Max-Planck-Institut für Gravitationsphysik
(Albert-Einstein-Institut), Potsdam
und
Institut für Physik und Astronomie Universität Potsdam

Tidal Disruption, Neutron Star Coalescences and Alternative Theories of Gravity in Numerical Relativity

Dissertation
zur Erlangung des akademischen Grades
doctor rerum naturalium (Dr. rer. nat.)

in der Wissenschaftsdisziplin
Gravitationsphysik

vorgelegt der
Mathematisch-Naturwissenschaftlichen Fakultät
der Universität Potsdam

vorgelegt von
Alan Tsz-Lok Lam

Potsdam
2025

Hauptbetreuer:	Prof. Dr. Tim Dietrich
Zweitbetreuer:	Prof. Dr. Masaru Shibata
Gutachter:	Prof. Dr. Thomas Baumgarte
Mentor:	Prof. Dr. Harald P. Pfeiffer
Weitere Kommissionsmitglieder:	
	Prof. Dr. Martin Pohl
	Prof. Dr. Christoph Pfrommer
	Prof. Dr. Jan Härter

Published online on the Publication Server of the University of Potsdam:
https://doi.org/10.25932/publishup-68491
https://nbn-resolving.org/urn:nbn:de:kobv:517-opus4-684915

Zusammenfassung

Die numerische Relativitätstheorie ist ein unverzichtbares Werkzeug für astrophysikalische Simulationen in starken Schwerefeldern. Sie ermöglicht es uns, die relativistische Dynamik um kompakte Objekte, einschließlich Neutronensterne und Schwarze Löcher, genau zu erfassen und die Gravitationswellensignale aus dem System zu extrahieren. In dieser Dissertation verwende ich numerische Relativitätssimulationen, um verschiedene astrophysikalische Systeme zu untersuchen, nämlich den Gezeiten-Sternzerriss eines Weißen Zwergs um ein supermassereiches Schwarzes Loch, die Verschmelzung von binären Neutronensternen (BNS) und den Kollaps von Sternen.

Im ersten Teil dieser Dissertation untersuche ich den Gezeiten-zerriss eines Weißen Zwergs um ein supermassereiches Schwarzes Loch. Gezeiten-Sternzerrissereignisse (GSZE) treten auf, wenn ein Stern sich über seinen Roche-Radius ausdehnt und durch die Gezeitenkräfte außerhalb des Schwarzen Lochs zerrissen wird. Der gravitativ gebundene Anteil der Sternfragmente fällt daraufhin auf das Schwarze Loch zurück und bildet ein Akkretionsscheibe mit potenziellem Jet-Ausbruch, der helle Emissionen von elektromagnetischer Strahlung, einschließlich optischer/UV- und Röntgenstrahlung, erzeugt. Weiße Zwerg GSZE sind besonders interessant, da sie Einblicke in die Entwicklung von Schwarzen Löchern mit Massen von $M_{\rm BH} \lesssim 10^5 M_\odot$ und deren Wachstum liefern können. Allerdings ist die Simulation von GSZE extrem schwierig, da sie eine große Spanne von Längenskalen und Zeitskalen umspannen. Um dies zu lösen, habe ich eine neue Methode für vollständig numerische Relativitätssimulationen entwickelt, die es mir ermöglicht, den Gezeiten-Sternzerriss eines Weißen Zwergs um ein supermassereiches Schwarzes Loch, zum ersten Mal, zu simulieren.

Der zweite Teil dieser Dissertation untersucht die Verschmelzung von Neutronensternpaaren in der massiven Skalar-Tensor-Theorie. Diese Theorie, vorgeschlagen von Damour und Esposito-Farèse, führt einen zusätzlichen skalaren Freiheitsgrad ein, welcher die Struktur von Neutronensternen ändert und zu unterscheidbaren Merkmalen in Gravitationswellensignalen führen kann. Ich habe eine Reihe von numerischen Simulationen durchgeführt, um die nichtlinearen Effekte dieser Theorie in BNS-Verschmelzungen zu quantifizieren und Signale in Gravitationswellensignalen zu untersuchen.

Im letzten Teil der Arbeit untersuche ich numerische Relativitätssimulationen unter achsensymmetrischen Konfigurationen. Die Einführung der Achsensymmetrie senkt die Rechenkosten für numerische Simulationen drastisch, indem sie die Größe des Problems auf zwei räumliche Dimensionen reduziert, was eine längere Simulationszeit für physikalische Systeme ermöglicht als dreidimensionale Simulationen. Zunächst betrachte ich das Kollapsar-System, bei dem ich ein annäherndes Freifallmodell konstruiere, das aus einem Schwarzen Loch und einfallendem Material besteht, das von massereichen Vorläufersternen ausgeht, um effiziente numerische Simulationen zu ermöglichen. Dann stelle ich `SACRA-2D` vor, einen neuen MPI- und OpenMP-parallelisierten, voll relativistischen Hydrodynamik Code in dynamischer Raumzeit unter axialer Symmetrie mit der Cartoon-Methode, der die von mir entwickelten Finite-Volumen-Schock-Capturing-Schemata für Hydrodynamik verwendet. Schließlich wird eine physikalische Anwendung von `SACRA-2D` vorgestellt, bei der das Wendepunktkriterium von differentiell rotierenden NS in der Skalar-Tensor-Theorie unter asymmetrischer Störung untersucht wird.

Abstract

Numerical Relativity is an essential tool for astrophysical simulations under strong gravity. It allows us to capture the relativistic dynamics around compact objects, including neutron stars and black holes, and accurately extract the gravitational wave signal from the system. In this thesis, I utilize numerical relativity simulations to study various astrophysical systems, namely the tidal disruption of a white dwarf around a supermassive black hole, binary neutron star (BNS) merger, and collapsar.

In the first part of this thesis, I investigate the tidal disruption of a white dwarf around a supermassive black hole. Tidal disruption events (TDEs) occur when a star passes closer to the tidal radius and gets torn apart by the tidal force outside the black hole's event horizon. The bounded fraction of tidal debris subsequently falls back onto the black hole and circularizes to form an accretion disk with potential jet launching, generating a luminous flare of electromagnetic radiation including optical/UV and X-ray emission. White dwarf TDEs are particularly interesting as they could provide insights into low-mass supermassive black holes $M_{\rm BH} \lesssim 10^5\ M_\odot$ and the growth of massive black holes. However, simulating TDEs is extremely challenging due to the vast range of length scales and time scales involved. To overcome this, I developed a new method for full numerical relativity simulations, allowing me to evolve the tidal disruption of a white dwarf around a supermassive black hole for the first time.

The second part of this thesis explores the BNS merger in the massive scalar tensor theory. This theory, proposed by Damour and Esposito-Farèse, introduces an additional scalar degree of freedom that can alter the structure of neutron stars and lead to distinctive features in gravitational wave (GW) signals. I conducted a series of numerical studies to quantify the non-linear effects of this theory in binary neutron star mergers and explore signatures in GW signals. My collaborators and I started by constructing initial data for quasi-equilibrium configurations of binary neutron stars that are self-consistent with the massive scalar-tensor theory, from which we suggested a constraint on the scalar mass. To further understand the scalar effect on the coalescence dynamics and the post-merger remnant, I extended the numerical relativity code SACRA-MPI to the massive scalar tensor theory and performed a set of numerical simulations. I found that the modified gravity effect in the massive scalar tensor theory can significantly alter the final fate of the merger remnant and provide various distinctive features that appear in a wide range of binary parameters. The presence of the scalar field can also provide additional support from gravitational collapse, modifying the final disk mass around the black hole and subsequent post-merger ejecta. I demonstrated that a gravitational effect like scalarization can lead to a violation in quasi-universal relations.

In the last part of the thesis, I explore numerical relativity simulations under axisymmetric configurations. Imposing axisymmetry drastically lowers the computation cost for numerical simulation by reducing the problem's size to two spatial dimensions, which facilitates a longer simulation time of physical systems than three-dimensional simulations. I first consider the collapsar system where I construct an approximate free-fall model consisting of a black hole and infalling material started from large-mass progenitor stars to facilitate efficient numerical simulations. Then, I introduce `SACRA-2D`, a new MPI and OpenMP parallelized, fully relativistic hydrodynamics (GRHD) code in dynamical spacetime under axial symmetry with the cartoon method, using the finite-volume shock-capturing schemes for hydrodynamics I developed. Finally, one physical application of `SACRA-2D` is presented, which examines the turning-point criterion of differential rotating NS in scalar-tensor theory under asymmetric perturbation.

Acknowledgements

I would like to express my deepest gratitude to the Max Planck Institute for Gravitational Physics, Potsdam for providing me with a stimulating and supportive environment for the past four years of my PhD journey. I am heartily grateful to my supervisor, Masaru Shibata, for his guidance and expertise throughout my research. I would not fulfill my PhD without his invaluable support.

I want to thank the entire CRA group, especially the director's assistant Matthias Blittersdorf, for their help, camaraderie, and enthusiasm, which made my time at the institute truly unforgettable. I also want to express my gratitude to my collaborators, Kenta Kiuchi, Sho Fujibayashi, Yong Gao, Kyohei Kawaguchi, and Daniela D. Doneva, with whom I always learn a lot from fruitful discussions. A special thank you goes to my officemate Hao-Jui Kuan, who enriched my physics knowledge and improved my scientific writing.

I am also deeply grateful to my family and my partner, Christy Yeung, who have been my rock throughout this journey, providing me with love, support, and encouragement whenever needed. Their sacrifices and understanding have not gone unnoticed, and I am forever grateful for their presence in my life. I would like to express my appreciation to Hao-Jui Kuan for his helpful feedback on the manuscript of the Introduction and Conclusion. A particularly kind support from Cédric Jockel for the German translation of the abstract is also highly appreciated.

Contents

Preface

I (**Alan Tsz-Lok, Lam**) claim that most results included in this thesis have been carried out by myself at the Max Planck Institute for Gravitational Physics (Potsdam), while contributions of my collaborators will be mentioned at the beginning of each Chapter. This doctoral dissertation is based on four peer-reviewed articles (Chapters 2 to 4 and 6), and three articles under review of a peer-reviewed journal (Chapters 5, 7 and 8). The numerical simulations were carried out in the workstation "yamazaki" and the cluster "sakura" that belongs to my host computational relativistic astrophysics department as well as in the cluster "raven" that belongs to the Max Planck Computing and Data Facility (MPCDF).

Results that are not original to me or my collaborative efforts with co-authors are cited where appropriate. A list of the articles upon which this thesis is based are detailed below:

- Chapter 2 is based on the publication: "*Numerical-relativity simulation for tidal disruption of white dwarfs by a supermassive black hole*" in Phys.Rev.D 107 (2023) 4, 043033 by **A. T.-L. Lam**, M. Shibata and K. Kiuchi.

- Chapter 3 is based on the publication: "*Binary neutron star mergers in massive scalar-tensor theory: Quasiequilibrium states and dynamical enhancement of the scalarization*" in Phys.Rev.D 108 (2023) 6, 064057 by H.-J. Kuan, K. V. Aelst, **A. T.-L. Lam** and M. Shibata.

- Chapter 4 is based on the publication: "*Binary neutron star mergers in massive scalar-tensor theory: Properties of postmerger remnants*" in Phys.Rev.D 110 (2024) 10, 104018 by **A. T.-L. Lam**, H.-J. Kuan, M. Shibata, K. V. Aelst and K. Kiuchi.

- Chapter 5 is based on the preprint: "*Accessing universal relations of binary neutron star waveforms in massive scalar-tensor theory*" in arXiv:2410.00137 by **A. T.-L. Lam**, Y. Gao, H.-J. Kuan, M. Shibata, K. V. Aelst and K. Kiuchi.

- Chapter 6 is based on the publication: "*Supernovalike explosions of massive rotating stars from disks surrounding a black hole*" in Phys.Rev.D 109 (2024) 2, 023031 by S. Fujibayashi, **A. T.-L. Lam**, M. Shibata and Y. Sekiguchi. The axisymmetric numerical code was developed by S. Fujibayashi, M. Shibata and Y. Sekiguchi.

- Chapter 7 is based on the preprint: "*SACRA-2D: New axisymmetric general relativistic hydrodynamics code with fixed mesh refinement*" in arXiv:2502.03223 by **A. T.-L. Lam** and M. Shibata.
- Chapter 8 is based on the preprint: "*Axisymmetric stability of neutron stars as extreme rotators in massive scalar-tensor theory*" in arXiv:2502.03973 by **A. T.-L. Lam**, K. V. Staykov, H.-J. Kuan, D. D. Doneva and S. S. Yazadjiev.

Acronyms

TDE	Tidal disruption event
WD	White dwarf
NS	Neutron star
BH	Black hole
BNS	Binary neutron star
GW	Gravitational wave
EOS	Equation of state
GR	General relativity
GRHD	General relativistic hydrodynamics
DEF	Damour-Esposito-Farèse scalar tensor theory
aLIGO	(advanced) Laser Interferometer Gravitational-Wave Observatory

Chapter 1

Introduction

Contents

This thesis is based on the publication [209, 293, 303, 304, 305, 306]. Throughout this thesis, the geometrical units of $c = 1 = G$ are used where c and G are the speed of light and the gravitational constant, respectively, but when it is necessary to clarify the units, G and c are recovered. The subscripts a, b, $c, \cdots$ denote the spacetime coordinates while i, j, $k, \cdots$ the spatial coordinates, respectively. This chapter provides an overview of the thesis and a basic introduction of numerical relativity.

1.1 Overview and motivationon

The first part of the thesis (Part I) is dedicated to studying the tidal disruption of white dwarfs by supermassive black holes through numerical relativity. Tidal disruption events (TDEs) occur when a star passes closer to the tidal radius and gets torn apart by the tidal force outside the event horizon of the black hole. The bounded fraction of tidal debris subsequently falls back onto the black hole and circularizes to form an accretion disk with potential jet launching, generating a luminous flare of radiation, including optical/UV and X-ray emission. With over one hundred events already detected in different telescopes and expected over several tens of thousands of detections in future transient surveys, TDEs act as an excellent and promising astrophysical laboratory to probe the parameters of massive black holes and the composition of the disrupted stars. This is particularly interesting if the companion star is a white dwarf, as white dwarf TDEs could occur for intermediate-mass black holes ($M_{\rm BH} \lesssim 10^5\ M_\odot$), potentially associated with GW signals, which could provide rich information on intermediate-mass black holes if detected and help understand the dwarf galaxy as well as the growth of massive black holes. However, numerical simulation of TDEs is extremely challenging because it requires resolving vastly different length scales over a long time. To address this, I developed a new method to evolve the tidal disruption of a white dwarf around a supermassive black hole using numerical relativity simulation (Chapter 2). The new formalism enables us to study the tidal disruption criteria in the relativistic regime for the first time.

Part II discusses the process of binary neutron star merger under the framework of alternative theories of gravity. Although Einstein's theory of general relativity (GR) passes many tests through observation of the Solar system and binary pulsars observation with flying colors, the incongruity of GR with quantum description demands a modification of gravity theory. The detection of the first GW signal from binary black holes mergers by Laser Interferometer Gravitational Observatory (LIGO) and Virgo collaborations [2] marks the beginning of the precision GW astrophysics era, providing us with a new and unique tool to stringently test GR in an extremely dynamical and strong field gravity regime. To better understand how detailed GW signatures correspond to specific features of alternative gravity, it is useful to conduct in-depth studies of specific alternative theories. One of the most established modified theories of gravity is the DEF type of scalar-tensor theory [142, 143] proposed as the low-energy limit of string theory where an additional scalar degree of freedom is introduced with the scalar field coupled to the spacetime curvature. In this theory class, a neutron star can spontaneously scalarize under specific conditions, altering its structure. The influence of the scalar field on the stellar structure is strongly degenerate with that of the supranuclear equation of states. That said, there are some effects exclusive to the scalar field. For example, the presence of scalar charge for neutron stars gives rise to additional dipolar radiation and speeds up the orbital decay of a binary due to the extra energy lost. This allows pulsar timing observations to rule out the massless DEF theory basically [419] and put a lower bound on the scalar mass of $\gtrsim 10^{-16}$ eV as the scalar effect is smeared off beyond the corresponding Compton wavelength. In Part II, my collaborator and I conducted a series of numerical studies aiming to quantify the non-linear feature of massive DEF theory in binary neutron star mergers and explore distinctive signatures in GW signals, paying particular attention to scalar mass in $\sim 10^{-11}$ eV with corresponding Compton wavelength ~ 20 km, which could have scalar interaction imprinted in the late inspiral phase. In Chapter 3, we constructed initial data for quasi-equilibrium configurations of binary neutron stars that are self-consistent with DEF theory. From that, we compared orbital energy obtained from the numerical data with the event GW170817 and suggested a constraint on scalar mass $\gtrsim 10^{-11}$ eV if both neutron stars are scalarized in the inspiral phase. To further understand the scalar effect on the dynamics of the coalescence and the postmerger remnant, in Chapter 4 we extended the numerical relativity code `SACRA-MPI` to the massive DEF theory and performed a set of numerical simulations to study comprehensively the dependence on scalar mass and coupling strength. In Chapter 5, we demonstrated a gravitational effect like scalarization could lead to a violation in quasi-universal relations of GW signals.

In the final part of the thesis, Part III, we explore the applications of numerical relativity under axisymmetric configurations. Numerical relativity simulations are a crucial tool for understanding the behavior of complex astrophysical systems, such as binary neutron star mergers and black hole-neutron star mergers. However, these simulations are often computationally expensive and require significant resources to perform. In contrast, some specific systems can be approximated to be axisymmetric, reducing the problem's size to two spatial dimensions and drastically lowering the computation cost for numerical simulation. For example, axisymmetric simulations have been useful in studying the long-term evolution of post-merger remnants from neutron star mergers and the core-collapse supernova. In particular, to speed up the simulation of the collapsar, we developed a free-fall model in Chapter 6 composed of a spinning black hole and infalling matter that self-consistently satisfies constraint equations of general relativity. We also implemented `SACRA-2D`, a new MPI and OpenMP parallelized, fully relativistic general-relativistic hydrodynamic (GRHD) code in dynamical spacetime under axial symmetry with the cartoon method, described in Chapter 7, which utilized the two-to-one fixed mesh refinement and the state-of-the-art HLLC Riemann solver. Finally, we apply `SACRA-2D` in Chapter 8 to study the dynamical stability of differentially rotating neutron stars in scalar-tensor theory.

1.2 Formulation in Numerical Relativity

1.2.1 The 3+1 decomposition

The Einstein equation connects the spacetime curvature and the stress-energy momentum tensor T_{ab} by

$$ {}^{(4)}R_{ab} - \frac{1}{2} g_{ab} {}^{(4)}R = \frac{8\pi G}{c^4} T_{ab}, \tag{1.1} $$

where g_{ab} is the metric, ${}^{(4)}R_{ab}$ is the Ricci tensor, ${}^{(4)}R := g_{ab} {}^{(4)}R^{ab}$ is the Ricci scalar. The non-linear nature of the Einstein equations makes it challenging to find even the approximate solutions for dynamical systems. Therefore, numerical simulation becomes a reliable way, sometimes the only method, to describe these systems accurately. To perform these simulations, one must reformulate the Einstein equations as an initial-value problem, which can be accomplished by the 3+1 decomposition. The following section will briefly outline the

3+1 decomposition of spacetime and summarize some useful relations that are often used in the later chapters. We refer the readers to the numerical relativity books from Baumgarte and Shapiro [56] and Shibata [430] for a more detailed introduction.

In 3+1 decomposition, the spacetime manifold is foliated into a set of non-intersecting spacelike hypersurfaces Σ_t, each defined as a level surface of the coordinate time t. We can construct the future-directed timelike unit four-vector n^a normal to Σ_t given by

$$n^a = g^{ab} n_b, \qquad n_a = -\alpha \nabla_a t, \qquad \alpha := \left(-g^{ab} \nabla_a t \nabla_b t\right)^{-1/2} \tag{1.2}$$

where the lapse function $\alpha > 0$ determines the proper time $\alpha \Delta t$ between consecutive hypersurfaces Σ_t and $\Sigma_{t+\Delta t}$, and ∇_a is the covarivant derivative associated with g_{ab}. The induced spatial metric γ_{ab} on the hypersurface can therefore be defined as

$$\gamma_{ab} := g_{ab} + n_a n_b. \tag{1.3}$$

This allows us to construct the spatial projection tensor $\gamma^a{}_b$ and the time projection tensor $N^a{}_b$ as

$$\gamma^a{}_b := \delta^a{}_b + n^a n_b, \qquad N^a{}_b := -n^a n_b, \tag{1.4}$$

which decomposes any generic four-vector V^a into spatial part $\gamma^a{}_b V^b$ and timelike part $N^a{}_b V^b$, and also define on Σ_t the corresponding spatial counterparts of Ricci tensor R_{ij}, Ricci scalar R, connection coefficients $\Gamma^i{}_{jk}$, as well as the covariant derivative D_a for generic tensor $T^{b_1 b_2 \cdots}{}_{c_1 c_2 \cdots}$ as

$$D_a T^{b_1 b_2 \cdots}{}_{c_1 c_2 \cdots} := \gamma_a{}^d \gamma^{b_1}{}_{e_1} \gamma^{b_2}{}_{e_2} \cdots \gamma_{c_1}{}^{f_1} \gamma_{c_2}{}^{f_2} \cdots \nabla_d T^{e_1 e_2 \cdots}{}_{f_1 f_2 \cdots}, \qquad \text{with } D_c \gamma_{ab} = 0. \tag{1.5}$$

Consequently, the time unit vector $t^a := (\partial/\partial t)^a$ can be decomposed as

$$t^a = \alpha n^a + \beta^a, \qquad \beta^a := \gamma^a{}_b t^b, \tag{1.6}$$

where β^a is the shift vector that measures the changes of spatial coordinates on the successive hypersurfaces. The extrinsic curvature K_{ab} is defined by the spatial projection of the gradient of n_a on Σ_t as

$$K_{ab} := -\gamma_a{}^c \nabla_c n_b = -\frac{1}{2} \mathcal{L}_{\mathbf{n}} \gamma_{ab}, \tag{1.7}$$

where $\mathcal{L}_{\mathbf{n}}$ is the Lie derivative with respect to n^a. Note that for pure spatial tensor, e.g., γ_{ab}, β^a and K_{ab}, it would be sufficient only to consider the spatial components, and hence only the spatial indices are shown (i.e., γ_{ij}, β^i and K_{ij}).

Under the 3+1 decomposition, the line element is therefore given by

$$ds^2 = -\alpha^2 dt^2 + \gamma_{ij}\left(\beta^i dt + dx^i\right)\left(\beta^j dt + dx^j\right), \tag{1.8}$$

and the stress-energy momentum tensor T_{ab} is decomposed into

$$T_{ab} = \rho_h n_a n_b + J_a n_b + J_b n_a + S_{ab}, \tag{1.9}$$

where

$$\rho_h = T_{cd} n^c n^d, \qquad J_a = -T_{cd}\gamma^c{}_a n^d, \qquad S_{ab} = T_{cd}\gamma^c{}_a\gamma^d{}_b. \tag{1.10}$$

In the Arnowitt–Deser–Misner (ADM) formulation [38, 532], the Einstein equations in Eq. (1.1) are rewritten into a set of constraint and evolution equations of the dynamical variables (γ_{ij}, K_{ij}) given by

$$\begin{aligned}
R - K_{ij}K^{ij} + K^2 &= 16\pi\rho_h, && \text{(Hamiltonian constraint)} && \text{(1.11a)}\\
D_j K_i{}^j - D_i K &= 8\pi J_i, && \text{(Momentum constraint)} && \text{(1.11b)}\\
\left(\partial_t - \beta^k\partial_k\right)\gamma_{ij} &= -2\alpha K + \gamma_{ik}\partial_j\beta^k + \gamma_{jk}\,\partial_i\beta^k, && \text{(Evolution for } \gamma_{ij}\text{)} && \text{(1.11c)}\\
\left(\partial_t - \beta^k\partial_k\right)K_{ij} &= \alpha\left(R_{ij} - 2K_{ik}K_j{}^k + KK_{ij}\right) && &&\\
&\quad - 8\pi\alpha\left[S_{ij} - \frac{1}{2}\gamma_{ij}\left(S^k{}_k - \rho_h\right)\right] && \text{(Evolution for } K_{ij}\text{)} && \text{(1.11d)}\\
&\quad - D_i D_j\alpha + K_{ik}\partial_j\beta^k + K_{jk}\partial_i\beta^k, && &&
\end{aligned}$$

where $K := \gamma^{ij}K_{ij}$ is the trace of the extrinsic curvature.

In addition to the 3+1 formulation, the conformal decomposition, originally developed by Lichnerowicz [310] and York [349, 530, 531] for initial data construction, is often used to factor out the gravitational potential part from the spatial metric in numerical relativity. Under such formulation, the conformal spatial metric $\tilde{\gamma}_{ij}$ and the conformal traceless extrinsic curvature $\tilde{A}_{ij}$ are defined by

$$\tilde{\gamma}_{ij} := \psi^{-4}\gamma_{ij}, \tag{1.12a}$$

$$\tilde{A}_{ij} := \psi^{-4}\left(K_{ij} - \frac{1}{3}\gamma_{ij}K\right), \tag{1.12b}$$

with the conformal factor ψ usually chosen to be

$$\psi := (\gamma/f)^{1/12}, \tag{1.13}$$

where $\gamma := \det(\gamma_{ij})$ and $f := \det(f_{ij})$ with f_{ij} being the flat spatial metric. The corresponding conformal Ricci tensor $\tilde{R}_{ij}$, Ricci scalar $\tilde{R}$, connection coefficient $\tilde{\Gamma}^i{}_{jk}$ and covariant derivative operator $\tilde{D}_i$ can be defined in a similar manner. The basic equations in the ADM formulation Eq. (1.11) can hence be rewritten in the conformal decomposition formulation for variables $(\tilde{\gamma}_{ij}, \tilde{A}_{ij}, \psi, K)$ with two additional algebraic constraints

$$\det(\tilde{\gamma}_{ij}) = f, \qquad\qquad \tilde{\gamma}^{ij}\tilde{A}_{ij} = 0. \tag{1.14}$$

1.2.2 The Baumgarte-Shapiro–Shibata–Nakamura formulation

Despite the well-definedness of the 3+1 formulation, it forms a weakly hyperbolic system and is not well-posed. If we numerically integrate the evolution equations directly, any small numerical error will grow inevitably without bound. A strongly hyperbolic reformulation is necessary to maintain a stable evolution. Shibata and Nakamura [433] recasted the equations by introducing a new independent variable $F_i := f^{jk}D^{(0)}_j\tilde{\gamma}_{ik}$ with $D^{(0)}_j$ being the covariant derivative associated with f_{ij} (the so-called F_i version). Later, Baumgarte and Shapiro [55] proposed the $\tilde{\Gamma}^i$ version by instead defining $\tilde{\Gamma}^i := -D^{(0)}_j\tilde{\gamma}^{ij}$, which gives essentially the same basic equations with slightly simpler form. This reformulation established the so-called Baumgarte-Shapiro–Shibata–Nakamura (BSSN) formulation, one of the most popular formulations in numerical relativity. The evolution equations of the BSSN formulation in the Cartesian coordinate are summarized below

$$(\partial_t-\beta^k\partial_k)W = \frac{1}{3}W\left(\alpha K - \partial_k\beta^k\right), \tag{1.15a}$$

$$(\partial_t-\beta^k\partial_k)\tilde{\gamma}_{ij} = -2\alpha\tilde{A}_{ij} + \tilde{\gamma}_{ik}\partial_j\beta^k + \tilde{\gamma}_{jk}\partial_i\beta^k - \frac{2}{3}\tilde{\gamma}_{ij}\partial_k\beta^k, \tag{1.15b}$$

$$\begin{aligned}(\partial_t-\beta^k\partial_k)\tilde{A}_{ij} &= W^2\left(\alpha R_{ij} - D_iD_j\alpha - 8\pi\alpha S_{ij}\right)^{\rm TF} + \alpha\left(K\tilde{A}_{ij} - 2\tilde{A}_{ik}\tilde{A}_j{}^k\right)\\ &\quad + \tilde{A}_{kj}\partial_i\beta^k + \tilde{A}_{ki}\partial_j\beta^k - \frac{2}{3}\tilde{A}_{ij}\partial_k\beta^k,\end{aligned} \tag{1.15c}$$

$$(\partial_t-\beta^k\partial_k)K = 4\pi\alpha(S^i{}_i + E) + \alpha\left(\tilde{A}_{ij}\tilde{A}^{ij} + \frac{1}{3}K\right) - D_iD^i\alpha, \tag{1.15d}$$

$$\begin{aligned}(\partial_t-\beta^k\partial_k)\tilde{\Gamma}^i &= -2\tilde{A}^{ij}\partial_j\alpha + 2\alpha\left(\tilde{\Gamma}^i_{jk}\tilde{A}^{jk} - \frac{1}{3}\tilde{\gamma}^{ij}\partial_jK - \frac{3}{W}\tilde{A}^{ij}\partial_jW - 8\pi\tilde{\gamma}^{ij}S_j\right)\\ &\quad + \frac{2}{3}\tilde{\gamma}^{jk}\tilde{\Gamma}^i{}_{jk}\partial_l\beta^l + \tilde{\gamma}^{jk}\partial_j\partial_k\beta^i + \frac{1}{3}\tilde{\gamma}^{ij}\partial_j\partial_k\beta^k - \tilde{\gamma}^{kl}\tilde{\Gamma}^j{}_{kl}\partial_j\beta^i,\end{aligned} \tag{1.15e}$$

where ${S_{ij}}^{\rm TF} := S_{ij} - \frac{1}{3}\gamma_{ij}S^k{}_k$ corresponds to the tracefree part of a tensor S_{ij} and $W := \psi^{-2}$ is introduced to avoid divergent term of ψ appeared in the black hole [328] ($\chi := \psi^{-4}$ is employed for some studies e.g., [119]).

1.2.3 Gauge conditions

The evolution equations from the 3+1 decomposition are not sufficient for numerical integration. One still has the gauge freedom to impose the coordinate conditions by specifying the lapse function α and the shift vectors β^i. A proper choice of coordinates should avoid any singularities, such as coordinate singularities and black hole singularity. One typical choice for lapse α is the maximal slicing condition defined as

$$K = 0 = \partial_t K, \tag{1.16}$$

which yields a continuity equation for proper volume $\sqrt{\gamma}$

$$\partial_t \sqrt{\gamma} = \partial_i \left(\sqrt{\gamma} \beta^i \right), \tag{1.17}$$

which shows γ remains regular as long as a regular shift β^i is chosen, suggesting this is likely to have a singularity-avoidance property. This time slicing condition forms an elliptic equation for α

$$\gamma^{ij} D_i D_j \alpha = \alpha \left[K_{ij} K^{ij} + 4\pi \left(\rho + S^k{}_k \right) \right] \tag{1.18}$$

which, combined with the Hamiltonian constraint, is often used in constructing the initial data given by

$$\tilde{\gamma}^{ij} \tilde{D}_i \tilde{D}_j \left(\alpha \psi \right) = \alpha \psi \left[\frac{7}{8} \tilde{A}_{ij} \tilde{A}^{ij} + \frac{1}{8} \tilde{R} + 2\pi \psi^4 \left(\rho + S^k{}_k \right) \right]. \tag{1.19}$$

The next issue is defining a spatial slicing condition with a "regular" shift β^i. Smarr and York [463] proposed the minimal distortion gauge defined by

$$D_j \left(\gamma^{-1/3} \partial_t \tilde{\gamma}^{ij} \right) = 0, \tag{1.20}$$

which minimizes the global change rate of $\tilde{\gamma}^{ij}$ in every hypersurface based on the action I

$$I = \int d^3 x \left(\partial_t \tilde{\gamma}_{ij} \right) \left(\partial_t \tilde{\gamma}_{kl} \right) \tilde{\gamma}^{ik} \tilde{\gamma}^{jl} \sqrt{\gamma}, \tag{1.21}$$

hence the name "minimal distortion". Provided that the initial condition does not contain large coordinate distortion, this gauge condition can eliminate coordinate-related fluctuations on $\tilde{\gamma}^{ij}$, which is desirable for long-term stable numerical evolution. The minimal distortion gauge can be further written into a vector elliptic equation for β^i by combining the evolution equation of $\tilde{\gamma}_{ij}$ as

$$\tilde{\gamma}^{jk} \tilde{D}_j \tilde{D}_k \beta^i + \frac{1}{3} \tilde{\gamma}^{ij} \tilde{D}_j \tilde{D}_k \beta^k + \tilde{R}^i{}_j \beta^j + \left(\tilde{\gamma}^{ik} \tilde{D}_k \beta^j + \tilde{\gamma}^{jk} \tilde{D}_k \beta^i - \frac{2}{3} \tilde{\gamma}^{ij} \tilde{D}_k \beta^k \right) \tilde{D}_j \ln \psi^6 \tag{1.22}$$

$$= 2\psi^{-6} \tilde{A}^{ij} \tilde{D}_j \alpha + \frac{4}{3} \alpha \tilde{\gamma}^{ij} D_j K + 16\pi \psi^4 \alpha S^i. \tag{1.23}$$

Despite the excellent physical property of the maximal slicing and minimal distortion gauge conditions, the fact that they take forms in elliptic type equations makes it computationally expensive for practical use. On the other hand, the dynamical gauge conditions, which take forms in hyperbolic equations, are numerically more favorable. In particular, the moving-puncture gauge [26, 42, 119] was established to become the standard gauge in numerical relativity written as

$$\left(\partial_t - \beta^k \partial_k\right) \alpha = -2\alpha K, \qquad \text{(1+log slicing)} \tag{1.24a}$$

$$\begin{aligned} \left(\partial_t - \beta^k \partial_k\right) \beta^i &= \frac{3}{4} B^i, \\ \left(\partial_t - \beta^k \partial_k\right) B^i &= \left(\partial_t - \beta^k \partial_k\right) \tilde{\Gamma}^i - \eta_B B^i, \end{aligned} \qquad \text{(hyperbolic Gamma-driver)} \tag{1.24b}$$

where B^i is a new auxiliary variable and η_B is a constant of order $1/M$ with M being the total mass of the system.

Part I

Tidal Disruption of white dwarfs by a supermassive black hole

Chapter 2

Tidal Disruption of white dwarfs by a supermassive black hole

Contents

Breakdown of Contributions

This chapter is based on the publication: "*Numerical-relativity simulation for tidal disruption of white dwarfs by a supermassive black hole*" in Phys.Rev.D 107 (2023) 4, 043033 [304] by **A. T.-L. Lam**, M. Shibata and K. Kiuchi. I modified the code `SACRA-MPI` developed by M. Shibata and K. Kiuchi to include the unequal levels in moving box structure and the trumpet black hole background for the tidal disruption project. I also constructed an initial data solver that consists of a supermassive black hole and a white dwarf in an elliptic orbit built upon the open-source code `octree-mg`. All the numerical simulations were carried out by me and all the plots were generated by me. K. Kiuchi provided constructive comments on the manuscript written partially by me and M. Shibata.

Overview

In this Chapter, we study tidal disruption of white dwarfs in elliptic orbits with the eccentricity of $\sim 1/3$–$2/3$ by a nonspinning supermassive black hole of mass $M_{\rm BH} = 10^5 M_\odot$ in fully general relativistic simulations targeting the extreme mass-ratio inspiral leading eventually to tidal disruption. Numerical-relativity simulations are performed by employing a suitable formulation in which the weak self-gravity of white dwarfs is accurately solved. We reconfirm that tidal disruption occurs for white dwarfs of the typical mass of $\sim 0.6M_\odot$ and radius $\approx 1.2 \times 10^4$ km near the marginally bound orbit around a nonspinning black hole with $M_{\rm BH} \lesssim 4 \times 10^5 M_\odot$.

2.1 Introduction

Tidal disruption of ordinary stars and/or white dwarfs by supermassive black holes has been revealed to be one of the major sources of bright electromagnetic transients (see, e.g., Refs. [27, 410, 505]), which have been actively observed in the last decade. In addition, gravitational waves emitted by tidal disruption of white dwarfs closely orbiting supermassive black holes could be observable by Laser Interferometer Space Antenna (LISA) [31]. Electromagnetic signals associated with tidal excitation (e.g., Ref. [506]) or mass stripping (e.g., Refs. [274, 313, 318, 335] for related works) or tidal disruption (e.g., Refs. [400, 401]) of white dwarfs can be an important electromagnetic counterpart of gravitational waves. Because the expected event rate is not so high [324] that the signal-to-noise ratio of gravitational waves for the LISA sensitivity is unlikely to be very high, the discovery of the possible electromagnetic counterparts will help extract gravitational waves from the noisy data in the LISA mission.

The condition for mass shedding and tidal disruption during the cross encounter of stars with supermassive black holes is often described by the so-called β-parameter defined by

$$\beta := \frac{r_t}{r_p}, \tag{2.1}$$

where r_p is the periastron radius for the orbit and r_t is the Hill's radius [240] defined by

$$r_t := R_* \left(\frac{M_{\rm BH}}{M_*}\right)^{1/3}, \tag{2.2}$$

with R_* the stellar radius, M_* the stellar mass, and $M_{\rm BH}$ the mass of the supermassive black hole, respectively. Since the early 1990s (see, e.g., Refs. [157, 273, 302]), a large number of numerical simulations have been performed in the last three decades (see, e.g., Refs. [325, 399] for reviews of the latest works and Refs. [212, 404, 405, 406, 407, 408] for some of the most advanced works). They have shown that mass stripping can take place at the close encounter if β is larger than about 0.5, and tidal disruption can take place if $\beta \gtrsim 1$ for stars in parabolic orbits (see, e.g., Refs. [222, 326, 399] for Newtonian simulation works, and also early semianalytical work [320, 321]). It is also shown that for close orbits around a black hole, the general relativistic effect can significantly reduce the critical value of β for the tidal disruption [407]. Indeed, general relativistic works show that for circular orbits near the innermost stable circular orbit of black holes, the mass shedding can occur even for $\beta \sim 0.4$ [190, 254].

However, the previous analyses have been carried out in Newtonian gravity or in relativistic gravity of a black hole with Newtonian (or no) gravity for the companion star or in a tidal approximation with a relativistic tidal potential [190, 254, 327]. To date, no fully general relativistic (the so-called numerical-relativity) simulation, i.e., a simulation with no approximation except for the finite differencing, has been done for the tidal disruption problem with $\beta \lesssim 1$ (but see Refs. [172, 174, 225] for a head-on and an off-axis collision).

Numerical-relativity simulation is suitable for the tidal disruption problem for the case that the orbit at the tidal disruption is highly general-relativistic. This is particularly the case for tidal disruption of white dwarfs by supermassive black holes because it can occur only for orbits very close to the black-hole horizon. Advantages of the numerical-relativity simulation are: (i) the redistribution of the energy and angular momentum of the star can be followed in a straightforward manner and (ii) we can directly follow the matter motion after the tidal disruption including the subsequent disk formation.

In this Chapter, we present a result of numerical-relativity simulations for tidal disruption of white dwarfs of typical mass (0.6–$0.8 M_\odot$) by a supermassive black hole with relatively low mass ($M_{\rm BH} = 10^5 M_\odot$) for the first time. For simplicity, the white dwarfs are modeled by the $\Gamma = 5/3$ polytropic equation of state. As a first step toward more detailed and systematic studies, we focus on tidal disruption of white dwarfs in mildly elliptic orbits aiming at confirming that our numerical-relativity approach is suitable for reproducing the criteria of tidal disruption, which has been already investigated in many previous works referred to above.

This Chapter is organised as follows. In Section 2.2, we describe our formulation for evolving gravitational fields, matter fields, and for providing initial data of a star in elliptic orbits around supermassive black holes. In Section 2.3, numerical results are presented paying particular attention to the criterion for tidal disruption. Section 2.4 is devoted to a summary.

2.2 Basic equations for the time evolution

2.2.1 Gravitational field

First, we reformulate the Baumgarte-Shapiro-Shibata-Nakamura (BSSN) formalism [55, 422] in numerical relativity to a form suitable for the simulation of high-mass ratio binaries, in particular for accurately computing a weak self-gravity of white dwarfs. Throughout this Chapter, high-mass ratio binaries imply those composed of a very massive black hole of mass $M_{\rm BH} \gtrsim 10^5 M_\odot$ and a white dwarf (or an ordinary star) of mass of $M_* = O(M_\odot)$ with the radius $R_* \gtrsim 10^3\,{\rm km}$, for which the compactness defined by M_*/R_* is smaller than 10^{-3}.

We consider the two-body problem with a compact orbit of the orbital separation $r \lesssim 30 M_{\rm BH}$. With such setting, the magnitude of the gravitational field generated by the black hole, which is defined by $g_{ab} - \eta_{ab}$ is, of order $M_{\rm BH}/r > 10^{-2}$. Here g_{ab} and η_{ab} are the spacetime metric and Minkowski metric, respectively. On the other hand, the magnitude of the gravitational field generated by white dwarfs and ordinary stars is of order $M_*/R_* < 10^{-3}$, which is much smaller than that by the black hole. To accurately preserve the nearly equilibrium state of such stars during their orbits, an accurate computation of the gravitational field by them is required. However, if we simply solve Einstein's equation, a numerical error for the computation of the black-hole gravitational field can significantly affect the gravitational field for the white dwarfs/ordinary stars. To avoid this numerical problem, we separate out the gravitational field into the black hole part and other part, although we still solve fully nonlinear equations. The idea employed here is similar to that of Ref. [174], but we develop a formalism based on the BSSN formalism (see Eq. (1.15) in Chapter 1).

In this problem, we employ a variation of puncture gauge [25], in which the evolution equations for α and β^i are written by replacing the advective derivatives $\partial_t - \partial_k \beta^k$ to ∂_t as

$$\partial_t \alpha = -2\alpha K, \tag{2.3a}$$

$$\partial_t \beta^i = \frac{3}{4} B^i, \tag{2.3b}$$

$$\partial_t B^i = \partial_t \tilde{\Gamma}^i - \eta_B B^i, \tag{2.3c}$$

where B^i is an auxiliary three-component variable and η_B is a constant of order $M_{\rm BH}^{-1}$.

By introducing a static black-hole solution for the geometric variables, α_0, β^i_0, $\tilde{\gamma}^0_{ij}$, W_0, $\tilde{A}^0_{ij}$, and K_0 and by writing all the variables by

$$\begin{aligned} &\alpha = \alpha_0 + \alpha_{\rm s}, \qquad && \beta^i = \beta^i_0 + \beta^i_{\rm s}, \qquad && \tilde{\gamma}_{ij} = \tilde{\gamma}^0_{ij} + \tilde{\gamma}^{\rm s}_{ij}, \qquad && W = W_0 + W_{\rm s}, \\ &\tilde{A}_{ij} = \tilde{A}^0_{ij} + \tilde{A}^{\rm s}_{ij}, && K = K_0 + K_{\rm s}, && \tilde{\Gamma}^i = \tilde{\Gamma}^i_0 + \tilde{\Gamma}^i_{\rm s}, && \end{aligned} \tag{2.4}$$

we then write down the equations for $\alpha_{\rm s}$, $\beta^i_{\rm s}$, $\tilde{\gamma}^{\rm s}_{ij}$, $W_{\rm s}$, $\tilde{A}^{\rm s}_{ij}$, $K_{\rm s}$, and $\tilde{\Gamma}^i_{\rm s}$ (these are denoted by a representative variable Q_s as follows). Specifically, the evolution equations Eq. (1.15) and Eq. (2.3) of the geometrical variables (denoted by a representative variable Q) are schematically written in the form

$$\partial_t Q = F(Q). \tag{2.5}$$

Then, for the decomposition of $Q = Q_0 + Q_{\rm s}$ with $F(Q_0) = 0$ (under the conditions of $\partial_t Q_0 = 0$), we write the equation for $Q_{\rm s}$ as

$$\partial_t Q_{\rm s} = F(Q_0 + Q_{\rm s}) - F(Q_0). \tag{2.6}$$

In numerical simulation, $F(Q_0)$ obtained from finite difference is nonzero, which contains the truncation error of evolving the stationary background metric numerically. Here, we added the second term in the right-hand side to explicitly subtract the leading error of evolving the background metric so that the right-hand side of the evolution equation of Q_s does not have the zeroth order terms in Q_s

Any static black-hole solutions can be used for α_0, $\beta^i_0, \cdots$, but in the BSSN formalism with the puncture gauge, the metric relaxes to a solution in the limit hypersurface with $K_0 = 0$. Using such a trumpet-puncture black hole also allows us to construct the initial data in the conformal-thin-sandwich (CTS) formalism [53] (see Section 2.2.3). Thus, in the present formalism, it is appropriate to employ such a solution. In the nonspinning black hole, the analytic solution is known and is written as [180]

$$\alpha_0 = \sqrt{1 - \frac{2M_\mathrm{BH}}{R} + \frac{27M_\mathrm{BH}^4}{16R^4}}, \tag{2.7a}$$

$$\beta^i_0 = \frac{3\sqrt{3}M_\mathrm{BH}^2}{4R^3}x^i, \tag{2.7b}$$

$$W_0 = \frac{r}{R}, \tag{2.7c}$$

$$\tilde{\gamma}^0_{ij} = \delta_{ij}, \quad \text{i.e.,} \quad \tilde{\Gamma}^i_0 = 0, \tag{2.7d}$$

$$\tilde{A}^0_{ij} = \frac{3\sqrt{3}M_\mathrm{BH}^2}{4R^3}\left(\delta_{ij} - 3\frac{x^i x^j}{r^2}\right), \tag{2.7e}$$

and $K_0 = 0$ where R is a function of r determined by [54]

$$\begin{aligned} r = &\left(\frac{2R + M_\mathrm{BH} + \sqrt{4R^2 + 4M_\mathrm{BH}R + 3M_\mathrm{BH}^2}}{4}\right) \\ &\times \left[\frac{(4+3\sqrt{2})(2R - 3M_\mathrm{BH})}{8R + 6M_\mathrm{BH} + 3\sqrt{8R^2 + 8M_\mathrm{BH}R + 6M_\mathrm{BH}^2}}\right]^{1/\sqrt{2}}. \end{aligned} \tag{2.8}$$

We note that $r = 0$ corresponds to $R = 3M_\mathrm{BH}/2$ and the event horizon is located at $R = 2M_\mathrm{BH}$ (i.e., $r \approx 0.78M_\mathrm{BH}$) in this solution.

2.2.2 Hydrodynamics

In this Chapter we model white dwarfs simply by the polytropic equation of state,

$$P = \kappa\rho^\Gamma, \tag{2.9}$$

where P and ρ are the pressure and rest-mass density, respectively, κ the polytropic constant, and Γ adiabatic index for which we set to be $5/3$. For the hydrodynamics, we solve the continuity and Euler equations,

$$\nabla_a(\rho u^a) = 0, \tag{2.10a}$$

$$\nabla_a T^a{}_k = 0, \tag{2.10b}$$

and

$$T_{ab} = (\rho + \rho\varepsilon + P)u_a u_b + P g_{ab}, \tag{2.11}$$

where ε and u^a are the specific internal energy and four velocity, respectively. In this work, we do not solve the energy equation, and determine ε simply by $\varepsilon = \kappa\rho^{\Gamma-1}/(\Gamma-1)$, which is derived from the condition that the specific entropy is conserved for the fluid elements. The continuity and Euler equations are solved in the same scheme as that used in Refs. [278, 526].

The motivation for using the polytropic equation of state comes from the fact that our primary purpose of this Chapter is to explore the tidal disruption condition for a relatively low value of $\beta < 1$ and the formation of shocks by the tidal compression does not play any role. We here focus only on the process of tidal disruption and subsequent short-term evolution of the tidally disrupted material. After the tidal disruption, the fluid is highly elongated and during the long-term evolution of the fluid elements with different specific energy and angular momentum, they collide and shocks are likely to be formed. For such a phase, the shock heating will play an important role. Our plan is to follow this phase by solving the energy equation with a more general equation of state.

2.2.3 Initial condition

First, we describe the formulation employed in this Chapter for computing the initial data in which white dwarfs are approximately in an equilibrium state in their comoving frame. From Eq. (2.10b), we have

$$\rho u^a \nabla_a(h u_i) + \nabla_i P = 0, \tag{2.12}$$

where h is the specific enthalpy defined by $h := 1 + \varepsilon + P/\rho$. To derive Eq. (2.12), we used Eq. (2.10a).

For the isentropic fluid, the first law of thermodynamics is written as

$$\rho dh = dP, \tag{2.13}$$

where dQ denotes the variation of a quantity Q in the fluid rest frame. In the polytropic equations of state employed in this work, we obtain the relation

$$h = \int \frac{dP}{\rho} \quad \text{and} \quad \ln h = \int \frac{dP}{\rho h}. \tag{2.14}$$

In this situation, Eq. (2.12) is rewritten to

$$u^a \nabla_a (h u_i) + \partial_i h = 0. \tag{2.15}$$

Then, we define $k^a := u^a/u^t$. Using this quantity, Eq. (2.15) is written to

$$u^t \mathcal{L}_k (h u_i) - u^t h u_a \nabla_i k^a + \partial_i h = 0, \tag{2.16}$$

where $\mathcal{L}_k$ denotes the Lie derivative with respect to k^a. The second term of Eq. (2.16) is written as

$$u^t h u_a \nabla_i k^a = u^t h u_a \nabla_i (u^a/u^t) = h \partial_i \ln u^t, \tag{2.17}$$

where we used $u^a u_a = -1$. Thus, Eq. (2.16) is written to

$$\mathcal{L}_k (h u_i) + \partial_i (h/u^t) = 0. \tag{2.18}$$

We consider an initial condition for a system composed of a star of mass M_* and radius R_*, for which the center is located on the x-axis, around a massive black hole of mass $M_{\rm BH} \gg M_*$ and $M_{\rm BH} \gg R_*$ which is located at a coordinate origin. We assume that the star predominantly moves toward the y-direction with the identical specific momentum. Thus we set $v^i := u^i/u^t = -\beta_0^i + V^i$ where $V^i = V \delta^i{}_y$ with V being a constant to be determined. Here the term of β_0^i is added to simplify the iteration process for computing quasiequilibrium states. Then, u^t is calculated from

$$u^t = \left[\alpha^2 - \gamma_{ij} (v^i + \beta^i)(v^j + \beta^j)\right]^{-1/2}. \tag{2.19}$$

In the present context, $\mathcal{L}_k (h u_i)$ can be assumed to be zero for $i = y$ and z, because the star has momentarily translation invariance for the motion toward the y- and z-directions. By contrast, with respect to the x-direction, the star receives the force from the massive black hole. Since the radius of the star, R_*, is much smaller than the orbital separation, x_0, and x_0 is larger than the black-hole radius of $\sim M_{\rm BH}$, $\mathcal{L}_k (h u_i)$ for the x–direction can be approximated by $\partial_i [A(x - x_0)]$ where we take A to be a constant, which should be approximately the Newtonian gravitational acceleration caused by the black-hole written as $\sim -M_{\rm BH}/x_0^2$ for $x_0 > 0$. Then, Eq. (2.18) is integrated to give

$$A(x - x_0) + \frac{h}{u^t} = C, \tag{2.20}$$

where C is an integration constant. We note that Eq. (2.20) is not an exact first integral of the Euler equation but can be considered as an approximate one for obtaining an initial condition in which the star is in an approximate equilibrium state.

For computing initial conditions, we assume the line elements of the form

$$ds^2 = -(\alpha^2 - \beta_k \beta^k)dt^2 + 2\beta_k dt dx^k + \psi^4 \delta_{ij} dx^i dx^j, \tag{2.21}$$

where ψ is the conformal factor. Using the Isenberg-Wilson-Mathews formalism [253, 516], the basic equations are written as

$$\Delta\psi = -2\pi\rho_h\psi^5 - \frac{\psi^{-7}}{8}\hat{A}_{ij}\hat{A}^{ij}, \tag{2.22a}$$

$$\Delta(\alpha\psi) = 2\pi\alpha\psi^5(\rho_h + 2S) + \frac{7}{8}\alpha\psi^{-7}\hat{A}_{ij}\hat{A}^{ij}, \tag{2.22b}$$

$$\partial_i \hat{A}^i{}_j = 8\pi J_j \psi^6, \tag{2.22c}$$

where

$$\rho_h = \rho h(\alpha u^t)^2 - P, \qquad S = \rho h[(\alpha u^t)^2 - 1] + 3P, \qquad J_i = \rho h \alpha u^t u_i, \tag{2.23}$$

and Δ is the flat Laplacian. $\hat{A}_{ij}$ is defined from the extrinsic curvature, $\tilde{A}_{ij}$, by $\hat{A}_{ij} = \psi^6 \tilde{A}_{ij}$ and K is set to be zero. Using the CTS decomposition [58, 533] with trumpet-puncture

$$\hat{A}^{ij} = \hat{A}^{ij}_0 + \frac{\psi^6}{2\alpha}\left(\mathbf{L}\beta_{\rm s}\right)^{ij}, \tag{2.24}$$

Eq. (2.22c) is rewritten as

$$\partial_j\partial^j\beta^i_{\rm s} + \frac{1}{3}\delta^{ij}\partial_j\partial_k\beta^k_{\rm s} = 16\pi\alpha\psi^4 J^i + \left(\mathbf{L}\beta_{\rm s}\right)^{ij}\partial_j \ln\left(\alpha\psi^{-6}\right), \tag{2.25}$$

where $\left(\mathbf{L}\beta_{\rm s}\right)^{ij} = \left(\delta^{ik}\partial_k\beta^j_{\rm s} + \delta^{jk}\partial_k\beta^i_{\rm s} - \frac{2}{3}\delta^{ij}\partial_k\beta^k_{\rm s}\right)$. Note that although there are some works in constructing binary black holes initial data with trumpet-puncture [131, 158, 250], this is, to our knowledge, the first attempt combining the CTS decomposition and puncture method with the limit (trumpet) hypersurface in constructing quasi-equilibrium initial data in nonvacuum spacetime. We assume that the contribution to the extrinsic curvature from the black hole is negligible because the orbital momentum of the black hole is negligible in this problem, and thus, we set the black hole at rest (however, it is straightforward to take into account the small black-hole motion [462] in our formalism.)

For a solution of the initial data, we have to determine the free parameters, A, C, and V. In the polytropic equation of state, we can consider κ as well as the central density ρ_c as free parameters. In the following, we first consider that V and the rest mass of the star are input parameters and A, C, and κ are parameters to be determined during the iteration process in numerical computation. Our method to adjust κ to a desired value will be described later.

To determine these three parameters we need three conditions, for which we choose the following relations. First, we fix the location of the surface of white dwarfs along the x-axis as $x = x_1$ (referred to as point 1) and $x = x_2$ (point 2). Typically, we choose $x_1 + x_2 = 2x_0$. At the surface, $h = 1$, and thus, Eq. (2.20) gives

$$A(x_1 - x_0) + \frac{1}{u^t_1} = A(x_2 - x_0) + \frac{1}{u^t_2} = C, \tag{2.26}$$

where u^t_1 and u^t_2 are the values of u^t at points 1 and 2. In addition, we fix the rest mass of the star which is defined by

$$m_* = \int d^3x \rho \alpha \psi^6 u^t, \tag{2.27}$$

where m_* is approximately equal to the gravitational mass M_* because the star is only weakly self-gravitating.

Using the condition (2.26), the values of C and A are determined, and subsequently, h is determined from Eq. (2.20). In the polytropic equation of state, the rest-mass density is written as

$$\rho = \left(\frac{(h-1)(\Gamma - 1)}{\kappa \Gamma} \right)^{1/(\Gamma-1)}, \tag{2.28}$$

and thus, from Eq. (2.27), κ is determined for given values of m_* and $x_2 - x_1$. Once these free parameters are determined, the rest-mass density is obtained from Eq. (2.28).

For a realistic setting, we have to obtain the desired values of the mass of the star and the value of κ. The value of κ is controlled by varying the stellar diameter $x_2 - x_1$ for a given value of m_*.

To take into account the effect of the black-hole gravity, we employ the puncture formulation by setting

$$\psi = \psi_0 + \phi, \qquad \alpha\psi = \alpha_0\psi_0 + X, \qquad \beta^k = \beta^k_0 + \beta^k_{\rm s}, \qquad \hat{A}_{ij} = \hat{A}^0_{ij} + \hat{A}^{\rm s}_{ij}, \tag{2.29}$$

where ψ_0, α_0, β^k_0, and $\hat{A}^0_{ij}$ denote the solutions of vacuum Einstein's equation shown already in Section 2.2.1. Then we numerically solve the equations for ϕ, X, $\beta^k_{\rm s}$, and $\hat{A}^{\rm s}_{ij}$ from Eqs. (2.22a), (2.22b), (2.24) and (2.25). The initial data is prepared using the `octree-mg` code [488], an open source multigrid library with an octree adaptive-mesh refinement (AMR) grid, which we modified to support a fourth-order finite-difference elliptic solver.

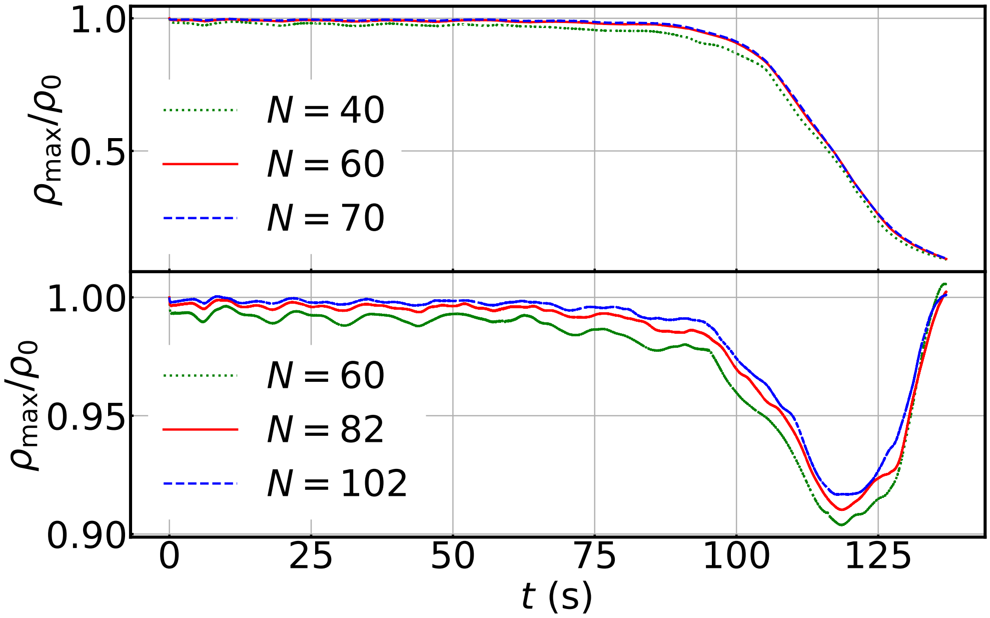

Figure 2.1: Maximum density as a function of time for model `M7V165` (top) with $N = 40$, 60, 70, and model `M8V17` (bottom) with $N = 60$, 82, 102. We find that a fair convergence is obtained with $N = 60$.

2.3 Numerical simulation

2.3.1 Setup

The simulation is performed using an AMR algorithm with the equatorial symmetry imposed on the $z = 0$ (equatorial) plane using the `SACRA-TD` code (for `SACRA` see Refs. [278, 526]). We prepare two sets of finer domains, one of which comoves with a white dwarf and the other of which is located around the center and covers the massive black hole. Because the radius of the white dwarf, R_*, is smaller than the black-hole horizon radius $\sim M_{\rm BH}$, we need to prepare more domains for resolving the white dwarf. In addition to these domains, we prepare coarser domains that contain both the finer domains in their inside. All the domains are covered by $(2N+1, 2N+1, N+1)$ grid points for (x, y, z) with N being an even number.

Specifically, each domain is labeled by i which runs as $0, 1, 2, \cdots, i_{\rm fix}, \cdots, i_{\rm BH}, \cdots, i_{\rm max}$. The grid resolution for the domains with $i_{\rm fix} \le i \le i_{\rm BH}$ is identical with that with $i_{\rm BH} + 1 \le i \le 2i_{\rm BH} - i_{\rm fix} + 1 (< i_{\rm max})$, respectively. For $0 \le i \le i_{\rm BH}$, the center of the domain is located at the origin, at which a black hole is present. Strictly speaking, the black hole moves due to the backreaction against the motion of the companion star, but this motion is tiny because of the condition $M_{\rm BH} \gg M_*$. For these domains, the ith level covers a half cubic region of $[-L_i : L_i] \times [-L_i : L_i] \times [0 : L_i]$ where $L_i = N\Delta x_i$, Δx_i is the grid spacing for the ith level, and the grid spacing for each level is determined by $\Delta x_{i+1} = \Delta x_i/2$ ($i = 0, 1, 2, \cdots, i_{\rm BH} - 1$ and $i = i_{\rm BH} + 1, \cdots, i_{\rm max} - 1$) with $\Delta x_{i_{\rm BH}+1} = \Delta x_{i_{\rm fix}}$ and $L_{i_{\rm BH}} \sim 0.8M_{\rm BH}$.

For the moving domains that cover the white dwarf, the center is chosen to approximately

Table 2.1: Models considered in this Chapter and the fate (last column). `M7V16a` and `M7V16b` correspond to the models with $R_* = 8.5 \times 10^3$ and 7.0×10^3 km, respectively. For other models, $R_* \approx 10^4 (M_*/0.7M_\odot)^{-1/3}$ km. r_p and $r_{p,A}$ are periastron radius in the present coordinates and the Schwarzschild coordinates, respectively. TD and OC denote tidal disruption and appreciable oscillation of white dwarfs, and NN denotes that no appreciable tidal effect is found.

ID	V	$M_*(M_\odot)$	$r_p/M_{\rm BH}$	$r_{p,A}/M_{\rm BH}$	$J/M_{\rm BH}$	β	Fate
`M6V16`	0.160	0.6	4.401	5.456	3.775	0.72	TD
`M7V16`	0.160	0.7	4.401	5.456	3.775	0.65	TD
`M7V16a`	0.160	0.7	4.401	5.456	3.775	0.55	TD
`M7V16b`	0.160	0.7	4.401	5.456	3.775	0.45	TD/OC
`M8V16`	0.160	0.8	4.401	5.456	3.775	0.59	TD
`M7V165`	0.165	0.7	5.770	6.813	3.897	0.52	TD
`M8V165`	0.165	0.8	5.770	6.813	3.897	0.47	TD/OC
`M6V17`	0.170	0.6	7.030	8.065	4.019	0.49	TD/OC
`M7V17`	0.170	0.7	7.030	8.065	4.019	0.44	OC
`M8V17`	0.170	0.8	7.030	8.065	4.019	0.40	OC
`M6V175`	0.175	0.6	8.317	9.346	4.142	0.42	OC
`M7V18`	0.180	0.7	9.681	10.707	4.265	0.33	NN

agree with the location of the density maximum. In the present context, the local density maximum is approximately located along a geodesic around the supermassive black hole. The size of the finest domain with $i = i_{\rm max}$, $L_{\rm max}$, is chosen so that it is 1.3–1.5R_*. We check the convergence of two different models with three grid resolutions as illustrated in Fig. 2.1. Higher resolution is used for model `M8V17` to measure the spin up of the white dwarf more accurately (see Section 2.3.2). We obtain good convergence for both models, and thus, we employ $N = 60$ as the standard resolution in this Chapter.

2.3.2 Numerical results

In this Chapter we focus on the case that the black-hole mass is $M_{\rm BH} = 10^5 M_\odot$, the white-dwarf mass is $M_* = 0.6$, 0.7, and $0.8M_\odot$. For the polytropic equation of state, the stellar radius, R_*, is proportional to $M_*^{(\Gamma-2)/(3\Gamma-4)}$ for a fixed value of κ. Thus, for $\Gamma = 5/3$, the stellar radius depends only weakly on the stellar mass. In the present case we basically choose the value of κ so that $R_* \approx 1.0 \times 10^4 (M_*/0.7M_\odot)^{-1/3}$ km. For $M_* = 0.7M_\odot$ and $V = 0.160$, we also prepare two additional cases where κ is chosen such that $R_* = 8.5 \times 10^3$ km and $R_* = 7.0 \times 10^3$ km.

The initial separation is set to be $x_0 = 20M_{\rm BH}$ (it is $\approx 21.01M_{\rm BH}$ in the Schwarzschild coordinates), and V is chosen to be 0.160, 0.165, 0.170, 0.175, and 0.180 (see Table 2.1). The corresponding specific angular momentum of the white dwarf is $J \approx 3.7748$, 3.8968, 4.0192, 4.142, and $4.2653M_{\rm BH}$, and the resulting periastron radius is $r_p/M_{\rm BH}(r_{p,A}/M_{\rm BH}) =$ 4.401(5.456), 5.770 (6.813), 7.030 (8.065), 8.317 (9.346), and 9.681 (10.707) where in the parenthesis the values in the Schwarzschild coordinate, i.e., areal radius (hereafter denoted by $r_{p,A}$), are described. In Fig. 2.2, we plot the geodesics only for one orbital period for

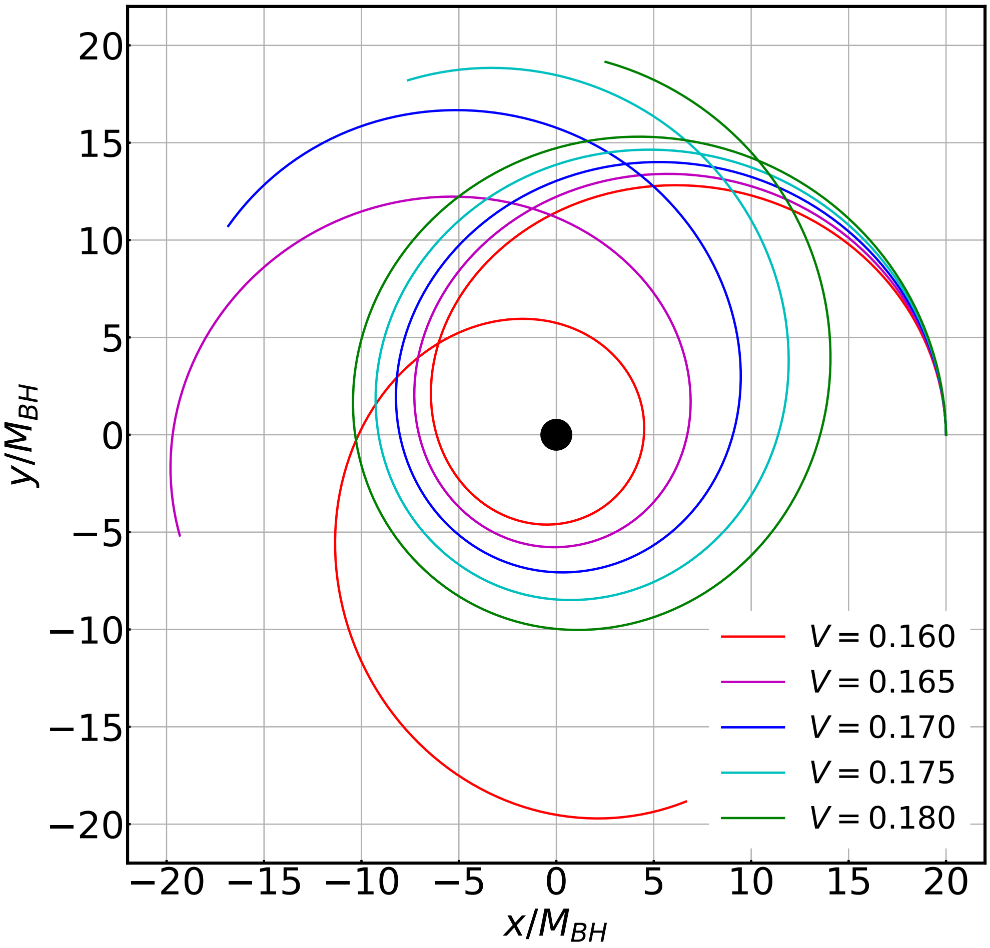

Figure 2.2: Geodesics for $V = 0.160$, 0.165, 0.170, 0.175 and 0.180 in the coordinates of g^0_{ab}. Those only for one orbital period started from $x = 20M_{\rm BH}$ and $y = z = 0$ are plotted. The filled circle at the center represents the black hole with the coordinate radius of its event horizon $r \approx 0.78M_{\rm BH}$.

$V = 0.160$, 0.165, 0.170, and 0.180.

With these settings, the white dwarf has an elliptic orbit around the black hole with the periastron at $r_p \approx (4.4\text{–}10)M_{\rm BH}$, and thus, the eccentricity is approximately defined by $e = (x_0 - r_p)/(x_0 + r_p)$ is $\approx 1/3\text{–}2/3$. Here, $x_0(= 20M_{\rm BH})$ and r_p are defined in the radial coordinates of the metric of g^0_{ab}, and thus, the values of e slightly change if we define it in the areal coordinate (Schwarzschild radial coordinate).

For the models mentioned above, the value of β is in the range between 0.33 and 0.72 and estimated by

$$\beta \approx 0.59 \left(\frac{R_*}{10^4\,{\rm km}}\right)\left(\frac{M_*}{0.7M_\odot}\right)^{-1/3}\left(\frac{r_{p,A}}{6M_{\rm BH}}\right)^{-1}\left(\frac{M_{\rm BH}}{10^5M_\odot}\right)^{-2/3}, \tag{2.30}$$

where the areal radius $r_{p,A}$ is used for the definition of β in this section. For $V = 0.160$ and 0.165 with $M_* = 0.6\text{–}0.8M_\odot$, we find $0.50 \le \beta \le 0.7$, and thus, the white dwarf is expected

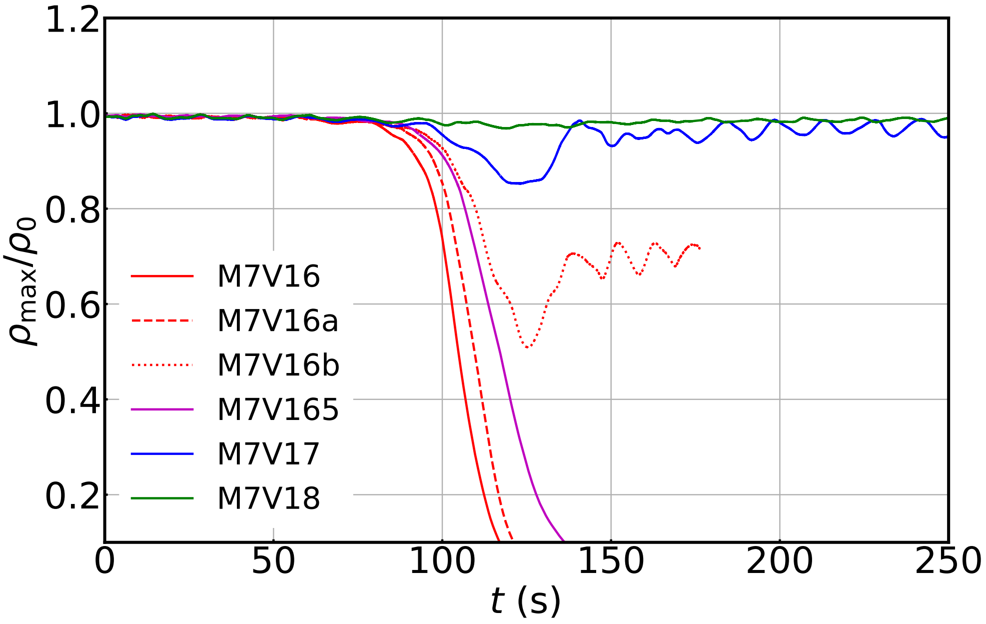

Figure 2.3: The maximum density as a function of time for $V = 0.160$, 0.165, 0.170, and 0.180 with $M_* = 0.7M_\odot$. The maximum density is normalized by the initial value denoted by ρ_0.

to be strongly perturbed by the black-hole tidal field for $M_* = 0.6$–$0.8M_\odot$. By contrast, for $V = 0.180$, $\beta < 0.35$ with $M_* = 0.7M_\odot$, and thus, the tidal force of the black hole is likely to be too weak to perturb the white dwarf.

For $V = 0.170$, $\beta \approx 0.49$, 0.44, and 0.40 with $M_* = 0.6$, 0.7, and $0.8M_\odot$ respectively. In these cases, tidal disruption is not very likely to take place but the tidal force from the black hole should induce the stellar oscillation on the white dwarf. Because for $\Gamma = 5/3$, the stellar radius depends only weakly on the stellar mass, the presence or absence of the tidal disruption is likely to depend primarily on the value of V (or the specific angular momentum of the white dwarfs) in the present setting. In the following, we will show that our code can reproduce all these expected phenomena.

Fig. 2.3 plots the evolution of the maximum density for $V = 0.160$, 0.165, 0.170, and 0.180 with $M_* = 0.7M_\odot$. We note that for $M_{\rm BH} = 10^5M_\odot$, the orbital period for these parameters are in the range from ≈ 220 s for $V = 0.160$ to ≈ 250 s for $V = 0.180$. The figure shows the results expected in the previous paragraphs: For `M7V16` and `M7V165`, the white dwarfs are tidally disrupted while approaching the black hole irrespective of the white-dwarf mass. For `M7V17` ($\beta = 0.44$), the white dwarf is perturbed by the black hole near the periastron but it is not tidally disrupted. After the close encounter, the white dwarf is in an oscillating state due to the instantaneous tidal force received from the black hole. By contrast, for `M7V18`, the maximum density is approximately preserved to be constant, suggesting no disruption occurs and the tidal effect is negligible. Note that such tidal field may still perturb the white dwarf and produce detectable electromagnetic or gravitational-wave signal if a sufficient amplitude

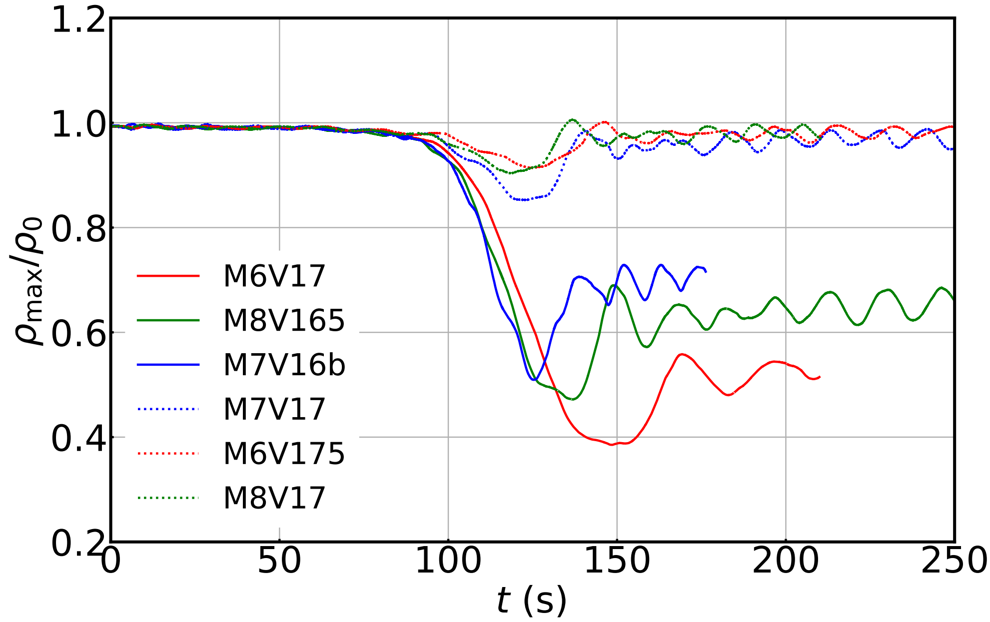

Figure 2.4: The maximum density as a function of time for the cases that stellar oscillation occurs ($0.5 \gtrsim \beta \gtrsim 0.4$). The red, blue, and green curves show the results with $M_* = 0.6M_\odot$, $0.7M_\odot$ and $0.8M_\odot$, respectively. The maximum density is normalized by the initial value denoted by ρ_0.

of oscillation is induced.

In Fig. 2.3, the results of `M7V16` ($\beta = 0.65$), `M7V16a` ($\beta = 0.55$) and `M7V16b` ($\beta = 0.45$) are also compared. As expected, for the first two models, the white dwarfs are tidally disrupted, while for the most compact white dwarf, the tidal disruption does not occur although it is perturbed significantly by the black-hole tidal force. This illustrates that the β parameter is a good indicator for assessing whether tidal disruption takes place or not irrespective of the white-dwarf radius.

Fig. 2.4 shows the evolution of the maximum density when stellar oscillation is induced. For `M6V17` ($\beta = 0.49$), the white dwarf is significantly elongated by the tidal force from the black hole; the central density is decreased to less than 50% of the original value after passing through the periastron. Associated with the tidal effect, the mass is lost from the white dwarf. However, with the increase of the orbital radius, the central density increases again, resulting in a less massive white dwarf. This is also the case for `M8V165` ($\beta = 0.47$) and `M7V16b` ($\beta = 0.45$). These results indicate that the critical value of β for the tidal disruption is ~ 0.50 and the threshold value for exciting a high-amplitude oscillation is $\beta \sim 0.45$. Fig. 2.4 also shows that even for $0.40 \lesssim \beta \lesssim 0.45$ an appreciable oscillation is excited by the tidal force.

In Fig. 2.5 and Table 2.1, we summarize the fates of white dwarfs as a result of the tidal interaction. It is found that for $\beta \gtrsim 0.5$ tidal disruption takes place and for $\beta \gtrsim 0.4$, the white dwarfs are perturbed appreciably by the black-hole tidal field. All these results agree

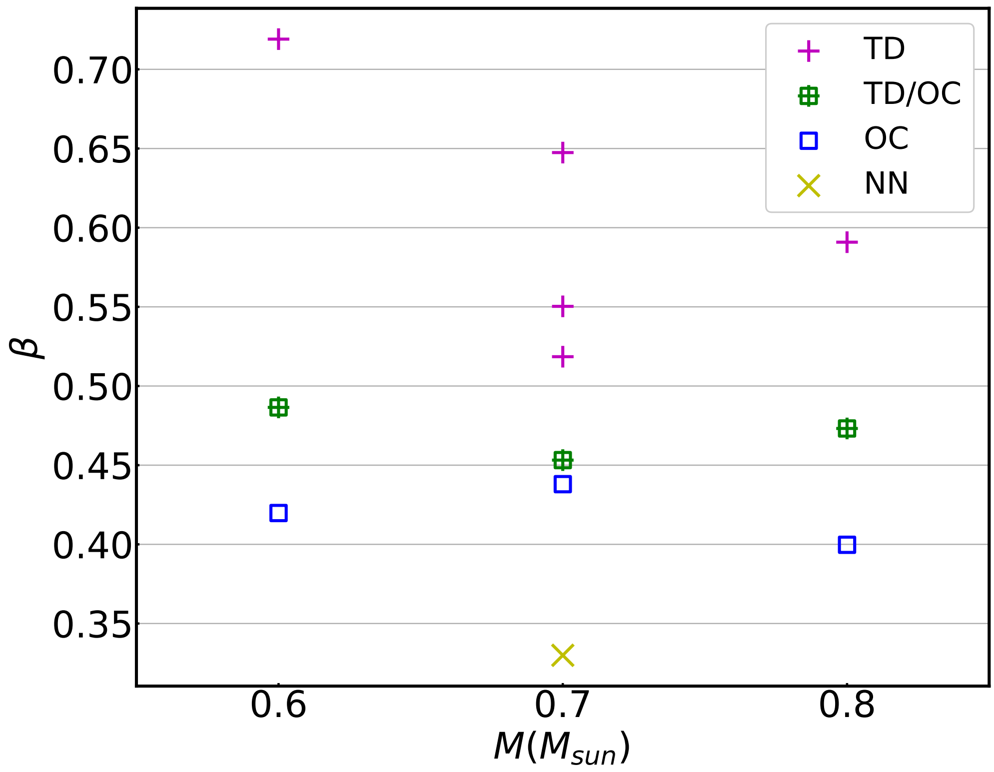

Figure 2.5: A summary for the fate of the white dwarfs in the plane of M_* and β. TD and OC denote that tidal disruption and appreciable oscillation of the white dwarfs are observed after the close encounter of the white dwarfs with the black hole. NN denotes that no appreciable tidal effect is observed.

approximately with the expectation from the previous studies.

For `M7V16`, tidal disruption takes place but only a small fraction of the white dwarf matter falls into the black hole because the fluid elements have specific angular momentum large enough to escape capturing by the black hole. Most of the tidally disrupted matter approximately maintains the original elliptic orbit (see Fig. 2.6) although the matter has an elongated profile. To clarify the eventual matter distribution around the black hole, we will need to follow the matter motion for more than 10 orbits. This topic is one of our major research targets in the future.

For $0.4 \lesssim \beta \lesssim 0.5$, the white dwarf will be continuously perturbed by the black-hole tidal force whenever it passes through the periastron. In addition, the angular momentum is transported during the tidal interaction, and it will lead to the transport of the orbital angular momentum to the white dwarf, resulting in a spin-up of it. According to a perturbation study for the stellar encounter, the energy deposition during the tidal interaction in one orbit is

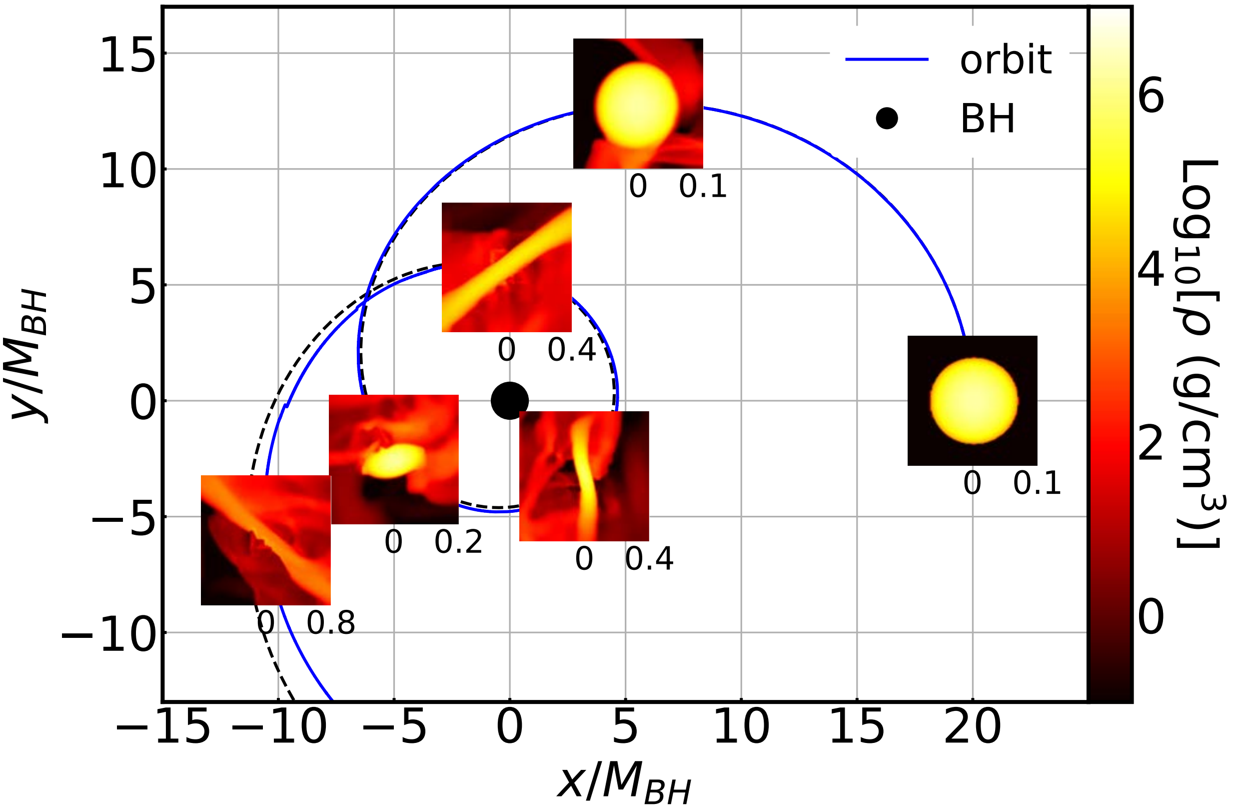

Figure 2.6: The density profiles of the tidally-disrupted white dwarf for the model $V = 0.160$ and $M_* = 0.7M_\odot$ (M7V16). The units of the length scale for the density plots are $GM_{\rm BH}/c^2 \approx 1.48 \times 10^5$ km. The solid and dashed curves show the time evolution for the location of the maximum density and the elliptic orbit shown in Fig. 2.2 for $V = 0.160$ (i.e., geodesic). The length scale of x and y axes is shown in units of $M_{\rm BH}$.

written approximately as [375]

$$\begin{aligned}\Delta E_{\rm tid} &= f_{\rm tid}\left(\frac{M_*^2}{R_*}\right)\left(\frac{M_{\rm BH}}{M_*}\right)^2\left(\frac{R_*}{r_{p,A}}\right)^6 \\ &= f_{\rm tid}\left(\frac{M_*^2}{R_*}\right)\beta^6.\end{aligned} \tag{2.31}$$

where $f_{\rm tid}$ is a factor of $O(0.1)$, which depends on β and the equation of state. Associated with the energy deposition near the periastron, the angular momentum deposition is also deposited. In one orbit it is approximately estimated by $\Delta J_{\rm spin} \approx \Delta E_{\rm tid}/\Omega_p$ [296] where $\Omega_p = \sqrt{M_{\rm BH}/r_{p,A}^3}$, and thus,

$$\begin{aligned}\Delta J_{\rm spin} &= f_{\rm spin} M_* \sqrt{M_* R_*}\left(\frac{M_{\rm BH}}{M_*}\right)^{3/2}\left(\frac{R_*}{r_{p,A}}\right)^{9/2} \\ &= f_{\rm spin} M_* \sqrt{M_* R_*}\beta^{9/2},\end{aligned} \tag{2.32}$$

where $f_{\rm spin}$ is a coefficient of the same order of the magnitude of $f_{\rm tid}$.

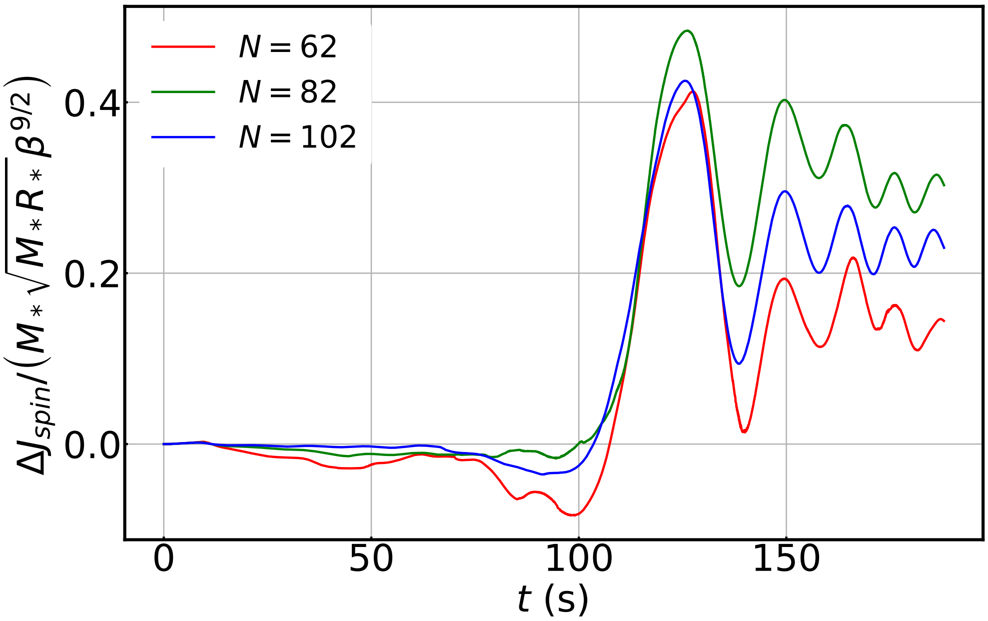

Figure 2.7: The rescaled change in angular momentum $\Delta J_{spin}/\left(M_*\sqrt{M_*R_*}\beta^{9/2}\right)$ as a function of time for the stellar oscillation scenario (`M8V17`). This agrees with the analytic expression Eq. (2.32) if $f_{\mathrm{spin}} \sim 0.1$–$0.3$.

Because the maximum spin angular momentum of the star is approximately written as $M_*\sqrt{M_*R_*}$, we find that ΔJ_{spin} can be more than 0.1% of the maximum spin if a white dwarf passes through a close orbit with $\beta \gtrsim 0.4$. We approximate the orbit angular momentum J_{orbit} and the spin angular momentum J_{spin} of the white dwarf as

$$J_{\mathrm{orbit}} = M_h \left(\langle x \rangle \langle u_y \rangle - \langle y \rangle \langle u_x \rangle\right), \tag{2.33a}$$

$$J_{\mathrm{spin}} = \int d^3x \psi^6 \rho h \left[\left(x - \langle x \rangle\right)\left(u_y - \langle u_y \rangle\right) - \left(y - \langle y \rangle\right)\left(u_x - \langle u_x \rangle\right)\right], \tag{2.33b}$$

where $M_h := \int d^3x\psi^6\rho h$ and the volume average of quantity q is defined as $\langle q \rangle := \frac{1}{M_h}\int d^3x\psi^6\rho h q$. In such decomposition, the sum of orbital and spin angular momentum equals the total angular momentum of the white dwarfs. We analyzed the spin angular momentum gain of the white dwarfs for `M8V17`, and we indeed find $\Delta J_{\mathrm{spin}}/(M_*\sqrt{M_*R_*}\beta^{9/2}) \approx 0.1$–$0.3$ as shown in Fig. 2.7. Note that the spin up of white dwarf ΔJ_{spin} is about 10^{-6} of the total angular momentum, and hence, it is not easy to determine ΔJ_{spin} accurately. Although we cannot achieve a good convergence in ΔJ_{spin}, we are able to obtain a noticeable rise in J_{spin} during the close encounter, which suggests $f_{\mathrm{spin}} \sim 0.1$–$0.3$, consistent with the above analytic result.

For close orbits, the tidal angular-momentum transport can dominate over the orbital angular momentum loss by gravitational-radiation reaction. Assuming that gravitational waves are most efficiently emitted near the periastron at which we may approximate the orbit to be circular, the angular momentum dissipation by gravitational waves in one orbit can be written as [368]

$$\Delta J_{\rm GW} \approx \frac{64\pi}{5}\frac{M_{\rm BH}^2 M_*^2}{r_{p,A}^2}\left(1+\frac{7e^2}{8}\right), \tag{2.34}$$

where e denotes the eccentricity. Thus, the ratio of $\Delta J_{\rm tid}$ to $\Delta J_{\rm GW}$ is written as

$$\frac{\Delta J_{\rm spin}}{\Delta J_{\rm GW}} \approx 23 f_{\rm spin}\left(\frac{r_{p,A}}{4M_{\rm BH}}\right)^{-5/2}\left(\frac{M_{\rm BH}}{10^5 M_\odot}\right)^{-3}\left(\frac{M_*}{0.7M_\odot}\right)^{-2}\left(\frac{R_*}{10^4\,{\rm km}}\right)^{5}\left(1+\frac{7e^2}{8}\right)^{-1}. \tag{2.35}$$

Thus it is larger than unity for $r_{p,A} \lesssim 7M_{\rm BH}/c^2$, $R_* \approx 10^4$ km, $M_{\rm BH} = 10^5 M_\odot$, $M_* = 0.7M_\odot$, and $f_{\rm spin} = 0.2$. This is also the case for the ratio of $\Delta E_{\rm tid}/\Delta E_{\rm GW}$ where $\Delta E_{\rm GW}$ is the energy dissipated by gravitational waves in one orbit. Thus, near the tidal disruption orbit, the orbital evolution would be primarily determined not by the gravitational-wave emission but by the tidal effect. To clarify the eventual fate of such a white dwarf, we obviously need a long-term accurate simulation. Such a topic is one of our future targets.

We note that both $\Delta J_{\rm spin}$ and $\Delta J_{\rm GW}$ are much smaller than the orbital angular momentum of order $M_*\sqrt{M_{\rm BH} r_{p,A}}$. Thus, the cumulative effect of the tidal angular momentum transport plays an important role just prior to the tidal disruption. By repeated tidal interaction, the spin angular velocity of the white dwarfs is likely to be enhanced up to $\sim M_{\rm BH}^{1/2}/r_p^{3/2} = \beta^{3/2} M_*^{1/2}/R_*^{3/2}$. In addition, the stellar oscillation for which the oscillation energy is comparable to or larger than the rotational kinetic energy should be excited. As a result, mass loss could be induced, resulting in the increase of the stellar radius and enhancing the importance of tidal interaction. In this type of the system, the tidal disruption is unlikely to take place by one strong impact by the black-hole tidal force but likely to do as a result of a secular increase of the stellar radius (see, e.g., Refs. [141, 313] for related studies).

2.4 Discussion

We reported a new numerical-relativity code which enables us to explore tidal disruption of white dwarfs by a relatively low-mass supermassive black hole. As a first step toward more detailed future studies, we paid attention to the condition for tidal disruption of white dwarfs with typical mass range in elliptic orbits by a nonspinning supermassive black hole. We showed that our code is capable of determining the condition for the tidal disruption. As expected from previous general relativistic works (e.g., Refs. [254, 407]), the tidal disruption takes place for $\beta \gtrsim 0.5$ and an appreciable oscillation of the white dwarfs are induced by the black-hole tidal effect for $\beta \gtrsim 0.4$ for orbits close to the black hole in the $\Gamma = 5/3$ polytropic equation of state. The critical value for the onset of the tidal disruption is smaller than that obtained by Newtonian analysis. For white dwarfs with $M_* = 0.6M_\odot$ and $R_* = 1.2 \times 10^4$ km, β can be larger than 0.4 even for $M_{\rm BH} \approx 4 \times 10^5 M_\odot$ if the periastron radius is

$r_{p,A} = 4M_{\rm BH}$. Our result indicates that in such systems with a relatively low-mass (but not intermediate-mass) supermassive black hole for which gravitational waves in the late inspiral phase can be detected by LISA [31], tidal disruption can occur for typical white dwarfs. For spinning black holes with the dimensionless spin parameter of $\gtrsim 0.9$, $r_{p,A}$ can be smaller than $\sim 1.7M_{\rm BH}$ [47]. For such black holes, tidal disruption of typical-mass white dwarfs may occur even for $M_{\rm BH} \approx 10^6 M_\odot$. Investigation of this possibility is a future issue.

There are several issues to be explored. The first one is to extend our implementation for spinning black holes. Since no analytic solution is known for the spacetime of spinning black holes on the limit hypersurface, we need to develop a method to provide g^0_{ab} for employing the formulation introduced in this Chapter. One straightforward way to prepare such data is just to numerically perform a simulation for a spinning black hole (in vacuum) until the hypersurface reaches the limit hypersurface as a first step, and then, the obtained data are saved and used in the subsequent simulations with white dwarfs. A more subtle issue along this line is to prepare the initial condition. For nonspinning black holes, we can assume that the conformal flatness of the three metric, and as a result, the initial-value equations are composed only of elliptic-type equations with the flat Laplacian. For the spinning black holes, the basic equations are composed of elliptic-type equations of complicated Laplacian, and hence, the numerical computation could be more demanding, although in principle it would be still possible to obtain an initial condition. We plan to explore this strategy in the subsequent work.

For modeling realistic white dwarfs it is necessary to implement a realistic equation of state. If we assume that the temperature of the white dwarfs is sufficiently low and the pressure is dominated by that of degenerate electrons, it is straightforward to implement this.

More challenging issue is to follow the hydrodynamics of tidally disrupted white-dwarf matter for a long term. After the tidal disruption, the matter of the white dwarf is likely to move around the black hole for many orbits. During such orbits, the matter collides each other, and eventually, a compact disk will be formed after the circularization. Such disks are likely to be hot due to the shock heating, and thus, it can be a source of electromagnetic counterparts of the tidal disruption. In the presence of magnetic fields, magnetorotational instability [43] occurs in the disk, and the magnetic fields will be amplified. If the amplified magnetic field eventually penetrates the black hole and if the black hole is appreciably spinning, a jet may be launched through the Blandford-Znajek effect [95]. After the amplification of the magnetic fields, a turbulent state will be developed in the disk and mass ejection could occur by the effective viscosity or magneto-centrifugal force [94]. The ejecta may be a source of electromagnetic signals. One long-term issue is to investigate such scenarios by general relativistic magnetohydrodynamics.

Part II

Binary neutron star mergers in massive scalar-tensor theory

Chapter 3

Quasi-equilibrium states and dynamical enhancement of the scalarization

Contents

Breakdown of Contribution

This chapter is based on the publication: "*Binary neutron star mergers in massive scalar-tensor theory: Quasiequilibrium states and dynamical enhancement of the scalarization*" in Phys.Rev.D 108 (2023) 6, 064057 [294] by H.-J. Kuan, K. V. Aelst, **A. T.-L. Lam** and M. Shibata. K. V. Aelst developed the initial data solver of binary neutron stars in massive scalar-tensor theory based on the open-source code `FUKA`. The modified gravitational field equations in quasi-equilibria were derived by H.-J. Kuan and me. I also proposed a change of scalar field variable to better capture the asymptotic exponential decay, and helped fixing some bugs during the development of the initial data code. The numerical calculation of the quasi-equilibrium sequences was performed by H.-J. Kuan. K. V. Aelst and I provided constructive comments on the manuscript written partially by H.-J. Kuan and M. Shibata.

Overview

In this Chapter, we study quasi-equilibrium sequences of binary neutron stars in the framework of Damour-Esposito-Farese-type scalar-tensor theory of gravity with a massive scalar field, paying particular attention to the case where neutron stars are already spontaneously scalarized at distant orbits, i.e., in the high coupling constant case. Although scalar effects are largely quenched when the separation a is $\gtrsim$ 3–6 times of the Compton length-scale that is defined by the scalar mass, we show that the interaction between the scalar fields of the two neutron stars generates a scalar cloud surrounding the binary at the price of orbital energy when $a \lesssim$ 3–6 times of the Compton length-scale. This enables us to constrain the scalar mass m_ϕ from gravitational-wave observations of binary neutron star mergers by inspecting the dephasing due to such phenomenon. In particular, the event GW170817 is suggestive of a constraint of $m_\phi \gtrsim 10^{-11}$ eV and the coupling strength should be mild if the neutron stars in this system were spontaneously scalarized.

3.1 Introduction

General relativity (GR) has been put against a variety of observations and yet been challenged, while it has also proven to be incomplete from the theoretical point of view for its nonrenormalizability (e.g., [50, 51]). Among the extensions to GR present in the literature, Damour-Esposito-Farese (DEF) type of scalar-tensor (ST) theory of gravity is perhaps most widely considered. In such theory, the gravity around a scalarized compact object acquires a distinct feature from that in GR, modifying the trajectory of orbiting companions. In particular, the motion of binaries will be influenced to deviate from the GR prediction if there is scalar interaction between the two components at play. In addition, scalar waves will be emitted from binaries consisting of differently scalarized components, constituting extra loss of orbital energy. Lacking the evidence of the aforementioned two effects in the pulsar timing observation of neutron star-white dwarf (NS-WD) binaries has placed strong constraints on ST theories with a *massless* scalar field [33, 74, 145, 197, 224, 419]. Such constraints are rather stringent for the presence of a scalar charge of neutron stars (NSs) [128, 538]. These constraints can, however, be mitigated by the inclusion of scalar mass m_ϕ [28, 385]. The scalar effects beyond the associated Compton length-scale $\lambdabar_{\rm comp} = \hbar c/m_\phi$ are smeared out, thus naturally accounting for the non-detection of scalar dynamics that could take place in these binaries. In particular, the constraints by the pulsar timing are lifted to a large extent if the scalar field has a light mass $m_\phi \gg 10^{-16}$ eV (corresponding to a Compton length-scale $\lambdabar_{\rm comp} \ll 1.5 \times 10^6$ km) [385]. With this small mass, the scalar interaction within NS-WD binaries and the emission of scalar waves from them are suppressed, leading to identical orbital evolution with that in GR. Therefore, including a scalar mass not only increases the dimension of the parameter space by one but unlocks the previously ruled-out region. However, NS-WD binaries could barely put constraints on the massive theory since a light scalar field is enough to lift the constraining power of pulsar timing observations. On the other hand, an ever-stringent lower bound on the scalar mass may be placed by pre-merger gravitational waves (GWs) from coalescing binary neutron stars (BNSs).

For BNS mergers, the growth of the scalar field can be activated by the gravitational compactness of the binary, defined as the ratio of the total mass to the orbital separation, forming another kind of scalarization [46, 409, 432, 450] (see also [270, 271, 361, 415] for semi-analytical modeling) other than the spontaneous ones [34, 143]. In the same spirit as pulsar timing constraints, the absence of both kinds of scalarization in the event GW170817 suggests that spontaneously scalarized NSs are unlikely present in the associated coalescing BNS if the scalar field is *massless* [537]. To probe massive ST theory by GW physics, a pursue of scalar masses 10^{-12}–10^{-11} eV is of particular interest since the associated Compton length-scale is comparable with or smaller than the typical orbital separation of $\sim$ 30–200 km when the BNS comes in the detection window.

It is widely known that the uncertainty on the theory of gravity is degenerate with that on the nuclear equations of state (EOS) [418, 469]. Among other things, the twin star in GR predicted from some EOS embracing hadron-quark phase transition has an analog in the ST theory [292]. Nonetheless, certain scalar-induced phenomena have no counterparts in GR, e.g., the presence of scalar-type GWs from binary motions [142], core-collapse of giant stars [39, 126, 216, 398, 473], and radial [466] and polar [289] oscillations of NSs (see [167] for a recent, extensive review). An observation of such ST-exclusive effects can therefore probe the nature of gravity, and limit the parameter space of ST theories without the potential for misinterpreting EOS effects. The dynamics during the late inspiral up to merger, and the associated GW emission from BNSs in a ST theory that admits spontaneous and/or dynamical scalarization may shed unique light on the nature of gravity [4, 15], thus deserving qualitative investigation.

For mass of $m_\phi \gtrsim 10^{-12}$ eV, the scalar effects are shielded in the early inspiral and the interaction only becomes dynamically important when the binary approaches merger. Since the effects occur in a highly non-linear regime of the theory, it can only be investigated numerically. Although certain attempts have been made in the massless case ($m_\phi = 0$) [46, 235, 323, 450, 486], numerical study of the BNS dynamics in theories with a massive scalar field has not been performed. We thus endeavour to address such issue numerically as a non-trivial scalar mass is necessary to account for the aforementioned observations. For this purpose, preparing appropriate initial data (ID) is rather imperative in order to guarantee accurate simulations.

As the first step towards the derivation of accurate BNS dynamics and the emitted GWs, we develop an ID code to generate equilibrium states of BNSs, which are expected to deliver certain information on the dynamics of coalescence since the sequence of equilibria can be viewed as the leading order approximations of the inspiraling process. In particular, the constructed equilibria can (i) offer an approximate estimate on the luminosity of GWs [442, 486], and (ii) qualitatively investigate scalar effects in the inspiral stage on top of (iii) paving the way toward future numerical-relativity studies of BNS mergers. By scrutinising the constructed sequences, we found that a lower bound of $m_\phi > 10^{-11}$ eV for strong couplings can be readily drawn. Although quantitative analysis of the waveforms can supplement the effort of waveform-modelling (e.g., [100]) to examine the imprint of modified gravity from GWs, the relevant investigation will be deferred to later work in this series.

In this Chapter, we pay particular attention to the sequences of BNSs in which each NS is spontaneously scalarized, i.e., the coupling constant B is high [see Eq. (3.2)]. Broadly speaking, inspiraling scalarized BNSs are speculated to be classified into three stages depending on the following three parameters: the orbital separation a, the gravitational wavelength $\lambdabar_{\rm gw}$, which is $\approx a^{3/2}M^{-1/2}/2(> a)$ for binaries in circular orbits with M the total mass of the binary, and the Compton length-scale $\lambdabar_{\rm comp}$. For (I) $\lambdabar_{\rm gw} > a \gg \lambdabar_{\rm comp}$, no effect associated with the scalar field appears and hence the sequences of BNSs can be identical to those in GR; (II) for $\lambdabar_{\rm gw} > \lambdabar_{\rm comp} \gtrsim a$, the scalar-wave emission is suppressed because of the relation $\lambdabar_{\rm gw} > \lambdabar_{\rm comp}$, while the interaction between the scalar clouds of the two NSs can play a role in modifying the binary orbit; (III) for $\lambdabar_{\rm comp} > \lambdabar_{\rm gw} > a$, both the scalar-wave emission and interaction of the two scalar clouds are present. For the categories (II) and (III), the orbital evolution of the BNSs can be different from that in GR. One of the primary purposes of this Chapter is to confirm these speculations.

This Chapter is organised as follows. Section 3.2 briefly reviews the ST theory under study, including the connection to other formalisms adopted in the literature, the equations to be solved for quasi-equilibrium states of binaries, and the constraints on the theory parameters from current observations of binary pulsar timing and GWs from coalescing BNS. In Sec. 3.3, we describe the asymptotic properties of stationary spacetimes in this theory, which provide quantitative measures for the quality of the quasi-equilibrium states constructed here. Section 3.4 forms the main part of the article, where the sequences of BNS are computed (Sec. 3.4.1), and demonstrates the scalar effects in the binary evolution especially in terms of the cycles in the GW (Sec. 3.4.2). An elaboration on how the enhancement of scalarization influences the onset of mass-shedding follows in Sec. 3.4.3. Discussion and potential implications of a detection of such effects are given in Sec. 3.5. Throughout this Chapter, the reduced Plank constant set to $\hbar = 1$.

3.2 Theoretical and observational aspects of the theory

3.2.1 Basic equations

The action of the scalar-tensor theory in the Jordan frame is written as [104, 259]

$$S =\frac{1}{16\pi}\int d^4x\sqrt{-g}\left[\phi\mathcal{R}-\frac{\omega(\phi)}{\phi}\nabla_a\phi\nabla^a\phi-U(\phi)\right]-\int d^4x\sqrt{-g}\rho(1+\varepsilon), \tag{3.1}$$

where $\mathcal{R}$ and ∇_a are the Ricci scalar and covariant derivative associated with the metric g_{ab}, ρ is the rest-mass density, and ε is the specific internal energy. In the action, $\omega(\phi)$ describes the coupling between the metric and the scalar field ϕ, for which the following expression:

$$\frac{1}{\omega(\phi)+3/2}=B\,\ln\phi, \tag{3.2}$$

is adopted in the present article with B as the dimensionless coupling constant [450]. For latter use, we introduce the variable φ via

$$2\ln\phi=\varphi^2, \tag{3.3}$$

with respect to which the scalar potential,

$$U(\phi)=\frac{2m_\phi^2\varphi^2\phi^2}{B}, \tag{3.4}$$

is chosen for the scalar mass m_ϕ [298]. Along with the scalar mass, a Compton length-scale,

$$\lambdabar_{\rm comp}\approx 19.7\,{\rm km}\left(\frac{m_\phi}{10^{-11}\ {\rm eV}}\right)^{-1} \tag{3.5}$$

is introduced.

Denoting the Einstein tensor associated with the metric g_{ab} as G_{ab}, the equation of motion associated with the action can then be written down as

$$\begin{aligned}G_{ab} =&8\pi\phi^{-1}T_{ab}+\omega(\phi)\phi^{-2}\left[\nabla_a\phi\nabla_b\phi-\frac{1}{2}g_{ab}\nabla_c\phi\nabla^c\phi\right]\\&+\phi^{-1}(\nabla_a\nabla_b\phi-g_{ab}\nabla_c\nabla^c\phi)-\frac{2m_\phi^2}{B}\phi\ln\phi g_{ab},\end{aligned} \tag{3.6}$$

and

$$\nabla_a\nabla^a\phi=\frac{1}{2\omega(\phi)+3}\left[8\pi T-\frac{d\omega}{d\phi}\nabla_c\phi\nabla^c\phi+\frac{4m_\phi^2\phi^2}{B}\right], \tag{3.7}$$

where $T={T_a}^a$. The equation of motion for the matter in the Jordan frame is the same as in GR, i.e.,

$$\nabla_a T^{ab} = 0. \tag{3.8}$$

The fluid is assumed to be a perfect fluid, for which the stress-energy tensor has the form

$$T^{ab} = \rho h u^a u^b + P g^{ab}, \tag{3.9}$$

where P is the pressure, $h = 1 + \varepsilon + P/\rho$ is the specific enthalpy, and u^a is the 4-velocity of the fluid, respectively.

3.2.2 Connection to the Einstein frame

To draw the connection to a large part of the literature, where the Einstein frame is often considered due to certain advantages with respect to the Jordan frame, we provide the relations between these two frames in this subsection, while we will stick to the Jordan frame in the rest of the article. The scalar field in the Einstein frame, denoted by $\bar{\varphi}$, is defined by assuming that the Weyl relation between the metric fields in the two frames is

$$g_{ab} = A(\bar{\varphi})^2 \tilde{g}_{ab}, \tag{3.10}$$

where $A(\bar{\varphi}) = \phi^{-1/2} = e^{\beta_0 \bar{\varphi}^2/2}$, and β_0 is a dimensionless constant. Thus,

$$\varphi = \sqrt{-2\beta_0}\bar{\varphi} = \sqrt{B}\bar{\varphi}. \tag{3.11}$$

In addition, the potential in the Einstein frame, V, related to U via $U = 4V\phi^2$, is given by

$$V = \frac{1}{2} m_\phi^2 \bar{\varphi}^2, \tag{3.12}$$

which makes clear the physical meaning of the parameter m_ϕ as the scalar mass.

The two parameters in the DEF theory are defined as the asymptotic values of the first and second derivative of the logarithmic coupling function [142, 143]. Let the asymptotic value of the Jordan frame scalar field be φ_0, thus the one in the Einstein frame being $\bar{\varphi}_0 = \varphi_0/\sqrt{B}$ by Eq. (3.11), one then has

$$\alpha_{\mathrm{DEF}} = \left.\frac{d \ln A}{d\bar{\varphi}}\right|_{\varphi_0} = \frac{\beta_0 \varphi_0}{\sqrt{B}}, \tag{3.13}$$

and

$$\beta_{\mathrm{DEF}} = \left.\frac{d^2 \ln A}{d\bar{\varphi}^2}\right|_{\varphi_0} = \beta_0 = -B/2. \tag{3.14}$$

As long as the transformations of the fields between the two frames are mathematically well-defined (e.g., one-to-one relations should be guaranteed [215]), the physics can be equally validly discussed in whichever frame [191].

3.2.3 Gravitational field equations in quasi-equilibria

We describe here the basic gravitational field equations for computing quasi-equilibria of BNSs in circular orbits. Following previous works [253, 515] (and see, e.g., [485] for a review), we solve the constraint equations under the maximal slicing condition, assuming conformal flatness for the 3-spatial metric $\gamma_{ij} = W^{-2} f_{ij}$, where W is a conformal factor and f_{ij} is the flat 3-metric.

The momentum constraint is written as

$$0 = \mathcal{M}_j = D_i K^i{}_j - D_j K - 8\pi\phi^{-1} J_j + \varphi K_j{}^i D_i\varphi - \left(1 + \frac{2}{B} - \frac{\varphi^2}{2}\right)\Phi D_j\varphi - \varphi D_j\Phi, \tag{3.15}$$

where $\Phi = -\alpha^{-1}(\partial_t - \beta^k\partial_k)\varphi$ is the "momentum" of the scalar field. The Hamiltonian constraint is written as

$$\begin{aligned} 0 = \mathcal{H} = R + K^2 - K_{ij}K^{ij} - 16\pi\phi^{-1}\rho_{\rm h} - \left(\frac{2}{B} - \frac{3}{2}\varphi^2\right)\left(\Phi^2 + D_k\varphi D^k\varphi\right) \\ - 2\left[-K\Phi\varphi + \varphi D_k D^k\varphi + (1+\varphi^2) D_k\varphi D^k\varphi\right] - \frac{2m_\phi^2\varphi^2\phi}{B}, \end{aligned} \tag{3.16}$$

where R is the Ricci scalar with respect to γ_{ij} and $\rho_{\rm h} = \alpha^2 T^{tt}$.

The elliptic equations for generating binary ID (assuming conformal flatness) are written down as (see [450, 486] for equations in ST theories with a massless scalar field)

$$\begin{aligned} \Delta\psi = &-\phi^{-1}\psi^5\left(2\pi\rho_{\rm h} + \frac{m_\phi^2\phi^2\varphi^2}{4B}\right) - \frac{1}{8}\psi^{-7}\bar{A}_{ij}\bar{A}^{ij} - \frac{1}{2}\pi B\psi^5\varphi^2 T\phi^{-1} - \frac{m_\phi^2\phi\varphi^2}{4}\psi^5 \\ &- \frac{\psi}{4}\left(1 + \frac{1}{B} - \frac{3}{4}\varphi^2\right) f^{ij}(\partial_i\varphi)(\partial_j\varphi) + \frac{1}{4}\chi^{-1}\varphi f^{ij}(\psi\partial_i\chi - \chi\partial_i\psi)(\partial_j\varphi), \end{aligned} \tag{3.17}$$

$$\begin{aligned} \Delta\chi = &\, 2\pi\phi^{-1}\chi\psi^4(\rho_{\rm h} + 2S) + \frac{7}{8}\chi\psi^{-8}\bar{A}_{ij}\bar{A}^{ij} - \frac{3}{2}\pi B\chi\psi^4\varphi^2 T\phi^{-1} - \left(\frac{3}{4} + \frac{5}{4B}\right)\chi\psi^4 m_\phi^2\varphi^2\phi \\ &- \frac{\chi}{4}\left(3 + \frac{1}{B} - \frac{3}{4}\varphi^2\right) f^{ij}(\partial_i\varphi)(\partial_j\varphi) - \frac{3}{4}\psi^{-1}\varphi f^{ij}(\psi\partial_i\chi - \chi\partial_i\psi)(\partial_j\varphi), \end{aligned} \tag{3.18}$$

$$\begin{aligned} \Delta\beta^i + \frac{1}{3}f^{ij}\partial_j(\partial_k\beta^k) = &\, 16\pi\phi^{-1}\chi\psi^{-1}f^{ij}J_j \\ &- 2\chi\psi^{-7}\bar{A}^{ij}(7\psi^{-1}\partial_j\psi - \chi^{-1}\partial_j\chi) - 2\chi\varphi\psi^{-7}\bar{A}^{ij}\partial_j\varphi, \end{aligned} \tag{3.19}$$

and

$$\Delta\varphi = 2\pi B\psi^4\varphi\phi^{-1}T - \varphi f^{ij}(\partial_i\varphi)\partial_j\varphi - f^{ij}(\chi^{-1}\partial_i\chi + \psi^{-1}\partial_i\psi)(\partial_j\varphi) + m_\phi^2\psi^4\varphi\phi, \tag{3.20}$$

where Δ denotes the flat Laplacian, $\psi = W^{-1/2}$, $\chi = \alpha\psi$, $S = T_{ij}\gamma^{ij}$, and we used the definition

$$\bar{A}^{ij} = \psi^{10}\left(K^{ij} - \frac{1}{3}\gamma^{ij}K\right). \tag{3.21}$$

We also assumed that the "momentum" of the scalar field φ, denoted by Φ, vanishes given that the scalar-radiation reaction time scale is much longer than the orbital time scale. From Eq. (3.20) we see that the asymptotic value of the scalar field, φ_0, can be oscillatory (e.g., [149]) or zero for stationary solutions. We adopt the latter case in the present work, i.e., $\varphi_0 = 0$. By modifying the elliptic equations (3.17)–(3.19) and introducing equation (3.20), we generalise the public spectral code FUKA [363] to this ST theory for generating the BNSs in quasi-equilibrium.

Note that, for large distances, FUKA uses a compactified domain to bring infinity to a finite numerical distance (this allows in particular to properly impose boundary conditions at infinity). Given the asymptotic exponential decay of the scalar field φ, its profile is better captured in such a domain if Eq. (3.20) is rewritten in terms of an auxiliary scalar field $\xi = \varphi\cosh(m_\phi r)$, which gives

$$\begin{aligned}\Delta\xi =& m_\phi^2\left[2\cosh^{-2}(m_\phi r) + \psi^4\phi - 1\right]\xi + \frac{2m_\phi\tanh(m_\phi r)}{r}\xi + 2m_\phi\tanh(m_\phi r)\hat{r}^i\partial_i\xi \\ &+ 2\pi B\psi^4\xi\phi^{-1}T - \cosh^{-2}(m_\phi r)\xi\Big[f^{ij}\partial_i\xi\partial_j\xi - 2m_\phi\xi\tanh(m_\phi r)\hat{r}^i\partial_i\xi \\ &+ m_\phi^2\xi^2\tanh^2(m_\phi r)\Big] - (\chi^{-1}\partial_i\chi + \psi^{-1}\partial_i\psi)\Big[f^{ij}\partial_j\xi - m_\phi\xi\tanh(m_\phi r)\hat{r}^i\Big],\end{aligned} \tag{3.22}$$

where $\hat{r}^i$ is the unit radial vector. The first term in the right-hand side suggests a Helmholtzian nature of the equation, which, however, asymptotically reduces to a Laplacian one under the assumption of this Chapter that $\phi \to 1$ at $r \to \infty$.

3.2.4 Spontaneous scalarization with massive fields

In isolated NSs and for a given coupling strength B, scalarization is triggered by tachyonic instability if the NS exceeds a threshold compactness determined by the theory parameters and the EOS. In particular, the conditions to be met for spontaneous scalarization in a spherical NS are approximately $k^2 > 0$ and $kR_\star \to \pi/2$ for $k^2 = -(2\pi BT + m_\phi^2)$ [298]. In the massless theory, the threshold is only weakly EOS-dependent for some coupling strength, given that $-T \approx \rho$ [30, 143, 450, 521]. However, this universality is lost from the non-vanishing m_ϕ [527]. Instead of studying the EOS dependence of the threshold, we focus on a

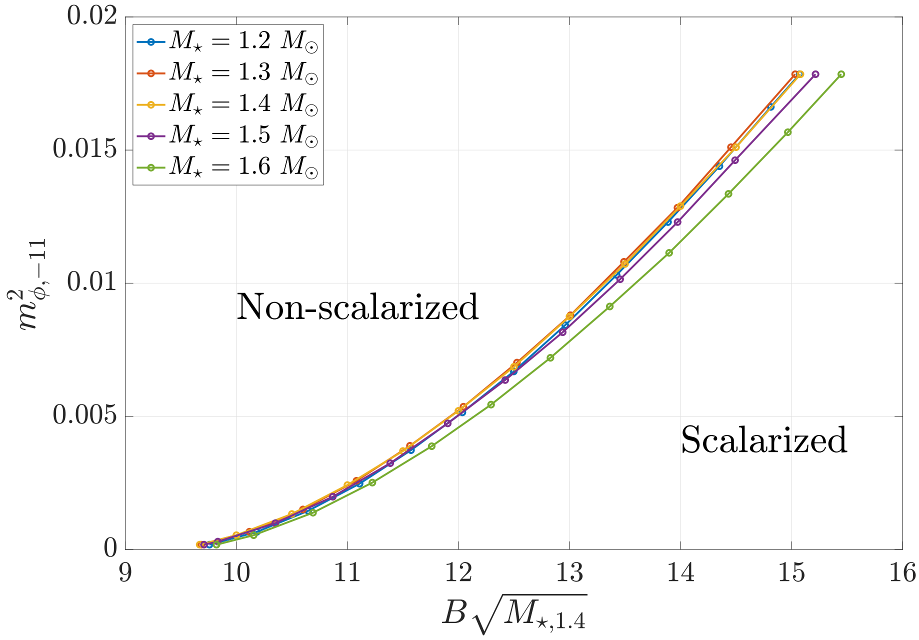

Figure 3.1: Boundaries of the scalarization projected on the $m_\phi^2 - B\sqrt{M_{\star,1.4}}$ plane for a variety of stellar masses, which separate the upper region where stars do not harbour a static scalar field from the lower region of scalarized NSs. Here the notations $M_{\star,1.4} = M_\star/1.4\ M_\odot$ and $m_{\phi,-11} = m_\phi/10^{-11}$ eV are used, and the APR4 EOS is adopted.

particular EOS (ARP4 [22]) and look at how the scalarization criterion is modified by m_ϕ.

In Fig. 3.1, we trace out the marginally-scalarized configuration on the m_ϕ^2–$B\sqrt{M_\star}$ plane where $M_\star$ denotes the mass of the NS (see Sec. 3.3.2 for more details on defining stellar mass). We observe that the critical coupling strength B for scalarization correlates approximately with the squared mass of the scalar field, and the relation depends only slightly on the specific stellar mass. For the considered EOS, we find the fitting formula

$$\left(\frac{m_\phi}{1.6\times 10^{-11}\,\text{eV}}\right)^2 \approx 1 - 2.52x + 1.54x^2, \tag{3.23}$$

where

$$x = \left(\frac{B}{10}\right)\left(\frac{M_\star}{1.4\,M_\odot}\right)^{1/2}. \tag{3.24}$$

Therefore, for a given scalar mass, the critical coupling strength is approximately a function of $M_\star$. In particular, the critical coupling strength B_crit for massless ST theories is solved as

$$B_\text{crit}^{m_\phi=0} \approx 9.6\left(\frac{M_\star}{1.4\,M_\odot}\right)^{-1/2}. \tag{3.25}$$

We see also that the critical coupling strength increases monotonically with m_ϕ (i.e., $\partial B_\text{crit}/\partial m_\phi >$

0). This tendency continues up to the mass large enough to eliminate scalarization for any coupling strength [385]. For NSs whose typical radius is ~ 10 km, mass of $m_\phi \gtrsim 2\times 10^{-11}\,\mathrm{eV}$ severely suppresses scalarization in NSs since the associated Compton length is shorter than the stellar size. We thus only consider masses smaller than this limit.

In addition, the presence of scalar hair provides extra supporting force, thus sustaining more matter for a given stellar mass (the meaning of stellar mass will be further clarified in Section 3.3.2), i.e., the stellar rest mass

$$M_{\mathrm{b}} = \int \rho u^t \sqrt{-g} d^3x \tag{3.26}$$

is larger for stronger scalarization. As an illustration, assuming $m_\phi = 1.33\times 10^{-11}\,\mathrm{eV}$, EOS APR4, and $M_\star = 1.35\,M_\odot$, one has $M_{\mathrm{b}} = 1.5021\,M_\odot$ for $B = 15.5$, while M_{b} increases by $0.015\,M_\odot$ for $B = 17$.

3.2.5 Current Constraints

Pulsar-timing observations in NS-WD binaries [33, 197, 419] or in galactic NS-NS binaries [287] can constrain the parameters of ST theories based on scalar-wave emissivity (assuming $m_\phi \lesssim 10^{-19}\,\mathrm{eV}$). In fact, the ST theory with a massless scalar field and a high coupling constant $B \gtrsim 9$ (i.e., $\beta_{\mathrm{DEF}} \lesssim -4.5$) is ruled out by the network of pulsar systems [128, 538]. However, a tiny value of $m_\phi > \lambdabar_{\mathrm{gw}}^{-1}$ (here $\lambdabar_{\mathrm{gw}}$ denotes the wavelength of scalar waves which is comparable to the gravitational wavelength) can account for the absence of scalar radiation and the reason is as follows. The propagation group speed of scalar waves (v_g) with the frequency ω_{gw} can be approximately written as

$$v_g = \sqrt{1 - m_\phi^2 \omega_{\mathrm{gw}}^{-2}} = (1 + m_\phi^2 \lambdabar_{\mathrm{gw}}^2)^{-1/2}, \tag{3.27}$$

where we note that the relation between the wavelength and frequency is $\lambdabar_{\mathrm{gw}} = (\omega_{\mathrm{gw}}^2 - m_\phi^2)^{-1/2}$. This speed is much slower than the speed of light for $\lambdabar_{\mathrm{gw}} \gg \lambdabar_{\mathrm{comp}}$, thus essentially prohibiting the scalar-wave emission (e.g., [28, 398]).

Aside from the scalar-wave emissivity, the gravitational field around scalarized NSs can be appreciably different from that in GR within a few times of $\lambdabar_{\mathrm{comp}}$ (see Fig. 3.2 below). Accordingly, the orbital motion around the scalarized NS should be modified for orbital separations comparable with $\lambdabar_{\mathrm{comp}}$. Such modification is, however, not seen in the observations. A small value of the mass $m_\phi \gg 1/a\,(\sim 10^{-16}\,\mathrm{eV}$ for observed NS-WD systems) is then necessary to circumvent the current observational constraint if the NSs are scalarized (e.g., [385]). We note that this mass range can also accommodate what is observed from the triple system PSR J0337+1715 [416] (see Fig. 2 therein). In addition, simultaneous mass-radius measurements by monitoring rotating hot spot patterns of pulsars can also probe the theory parameters [152, 497], while the constraints obtained in this way are currently weaker than the aforementioned ones.

The tensorial gravitational waveforms observed for a BNS can constrain the theory by measuring the scalar-radiation-induced phase shift [378]. For the specific event GW170817, the observation does not support significant scalar effects in inspiral stages [331, 537], while the induced/dynamical scalarization in late-inspiral-to-merger phase remains unconstrained due to the insufficient sensitivity to the late inspiral waveform. An upper limit of $B \lesssim 9-9.4$ is thus suggested for *massless* scalar field if the two NSs are slowly rotating (cf. Fig. 13 in [537]; we note again that their parameter is $\beta = -B/2$). This constraint substantially prevents spontaneous scalarization in NSs. In order to revive the existence of scalarized NSs, the Compton length-scale has to be much smaller than the constraint from the pulsar systems, because the orbital separation of inspiraling BNSs in the range of GW observations is quite small, within $\sim$ 20–200 km. However, the scalar effects in this regime is not trivial, so that the present numerical work is required; see Sec. 3.4 for more details.

Although much less stringent, the gravitational phenomena in the solar system (e.g., Shapiro time delay measured by Cassini tracking) put constraints on the scalar mass $m_\phi \gtrsim 10^{-17}\,\mathrm{eV}$ [28, 365]. Possible constraints on the massive theories may also be placed by extreme mass-ratio inspirals (EMRIs) where superradiance modifies orbital dynamics [109], e.g., with the presence of floating orbits on resonance ‘islands’ [535], thus leading to phase shifts in gravitational waveforms (much similar to the ramification of non-Kerr black hole spacetimes [155, 156]). However, it has recently been pointed out that the scalar imprint in the waveforms may be indistinguishable from GR waveform baselines for $m_\phi \lesssim 4 \times 10^{-12}\,\mathrm{eV}$ [49].

3.3 Virial theorem, tensor mass, and asymptotic behavior of the geometry

In the present article, we assume the conformally flat (Isenberg-Wilson-Mathews [253, 515]) approximation (see [199, 445, 501, 502] for a construction without this approximation), helical symmetry, and maximal slicing (i.e., $K = 0$) for the spacetime. The quasi-equilibrium states in this formalism satisfy the viral relation [99, 199, 432, 445]. Thus, we will validate the numerical solutions of the quasi-equilibria by the virial theorem, which is described for massive ST theory in Sec. 3.3.1. We then define the tensor mass in Sec. 3.3.2, which characterizes the physical mass of the system.

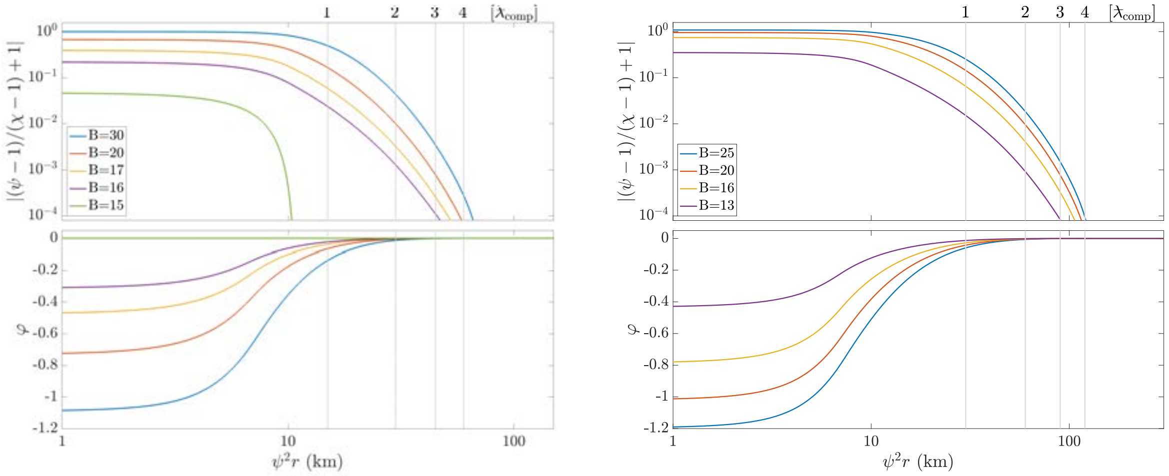

Figure 3.2: Relevant properties of isolated NSs in ST theories: Deviation between $(\psi-1)$ and $(\chi-1)$ as a function of the areal radius $\psi^2 r$ (top) and the profile of the scalar field (bottom) for NSs with $M_\star = 1.35\,M_\odot$. Theories with $\lambdabar_{\rm comp} = 15\,{\rm km}$ ($m_\phi = 1.33\times10^{-11}\,{\rm eV}$; left) and $\lambdabar_{\rm comp} = 30\,{\rm km}$ ($m_\phi = 6.65\times10^{-12}\,{\rm eV}$; right) are considered. For each scalar mass, four coupling strengths are adopted and listed in the legend. Note that the NS for $B = 15$ and $\lambdabar_{\rm comp} = 15\,{\rm km}$ is not scalarized, and thus, the geometry is the same as in GR. Vertical lines mark the first four times of the associated Compton length-scale. The stellar radius (areal radius) for this model is $\approx 11.1\,{\rm km}$.

3.3.1 Virial theorem

Given that the asymptotic behavior of the scalar field in the Einstein frame reads

$$\bar{\varphi} = \bar{\varphi}_0 + \frac{M_{\bar{\varphi}}}{r} e^{-m_\phi r} + O(r^{-2}), \tag{3.28}$$

we have the following relations for $r \to \infty$,

$$\varphi = \varphi_0 + \frac{\sqrt{B} M_{\bar{\varphi}}}{r} e^{-m_\phi r} + O(r^{-2}). \tag{3.29}$$

Since φ approaches φ_0 exponentially at $r \to \infty$, the scalar charges $\sqrt{B} M_{\bar{\varphi}}$ does not contribute to the mass in the system. Thus, the virial relation is written in the same form as in GR (cf. [432])

$$M_{\rm K} = M_{\rm ADM}, \tag{3.30}$$

where $M_{\rm ADM}$ is the Arnowitt–Deser–Misner (ADM) mass and $M_{\rm K}$ denotes the Komar mass defined by

$$M_{\rm K} = -\frac{1}{4\pi\phi_0} \oint_\infty dS_a n_b \phi \nabla^a \xi^b, \tag{3.31}$$

where we have assumed the existence of a timelike Killing vector ξ^a fulfilling $n_a \xi^a = -\alpha$.

3.3.2 Tensor Mass

As the ADM mass in the Einstein frame decreases monotonically when GWs propagate away and is positively defined [309, 411, 412], we refer it to the mass of a given system following, e.g., [165, 432], and define it as the tensor mass $M_{\rm T}$ to be distinguishable from the ADM mass in the Jordan frame ($M_{\rm ADM}$). As a specific example, the stellar mass refers to the tensor mass of a NS, i.e., $M_\star = M_{\rm T}$. In the massless ST theories, the tensor mass is written as the sum of the ADM mass and scalar charge [309]. As mentioned in Sec. 3.3.1, the scalar charge does not contribute to the mass of the system in the massive ST theories. Thus, we simply have $M_{\rm T} = M_{\rm ADM}$. If the virial theorem is satisfied, the tensor mass is also equal to the Komar mass.

3.3.3 Asymptotic behavior of the geometry

In GR, the asymptotic behavior of ψ and χ at a large distance in isotropic coordinates is described as (e.g., [199])

$$\psi = 1 + \frac{M_{\rm ADM}}{2r} + O(r^{-2}), \tag{3.32a}$$

$$\chi = 1 - \frac{2M_{\rm K} - M_{\rm ADM}}{2r} + O(r^{-2}). \tag{3.32b}$$

Thus, the equality

$$(\psi - 1)r = -(\chi - 1)r, \tag{3.33}$$

holds at $r \to \infty$, if the virial relation is satisfied. For spherical stars in equilibrium, this relation is satisfied for the entire region outside the stellar surface, $r = R_\star$, because of the presence of Birkhoff's theorem in GR [89, 258].

By contrast, Eq. (3.33) is satisfied only at $r \to \infty$ in ST theories because the scalar clouds contribute to ψ and χ in a different way. The deviation from the equality of Eq. (3.33) outside the star is considered as a manifestation of ST theories. In particular, we plot in Fig. 3.2 the violation of the equality of $\psi - 1 = 1 - \chi$ (upper panels) and the profile of φ (lower panels) for spherical NS models with $M_\star = 1.35\,M_\odot$. Two scalar masses are considered with the associated Compton length-scale being $\lambdabar_{\rm comp} \simeq 15\,{\rm km}$ (left) and $30\,{\rm km}$ (right). By picking several values of B for each value of m_ϕ, we consider NSs scalarized to different extents. We see that the equality (3.33) holds for $r \gg \lambdabar_{\rm comp}$, while the deviation can be $\gtrsim 10^{-2}\%$ for $\psi^2 r \lesssim 4\lambdabar_{\rm comp}$ where the amplitude of the scalar field is appreciably non-zero. This clearly indicates that the presence of the scalar cloud can appreciably modify the binary motion if the orbital separation is smaller than a few times of $\lambdabar_{\rm comp}$.

It is also found that for larger values of B, the maximum value of $|\varphi|$ is larger, and as a result, the region, in which the equality of Eq. (3.33), is breached is wider. Thus, for larger

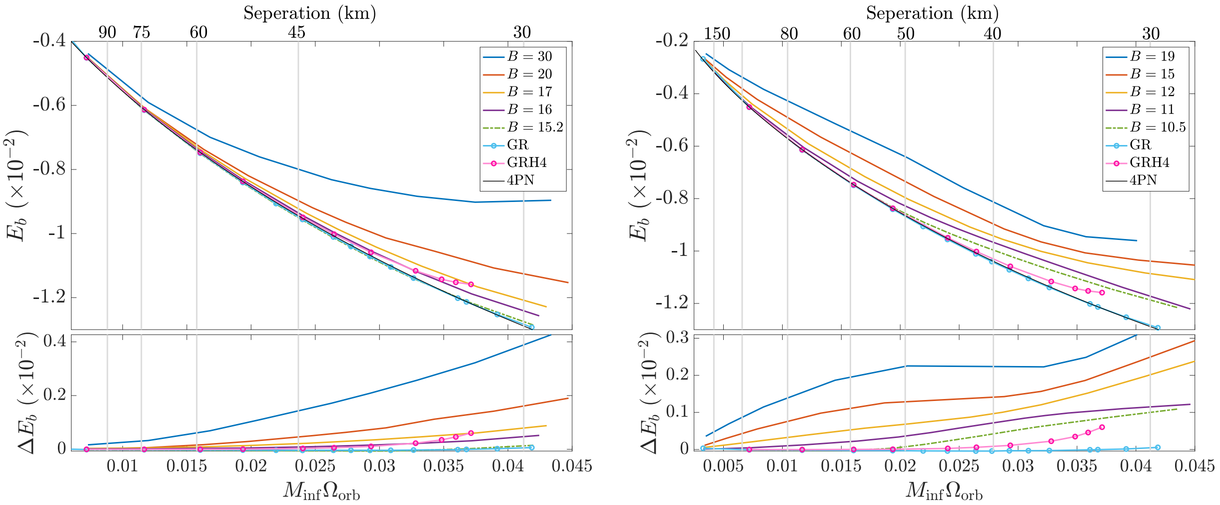

Figure 3.3: Quasi-equilibrium sequences for symmetric binaries with each NS having $1.35\,M_\odot$. The binding energy is plotted as a function of orbital frequency in the top, while the deviation of various theories from the 4PN analytic estimates of GR is shown in the bottom. Two EOS have been adopted for GR sequences, viz. APR4 (blue-circle) and H4 (pink-circle), while two scalar masses, $m_\phi = 1.33 \times 10^{-11}$ eV (left; $\lambda\!\!\!^{-}_{\rm comp} \simeq 15$ km) and $m_\phi = 4 \times 10^{-12}$ eV (right; $\lambda\!\!\!^{-}_{\rm comp} \simeq 50$ km), are considered for ST sequences. Depending on different ST parameters, scenarios of dynamical enhancement of the scalarization (colorful solid) and dynamical scalarization (dash-dotted) manifest. The vertical gray lines relate the binary separation and $M_{\rm inf}\Omega_{\rm orb}$ based on the GR sequence.

values of B, the scalar could modify the binary motion from a larger distance (see Sec. 3.4.1).

3.4 Binary neutron stars in quasi-equilibria

The major purpose of this Chapter is to clarify in which cases the effect of the scalarization of NSs can be identified by observing GWs from inspiraling BNSs. Given that the current GW detectors are able to detect signals for $f \approx 20$–10^3 Hz, where the separation between the members of a BNS is less than $\sim 200\,$km (for NS masses of $\sim 1.4 M_\odot$), the scalar mass of interest will then be

$$m_\phi \geq 1 \times 10^{-12}\,\text{eV}, \tag{3.34}$$

associated with Compton length scales of $\leq 200\,$km. We consider $m_\phi = 4 \times 10^{-12}\,$eV ($\lambda\!\!\!^{-}_{\rm comp} \approx 50\,$km) and $m_\phi = 1.33 \times 10^{-11}\,$eV ($\lambda\!\!\!^{-}_{\rm comp} \approx 15\,$km) as two canonical cases to demonstrate the role played by the scalar mass, as well as coupling strength, in the last several orbits of BNSs. To model the hydrodynamical equilibria of NSs, we adopted the piecewise-polytropic approximated EOS APR4 [386]. The details of our implementation are essentially the same as those in [485], and thus we will not repeat them here.

Denoting the tensor masses of the two NSs when they were in isolation as $M_{\star,1}$ and $M_{\star,2}$, the total mass $M_{\rm inf} = M_{\star,1} + M_{\star,2}$ is kept constant along each binary sequence. In

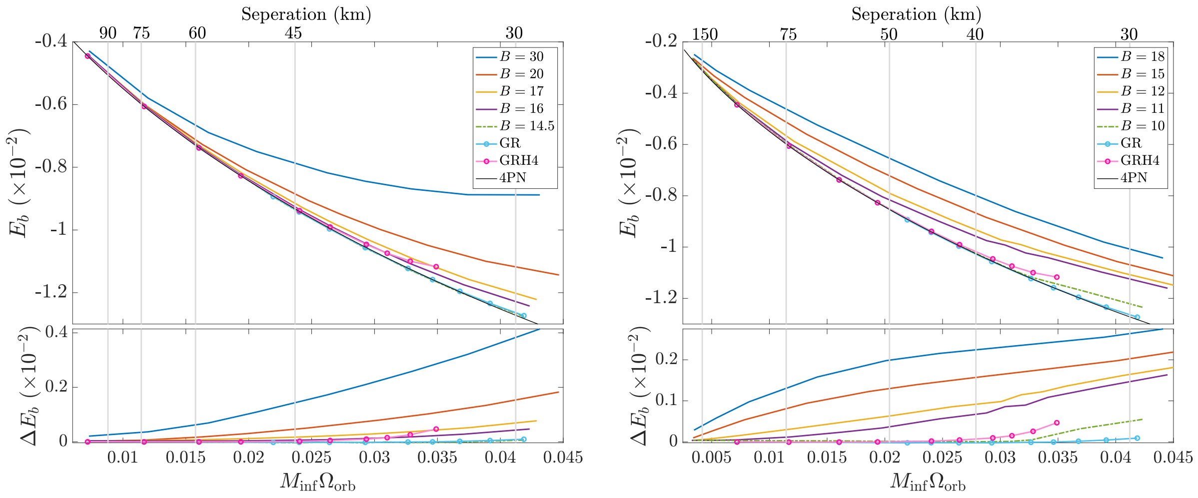

Figure 3.4: Same as Fig. 3.3, but for asymmetric binaries with $1.5\,M_\odot + 1.2\,M_\odot$.

this work, we choose $M_{\rm inf} = 2.7\,M_\odot$, while consider two values for the mass ratio, viz. $q = M_{\star,2}/M_{\star,1} = 1$ and 0.8. Each quasi-equilibrium state on a particular sequence is characterized by a dimensionless orbital angular velocity $M_{\rm inf}\Omega_{\rm orb}$ and the orbital binding energy defined by

$$E_{\rm b} = \frac{M_{\rm T} - M_{\rm inf}}{M_{\rm inf}}. \tag{3.35}$$

We compare the curves of $E_{\rm b}$ as a function of $M_{\rm inf}\Omega_{\rm orb}$ with that in GR and identify the effect of the scalar field. Specifically, we will show that the scalar-related dynamical response in the late time can noticeably expedite the merger (Sec. 3.4.2), while the orbital frequency at the last orbit increases only slightly compared to the GR value [255, 260] (see also Section 3.4.3).

The quality of the constructed configurations is examined by checking the violation of Eq. (3.30), i.e.,

$$\mathcal{E}_{\rm virial} = \frac{|M_{\rm K} - M_{\rm ADM}|}{M_{\rm ADM}}, \tag{3.36}$$

which has been found to be less than 0.06% for our results. In addition, we evolved some of the obtained quasi-equilibrium states with our numerical code (developed from the previous code [450]) for a few orbits to validate our ID solver. We confirmed that the BNSs have quasi-circular orbits with a small eccentricity of 10^{-2}, which is approximately the same magnitude as that in [486].

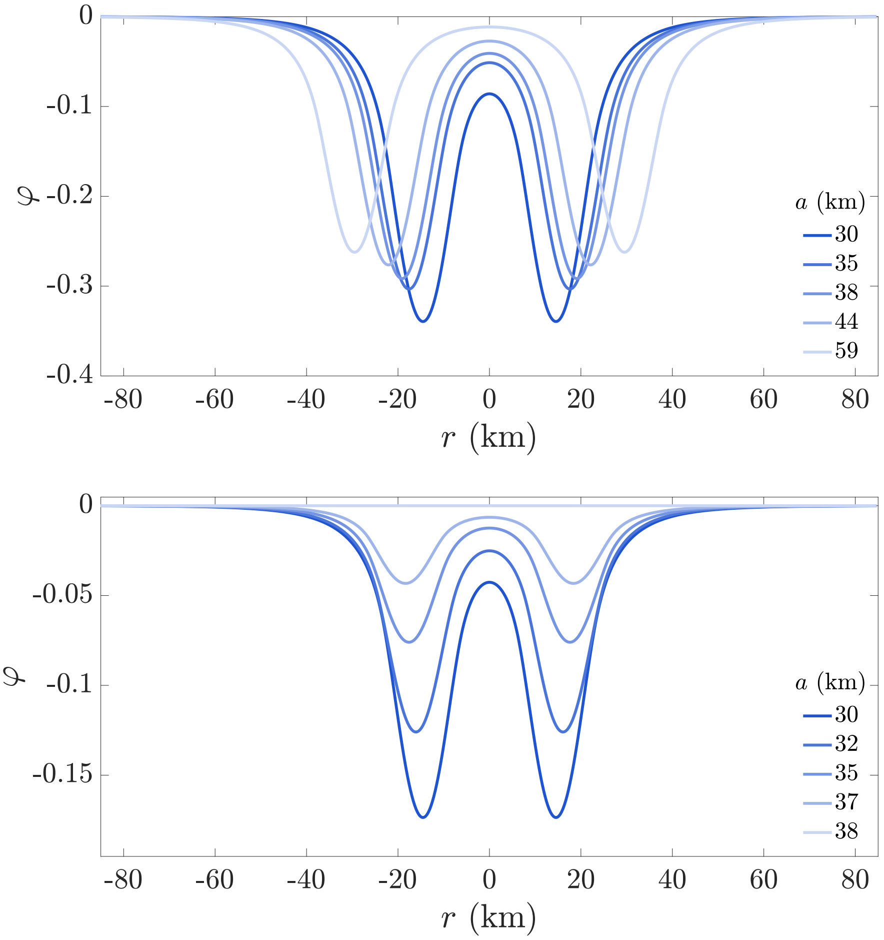

Figure 3.5: Radial profile of the scalar field for equal-mass binaries at different stages, undergoing enhancement of scalarization (top) and dynamical scalarization (bottom). The color is darker for closer separation with the orbital separation a listed in the legend. The coupling strengths are set to $B = 15.8$ (top) and $B = 15.2$ (bottom), respectively, while the scalar mass is assumed to be $m_\phi = 1.33 \times 10^{-11}$ eV. We adopt the APR4 EOS for NSs.

3.4.1 Quasi-equilibrium sequences

In Figs. 3.3 and 3.4, we plot the binding energy of binaries as a function of their orbital frequency. To represent the evolution track of a BNS, at least to the leading order, the rest mass of binaries is constant along each sequence [500], while we note that it may vary from one sequence to another depending on B and m_ϕ (see Sec. 3.2.4). The virial violation (3.36) for the constructed binaries is at most 0.06%, i.e., much smaller than the absolute value of the orbital binding energy. In both figures, we also show the GR curve (solid-circle) constructed by the original FUKA library [363] for the EOS APR4 (light blue) and H4 (pink), and 4th order post-Newtonian (PN) approximation [78, 93] to clarify the scalar imprints. The deviation of the numerically constructed sequences from the 4PN prediction is denoted by ΔE_b (bottom panels). Estimating the adiabatic tidal contribution by the difference between the GR sequence and the 4PN estimates, we see that scalar effects are similar to the enhanced tidal response for equal-mass binaries, so that systems with a soft EOS in ST theory could accidentally be identified as GR binaries with a *stiffer* EOS (see also below).

For each considered scalar mass, we choose 4 coupling strengthes that admit spontaneous scalarization (solid), as well as one slightly below the critical value (dashed-dotted). The former leads to the scenario of dynamical enhancement of the scalarization at a close orbit, resulting from the scalar-cloud interaction (see the upper panel of Fig. 3.5), while for the latter, the scenario is similar to the so-called dynamical scalarization (see the lower panel of Fig. 3.5), although the mechanism of the scalar-field enhancement is identical for both cases. The dynamical scalarization takes place for an orbital separation of $a \lesssim 1.7\lambda\!\!\!^{-}_\mathrm{comp}$, slightly outside the Compton length scale, while the dynamical enhancement of the scalarization can do for more distant orbits of $a \lesssim 3$–$6\lambda\!\!\!^{-}_\mathrm{comp}$ mainly contingent on the scalar mass. This enhancement starts at more distant orbits for larger values of B. The reason for this enhancement of the scalar fields outside the Compton length-scale is that even though the scalar field amplitude of one star decays exponentially outside that scale, it still has an appreciable value along the line connecting to its companion when the orbital separation is close enough. The same applies to the scalar field in the companion. The interaction between the tails of the scalar field induces a phenomenon similar to dynamical scalarization, leading to the enhancement of the scalar cloud around each NS. We note that for lower values of B with which the maximum amplitude of the scalar field is low, i.e., $\varphi \lesssim 10^{-2}$, the enhancement of the scalar amplitude does not appreciably take place.

It is worth noting that BNSs follow the same evolution track as in GR even if spontaneously scalarized NS is present when $a \gtrsim 3$–$6\lambda\!\!\!^{-}_\mathrm{comp}$ for the cases considered here, viz. $m_\phi = 1.33 \times 10^{-11}$ eV (left panels) and $m_\phi = 4 \times 10^{-12}$ eV (right panels) cases. This critical distance within which the scalar imprint reveals matches well with the size of the scalar cloud of an isolated NS (Fig. 3.2). During this epoch [Stage (I) defined in Sec. 3.1], the scalar-wave emission is also negligible because the relation $\lambdabar_{\rm gw} > \lambdabar_{\rm comp}$ is satisfied, and therefore, the ST theory is likely indistinguishable from GR. This indicates that for $\lambdabar_{\rm comp} \lesssim 10\,{\rm km}$ (i.e., $m_\phi \gtrsim 2 \times 10^{-11}\,{\rm eV}$), the orbital evolution in this ST theory agrees with that in GR.

As the binary separation shrinks to $a \lesssim 3$–$6\lambdabar_{\rm comp}$ while $\lambdabar_{\rm gw}$ is still larger than $\lambdabar_{\rm comp}$ [Stage (II)], we can observe the bifurcation of scalarized sequences from GR ones in both figures, though the scalar-emission is expected to be highly suppressed by the scalar mass. This m_ϕ-induced suppression will however be eventually avoided when the binary evolves to Stage (III). The difference between (II) and (III) cannot be seen in quasi-equilibrium sequences since the radiation is approximately ignored in construction. In a future work, we will revisit this aspect.

A word of caution is appropriate here. The curves of $E_{\rm b}$ for a non-zero mass m_ϕ cases are similar to those in GR assuming a stiffer NS EOS, where the NS radius (i.e. tidal deformability) is high enough (see e.g., [485]). For example, we plot in Fig. 3.6 the deviation from 4PN binding energy for a sequence of a particular ST theory with the EOS APR4, and for a GR sequence with the EOS H4, for which the tidal deformability is about 3.5 times larger than that for EOS APR4 [246]. We see that the two curves coincide when $M_{\rm inf}\Omega_{\rm orb} < 0.03$, indicating that the effect of the scalar-field interaction entangles with that of the NS EOS until late-inspiral. On the other hand, the curves of $E_{\rm b}$ for $m_\phi = 4 \times 10^{-12}$ eV cannot be reproduced by the NS EOS effect because the deviation from the GR curve sets in at a distant orbit. An approximate estimate taking into account the previous GR studies (e.g., [485]) gives that the tidal effect of the NS is appreciable only for $M_{\rm inf}\Omega_{\rm orb} \gtrsim 0.02$ (i.e., an orbital separation of $\sim 50\,{\rm km}$) for a NS with a radius of $\sim 15\,{\rm km}$. Therefore, if $\lambdabar_{\rm comp} \gtrsim 20\,{\rm km}$, the scalar-field interaction effect may be distinguished from the NS EOS effect assuming that the NS radius is less than $14\,{\rm km}$ [6, 16]. This suggests that by observing GWs from BNSs, the mass of the scalar field could be bounded from below for a hypothetically high value of B.

3.4.2 Cycles in gravitational waveform

The above conclusion can be further evidenced by looking at the number of cycles, $\mathcal{N}$, from a given orbital frequency up to merger. Here we estimate $\mathcal{N}$ in an adiabatic manner by integrating the orbital frequency along the quasi-equilibrium states. Following [485, 486], we express the energy balance equation as

$$\frac{dE_{\rm b}}{dt} = -\mathcal{F}, \tag{3.37}$$

whereby the orbit shrinks at the rate,

$$\frac{d\Omega_{\rm orb}}{dt} = -\frac{\mathcal{F}}{dE_{\rm b}/d\Omega_{\rm orb}}. \tag{3.38}$$

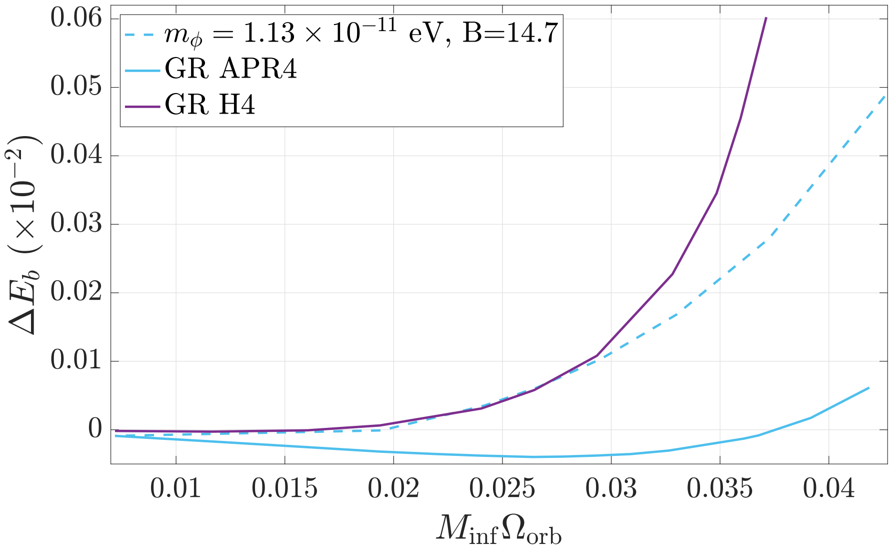

Figure 3.6: Deviation from 4PN approximant in the binding energy as a function of orbital frequency. Two EOSs, APR4 (blue curves) and H4 (purple curve), are employed. Einstein's gravity is assumed for both EOSs (solid curves), on top of which the curve of one specific ST theory with EOS APR4 is overplotted (dash-dot curve).

Binary components	$(m_\phi,\, B)$	$\mathcal{N}$
$1.35M_\odot + 1.35M_\odot$	(0.03, 10.5)	25.66
	(0.03, 11)	24.62
	(0.03, 12)	23.33
	(0.03, 15)	21.86
	(0.03, 19)	19.80
	(0.1 , 15.2)	27.27
	(0.1 , 16)	26.65
	(0.1 , 17)	25.92
	(0.1 , 20)	22.13
	(0.1 , 30)	21.13
$1.5M_\odot + 1.2M_\odot$	(0.03, 10)	27.46
	(0.03, 11)	24.60
	(0.03, 12)	23.74
	(0.03, 15)	22.34
	(0.03, 18)	20.60
	(0.1 , 14.5)	27.71
	(0.1 , 16)	27.34
	(0.1 , 17)	26.64
	(0.1 , 20)	24.60
	(0.1 , 29)	20.84

Table 3.1: Number of cycles when the binary evolves during $f_{\rm gw} = 240$–957 Hz for a variety of ST parameters. In this table we present the dimensionless scalar mass with a note that $m_\phi = 0.1 = 1.33 \times 10^{-11}$ eV.

.

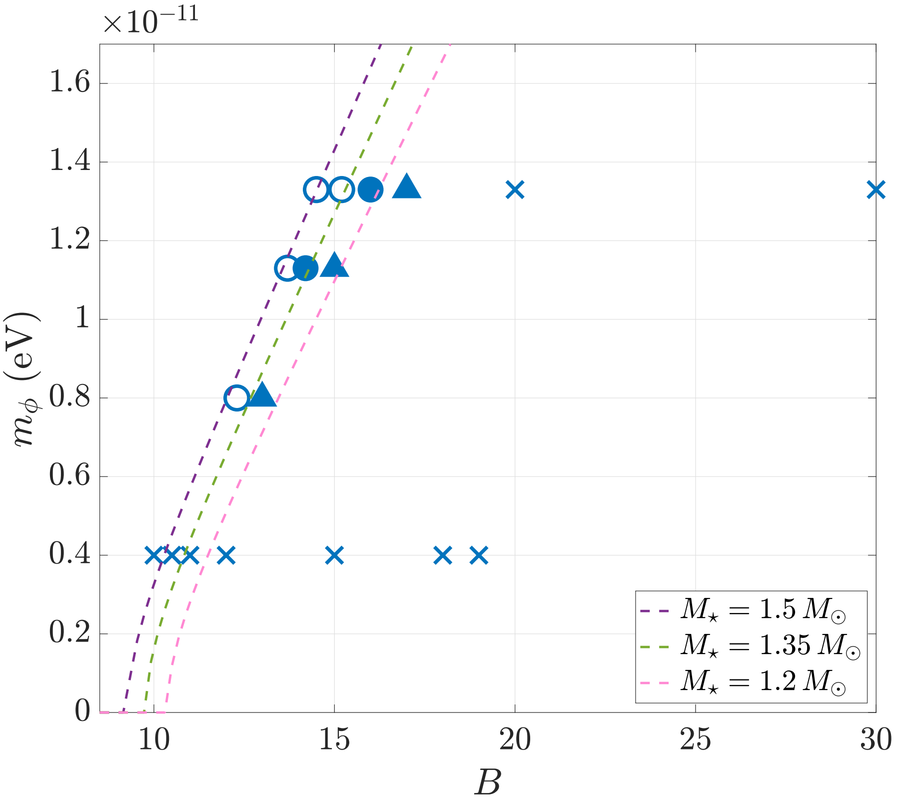

Figure 3.7: Parameter space of the considered massive ST theory. Relation (3.23) for stellar masses of $1.5\,M_\odot$ (purple), $1.35\,M_\odot$ (green), and $1.2\,M_\odot$ (pink) are plotted as dashed lines. The markers present the viability of the corresponded ST theory after GW170817 especially for binaries with spontaneously scalarized NSs (filled markers). Specifically, circles (crosses) denote (un)acceptable parameters concerning with the two chosen binary configurations, while triangle marks the theory only allowed by the $1.5\,M_\odot + 1.2\,M_\odot$ binary.

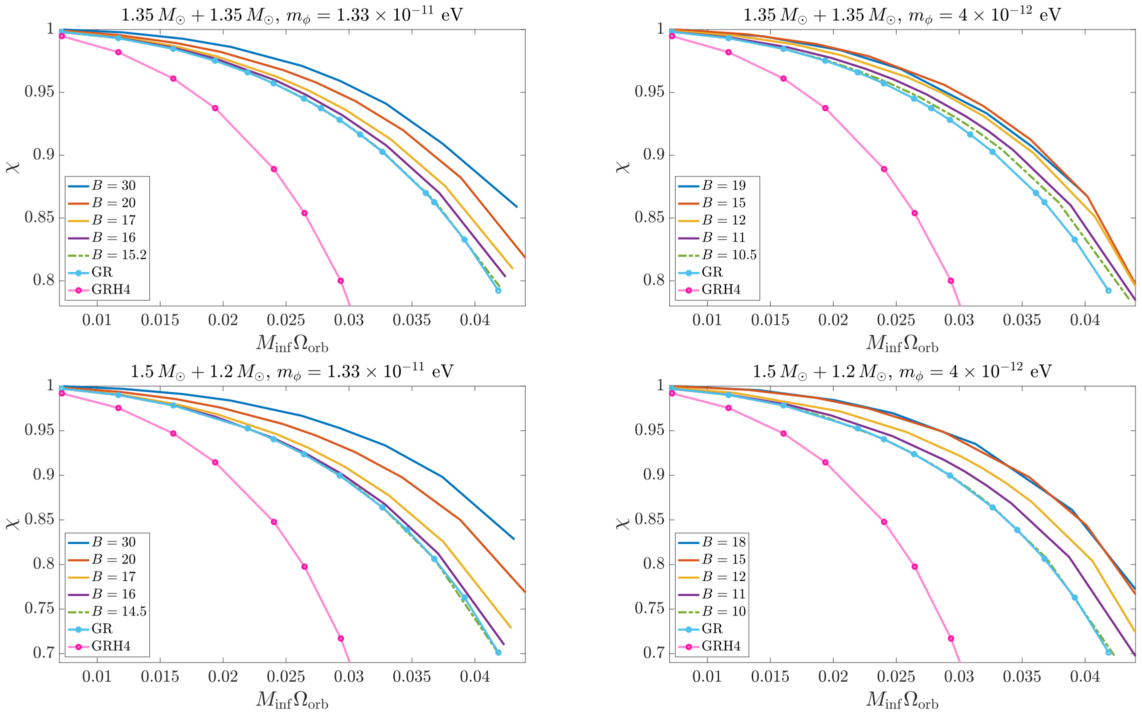

Figure 3.8: Mass-shedding indicator as a function of orbital frequency for binaries $1.35\,M_\odot + 1.35\,M_\odot$ (top) and $1.5\,M_\odot + 1.2\,M_\odot$ (bottom). Sequences with dynamical enhancement of the scalarization are shown as solid curves, those with dynamical scalarization as dashed-dotted curves, and the GR sequence is the dotted-solid curve. The ARP4 EOS is employed to model NSs.

An orbit number of

$$\begin{aligned}\mathcal{N} &= \frac{1}{2\pi}\int \frac{\Omega_{\rm orb}}{d\Omega_{\rm orb}/dt}\,d\Omega_{\rm orb}\\ &= -\frac{1}{2\pi M_{\rm inf}}\int \frac{x^{3/2}}{\mathcal{F}(x)}\frac{dE_{\rm b}}{dx}\,dx\end{aligned}$$

will accumulate during the inspiral when the orbital frequency evolves from $\Omega_{\rm i}$ to $\Omega_{\rm e}$, where we introduce $x = (M_{\rm inf}\Omega_{\rm orb})^{2/3}$. In numerical integration of Eq. (3.39), we adopt the ansatz (cf. Eq. (68) of [485]),

$$E_{\rm b} = E_{\rm b}^{\rm 4PN} + a x^6 + b x^7 + c x^8, \tag{3.39}$$

to fit the derivative of binding energy with respect to $\Omega_{\rm orb}$. Here we adopt 4PN result of the binding energy as the principle part ($E_b^{\rm 4PN}$; Eq. (5.6) of [78]), and a, b, and c are the fitting coefficients. In our consideration of energy flux, we ignore the scalar radiation based on two reasons: (i) the emissivity of such radiation is limited over most of the orbital evolution, and (ii) the energy lost via scalar channel is already subdominant to that via traditional GW in the massless ST theory as estimated by [486], let alone the situation in massive ST theory. Therefore, we adopt the 3.5PN approximation for the energy flux, which is given by

(Eq. (314) of [92])

$$
\begin{aligned}
\mathcal{F} = \frac{32}{5}\nu^2 x^5 \Bigg\{ & 1 + \left(-\frac{1247}{336} - \frac{35}{12}\nu\right) x + 4\pi x^{3/2} + \left(-\frac{44711}{9072} + \frac{9271}{504}\nu + \frac{65}{18}\nu^2\right) x^2 \\
& + \left(-\frac{8191}{672} - \frac{583}{24}\nu\right)\pi x^{5/2} + \Bigg[\frac{6643739519}{69854400} + \frac{16}{3}\pi^2 - \frac{1712}{105}\gamma_{\mathrm{E}} - \frac{856}{105}\ln(16x) \\
& + \left(-\frac{134543}{7776} + \frac{41}{48}\pi^2\right)\nu - \frac{94403}{3024}\nu^2 - \frac{775}{324}\nu^3\Bigg] x^3 \\
& + \left(-\frac{16285}{504} + \frac{214745}{1728}\nu + \frac{193385}{3024}\nu^2\right)\pi x^{7/2} \Bigg\},
\end{aligned}
\tag{3.40}
$$

where $\nu = q/(1+q)^2$ is the symmetric mass ratio.

Regulating the upper and lower limits of the integration such that the associated GW frequencies are $f_{\mathrm{gw}} \simeq 240$ Hz ($M_{\mathrm{inf}}\Omega_{\mathrm{orb}} = 0.01$) and $f_{\mathrm{gw}} \simeq 957$ Hz ($M_{\mathrm{inf}}\Omega_{\mathrm{orb}} = 0.04$), we list the accumulated GW cycles in Tab. 3.1. The almost stiffest and softest EOS that are allowed by GW170817 have been estimated to be H4 and APR4, respectively, through the analysis where GR is assumed as the theory of gravity [8]. We, however, adopt them to elaborate possible constraints on the ST theory that could be placed by this event. The number of cycles obtained in GR are 27.45 and 26.24 for APR4 and H4, respectively, for $q = 1$, while there are 27.71 and 26.03 cycles for $q = 0.8$. Therefore, the uncertainty in the EOS can also be interpreted as the ambiguity of the gravity theory if the resulted $\mathcal{N}$ in a certain ST theory lies between those for EOS APR4 and H4.

Together with cases with other values of m_ϕ not shown in the table, our results are summarized in Fig. 3.7 where the circles and crosses denote the acceptable and unacceptable parameters with respect to the observational results of GW170817. Focusing on systems involving spontaneously scalarized NSs (filled markers), we see that scalar mass of $m_\phi \leq 10^{-11}$ eV can hardly account for the variation due to EOS, and thus are disfavored after GW170817 in the event that one of the NSs is spontaneously scalarized. It is also interesting to note that there are some parameters allowed by $1.5\,M_\odot + 1.2\,M_\odot$ binaries that are exhibited by equal-mass binaries, and thus a more stringent constraint is concluded from the cases with $q = 1$. For systems with small mass ratio, the scalarization in the lighter star is much weaker than that in the heavier star, and thus the strength of scalar interaction between the binary is inconsequential. This somehow contradicts the intuitive feeling that one gained from the experience that the more strict constraint is obtained from increasingly asymmetric binaries when analysing the pulsar timing observations in the massless theory, where the emissivity of the scalar wave will not be switched off by the scalar mass. Here, instead, the merger is accelerated due to the excess in the lost of orbital energy when developing scalar cloud in the binary.

3.4.3 Mass-shedding Criterion

The contact of the two NSs could be understood as the moment when one of them loses the feature of being individual. An indicator of such loss of integrity is the formation of a cusp along the direction towards the companion, which can be quantitatively assessed through the ratio between the radial gradient of enthalpy at the pole and at the equatorial point facing the companion [221, 485]. In particular, a dimensionless factor [221],

$$\chi_{\rm ms} = \left(\frac{\partial \ln h}{\partial r}\right)_{\rm eq} \left(\frac{\partial \ln h}{\partial r}\right)^{-1}_{\rm pole} , \tag{3.41}$$

is useful to identify cusp formation: $\chi_{\rm ms} = 1$ for static NSs, while $\chi_{\rm ms} = 0$ when the cusp is constituted. Since spectral methods cannot resolve well the NS if a cusp is formed at the region closest to the companion, it is unfeasible to construct a configuration with $\chi_{\rm ms} \ll 1$. In addition, conformal flatness is unlikely to be a fair approximation at very close orbits. In this work, the closest configurations we generated are at a stage less than 1 orbit, i.e., $\lesssim 2$ ms, before merger.

Figure 3.8 shows the mass-shedding indicator $\chi_{\rm ms}$ as a function of the orbital frequency for the symmetric (top panels) and asymmetric (bottom panels) binaries under our consideration. Several features are observed, including (i) the binaries pertaining to the stiffer EOS H4 start to contact at a lower orbital frequency since the tidal effect is more pronounced; (ii) dynamical scalarization does not affect much $\Omega_{\rm orb}$ at the onset of mass shedding; (iii) the deformation indicator χ at a given $\Omega_{\rm orb}$ is less for increasingly scalarized configuration, which is due to the extra attractive force provided by the scalar field, and is in line with the finding of [450] that the central density of NS components keep increasing until merger while a decrease is seen shortly before the merger in GR. However, for the viable ST parameters summarised in Fig. 3.7, the onset of mass-shedding is not sizeably affected by scalar effects.

3.5 Discussion

In order to consistently investigate the constraints that could be obtained from observed gravitational waveforms, a detailed understanding of the dynamics during late-inspiral-to-merger is requisite. Owing to the non-linearity manifesting in this regime, numerical-relativity simulation is crucial and serves as the unique tool for this purpose. Constructing quasi-equilibrium states as ID is therefore the first step for the accurate modelling of the gravitational waveforms. We provided reliable ID of binaries consisting of two spontaneously scalarized NSs in massive ST theories since a massless scalar field is excluded by pulsar-timing observations for theories with a high coupling constant B. The scalar mass gives rise to certain hurdles in solving the elliptic-type equation (3.20) due to the exponentially-decaying behavior of the scalar field [Eq. (3.28)]. An auxiliary scalar field ξ is introduced for better treatment by the spectral code FUKA [363], and is solved for according to the modified equation (3.22).

For equilibrium states of binaries generated here, the asymptotic equality (3.30), dictated by the virial theorem, is met within 0.06%, and some of them have been evolved for a few orbits to reaffirm that the quasi-circular motion is guaranteed. The constructed binary configurations thus provide the essential setup for future numerical-relativity study of BNSs in massive ST theories. In addition to future use, qualitative characteristics of the scalar influence can be readily extracted by comparing the equilibria to GR ones. In particular, it is confirmed that the quasi-equilibrium sequences in the ST theory are indistinguishable from that in GR until the orbital separation becomes approximately 3–6 times the Compton length scale of the scalar field, i.e., $a \gtrsim 3\text{–}6\lambdabar_{\rm comp}$. Then, at $a \sim 3\text{–}6\lambdabar_{\rm comp}$, the enhancement of the scalar field sets in due to the interaction of the scalar clouds of the two NSs (Figs. 3.3 and 3.4). Accordingly, the gravitational fields will be modified, resulting in the deviation of the quasi-equilibrium sequences from GR.

To quantify the deviation of sequences in ST from those in GR, we estimate the number of cycles in GWs accumulating over a certain range of orbital frequency [Eq. (3.39)]. The tolerance in the stiffness of EOS concluded from GW170817 roughly spans over from the EOS APR4 to H4 [4, 16], and thus we adopt the EOS APR4 to derive conservative bounds on the ST parameters, provided that the scalar effects contribute to waveforms in a similar way as tidal effects (Fig. 3.6). We found that the cycles undergone by GWs indeed decrease with a stronger scalar cloud (Tab. 3.1) and/or a stiffer EOS. The error budget in $\mathcal{N}$ defined by the EOS APR4 to H4 can thus be translated to the upper bound on the scalar-induced dephasing in waveforms. Comparing the cycles of ST binaries pertaining to the EOS APR4 to those of GR binaries following the EOS H4, our results are summarised in Fig. 3.7, where a lower bound of $m_\phi \gtrsim 10^{-11}\,\mathrm{eV}$ can be reckoned. We also noticed that the most stringent limit is placed by equal-mass binaries, implying that the derived constraint on the scalar mass assuming a spontaneously scalarized NS is in part of the BNS should be robust even though we do not span over a wide range of mass ratio. For $m_\phi \gtrsim 10^{-11}\,\mathrm{eV}$ and a mild coupling strength $B \lesssim 17$, the scalar-cloud interaction effect is not appreciable during the inspiral stage of BNSs despite that both members are scalarized, and can be seen only when the binary is just outside the last stable orbit. The onset of mass-shedding for plausible ST theories essentially matches to the GR cases (cf. Figs. 3.7 and Fig. 3.8).

It is important to note yet another layer of complication for the degeneracy between tidal effects, both adiabatic [146] and dynamical ones, and the late enhancement of scalarization, either dynamically triggered or through interacting scalar clouds as suggested by Figs. 3.3 and 3.4 (see also [323]). It has been known that NSs' tidal response will be modified in ST theories with a massless scalar field so that (i) the tidal effect will appear at 3PN order [145] or even at 1PN order [179] in the case of dynamical scalarization, (ii) the Love number will increase or decrease depending on the compactness and the ST parameters [112, 248, 362, 528], and (iii) a novel class of Love number is introduced by the scalar field, leading to, e.g., dipolar tidal effects [77, 504]. Relevant studies in the massive ST theory have not been addressed to our knowledge, and a numerical study of scalar-induced modulation in finite-size effects will constitute an essential step toward testing ST theories with GW physics. In this series of investigation, we hope to address this issue to some extent.

Chapter 4

Properties of post-merger remnants

Contents

Breakdown of Contribution

This chapter is based on the publication: "*Binary neutron star mergers in massive scalar-tensor theory: Properties of postmerger remnants*" in Phys.Rev.D 110 (2024) 10, 104018 [305] by **A. T.-L. Lam**, H.-J. Kuan, M. Shibata, K. V. Aelst and K. Kiuchi. I extended the code `SACRA-MPI` developed by M. Shibata and K. Kiuchi to the massive scalar-tensor theory. All the numerical simulations of the binary neutron stars mergers were carried out by me. The initial data used in the simulations were constructed by me and H.-J. Kuan using the code developed by K. V. Aelst. I analysed the data and generated all the figures. H.-J. Kuan, M. Shibata and K. Kiuchi provided constructive comments on the manuscript written by me.

Overview

In this Chapter, we investigate the properties of post-merger remnants of binary neutron star mergers in the framework of Damour-Esposito-Farese-type scalar-tensor theory of gravity with a massive scalar field by numerical relativity simulation. It is found that the threshold mass for prompt collapse is raised in the presence of the excited scalar field. Our simulation results also suggest the existence of long-lived $\phi-$mode in hypermassive neutron stars due to the presence of the massive scalar field which enhances the quasi-radial oscillation in the remnant. We investigate the descalarization condition in hypermassive neutron stars and discover a distinctive signature in post-merger gravitational waves.

4.1 Introduction

After the monumental event GW170817 [4, 5, 6, 265], huge effort has been devoted to modeling the physics involved in the course of binary neutron star (BNS) mergers with the hope of learning more about the nuclear equation of state (EOS) of matters in extreme environment, exploring r-process nucleosynthesis in the merger ejecta, and understanding the non-linear nature of gravity. In particular, through measuring the size of matter effects of the neutron star (NS) members in the late inspiral stages for this event, the stiffness of the EOS has been constrained to a narrow range [8, 35, 121, 147, 162]. In addition, general relativity (GR) has been proven to reproduce gravitational effects accurately, at least up to the stage shortly before the merger. Considering the Damour-Esposito-Farese type extension to GR (DEF theory in what follows), this can be translated to an upper bound on the coupling constant, which prohibits spontaneous scalarization in isolated NSs for massless scalar field [537] while admitting of mild scalarization for massive cases as shown in Chapter 3. A plausible agent to push the known constraints further is the remnant system in the aftermath of the merger, where higher-energy physics, for which details have not been yet understood, can play an important role. The evolution process of BNS remnants is also the key determinant of multimessenger signals [79, 431]: the properties of the electromagnetic (EM) signals depend strongly on the mass and the composition of ejecta from the remnant including some ultra-relativistic jets [267], and post-merger gravitational waves (GWs) encode information about BNS parameters [245, 276, 428].

Joint detection of EM and GW signals provides a unique avenue to learn the details of post-merger systems such as the lifetime of the remnant NSs. The latter quantity is sensitive to the EOS and underlying gravitational theory. Although GR functions quite well throughout the inspiral history of binaries, beyond-GR signatures may reveal shortly before, during, and after the merger. For example, the DEF theory can admit dynamical scalarization and/or enhanced scalar cloud in the parameter region corresponding to GW170817 as mentioned in Chapter 3. Besides, the additional scalar degree of freedom can lead to qualitative differences in the post-merger waveform, and impact the evolution of the object produced in the merger. The goal here is thus to extensively investigate the outcomes of BNS mergers in the DEF theory, whereas magnetic, neutrino, and thermal physics are not taken into account as we focus on the post-merger stage only for a short timescale.

In most BNS mergers, either a hypermassive neutron star (HMNS, which is stabilized by a high degree of angular momentum with a differential rotation [57, 425, 441]) is formed and lives for some time before collapsing to a black hole, or a prompt collapse occurs if the total mass of the BNS exceeds a threshold $M_{\rm thr}$. The threshold mass for the prompt collapse is sensitive to the nuclear EOS [431, 439]. On the other hand, it is expected to be rare that a supramassive NS is produced from a BNS since the total mass of the system should be less than the maximum mass that is supportable by rigid rotation (M_c). An empirical relation of such critical value is $M_c \simeq 1.2 M_{\rm TOV}$ with $M_{\rm TOV}$ the maximum mass of a spherical cold NS of a given EOS [134, 135, 136], which then suggests $M_c \lesssim 2.6\, M_\odot$ (e.g., [394, 452]). Some population studies thus suggest that only $\lesssim 15\%$ of BNSs has a total mass lower than M_c [185] (see also [487]). In the present work, we focus on scenarios with total mass larger than M_c, i.e., a black hole + torus will be formed either shortly after the merger or after the rotational profile is modified within the HMNS [168, 243].

The presence of a torus surrounding the black hole plays an essential role in determining the post-merger emissions, such as short gamma ray bursts [277, 439] and kilonovae [133, 140, 203, 268]. The amount of matter ejected to form the torus depends strongly on the total mass, and the nuclear EOS for both prompt collapse and HMNS formation scenarios [160, 242, 244, 276] (see also [431] for a review). In the latter scenario, the lifetime of HMNS, $\tau_{\rm H}$, is the main factor that determines the torus mass especially when the BNS is of (nearly) equal mass, since the matter injection from the central object ceases upon the formation of the black hole [243].

It has been known that the value of $\tau_{\rm H}$ for short-lived HMNSs is determined primarily by the BNS's total mass if the system is moderately symmetric (e.g., [64, 79, 242, 264, 286, 439]) in GR. Under the framework of the DEF theory, the lifetime of HMNSs is also likely to be sensitive to the scalar parameters, which are the strength of the coupling (B) of the scalar field to the metric functions, and the mass of the scalar field (m_ϕ). In addition to their lifetime, the scalar field can also exist in the HMNSs for a certain time, $\tau_{\rm S} (\leq \tau_{\rm H})$. Depending on $\tau_{\rm H}$, three possibilities for the outcome are generically expected: (i) prompt collapse to a black hole, (ii) short-lived HMNS formation, and (iii) long but finite lived HMNS formation. In the presence of an excited scalar field in the DEF theory, $\tau_{\rm S}$ further divides channel (iii) into (iii.a) long-lived scalarized HMNSs and (iii.b) those descalarizing at some point. The two characteristic time-scales are dependent on the source and theory parameters, namely, the total mass and mass ratio of the BNSs, ($M_{\rm tot}$, q), the EOS, B, and m_ϕ. The main goal of the present study is to investigate how the two crucial timescales are modified by the scalar quantities by performing numerical-relativity simulations for equal-mass BNSs.

This Chapter is organized as follows. Section 4.2 briefly introduces the DEF theory, the associated $3+1$ decomposition for numerical evolution, the EOS employed, the details of the numerical setup, and the parameters we consider in this work. In Section 4.3 we discuss in detail the post-merger scenarios including the formation of a long-lived HMNS, a short-lived

HMNS, and prompt collapse to a black hole, and investigate the effect of the scalar field on the HMNS lifetime and the threshold mass. The properties of the remnant including dynamical ejecta, GW signal, mass of the final black hole and disk with potential quantities relevant to observation are given in Section 4.4. Section 4.5 is devoted to summary and discussion. Throughout this Chapter, the reduced Plank constant set to $\hbar = 1$.

4.2 Formalism

4.2.1 Evolutionary Equations

The associated equations for the metric and scalar fields in the DEF theory are written in Eqs. (3.6) and (3.7). Since we evolve the scalar field quantity $\varphi := \sqrt{2\ln\phi}$ rather than ϕ, we rewrite Eq. (3.7) in terms of φ as

$$\nabla_a\nabla^a\varphi = 2\pi\phi^{-1}BT\varphi - \varphi(\nabla_c\varphi)(\nabla^c\varphi) + m_\phi^2\varphi\phi, \tag{4.1}$$

which will be used to derive the evolution equation for the auxiliary scalar field.

The evolution equations for gravitational and scalar fields can be derived by 3+1 decomposition (see Ref. [450] for the detailed derivation in the massless DEF case). Following the Baumgarte-Shapiro-Shibata-Nakamura (BSSN) formalism [55, 433], we can obtain the modified evolution equations in the Cartesian coordinates as follows [298]:

$$(\partial_t - \beta^k\partial_k)W = \frac{1}{3}W\left(\alpha K - \partial_k\beta^k\right), \tag{4.2a}$$

$$(\partial_t - \beta^k\partial_k)\tilde{\gamma}_{ij} = -2\alpha\tilde{A}_{ij} + \tilde{\gamma}_{ik}\partial_j\beta^k + \tilde{\gamma}_{jk}\partial_i\beta^k - \frac{2}{3}\tilde{\gamma}_{ij}\partial_k\beta^k, \tag{4.2b}$$

$$\begin{aligned}(\partial_t - \beta^k\partial_k)\tilde{A}_{ij} = {} & W^2\left[\alpha R_{ij} - D_iD_j\alpha - 8\pi\alpha\phi^{-1}S_{ij}\right]^{\mathrm{TF}} + \alpha\left(K\tilde{A}_{ij} - 2\tilde{A}_{ik}\tilde{A}_j{}^k\right)\\ & + \tilde{A}_{kj}\partial_i\beta^k + \tilde{A}_{ki}\partial_j\beta^k - \frac{2}{3}\tilde{A}_{ij}\partial_k\beta^k + \alpha\tilde{A}_{ij}\varphi\Phi\\ & - \alpha W^2\left[\omega\varphi^2 D_i\varphi D_j\varphi + \phi^{-1}D_iD_j\phi\right]^{\mathrm{TF}},\end{aligned} \tag{4.2c}$$

$$\begin{aligned}(\partial_t - \beta^k\partial_k)K = {} & 4\pi\alpha\phi^{-1}(S^i{}_i + \rho_{\mathrm{h}}) + \alpha K_{ij}K^{ij} - D_iD^i\alpha\\ & + \alpha\omega\varphi^2\Phi^2 - \left(\frac{3}{2} + \frac{1}{B}\right)\alpha m_\phi^2\varphi^2\phi\\ & + \alpha\phi^{-1}\Big[D_iD^i\phi - K\Phi\phi\varphi - 3\pi\varphi^2 BT + \frac{3}{2\varphi^2\phi}\left(\Phi^2\phi^2\varphi^2 - D_k\phi D^k\phi\right)\Big],\end{aligned} \tag{4.2d}$$

$$\begin{aligned}(\partial_t - \beta^k\partial_k)\tilde{\Gamma}^i = {} & 2\alpha\left(\tilde{\Gamma}^i_{jk}\tilde{A}^{jk} - \frac{2}{3}\tilde{\gamma}^{ij}\partial_j K - \frac{3}{W}\tilde{A}^{ij}\partial_j W\right) \\ & - 2\tilde{A}^{ij}\partial_j\alpha - 2\alpha\tilde{\gamma}^{ij}\left[8\pi\phi^{-1}J_j - \varphi K_j{}^k D_k\varphi + \left(1 + \frac{2}{B} - \frac{\varphi^2}{2}\right)\Phi D_j\varphi + \varphi D_j\Phi\right] \\ & + \tilde{\gamma}^{jk}\partial_j\partial_k\beta^i + \frac{1}{3}\tilde{\gamma}^{ij}\partial_j\partial_k\beta^k - \tilde{\gamma}^{kl}\tilde{\Gamma}^j{}_{kl}\partial_j\beta^i + \frac{2}{3}\tilde{\gamma}^{jk}\tilde{\Gamma}^i{}_{jk}\partial_l\beta^l,\end{aligned} \tag{4.2e}$$

$$(\partial_t - \beta^k\partial_k)\varphi = -\alpha\Phi, \tag{4.2f}$$

$$\begin{aligned}(\partial_t - \beta^k\partial_k)\Phi = {} & -\alpha D_i D^i\varphi - (D_i\alpha)D^i\varphi - \alpha\varphi(\nabla_a\varphi)\nabla^a\varphi \\ & + \alpha K\Phi + 2\pi\alpha\phi^{-1}BT\varphi + \alpha m_\phi^2\varphi\phi.\end{aligned} \tag{4.2g}$$

We adopt the moving-puncture gauge Eq. (1.24) for the lapse function and shift vector. The Hamiltonian and momentum constraints are listed in Eqs. (3.15) and (3.16), and will not be repeated here.

In the Jordan frame, the scalar field does not affect the matter evolution explicitly, and thus, the equations of motion for matter are the same as those in GR. We assume a perfect fluid in form Eq. (3.9). In addition to Eq. (3.8), we solve the continuity equation, $\nabla_a(\rho u^a) = 0$.

4.2.2 Equation of state

We adopt the piecewise-polytropic approximation [386] for the barotropic EOS APR4 [23], MPA1 [347], and H4 [301], which cover a range of stiffness favored by GW170817 [8, 162, 186]. In addition, we adopt the following description for the thermal pressure, which is associated with the generation of shocks in the plunge and post-merger stages:

$$P = P_{\rm cold}(\rho) + P_{\rm th}(\rho, \epsilon), \tag{4.3}$$

where the cold contribution to the pressure, $P_{\rm cold}(\rho)$, is dictated by the cold EOS, and the thermal contribution is assumed to take the form [256]

$$P_{\rm th} = (\Gamma_{\rm th} - 1)\rho\epsilon_{\rm th}, \tag{4.4}$$

with the adiabatic index $\Gamma_{\rm th}$ for heated matter, and $\epsilon_{\rm th} = \epsilon - \epsilon_{\rm cold}$ is the residual in the specific internal energy that is not included in the cold EOS. In general, $\Gamma_{\rm th}$ depends on the temperature and rest mass density [62], while it has been suggested that a (reasonable) constant approximation suffices for investigating the fate of the merger remnant [64, 242, 446]. We choose $\Gamma_{\rm th} = 1.8$ for our simulations. Depending on the EOS and theory parameters, NSs in a coalescing BNS can remain unscalarized up to merger, be dynamically scalarized in the late inspiral, or be spontaneously scalarized at large separation [46, 361, 415, 450, 486].

4.2.3 Numerical setup

We implement the Z4c version of the evolution equations by extending the code developed in [526], which was parallellised to `SACRA-MPI` in [278]. `SACRA-MPI` employs a box-in-box adaptive mesh refinement with 2:1 refinement and imposes equatorial mirror symmetry on the $z = 0$ orbital plane. For the simulations shown in this article, each NS is covered by 4 comoving finer concentric boxes, with 6 coarser domains underneath containing both piles of the finer domains. The size of the finest domain is chosen to be about 1.3 to 1.5 times of NS radius. All domains are covered by $(2N, 2N, N)$ grid points for (x, y, z) with N being an even number. We employ the finite-volume scheme with a reflux prescription and Harten-Lax-van Leer contact (HLLC) Riemann solver, as that implemented in [281], for hydrodynamics evolution to better conserve the total baryon mass of the system.

For the outer boundary condition, we use the outgoing boundary condition for metric variables following [433] and specifically include an additional term for the scalar field variables $Q = (\varphi, \Phi)$ as

$$Q(t,r) = \left(1 - \frac{\Delta r}{r}\right) Q(t - \Delta t, r - \Delta r) e^{-m_\phi \Delta r}, \tag{4.5}$$

to capture the exponential decay tail due to the mass term m_ϕ. Here, $\Delta r = c\Delta t$ with Δt the time step in numerical computation. We test the convergence of our code in three different resolutions (see Section 4.6). Unless otherwise specified, we adopt $N = 94$ as the standard resolution of this Chapter which corresponds to $\Delta x = 157$ m in the finest box. The details of the numerical setup can be found in Table 4.1 in Section 4.6.

The primary purpose of this Chapter is to investigate how the scenarios of post-merger remnants depend on the binary mass, B, m_ϕ, and the EOS while restricting ourselves to equal-mass binaries. However, rather than specifying the binary mass as the sum of the ADM masses of the two NS members, we identify the binary mass as the total *rest mass*,

$$M_b := \int \rho u^t \sqrt{-g} d^3x, \tag{4.6}$$

contained in the binary. Taking into account the GW event GW170817, scalar masses of $m_\phi \gtrsim 10^{-11}$ eV are favored unless the coupling constant B is so small that the NSs in the observed system are non-scalarized as described in Chapter 3. This condition on m_ϕ is several orders of magnitude greater than the constraint concluded from the pulsar timing observations, which is $m_\phi \gtrsim 10^{-15}$ eV [150, 385, 527], while more rigorous Bayesian inference studies are required to transform the suggestion of $m_\phi \gtrsim 10^{-11}$ eV into a constraint (for strong couplings). On the other hand, a mass of $m_\phi \gtrsim 2 \times 10^{-11}$ eV would significantly suppress scalarization in NSs since the associated Compton length is shorter than the stellar size. Aiming to study the scalar's influence on BNS mergers, we focus on cases where NSs can

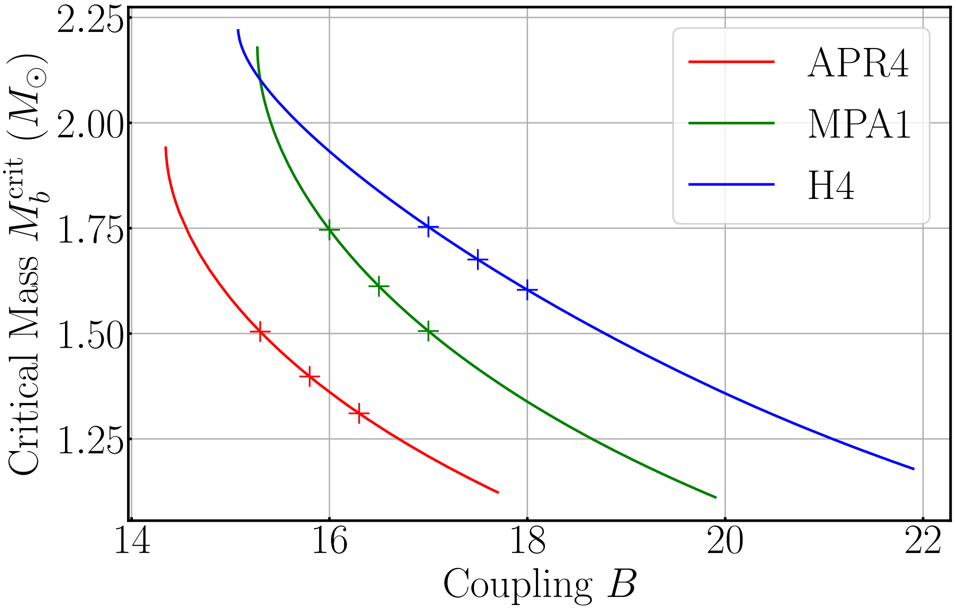

Figure 4.1: Critical baryon rest-mass of NSs that are marginally scalarized when isolated as functions of the coupling constant B for $m_\phi = 1.33 \times 10^{-11}$ eV. The plus markers indicate the coupling strength which we choose to generate the mass sequences for each EOS.

develop scalar cloud before and/or after merger, and thus the range of interest of m_ϕ is narrow. We will consider only one canonical value for the scalar mass, viz. $m_\phi = 1.33 \times 10^{-11}$ eV ($\lambda\!\!\!^{-}_{\rm comp} = 14.8$ km), to quantitatively study how B influences the lifetimes of the HMNSs ($\tau_{\rm H}$) and scalar cloud ($\tau_{\rm S}$) in post-merger systems.

For each EOS, we choose three different coupling strengthes B such that an isolated NS with $M_b = 1.60 M_\odot$ would be either non-scalarized, marginally scalarized or spontaneously scalarized as illustrated in Fig. 4.1. We explore a wide range of NS's baryon mass spanning from $1.60 M_\odot$ to $1.90 M_\odot$ as summarized in Section 4.7 with Tables 4.3 to 4.5 for APR4, MPA1 and H4 EOS, respectively, to investigate different outcomes of post-merger remnants. Each model is referred to in the manner of the example: `MPA1_B16.5_M1.70` corresponds to the equal mass binary with the MPA1 EOS, $B = 16.5$, and $M_b = 1.70 M_\odot$ for an individual NS. Since the coupling strengthes considered are not very strong, the ADM mass ($M_{\rm ADM}$) of the isolated NS deviates only slightly ($\lesssim 10^{-3}$ $M_\odot$) from the star having the same baryon mass in GR.

We construct the BNS initial data in a quasi-equalibrium state by generalizing the public spectral code FUKA [363] to the massive DEF theory. The BNS configurations are prepared with an initial separation of 44.31 km, with which the BNS models experience 3–5 orbits before merger. Note that in our numerical simulation, the virial error of the initial data defined by the relative difference of ADM mass and Komar mass, are always smaller than 0.04%. We refer the readers to Chapter 3 for the detailed initial data formulation for constructing quasi-equilibrium states of BNS in the massive DEF theory.

4.2.4 Gravitational Wave Extraction

The information of GWs emitted is obtained by extracting the complex Weyl scalar Ψ_4 in the local wave zone (see, e.g., [278, 280, 526] for details). The Weyl scalar Ψ_4 is decomposed into (l, m) modes with spin-weighted harmonics as

$$\Psi_4(t_{\rm ret}) = \sum_{l,m} \Psi_4^{l,m}(t_{\rm ret})_{-2}Y_{lm}(\theta, \phi), \tag{4.7}$$

where the retarded time $t_{\rm ret}$ is defined by [245, 278]

$$t_{\rm ret} := t - D - 2M_{\rm inf} \ln\left(\frac{D}{2M_{\rm inf}} - 1\right). \tag{4.8}$$

Here, $M_{\rm inf} := M_{1,\rm ADM} + M_{2,\rm ADM}$ is the total ADM mass of the isolated NSs separated at spatial infinity and D is the areal radius of the extraction sphere approximated as [278]

$$D \approx R_0 \left(1 + \frac{M_{\rm inf}}{2R_0}\right)^2, \tag{4.9}$$

by assuming isotropic coordinates of non-rotating black holes in the wave zone with R_0 being the corresponding coordinate radius. We evaluate Ψ_4 at the finite radius $R_0 = 480\ M_\odot \approx 709$ km and then analytically extrapolate the waveform toward null infinity by Nakano's method [317, 350, 351]. We shall focus only on the dominant $(l, |m|) = (2, 2)$ mode in this work because the contribution from other higher-multipole modes is minor for the equal-mass BNSs. The harmonic mode of GWs can be evaluated by integrating $\Psi_4^{l,m}$ twice in time given by

$$\begin{aligned} h^{l,m}(t_{\rm ret}) &= h_+^{l,m}(t_{\rm ret}) - ih_\times^{l,m}(t_{\rm ret}) \\ &= -\int^{t_{\rm ret}} dt' \int^{t'} \Psi_4^{l,m}(t'')dt'' \\ &= \int df' \frac{\tilde{\Psi}_4^{l,m}(f')}{(2\pi \max(f', f_{\rm cut}))^2} e^{2\pi i f' t_{\rm ret}}, \end{aligned} \tag{4.10}$$

where the last line shows the fixed frequency method of [389] we employed for the calculation and $f_{\rm cut}$ is the cutoff frequency set to be $0.8M_{\rm inf}\Omega_0/(2\pi)$ with Ω_0 being the initial angular velocity of the binary obtained from the initial data. The merger time $t_{\rm merge}$ is defined at the time of the peak GW strain $h^{2,2} := h_+^{2,2} - ih_\times^{2,2}$, where $h_+^{2,2}$ and $h_\times^{2,2}$ are the plus and cross polarization of $l = m = 2$ GWs, respectively. We also calculate the instantaneous frequency $f_{\rm GW}$ of the $(2, 2)$ mode by

$$f_{\rm GW} = \frac{1}{2\pi}{\rm Im}\left(\frac{h^{*2,2}\dot{h}^{2,2}}{|h^{2,2}|^2}\right), \tag{4.11}$$

where the asterisk and dot symbols denote the complex conjugate and the time derivative, respectively. The interval between $t_{\rm merge}$ and the apparent horizon formation time $t_{\rm AH}$ defines the lifetime of HMNSs (i.e., $\tau_{\rm H} := t_{\rm AH} - t_{\rm merge}$), and the lifetime of the scalar cloud, $\tau_{\rm S}$, is determined by the interval between the merger and the descalarization in the HMNSs (if at all).

We obtain the amplitude of the Fourier spectrum of GWs following [242, 276]

$$\tilde{h}(f)^{2,2} = \sqrt{\frac{|\tilde{h}_{+}^{2,2}(f)|^2 + |\tilde{h}_{\times}^{2,2}(f)|^2}{2}}, \tag{4.12}$$

from the Fourier transforms of plus $\tilde{h}_{+}^{2,2}(f)$ and cross $\tilde{h}_{\times}^{2,2}(f)$ polarization of GWs with f being the GW's frequency. The dimensionless effective amplitude $h_{\rm eff}(f)$ of GWs is defined by

$$h_{\rm eff}(f) := f\tilde{h}^{2,2}(f). \tag{4.13}$$

The propagation group velocity of scalar waves (v_g) is stretched by m_ϕ, and the dispersion relation is given by [40, 294] (see also Chapter 3)

$$v_g = \left(1 + m_\phi^2 \lambda_{\rm gw}^2\right)^{-1/2}, \tag{4.14}$$

with $\lambda_{\rm gw}$ being the wavelength of the scalar wave. For $\lambda_{\rm gw} \gg \lambda_{\rm comp}$, the speed of scalar waves is much lower than the speed of light, and thus, essentially prohibiting the emission of scalar waves [29, 398]. In this work, we consider a zero asymptotic value for the scalar field ($\varphi_0 = 0$), and consequently, scalar waves do not couple to the interferometer leaving no extra mode such as the breathing and longitude modes in emitted GWs.

4.3 Post-merger scenarios

In GR, the final fate of the post-merger remnant of BNSs depends primarily on the total mass and the EOS, while the mass of dynamical ejecta and the torus formed around the post-merger black hole (if at all) should be also sensitive to the mass ratio [160, 393, 444]. In terms of the HMNS's lifetime, we categorise the final outcome of BNS mergers into three different scenarios:

1. prompt collapse to black hole,
2. short-lived HMNS formation ($\tau_{\rm H} < 10$ ms),
3. long-lived HMNS formation ($\tau_{\rm H} > 10$ ms),

where the criteria of 10 ms is a subjective choice. On top of the above categorization for

BNS remnants, the presence of a scalar field introduces more variety in the final states (see Fig. 4.2).

All the possible outcomes are showcased in Fig. 4.3, where the evolution of the relative difference of maximum rest-mass density,

$$\delta\rho_{\max} := \rho_{\max}(t)/\rho_{\max}(t=0) - 1, \tag{4.15}$$

and the maximum scalar-field amplitude[1],

$$\varphi_{\text{amp}} := \text{sgn}(\varphi)\max(|\varphi|), \tag{4.16}$$

are plotted for four selected models with MPA1 EOS and scalar-field parameters $(B, m_\phi) = (16, 1.33 \times 10^{-11}\text{ eV})$. We briefly summarize all the possible scenarios of the scalar field evolution according to Fig. 4.3, and leave the in-depth discussion to the following sections. In the pre-merger phase, the scalar field can be excited if the NSs are compact enough to undergo spontaneous scalarization (blue and yellow lines) or dynamical scalarization (green line). Otherwise, the scalar field remains insignificant up to merger (red line). As we will show in Section 4.3.3, the scalarization history of the BNS plays an important role in the prompt-collapse threshold mass. In the post-merger phase, depending on the final mass of the HMNS, it can either be spontaneously scalarized (red) or "descalarize" after a certain time to form an oscillating scalar cloud with appreciable amplitude. In the case where black holes are formed (blue and yellow), the scalar field does not dissipate away entirely, and an oscillating scalar cloud forms from the fossil scalar field instead. Although we will discuss different outcomes of BNS mergers based on the lifetimes of the HMNS and the scalar cloud, it should be noted that these timescales are not to be taken as exact for simulated models. In fact, it is impossible to determine accurately the lifetimes in the numerical simulation in practice since the HMNS after the merger is close to a marginally stable state, and any small perturbation (including numerical errors) will alter its collapse time and thus the dynamics is extremely sensitive to the grid resolution. Thus, the values can be considered as an approximate estimate and the scenarios characterized by them are still qualitatively robust.

It can be noticed that the scalar field φ_{amp} experiences $\sim 10\%$ perturbation for scalarized binaries in the inspiral phase, which indicates that the scalar field has not yet perfectly reached the quasi-equilibrium state. One possible reason is the insufficient grid resolution to resolve the exponential falloff tail of the scalar field in our initial data solver. The other possible reason is that the zero scalar field "momentum" $\Phi = 0$ condition employed in our initial data formulation [294] described in Chapter 3 could possibly induce some initial perturbation in the system. While any initial perturbation of the scalar field in the massless

---

[1] Since the change of sign of $\varphi \to -\varphi$ does not alter the evolution of the system, we adopt the convention of negative value of φ when spontaneous scalarization happens. Therefore, we flip the sign of φ in the plots if positive φ arises when the HMNS is spontaneously scalarized unless φ experiences change of sign in the scalarization/descalarization process.

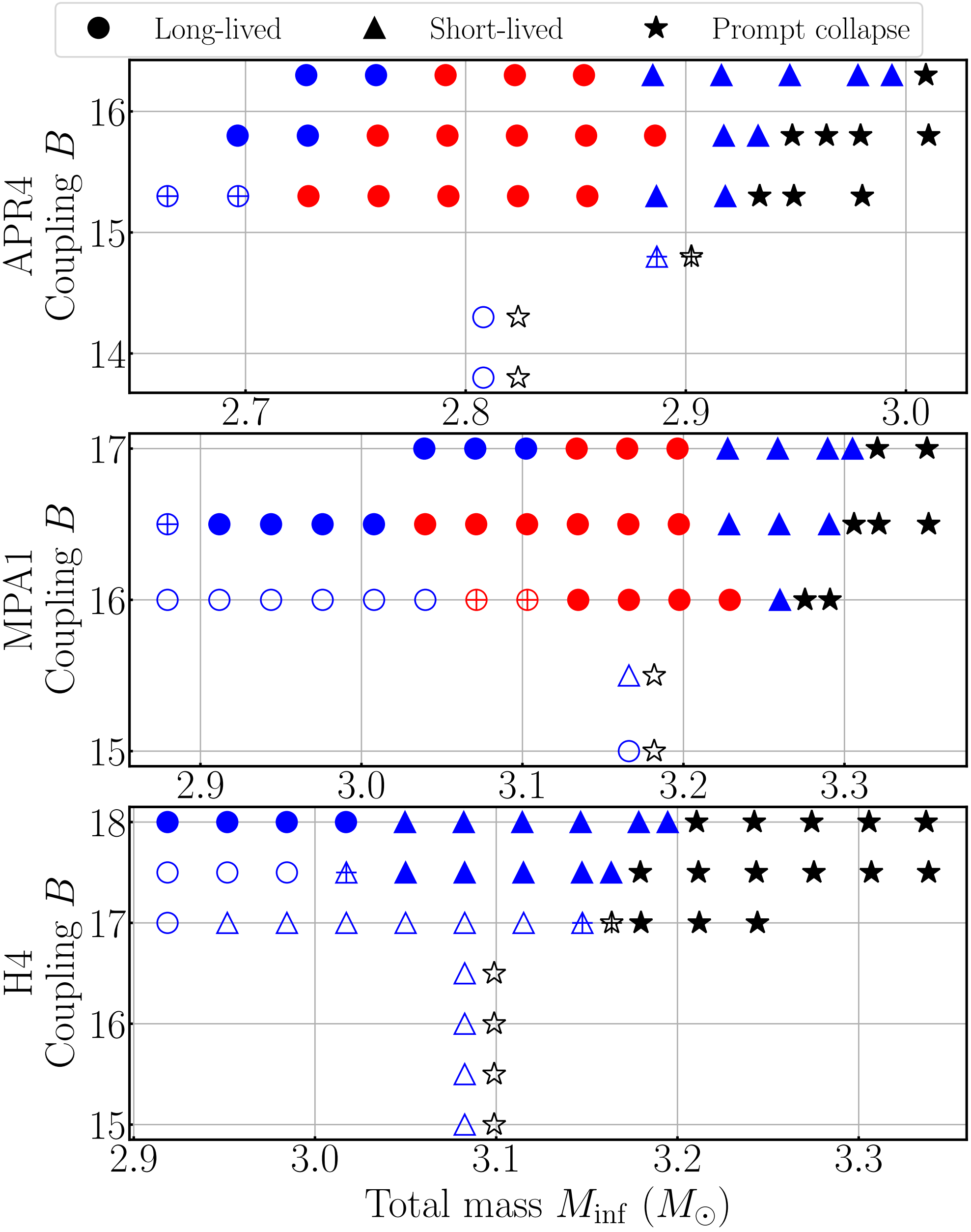

Figure 4.2: Summary of all the models in this work. The circle, triangle and black star markers represent the final fate of postmerger remnant as long-lived HMNSs, short-lived HMNSs, and prompt collapse to a black hole, respectively. The filled (resp. hollow) markers indicate the presence (resp. absence) of spontaneous scalarization for isolated NS while the plus markers indicate the occurrence of dynamical scalarization. The models that undergo descalarization are marked in the red color.

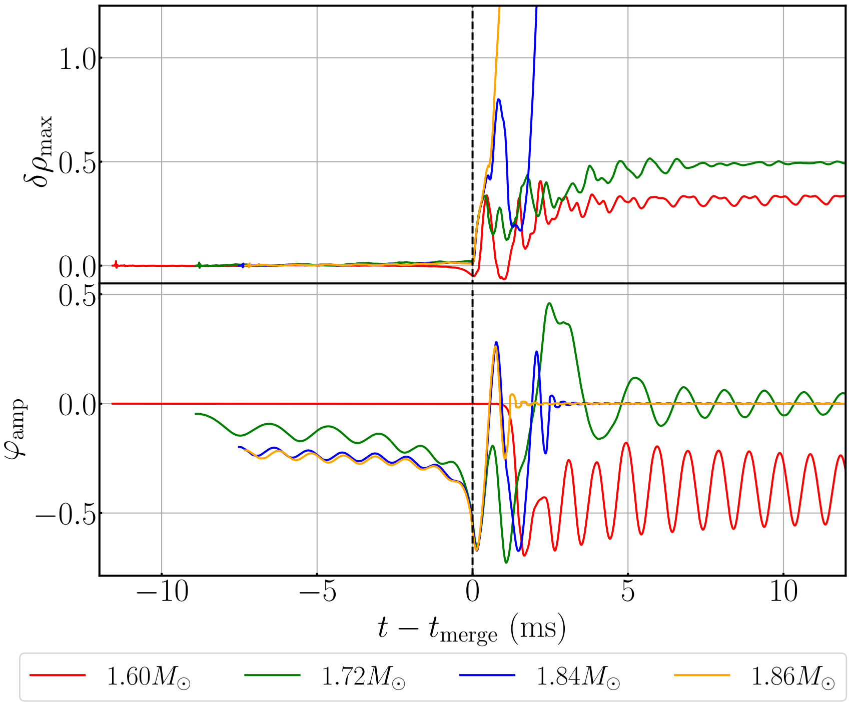

Figure 4.3: Evolution of the relative difference of maximum rest-mass density $\delta\rho_{\max} := \rho_{\max}(t)/\rho_{\max}(t=0)-1$ (top) and of the maximum scalar field amplitude $\varphi_{\rm amp}$ (bottom) with different initial baryon rest mass of individual NS with MPA1 EOS. The scalar-field parameters are set as $B = 16$ and $m_\phi = 1.33 \times 10^{-11}$ eV.

DEF theory [450, 486] can freely propagate out and dissipate quickly, in the presence of non-zero scalar mass m_ϕ perturbations with a wavelength smaller than the Compton wavelength will be trapped and remain in the vicinity of the system. Nonetheless, the initial perturbation of the rest-mass density $\delta\rho_{\max}$ is less than 1%, and hence, we believe that the effect of the scalar field perturbation is minor.

4.3.1 Long-lived neutron star remnant

We first recap the key criterion for spontaneous scalarization in a single star following [143, 298, 450], which is also useful in explaining the evolution of the scalar field in the HMNS. The onset of scalarization can be approximately described by taking the weak field limit of Eq. (4.1) with an average value of T within the star radius R, $\bar{T}$, as

$$(\Delta - m_\phi^2)\varphi = 2\pi B\bar{T}\varphi, \tag{4.17}$$

where Δ is the flat Laplacian. Denoting $k^2 := -(2\pi B\bar{T}+m_\phi^2)$, the conditions for scalarization are given as $k^2 > 0$ and $kR \to \pi/2$ for R the NS's radius [298, 450]. For the case of $B > 0$ and assuming that the relativistic corrections to matter are small (i.e., $\bar{T} \sim -\rho$), scalarization is likely to happen if $\bar{T} \sim -\rho < T_{\rm crit} := -m_\phi^2/(2\pi B)$. However, scalarization is unlikely to

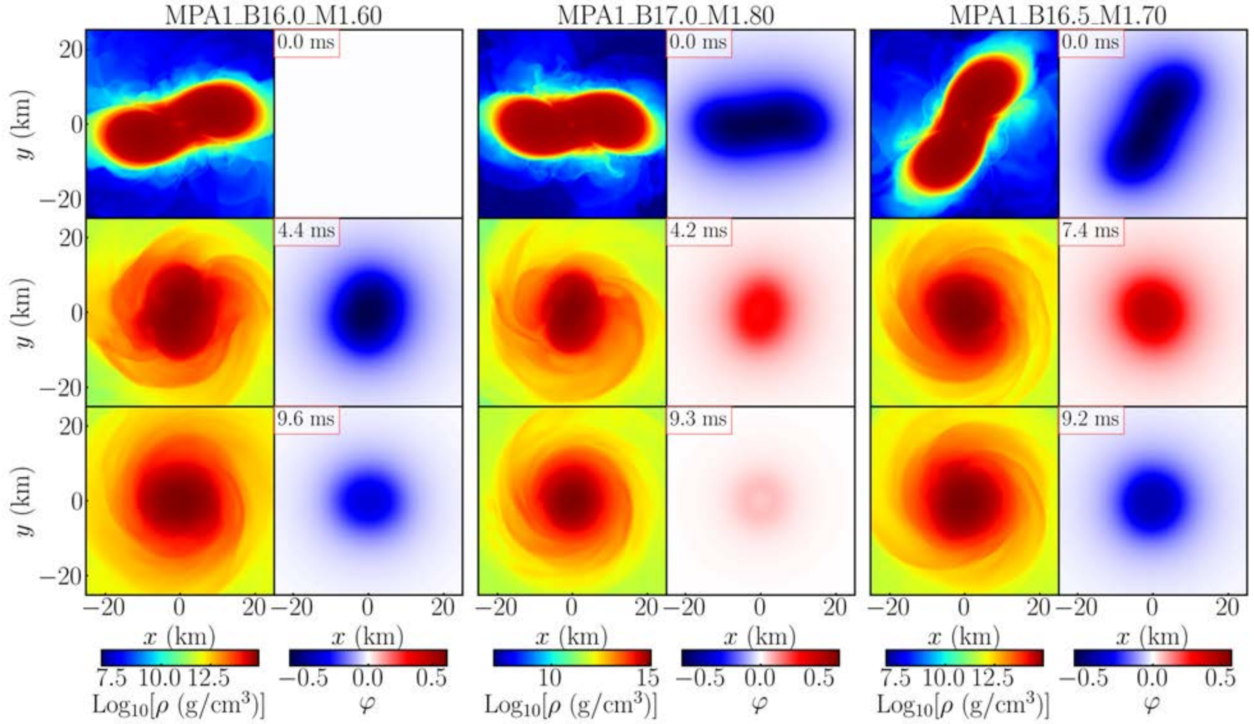

Figure 4.4: Snapshots of the rest-mass density ρ (left column of each panel) and scalar field φ (right column of each panel) on the equatorial plane for the cases of long-lived HMNS formation with the MPA1 EOS. The baryon mass M_b of each NS in units of $M_\odot$ and coupling strength B are $(M_b, B) = (1.60, 16.0)$ (left) $(M_b, B) = (1.80, 17.0)$ (middle) $(M_b, B) = (1.70, 16.5)$ (right). The time for each snapshot is indicated in the red boxes with time measured from the onset of merger.

occur if a bulk of HMNS's interior is ultrarelativistic with $T = -\rho h + 4P > T_{\rm crit}$. The critical value of $\bar{T}$ depends on the actual profile of the star, while $T_{\rm crit}$ still serves as a good indicator for understanding the scalarization criterion (see below).

Shortly after the merger, an ultrarelativistic region can be formed in the HMNS for some cases, where the descalarization soon ensues. However, the core of a natal HMNS may not be in an ultrarelativistic regime even though possessing a much higher central density than that of the progenitors. In this case, scalarization may occur in the HMNS even if the progenitors remain unscalarized up to the merger (i.e., for a not-extremely large value of B). However, the subsequent mass accretion may lead to the emergence of a region with $\bar{T} > T_{\rm crit}$, resulting in a descalarization. In the event of a *marginal* descalarization, the scalar cloud trapped by the central object oscillates with a larger amplitude than the case where the condition of $\bar{T} > T_{\rm crit}$ is conspicuously satisfied.

Before delineating different scalarization and descalarization scenarios for long-lived HMNSs in the following subsections, we demonstrate each channel by a representative model in Fig. 4.4, in which the snapshots of rest-mass density (left column of each panel) and scalar field (right column of each panel) on the equatorial plane in the post-merger phase are displayed. For `MPA1_B16.0_M1.60`, the HNMS never reaches the ultrarelativistic regime and remains scalarized until the end of the simulation, while the descalarization upon the criterion is met fully and marginally for `MPA1_B17.0_M1.80` and `MPA1_B16.5_M1.70`, respectively.

4.3.1.1 Long-lived scalarized HMNS

Fig. 4.5 shows the evolution of the maximum rest-mass density $\rho_{\rm max}$ and scalar-field amplitude $\varphi_{\rm amp}$ for selected models that yield a long-lived HMNS for three different EOSs. We first focus on the cases for which the HMNS confidently (solid) and marginally (dashed; present only for the H4 EOS) remains spontaneous scalarized at $t - t_{\rm merge} = 10$ ms. Some models with small values of B do not exhibit dynamical scalarization during the inspiral phase, but scalarization can still occur in the post-merger phase (e.g., `MPA1_B16.0_M1.60`), because the HMNS has a higher compactness compared to the corresponding isolated NS so that even for a small value of B, $\sqrt{-T}R \sim \sqrt{\rho}R \sim \sqrt{M/R}$ in the resulting HMNS can be high enough to fulfill the criterion of spontaneous scalarization.

Generally, the scalar field for scalarized HMNSs first gets amplified during merger and then settles down to a certain saturation level ($|\varphi| \sim 0.5 - 0.7$ in our cases) in a time interval of ~ 2 ms. The exact timescale depends on the coupling strength B; for example, the scalar field for `H4_B17.5_M1.60` takes ≈ 1.7 ms to grow to the peak value after merger, while for `H4_B17.0_M1.60` it takes ≈ 2.1 ms. This illustrates that it typically takes longer for the scalar field to grow to saturation for a weaker coupling, in line with the previous numerical studies where massless scalar field is considered [450].

The enhancement or activation of the scalar field during merger introduces an oscillation

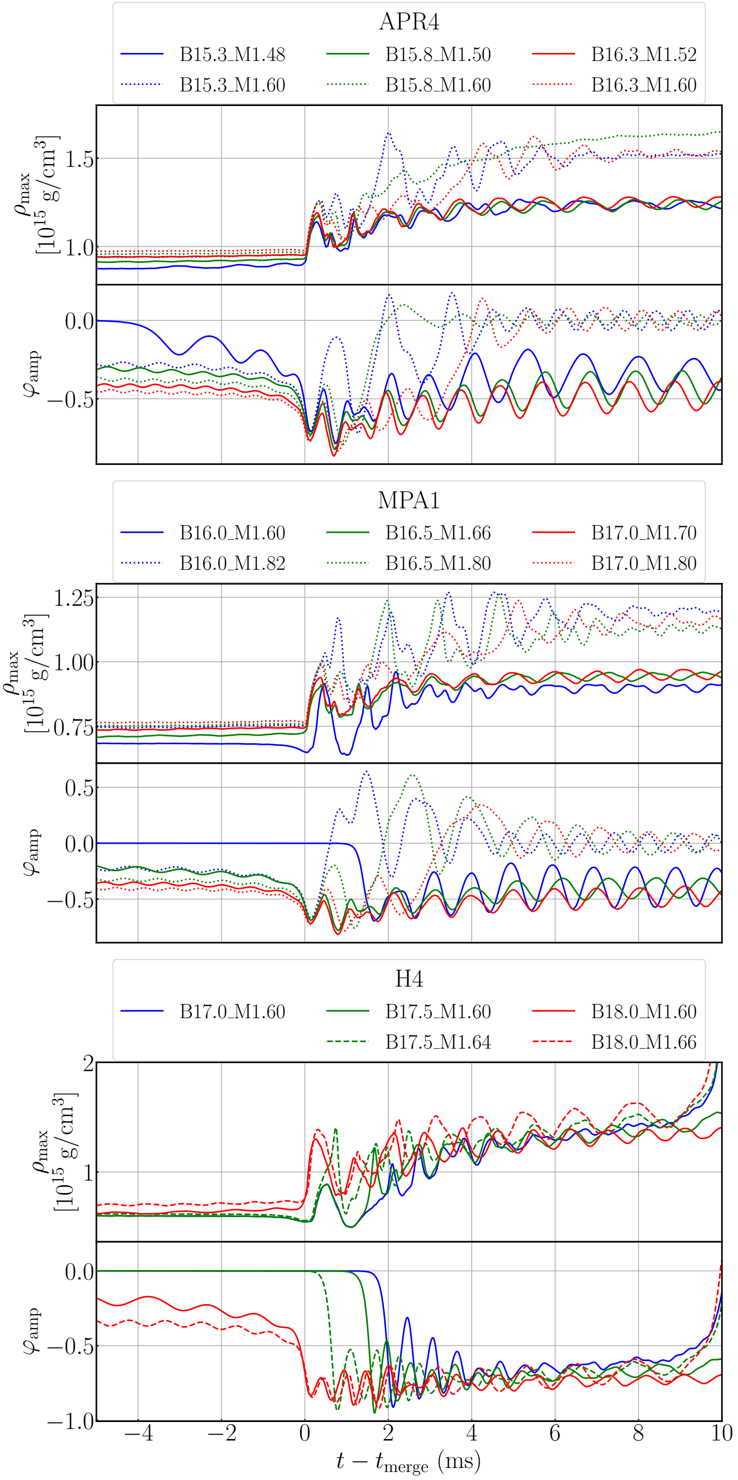

Figure 4.5: Evolution of the maximum rest-mass density $\rho_{\rm max}$ and scalar-field amplitude $\varphi_{\rm amp}$ for the long-lived HMNS formation with APR4 (top), MPA1 (middle), and H4 (bottom) EOS. The solid and dashed curves correspond to spontaneously scalarized HMNS formation, and the dotted curves correspond to models in which descalarization happens within 10 ms after the merger.

for it in the HMNS. Due to the non-zero mass of the scalar field, this oscillation does not dissipate quickly in contrast to the massless case [450], but instead gets trapped and persists for a timescale longer than 10 ms after the onset of merger with appreciable oscillation amplitude $\lesssim 0.1$ for φ. The oscillation frequency of the scalar field coincides with the one for the rest-mass density at around 1 kHz. The mode associated with this pattern is believed to attribute to the radial $\phi-$mode since it falls in the band of a radial mode [333] of scalarized HMNSs.

For `H4_B17.0_M1.60` (blue solid line), `H4_B17.5_M1.64` (green dashed), and `H4_B18.0_M1.66` (red dashed) in the bottom panel of Fig. 4.5, we find a unique feature. For these models, the scalar fields go to zero at ~ 10 ms after the onset of merger, and a black hole forms very soon afterward as we can see that the rest-mass density is also growing rapidly. The descalarization shortly prior to the black hole formation is not triggered by the criterion $\bar{T} > T_{\rm crit}$, but rather should be attributed to the no-hair theorem in the DEF theory (e.g., [470] and the references therein).

4.3.1.2 Descalarized HMNS

In this section, we pay attention to the models for which the long-lived HMNSs undergo descalarization that is induced by the secular contraction of the HMNS due to the GW emission and angular momentum redistribution via gravitational torque associated with the non-axisymmetric structure of the merger remnant.

The dotted curves in Fig. 4.5 show the evolution of models that descalarize over a dynamical timescale after the onset of merger. Taking `MPA1_B16.0_M1.82` as an example (blue dotted curve in the middle panel), we find that the scalar field promptly goes to zero when the maximum density rises to become ultrarelativistic during the post-merger evolution. However, the scalar field does not stop at zero but instead form an oscillating scalar cloud around the HMNS with an appreciable amplitude of $\lesssim 0.1$, which differs from the massless case in which the scalar field is completely turned off after descalarization [450]. A note is necessary here to say that the term “descalarized HMNS” does not mean the scalar field is totally dissipated, but rather, it represents an HMNS with a long-lived oscillating scalar field with the zero time-averaged value $\langle \varphi_{\rm amp} \rangle = 0$. Owing to the residue scalar cloud, it is non-trivial to determine definitely the time when descalarization happens, and we simply define the descalarization time $\tau_{\rm S}$ as the time of the first zero crossing of the scalar field amplitude $\varphi_{\rm amp}$ during the post-merger phase.

To further understand the condition of the descalarization, we show the evolution of the scalar-field amplitude $\varphi_{\rm amp}$ together with T at the maximum density, $T(\rho_{\rm max})$, in Fig. 4.6 for model `MPA1_B16.0_M1.82` for which the prompt descalarization happens during the post-merger phase with $\tau_{\rm S} = 0.60$ ms. Here, $T(\rho_{\rm max})$ in units of the nuclear saturation density $\rho_{\rm nuc}$ $(= 2 \times 10^{14}\,{\rm g/cm^3})$ is plotted. In the inspiral phase, the NSs are initially spontaneously

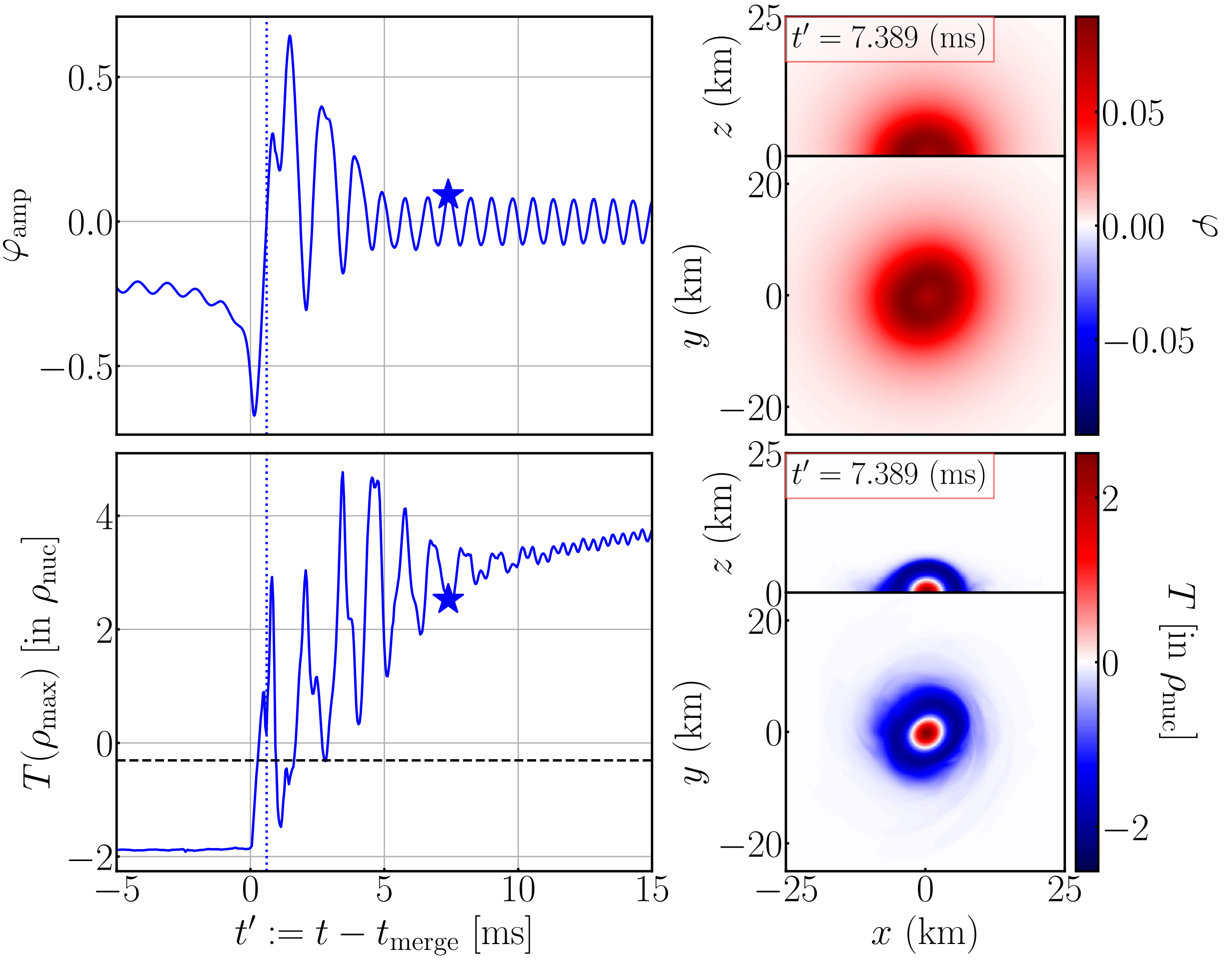

Figure 4.6: For a prompt descalarization scenario `MPA1_B16.0_M1.82`, left panels show the evolution of the scalar-field amplitude $\varphi_{\rm amp}$ (top left) and trace of stress-energy momentum tensor $T := T^a{}_a$ (bottom left) in units of the nuclear saturation density $\rho_{\rm nuc} = 2 \times 10^{14}$ g/cm^3 at maximum density $\rho_{\max}$ point. The blue dotted vertical line and the black dashed horizontal line show the descalarization time $\tau_{\rm S}$ and the critical value $T_{\rm crit}$, respectively. The blue stars indicate the time of the snapshots of φ (top right) and T (bottom right) on equatorial (x-y) and vertical (x-z) planes.

scalarized which is consistent with the scalarization condition $T(\rho_{\max}) < T_{\rm crit}$ as the central value of $T \approx -2\rho_{\rm nuc}$. Once the NSs merge, $T(\rho_{\max})$ raises rapidly due to the increase in maximum density and thermal contribution from shock heating, and immediately flips sign to become positive. Soon after the scalar field crosses $T_{\rm crit}$, the descalarization occurs. Note that $T(\rho_{\max})$ fluctuates around $T_{\rm crit}$ for a few times due to the radial oscillation, temporally satisfying the scalarization condition ($T < T_{\rm crit}$) during those cycles. As it turns out, the scalar field is likely to temporarily reach a high value as in spontaneous scalarization, and hence introduces large oscillation after $\tau_{\rm S}$.

As $T(\rho_{\max})$ shifts further away from $T_{\rm crit}$, the scalar field quickly damps, leaving an oscillating scalar cloud around the HMNS. In contrast to the ϕ-mode in spherical NSs in the massless DEF theory, for which the damping time of φ is $\lesssim 1$ ms [333], the residual scalar cloud persists for more than 10 ms in the massive case, forming a long-lived quasi-normal mode with appreciable amplitude $\sim \mathcal{O}(0.1)$. Such a long-lived ϕ-mode observed in both scalarized and descalarized cases is consistent with the results of [319], which suggests that the presence of mass term m_ϕ could significantly extend the lifetime of the radial $\phi-$mode in the massive Brans-Dicke scalar-tensor theory. Also shown in the right panels of Fig. 4.6 are the snapshots of the scalar field φ and T at 7.389 ms after the onset of merger. Despite of the large value of $T \sim 2\rho_{\rm nuc}$ at the center which forbids the HMNS from being spontaneously scalarized, it still contains considerable matter with $T < T_{\rm crit}$ surrounding the center, whose size is comparable to the Compton wavelength $\lambda\!\!\!^{-}_{\rm comp} = 14.8$ km. This creates an off-centered potential well in the right-hand-side of Eq. (4.17) and as such traps the scalar field in a hollow sphere shape as shown in Fig. 4.6, which is different from the scalar field profile of spontaneous scalarized HMNSs in Fig. 4.4, for which the peak value of φ is located at the center of the NSs (see also [474]).

Other than the prompt descalarization scenario, the HMNS can still be subsequently descalarized due to the secular contraction. In some models shown as red dotted curves in Fig. 4.5, such as `APR4_B16.3_M1.60` and `MPA1_B17.0_M1.80`, the HMNSs remain spontaneously scalarized for a few ms after the onset of merger. Meanwhile the rest-mass density $\rho_{\max}$ continues increasing due to the contraction resulting from the angular momentum dissipation by the GW emission and the angular momentum redistribution via gravitational torque associated with the non-axisymmetric structure of the HMNS until it reaches the ultrarelativistic limit and triggers the descalarization. However, if the maximum rest-mass density of the HMNS settles down to a value very close to the critical value for scalarization, the HMNS may undergo several cycles going between states of scalarization and descalarization due to the density fluctuation caused by the radial oscillation. Fig. 4.7 shows the evolution of maximum density $\rho_{\max}$ and scalar-field amplitude $\varphi_{\rm amp}$ for the marginally descalarized models, which are denoted as the least massive descalarized HMNS along the mass sequence. As the transition state between scalarized and descalarized HMNSs, any perturbation in den-

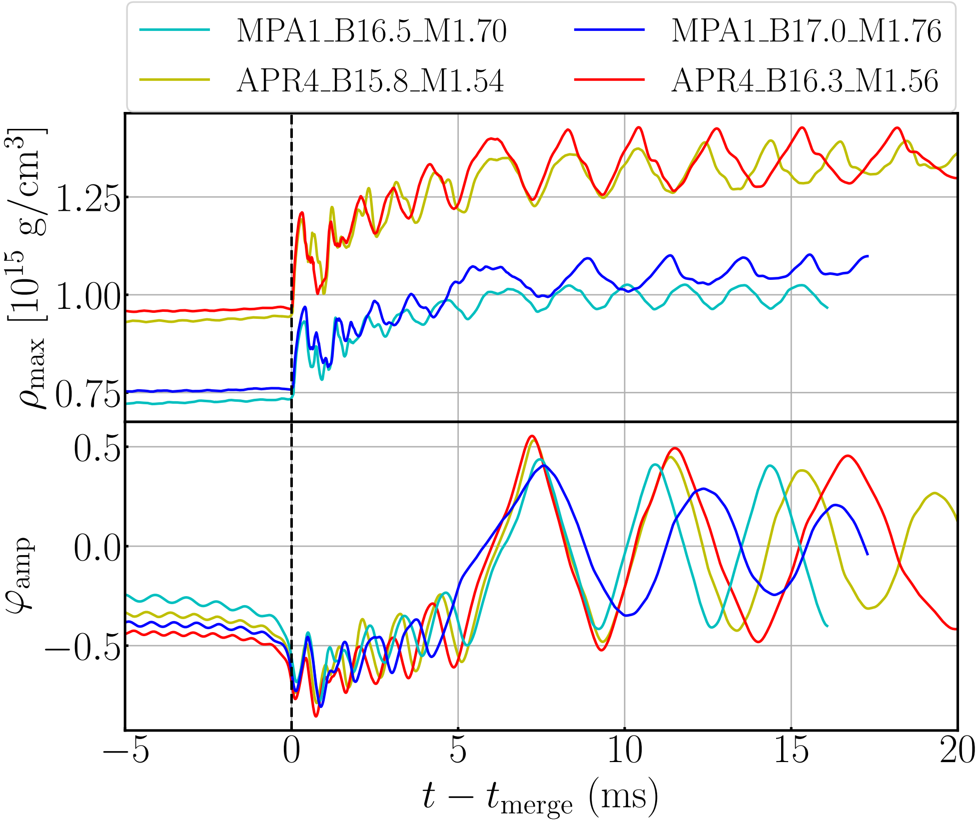

Figure 4.7: Evolution of the maximum density $\rho_{\rm max}$ (top) and scalar-field amplitude $\varphi_{\rm amp}$ for marginally descalarized models with APR4 and MPA1 EOSs.

sity allow the HMNS to temporarily reach the scalarization criteria and drive the scalar field towards the level of the spontaneously scalarized HMNS. Different from the hollow spherical scalar clouds formed around the descalarized HMNS, the scalar cloud's profile still peaks at the center, similar to the spontaneously scalarized models in the marginally descalarized as illustrated in Fig. 4.4 for model `MPA1_B16.5_M1.70` (right panel). Therefore, it contains a much stronger oscillation in φ than for other descalarized models with the amplitude ~ 0.5.

In addition to the strong scalar-cloud oscillation, the marginally descalarized models also have a much lower frequency of ϕ–mode with $\lesssim 500$ Hz. We perform Fourier transform of $\varphi^2_{\rm amp}$ for the post-merger phase of long-lived HMNSs to obtain the characteristic frequency[2] since the scalar field enters the modified Einstein field equations, Eq. (3.6), as $\phi \sim \varphi^2$ and thus φ^2 is physically more relevant to hydrodynamics. Indeed, we find a better agreement between the Fourier spectrum of $\rho_{\rm max}$[3] and $\varphi^2_{\rm amp}$. To obtain a cleaner spectrum, we cut the transient evolution of scalar field after the change of the scalarization state, which is the first

---

[2] Note that instead of the conventional choice $\varphi_{\rm amp}$ used in other studies [319, 333], we choose specifically $\varphi^2_{\rm amp}$ for the Fourier analysis which introduces an extra factor of 2 in frequency for the perturbation of φ if the background scalar field is zero (i.e. in the case of a descalarized HMNS with time-averaged $\langle\varphi_{\rm amp}\rangle = 0$). However, this choice does not alter the frequency of the Fourier spectrum for the spontaneously scalarized HMNS case.

[3] While the perturbation of rest-mass density ρ is decoupled with φ in the GR branch of static spherical stars [333], the evolution of ρ would still be affected by φ even for the descalarized HMNS case in full dynamical simulation.

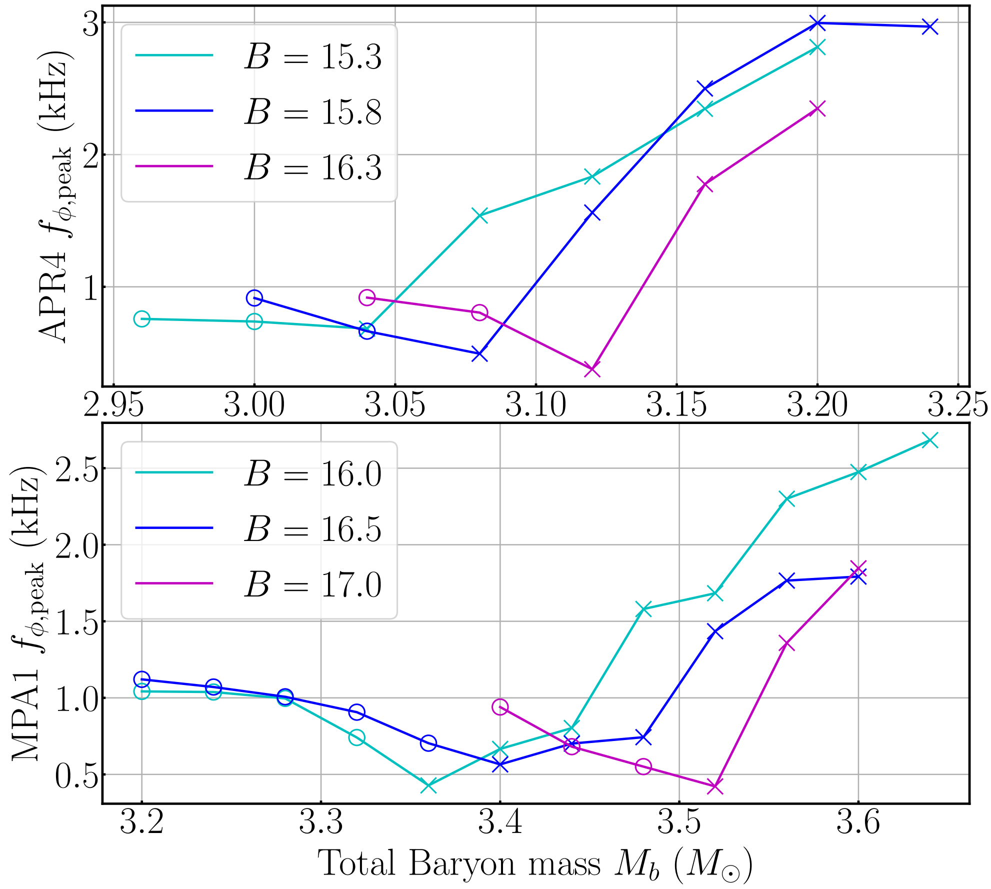

Figure 4.8: The peak frequency of φ_{amp} for EOS APR4 (top) and MPA1 (bottom) with respect to the total baryon mass of the system for the long-lived HMNS scenario. The cross and circle markers indicate the models with and without descalarization, respectively.

2 ms after the onset of merger for the scalarized cases, while for the descalarized cases we cut the first few ms after the descalarization happened until the scalar field reaches at most twice of its final amplitude.

Denoting $f_{\phi,\text{peak}}$ as the peak frequency of the Fourier spectrum of φ^2_{amp}, which is believed to be the ϕ-mode of the HMNS, Fig. 4.8 summerizes how $f_{\phi,\text{peak}}$ varies along the mass sequence for the APR4 and MPA1 EOSs, for which a descalarized HMNS can be formed. The cross and circle markers indicate the models with and without descalarization, respectively. As the total baryon rest-mass of the scalarized HMNS increases, $f_{\phi,\text{peak}}$ drops and eventually reaches its minimum at the marginally descalarized models. After that, $f_{\phi,\text{peak}}$ rises along the mass sequence for the descalarized HMNS. This is consistent with the characteristics of ϕ-mode as shown in Fig. 2c in [333] for which the mode frequency of the spontaneously scalarized branch first drops to zero at the bifurcation point, indicating the end of the scalarized state due to the mode instability, and then rises again in the GR branch. Therefore, we believe that the dominant mode in φ^2_{amp} is the radial ϕ-mode and the zero-frequency point of $f_{\phi,\text{peak}}$ at the marginally descalarized model indicates the bifurcation point of scalarized and GR

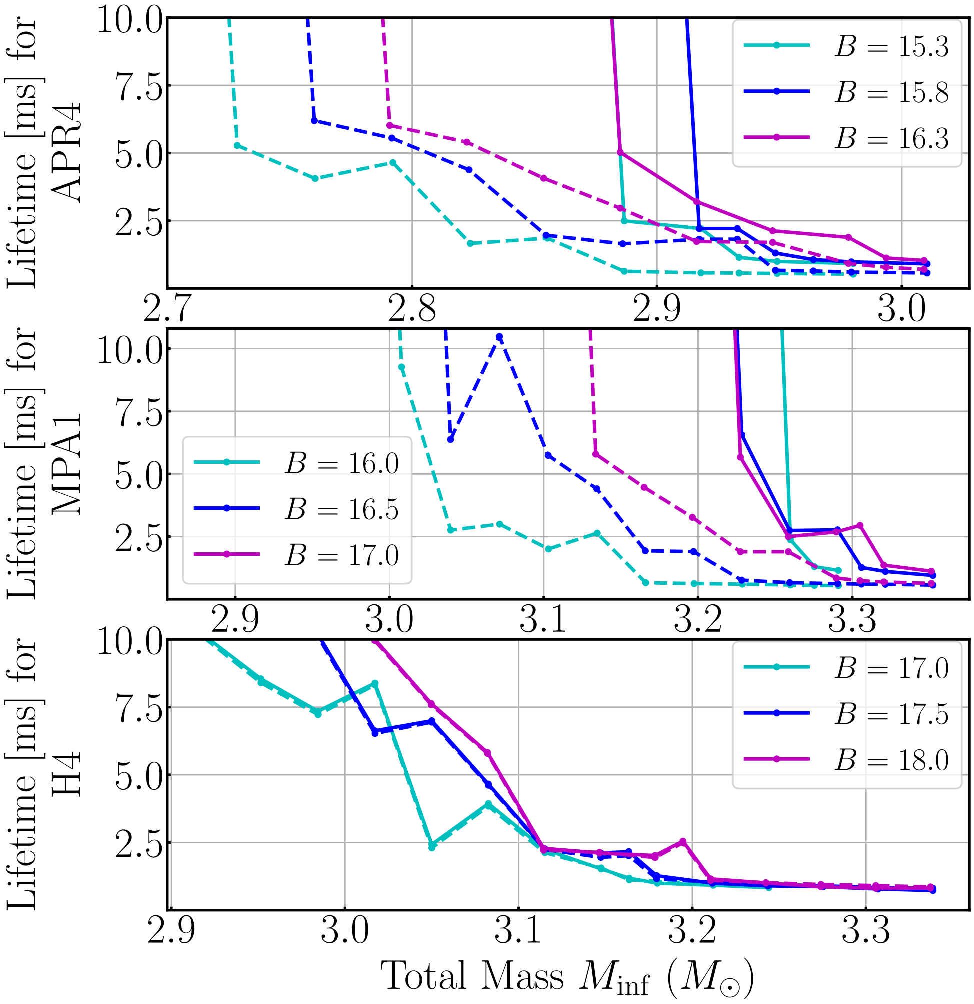

Figure 4.9: Lifetimes of the excited scalar field (dashed) and HMNS (solid) for the DEF theory with $m_\phi = 1.33 \times 10^{-11}$ eV while various coupling strengths as functions of the total mass $M_{\mathrm{inf}} := M_{\mathrm{ADM},1} + M_{\mathrm{ADM},2}$ of NSs for APR4 (top) MPA1 (middle), and H4 (bottom) EOSs.

branches.

We summerize τ_{H} (solid) and τ_{S} (dashed) for the simulated models whenever they can be determined in Fig. 4.9. The scalar cloud's lifetime τ_{S} depends strongly on the coupling strength B as shown by the dashed curves in Fig. 4.9. In general, τ_{S} is longer for the larger values of B. It is noticed that the descalarization of HMNSs only occurs in APR4 and MPA1 EOSs, while all the models with the H4 EOS (bottom panel) only descalarize right before the collapse, i.e., the lifetimes τ_{H} and τ_{S} overlapped with each other. Although we pick up weak coupling strengths that induces the scalarization for the static spherical NSs, ranging from $B = 17$ to 18 for H4 EOS, the critical coupling strength B for the marginally scalarization decreases rapidly for more massive NSs as shown in Fig. 4.1. For static spherical NSs with total baryon mass greater than $2M_\odot$, spontaneously scalarization can happen for much lower coupling $B < 16$ in H4 EOS, and we expect such critical value of B could go even lower for more massive HMNSs with $M_b > 3M_\odot$. Therefore, the coupling constant B we covered is relatively strong for HMNSs, prolonging the scalarization time and thus explain the strong scalarization behavior.

4.3.2 Delayed collapse

When the total mass of merger remnants is slightly below the threshold mass $M_{\rm thr}$, the HMNS survives for a short period of time and then collapses to a black hole after subsequent angular momentum dissipation by the GW emission and angular momentum transport via the gravitational torque associated with non-axisymmetric structure of the HMNS. We classify these delayed collapse models with $\tau_{\rm H} < 10$ ms as a short-lived HMNS. We expect that the collapse could be further delayed if the HMNS is spontaneously scalarized since the scalar field will weaken the gravitational force on the surrounding matter. Fig. 4.10 shows the evolution of $\rho_{\rm max}$ and $\varphi_{\rm amp}$ for short-lived HMNS models. HMNSs with the H4 EOS always remain spontaneously scalarized until the formation of a black hole because of the choice of the relatively strong coupling strength. Then, the descalarization occurs when the black hole is formed and the scalar field is quickly dissipated due to the no-hair theorem. On the other hand, HMNSs pertaining to the APR4 and MPA1 EOSs undergo descalarization earlier before the black hole formation, leaving an oscillating scalar cloud. These descalarized HMNSs have a mass $> M^{\rm GR}_{\rm thr}$ and yet they still survive for a few ms before forming a black hole. This indicates that the small-amplitude scalar cloud $|\varphi| \lesssim 0.1$ provides a temporal support to stave off the collapse.

Taking one particular model as an example (same one as the red curve for MPA1 in Fig. 4.10), we find that the evolution of the scalar field and the HMNS in this scenario is visualized in Fig. 4.11 through the snapshots of the rest-mass density (left) and scalar field (right) on the equatorial plane. The HMNS descalarizes at $\lesssim 2$ ms after the onset of merger and forms a hollow spherical scalar cloud around it (middle), similar to the scalar profile of the descalarized models (cf, Fig. 4.6). The scalar cloud delays the collapse of the HMNS until 5.67 ms after the onset of merger. Eventually, a black hole is formed, which is surrounded by a long-lived quasi-bound state of the scalar cloud with the amplitude of $\sim 10^{-4}$ (bottom) because of the non-zero mass of the scalar field (see more details in Section 4.3.3).

4.3.3 Prompt collapse and the threshold mass

Shortly after the fully GR BNS merger simulations were feasible, Refs. [444, 446] showed that there is a mass limit on the BNSs beyond which they immediately collapse into a black hole within a dynamical timescale $\lesssim 1$ ms. In GR, the threshold mass $M^{\rm GR}_{\rm thr}$ of NSs for which the prompt collapse proceeds has been vastly studied for different EOSs, whereby it was found that this threshold mass varies for different EOSs [64, 79, 242, 264, 286, 439], but is not

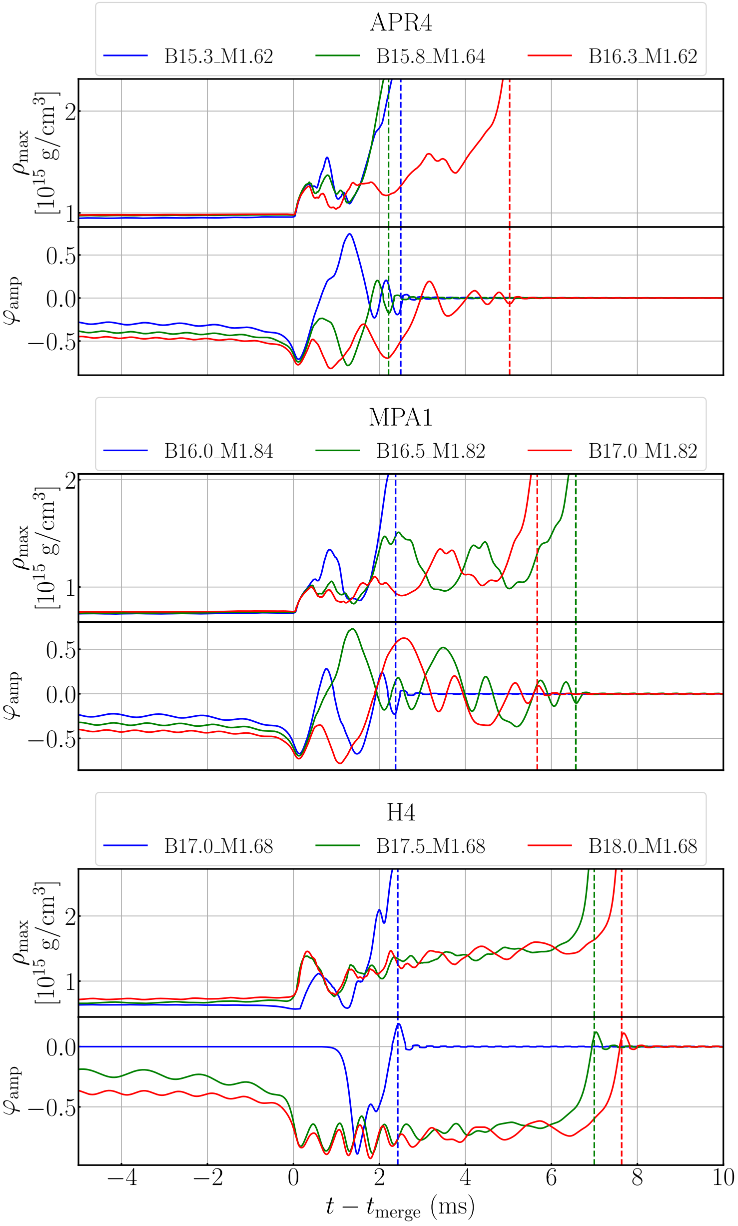

Figure 4.10: Evolution of maximum density $\rho_{\max}$ (top) and scalar field amplitude φ_{amp} for short-lived HMNS cases. The dashed line indicate the collapse time for the corresponding models.

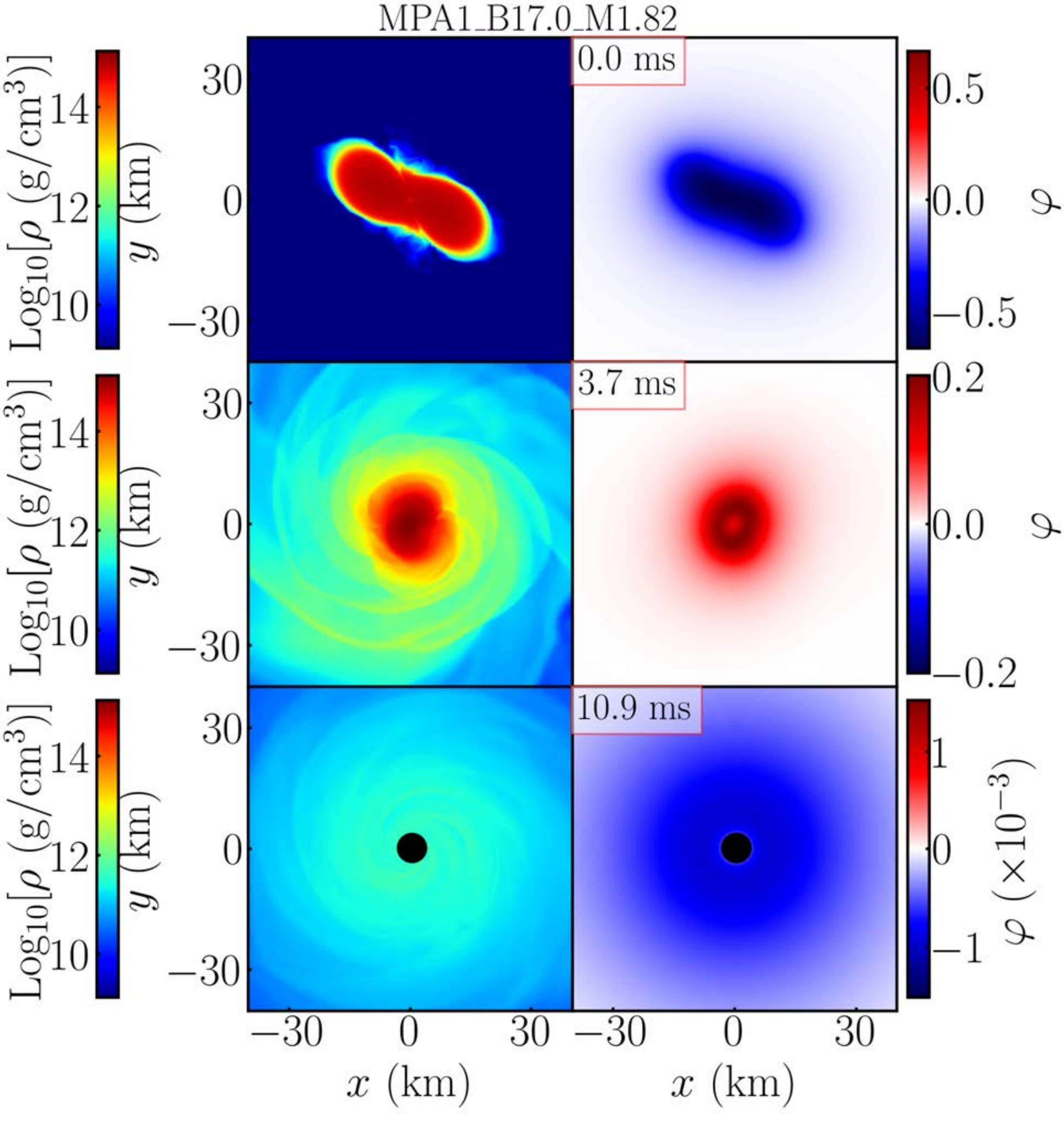

Figure 4.11: Snapshots of rest-mass density ρ and scalar field φ on the equatorial plane for a short-lived HMNS model `MPA1_B17.0_M1.82` at the onset of merger (top), before the formation of apparent horizon (middle), and at 10.9 ms after the onset of merger (bottom). The time after the onset of merger is indicated in the red box and the black filled circles plotted at the bottom panels show the location of the black hole. Notice the varying scale rule for φ in different panels.

sensitive to the mass ratio unless the system is appreciably asymmetric as $q < 0.7$ [71]. The threshold masses for the considered EOSs, APR4, MPA1, and H4, have been found to be $2.825\ M_\odot$, $3.225\ M_\odot$ and $3.125\ M_\odot$, respectively, in [70] with GR hydrodynamics simulations under conformal flatness approximation. In addition to dynamical studies, the threshold mass can also be approximately determined by the maximum mass of differentially rotating NSs along a constant angular momentum sequence for a given EOS, i.e., the turning-point criteria is approximately valid to a large extent, provided that the rotational law can be phenomenologically modeled [262, 346, 511]. However in the DEF theory, there could emerge a scalarized branch of equilibrium under the same EOS, angular momentum, and rotational law. The presence of the scalar field in spontaneously scalarized NS will effectively increase the stiffness of the EOS, providing additional support against gravitational collapse and thus the maximum achievable on the scalar branch has been shown to exceed that on the GR-sequence [474]. This suggests the existence of HMNSs heavier than the prompt collapse threshold in GR, i.e., the final remnant with mass greater than $M_{\rm thr}$ in GR may not undergo prompt collapse if it is scalarized.

In practical simulations, there is no clear criterion to classify the outcome as the prompt collapse scenario. Some studies [242] used monotonically increasing feature of $\rho_{\rm max}$ after the onset of merger as an indication of the prompt collapse, while some used monotonically decreasing feature of the minimum value of the lapse function, $\alpha_{\rm min}$, toward zero as a criterion [71]. In this study, we employ the minimum lapse function $\alpha_{\rm min}$ as the indicator for the prompt collapse when it decreases monotonically in the merger phase. Although $\alpha_{\rm min}$ is a gauge dependent variable, it directly reflects the geometrical property compared to the maximum rest-mass density $\rho_{\rm max}$ in the DEF framework since the contribution of hydrodynamics is coupled to the scalar field as $\phi^{-1}T_{ab}$ [cf. Eq. (3.6)]. When the remnant undergoes gravitational collapse, the scalar field $|\varphi|$ drops to zero drastically due to the no-hair theorem and causes a small bump in the evolution of the rest-mass density $\rho_{\rm max}$

To better resolve the threshold mass for prompt collapse, we increase the grid resolution in binary mass sequence such that the least massive prompt collapse model and the most massive delayed collapse model differ by $\Delta M_b = 0.02\ M_\odot$ in total baryon mass (i.e., $\Delta M_b = 0.01\ M_\odot$ for each NS). We define the threshold mass as $M_{\rm thr} := (M_{\rm inf,PC} + M_{\rm inf,SL})/2$ following [70] in which $M_{\rm inf,PC}$ and $M_{\rm inf,SL}$ are the ADM masses of least massive prompt collapse model and most massive delayed collapse model at infinite orbital separation, respectively.

Fig. 4.12 shows the threshold mass of NSs with different values of B for the three EOSs considered. We investigate the dependence of $M_{\rm thr}$ on B until it reaches the minimum coupling strength $B^{\rm crit}$ (circle markers in Fig. 4.12) with which spontaneous scalarization is possible for spherically symmetric NSs as shown in Fig. 4.1. The shaded region indicates the error bar given by $M_{\rm inf,PC}$ and $M_{\rm inf,SL}$. For the weak coupling case $B \lesssim B^{\rm crit}$, the NSs are not scalarized in the inspiral phase, and thus, the contribution of the scalar field is

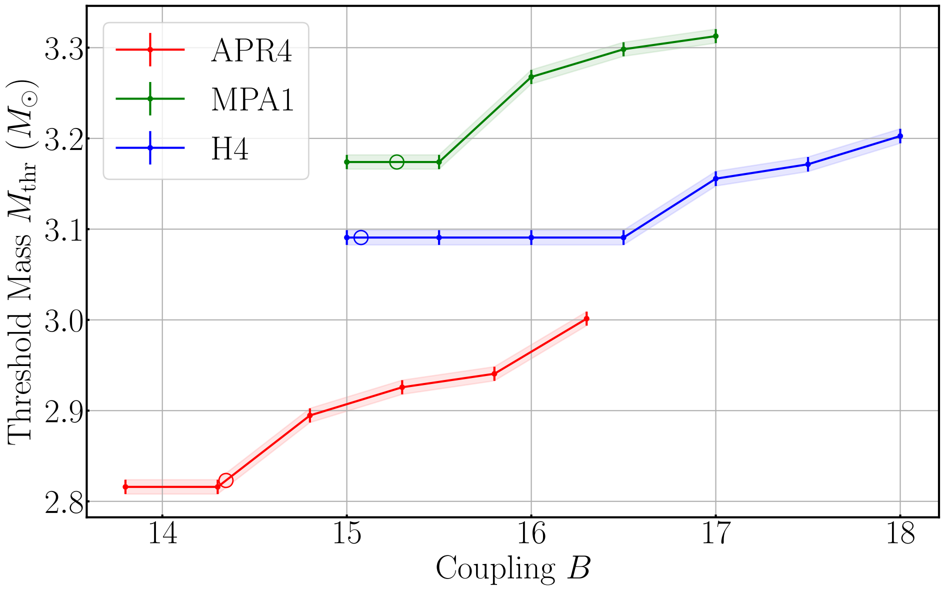

Figure 4.12: Threshold mass $M_{\rm thr}$ for equal-mass BNSs as a function of the coupling constant B for APR4 (red), MPA1 (green), and H4 (blue) EOSs. The circle markers indicate the minimum value of the coupling strength $B^{\rm crit}$ with which spontaneous scalarization is possible for sphereically symmetric NSs. The width of each curve reflects the bin size of the mass sampling.

negligible. For this case, the resultant threshold masses are essentially the same as in GR with $M_{\rm thr}^{\rm GR} = 2.816M_\odot$, $3.174M_\odot$, and $3.091M_\odot$ for APR4, MPA1, and H4 EOSs, respectively. Although the obtained threshold masses $M_{\rm thr}^{\rm GR}$ are by $\sim 1\%$ lower than the corresponding values found in [70], this could be due to the systematic error caused by the conformal flatness approximation employed in their study which cannot accurately evolve spacetime with high angular momentum. This is in agreement with [286] in which the obtained $M_{\rm thr}$ is also lower than those in [66].

As the coupling strength B increases, the threshold mass $M_{\rm thr}$ begins to rise when the scalar effect becomes important. Note that whether the threshold mass $M_{\rm thr}$ is modified from GR is determined by scalarization history of the BNS in the inspiral phase. If spontaneous scalarization or dynamical scalarization happens before the merger, the scalar field is large enough to alter the subsequent evolution of the remnant HMNS. Otherwise, even if the final remnant could be potentially scalarized with the associated mass and angular momentum, the scalarization time is longer than the dynamical time of the remnant so that the prompt collapse can happen before the HMNS reaches a state of spontaneous scalarization. This can be found in model `H4_B16.5_M1.71` shown in Fig. 4.13 (red) for which the scalar field grows exponentially in the merger phase, hinting a sign of scalarization. However, the remnant undergoes prompt collapse before the scalar field is significantly amplified, and hence, the scalar effect is negligible throughout the evolution process. On the other hand, dynamical scalarization kicks in and gets saturated at 2–3 ms before merger for model `APR4_B14.8_M1.62`

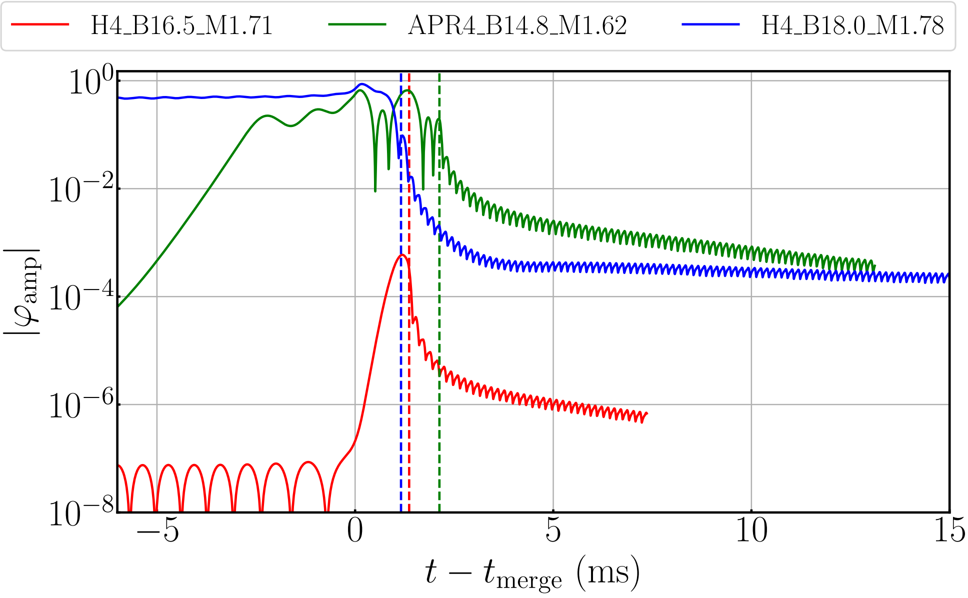

Figure 4.13: Evolution of the maximum scalar-field amplitude $|\varphi_{\rm amp}|$ for three different collapse models. The `H4_B16.5_M1.71` (red) and `H4_B18.0_M1.78` (blue) are prompt collapse models while `APR4_B14.8_M1.62` (green) is a delayed collapse model. The colored dotted lines show the collapse times for the corresponding models.

(green in Fig. 4.13). Hence, the final remnant is evaded from prompt collapse with total massof $2.887 M_\odot$ greater than threshold mass in GR $M_{\rm thr}^{\rm GR}$ of $2.816 M_\odot$ because appreciable scalar field is built up in the inspiral phase through the scalarization process.

As mentioned in Section 4.3.2, after the HMNS collapses, a quasi-bound state of the oscillating scalar cloud will form around the black hole from the fossil scalar field if the system undergoes scalarization beforehand. Fig. 4.13 shows that the scalar field for model `H4_B18.0_M1.78` (blue) quickly dissipates most of its energy after the prompt collapse. Nonetheless, a small fraction of the original scalar field remains and settles down to a long-lived oscillating cloud with the amplitude $\sim 10^{-4}$. The final scalar cloud contains dominantly a monopole component as illustrated at the bottom panels of Fig. 4.11 and Fig. 4.14.

4.4 Properties of remnants

4.4.1 Dynamical ejecta

First, we briefly discuss the material ejected from the BNS merger in the DEF theory.

One common method to identify the unbounded fluid element is to use geodesic criteria $u_t \leq -1$ for particles moving on ballistic trajectories [85, 244, 266, 352, 379]. We define the total baryon rest-mass $M_{\rm ej}$, total energy $E_{\rm ej}$, and total internal energy $U_{\rm ej}$ of the ejected

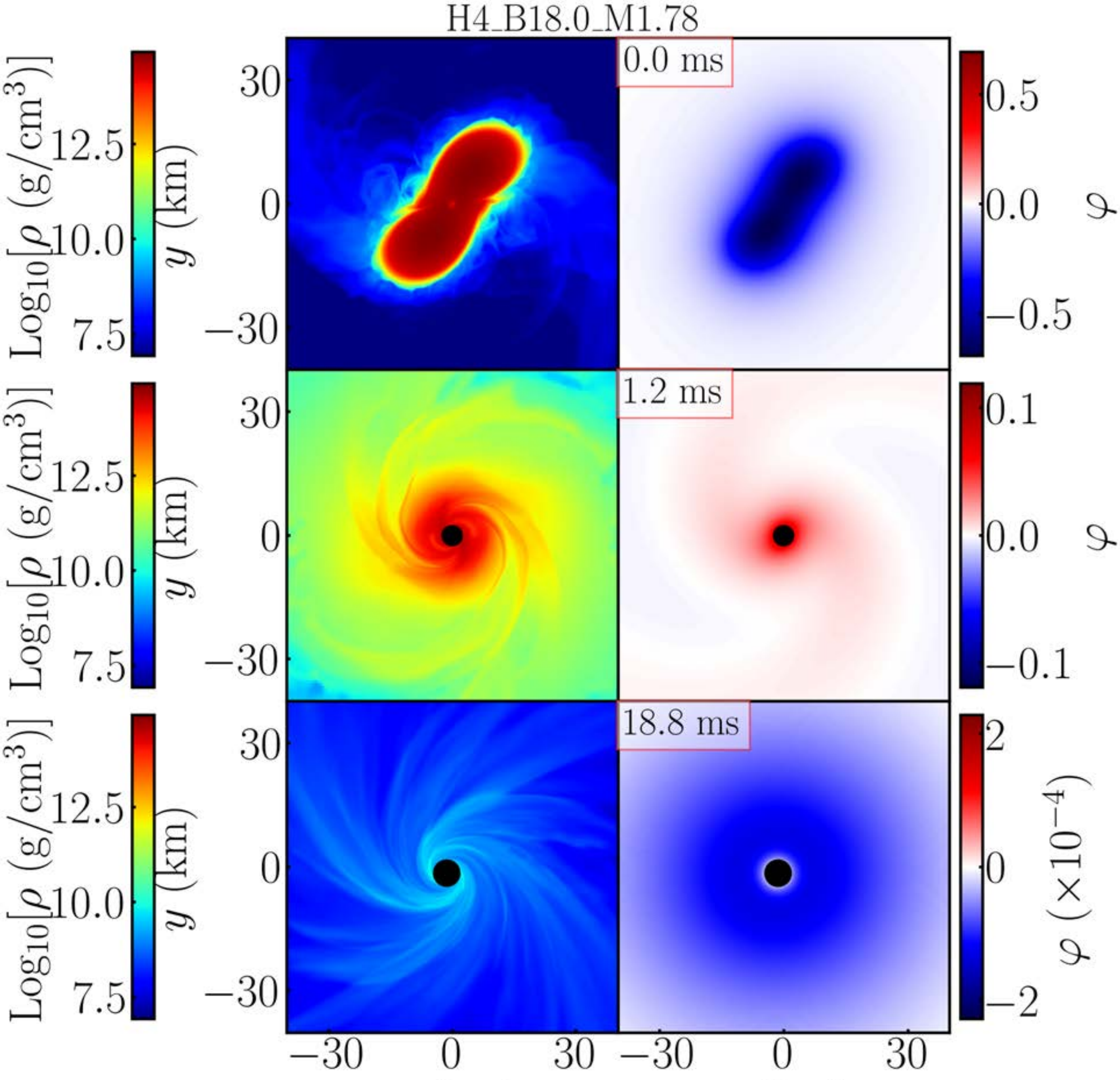

Figure 4.14: Snapshots of rest-mass density ρ and scalar field φ on the equatorial plane for a prompt collapse model `H4_B18.0_M1.78` at three different time slices. The time after the onset of merger is indicated in the red box and the black filled circles denote the black hole.

material by

$$M_{\rm ej}(t) := \int_{u_t \leq -1} \rho u^t \sqrt{-g} d^3x, \tag{4.18a}$$

$$E_{\rm ej}(t) := \int_{u_t \leq -1} T_{\mu\nu} n^\mu n^\nu \sqrt{\gamma} d^3x, \tag{4.18b}$$

$$U_{\rm ej}(t) := \int_{u_t \leq -1} \rho u^t \epsilon \sqrt{-g} d^3x, \tag{4.18c}$$

and approximate the kinetic energy $T_{\rm ej}$ as

$$T_{\rm ej}(t) := E_{\rm ej} - M_{\rm ej} - U_{\rm ej}. \tag{4.19}$$

Assuming that the ejecta has non-relativistic motion, we then estimate the average velocity $v_{\rm ej}$ of it as [244]

$$v_{\rm ej}(t) := \sqrt{\frac{2T_{\rm ej}}{M_{\rm ej}}}. \tag{4.20}$$

However, the influence of gravitational potential still remains in $T_{\rm ej}$ as evaluated within the computation domain $\lesssim$ 7500 km, hence overestimating the ejecta velocity. We therefore further estimate the extrapolated velocity $v_{\rm ej,ex}$ following [125, 233] as

$$v_{\rm ej,ex}(t) := \sqrt{v_{\rm ej}^2 - 2\frac{M_{\rm inf}}{v_{\rm ej} \times (t - t_{\rm merge})}}, \tag{4.21}$$

where $v_{\rm ej}$ is evaluated at time t. In this Chapter we define the mass $M_{\rm dyn}$ and the average velocity $v_{\rm dyn}$ of unbounded dynamical ejecta at 10 ms after the onset of merger from $M_{\rm ej}$ and $v_{\rm ej,ex}$, respectively. Note that due to the residual eccentricity $e \sim 10^{-2}$ in our simulations and limited grid resolution, the total mass of the ejected material could be altered by $\mathcal{O}(10\%)$ compared to circular orbits [196].

Fig. 4.15 summaries the total mass $M_{\rm dyn}$ and extrapolated average velocity $v_{\rm dyn}$ of the dynamical ejecta. The circle, triangle, and cross markers represent long-lived HMNS, short-lived HMNS and prompt collapse models, respectively. The error bars are estimated by the convergence test for long-lived HMNSs, short-lived HMNSs and prompt collapse cases: see Section 4.6. Since the collapse time is very sensitive to the grid resolution in the short-lived HMNS formation and hence alters the final ejecta properties, the corresponding error bar is much larger than the other two cases. The ejecta mass $M_{\rm dyn}$ falls in the range of 10^{-3}–10^{-2} $M_\odot$ depending on the EOS for the long-lived HMNS formation case with the average velocity $v_{\rm dyn} \sim 0.2c$–$0.3c$. The ejecta mass is found to be often very low as $\lesssim 10^{-3}$ $M_\odot$ for the prompt collapse case (in particular for the H4 EOS) due to inefficient time for outward angular

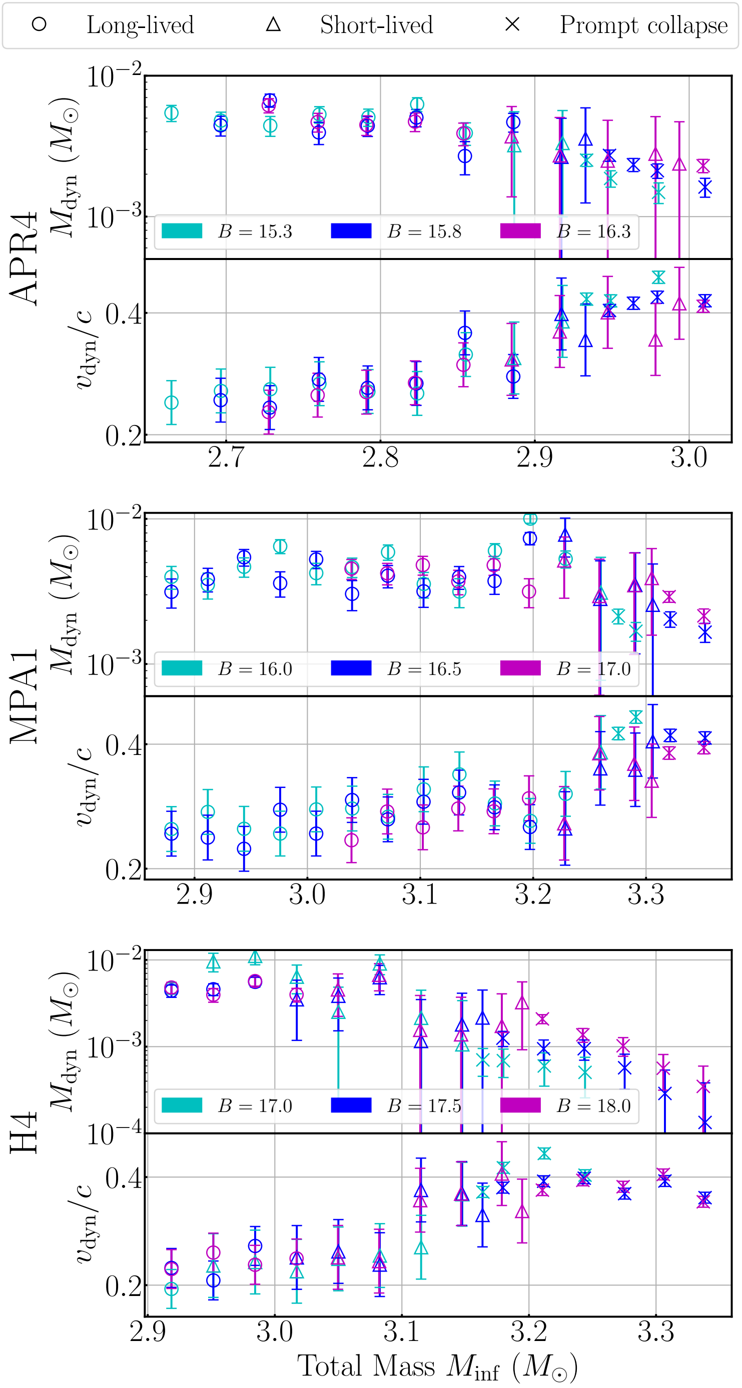

Figure 4.15: Dynamical ejecta mass ($M_{\rm dyn}$) and extrapolated average velocity ($v_{\rm dyn}$) as functions of mass $M_{\rm inf}$ for all the simulated BNS models. Each panel refers to a given EOS, while different coupling strengths B are distinguished by different colors. The circle, triangle, and cross markers represent long-lived HMNS, short-lived HMNS, and prompt collapse models, respectively. The error bars are estimated from the convergence test shown in Section 4.6.

momentum transport. For the APR4 and MPA1 EOSs, the ejecta mass is not extremently low as $\gtrsim 10^{-3}M_\odot$. The reason for this is that we pay particular attention to the BNS mass which is close to the threshold of the prompt collapse, and thus, shock heating effects at the merger induce a certain amount of the dynamical mass ejection. For these models the ejecta velocity becomes fairly high 0.3–0.4c because the shock heating is the dominant source of the dynamical mass ejection.

We find that the ejecta properties are determined primarily by the lifetime of HMNSs while the scalar effect is minor for the long-lived/short-lived HMNS formation case. This is reasonable because the dynamical ejecta quickly escapes the Compton wavelength $\lambdabar_{\rm comp} \approx$ 15 km of the scalar field, and hence, the ejecta evolution is not significantly influenced by the scalar effect. This picture may change for lower values of m_ϕ, while observationally allowed values of B will be further bounded to lower values.

4.4.2 Black hole and disk

For models that undergoes gravitational collapse to a black hole, we estimate the parameters of the black hole from the equatorial circumferential radius $C_{\rm e}$ and the area $A_{\rm AH}$ of the apparent horizon by assuming that the spacetime is approximately stationary with negligible effect from the matter. The black hole's mass $M_{\rm BH}$ and dimensionless spin parameter $\chi_{\rm BH}$ can be approximately computed via [449]

$$M_{\rm BH} = \frac{C_{\rm e}}{4\pi}, \tag{4.22}$$

$$\chi_{\rm BH} = \sqrt{1-\left(\frac{A_{\rm AH}}{8\pi M_{\rm BH}^2}-1\right)^2}, \tag{4.23}$$

respectively. Here, we evaluate $M_{\rm BH}$ and $\chi_{\rm BH}$ at 10 ms after the apparent horizon is formed. The total bounded baryon rest mass outside the apparent horizon is determined via

$$M_{\rm disk}(t) := \int_{r>r_{\rm AH}} \rho u^t \sqrt{-g}\, d^3x - M_{\rm ej}(t), \tag{4.24}$$

with $r_{\rm AH} = r_{\rm AH}(\theta,\phi)$ being the coordinate radius of the apparent horizon. We also refer to the final disk mass $M_{\rm disk,0}$ as $M_{\rm disk}(t - t_{\rm AH} = 10\,{\rm ms})$, where we recall that $t_{\rm AH}$ is the first formation time of the apparent horizon.

We summarize the properties of the black hole and disk in Fig. 4.16 for short-lived HMNS formation and prompt collapse models. For the prompt collapse models (cross markers), the remnant disk mass is significantly suppressed with $M_{\rm disk,0} \lesssim 10^{-3}\ M_\odot$ due to the insufficient time for angular momentum to be transported outwards and hence most of the matter falls into the BH as shown by the relatively high $M_{\rm BH}/M_{\rm inf}$ factor and dimensionless spin parameter $\chi_{\rm BH}$. Nonetheless, the dynamical timescale for the remnant to collapse to a

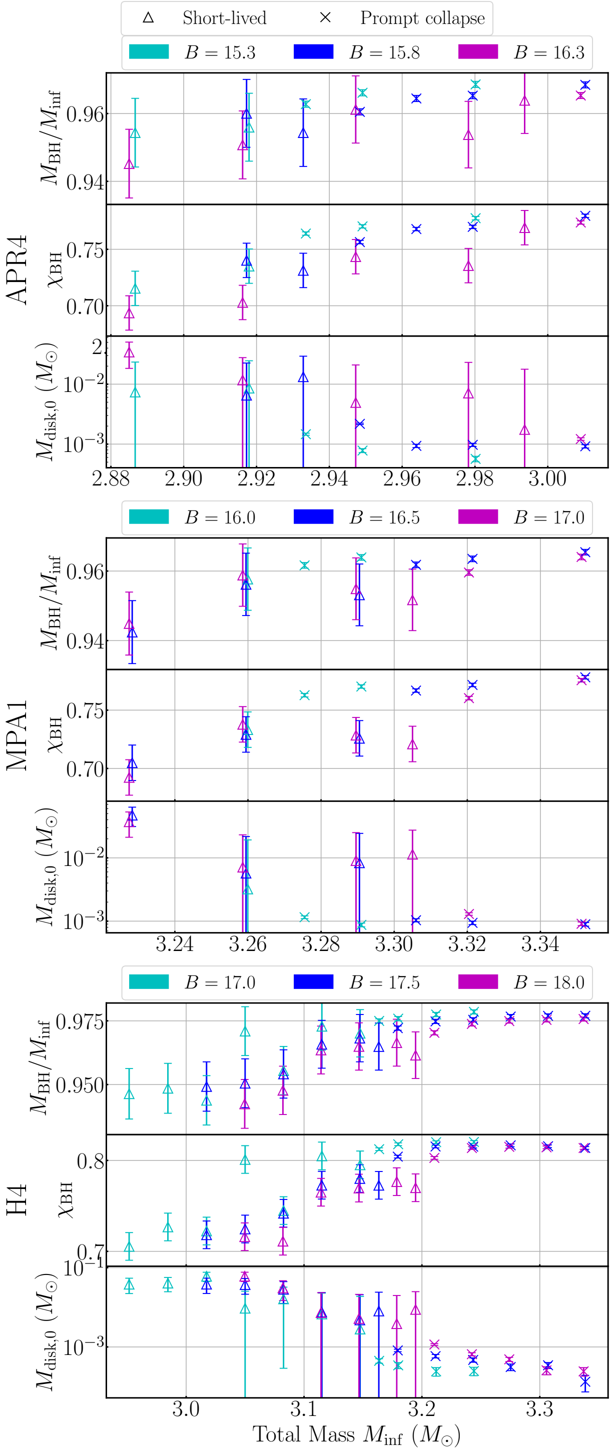

Figure 4.16: Summary of final black hole and disk properties for short-lived HMNS formation (dot markers) and prompt collapse (cross markers) cases with APR4 (top), MPA1 (middle), and H4 (bottom) EOSs. For each EOS subplot, the black hole mass scaled by the total mass $M_{\rm BH}/M_{\rm inf}$ (top), dimensionless spin parameter $\chi_{\rm BH}$ (middle), and the final disk mass $M_{\rm disk,0}$ (bottom) are shown. The error bars are estimated from the convergence test shown in Section 4.6.

black hole is slightly extended for larger values of B due to the decrease in compactness of isolated NSs. For example, the lifetime $\tau_{\rm H}$ rises from 0.83 ms in `H4_B17.0_M1.80` to 1.01 ms in `H4_B18.0_M1.80` as the coupling strength B is increased from 17 to 18. As a result, more matter remains outside the black hole, yielding a slight decrease in $M_{\rm BH}$ and $\chi_{\rm BH}$.

For the short-lived HMNS formation case, the disk mass is much higher than for the prompt collapse case, and typically falls in the range of $\sim 10^{-2} - 10^{-3}\ M_\odot$. Simultaneously, the resultant black hole mass and spin are lower. This result is consistent with that found in GR hydrodynamics; the lifetime of the HMNS primarily determines the final disk mass in the case of equal-mass BNSs. Since $M_{\rm thr}$ could be modified for large enough values of B in the DEF theory, the disk mass could be significantly modified compared to in GR with the same value of $M_{\rm inf}$.

Fig. 4.17 shows the snapshots of the disk on the x-z plane at 10 ms after the formation of the apparent horizon for `MPA1_B16.0_M1.86` and `MPA1_B17.0_M1.86`. Despite of their similar masses $M_{\rm inf}$ ($\Delta M_{\rm inf} < 0.002 M_\odot$), the short-lived HMNS formation model `MPA1_B17.0_M1.86` has a thick torus with mass $M_{\rm disk,0} = 7.3 \times 10^{-3} M_\odot$ outside the horizon, while only a thin disk with tiny mass $M_{\rm disk,0} = 5.1 \times 10^{-4} M_\odot$ remains in the black hole's proximity for the prompt collapse model `MPA1_B16.0_M1.86`.

4.4.3 Characteristics of gravitational waves from descalarized HMNS

In this Chapter, we focus on the discussion for a property of post-merger waveforms that is special to the scenarios involving a descalarization, while leaving more extensive investigation about other scenarios to future paper (Lam et al., in preparation). Taking model `APR4_B15.8_M1.56` as an example, Fig. 4.18 shows the plus polarization (top) and simultaneous frequency [Eq. (4.11); bottom] of the GW signal. We denote the instantaneous frequency at the onset of merger at which the absolute amplitude $|h|$ reaches its maximum as $f_{\rm merge}$, which is sometimes denoted as $f_{\rm peak}$ or $f_{2,\rm max}$ in the literature. We also define $f_{2,\rm peak}$ as the frequency as the dominant peak in the Fourier spectrum of $h_{\rm eff}$ in the post-merger phase, which is attributed to the $l = m = 2$ mode of the HMNS [194, 242, 428, 477, 483, 484]. The acceleration spectral density (ASD) $\tilde{h}\sqrt{f}$ (Hz$^{-1/2}$) is plotted in Fig. 4.19 for this model assuming a source distance of 50 Mpc. Since the HMNS in this model undergoes descalarization at 5.6 ms after the onset of merger, we perform the Fourier analysis of the waveform within two different time segments before and after descalarization indicated by the solid blue curves on the top and bottom panels in Fig. 4.19, respectively, while the spectrum of the whole waveform is shown by the black dashed curve. By comparing the spectrum of the whole waveform to that of the two time windows, we find that the $f_{2,\rm peak}$ is determined primarily by the state of the HMNS at a few ms after the onset of merger. In the later time window, we find an up-wind shift in $f_{2,\rm peak}$ after the descalarization since the compactness of the HMNS increase during this process. Both the increased compactness and the higher

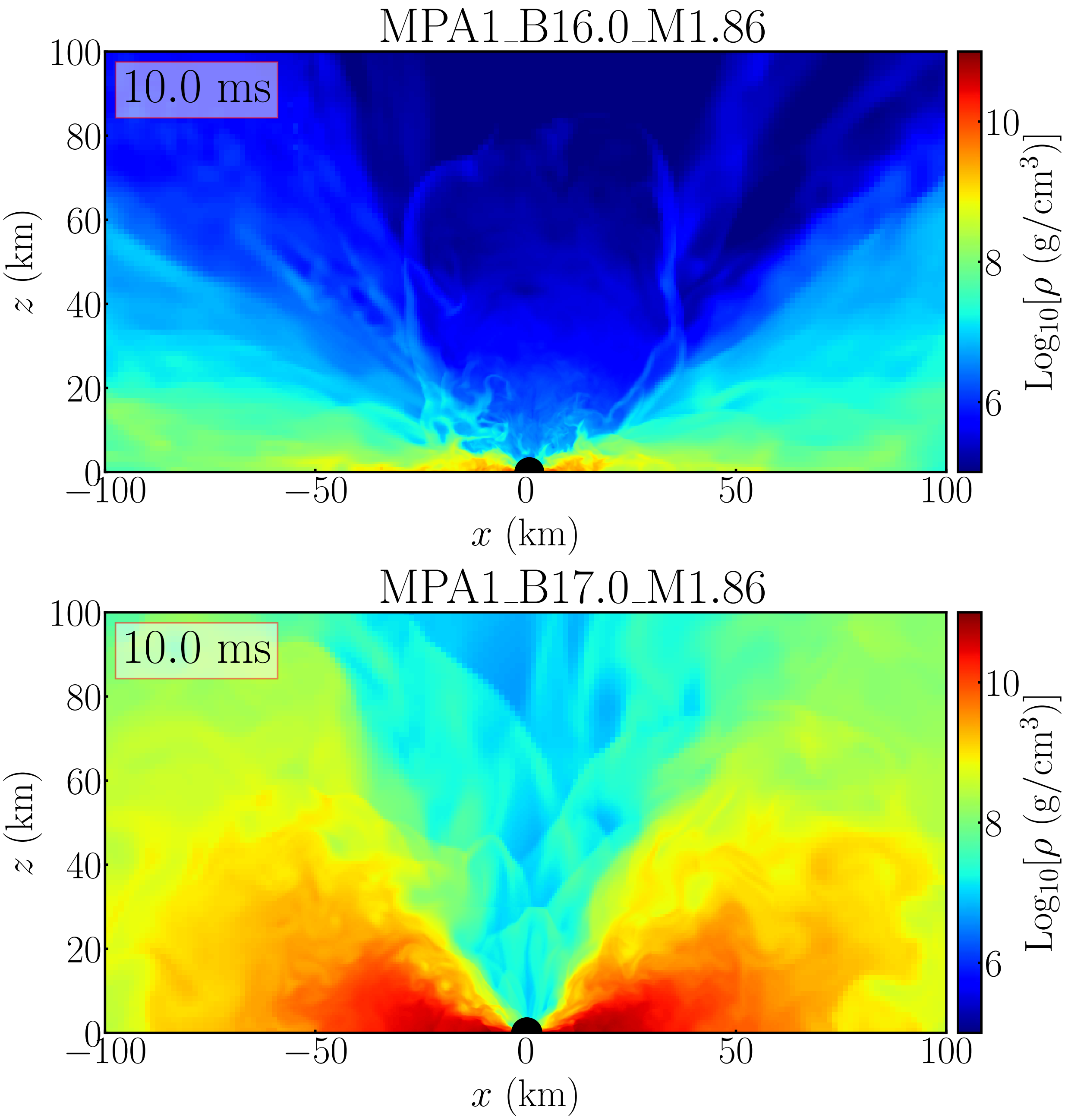

Figure 4.17: Snapshots of rest-mass density ρ on the x-z plane for a prompt collapse model `MPA1_B16.0_M1.86` (top) and a short-lived HMNS formation model `MPA1_B17.0_M1.86` (bottom) at 10 ms after the formation of apparent horizon. The black filled circles at the center denote the black hole.

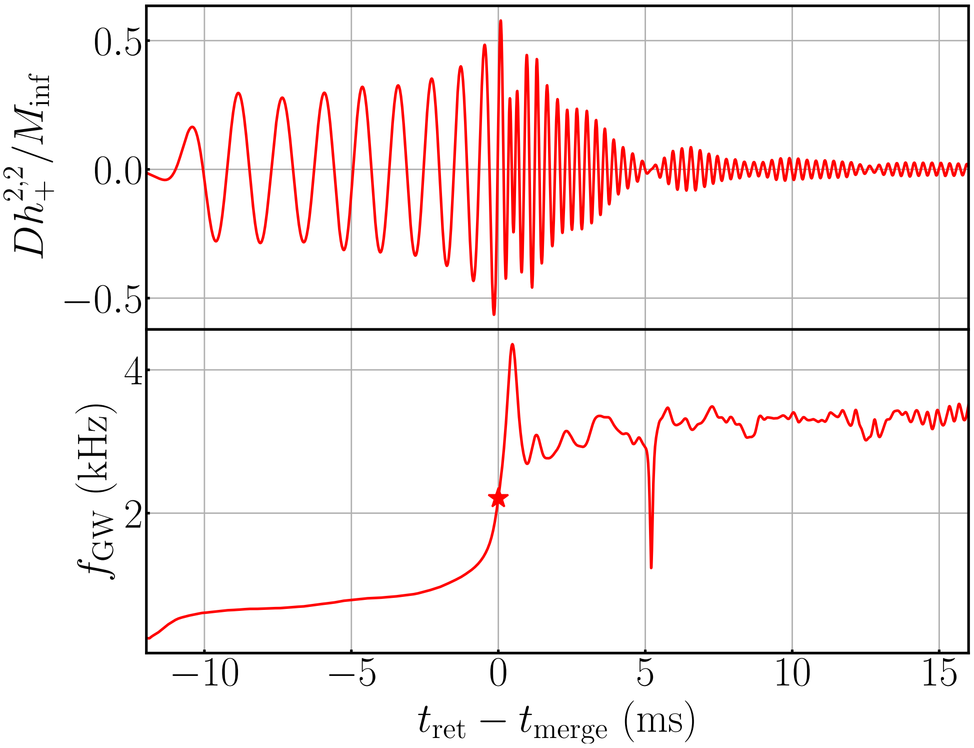

Figure 4.18: GWs emitted by `APR4_B15.8_M1.56`. The top panel shows the plus h_+ (red) polarization of GWs normalized by the extraction radius $D = 480\ M_\odot$ and initial ADM mass of BNSs, $M_{\rm inf}$, as a function of retarded time $t_{\rm ret} - t_{\rm merge}$. The bottom panel shows the instantaneous GW frequency $f_{\rm GW}$. The red star marker indicates the merge frequency $f_{\rm merge}$.

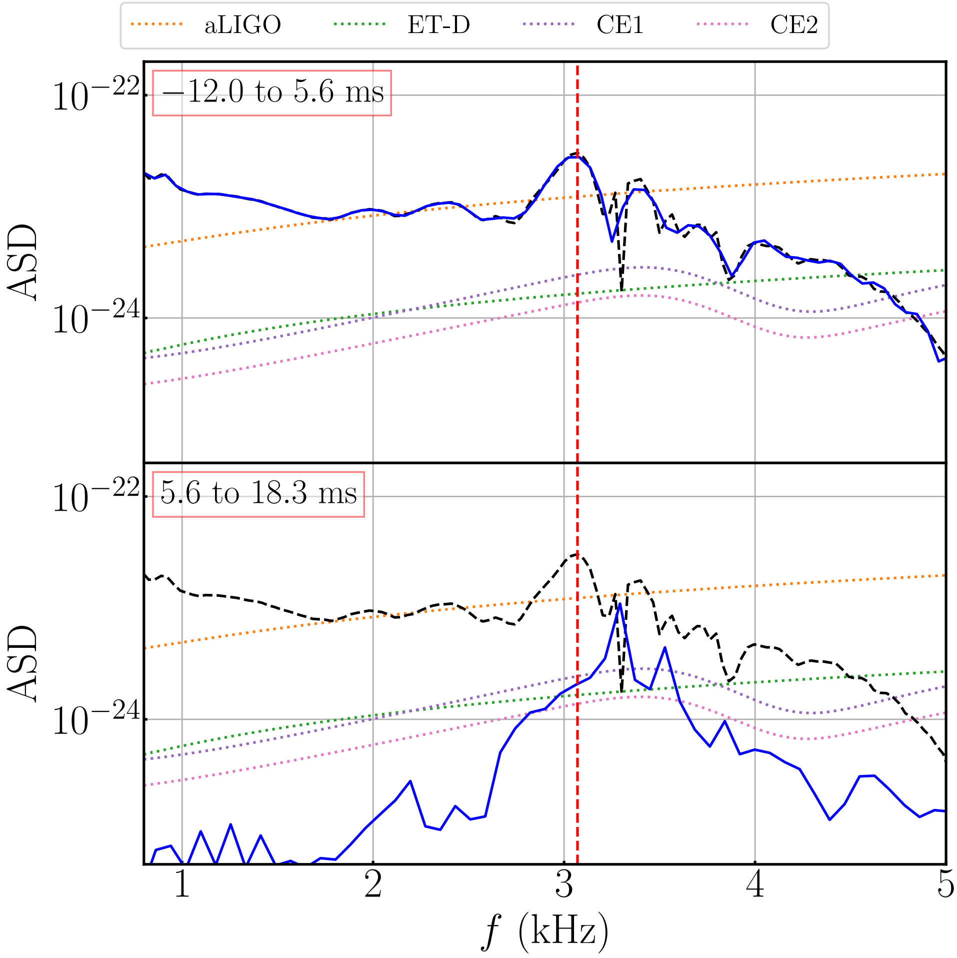

Figure 4.19: ASD $\tilde{h}\sqrt{f}$ ($\mathrm{Hz}^{-1/2}$) of `APR4_B15.8_M1.56` at a distance of 50 Mpc. The black dashed curve indicates the ASD of the the whole waveform and the vertical red dashed line indicates the $f_{2,\mathrm{peak}}$. The blue line in the upper and lower panels show respectively the ASD of the waveform before and after the onset of descalarization (5.6 ms after merge).

$f_{2,\mathrm{peak}}$ are similar characteristics of the GW signature shared with the influence of a phase transition from confined hadronic matter to deconfined quark matter (e.g., [68, 69, 91, 512]).

For comparison, we show in Fig. 4.20 the ASD in two time segments separated by 5 ms after the onset of merger for model `H4_B18.0_M1.64`, whereas the remnant HMNS remains scalarization in the post-merger phase. The $f_{2,\mathrm{peak}}$ does not shift in the absence of a state transition in the HMNS throughout the post-merger phase, which verifies that the shift in $f_{2,\mathrm{peak}}$ is indeed caused by the state transition of descalarization.

4.5 Summary and Discussion

We performed numerical relativity simulations to study the properties of post-merger remnants and GW emission from BNS mergers in the DEF theory with a massive scalar field.

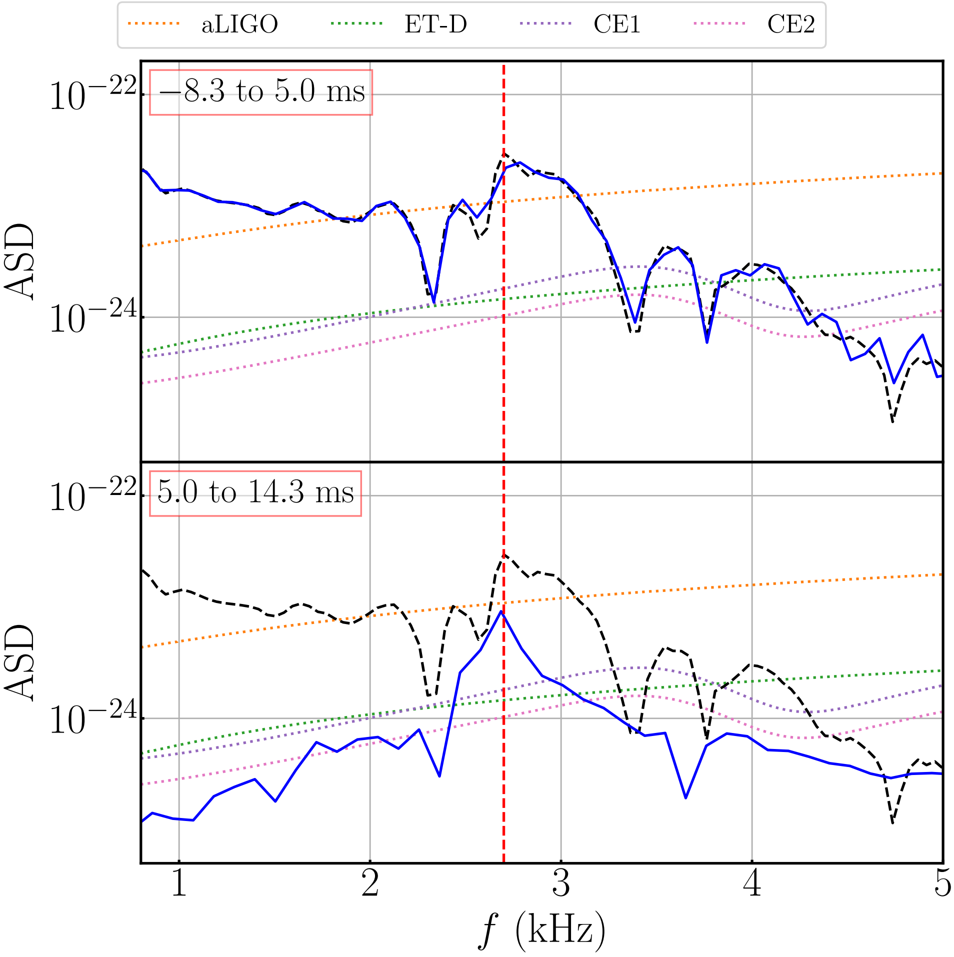

Figure 4.20: ASD $2\tilde{h}\sqrt{f}$ ($\mathrm{Hz}^{-1/2}$) of `H4_B18_M1.64` at a distance of 50 Mpc. The black dashed curvee indicates the ASD of the the whole waveform and the vertical red dashed line indicates the $f_{2,\mathrm{peak}}$. The blue line in the upper and lower panels show, respectively, the ASD of the waveform before and after $t - t_{\mathrm{merge}} =$ 5 ms.

We focused on a canonical scalar mass of $m_\phi = 1.33 \times 10^{-11}$ eV suggested in Chapter 3 to explore a wide range of NS mass and coupling strength B for the APR4, MPA1, and H4 EOSs. In the framework of the DEF theory, a scalar cloud can be induced in NSs and HMNSs by spontaneous scalarization or through dynamical scalarization in the binary system. This additional scalar field modifies the classic picture of BNS post-merger remnants. In the presence of scalarization, the lifetime of the HMNSs is prolonged due to the extra support from the scalar field. This raises the threshold mass for the prompt collapse by 0.1–0.2 $M_\odot$, which depends on the EOS (Fig. 4.12).

For lower BNSs from which a long-lived HMNS is formed, the excited scalar field also changes its dynamics from GR one. We find that the remnant can undergo descalarization if the maximum density reaches a certain critical value to become ultrarelativistic (Fig. 4.6), either due to the merger or subsequent post-merger evolution by the GW emission and the angular momentum redistribution via gravitational torque associated with the non-axisymmetric structure of the remnant. Afterward, an oscillating scalar cloud remains in the vicinity of the descalarized HMNS, and lasts over 10 ms after descalarization with appreciable amplitude $\Delta\varphi \lesssim 0.1$ (Figs. 4.5 and 4.7) instead of rapidly dissipating away as that would happen for a massless scalar field. Not only in a descalarized HMNS can we observe a long-lived ϕ-mode. Even for HMNSs that remain scalarized to the end of the simulation, the $\phi-$mode excited during merger is exhibited (Fig. 4.5), and helps enhancing a quasi-radial oscillation in the HMNS. Such a long-lived scalar cloud can also be found even after the HMNS collapses to a black hole while with much smaller amplitude (Fig. 4.13).

The scalar field alters the lifetime of HMNSs (Fig. 4.9), which in turn modifies the dynamical ejecta mass and disk mass. This may give a different kilonova signature from the GR prediction for a system with the same mass. We also observe an upward shift in $f_{2,\mathrm{peak}}$ frequency in post-merger GW signal due to the transition in the HMNS's state caused by descalarization (Fig. 4.19), which assembles the characteristics of the EOS phase transition when deconfined quark matter reveals. The result for more detailed analysis of gravitational waveforms and their spectra will be presented in a separate paper.

4.6 Convergence test

We summarize the details of numerical setup used in the simulations in Table 4.1. We adopt $N = 94$ as the standard resolution throughout this Chapter.

Fig. 4.21 shows a result of the convergence test considering models of long-lived HMNSs, `MPA1_B16.5_M1.76` (Fig. 4.21a), short-lived HMNSs, `MPA1_B16.5_M1.82` (Fig. 4.21b), and prompt collapse, `MPA1_B16.5_M1.88` (Fig. 4.21c) with three different grid-resolutions as $N = (110, 94, 78)$. We obtain convergent result in the inspiral phase , while the poor resolution in the post-merger phase become notable in the presence of shocks. In particular for the short-

Table 4.1: Numerical setups for the simulations. The grid number for covering one positive direction (N), the grid spacing in the finest refinement level (Δx), the total size of computation domain $[-L, L]$, total number of moving boxes (n_{fix}) and fixed (non-moving) boxes (n_{fix}), total number of refinement depths (d) and the extraction radius (r_{ex}).

N	Δx (m)	L $(10^6 m)$	n_{mv}	n_{fix}	d	r_{ex} (km)
78	189	7.56	8	6	10	709
94	157	7.56	8	6	10	709
110	134	7.56	8	6	10	709

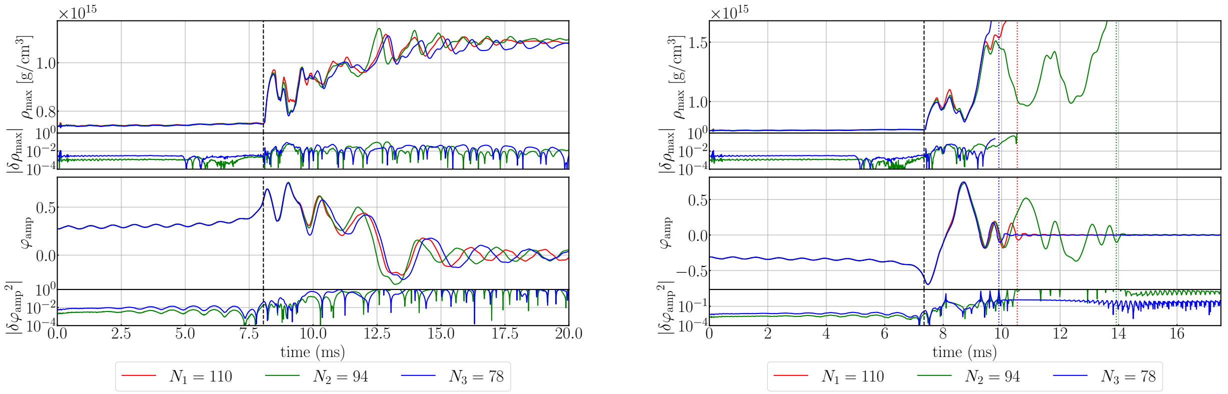

(a) Long-lived HMNS `MPA1_B16.5_M1.76`.

(b) Short-lived HMNS`MPA1_B16.5_M1.82`.

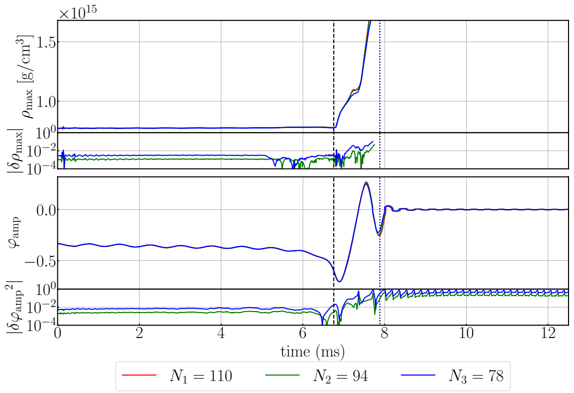

(c) Prompt collapse `MPA1_B16.5_M1.88`.

Figure 4.21: Convergence test for three different models. In each subplot, the upper panel shows the evolution of maximum density ρ_{max} with resolution $N_1 = 110$ (red), $N_2 = 94$ (green) and $N_3 = 78$ (blue), together with the relative error $|\delta\rho_{\text{max}}| := |\rho_{\text{max}}/\rho_{1,\text{max}} - 1|$ in $N_{2,3}$ with respect to the highest resolution $\rho_{1,\text{max}}$. The lower panel shows the evolution of scalar field φ_{amp} and the relative error $|\delta\varphi_{\text{amp}}{}^2| := |\varphi_{\text{amp}}{}^2/\varphi_{1,\text{amp}}{}^2 - 1|$ in the corresponding resolutions. The black dashed line shows the merger time in N_1 while the colored dotted lines in (b) and (c) show the collapse time in different resolutions respectively.

Table 4.2: Errors of remnant properties for long-lived HMNSs, short-lived HMNSs and prompt collapse cases.

Models	$\Delta M_{\rm dyn}$ $10^{-4}M_\odot$	$\Delta v_{\rm dyn}$ 10^{-2}	$\Delta M_{\rm disk}$ $M_\odot$	$\Delta M_{\rm BH}$ $10^{-3}M_\odot$	$\Delta\chi_{\rm BH}$ 10^{-3}
Long-lived HMNS	2.5	1.0	-	-	-
Short-lived HMNS	23.3	5.9	5.9×10^{-5}	2.7	1.5
Prompt Collapse	7.1	3.6	1.6×10^{-2}	29.2	15.2

lived HMNS formation model, `MPA1_B16.5_M1.82` (Fig. 4.21b), $\rho_{\rm max}$ and $\varphi_{\rm amp}$ deviate significantly at 2 ms after the onset of merger with non-converging collapse time since the evolution of the marginally stable HMNS is extremely sensitive to the grid resolution. Nonetheless, we find consistent evolution of $\rho_{\rm max}$ and $\varphi_{\rm amp}$ for the cases of long-lived HMNS formation model, `MPA1_B16.5_M1.76` (Fig. 4.21a), and prompt collapse model, `MPA1_B16.5_M1.88` (Fig. 4.21c). In addition, the descalarization time $\tau_{\rm S}$ and the collapse time in `MPA1_B16.5_M1.76` and `MPA1_B16.5_M1.88`, respectively, have a good convergence. This indicates that the standard resolution $\Delta x = 157$ m we employed throughout this Chapter is acceptable to explore the scenarios of long-lived HMNS formation and prompt collapse.

We estimate the errors of dynamical ejecta mass $M_{\rm dyn}$ and velocity $v_{\rm dyn}$, remnant disk mass $M_{\rm disk}$ and black hole parameters $M_{\rm BH}$, $\chi_{\rm BH}$ by their difference under the three resolutions considered, which are given by Table 4.2.

4.7 List of the selected Models

In Tables 4.3, 4.4, 4.5, we summarize the outcomes for all the models considered in this paper.

Table 4.3: Summary of outcomes for the BNS mergers in the massive DEF theory with APR4 EOS. The first column lists the model name which combines EOS, coupling strength B, and baryon mass of each NS in units of $M_\odot$. The second column shows the ADM mass $M_{\rm ADM}$ of each isolated NS. The third column shows the state of pre-merger scalarization with symbols ×, △ and ○ corresponding to no scalarization, dynamical scalarization, and spontaneous scalarization in the pre-merger phase, respectively. The fourth column lists the post-merger remnants with LL, SL and PC being a long-lived HMNS, a short-lived HMNS, and prompt collapse. The last two columns summerize the lifetime of the HMNS $\tau_{\rm H}$ and scalar cloud $\tau_{\rm S}$ for the cases of LL and SL, with '-' representing the absence of descalarization in the post-merger phase.

Model name	$M_{\rm ADM}$ ($M_\odot$)	Pre-merger φ	Fate	$\tau_{\rm H}$ (ms)	$\tau_{\rm S}$ (ms)
APR4_B13.8_M1.57	1.4041	×	LL	> 10	-
APR4_B13.8_M1.58	1.4119	×	PC	1.13	-
APR4_B14.3_M1.57	1.4041	×	LL	> 10	-
APR4_B14.3_M1.58	1.4119	×	PC	1.13	-
APR4_B14.8_M1.62	1.4436	△	SL	2.13	0.52
APR4_B14.8_M1.63	1.4514	△	PC	1.17	0.50
APR4_B15.3_M1.48	1.3323	△	LL	> 10	-
APR4_B15.3_M1.50	1.3500	△	LL	> 10	-
APR4_B15.3_M1.52	1.3643	○	LL	> 10	5.28
APR4_B15.3_M1.54	1.3802	○	LL	> 10	4.06
APR4_B15.3_M1.56	1.3961	○	LL	> 10	4.65
APR4_B15.3_M1.58	1.4118	○	LL	> 10	1.66
APR4_B15.3_M1.60	1.4277	○	LL	> 10	1.86
APR4_B15.3_M1.62	1.4433	○	SL	2.50	0.63
APR4_B15.3_M1.64	1.4590	○	SL	2.21	0.58
APR4_B15.3_M1.65	1.4668	○	PC	1.15	0.57
APR4_B15.3_M1.66	1.4747	○	PC	1.00	0.55
APR4_B15.3_M1.68	1.4900	○	PC	0.92	0.53
APR4_B15.8_M1.50	1.3481	○	LL	> 10	-
APR4_B15.8_M1.52	1.3642	○	LL	> 10	-
APR4_B15.8_M1.54	1.3800	○	LL	> 10	6.20
APR4_B15.8_M1.56	1.3960	○	LL	> 10	5.55
APR4_B15.8_M1.58	1.4116	○	LL	> 10	4.38
APR4_B15.8_M1.60	1.4274	○	LL	> 10	1.97
APR4_B15.8_M1.62	1.4430	○	LL	> 10	1.65
APR4_B15.8_M1.64	1.4586	○	SL	2.21	1.82
APR4_B15.8_M1.65	1.4664	○	SL	3.06	0.82
APR4_B15.8_M1.66	1.4742	○	PC	1.31	0.67
APR4_B15.8_M1.67	1.4820	○	PC	1.06	0.64
APR4_B15.8_M1.68	1.4897	○	PC	0.98	0.60
APR4_B15.8_M1.70	1.5052	○	PC	0.91	0.57
APR4_B16.3_M1.52	1.3637	○	LL	> 10	-
APR4_B16.3_M1.54	1.3797	○	LL	> 10	-
APR4_B16.3_M1.56	1.3955	○	LL	> 10	6.02
APR4_B16.3_M1.58	1.4111	○	LL	> 10	5.40
APR4_B16.3_M1.60	1.4268	○	LL	> 10	4.07
APR4_B16.3_M1.62	1.4425	○	SL	5.03	2.97
APR4_B16.3_M1.64	1.4580	○	SL	3.21	1.73
APR4_B16.3_M1.66	1.4737	○	SL	2.23	1.70
APR4_B16.3_M1.68	1.4891	○	SL	1.89	0.92
APR4_B16.3_M1.69	1.4967	○	SL	1.12	0.78
APR4_B16.3_M1.70	1.5046	○	PC	1.03	0.71

Table 4.4: Same as Table 4.3 but for the MPA1 EOS.

Model name	M_{ADM} ($M_{\odot}$)	Pre-merger φ	Fate	τ_{H} (ms)	τ_{S} (ms)
MPA1_B15.0_M1.78	1.5830	×	LL	> 10	-
MPA1_B15.0_M1.79	1.5910	×	PC	1.18	-
MPA1_B15.5_M1.78	1.5830	×	SL	3.06	-
MPA1_B15.5_M1.79	1.5910	×	PC	1.18	-
MPA1_B16.0_M1.60	1.4399	×	LL	> 10	-
MPA1_B16.0_M1.62	1.4559	×	LL	> 10	-
MPA1_B16.0_M1.64	1.4721	×	LL	> 10	-
MPA1_B16.0_M1.66	1.4880	×	LL	> 10	-
MPA1_B16.0_M1.68	1.5040	×	LL	> 10	9.27
MPA1_B16.0_M1.70	1.5200	×	LL	> 10	2.76
MPA1_B16.0_M1.72	1.5358	△	LL	> 10	3.00
MPA1_B16.0_M1.74	1.5537	△	LL	> 10	2.01
MPA1_B16.0_M1.76	1.5674	○	LL	> 10	2.64
MPA1_B16.0_M1.78	1.5832	○	LL	> 10	0.66
MPA1_B16.0_M1.80	1.5989	○	LL	> 10	0.63
MPA1_B16.0_M1.82	1.6145	○	LL	> 10	0.61
MPA1_B16.0_M1.84	1.6299	○	SL	2.37	0.57
MPA1_B16.0_M1.85	1.6377	○	PC	1.30	0.56
MPA1_B16.0_M1.86	1.6456	○	PC	1.15	0.55
MPA1_B16.5_M1.60	1.4399	△	LL	> 10	-
MPA1_B16.5_M1.62	1.4559	○	LL	> 10	-
MPA1_B16.5_M1.64	1.4719	○	LL	> 10	-
MPA1_B16.5_M1.66	1.4880	○	LL	> 10	-
MPA1_B16.5_M1.68	1.5039	○	LL	> 10	-
MPA1_B16.5_M1.70	1.5197	○	LL	> 10	6.38
MPA1_B16.5_M1.72	1.5357	○	LL	> 10	10.5
MPA1_B16.5_M1.74	1.5514	○	LL	> 10	5.74
MPA1_B16.5_M1.76	1.5673	○	LL	> 10	4.41
MPA1_B16.5_M1.78	1.5830	○	LL	> 10	1.94
MPA1_B16.5_M1.80	1.5986	○	LL	> 10	1.90
MPA1_B16.5_M1.82	1.6142	○	SL	6.57	0.76
MPA1_B16.5_M1.84	1.6296	○	SL	2.75	0.67
MPA1_B16.5_M1.86	1.6453	○	SL	2.77	0.62
MPA1_B16.5_M1.87	1.6531	○	PC	1.27	0.61
MPA1_B16.5_M1.88	1.6607	○	PC	1.11	0.60
MPA1_B16.5_M1.90	1.6761	○	PC	0.95	0.57
MPA1_B17.0_M1.70	1.5196	○	LL	> 10	-
MPA1_B17.0_M1.72	1.5353	○	LL	> 10	-
MPA1_B17.0_M1.74	1.5511	○	LL	> 10	-
MPA1_B17.0_M1.76	1.5670	○	LL	> 10	5.79
MPA1_B17.0_M1.78	1.5824	○	LL	> 10	4.47
MPA1_B17.0_M1.80	1.5981	○	LL	> 10	3.27
MPA1_B17.0_M1.82	1.6139	○	SL	5.67	1.90
MPA1_B17.0_M1.84	1.6293	○	SL	2.50	1.90
MPA1_B17.0_M1.86	1.6447	○	SL	2.69	0.85
MPA1_B17.0_M1.87	1.6525	○	SL	2.95	0.74
MPA1_B17.0_M1.88	1.6601	○	PC	1.36	0.69
MPA1_B17.0_M1.90	1.6757	○	PC	1.12	0.64

Table 4.5: Same as Table 4.3 but for the H4 EOS.

Model name	M_{ADM}	Pre-merger	Fate	τ_{H} (ms)	τ_{S} (ms)
	($M_{\odot}$)	φ			
H4_B15.0_M1.70	1.5414	×	SL	3.69	-
H4_B15.0_M1.71	1.5494	×	PC	1.37	-
H4_B15.5_M1.70	1.5414	×	SL	2.59	-
H4_B15.5_M1.71	1.5494	×	PC	1.37	-
H4_B16.0_M1.70	1.5414	×	SL	2.68	-
H4_B16.0_M1.71	1.5494	×	PC	1.37	-
H4_B16.5_M1.70	1.5414	×	SL	2.84	-
H4_B16.5_M1.71	1.5494	×	PC	1.36	-
H4_B17.0_M1.60	1.4594	×	LL	> 10	-
H4_B17.0_M1.62	1.4758	×	SL	8.54	8.40
H4_B17.0_M1.64	1.4923	×	SL	7.35	7.22
H4_B17.0_M1.66	1.5087	×	SL	8.39	8.32
H4_B17.0_M1.68	1.5251	×	SL	2.43	2.30
H4_B17.0_M1.70	1.5414	×	SL	3.94	3.84
H4_B17.0_M1.72	1.5575	×	SL	2.24	2.13
H4_B17.0_M1.74	1.5738	△	SL	1.52	1.56
H4_B17.0_M1.75	1.5867	△	PC	1.18	1.12
H4_B17.0_M1.76	1.5899	○	PC	1.00	1.06
H4_B17.0_M1.78	1.6060	○	PC	0.92	0.95
H4_B17.0_M1.80	1.6221	○	PC	0.83	0.87
H4_B17.5_M1.60	1.4594	×	LL	> 10	-
H4_B17.5_M1.62	1.4758	×	LL	> 10	-
H4_B17.5_M1.64	1.4922	×	LL	> 10	-
H4_B17.5_M1.66	1.5087	△	SL	6.63	6.53
H4_B17.5_M1.68	1.5251	○	SL	7.00	7.95
H4_B17.5_M1.70	1.5413	○	SL	4.66	4.62
H4_B17.5_M1.72	1.5575	○	SL	2.27	2.24
H4_B17.5_M1.74	1.5736	○	SL	2.11	1.95
H4_B17.5_M1.75	1.5818	○	SL	2.16	2.01
H4_B17.5_M1.76	1.5898	○	PC	1.27	1.16
H4_B17.5_M1.78	1.6058	○	PC	1.00	1.03
H4_B17.5_M1.80	1.6216	○	PC	0.90	0.96
H4_B17.5_M1.82	1.6377	○	PC	0.87	0.90
H4_B17.5_M1.84	1.6535	○	PC	0.78	0.83
H4_B17.5_M1.86	1.6694	○	PC	0.73	0.81
H4_B18.0_M1.60	1.4594	○	LL	> 10	-
H4_B18.0_M1.62	1.4758	○	LL	> 10	-
H4_B18.0_M1.64	1.4922	○	LL	> 10	-
H4_B18.0_M1.66	1.5086	○	LL	> 10	9.96
H4_B18.0_M1.68	1.5249	○	SL	7.63	7.59
H4_B18.0_M1.70	1.5410	○	SL	5.82	5.79
H4_B18.0_M1.72	1.5572	○	SL	2.29	2.22
H4_B18.0_M1.74	1.5733	○	SL	2.11	2.14
H4_B18.0_M1.76	1.5894	○	SL	2.02	1.95
H4_B18.0_M1.77	1.5973	○	SL	2.55	2.49
H4_B18.0_M1.78	1.6053	○	PC	1.16	1.10
H4_B18.0_M1.80	1.6212	○	PC	1.01	1.02
H4_B18.0_M1.82	1.6371	○	PC	0.87	0.95
H4_B18.0_M1.84	1.6529	○	PC	0.81	0.91
H4_B18.0_M1.86	1.6687	○	PC	0.82	0.86

Chapter 5

Accessing universal relations of binary neutron star waveforms in massive scalar-tensor theory

Contents

Breakdown of Contribution

This chapter is based on the preprint submitted to Phys. Rev. Lett.: "*Accessing universal relations of binary neutron star waveforms in massive scalar-tensor theory*" in arXiv:2410.00137 [306] by **A. T.-L. Lam**, Y. Gao, H.-J. Kuan, M. Shibata, K. V. Aelst and K. Kiuchi. The tidal deformability of the neutron stars in scalar-tensor theory was calculated by Y. Gao. All the numerical simulations were carried out by me using the massive scalar-tensor extension of `SACRA-MPI` developed by me. The initial data were constructed by me using the initial data solver developed by K. V. Aelst. The simulation results were analysed by me and all the figures except figure 1 were generated by me. M. Shibata and K. Kiuchi provided constructive comments on the manuscript partially written by me, H.-J. Kuan and Y. Gao.

Overview

In this Chapter, we investigate how the quasi-universal relations connecting tidal deformability with gravitational waveform characteristics and/or properties of individual neutron stars that were proposed in the literature within general relativity would be influenced in the massive Damour-Esposito-Farese-type scalar-tensor gravity. For this purpose, we systematically perform numerical relativity simulations of ~ 120 binary neutron star mergers with varying scalar coupling constants. Although only three neutron-star equations of state are adopted, a clear breach of universality can be observed in the datasets. In addition to presenting difficulties in constructing quasi-universal relations in alternative gravity theories, we also briefly compare the impacts of non-general-relativity physics on the waveform features and those due to the first order or cross-over quantum chromodynamical phase transition.

5.1 Introduction

Coalescence of binary neutron stars (BNSs) offers a unique avenue to test gravity in its strong regime and to probe thermodynamic states of matter at subatomic densities. The gravitational wave (GW) signal originating from such a process was detected for the first time in 2017 by LIGO and VIRGO observatories [1, 20], though only in the late-inspiral epoch. This event, GW170817 [6, 11, 12], has led to certain constraints on gravitation [10, 87, 366] and the equation of state (EOS) of nuclear matter [7, 122, 163, 381]. The analysis was conducted assuming general relativity (GR) as the underlying theory of gravity to agnostically bound the observation's deviation from the prediction of GR. However, tests of a specific alternative theory of gravity require the development of waveform templates within the theory and may entail certain modifications in the data analysis formalism. Although analytic efforts in waveform modeling have been devoted to some theories, e.g., the scalar-tensor theory and the scalar-Gauss-Bonnet theory, a lot remains to be done to establish machinery at the same level of sophistication as that in GR to analyze GWs.

GWs emitted during and in the aftermath of the merger would lie in the frequency band of 2–4 kHz if the system produces a hypermassive neutron star (HMNS) as a transient remnant [60, 242, 447]. The current ground-based GW detectors are less sensitive in these bands [3, 13, 17]; in fact, even with the design sensitivity of Advanced LIGO, the postmerger waveform of a GW170817-like event might only have a SNR of $\sim$ 2–3, which can hardly be detected. However, waveforms at a few kHz may be reachable with the next-generation detectors such as the Einstein Telescope [101, 238, 377] and the Cosmic Explorer [18, 184, 390], for which the sensitivity is by a factor of $\gtrsim 10$ higher than those of current detectors.

Postmerger waveforms are informative of the dynamics of remnant systems. Of particular interest are the mergers that lead to an HMNS temporarily supported by differential rotations [57, 446] and high thermal pressure [62, 243, 262, 346]. The fluid motions within these remnants will emit a loud GW transient over $\sim$ 10–20 ms with characteristic frequencies corresponding to the oscillation modes excited in the remnant massive NS [60, 243, 358, 428, 444, 446, 483, 484]. The dominant peak in the spectrum can be related to the fundamental mode of the remnant, whose frequency depends sensitively on both the EOS and the underlying gravitational theory [96, 289, 468]. Therefore, the measurement of this frequency provides combined information about the nature of gravity and supranuclear matters.

However, to what extent we can learn about the gravitation and the EOS is subject to at least these technical and theoretical challenges: (i) the morphology of the postmerger waveforms are qualitatively different from that of inspiral, requiring different modeling and analysis strategies [123, 130, 367], and (ii) the influences of the microphysics and the gravitational aspects of the problem on waveforms are strongly degenerate [418], which hinders a clear determination of matter effects and deviations from GR. One of the cogent proposals to address the latter issue appeals to quasi-universal relations that connect the spectral properties of postmerger waveforms with properties of cold stars in isolation or participating in a coalescing binary.

Within GR, these quasi-universal relations are leveraged to infer quantities that are not directly observable [124, 330, 494, 522, 523, 524], facilitate efficient Bayesian analysis [105, 106, 376, 479, 514], and develop phenomenological waveform models by reducing the matter's degrees of freedom [66, 82, 484, 525]. In alternative theories, the EOS-insensitive feature of these relations will be useful in disentangling the EOS effects from gravity, and thus can help to distinguish non-GR imprints from the uncertainties of EOS. However, this method requires a cautious evaluation of the reliability of these relations in the gravity theory under study to prevent any contamination in the inference. Taking the massive Damour-Esposito-Farese-type (DEF; [142, 143, 144, 145]) scalar-tensor theory of gravity as an example, whose action is given as Eq. (3.1) [294, 298, 305] (see also Chapters 3 and 4), we illustrate in the remainder of this chapter that many (if not all) of the quasi-universal relations on the market are actually breached, hinting at a strong caveat of using them for Bayesian analysis. The scalar mass has been constrained by pulsar observations [32, 419, 538] as $m_\phi > 10^{-15}$ eV [385, 527] . In addition, GW170817 can tentatively suggest a lower bound on scalar mass as $m_\phi > 10^{-12}$ eV [294, 536] (see also Chapter 3). In this chapter, we will consider $m_\phi = 1.33 \times 10^{-11}$ eV (Compton wavelength of $\approx$ 15 km), which suffices to demonstrate the main conclusion: we will emphasize the violation of the quasi-universal relations, which can only be more profound for smaller m_ϕ.

For the simulations considered in this chapter, the coupling constants have been chosen such that the non-GR effects can only marginally appear during inspiral to respect the observation of GW170817 in Chapter 4 In particular, the radius-mass and tidal deformability-mass relations are shown in Fig. 5.1 (see Section 5.6 for the equations for computing tidal deformability in the massive DEF theory). We can see a qualitative difference between the sequence of the H4 EOS and those of the other two EOS: the scalarized sequence of equilibria of static, spherical stars does not merge into the GR branch in the high-density regime. The steep softening behavior of the H4 EOS at the high density prevents the revealing of a core that features a negative trace of the energy-stress tensor, staving off the conditions for descalarization (see, e.g., the discussion in Sec. III of [450]). The complete catalog of the simulated system is listed in Section 5.6, while the details of numerical schemes and setups can be found in Chapter 4 as well as in [450, 486]. We also note that the simulations included in this chapter focus on the post-merger evolution and thus the quasi-equilibrium states of binaries were prepared at < 5 orbits before the merger as initial data.

Throughout, we denote the ratio between the masses of binary as $q = m_2/m_1 \leq 1$, the instantaneous frequency of GWs at the merger as $f_{\rm peak}$, the GW amplitude at the merger as $h_{\rm peak}$ (here the merger time is defined as the moment when the GW amplitude reaches the maximal), the threshold mass for prompt collapse to a black hole as $M_{\rm thr}$, and the frequency of the dominant peak in the post-merger waveform as f_2. The numerical results presented here are limited to simulations of equal-mass binaries, including those performed in the recent work included in Chapter 4 using theory-consistent quasi-equilibrium states as initial data described in Chapter 3 and some simulations within GR newly performed here.

5.2 Correlations between $\tilde{\Lambda}$ and GW characteristics

The main tidal signature in inspiral waveforms depends predominantly on the binary tidal deformability $\tilde{\Lambda} = 16(m_1 + 12m_2)m_1^4\Lambda_1/13M^5 + (1 \leftrightarrow 2)$, where $M = m_1 + m_2$ and the tidal deformability of the individual stars are Λ_1 and Λ_2, respectively [187, 192, 241, 248, 509]. The estimate on $\tilde{\Lambda}$ for GW170817 yielded, though loosely, the first constraints on the yet unknown EOS of NS while assuming GR as the gravitational theory. On the observation front, measurability of $\tilde{\Lambda}$ is within the uncertainty of $\sigma_{\tilde{\Lambda}} \sim 400$ at the 2σ level with current detectors [11, 247, 312] and is expected to be improved to $\sigma_{\tilde{\Lambda}} \lesssim 50$ at the 1σ level in the fifth observation mission [374, 383]. It is owing to this dominant role of $\tilde{\Lambda}$ in affecting the phasing of waveforms that several quasi-universal relations have been proposed to relate it with GW properties as introduced as follows.

Using numerical simulations, a quasi-universal relation between $\tilde{\Lambda}$ and $f_{\rm peak}$ is found for $1.35 + 1.35\,M_\odot$ irrotational binaries [82, 387]. The validity of this relation is extended in [84, 391, 484] to binaries with individual NSs having a mass of 1.2–1.65 $M_\odot$ while keeping binaries as symmetric and irrotational. Aside from reading off the numerical results, Bernuzzi et al. [82] also discover this universality by inspecting effective-one-body waveform models, where the mass range is further extended to include the mass close to the Tolman–Oppenheimer–Volkoff limit for the respective EOS and includes a small spin up to

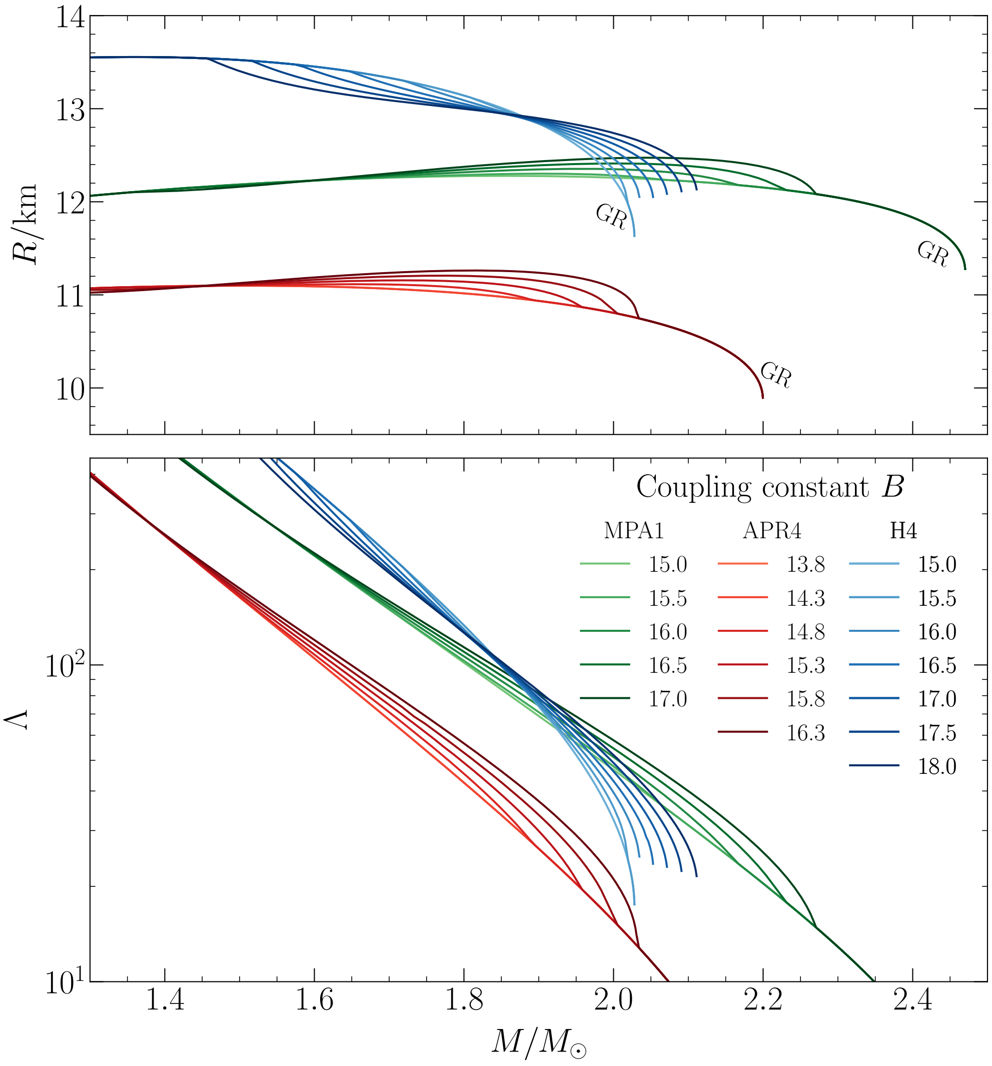

Figure 5.1: The radius-mass (top), and the tidal deformability-mass (bottom) relations for the considered theories. The lines labeled ”GR” represent the cases identical to those in GR. Three EOSs are considered in the piecewise-polytropic approximation [386]rezz16. For each EOS, a variety of scalar coupling constants (labels on the plot) are adopted while fixing the scalar mass as $m_\phi = 1.33 \times 10^{-11}$ eV.

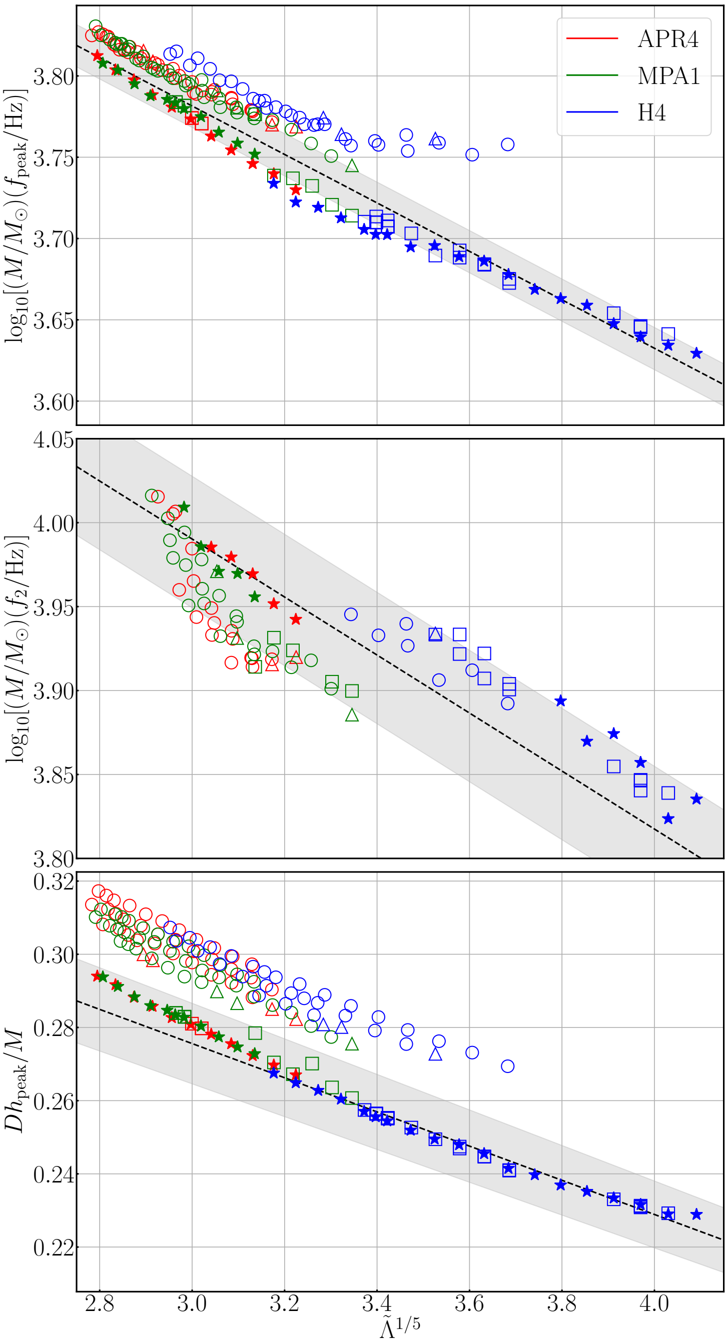

Figure 5.2: Relations between binary tidal deformability $\tilde{\Lambda}$ and the GW's frequency at the moment of merger (top), the frequency of the dominant peak of the postmerger waveform (middle), and the maximal strain of emitted GWs (bottom). The filled stars are the results of our simulations in GR, while open circles, triangles, and squares are for models with spontaneous scalarization, dynamical scalarization and no scalarization in the inspiral phase, respectively. The dashed lines are the fitting formula proposed in [280].

$|\chi| = 0.1$. The influence of mass-ratio on this relation is pointed out later on, which is evidenced by the simulations of asymmetric, irrotational binaries with varying mass ratios between 0.734–1 [278, 280]. This motivates Kiuchi et al. [280] to generalize the relation to capturing the effect of asymmetry, and subsequently, the coefficients of the fitting formula acquire a q-dependence.

The top panel of Fig. 5.2 shows our numerical results[1] (the filled markers denote the GR data) together with the relation established in [280] when setting the coefficients for equal-mass binaries (dashed line). First we see that the GR data deviates slightly from the fitting formula, but this is within the uncertainty of the fitting formula itself (4%; shaded area). The largest deviation is found as $\lesssim 5.8\%$ in the middle range of $\tilde{\Lambda}$, which is near the low (high) end of our H4 (APR4 and MPA1) samples. We can also notice that the binaries that do not exhibit scalarization before the merger (squares) obey well the quasi-universal relation, which can be expected since the inspiral dynamics leading up to the merger are equivalent to in GR for these cases.

On the other hand, the relation tends to underestimate $f_{\rm peak}$ for a given $\tilde{\Lambda}$ for either spontaneously (circles) or dynamically (triangles) scalarized mergers, indicating that the orbital frequency right before the merger is systematically enhanced compared to the case where the scalar phenomenon is silent. Although the deviation is still within the formula's uncertainty and does not show a decisive violation, the mergers with large $\tilde{\Lambda}$ (i.e., the stiff EOS H4) display a clear disagreement with the formula. In particular, $f_{\rm peak}$ for the EOS H4 is roughly constant for $\tilde{\Lambda}^{1/5} \gtrsim 3.4$, and thus differ further from the relation to the right of the plot.

On top of the GW frequency at the merger, Refs. [83, 105, 107, 280] demonstrated that $\tilde{\Lambda}$ can also be quasi-universally related to f_2 for a quite wide range of mass ratios ($0.67 \leq q \leq 1$) while commenting on a possible violation of the universality when including spinning and/or magnetized binaries. The relation is also proposed in [391, 484], while their simulations were limited to nearly equal-mass binaries. Our data together with the formula in [280] are shown in the middle panel of Fig. 5.2, where the shaded area presents the fitting uncertainty of 9%. We note that mergers promptly collapsing into a black hole are not shown here since no information of f_2 can be extracted. For the GR cases, data points with the APR4 and MPA1 EOSs lie on the line within a minor deviation of $< 1\%$, while those with the H4 EOS are on the boundary of the fitting uncertainty. In contrast to the $\tilde{\Lambda}$-$Mf_{\rm peak}$ relation, the scalar field is always activated in the aftermath of the merger for the adopted coupling constants. Therefore, f_2 is naturally expected to be different from what would be predicted in GR. Indeed, we observe a systematic reduction in f_2 when $\tilde{\Lambda}^{1/5} \lesssim 3.4$, for the chosen samples with the soft EOSs APR4 and MPA1. However, the cases with the H4 EOS are

---

[1] Numercial uncertainties in determining the considered characteristic properties is much less then the uncertainties of each fitting formula, and thus are not shown on Fig. 5.2. However, we provide some information about the numerical uncertainties in Section 5.6.

quite consistent between GR and the considered DEF theories. The reason could be that the scalar cloud is already developing shortly before the merger for the APR4 and MPA1 EOS, as indicated by the larger GW strain (cf. Fig. 5.2 for $h_{\rm peak}$). By contrast, the scalar field only started to grow after the merger for the simulations with the H4 EOS. The influence of the scalar field on the f_2 is therefore minor in the first few milliseconds, i.e., during the strongest emitting window of f_2 mode. That said, there is still a difference between GR and the DEF scenarios: a prompt collapse realizes for $\tilde{\Lambda}^{1/5} \lesssim 3.8$ in GR, while an HMNS can still be formed until $\tilde{\Lambda}^{1/5} \lesssim 3.4$ depending on B.

Kiuchi et al. [280] further provide relations of $\tilde{\Lambda}$ to $h_{\rm peak}$. We again compare our numerical data of $h_{\rm peak}$ with their formula, shown in the bottom panel of Fig. 5.2. Our GR results progressively exceed the fitting formula for lower $\tilde{\Lambda}$, and the deviation reaches $\lesssim 3.3\%$ to the left side of the plot. In general, cases that are not scalarized in the inspiral epoch, including those in the DEF theory with weak scalar coupling and those in GR, align well with quasi-universal relations. However, binaries endowed with a scalar cloud during inspiral exhibit a systematic upward shift from this trend.

5.3 Correlations between f_2 and properties of individual NS

On top of the above relations, the frequency of the dominant mode in postmerger waveforms can also be universally connected to the certain properites of a cold spherical neutron star in isolation, e.g., the Love number ($\Lambda_{1.6}$) and radius ($R_{1.6}$) of the 1.6 $M_\odot$ NS, assuming no strong phase transitions. In particular, Bauswein *et al.* proposed a f_2-$R_{1.6}$ relation [63, 65] (see also [60]) from their simulations of $1.35 + 1.35\, M_\odot$ binaries while adopting the conformal flatness condition (CFC). The data set for seeking such a relation has been significantly extended by including different M while keeping $q = 1$ in [314]. In the above work, the authors found different relations for each M and this dependence on M is also found later in [123]. On the other hand, focusing on binaries with similar total binary mass (viz. 2.7 and 2.6 $M_\odot$) for mass ratios $0.8 \leq q \leq 1$, Refs. [67, 243] showed a consistent fitting, while the data spread broader away from the fitting formula as quantified in [280]. This relation is substantially revised by including also the chirp mass as additional fitting parameter in [508]. In that work, the authors adopted the combined numerical results of equal-mass binary mergers under CFC with individual NS' mass ranging from 1.2–1.9 $M_\odot$, and the simulations withdrawing CFC of unequal-mass binaries with $q \geq 0.49$ for a mass range of 0.94–1.94 $M_\odot$ released in the CoRe database [161].

In Fig. 5.3, we show the comparison with the quasi-universal relation obtained in [67]. Even in GR, the formula can only approximately describe the cases with the EOS H4, while the systems with the other softer EOSs are significantly below. The relative deviation is depicted in the bottom panel, where we see that the formula tends to overestimate f_2 frequency by

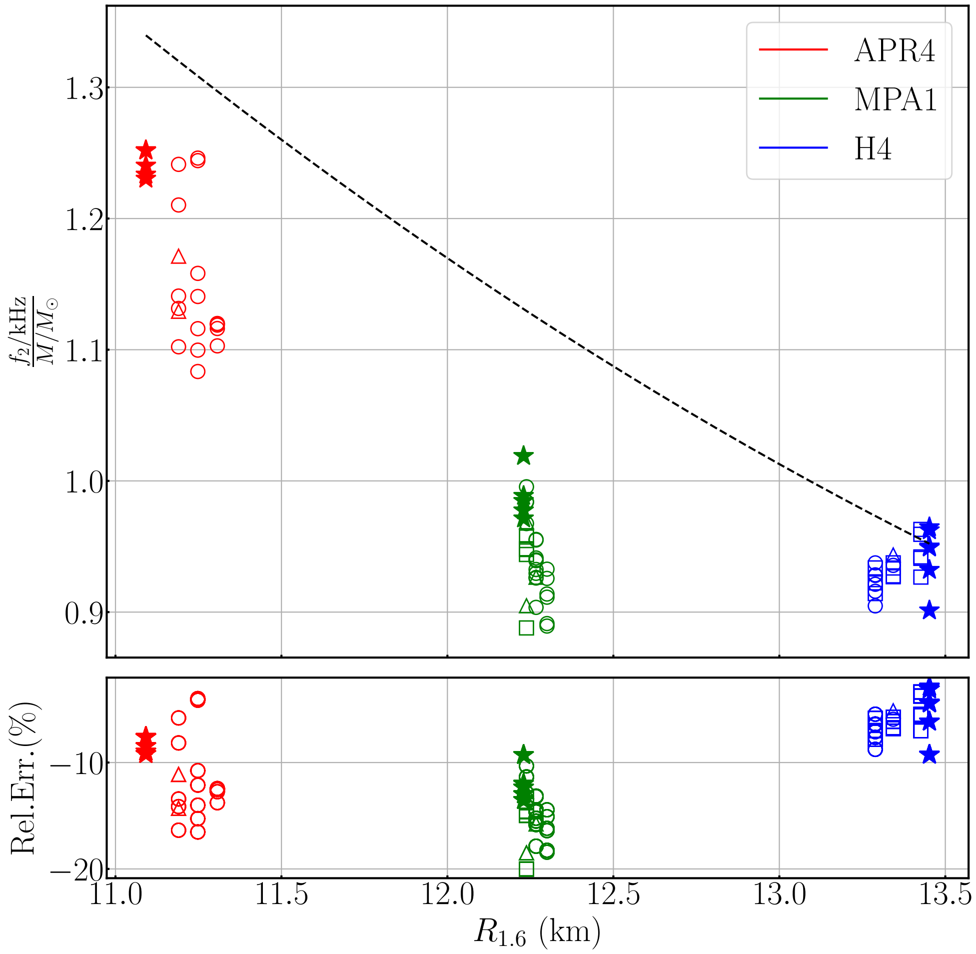

Figure 5.3: Correlation between f_2/M and $R_{1.6}$ for the considered EOS (see plot legends) and various of B. The numerical results are denoted in the same manner as in Fig. 5.2. The quasi-universal relation proposed in [67] is shown as the dashed curve, while the relative deviation of our numerical results to the formula is given in the bottom panel.

$\gtrsim 10\%$ for the APR4 and MPA1 EOSs. Focusing on the numerical data, it can be noticed that $R_{1.6}$ is larger in the DEF theories for the APR4 and MPA1 EOSs, while the trend is reversed for the H4 EOS. The overall reduced value of f_2 in the DEF theories can seemingly be explained by the effective stiffening for the APR4 and MPA1 EOSs. However, such a rationale does not apply to the H4 EOS, indicating that the interplay between gravity and matter is non-trivial and more investigation is needed to understand their competition in determining the stellar structure.

We have also compared the numerical results with the f_2-$\Lambda_{1.6}$ relation in Lioutas et al. [314]. The situation is more or less the same as the comparison with f_2-$R_{1.6}$ relation, and therefore we do not present it here.

5.4 Degeneracy with QCD phase transition

Certain caveats have already been raised that the tightness of quasi-universal relations can be broadened by including a wider set of EOS [382] or violated by either a strong, first-order [68, 91, 210, 228, 311, 345, 372, 373, 383, 512] or cross-over phase transition [249]. Consequently, an inconsistency between the inference on the EOS from the inspiral and postmerger waveforms is speculated as an indicator of phase transitions occurring during the merger process. In particular, the f_2 peak will have a higher frequency than what would be predicted by the quasi-universal relations for EOS with first-order phase transition since matters will be softened when the new degree of freedom emerges. On the other hand, matters will experience a stiffening at 3–4 n_0 followed by a softening at 4–5 n_0 for the cross-over phase transition scenario [72, 73], leading to a reduced f_2. Here $n_0 = 0.16$ fm^{-3} is the nuclear saturation number density.

However, the connection between the violation in the quasi-universal relations and matter phase transition should be carefully revisited as it can also arise from a modification in the underlying gravitational theory, as shown in this chapter. The similarity between modified gravity and QCD phase transition in terms of postmerger waveforms does not end here. After baryons crush to form exotic particles, the EOS can be stiffened or softened depending on the nature of the QCD phase transition (see above). In turn, the core can become less or more compact thereby adjusting the frequency of fluid oscillation and the associated GWs [90, 512]. This process can also manifest in scalarized HMNSs (cf. Fig. 5.2). In particular, the scalar activity in HMNSs pertaining to H4 can lead to a higher f_2 than the prediction by the quasi-universal relation (see the deviation in f_2 for $3.3 \lesssim \tilde{\Lambda}^{1/5} \lesssim 3.7$ in Fig. 5.2), reminiscent of the influence of a first-order nuclear phase transition. On the other hand, the coupling between the scalar field and matter tends to reduce f_2 for the EOSs APR4 and MPA1, mimicking the cross-over phase transition (see the deviation in f_2 for $\tilde{\Lambda}^{1/5} \lesssim 3.4$ in Fig. 5.2).

There is a distinction between the QCD phase transition and the gravitational transition of states: an interface (e.g., quark-hadron) will reveal in the former process, supporting a class of oscillation modes (i-mode) that may leave certain imprints in GW signals [308, 492, 540]. On the other hand, there is a class of mode linked to the scalar field, i.e., ϕ-mode [96, 333]. In principle, the quadrupole member of ϕ-mode can emit GWs as a result of the entrained fluid motions. Both the i- and ϕ-modes have typically the frequency of several hundred Hz, and the largely overlapped frequency band makes it non-trivial to tell them apart even if this weak emission could be detected.

5.5 Conclusion

We systematically performed numerical simulations of BNS mergers in GR and DEF theories to solve for the waveforms throughout inspiral up to the merger, where the considered scalar coupling constants are summarized in Fig. 5.1. Based on the numerical data, we examine several quasi-universal relations connecting the binary tidal deformability to waveform characteristics. For the mergers that scalarization does not realize before merger, the GW's frequency and amplitude at the merger in the DEF theories aligned well with the fitting formula valid in GR (cf. the top and bottom panels of Fig. 5.2). These two relations can, however, be significantly violated if scalarization occurs in the inspiral phase.

Although we only take three EOSs into account, our results already suggest a serious caveat when applying quasi-universal relations established in GR to probe the EOS and gravity in modified gravity. In particular, we demonstrated that a gravitational effect like scalarization could also lead to a violation in quasi-universal, mimicking the similar violation that could be caused by a strong phase transition. This indicates that one cannot take the future disagreement between the detected GW signal and the predictions of quasi-universal relations as a smoking gun of either effect. Recent studies [138, 139] show that three distinct kinds of finite-size effects are present in the DEF theory attributing to the matter, scalar field and a mixed type, respectively. The imprint of each of them on the waveform differs in sign and/or the scaling with frequency. Measuring these effects within sufficiently small statistical error with future detectors could thus help disentangle EOS and gravity effects. In any case, much more investigation remains to be done to further discriminate one effect from the other. Also, thermal effects in postmerger signals still remain to be explored [62, 83, 188, 189, 339, 384, 446], and thus the quasi-universal relations are to be inspected even for EOS without phase transition and within GR.

5.6 Supplemental materials

This section provides the formalism for computing the tidal deformability of scalarized neutron stars in the massive Damour-Esposito-Farese-type scalar-tensor theory. In addition, the catalogs of the coupling constants, binary parameters, and the equations of state adopted in the numerical simulations are summarized, and the quantities associated with the gravitational waves are also listed.

5.6.1 Tidal deformability of neutron stars in massive scalar tensor gravity

The action of Damour-Esposito-Farese-type (DEF) scalar-tensor theory of gravity in Jordan frame is given by Eq. (3.1). The field equations are conveniently formulated using the metric $\tilde{g}_{ab}$ in the Einstein frame. This metric is related to the Jordan frame metric g_{ab} through a conformal transformation given by Eq. (3.10).

The line element of the spherical background in the Einstein frame can be written as

$$\mathrm{d}s^2 = \tilde{g}_{\mu\nu}\mathrm{d}x^\mu \mathrm{d}x^\nu = -e^{\nu(r)}\mathrm{d}t^2 + \frac{1}{1-2m(r)/r}\mathrm{d}r^2 + r^2\left(\mathrm{d}\theta^2 + \sin^2\theta \mathrm{d}\phi^2\right) , \tag{5.1}$$

In general relativity, the metric component $\tilde{g}_{tt}$ of a tidally-deformed neutron star can be expanded as

$$-\frac{(1+\tilde{g}_{tt})}{2} = -\frac{M}{r} - \frac{3Q_{ij}}{2r^3}\left(n^i n^j - \frac{1}{3}\delta^{ij}\right) + O\left(\frac{1}{r^4}\right) + \frac{1}{2}\mathcal{E}_{ij}x^i x^j + O\left(r^3\right) , \tag{5.2}$$

where $\mathcal{E}_{ij}$ is the tidal field generated by the companion star, Q_{ij} is the quadrupolar moment of the neutron star induced by the tidal field, and $n^i \equiv x^i/r$. To the linear order of $\mathcal{E}_{ij}$, the induced quadrupole Q_{ij} can be written as

$$Q_{ij} = -\lambda \mathcal{E}_{ij} \, . \tag{5.3}$$

Here the parameter λ measures the tidal deformability of the star and can be related to the $l = 2$ tidal Love number via $k_2 = 3\lambda R^{-5}/2$ for R the circumferential radius of the star [192, 241].

In the massive Damour-Esposito-Farese-type scalar-tensor theory considered in the main text, both the scalar and tensor fields respond to the external tidal field induced by either tensor or scalar fields. Therefore, we should also expand the metric in terms of perturbations in the scalar field besides $\mathcal{E}_{ij}$ to determine the tidal deformability. In addition to the tensor and scalar tidal deformabilities, one also needs to consider a third kind of tidal deformability describing the tensor/scalar multipole moments induced by a scalar/tensor field as noted by Creci et al. [138]. However, the asymptotic behavior of a massive scalar field $\bar{\varphi}$ and its perturbation $\delta\bar{\varphi}$ read

$$\bar{\varphi},\ \delta\bar{\varphi} \to \frac{1}{r}e^{-r/\lambda_{\bar{\varphi}}}, \tag{5.4}$$

where $\lambda_{\bar{\varphi}} = 2\pi\hbar c/m_{\bar{\varphi}}$ is the Compton length scale of the Yukawa suppression associated with the scalar mass $m_{\bar{\varphi}}$. Such exponential decay does not affect the expansion in Eq. (5.2) on any order of $1/r$, which is different from the massless case [113, 138, 362]. We thus only need to consider the tensor tidal deformability of scalarized NSs for the massive theories considered in the present work.

Restriciting to the even-parity, static, and $l = 2$ perutrbations in the Reege-Wheeler gauge, the perturbation in the metric and the scalar field can be, respectively, written as

$$\delta\tilde{g}^{(2m)}_{\mu\nu} = Y_{2m}(\theta,\phi)\begin{bmatrix} e^{\nu}H_0 & H_1 & 0 & 0 \\ H_1 & H_2/\left(1-\frac{2m(r)}{r}\right) & 0 & 0 \\ 0 & 0 & r^2K & 0 \\ 0 & 0 & 0 & r^2\sin^2\theta K \end{bmatrix}, \tag{5.5}$$

and

$$\delta\bar{\varphi}^{(2m)} = \delta\bar{\varphi}Y_{2m}(\theta,\phi)\,, \tag{5.6}$$

where H_0, H_2, K, and $\delta\bar{\varphi}$ are perturbed quantities depending r, and Y_{2m} are the spherical harmonics.

Following the procedure in Hinderer [241], we substitute Eqs. (5.5-5.6) into the linearized Einstein equations $\delta G^{\mu}_{\nu} = 8\pi\delta T^{\mu}_{\nu}$ and denote $H_0 = -H_2 = H(r)$ to obtain

$$H_1 = 0\,, \tag{5.7a}$$

$$K' = -H' - \nu' H - 4\delta\bar{\varphi}\bar{\varphi}'\,, \tag{5.7b}$$

$$H'' + c_1 H' + c_0 H = c_s\delta\bar{\varphi}, \tag{5.7c}$$

$$\delta\bar{\varphi}'' + d_1\delta\bar{\varphi}' + d_0\delta\bar{\varphi} = d_s H. \tag{5.7d}$$

Here ($'$) denotes the derivative respect to r, and

$$c_1 = d_1 = -\frac{r^3\left(8\pi A^4(e-p)+V\right)+4m-4r}{2r(r-2m)}\,, \tag{5.8a}$$

$$\begin{aligned} c_s = 4d_s = &\left[r^2\left(-8\pi\alpha A^4\left[(\frac{\partial e}{\partial p}-1)e+(\frac{\partial e}{\partial p}-9)p\right]+2r\bar{\varphi}'\left(16\pi A^4p-V\right)\right.\right. \\ &\left.\left.+4(r-2m)\bar{\varphi}'^3-\frac{\mathrm{dV}}{\mathrm{d}\bar{\varphi}}\right)+8m\bar{\varphi}'\right]\times\frac{1}{r(r-2m)}\,, \end{aligned} \tag{5.8b}$$

$$
\begin{aligned}
c_0 = {} & \frac{4\pi A^4 r(e+p)}{r-2m}\frac{\partial e}{\partial p} + \frac{\left[r^3\left(V-16\pi A^4 p\right)-4m\right]\bar{\varphi}'^2}{r-2m} - r^2\bar{\varphi}'^4 \\
& + \frac{r\left(8\pi r^3 A^4 p+4m-r\right)V}{(r-2m)^2} - \frac{r^4V^2}{4(r-2m)^2} \\
& + \frac{-64\pi^2A^8p^2r^6+4\pi A^4r^3(5e(r-2m)-26mp+9pr)-4m^2+12mr-6r^2}{r^2(r-2m)^2}\,,
\end{aligned}
\tag{5.8c}
$$

$$
\begin{aligned}
d_0 = {} & \frac{4\pi\alpha^2A^4r(e+p)}{r-2m}\frac{\partial e}{\partial p} \\
& - \frac{96\pi\alpha^2A^4r^2(e-p)+16\pi A^3r^2\frac{\mathrm{d}^2A}{\mathrm{d}\bar{\varphi}^2}(e-3p)+16r(r-2m)\bar{\varphi}'^2+r^2\frac{\mathrm{d}^2V}{\mathrm{d}\bar{\varphi}^2}+24}{4r(r-2m)}\,.
\end{aligned}
\tag{5.8d}
$$

In general relativity, we have $c_s = d_s = 0$, and the perturbations for the tensor field and the scalar field decouple.

Eqs. (5.7c-5.7d) are linear equations for H and $\delta\bar{\varphi}$. Thus, to solve them, one can integrate the coupled equations twice with the following initial values [248, 362]

$$
H|_{r_0} = r_0^2, \quad H'|_{r_0} = 2r_0, \quad \delta\bar{\varphi}|_{r_0} = 0, \quad \delta\bar{\varphi}'|_{r_0} = 0 \tag{5.9}
$$

$$
H|_{r_0} = 0, \quad H'|_{r_0} = 0, \quad \delta\bar{\varphi}|_{r_0} = r_0^2, \quad \delta\bar{\varphi}'|_{r_0} = 2r_0 \tag{5.10}
$$

for r_0 a tiny radius near the center of the star. Then one makes a linear combination of the two integrated results to construct a solution whose asymptotic value of $\delta\bar{\varphi}$ vanishes at $r \gg \lambda_{\bar{\varphi}}$.

In practice, we integrate the system to a sufficiently large radius $r = r_{\mathrm{b}}$ and ignore the scalar field for $r > r_{\mathrm{b}}$. Defining

$$
C = \left.\frac{m}{r}\right|_{r\to r_{\mathrm{b}}}, \quad \text{and} \quad y = \left.\frac{rH'}{H}\right|_{r\to r_{\mathrm{b}}}, \tag{5.11}
$$

the tidal deformability, which is in the same form as the GR case, can be calculated as (e.g., [241])

$$
\begin{aligned}
\lambda = {} & \frac{2}{3}r_{\mathrm{b}}^5\frac{8C^5}{5}(1-2C)^2[2+2C(y-1)-y] \times \left\{4C^3\left[13-11y+C(3y-2)+2C^2(1+y)\right]\right. \\
& \left. + 3(1-2C)^2[2-y+2C(y-1)]\ln(1-2C)+2C[6-3y+3C(5y-8)]\right\}^{-1}.
\end{aligned}
\tag{5.12}
$$

The tidal deformability used in the main text is then obtained as $\Lambda = \lambda/M^5$ for M the mass of the star.

5.6.2 Catalog of simulated binaries and theories

We list in Tables 5.1 to 5.3 the information for every simulations, including the ADM mass of coalescing neutron stars, binary tidal deformability, parameters of the DEF theories, the status of scalar field before merger, spectral properties of GWs, and the total energy lost via GWs. In particular, we performed a convergence study on model `MPA_B16.5_M1.76` with numerical setup outlined in Section 4.6. The results of the convergence test are also listed in the last two rows in Table 5.2 as `MPA_B16.5_M1.76_lr` and `MPA_B16.5_M1.76_hr` for low and high resolution respectively. For each resolution, we determine f_{peak} as the GW's frequency where its strain reaches maximum, and evaluate f_2 by conducting a Fast Fourier Transform (FFT) to the GW data from merger time up to 25 ms post-merger. A cubic-spline interpolation is then applied to the spectrum to identify the dominant peak as the f_2 mode. We found that the f_2 estimated from simulations with different resolutions agree within 20 Hz, which is smaller than the FFT frequency bin size of 50 Hz, i.e., the deviation is less than the bin size of frequency domain analysis. Even when taking the frequency bin size as a conservative estimate of uncertainty, this corresponds to an uncertainty of less than $< 2\%$. The deviation in f_{peak} is even lower as $< 1\%$. We note that the deviation quoted here is for the value of f_{peak} and f_2 *per se*, whereas the uncertainties in the fitting formula provided in the main text are expressed in terms of logarithmic values. Therefore, the numerical uncertainties presented here are significantly smaller than those associated with the fitting formula.

Table 5.1: Summary of outcomes for the BNS mergers in the massive DEF theory with APR4 EOS. The first column lists the model name which combines EOS, coupling strength B, and baryon mass of each NS in units of $M_\odot$. The second column shows the ADM mass $M_{\rm ADM}$ of each isolated NS. The third column shows the state of pre-merger scalarization with symbols $\times$, $\triangle$ and $\bigcirc$ corresponding to no scalarization, dynamical scalarization, and spontaneous scalarization in the pre-merger phase, respectively. The fourth column lists the binary tidal deformability $\tilde{\Lambda}$. The last four columns summarize the properties of GWs.

Model name	$M_{\rm ADM}$ ($M_\odot$)	Inspiral $\bar{\varphi}$	$\tilde{\Lambda}$	$f_{\rm peak}$ (kHz)	f_2 (kHz)	$Dh_{\rm peak}/M$
`APR4_B13.8_M1.57`	1.4041	$\times$	251.5	2.100	-	0.280
`APR4_B13.8_M1.58`	1.4119	$\times$	242.8	2.105	-	0.281
`APR4_B14.3_M1.57`	1.4041	$\times$	251.5	2.101	-	0.280
`APR4_B14.3_M1.58`	1.4119	$\times$	242.8	2.105	-	0.281
`APR4_B14.8_M1.62`	1.4436	$\triangle$	210.5	2.231	-	0.298
`APR4_B14.8_M1.63`	1.4514	$\triangle$	203.2	2.252	-	0.300
`APR4_B15.3_M1.48`	1.3323	$\triangle$	348.8	2.204	3.121	0.282
`APR4_B15.3_M1.50`	1.3500	$\triangle$	321.6	2.181	3.049	0.285
`APR4_B15.3_M1.52`	1.3643	$\bigcirc$	300.7	2.199	3.008	0.288
`APR4_B15.3_M1.54`	1.3802	$\bigcirc$	279.6	2.213	3.123	0.292
`APR4_B15.3_M1.56`	1.3961	$\bigcirc$	260.4	2.201	3.186	0.294
`APR4_B15.3_M1.58`	1.4118	$\bigcirc$	242.9	2.215	3.417	0.298
`APR4_B15.3_M1.60`	1.4277	$\bigcirc$	226.7	2.232	3.544	0.300
`APR4_B15.3_M1.62`	1.4433	$\bigcirc$	212.0	2.226	-	0.303
`APR4_B15.3_M1.64`	1.4590	$\bigcirc$	198.4	2.237	-	0.304
`APR4_B15.3_M1.65`	1.4668	$\bigcirc$	192.0	2.224	-	0.305
`APR4_B15.3_M1.66`	1.4747	$\bigcirc$	185.7	2.220	-	0.307
`APR4_B15.3_M1.68`	1.4900	$\bigcirc$	174.3	2.246	-	0.308
`APR4_B15.8_M1.50`	1.3481	$\bigcirc$	321.4	2.192	3.075	0.290
`APR4_B15.8_M1.52`	1.3642	$\bigcirc$	299.3	2.204	3.045	0.294
`APR4_B15.8_M1.54`	1.3800	$\bigcirc$	279.3	2.217	2.990	0.296
`APR4_B15.8_M1.56`	1.3960	$\bigcirc$	260.9	2.209	3.070	0.299
`APR4_B15.8_M1.58`	1.4116	$\bigcirc$	244.3	2.183	3.270	0.301
`APR4_B15.8_M1.60`	1.4274	$\bigcirc$	228.8	2.203	3.557	0.304
`APR4_B15.8_M1.62`	1.4430	$\bigcirc$	214.5	2.221	3.591	0.305
`APR4_B15.8_M1.64`	1.4586	$\bigcirc$	201.3	2.218	-	0.308
`APR4_B15.8_M1.66`	1.4742	$\bigcirc$	189.0	2.222	-	0.310
`APR4_B15.8_M1.67`	1.4819	$\bigcirc$	183.3	2.222	-	0.311
`APR4_B15.8_M1.68`	1.4897	$\bigcirc$	177.7	2.239	-	0.312
`APR4_B15.8_M1.70`	1.5052	$\bigcirc$	167.0	2.220	-	0.314
`APR4_B16.3_M1.52`	1.3637	$\bigcirc$	300.1	2.204	3.044	0.297
`APR4_B16.3_M1.54`	1.3797	$\bigcirc$	280.6	2.196	3.090	0.299
`APR4_B16.3_M1.56`	1.3955	$\bigcirc$	263.0	2.216	3.123	0.302
`APR4_B16.3_M1.58`	1.4111	$\bigcirc$	246.8	2.179	3.113	0.304
`APR4_B16.3_M1.60`	1.4268	$\bigcirc$	231.9	2.212	3.196	0.307
`APR4_B16.3_M1.62`	1.4425	$\bigcirc$	217.9	2.205	-	0.309
`APR4_B16.3_M1.64`	1.4580	$\bigcirc$	205.0	2.203	-	0.311
`APR4_B16.3_M1.66`	1.4737	$\bigcirc$	193.0	2.231	-	0.313
`APR4_B16.3_M1.68`	1.4891	$\bigcirc$	181.8	2.215	-	0.315
`APR4_B16.3_M1.69`	1.4967	$\bigcirc$	176.6	2.229	-	0.316
`APR4_B16.3_M1.70`	1.5046	$\bigcirc$	171.4	2.231	-	0.317

Table 5.2: Same as Table 5.1 but for the MPA1 EOS.

Model name	$M_{\rm ADM}$ ($M_\odot$)	Inspiral $\bar{\varphi}$	$\tilde{\Lambda}$	$f_{\rm peak}$ (kHz)	f_2 (kHz)	$Dh_{\rm peak}/M$
MPA1_B15.0_M1.78	1.5830	×	236.4	1.911	-	0.283
MPA1_B15.0_M1.79	1.5910	×	229.1	1.911	-	0.284
MPA1_B15.5_M1.78	1.5830	×	236.4	1.911	-	0.283
MPA1_B15.5_M1.79	1.5910	×	229.1	1.910	-	0.284
MPA1_B16.0_M1.60	1.4399	×	419.3	1.798	2.757	0.261
MPA1_B16.0_M1.62	1.4559	×	392.9	1.806	2.761	0.264
MPA1_B16.0_M1.64	1.4721	×	368.0	1.834	-	0.270
MPA1_B16.0_M1.66	1.4880	×	345.1	1.834	2.820	0.267
MPA1_B16.0_M1.68	1.5040	×	323.6	1.821	2.839	0.270
MPA1_B16.0_M1.70	1.5200	×	303.5	1.966	2.699	0.278
MPA1_B16.0_M1.72	1.5358	△	285.0	1.964	2.779	0.287
MPA1_B16.0_M1.74	1.5537	△	265.5	1.989	3.011	0.290
MPA1_B16.0_M1.76	1.5674	○	251.4	2.001	3.033	0.292
MPA1_B16.0_M1.78	1.5832	○	236.4	1.978	3.116	0.294
MPA1_B16.0_M1.80	1.5989	○	222.5	1.987	3.146	0.296
MPA1_B16.0_M1.82	1.6145	○	209.6	1.977	3.214	0.299
MPA1_B16.0_M1.84	1.6299	○	197.7	1.984	-	0.302
MPA1_B16.0_M1.85	1.6377	○	192.0	2.000	-	0.303
MPA1_B16.0_M1.86	1.6456	○	186.4	2.006	-	0.304
MPA1_B16.5_M1.60	1.4399	△	419.3	1.930	2.668	0.276
MPA1_B16.5_M1.62	1.4559	○	391.9	1.934	2.735	0.277
MPA1_B16.5_M1.64	1.4719	○	366.7	1.948	2.812	0.280
MPA1_B16.5_M1.66	1.4880	○	343.3	1.965	2.756	0.284
MPA1_B16.5_M1.68	1.5039	○	322.0	1.970	2.787	0.286
MPA1_B16.5_M1.70	1.5197	○	302.5	1.955	2.746	0.288
MPA1_B16.5_M1.72	1.5357	○	284.2	1.965	2.864	0.291
MPA1_B16.5_M1.74	1.5514	○	267.6	1.970	2.916	0.294
MPA1_B16.5_M1.76	1.5673	○	251.9	1.971	2.914	0.296
MPA1_B16.5_M1.78	1.5830	○	237.5	1.966	2.980	0.298
MPA1_B16.5_M1.80	1.5986	○	224.2	1.975	3.053	0.301
MPA1_B16.5_M1.82	1.6142	○	211.6	1.973	-	0.303
MPA1_B16.5_M1.84	1.6296	○	200.1	1.979	-	0.304
MPA1_B16.5_M1.86	1.6453	○	189.1	1.988	-	0.306
MPA1_B16.5_M1.87	1.6531	○	183.9	1.996	-	0.307
MPA1_B16.5_M1.88	1.6607	○	178.9	2.000	-	0.308
MPA1_B16.5_M1.90	1.6761	○	169.4	2.019	-	0.310
MPA1_B17.0_M1.70	1.5196	○	302.2	1.967	2.777	0.292
MPA1_B17.0_M1.72	1.5353	○	285.0	1.951	2.842	0.294
MPA1_B17.0_M1.74	1.5511	○	268.8	1.946	2.759	0.297
MPA1_B17.0_M1.76	1.5670	○	253.7	1.953	2.856	0.300
MPA1_B17.0_M1.78	1.5824	○	239.9	1.972	2.821	0.302
MPA1_B17.0_M1.80	1.5981	○	226.8	1.968	2.981	0.303
MPA1_B17.0_M1.82	1.6139	○	214.4	1.969	-	0.305
MPA1_B17.0_M1.84	1.6293	○	203.1	1.990	-	0.307
MPA1_B17.0_M1.86	1.6447	○	192.4	1.999	-	0.309
MPA1_B17.0_M1.87	1.6525	○	187.3	1.998	-	0.310
MPA1_B17.0_M1.88	1.6601	○	182.5	1.992	-	0.311
MPA1_B17.0_M1.90	1.6757	○	172.9	1.994	-	0.312
MPA1_B16.5_M1.76_lr	1.5673	○	251.9	1.956	2.893	0.295
MPA1_B16.5_M1.76_hr	1.5673	○	251.9	1.962	2.909	0.296

Table 5.3: Same as Table 5.1 but for the H4 EOS.

Model name	M_{ADM} ($M_{\odot}$)	Inspiral $\bar{\varphi}$	$\tilde{\Lambda}$	f_{peak} (kHz)	f_2 (kHz)	Dh_{peak}/M
H4_B15.0_M1.70	1.5414	×	470.0	1.653	-	0.255
H4_B15.0_M1.71	1.5494	×	453.2	1.655	-	0.256
H4_B15.5_M1.70	1.5414	×	470.0	1.654	-	0.255
H4_B15.5_M1.71	1.5494	×	453.2	1.655	-	0.256
H4_B16.0_M1.70	1.5414	×	470.0	1.654	-	0.255
H4_B16.0_M1.71	1.5494	×	453.2	1.655	-	0.256
H4_B16.5_M1.70	1.5414	×	470.0	1.668	-	0.255
H4_B16.5_M1.71	1.5494	×	453.2	1.669	-	0.257
H4_B17.0_M1.50	1.3762	×	986.3	1.607	2.551	0.231
H4_B17.0_M1.60	1.4594	×	680.3	1.612	2.747	0.241
H4_B17.0_M1.62	1.4758	×	632.1	1.637	2.831	0.245
H4_B17.0_M1.64	1.4923	×	587.0	1.634	2.874	0.247
H4_B17.0_M1.66	1.5087	×	545.2	1.621	2.842	0.249
H4_B17.0_M1.68	1.5251	×	506.1	1.655	-	0.253
H4_B17.0_M1.70	1.5414	×	470.0	1.653	-	0.255
H4_B17.0_M1.72	1.5575	×	436.6	1.648	-	0.257
H4_B17.0_M1.74	1.5738	△	405.1	1.846	-	0.280
H4_B17.0_M1.75	1.5867	△	381.9	1.874	-	0.281
H4_B17.0_M1.76	1.5899	○	370.3	1.851	-	0.283
H4_B17.0_M1.78	1.6060	○	336.8	1.868	-	0.286
H4_B17.0_M1.80	1.6220	○	307.6	1.878	-	0.289
H4_B17.5_M1.50	1.3762	×	986.3	1.606	2.553	0.231
H4_B17.5_M1.60	1.4594	×	680.3	1.622	2.725	0.241
H4_B17.5_M1.62	1.4758	×	632.1	1.636	2.736	0.245
H4_B17.5_M1.64	1.4923	×	587.0	1.651	2.798	0.247
H4_B17.5_M1.66	1.5087	△	545.2	1.913	2.847	0.273
H4_B17.5_M1.68	1.5251	○	498.2	1.903	2.854	0.275
H4_B17.5_M1.70	1.5413	○	451.2	1.867	-	0.279
H4_B17.5_M1.72	1.5575	○	410.4	1.852	-	0.283
H4_B17.5_M1.74	1.5736	○	374.8	1.872	-	0.287
H4_B17.5_M1.75	1.5818	○	358.3	1.863	-	0.288
H4_B17.5_M1.76	1.5898	○	343.1	1.877	-	0.289
H4_B17.5_M1.78	1.6058	○	315.3	1.877	-	0.291
H4_B17.5_M1.80	1.6216	○	290.6	1.910	-	0.294
H4_B17.5_M1.82	1.6377	○	268.0	1.915	-	0.297
H4_B17.5_M1.84	1.6535	○	247.9	1.956	-	0.301
H4_B17.5_M1.86	1.6694	○	229.5	1.957	-	0.304
H4_B18.0_M1.48	1.3594	×	1062.8	1.610	2.539	0.229
H4_B18.0_M1.50	1.3762	×	986.3	1.609	2.516	0.231
H4_B18.0_M1.52	1.3929	×	916.2	1.618	2.569	0.233
H4_B18.0_M1.60	1.4594	○	677.4	1.962	2.673	0.269
H4_B18.0_M1.62	1.4758	○	609.6	1.912	2.767	0.273
H4_B18.0_M1.64	1.4922	○	551.2	1.923	2.700	0.276
H4_B18.0_M1.66	1.5086	○	500.5	1.880	2.800	0.279
H4_B18.0_M1.68	1.5249	○	456.4	1.877	2.809	0.283
H4_B18.0_M1.70	1.5410	○	417.9	1.855	2.861	0.286
H4_B18.0_M1.72	1.5572	○	383.6	1.892	-	0.289
H4_B18.0_M1.74	1.5733	○	353.0	1.890	-	0.292
H4_B18.0_M1.76	1.5894	○	325.7	1.899	-	0.294
H4_B18.0_M1.77	1.5973	○	313.3	1.907	-	0.295
H4_B18.0_M1.78	1.6053	○	301.3	1.903	-	0.297
H4_B18.0_M1.80	1.6212	○	279.3	1.931	-	0.300
H4_B18.0_M1.82	1.6371	○	259.2	1.947	-	0.302
H4_B18.0_M1.84	1.6529	○	241.0	1.937	-	0.305
H4_B18.0_M1.86	1.6687	○	224.3	1.950	-	0.307

Table 5.4: Same as Table 5.1 but for the APR4, MPA1 and H4 EOSs in GR. The first column lists the model name which combines EOS and baryon mass of each NS in units of $M_\odot$.

Model name	$M_{\rm ADM}$ ($M_\odot$)	$\tilde{\Lambda}$	$f_{\rm peak}$ (kHz)	f_2 (kHz)	$Dh_{\rm peak}/M$
APR4_M1.48	1.3323	348.5	2.015	3.287	0.267
APR4_M1.50	1.3483	323.5	2.037	3.318	0.270
APR4_M1.52	1.3643	300.9	2.042	3.417	0.272
APR4_M1.54	1.3802	279.2	2.058	3.456	0.276
APR4_M1.56	1.3961	260.2	2.075	3.463	0.278
APR4_M1.58	1.4119	241.8	2.102	-	0.281
APR4_M1.60	1.4277	225.7	2.114	-	0.283
APR4_M1.62	1.4434	210.2	2.128	-	0.286
APR4_M1.64	1.4591	196.1	2.150	-	0.288
APR4_M1.66	1.4747	182.9	2.158	-	0.292
APR4_M1.68	1.4903	170.5	2.178	-	0.294
MPA1_M1.70	1.5198	303.0	1.858	2.971	0.273
MPA1_M1.72	1.5357	285.4	1.868	3.036	0.275
MPA1_M1.74	1.5515	267.3	1.878	3.014	0.277
MPA1_M1.76	1.5673	250.9	1.900	3.087	0.280
MPA1_M1.78	1.5831	236.0	1.903	3.226	0.283
MPA1_M1.79	1.5909	228.5	1.909	-	0.283
MPA1_M1.80	1.5988	221.9	1.909	-	0.285
MPA1_M1.82	1.6144	208.6	1.900	-	0.286
MPA1_M1.84	1.6300	196.6	1.914	-	0.288
MPA1_M1.86	1.6456	184.6	1.933	-	0.291
MPA1_M1.88	1.6611	174.2	1.934	-	0.294
H4_M1.46	1.3426	1145.9	1.586	2.549	0.229
H4_M1.48	1.3594	1062.8	1.585	2.451	0.229
H4_M1.50	1.3762	986.3	1.584	2.615	0.232
H4_M1.52	1.3929	916.2	1.595	2.688	0.233
H4_M1.54	1.4096	850.3	1.617	2.628	0.235
H4_M1.56	1.4262	789.4	1.614	2.745	0.237
H4_M1.58	1.4428	732.9	1.616	-	0.240
H4_M1.60	1.4593	678.9	1.632	-	0.241
H4_M1.62	1.4758	631.7	1.644	-	0.246
H4_M1.64	1.4923	586.0	1.637	-	0.248
H4_M1.66	1.5086	543.9	1.644	-	0.250
H4_M1.68	1.5250	505.1	1.624	-	0.252
H4_M1.70	1.5413	469.2	1.635	-	0.254
H4_M1.71	1.5494	452.4	1.627	-	0.256
H4_M1.72	1.5576	436.0	1.630	-	0.257
H4_M1.74	1.5738	404.5	1.640	-	0.260
H4_M1.76	1.5899	375.4	1.647	-	0.263
H4_M1.78	1.6061	348.4	1.643	-	0.265
H4_M1.80	1.6221	323.4	1.670	-	0.268

Part III

Numerical Relativity in axisymmetry

Chapter 6

Supernova-like explosion of massive rotating stars from disks surrounding a black hole

Contents

Breakdown of Contribution

This chapter is based on the publication: "*Supernovalike explosions of massive rotating stars from disks surrounding a black hole*" in Phys.Rev.D 109 (2024) 2, 023031 [209] by S. Fujibayashi, **A. T.-L. Lam**, M. Shibata and Y. Sekiguchi. The axisymmetric numerical code was developed by S. Fujibayashi, M. Shibata and Y. Sekiguchi. I developed a free-fall model of a massive rotating star to approximate the stage when a rotating black hole is formed after the gravitational collapse of the star with an envelope in a free-fall state. The initial data were constructed by me using the open-source code `octree-mg` modified by me. S. Fujibayashi carried out all the numerical simulations and generated all the figures. Y. Sekiguchi provided constructive comments on the manuscript partially written by S. Fujibayashi, M. Shibata and me.

Overview

In this Chapter, we perform a new general-relativistic viscous-radiation hydrodynamics simulation for supernova-like explosion associated with stellar core collapse of rotating massive stars to a system of a black hole and a massive torus paying particular attention to large-mass progenitor stars with the zero-age main-sequence mass of $M_{\rm ZAMS} = 20$, 35, and $45M_\odot$ of Ref. [21]. Assuming that a black hole is formed in a short timescale after the onset of the stellar collapse, the new simulations are started from initial data of a spinning black hole and infalling matter that self-consistently satisfy the constraint equations of general relativity. It is found that with a reasonable size of the viscous parameter, the supernova-like explosion is driven by the viscous heating effect in the torus around the black hole irrespective of the progenitor mass. The typical explosion energy and ejecta mass for the large-mass cases ($M_{\rm ZAMS} = 35$ and $45M_\odot$) are $\sim 10^{52}\,$erg and $\sim 5M_\odot$, respectively, with ^{56}Ni mass larger than $0.15M_\odot$. These are consistent with the observational data of stripped-envelope and high-energy supernovae such as broad-lined type Ic supernovae. This indicates that rotating stellar collapses of massive stars to a black hole surrounded by a massive torus can be a central engine for high-energy supernovae. By artificially varying the angular velocity of the initial data, we explore the dependence of the explosion energy and ejecta mass on the initial angular momentum and find that the large explosion energy $\sim 10^{52}\,$erg and large ^{56}Ni mass $\geq 0.15M_\odot$ are possible only when a large-mass compact torus with mass $\gtrsim 1M_\odot$ is formed.

6.1 Introduction

Gravitational-wave observations by advanced LIGO and advanced Virgo have shown that stellar-mass black holes with a wide mass range between $\sim 3M_\odot$ and $\sim 100M_\odot$ are commonplace in the universe [19, 489]. It is natural to consider that a majority of these black holes are formed from core collapse of massive stars. In particular for large black-hole mass, $M_{\rm BH} \gtrsim 20M_\odot$, the black holes are likely to be formed shortly after the stellar core collapse with a short proto-neutron star stage or directly during the stellar core collapse. However, it is still not very clear how these black holes are formed. One way to understand the formation process of the black holes is to detect electromagnetic signals emitted during the formation and subsequent evolution processes such as gamma-ray bursts [370, 518]. However, the observational information of the stellar center is limited because the formed black hole is hidden by the dense matter surrounding it. Therefore, to understand the formation and evolution processes of the black holes during the stellar core collapse, theoretical studies play a crucial role.

A numerical-relativity simulation incorporating the relevant physics such as neutrino transfer, equation of state for high-density matter, and angular-momentum transport is the chosen way to theoretically understand the formation and evolution processes of stellar-mass black holes. In our previous work [205], we performed numerical-relativity simulations with approximate neutrino transfer and shear viscous hydrodynamics employing relatively low-mass (9 and $20M_\odot$), compact, rotating progenitor stars derived by stellar evolution calculations of Ref. [21]. We showed that these stars collapse to a black hole shortly after the formation of a proto-neutron star and subsequently the black holes grow due to the mass accretion from the infalling envelope. In the long-term (several seconds) evolution, an accretion disk is developed due to the centrifugal force of late-time infalling matter. The disk subsequently becomes a geometrically thick torus by the effects of viscous heating, viscous angular momentum transport, and shock heating. During an early stage in which the neutrino cooling efficiency and the ram pressure by the infalling matter are high, the outflow of the matter from the torus is prohibited. However, in a later stage, the neutrino cooling efficiency and the ram pressure become low enough to induce the mass outflow from the system, leading to a supernova-like explosion for the entire progenitor star (see also Ref. [261] for a related work).

The previous work [205] also showed that the explosion energy may be larger than that of the typical supernovae if the progenitor stars are rapidly rotating and a high mass-infall rate onto the torus is achieved. In such a case, a compact and massive ($\gtrsim 1M_\odot$) disk/torus can be formed around a black hole and the viscous and shock heating on the disk/torus can provide a large amount of the thermal energy, which can be the source for an energetic explosion. The viscous heating rate in a disk is written approximately as $\dot{E}_\nu \sim \nu M_{\rm torus}\Omega^2$ with the torus mass $M_{\rm torus}$, angular velocity Ω, and shear viscous coefficient ν. In the alpha viscous prescription [417], ν is written as

$$\nu = \alpha_\nu c_{\rm s} H, \tag{6.1}$$

where α_ν is the so-called alpha parameter, $c_{\rm s}$ is the sound velocity, and H is the scale height of the torus approximately written as $H = c_{\rm s}/\Omega$. Then, the viscous heating rate is

$$\begin{aligned} \dot{E}_\nu &\sim 4\times 10^{52}\,{\rm erg/s}\left(\frac{\alpha_\nu}{0.03}\right)\left(\frac{M_{\rm torus}}{M_\odot}\right) \\ &\times \left(\frac{c_{\rm s}}{10^9\,{\rm cm/s}}\right)^2\left(\frac{M_{\rm BH}}{10M_\odot}\right)^{-1/2}\left(\frac{R}{10M_{\rm BH}}\right)^{-3/2}, \end{aligned} \tag{6.2}$$

where we used $\Omega \approx \sqrt{M_{\rm BH}/R^3}$ with $M_{\rm BH}$ and R being the black hole mass and cylindrical radius of the torus. Here, the viscosity is supposed to be induced effectively by magnetohydrodynamics turbulence; see e.g., Refs [44, 232, 234, 237, 279, 420, 481], which shows $\alpha_\nu = O(10^{-2})$. In the presence of matter infall onto the disk/torus, strong shear layers are also formed at the shock surfaces outside the disk/torus, and hence, the viscous heating can be even more enhanced.

The timescale of the viscous heating in the disk/torus is written as

$$\begin{aligned} t_\nu &:= \frac{R^2}{\alpha_\nu c_{\rm s} H} \\ &\approx 4.7\,{\rm s}\left(\frac{\alpha_\nu}{0.03}\right)^{-1}\left(\frac{c_{\rm s}}{10^9\,{\rm cm/s}}\right)^{-2}\left(\frac{M_{\rm BH}}{10M_\odot}\right)^{1/2}\left(\frac{R}{10M_{\rm BH}}\right)^{1/2}, \end{aligned} \tag{6.3}$$

and thus, the total dissipated energy is approximately

$$\begin{aligned} \dot{E}_\nu t_\nu &\sim \frac{M_{\rm torus}M_{\rm BH}}{R} \\ &\approx 1.8\times 10^{53}\,{\rm erg}\left(\frac{M_{\rm torus}}{M_\odot}\right)\left(\frac{10M_{\rm BH}}{R}\right). \end{aligned} \tag{6.4}$$

Hence, if a fraction of the energy released by the viscous heating contributes to the outflow of the matter, it is possible to achieve a supernova-like explosion with a very large explosion energy of order 10^{52} erg in the presence of a compact and large-mass torus of $M_{\rm torus} \sim 0.1$–$1M_\odot$.

In this chapter, we continue our exploration of this problem for more massive progenitor stars with zero-age main-sequence mass $M_{\rm ZAMS} = 35$ and $45M_\odot$ as well as $M_{\rm ZAMS} = 20M_\odot$. Following our previous work, we employ the stellar evolution models by Aguilera-Dena et al. [21]. Since these stars have compact and very massive cores at the onset of the collapse, we may expect formation of a black hole shortly after the core bounce [357] (but see Ref. [118] for a counter example). In this work, therefore, we assume the black-hole formation after the core bounce without an explosion in the proto-neutron star stage. Under this assumption, we prepare an initial condition composed of a spinning black hole and infalling matter that self-consistently satisfy constraint equations of general relativity. The initial condition is prepared for a stage with no accretion disk/torus formation. With such initial data, we perform a neutrino-radiation viscous hydrodynamics simulation in full general relativity paying particular attention to the disk/torus formation and evolution, and subsequent development of the matter outflow, which leads to a supernova-like explosion.

This chapter is organized as follows: In Sec. 6.2, we summarize the progenitor models which we employ and then describe how to set up the initial condition composed of a spinning black hole and infalling matter. Section 6.3 presents the results of numerical-relativity simulations focusing on the mechanism of the explosion, the explosion energy, the ejecta property, and predicted light curves of the supernova-like explosion. Section 6.4 is devoted to a summary. In Section 6.5, we describe a formulation for the initial-value problem of general relativity that we employ in this chapter. In Sections 6.6 and 6.7, supplemental numerical results are presented. Throughout this chapter, $k_{\rm B}$ denotes Boltzmann's constant.

6.2 Models and initial conditions

We employ massive and very compact progenitor stars among the stellar evolution models of Ref. [21]. Specifically, we select the stars with the mass of the zero-age main-sequence state, $M_{\rm ZAMS} = 20$, 35, and $45M_\odot$. For these stars, we may suppose that a black hole would be formed in a short timescale after the core bounce because the compactness parameter of Ref. [357] is very large. [1]

Assuming the conservation of the specific angular momentum during the formation and subsequent growth of a black hole, it is possible to approximately determine the mass and angular momentum of the formed black hole for a given profile of the specific angular momentum as a function of the enclosed mass $j(m)$ [427, 438], if the region with the enclosed mass m collapses to the black hole without forming a disk. In the following, we assume that the angular velocity profile Ω is a function of spherical radius only, as is done in the stellar evolution calculation [21], and thus, the specific angular momentum j represents the angular average as

$$j = \frac{1}{4\pi r^2}\int_0^{2\pi}\int_0^{\pi}\Omega(r)r^4\sin^3\theta d\theta d\varphi = \frac{2}{3}r^2\Omega(r). \tag{6.5}$$

Since j is a function of r, m is as well.

Then, we choose the mass of the black hole, $M_{\rm BH,0}$, which is much larger than the maximum mass of neutron stars of $\lesssim 3M_\odot$. The resulting angular momentum, $J_{\rm BH,0}$, of the black hole is written as

$$J_{\rm BH,0} = \int_0^{M_{\rm BH,0}} j(m')dm'. \tag{6.6}$$

We note that for the choice of $M_{\rm BH,0}$, $j(m)$ with any value of $m \le M_{\rm BH,0}$ has to be smaller than the specific angular momentum of the innermost stable circular orbit $j_{\rm ISCO}$ [48] of the black hole of mass m and angular momentum

$$J(m) = \int_0^{m} j(m')dm'. \tag{6.7}$$

Since the angular momentum of the black hole is determined by specifying the enclosed mass, $j_{\rm ISCO}$ is a function of the enclosed mass m in this context.

Figure 6.1 shows j as a function of m for $M_{\rm ZAMS} = 9$, 20, 35, and $45M_\odot$ of Ref. [21] (solid curves). We also plot $j_{\rm ISCO}$ by the dotted curves. The filled circles denote the points at which $j = j_{\rm ISCO}$ is satisfied (we refer to the corresponding mass as $M_{\rm ISCO}$). This figure shows that for any model, $j(m) < j_{\rm ISCO}$ is satisfied for $m < M_{\rm ISCO}$ and indicates that for the progenitor models with $M_{\rm ZAMS} = 20$, 35, and $45M_\odot$, a black hole is likely to grow to $M_{\rm BH} = M_{\rm ISCO} \approx 8$, 15, and $22M_\odot$ prior to the disk formation. In the presence of the viscous

---

[1] Even for extremely compact progenitor stars, a supernova explosion may occur and a black hole may not be formed via neutrino heating [118] and/or via magnetohydrodynamics effects [117, 355, 356], although our previous simulations for the $20M_\odot$ progenitor model indicate that the assumption of the black-hole formation may be valid for the progenitor models of Ref. [21].

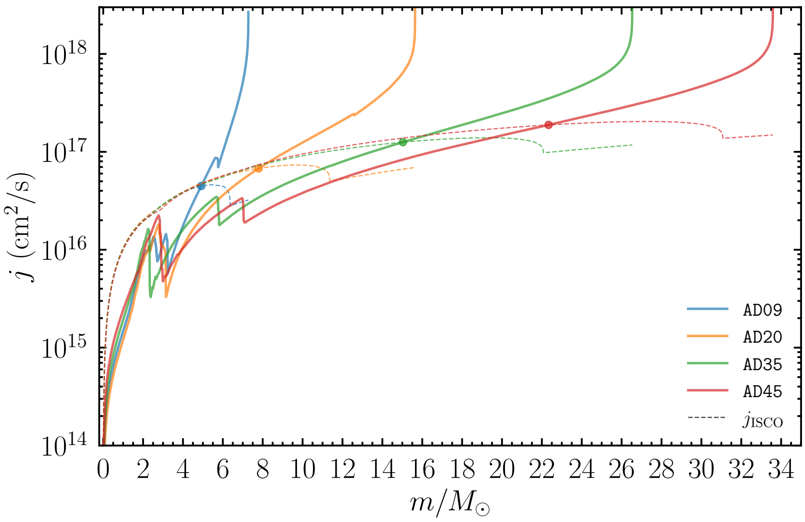

Figure 6.1: Specific angular momentum, j, as a function of the enclosed mass, m, for the models of $M_{\rm ZAMS} = 9$, 20, 35, and $45M_\odot$ in Ref. [21] (solid curves). We also plot $j_{\rm ISCO}$ for a given black hole of mass m and corresponding angular momentum $J(m)$ by the dotted curves. The filled circles denote the points at which $j = j_{\rm ISCO}$ is satisfied for each stellar model.

angular-momentum transport, the disk formation is delayed and black holes with larger mass can be formed before the disk formation.

The next step is to determine the profile of the infalling matter located outside the black hole. For this, we approximate that the envelope in the progenitor stars is in a free-fall state during the collapse. To characterize the profile, we employ a solution of Oppenheimer-Snyder collapse (e.g., Ref. [369]) for our free-fall approximation because the centrifugal effect before the disk formation is minor for the collapsing matter. Then, the fluid motion in the stellar envelope during the collapse is given by

$$r_m(\tau_m) \quad = \quad \frac{1}{2} r_{m,0} \left(1 + \cos\eta\right), \tag{6.8}$$

$$\tau_m \quad := \quad \max(\tau - \tau_{m,0}, 0) = \sqrt{\frac{r_{m,0}^3}{8m}} \left(\eta + \sin\eta\right), \tag{6.9}$$

where r_m is the areal radius of the mass shell with the enclosed mass m, $r_{m,0} = r_m(\tau_m = 0)$, $\tau_{m,0}$ is the starting time of the free-fall (see below), τ_m is the free-fall time of the mass shell, and η is an auxiliary parameter. For simplicity, we assume that the matter in the envelope has zero radial velocity initially and begins to free-fall when the sound wave propagated from the center reaches the radius at

$$\tau_{m,0} = \int_0^{r_{m,0}} \frac{dr}{c_{\rm s}(r)}. \tag{6.10}$$

Table 6.1: Model description. Model name, mass of the zero-age main-sequence stars, $M_{\rm ZAMS}$, employed angular velocity profile, initial rest mass (including the fraction which is transformed to the black hole), initial mass and dimensionless spin of the black hole, the ratio of the matter angular momentum $J_{\rm mat}$ to the black-hole angular momentum $J_{\rm BH,0} = M_{\rm BH,0}^2 \chi_0$, alpha parameter for viscosity, and grid spacing for the central region, Δx_0, respectively. The last two columns present the mass and dimensionless spin of the black hole at the termination of the simulations. Note that for model `AD20-7.8`, we stopped the simulation on the way of further significant black-hole growth (see Fig. 6.5). The results for model `AD20x1` are taken from Ref. [205].

Model	$M_{\rm ZAMS}$	Ω profile	$M_{*,0}$ ($M_\odot$)	$M_{\rm BH,0}$ ($M_\odot$)	χ_0	$J_{\rm mat}$ $/J_{\rm BH,0}$	α_ν	Δx_0 (m)	$M_{\rm BH,f}$ ($M_\odot$)	$\chi_{\rm BH,f}$
`AD20-7.8`	$20M_\odot$	original	15.1	7.8	0.60	9.93	0.03	250	(10.4)	(0.74)
`AD20-9`	$20M_\odot$	original	15.1	9.0	0.72	5.60	0.03	216	10.8	0.79
`AD20-10`	$20M_\odot$	original	15.0	10.0	0.83	3.86	0.03	240	10.9	0.84
`AD35-15`	$35M_\odot$	original	25.5	15.0	0.66	4.32	0.03	360	20.2	0.81
`AD35-15-hi`	$35M_\odot$	original	25.4	15.0	0.66	4.53	0.03	300	19.6	0.81
`AD35-15-mv`	$35M_\odot$	original	25.5	15.0	0.66	4.33	0.06	360	19.6	0.79
`AD35-15-hv`	$35M_\odot$	original	25.5	15.0	0.66	4.32	0.10	360	18.9	0.78
`AD35x0.5-21.5`	$35M_\odot$	original×0.5	25.5	21.5	0.48	0.84	0.03	516	25.1	0.60
`AD35x0.6-21.5`	$35M_\odot$	original×0.6	25.5	21.5	0.58	0.84	0.03	516	24.5	0.66
`AD35x0.8-18`	$35M_\odot$	original×0.8	25.4	18.0	0.63	2.13	0.03	432	22.2	0.75
`AD35x1.2-12.5`	$35M_\odot$	original×1.2	25.5	12.5	0.69	8.18	0.03	300	18.2	0.85
`AD45-22`	$45M_\odot$	original	32.6	22.0	0.64	2.71	0.03	528	28.0	0.77
`AD45-25`	$45M_\odot$	original	32.4	25.0	0.73	1.45	0.03	600	27.7	0.75
`AD45-25-hv`	$45M_\odot$	original	32.4	25.0	0.73	1.45	0.10	600	26.8	0.74
`AD20x1`	$20M_\odot$	original	15.1	—	—	—	—	175	11.2	0.73

Then, the black-hole formation time $\tau = \tau_{\rm BH}$ can be estimated as

$$\tau_{\rm BH} = \sqrt{\frac{R_{\rm BH,0}^3}{8M_{\rm BH,0}}} \left(\eta_{\rm BH} + \sin\eta_{\rm BH}\right) + \int_0^{R_{\rm BH,0}} \frac{dr}{c_{\rm s}(r)}, \tag{6.11}$$

where $\cos\eta_{\rm BH} = 4M_{\rm BH,0}/R_{\rm BH,0} - 1$ and $R_{\rm BH,0}$ is the areal radius of a mass shell with enclosed mass $M_{\rm BH,0}$. Note that the mass shell for $\tau_{m,0} > \tau_{\rm BH}$ does not start infalling. The radial velocity of the matter is then given approximately by

$$u^r = \frac{\partial r_m}{\partial \tau} = \sqrt{\frac{2m\left(r_{m,0} - r_m(\tau_m)\right)}{r_{m,0}r_m(\tau_m)}}. \tag{6.12}$$

Since we use the spinning black-hole puncture in quasi-isotropic coordinates for the initialization of geometric variables (see Section 6.5), we need to perform coordinate transformation to quasi-isotropic coordinates $(\bar{r}, \theta, \varphi)$ for consistency as

$$\bar{r} = \frac{1}{2}\left(r_m - m + \sqrt{r_m^2 - 2mr_m + a_m^2}\right), \tag{6.13}$$

where $a_m = J(m)/m$ and we assumed the conservation of the rest mass, m, and angular momentum $J(m)$ along radial geodesics of infalling mass shells. As a result, the weighted rest-mass density ρ_*, angular momentum density $\hat{J}_\varphi$, and radial velocity $u_{\bar{r}}$ (see Section 6.5

for the definition of them) are given by

$$\begin{aligned}
\rho_* &= \frac{1}{4\pi\bar{r}^2}\frac{\partial m}{\partial \bar{r}}, && (6.14)\\
\hat{J}_\varphi &= \frac{3}{8\pi\bar{r}^2}\frac{\partial J(m)}{\partial \bar{r}}\sin^2\theta, && (6.15)\\
u_{\bar{r}} &= \frac{r_m^2}{\bar{r}^2}\frac{\partial \bar{r}}{\partial r_m}u^r\\
&= \frac{r_m^2}{\bar{r}\left(m+2\bar{r}-r_m\right)}\sqrt{\frac{2m\left(r_{m,0}-r_m\right)}{r_{m,0}r_m}}, && (6.16)
\end{aligned}$$

while other thermodynamical quantities such as the specific enthalpy (h) and temperature (T) are obtained from the initial entropy of the matter assuming the adiabatic flow. In addition, we assume that the electron fraction is unchanged in the free-fall. After all the hydrodynamical quantities are set, we initialize the geometrical quantities following an initial-value formulation presented in Section 6.5.

The initial data is prepared using the multigrid solver code modified based on octree-mg [488], an open source multigrid library, with an octree adaptive-mesh refinement (AMR) grid. This code can provide more accurate initial data than in our previous chapter [205], and hence, enables us to explore the explosion energy and ejecta mass, which are sensitive to the accuracy of the gravitational field in the outer region of progenitor stars, with a better accuracy.

In numerical computation, we cut out the outer part of the progenitor stars with $r \gtrsim 10^5$ km, because our simulation time is at most ~ 20 s, and hence, the matter in such an outer region does not fall into the central region, i.e., it does not give any effect on the evolution of a black hole and a disk/torus.

Table 6.1 lists the models employed and their parameters, i.e., the initial total rest mass in the computational domain (including that of the matter transformed to the black hole), the initial mass and dimensionless spin of the black hole, the ratio of the matter angular momentum to the black-hole angular momentum, the alpha viscous parameter (see Sec. 6.3 for the definition), the grid spacing that covers the central region as well as the mass and dimensionless spin of the black hole at the termination of each simulation. The last number for the model name denotes the initial black-hole mass. Here, the black-hole mass is determined from the equatorial circumferential radius, C_e, of apparent horizons (e.g., see Ref. [430]) by

$$M_{\rm BH} = \frac{C_e}{4\pi}. \tag{6.17}$$

The dimensionless spin, χ, is determined from the ratio of the meridian circumferential radius C_p to C_e using the relation between χ and C_e/C_p for Kerr black holes [430]. We also confirm that the area of the apparent horizons, $A_{\rm AH}$, is written as $A_{\rm AH} = 8\pi M_{\rm BH}^2(1+\sqrt{1-\chi^2})$ for the given set of $M_{\rm BH}$ and χ within 0.1% error.

For the models with $M_{\rm ZAMS} = 20$, 35, and $45 M_\odot$, the rest-mass of the matter located outside the black hole is ≈ 7, 10, and $10 M_\odot$ for $M_{\rm BH,0} = 8$, 15, and $22 M_\odot$. This suggests that for the $35 M_\odot$ and $45 M_\odot$ models, the energy source available for the explosion is larger. For the stellar models of Ref. [21], the stellar radius $R_* \sim 3 \times 10^5$ km depends only weakly on the stellar mass M_* at the onset of the stellar core collapse. This implies that a compactness, defined by $C_* = GM_*/(c^2 R_*)$, and the density at a given radius are larger for the larger values of $M_{\rm ZAMS}$, leading to a higher mass infall rate. This dependency is reflected in the explosion energy as discussed in Sec. 6.3.4. It should be also mentioned that the angular momentum of the matter outside the black hole, $J_{\rm mat}$, is larger than that of the black hole, $J_{\rm BH,0} = \chi_0 {M_{\rm BH,0}}^2$, for all the models with the original angular velocity.

In this chapter, the model with $M_{\rm ZAMS} = 35 M_\odot$ and $\alpha_\nu = 0.03$ (`AD35-15`) is taken as a fiducial model. We perform additional simulations by uniformly multiplying constant factors 0.5, 0.6, 0.8, and 1.2 to the angular velocity of this fiducial model (each is referred to as `AD35-15x0.5`, `AD35-15x0.6`, `AD35-15x0.8`, and `AD35-15x1.2`). This exploration is motivated by the fact that the stellar evolution calculation is carried out assuming the spherical morphology and the results for the angular velocity profile may have a systematic uncertainty. By varying the angular velocity we explore the dependence of the ejecta mass and explosion energy on the initial angular momentum. We also perform simulations with $\alpha_\nu = 0.06$ and 0.10 for the model with $M_{\rm ZAMS} = 35 M_\odot$.

As we already mentioned, Fig. 6.1 indicates that it would be safe to choose $M_{\rm BH,0} \approx 8$, 15, and $22 M_\odot$ at which a disk starts forming. By performing numerical simulations, we find that it is practically possible to employ larger values of $M_{\rm BH,0}$, because in an early stage of the disk evolution during which the viscous timescale of the disk is shorter than its growth timescale, the matter in the disk quickly falls into the black hole. Thus, we also employ $M_{\rm BH,0} = 9$ and $10 M_\odot$ for $M_{\rm ZAMS} = 20 M_\odot$ and $M_{\rm BH,0} = 25 M_\odot$ for $M_{\rm ZAMS} = 45 M_\odot$. With these settings, the computational costs are saved because we can employ a larger grid spacing (see Sec. 6.3). Although the setting is different from the more reliable one (with a smaller value of $M_{\rm BH,0}$), it is indeed found that the results for the explosion energy and ejecta mass depend only weakly on the initial choice of $M_{\rm BH,0}$ if the boost of $M_{\rm BH,0}$ is within $\sim 15\%$. However, $M_{\rm BH,0}$ should not be taken to be too large. For example, for $M_{\rm ZAMS} = 20 M_\odot$ with $M_{\rm BH,0} = 10 M_\odot$, the final black-hole spin is overestimated, because a part of the high-angular-momentum matter that should form the disk in reality is incorrectly taken inside the black hole for the initial condition.

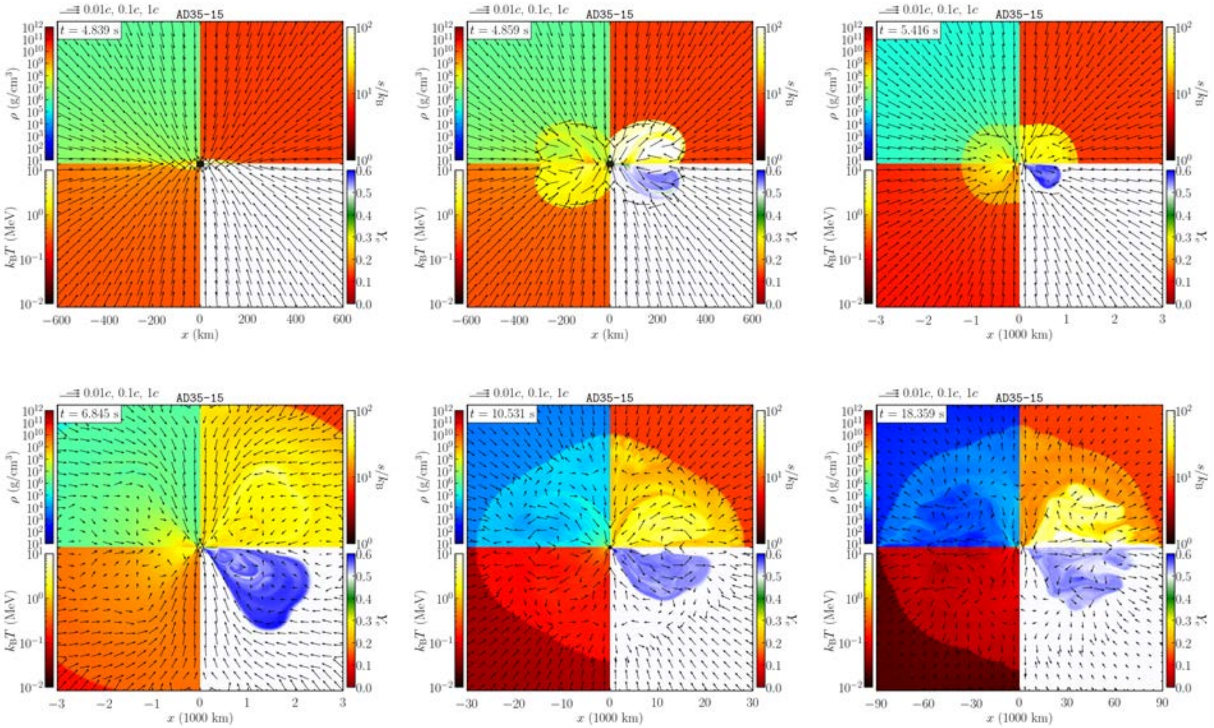

Figure 6.2: Snapshots of the profiles for several quantities at selected time slices for model `AD35-15`. At each time, the rest-mass density (top-left), entropy per baryon (top-right), temperature (bottom-left), and electron fraction (bottom-right) are displayed. The poloidal velocity field is depicted with arrows, the length of which is logarithmically proportional to the magnitude of the poloidal velocity. See the key shown in the top-left legend for the scale. Note that for the third to sixth panels, the regions displayed are wider than those for the first and second panels. The filled circles at the center denote the inside of apparent horizons. An animation for this model can be found in https://www2.yukawa.kyoto-u.ac.jp/~sho.fujibayashi/share/AD35-15-multiscale.mp4

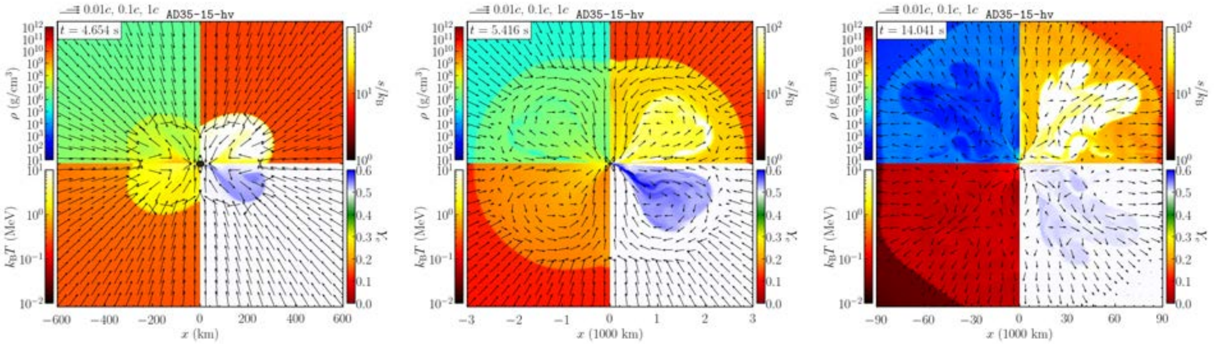

Figure 6.3: The same as Fig. 6.2 but for larger viscosity model `AD35-15-hv`. An animation for this model can be found in https://www2.yukawa.kyoto-u.ac.jp/~sho.fujibayashi/share/AD35-15-hv-multiscale.mp4

6.3 Numerical results

6.3.1 Set-up

Numerical simulations are performed employing the same formulations as in our previous studies [201, 202, 203]. For the viscous hydrodynamics simulation, we have to give the viscous parameter ν [201, 202, 203]. Following our previous works we write it in the form

$$\nu = \min(c_{\rm s}, 0.1c)\ell_{\rm tur}, \tag{6.18}$$

where $\ell_{\rm tur} := \alpha_\nu H$ is considered as a typical eddy scale in the turbulence. To conservatively incorporate the viscous effect, we set up the upper limit ($0.1c$) for the term proportional to the sound velocity in this chapter. Following previous works, we choose $H = 2GM_{\rm BH}/c^2$, where the black-hole mass $M_{\rm BH}$ is determined by Eq. (6.17) at each time (see Sec. 6.2). This choice of H is conservative because it should be much larger than $2GM_{\rm BH}/c^2$ in an outer region of the disk/torus. However, we will show that even with such a conservative choice, the viscous effect becomes strong enough to induce a stellar explosion. In other words, the key to the explosion is the viscous effect in an inner region of the torus.

The simulation is performed on a two-dimensional domain of R and z as in our previous works [201, 202]. For both directions, the following nonuniform grid is used for the present numerical simulation: For $x \lesssim 7GM_{\rm BH,0}/4c^2$ ($x = R$ or z), a uniform grid with the grid spacing, typically, of $\Delta x_0 \approx 0.016GM_{\rm BH,0}/c^2$ is used, while outside this region, the grid spacing Δx_i is increased uniformly as $\Delta x_{i+1} = 1.01\Delta x_i$, where the subscript i denotes the i-th grid. The black-hole horizon is always located in the uniform grid zone.

For the fiducial model with $M_{\rm ZAMS} = 35M_\odot$ and $\alpha_\nu = 0.03$, we additionally perform a high-resolution simulation with $\Delta x \approx 0.0135M_{\rm BH,0}$ to examine the numerical convergence (model `AD35-15-hi`). For this we also prepare the uniform grid for $x \lesssim 7GM_{\rm BH,0}/4c^2$ and non-uniform one with $\Delta x_{i+1} = 1.01\Delta x_i$ for the outer region. The dependence of the numerical results on the grid resolution is briefly summarized in Section 6.7.

Because we start from the initial data of a black hole and infalling matter, we can take a large value of Δx_0 from the beginning of the simulation. For example, for $M_{\rm BH,0} = 15M_\odot$, Δx_0 is chosen as 360 m (i.e., $\Delta x_0 \approx 0.016M_{\rm BH,0}$). If we started the same simulation from the pre-collapse star, we had to prepare a computational domain that could resolve the black-hole formation and subsequent evolution. At the formation of the black hole, its mass is $\sim 3M_\odot$, and hence, if we require the grid spacing that can resolve the black hole at birth with an accuracy as good as the present setting, we have to prepare $\Delta x_0 \approx 72$ m. Therefore by starting the simulation from a black hole and infalling matter, we can save the computational costs significantly.

A caution is appropriate here: For the lower grid resolutions (larger values of $\Delta x_0/M_{\rm BH}$), the black hole is less accurately resolved, leading to the overestimation of the black-hole mass and underestimation of the black-hole spin in our implementation [201] (see also Section 6.6). This is in particular the case for model `AD20-7.8` as well as for model `AD20x1` for which the early evolution of the black hole during the stage of $M_{\rm BH} \approx 3M_\odot$ is less accurately computed. For other models, we choose $\Delta x_0 \leq 0.016 G M_{\rm BH}/c^2$, with which the black hole is evolved in a good accuracy (see Section 6.6).

As we mentioned in Sec. 6.2, we cut out the matter for $r \gtrsim 10^5$ km although the original stellar surface is located at $\sim 3 \times 10^5$ km. The matter in the outer region can affect the explosion dynamics when the exploded matter interacts with it. However, the total mass of the cut-out matter is about 0.6, 1.1, and $1.3M_\odot$ for $M_{\rm ZAMS} = 20$, 35, and $45M_\odot$ [21], and thus, they are much smaller than the ejecta mass for most of the models (see Sec. 6.3).

We stop the simulation when a shock wave associated with the explosion from the disk/torus reaches the outer boundary (at $r \approx 10^5$ km) for $M_{\rm BH} = 35M_\odot$ and $45M_\odot$. For $M_{\rm BH} = 20M_\odot$ for which Δx_0 is small and more computational resources are required for a long-term computation, we stopped the simulations before the explosion energy and ejecta mass saturate to save the computational time, because our main focus in this chapter is the explosion property for large-mass progenitor stars.

6.3.2 Explosion mechanisms

6.3.2.1 General feature

First, we summarize how the disk and torus are formed and evolved, leading to the eventual explosion (see Figs. 6.2 and 6.3). As we find from Fig. 6.1, broadly speaking, the specific angular momentum of the infalling matter increases with the enclosed mass, thus with the radius. The matter located in the inner region does not have the specific angular momentum large enough to form a disk or torus around the black hole. Thus, in an early stage of the black-hole evolution, most of the infalling matter simply falls into the black hole. During this stage, the centrifugal force of the infalling matter does not play an important role. Subsequently, the matter with sufficiently large specific angular momentum starts forming a geometrically thin disk (see the first panel of Fig. 6.2). After the formation of the disk, a strong shear layer is established between the infalling matter and the shock surface outside the disk. Thus, viscous heating efficiently generates the thermal energy. Also, shock dissipation efficiently proceeds around the shock surface. By these heating mechanisms, the disk subsequently becomes geometrically thick, leading to the formation of a torus (see the second panel of Fig. 6.2).

After its formation, the torus gradually grows due to the continuous matter infall, while the black hole grows due to the matter infall primarily from the polar region. During the evolution of the torus, the kinetic energy of the infalling matter is dissipated around the shock

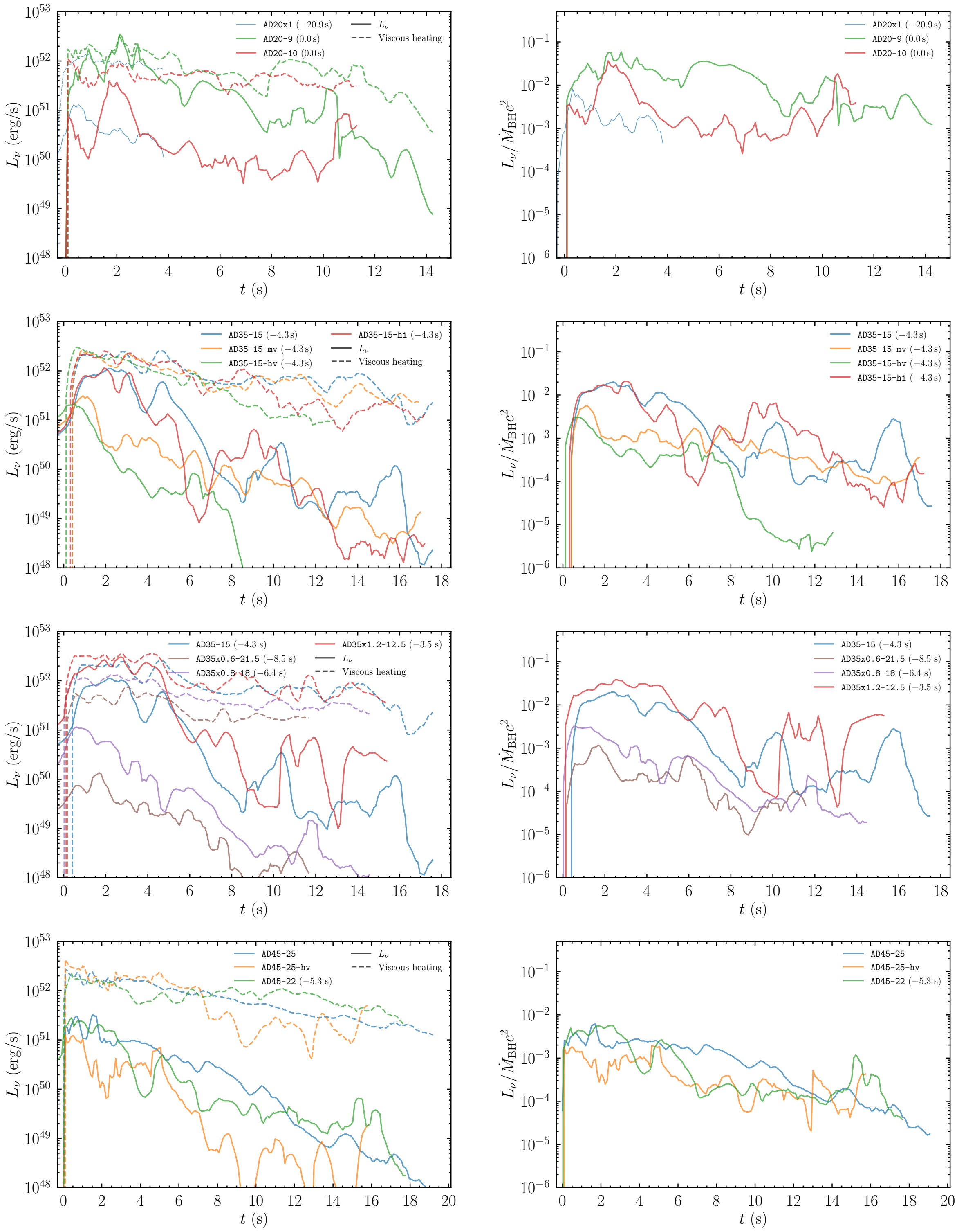

Figure 6.4: Time evolution of the total neutrino luminosity (left) and cooling efficiency (right) for models of $M_{\rm ZAMS} = 20M_\odot$ (top panels), $35M_\odot$ with three different values of the viscous coefficient (second top panels), $35M_\odot$ with different initial angular momentum (third top panels), and $45M_\odot$ (bottom panels). The time is shifted so that $t = 0$ corresponds to the torus formation time for each model. The time offsets are shown in the legend.

surface just outside the torus, which increases the temperature and entropy per baryon of the torus (see the second and third panels of Fig. 6.2 and the first panel of Fig. 6.3). Since the shock surface is non-spherical while the matter infall proceeds nearly spherically, the shear layer is also formed, enhancing the viscous heating. The oblique shocks formed around the shock surface play a role in enhancing the matter infall onto the black hole and inner region of the torus from the polar region. This enhances the efficiency of the viscous heating in the inner region.

In the early stage of the torus evolution, the ram pressure of the infalling matter is too high to induce an outflow from the torus. In addition, the neutrino cooling suppresses the viscous heating effect. However, the ram pressure of the infalling matter continuously decreases because of the decrease in its density, and also, the neutrino cooling efficiency becomes lower in a later stage (see below for more details). As a result, the thermal pressure of the torus generated by the viscous and shock heating eventually exceeds the ram pressure. Then, an outflow from the torus sets in, inducing the explosion of the entire star (see the fourth, fifth, and sixth panels of Fig. 6.2 and the second and third panels of Fig. 6.3).

The viscous heating as well as the shock dissipation are most efficient around the shock surface in the vicinity of the torus. Thus, the outward motion of the outflow is initially induced along the torus surface. The matter of the outward motion has high entropy per baryon, and thus, the outward motion accompanies convective motion, which redistributes the thermal energy to a wide region. Thus, although the matter initially moves toward a particular direction, subsequent motion becomes quasi-isotropic, and the explosion occurs in a nearly spherical way.

Although the viscous and shock heating are universally the explosion sources, the efficiency of the heating and evolution process of the torus depend on the neutrino cooling (see Fig. 6.4). In the presence of an efficient cooling by neutrinos, the torus relaxes to a neutrino-dominated-accretion-flow (NDAF) state. On the other hand, if the neutrino cooling is not efficient, the explosion takes place in the absence of the NDAF state and the explosion sets in earlier. For example, for model `AD35-15` for which the NDAF stage is present the explosion sets in at $t \sim 7\,\mathrm{s}$ while for model `AD35-15-hv` for which the NDAF stage is absent the explosion set is at $t \sim 5\,\mathrm{s}$ (compare Figs. 6.2 and 6.3).

Even after the onset of the explosion, the matter infall continues for at least several seconds near the rotational axis, around which the matter with small specific angular momentum continuously falls onto the black hole and the inner region of the torus. This matter infall to the torus contributes to the efficient viscous and shock heating, sustaining the explosion.

6.3.2.2 Dependence of the progenitor mass

As mentioned in Sec. 6.2, more massive progenitor stars are more compact and thus have higher mass-infall rates, which are advantageous for generating more thermal energy (see below). By contrast, the neutrino luminosity tends to be smaller for more massive progenitor stars at the torus formation (compare the models with original rotation profiles `AD20-9`, `AD35-15`, and `AD45-25`: see left panels of Fig. 6.4). This is due to the larger radius of the innermost stable circular orbit around the black hole for more massive models. That is, for more massive models, which form more massive black holes, the density and temperature of the torus are lower [202], and the neutrino luminosity is also lower. Consequently, the thermal energy generated by the viscous heating is efficiently used for the explosion of the system. Indeed the right panel of Fig. 6.4 shows that the neutrino cooling efficiency defined by $L_\nu/\dot{M}_{\rm BH}c^2$ is lower for more massive progenitor models. This results in a shorter (or no) NDAF phase, leading to a quick explosion. The lower neutrino cooling efficiency, in addition to the higher mass-infall rate, is advantageous for large explosion energy (see Sec. 6.3.4). This situation is in contrast to the usual core-collapse supernova explosion, in which higher neutrino luminosity of proto-neutron stars is advantageous for an earlier explosion (e.g., Ref. [257]).

For the fixed viscous parameter $\alpha_\nu = 0.03$, $M_{\rm ZAMS} = 20$ and $35 M_\odot$ models (`AD20-9` and `AD35-15`) have high neutrino cooling efficiency appreciably exceeds 0.01 (see Fig. 6.4), and have a NDAF phase. As a result, the explosion for these models is delayed after the torus formation. By contrast, no NDAF phase is found for $45 M_\odot$ models (`AD45-22` and `AD45-25`), which drive the explosion shortly after the torus formation. We note that the presence or absence of the NDAF phase depends not only on the progenitor stars but also on the viscous coefficient and the initial angular momentum of the progenitor star, as discussed in the following subsections.

6.3.2.3 Dependence on the viscous coefficient

For the $35 M_\odot$ progenitor, we perform three simulations varying the viscous coefficient and find that the evolution of the system depends qualitatively on the magnitude of α_ν. For large values of α_ν, i.e., 0.06 and 0.10, the evolution toward the explosion is the qualitatively same as those for the $45 M_\odot$ models: The explosion sets in in a relatively short timescale after the formation of the torus with no NDAF phase (cf. Fig. 6.3). By contrast, for $\alpha_\nu = 0.03$, the explosion is delayed because the neutrino cooling efficiency is sufficiently high to suppress the outward motion of the matter by the viscous and shock heating in the early evolution stage of the torus. For this model, the explosion is started only when the mass infalling rate is sufficiently low. This difference results from the stronger effects of the viscous heating and angular momentum transport for the larger viscosity, by which the torus expands more rapidly, reducing the neutrino cooling efficiency in an early stage.

6.3.2.4 Dependence on the initial angular momentum

The dependence of the evolution process of the system on the initial angular momentum is explored for the models of $M_{\rm ZAMS} = 35M_\odot$ with a fixed value of $\alpha_\nu (= 0.03)$. For our models, a disk and/or a torus surrounding a black hole is always formed, but their mass depends strongly on the initial angular momentum: For larger initial angular momentum, it is larger and, as a result, the explosion can be more energetic and mass ejection is more enhanced (see Sec. 6.3.4).

Models `AD35-15` and `AD35x1.2-12.5` achieve a high neutrino cooling efficiency and NDAF phase after the formation of tori (see Fig. 6.4). By contrast models `AD35x0.6-21.5` and `AD35x0.8-18.0` do not achieve the NDAF phase. This illustrates that larger angular momentum stars are more subject to the NDAF phase after the formation of a torus around a black hole.

For a model with sufficiently reduced angular momentum (`AD35x0.5-21.5`), the disk is too sparse and low-mass ($\lesssim 0.5M_\odot$) to find explosion in our simulation time. In this case, the geometrically-thick torus formation is not also found in the simulation time. Even for this case, however, a low-mass disk may be a source of a transient at a very late stage, i.e., $t \gg 10\,{\rm s}$: As discussed in Ref. [263], in this case, the final configuration is likely to be a black hole surrounded only by a low-mass low-compactness disk, which could be evolved by a viscous hydrodynamics effect (resulting from magnetohydrodynamics turbulence) leading to mass ejection. If this happens, a blue, rapidly varying optical transient may be generated after long-term evolution of the accretion disk formed in late time [263].

6.3.3 Evolution of black holes

Figure 6.5 shows the evolution of the mass and dimensionless spin of the black holes for all the models studied in this chapter. Note that for model `AD20-10`, we stopped the evolution of the gravitational field at $t \approx 8\,{\rm s}$ to save computational time because the total mass of the matter in the computational region was smaller than 10% of the black-hole mass, and moreover, model `AD20-9` is our main model for $M_{\rm ZAMS} = 20M_\odot$. Both the mass and dimensionless spin increase steeply prior to the onset of the explosion, but after that, they relax toward final values. The final black-hole mass is 50–60% of $M_{\rm ZAMS}$; large-mass black holes such as observed by gravitational-wave observations [19, 489] are naturally formed from the progenitor models of Ref. [21]. For the models with larger values of α_ν, the final mass and dimensionless spin of the black hole are slightly smaller, because higher viscous heating efficiency as well as viscous angular momentum transport enhances the mass ejection while preventing the matter infall onto the black hole. However the dependence on α_ν is not very strong; the mass and dimensionless spin decrease by $\sim 1M_\odot$ and 0.03, respectively, for the change of α_ν from 0.03 to 0.1.

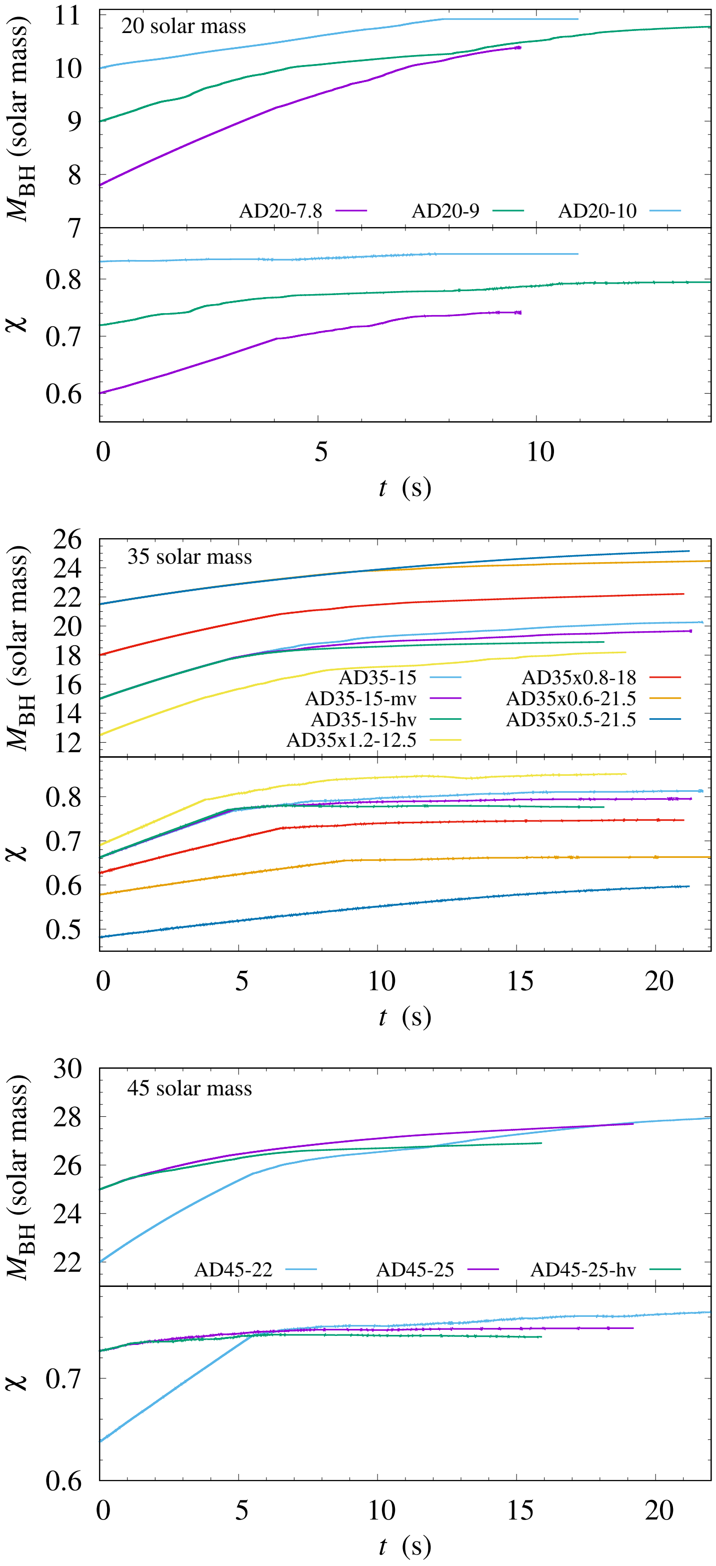

Figure 6.5: Time evolution of the mass and dimensionless spin of the black holes for models of $M_{\rm ZAMS} = 20 M_\odot$ (upper panels), $35 M_\odot$ (middle panels), and $45 M_\odot$ (lower panels). Note that for model `AD20-10`, we stopped the evolution of the gravitational field at $t \approx 8\,$s, and thus, the actual final black-hole mass may be larger.

Table 6.2: Summary of the quantities associated with the explosion for the models for which the simulation is performed for sufficiently long time: Time at the onset of the explosion measured from the torus formation time, $t_{\rm exp}$ (the values in the parenthesis denote the simulation time), explosion energy, $E_{\rm exp}$, and ejecta mass, $M_{\rm ej}$, measured at the termination of the simulation, the ejecta velocity defined by $v_{\rm ej} = \sqrt{2E_{\rm exp}/M_{\rm ej}}$, and synthesized ^{56}Ni mass $M_{\rm Ni}$. In the last two columns, we also list the mass of an ejecta component with the temperature satisfying $T > 5 \times 10^9$ K during the ejection process and the average value of the entropy per baryon for the ejecta. For model `AD35x0.5-21.5`, we do not find explosion. For most of the models, the explosion energy was still increasing at the termination of the simulations, and thus, the values shown here are considered as the lower bound.

Model	$t_{\rm exp}$ (s)	$E_{\rm exp}$ (10^{51} erg)	$M_{\rm ej}$ ($M_\odot$)	$v_{\rm ej}$ (10^9 cm/s)	$M_{\rm Ni}$ ($M_\odot$)	$M_{>5\,{\rm GK}}$ ($M_\odot$)	$\langle s\rangle/k_{\rm B}$
`AD20-9`	3.8 (3.8)	2.2	2.2	1.0	0.24	0.44	17
`AD20-10`	<0.1 (0.1)	2.6	2.6	1.0	0.20	0.44	17
`AD35-15`	2.8 (7.1)	6.5	4.2	1.2	0.18	0.55	23
`AD35-15-hi`	2.0 (6.3)	7.0	5.0	1.2	0.24	0.72	28
`AD35-15-mv`	0.8 (5.1)	8.1	4.1	1.4	0.41	1.02	26
`AD35-15-hv`	0.5 (4.8)	10.1	5.5	1.4	0.15	0.69	39
`AD35x0.5-21.5`	—	—	—	—	—	—	—
`AD35x0.6-21.5`	0.7 (9.2)	2.1	1.0	1.5	0.04	0.16	34
`AD35x0.8-18`	0.8 (7.2)	4.4	2.6	1.7	0.15	0.52	32
`AD35x1.2-12.5`	3.9 (7.4)	6.8	5.3	1.1	0.38	0.90	23
`AD45-22`	0.6 (5.9)	11.5	3.7	1.8	0.28	0.95	33
`AD45-25`	<0.1 (0.1)	8.4	4.3	1.4	0.46	1.15	27
`AD45-25-hv`	<0.1 (0.1)	13.0	4.7	1.7	0.25	0.87	43

Accompanied with the formation of a massive disk/torus around a black hole, the black-hole spin is naturally increased. For all the models with no modification of the initial angular momentum, the dimensionless spin of the black holes is ~ 0.75–0.85 at the termination of the numerical simulation (cf. Table 6.1). The high spin is advantageous for efficiently converting the released gravitational potential energy to the thermal energy.

For smaller and larger initial angular momentum models with $M_{\rm ZAMS} = 35 M_\odot$, the resulting final value of the dimensionless spin of the black hole, $\chi_{\rm f}$, is smaller and larger, respectively, while the final black-hole mass is larger and smaller, respectively. However, $\chi_{\rm f}$ varies only ± 0.05 for the change of the initial angular momentum by $\pm 20\%$ (compare the results for models `AD35x0.8-18`, `AD35-15`, and `AD35x1.2-12.5`). Thus, the final black hole spin is likely to be fairly high as long as a disk/torus with a few $M_\odot$ is formed around the black hole. By contrast, for model `AD35x0.5-21.5`, for which a substantial amount of the infalling matter falls into the black hole, the final value of χ is much smaller than those of the other $35 M_\odot$ models, while the final mass is much larger than others.

Models `AD45-22` and `AD45-25` started the simulations from different black-hole mass. However, the final mass and dimensional spin for these models have similar values. This appears to be also the case for models `AD20-7.8` and `AD20-9`. These results indicate that in the early stage of the disk evolution, a substantial fraction of the matter in the disk quickly falls into the black hole by the viscous effect, and the simulation may be started from a black-hole mass which is slightly larger than those predicted from Fig. 6.1.

6.3.4 Ejecta mass and explosion energy

Figure 6.6 shows the time evolution of the explosion energy (left panels) and ejecta mass (right panels) for all the models studied in this chapter (see also Table 6.2) except for model `AD35x0.5-21.5`, for which explosion is not found in the simulation time. At the termination of the simulations, the explosion energy is still increasing for most of the models, and hence, the values listed in Table 6.2 are considered to be the lower bound. However, broadly speaking, we may conclude that (i) for $M_{\rm ZAMS} = 20M_\odot$, the explosion energy is a few times 10^{51} erg, i.e., comparable to or slightly larger than that of the ordinary supernovae, while (ii) for $M_{\rm ZAMS} = 35M_\odot$ and $45M_\odot$, it is $\sim 10^{52}$ erg, i.e., about one order of magnitude larger than the ordinary supernovae, for the original progenitor models with no modification of the angular momentum profile.

The increasing explosion energy at the termination of the simulation stems from the fact that there is still matter infalling into the vicinity of the black hole. As seen in the left panels of Fig. 6.4, there is still viscous heating of order 10^{51} erg/s, which increases the explosion energy even in the later phase at which the shock wave reaches the outer boundary and ejecta mass does not increase any longer.

The large explosion energy of the massive progenitor models stems from their relatively large compactness. As we already mentioned in Sec. 6.2, for the pre-collapse models of Ref. [21], the compactness of the progenitor star $C_* = GM_*/(c^2R_*)$ is larger for the more massive stellar models. Broadly speaking, the mass infall rate during the collapse is proportional to $M_*/t_{\rm ff} \propto C_*^{3/2}$, where $t_{\rm ff} = \sqrt{R_*^3/M_*}$ is the free-fall timescale. Thus, the mass-infall rate is higher for the larger-compactness progenitor models. The higher mass-infall rate enhances the viscous and shock heating rates around the inner region of the disk/torus, which result in the larger explosion energy for the more massive progenitor models.

For models with larger values of α_ν, the explosion energy and ejecta mass are naturally larger. Fundamentally, the viscous effect should come effectively from the magnetohydrodynamical turbulence and hydrodynamical shear in the present context. Thus, the explosion energy and ejecta mass can be accurately determined only by a magnetohydrodynamics simulation. However, the present study indicates that the dependence of these quantities on α_ν is not very strong; even for the 10/3 times larger value of α_ν, the explosion energy and ejecta mass increase within a factor of 2. In particular, the explosion energy and ejecta mass show similar values for $M_{\rm ZAMS} = 35M_\odot$ with $\alpha_\nu = 0.03$ and 0.06. Therefore it is reasonable to conclude that the explosion energy can reach $E_{\rm exp} \sim 10^{52}$ erg with the ejecta mass of $M_{\rm ej} = 4$–$5M_\odot$ for the present choice of the massive progenitor stars, if the turbulent state is excited and the resulting effective viscosity with $\alpha_\nu = \mathcal{O}(10^{-2})$ is generated around the inner region of the accretion disk/torus.

The modification of the initial angular momentum profile for the progenitor stars of

$M_{\rm ZAMS} = 35M_\odot$ has an impact on the explosion energy and ejecta mass, in particular for the case that we reduce it by more than 40%. The ejecta mass decreases monotonically with the decrease of the initial angular momentum because the total mass outside the black hole is initially smaller and the mass of the resulting disk/torus becomes smaller for the smaller initial angular momentum. The ejecta mass becomes $\sim 1M_\odot$ for the reduction of the angular momentum by 40% (model `AD35x0.6-21.5`) and smaller than $0.4M_\odot$ (i.e., $< M_{*,0} - M_{\rm BH,f}$) by the 50% reduction (model `AD35x0.5-21.5`). For model `AD35x0.6-21.5`, the explosion energy is $\sim 2 \times 10^{51}$ erg, which is comparable to that of ordinary supernovae. This suggests that a rapid rotation as well as the large compactness of the progenitor star is the key to the large explosion energy.

For the models of $M_{\rm BH} = 20M_\odot$ and $45M_\odot$, we performed simulations with different initial black-hole mass. We find a fair agreement of the final values of explosion energy and ejecta mass, although their time evolution depends weakly on the initial setting. Thus, the ejecta-related quantities can be approximately obtained even if we start the simulations with black-hole mass larger than the value expected at the disk formation (see Sec. 6.2).

For $M_{\rm ZAMS} = 20M_\odot$, we compare the present results with that in our previous work [205]. We find that both the explosion energy and ejecta mass were underestimated in the previous study because the simulation time was too short. For obtaining the accurate explosion energy and ejecta mass for this case, we needed a long-term simulation with the duration of $\gtrsim 10\,$s after the onset of the explosion.

Even in the present study, the ejecta mass for $M_{\rm BH} = 20M_\odot$ does not relax to a saturated value at the termination of the simulation. For this model, the expanding shock is still inside the computational domain, and a significant amount of unshocked, bound matter is present in the outer region of the star. The progenitor star for this model is less compact than the more massive progenitor stars, and hence, it takes more time (in units of $M_{\rm BH}$) to follow the ejecta generation. In the longer-term energy injection from the accretion torus, the ejecta mass may be increased to $M_{*,0} - M_{\rm BH,f} \sim 4M_\odot$.

At the termination of the simulations for $M_{\rm ZAMS} = 35M_\odot$ and $45_\odot$, we typically find $M_{*,0} - M_{\rm BH,f} - M_{\rm ej} \approx 1$–$2M_\odot$, which is still bound by the black hole. Since the black-hole mass increases slowly with time even at the termination of the simulations, most part of this mass will eventually fall into the black hole, and a fraction will be ejected from the system via the viscous heating and viscous angular momentum transport. However, this is a minor part compared with the matter ejected earlier.

As mentioned in Sec. 6.2, we discard the stellar matter with $r > 10^5\,$km in our simulation for which the mass is $\sim 1M_\odot$. Thus the ejecta mass may be larger than those listed in Table 6.2 by this amount, but this possible increase is a small fraction of the numerical result of $M_{\rm ej}$ for most of the models.

6.3.5 Nickel mass and predicted light curve

Using the time evolution of the thermodynamical quantities on the tracer particles [205], post-process nucleosynthesis calculations are performed with a open-source nuclear reaction network code `torch` [491] with 495 isotopes, paying particular attention to the ^{56}Ni production.

Table 6.2 lists the mass of ^{56}Ni, $M_{\rm Ni}$, for selected models. The ^{56}Ni mass is found to be always larger than $0.15 M_\odot$ and $\sim$ 3–11% of the total ejecta mass for all the models except for the models with significant angular momentum reduction (`AD35x0.5-21.5` and `AD35x0.6-21.5`). The ^{56}Ni mass does not have strong correlation with the ejecta mass because the ^{56}Ni production efficiency depends strongly on the thermal history of the matter during the explosion. In Table 6.2, we also show the mass of the ejecta that experiences a state with $T > 5\,{\rm GK}$ $(= 5 \times 10^9\,{\rm K})$, $M_{>5\,{\rm GK}}$, and the average entropy per baryon, $\langle s \rangle / k_{\rm B}$, for the ejecta. The ^{56}Ni production primarily occurs for $T \gtrsim 5$ GK, while it is suppressed for the ejecta with a high entropy per baryon [480]. No clear correlation between $M_{\rm Ni}$ and the viscous coefficient is found (compare the results for models `AD35-15`, `AD35-15-mv`, and `AD35-15-hv`). This stems from the fact that the high viscous heating can enhance not only the fraction of the ejecta with $T > 5\,{\rm GK}$, but also the entropy per baryon. In our results, the ^{56}Ni mass is approximately written as (see Fig. 6.7)

$$M_{\rm Ni} \approx \frac{M_{>5\ {\rm GK}}}{2} \left(\frac{\langle s \rangle}{17 k_{\rm B}} \right)^{-4/5}. \tag{6.19}$$

It is also worth pointing out that $M_{>5\,{\rm GK}}$ is by more than a factor of ~ 2 larger than $M_{\rm Ni}$ for the models studied in this chapter. Thus, $M_{>5\,{\rm GK}}$ overestimates the ^{56}Ni mass for the present models.

By contrast, a clear correlation is found between $M_{\rm Ni}$ and the angular momentum of the progenitor stars for the $M_{\rm ZAMS} = 35 M_\odot$ model; larger angular momentum results in the larger ^{56}Ni mass. This correlation stems from the larger mass and lower entropy per baryon of the ejecta for the larger initial angular momentum. The latter is associated with the difference in the evolution of the torus before the explosion sets in. For larger-angular-momentum models `AD35-15` and `AD35x1.2-12.5`, the explosion takes place after a quasi-stationary NDAF phase of the torus, during which neutrino emission extracts the entropy of the torus efficiently. In addition, the explosion after the quasi-stationary phase is less violent [205]. These factors result in the lower entropy of the ejecta. This situation is in clear contrast with those for smaller-angular-momentum models `AD35x0.6-21.5` and `AD35x0.8-18.0`, for which the explosion takes place in a relatively short timescale after the formation of the torus because of the lower neutrino cooling efficiency and lower ram pressure of infalling matter. For these models, a high entropy generated by the shock dissipation at the formation of the torus is directly reflected in that of the ejecta.

For the $M_{\rm ZAMS} = 45M_\odot$ models, the ^{56}Ni mass is larger, $\geq 0.25M_\odot$, reflecting the large mass fraction of the high-temperature ejecta component. The larger values of $M_{>5\,\rm GK}$ for these models result from the earlier explosion than for less massive progenitor models (see Sec. 6.3.2). A significant difference is found between the results of models `AD45-22` and `AD45-25` in spite of the facts that for these models the explosion energy and ejecta mass show similar values. This illustrates that the ^{56}Ni mass depends sensitively on the thermal condition of the ejecta.

Figure 6.8 displays the ^{56}Ni mass as a function of the explosion energy (left panel) and the average ejecta velocity (right panel). Together with the numerical results shown by the filled symbol, we plot the observational data for stripped-envelope supernovae, some of which are broad-lined type Ic supernovae, taken from Refs. [217, 482], by the open symbols. It is found that our numerical results reproduce the relations between $M_{\rm Ni}$ and $E_{\rm exp}$ or $M_{\rm Ni}$ and $v_{\rm ej}$ for high-energy supernovae with $E_{\rm exp} = 2$–$10 \times 10^{51}\,$erg and with $v_{\rm ej} = 1$–$2 \times 10^9\,$cm/s, suggesting that a fraction of these supernovae may be driven by the explosion from a torus surrounding a massive black hole of $M_{\rm BH} \approx 10$–$30M_\odot$. Our result is consistent with a recent model [211].

Using the explosion energy, ejecta mass, and ^{56}Ni mass as input parameters, we derive model light curves for the supernova-like explosion using the Arnett's model [37]. In this modelling, we use the same prescription as described in our previous work [205]. The resulting light curves are displayed in Fig 6.9. As predicted from the explosion energy, ejecta mass, and ^{56}Ni mass, the peak luminosity and timescale of the luminosity decline for most of the models are in good agreement with the observed data for high-energy supernovae like the broad-lined type Ic supernovae or type Ib/Ic supernovae. For model `AD35x0.6-21.6`, the peak luminosity is lower than those for other models due to the smaller ejecta mass and explosion energy, indicating that a rapid rotation may be necessary to reproduce the brightness of high-energy supernovae.

We note that the luminosity predicted by the Arnett model for given ^{56}Ni mass may be underestimated by a factor of a few (see Refs. [153, 154, 272]). Thus, the explosion models presented in this chapter may show more luminous light curves than in Fig. 6.9, i.e., most of them may be good models for broad lined type Ic supernovae, as Fig. 6.8 indicates. To clarify this point, we need a more detailed radiation transfer study for deriving the light curves in follow-up work.

6.4 Summary

We studied the fate after the collapse of rotating massive stars that form a black hole and a disk/torus by performing a neutrino-radiation viscous-hydrodynamics simulation in general relativity and employing the stellar evolution models by Aguilera-Dena et al. [21] as initial data. Specifically, we employed rapidly rotating and compact progenitor stars as base models and constructed a system of a spinning black hole and infalling matter as the initial conditions. For most of the models we employed, a system of a black hole surrounded by a massive torus is formed during the time evolution.

Due to the viscous heating as well as shock heating around the surface of the torus, thermal energy is generated and becomes the source for the explosion of the system. For the massive models ($M_{\rm ZAMS} = 35M_\odot$ and $45M_\odot$), the ejecta mass is 4–$5M_\odot$ and the explosion energy is $\sim 10^{52}$ ergs, i.e., much larger than typical supernovae. The explosion energy is enhanced for larger viscous coefficients. By contrast, the explosion energy for the $20M_\odot$ model is of order 10^{51} erg. The primary reason for this difference is that for the more massive models, the compactness of the progenitor stars is larger, the mass infall rate to the central part is higher, and as a result, the viscous and shock heating efficiency are enhanced to get large explosion energy.

For $M_{\rm ZAMS} = 35M_\odot$, we performed simulations artificially varying the initial angular momentum for a fairly wide range. For its change by ±20%, the explosion energy and ejecta mass do not vary significantly. However, for the reduction by 50%, we did not find the torus formation and explosion in our simulation time, although a small-mass disk is formed. This indicates that for high-energy explosion from the torus, a rapid rotation of the progenitor stars that results in a rapidly spinning black hole with $\chi \gtrsim 0.7$ and a massive torus with mass $\gtrsim 1M_\odot$ is necessary.

For the simulations with the original progenitor models of Ref. [21], the final black-hole spin is always 0.75–0.85, and thus, a rapidly spinning black hole is the outcome. The final black-hole mass is ≈ 10–$30M_\odot$, which are 50–60% of the progenitor mass. Even for the model with initially reduced angular momentum (model `AD35x0.5-21.5`) the final dimensionless spin is ≈ 0.6. Since the black-hole dimensionless spin is high, in the presence of electromagnetic fields, the Blandford-Znajek effect is likely to play an important role [95] for launching an energetic jet or outflow along the spin axis of the black hole. If a relativistic jet is produced, a gamma-ray burst will be also launched (see Refs. [110, 219, 285] for simulation works). Our present explosion models may naturally explain the association between the gamma-ray burst and supernova-like explosion [120] if a jet is really launched. To demonstrate that a relativistic jet is indeed launched, it is necessary to perform a magnetohydrodynamics simulation, which is one of our follow-up works to be done. In the presence of a jet, energy available for the explosion and ^{56}Ni production is additionally injected, and also, observed relativistic motion in supernova-associated gamma-ray bursts will be naturally modelled [120]. Exploring this additional effect is an important subject for developing a model for supernova-associated gamma-ray bursts.

For model `AD35x0.5-21.5`, energetic explosion from the torus is not found although a fairly rapidly spinning black hole is formed. In such a case, a gamma-ray burst may be launched in the presence of a strong magnetic field penetrating the black hole, while supernova-like explosion is likely absent. A wide variety of the final outcomes, which the present work illustrates, suggest that there may be a variety of possibilities on the high-energy phenomena depending on the initial angular momentum profiles in the progenitor stars.

For the case that an explosion occurs, an appreciable amount of ^{56}Ni is synthesized. We find that the ^{56}Ni mass is always larger than $0.15 M_\odot$ and ~ 3–11% of the total ejecta mass for rapidly rotating progenitor stars. For the models with reduced angular momentum, the ^{56}Ni mass is significantly smaller. This illustrates that rapidly rotating progenitor stars are necessary for the significant ^{56}Ni production.

The relations between the explosion energy and ^{56}Ni mass and between the average ejecta velocity and ^{56}Ni mass are similar to the observational data for stripped-envelope supernovae with large explosion energy $> 10^{51}$ erg. As a natural consequence, the model light curves derived from our numerical results are also in good agreement with the observational data. This suggests a possibility that some of high-energy stripped-envelope supernovae may take place from a system of a spinning black hole and a massive torus. As discussed above, a gamma-ray burst is likely to accompany with such supernovae if a strong magnetic field penetrating the spinning black hole is developed. Therefore, supernova-associated gamma-ray bursts may be naturally explained in this model.

6.5 Initial data for collapsing stars onto a spinning black hole

We consider an axisymmetric initial data with the line element written in the form

$$dl^2 = \psi^4 \hat{\gamma}_{ij} dx^i dx^j = \psi^4 \left[e^{2q}(dR^2 + dz^2) + R^2 d\varphi^2 \right], \tag{6.20}$$

where $\hat{\gamma}_{ij}$ is the conformal three metric and ψ is a conformal factor, both of which are functions of R and z. We suppose that q is a given function of R and z. We require that the metric reduces to that of Kerr black holes in the quasi-isotropic coordinates in the absence of matter [288], i.e.,

$$\psi = \psi_{\rm K} = \frac{\Xi_{\rm K}^{1/4}}{r^{1/2} \Sigma_{\rm K}^{1/4}}, \tag{6.21}$$

$$e^q = e^{q_{\rm K}} = \frac{\Sigma_{\rm K}}{\Xi_{\rm K}^{1/2}}, \tag{6.22}$$

where

$$\begin{aligned}\Xi_{\rm K} &= (r_{\rm K}^2+a^2)\Sigma_{\rm K}+2Ma^2 r_{\rm K}\sin^2\theta, && (6.23)\\ \Sigma_{\rm K} &= r_{\rm K}^2+a^2\cos^2\theta, && (6.24)\end{aligned}$$

M is the black-hole mass, a is the black-hole spin, $r_{\rm K}$ is the radial coordinate in the Boyer-Lindquiest coordinates of Kerr black holes, $r=\sqrt{R^2+z^2}$, and $\tan\theta = R/z$. The relation between $r_{\rm K}$ and r is

$$r_{\rm K} = r + M + \frac{r_{\rm s}^2}{r}, \qquad (6.25)$$

where $r_{\rm s} := \sqrt{M^2-a^2}/2$ denotes the location of the black-hole horizon in the quasi-isotropic coordinates. In the following, we assume $q = q_{\rm K}$. We note that for $r \to 0$, $\Psi_{\rm K} \to r_{\rm s}/r$ and $q_{\rm K} \to 0$.

From the extrinsic curvature K_{ij}, we define $\hat{K}_{ij} = \psi^2 K_{ij}$, $\hat{K}^i{}_j = \psi^6 K^i{}_j$, $\hat{K}^{ij} = \psi^{10} K^{ij}$, and the subscripts of $\hat{K}_{ij}$ is raised by $\hat{\gamma}^{ij}$. In the following, we assume that the trace of the extrinsic curvature is zero, i.e., $(\hat{K}^{RR}+\hat{K}^{zz})e^{2q}+\hat{K}^{\varphi\varphi}R^2 = 0$. Then, for the metric of Eq. (6.20), the momentum constraint is written in the form:

$$\begin{aligned}&\frac{1}{R}\partial_R(R\hat{K}_{RR})+\partial_z\hat{K}_{Rz}-(\hat{K}_{RR}+\hat{K}_{zz})(\partial_R q - R^{-1}) = 8\pi J_R \psi^6 e^{2q}, && (6.26)\\ &\frac{1}{R}\partial_R(R\hat{K}_{Rz})+\partial_z\hat{K}_{zz}-(\hat{K}_{RR}+\hat{K}_{zz})\partial_z q = 8\pi J_z \psi^6 e^{2q}, && (6.27)\\ &\frac{1}{R}\partial_R(R\hat{K}_{R\varphi})+\partial_z\hat{K}_{z\varphi} = 8\pi J_\varphi \psi^6 e^{2q}, && (6.28)\end{aligned}$$

where $J_i = \alpha T^t{}_i$ with α the lapse function and $T^{\mu\nu}$ the energy-momentum tensor. In the formalism presented here, we will give J_i to determine the geometric quantities, and hence, we do not have to specify α.

We then write the conformal-tracefree extrinsic curvature as

$$\hat{K}_{ij} = \hat{D}_i W_j + \hat{D}_j W_i - \frac{2}{3}\hat{\gamma}_{ij}\hat{D}_k W^k + \hat{K}^{\rm K}_{ij}, \qquad (6.29)$$

where $\hat{D}_i$ is the covariant derivative with respect to $\hat{\gamma}_{ij}$, W^i is a conformal three vector, i.e., $W_j = \hat{\gamma}_{jk}W^k$, and $\hat{K}^{\rm K}_{ij}$ is the contribution from the black hole, which is tracefree. Each component of $\hat{K}_{ij}$, necessary for the momentum constraint, is written as

$$\begin{aligned}
\hat{K}_{RR} &= \partial_R W_R - \frac{W_R}{R} - \partial_z W_z - 2W_R \partial_R q + 2W_z \partial_z q + \frac{1}{3}\mathrm{div}W, \\
\hat{K}_{Rz} &= \partial_R W_z + \partial_z W_R - 2W_R \partial_z q - 2W_z \partial_R q, \\
\hat{K}_{zz} &= \partial_z W_z - \partial_R W_R - \frac{W_R}{R} + 2W_R \partial_R q - 2W_z \partial_z q + \frac{1}{3}\mathrm{div}W, \\
\hat{K}_{R\varphi} &= \partial_R W_\varphi - 2\frac{W_\varphi}{R} + \hat{K}^{\mathrm{K}}_{R\varphi}, \\
\hat{K}_{z\varphi} &= \partial_z W_\varphi + \hat{K}^{\mathrm{K}}_{z\varphi},
\end{aligned} \tag{6.30}$$

where $\mathrm{div}W = \partial_R W_R + W_R/R + \partial_z W_z$,

$$\hat{K}^{\mathrm{K}}_{R\varphi} = \frac{H_E R^3}{r^5} + \frac{H_F R z}{r^4}, \tag{6.31}$$

$$\hat{K}^{\mathrm{K}}_{z\varphi} = \frac{H_E R^2 z}{r^5} - \frac{H_F R^2}{r^4}, \tag{6.32}$$

and H_E and H_F are [102, 103]

$$H_E = \frac{Ma\left[(r_{\mathrm{K}}^2 - a^2)\Sigma_{\mathrm{K}} + 2r_{\mathrm{K}}^2(r_{\mathrm{K}}^2 + a^2)\right]}{\Sigma_{\mathrm{K}}^2}, \tag{6.33}$$

$$H_F = -\frac{2Ma^3 r_{\mathrm{K}}\sqrt{r_{\mathrm{K}}^2 - 2Mr_{\mathrm{K}} + a^2}\sin^2\theta\cos\theta}{\Sigma_{\mathrm{K}}^2}. \tag{6.34}$$

Here, $\hat{K}^{\mathrm{K}}_{ij}$ satisfies the φ-component of the momentum constraint for $J_\varphi = 0$

$$\frac{1}{R}\partial_R(R\hat{K}^{\mathrm{K}}_{R\varphi}) + \partial_z \hat{K}^{\mathrm{K}}_{z\varphi} = 0. \tag{6.35}$$

Then the equations for W_i are written as

$$\begin{aligned}
&\left[\Delta - \frac{1}{R^2}\right] W_R + \frac{1}{3}\partial_R(\mathrm{div}W)2\left(\partial_R^2 q + \partial_z^2 q\right) W_R - \left(\frac{8}{3}\mathrm{div}W - \frac{2W_R}{R}\right)\partial_R q \\
&\quad +2\left(\partial_R W_z + \frac{W_z}{R} - \partial_z W_R\right)\partial_z q = 8\pi J_R \psi^6 e^{2q},
\end{aligned} \tag{6.36}$$

$$\begin{aligned}
&\Delta W_z + \frac{1}{3}\partial_z(\mathrm{div}W)2\left(\partial_R^2 q + \partial_z^2 q\right) W_z - \left(\frac{8}{3}\mathrm{div}W - \frac{2W_R}{R}\right)\partial_z q \\
&\quad -2\left(\partial_R W_z + \frac{W_z}{R} - \partial_z W_R\right)\partial_R q = 8\pi J_z \psi^6 e^{2q},
\end{aligned} \tag{6.37}$$

$$\left[\Delta - \frac{1}{R^2}\right] W^{\bar{\varphi}} = 8\pi J_\varphi \psi^6 e^{2q} R^{-1}, \tag{6.38}$$

where $W^{\bar{\varphi}} := W^{\varphi}/R$ and Δ denotes the flat Laplacian,

$$\Delta = \partial_R^2 + \frac{1}{R}\partial_R + \partial_z^2. \tag{6.39}$$

For a given function of $J_{\varphi}\psi^6 e^{-2q}$, the equation for $W^{\bar{\varphi}}$ is solved with the outer boundary condition of $W^{\bar{\varphi}} \propto r^{-2}$ and the inner boundary conditions, $W^{\bar{\varphi}} \propto R$ for $R \to 0$ and $\partial_z W^{\bar{\varphi}} = 0$ at $z = 0$.

To simplify the procedure for the numerical solution of W_R and W_z, we may rewrite these variables using (see, e.g., Ref. [430] for a similar formulation in Cartesian coordinates)

$$W_i = B_i - \frac{1}{8}\partial_i(\chi + B_R R + B_z z), \tag{6.40}$$

where χ and B_i are new functions to be solved instead of W_R and W_z, and i denotes R or z. With this prescription, we find

$$\left[\Delta - \frac{1}{R^2}\right] W_R + \frac{1}{3}\partial_R(\mathrm{div}W) \tag{6.41}$$

$$= \left[\Delta - \frac{1}{R^2}\right] B_R - \frac{1}{6}\partial_R\left[\Delta\chi + R(\Delta - R^{-2})B_R + z\Delta B_z\right] \tag{6.42}$$

and

$$\Delta W_z + \frac{1}{3}\partial_z(\mathrm{div}W) = \Delta B_z - \frac{1}{6}\partial_z\left[\Delta\chi + R(\Delta - R^{-2})B_R + z\Delta B_z\right]. \tag{6.43}$$

Thus, by choosing the equation for $\Delta\chi$ as

$$\Delta\chi = -R(\Delta - R^{-2})B_R - z\Delta B_z, \tag{6.44}$$

we obtain the equations for B_R, B_z, and χ in simple forms as

$$\left[\Delta - \frac{1}{R^2}\right] B_R = S_R, \tag{6.45}$$

$$\Delta B_z = S_z, \tag{6.46}$$

$$\Delta\chi = -RS_R - zS_z, \tag{6.47}$$

where

$$\begin{aligned} S_R &= 2\left(\partial_R^2 q + \partial_z^2 q\right) W_R + \left(2\mathrm{div}B - \frac{2W_R}{R}\right)\partial_R q \\ &\quad -2\left(\partial_R B_z + \frac{W_z}{R} - \partial_z B_R\right)\partial_z q + 8\pi J_R \psi^6 e^{2q}, \qquad (6.48)\\ S_z &= 2\left(\partial_R^2 q + \partial_z^2 q\right) W_z + \left(2\mathrm{div}B - \frac{2W_R}{R}\right)\partial_z q \\ &\quad +2\left(\partial_R B_z + \frac{W_z}{R} - \partial_z B_R\right)\partial_R q + 8\pi J_z \psi^6 e^{2q}, \qquad (6.49) \end{aligned}$$

and

$$\mathrm{div}B\left(= \frac{4}{3}\mathrm{div}W\right) = \partial_R B_R + \frac{1}{R}B_R + \partial_z B_z. \qquad (6.50)$$

We note that in S_R and S_z the second spatial derivative of B_R, B_z, and χ is not present.

Because S_R and S_z fall off sufficiently rapidly in the far region (with $O(r^{-6})$), the elliptic equations (6.45)–(6.47) can be solved in a straightforward manner with the outer boundary conditions

$$B_R \propto \frac{R}{r^3}, \qquad B_z \propto \frac{z}{r^3}, \qquad \chi \propto \frac{1}{r}. \qquad (6.51)$$

The boundary conditions at $R = 0$ are

$$B_R \propto R, \qquad \partial_R B_z = 0 = \partial_R \chi, \qquad (6.52)$$

and the boundary conditions at $z = 0$ are

$$\partial_z B_R = 0 = \partial_z \chi, \qquad B_z \propto z. \qquad (6.53)$$

For the equation of B_R, it may be better to solve the equation for $B_{\bar{R}} = B_R/R$ to guarantee the boundary condition, $\partial_R B_{\bar{R}} = 0$, at $R = 0$. For this case the kernel operator of the equation becomes

$$\left(\partial_R^2 + \frac{3}{R}\partial_R + \partial_z^2\right) B_{\bar{R}} = \frac{S_R}{R}. \qquad (6.54)$$

Here, we note that $J_R \propto R$ and $q \propto \sin^2\theta$ at $\theta \to 0$, and thus, the regularity of S_R/R at $R = 0$ is guaranteed.

If we consider that $J_i\psi^6 e^{2q}$ is a given function, the Hamiltonian constraint is solved for an obtained numerical solution of $\hat{K}_{ij}$. In this context, the Hamiltonian constraint is written as

$$\Delta\psi = \frac{1}{8}\psi e^{2q}\hat{R} - 2\pi\rho_{\mathrm{H}}\psi^5 e^{2q} - \frac{1}{8\psi^7}\hat{K}_{ij}\hat{K}^{ij}, \qquad (6.55)$$

where $\rho_{\mathrm{H}} = \alpha^2 T^{tt}$ and $\hat{R}$ is the Ricci scalar with respect to the given conformal metric, $\hat{\gamma}_{ij}$, i.e., $q = q_{\rm K}$. In the present context (e.g., Ref. [429]),

$$\hat{R} = -2e^{-2q}(\partial_R^2 + \partial_z^2)q. \tag{6.56}$$

We also note that we will consider to give $\rho_{\rm H}$ (not T^{tt}), and hence, we do not have to specify α.

For the decomposition of $\psi = \psi_{\rm K} + \phi$, Eq. (6.55) is rewritten as

$$\Delta\phi \;=\; \frac{1}{8}\phi e^{2q}\hat{R} - 2\pi\rho_{\rm H}\psi^5 e^{2q} - \frac{1}{8\psi^7}\hat{K}_{ij}\hat{K}^{ij} + \frac{1}{8\psi_{\rm K}^7}\hat{K}^{\rm K}_{ij}\hat{K}^{{\rm K}ij}, \tag{6.57}$$

where we used

$$\Delta\psi_{\rm K} = \frac{1}{8}\psi_{\rm K}e^{2q}\hat{R} - \frac{1}{8\psi_{\rm K}^7}\hat{K}^{\rm K}_{ij}\hat{K}^{{\rm K}ij}. \tag{6.58}$$

The boundary conditions for ϕ are

$$\partial_r[r(\phi-1)] = 0 \ \text{ at } \ r \to \infty, \tag{6.59}$$
$$\partial_R\phi = 0 \ \text{ at } \ R = 0, \tag{6.60}$$
$$\partial_z\phi = 0 \ \text{ at } \ z = 0. \tag{6.61}$$

For $r \to 0$, $\psi_{\rm K} \propto r^{-1}$, $K^{\rm K}_{ij}K^{{\rm K}ij} \propto r^{-6}$, and $\hat{R} \to 2a^2/r_{\rm s}^4$, the right-hand side of Eq. (6.57) is regular anywhere. Thus, it is also straightforward to solve this equation under the boundary conditions shown above.

For the perfect fluid,

$$T^{\mu\nu} = \rho h u^\mu u^\nu + P g^{\mu\nu}, \tag{6.62}$$

where ρ, h, u^μ, P, and $g^{\mu\nu}$ are the rest-mass density, specific enthalpy, four velocity, pressure, and spacetime metric. Then we obtain

$$\hat{J}_i := J_i\psi^6 e^{2q} \;=\; \rho h\alpha u^t u_i \psi^6 e^{2q} = \rho_* h u_i, \tag{6.63}$$
$$S_0 := \rho_{\rm H}\psi^6 e^{2q} \;=\; \rho_* h(\alpha u^t) - P\psi^6 e^{2q}, \tag{6.64}$$

where $\rho_* = \rho\alpha u^t\psi^6 e^{2q}$ is the weighted rest-mass density which satisfies the continuity equation,

$$\partial_t\rho_* + \frac{1}{R}\partial_R\left(R\rho_* v^R\right) + \partial_z(\rho_* v^z) = 0, \tag{6.65}$$

with $v^i = u^i/u^t$ and $\alpha u^t = \sqrt{1+\psi^{-4}\hat{\gamma}^{ij}u_i u_j}$. Thus, the total rest mass of the system is obtained by

$$M_* = 2\pi\int RdRdz\,\rho_*. \tag{6.66}$$

The angular momentum of the matter is also obtained by

$$J = 2\pi \int R dR dz\, \hat{J}_{\varphi}. \tag{6.67}$$

In numerical computation, $\left(\rho_*, Y_e, T, \hat{J}_\phi, u_R, u_z\right)$ are provided using the data of the collapsing matter (see Sec. 6.2), and the field equations, e.g., (6.45), (6.46), (6.47), and (6.57), are solved iteratively until the rest-mass density ρ and all metric variables converge.

6.6 Accuracy of the black-hole quantities

To ascertain numerical accuracy in evaluating the mass and dimensionless spin of black holes, we evolve isolated spinning black holes using similar grid resolutions to those used in the present work, initially preparing a Kerr black hole in quasi-isotropic coordinates [288] with $\chi = 0.8$. Numerical evolution is carried out until $t = 80,000 M_{\rm BH}$. To save the computational costs, the outer boundary is located at $\approx 800 M_{\rm BH}$ along each axis. The simulations are performed for $\Delta x / M_{\rm BH} = 0.012$, 0.016, and 0.020 which are employed for the uniform grid zone with $x \leq 0.72 M_{\rm BH}$ where x denotes R or z. For $x > 0.72 M_{\rm BH}$ the grid spacing is increased with the rate of 1.01 as in viscous hydrodynamics simulations. In this section, the results are shown in units of $M_{\rm BH} = 1$ (with $c = 1 = G$). For example, for $M_{\rm BH} = 15 M_\odot$, $80,000 M_{\rm BH} \approx 5.9\,{\rm s}$ and $800 M_{\rm BH} \approx 1.8 \times 10^4\,{\rm km}$.

Figure 6.10 shows the evolution of the mass and dimensionless spin. A bump found at $t \approx 1,600 M_{\rm BH}$ is due to a slight reflection of numerical errors from the outer boundary: In this test simulations, the initial data are Kerr black holes in the quasi-isotropic coordinates, and thus, during the time evolution, the metric form is varied due to the change of the slicing, approaching those on the limiting hypersurface (trumpet hypersurface). During this variation, the gauge modes are propagated outward with the speed of light and some of the modes are reflected at the outer boundary toward the inner region causing a high-frequency numerical noise. This oscillation spuriously and slightly perturbs the horizon in particular for the high-resolution runs, but the oscillation does not grow in time and the error size associated with this is minor.

Besides this numerical error, the accuracy of the mass and the area of the apparent horizon converge approximately at fourth order with respect to the grid spacing Δx. The numerical error for the mass and dimensionless spin increase approximately linearly in time, but for $\chi = 0.8$ with $\Delta x \leq 0.016 M_{\rm BH}$, which is the typical grid resolution of the present chapter, the errors in mass and dimensionless spin are within $\approx 1.6\%$ and $\Delta\chi \approx 0.004$, respectively, at $t = 80,000 M_{\rm BH}$. For $\Delta x = 0.020 M_{\rm BH}$, the error size is more than twice as large as that with $\Delta x = 0.016 M_{\rm BH}$. This illustrates that a sufficiently high grid resolution is necessary to accurately evolve the black hole. For model `AD20-7.8` with $\Delta x / M_{\rm BH,0} \approx 0.0215$, the grid resolution in the early stage of the black-hole evolution is so low that the mass and dimensionless spin are likely to be overestimated and underestimated, respectively. This is also the case for model `AD20x1` [205]. For this model the grid resolution for the early black-hole evolution was not so high that the black-hole mass and dimensionless spin were overestimated and underestimated, respectively. As a result, the specific angular momentum at the innermost stable circular orbit around the black hole was spuriously overestimated in the numerical computation, and thus, the matter around the black hole were more subject to falling into the black hole. This leaded to the overestimation of the black-hole mass and underestimation of the disk/torus mass. For this model, the NDAF phase was not found [205], but this might be a spurious result due to the poor grid resolution.

6.7 Dependence on the grid resolution

In this section, we compare the results of models `AD35-15` and `AD35-15-hi` as a convergence test. Figure 6.11 shows the evolution of the mass and dimensionless spin (left) and the explosion energy and ejecta mass (right). We find a fair agreement between the results for different grid resolutions. For the black-hole mass, the higher-resolution results slightly in smaller mass. The primary reason for this is that with the higher-resolution, the viscous heating is more efficient, enhancing larger ejecta mass (see the right upper panel) while suppressing the accretion onto the black hole. Thus the black-hole mass presented in Fig. 6.5 may be slightly overestimated for their late stages while the ejecta mass may be underestimated in Fig. 6.6. The explosion energy are also slightly larger for the higher grid resolution, reflecting more energy injection from the viscous heating.

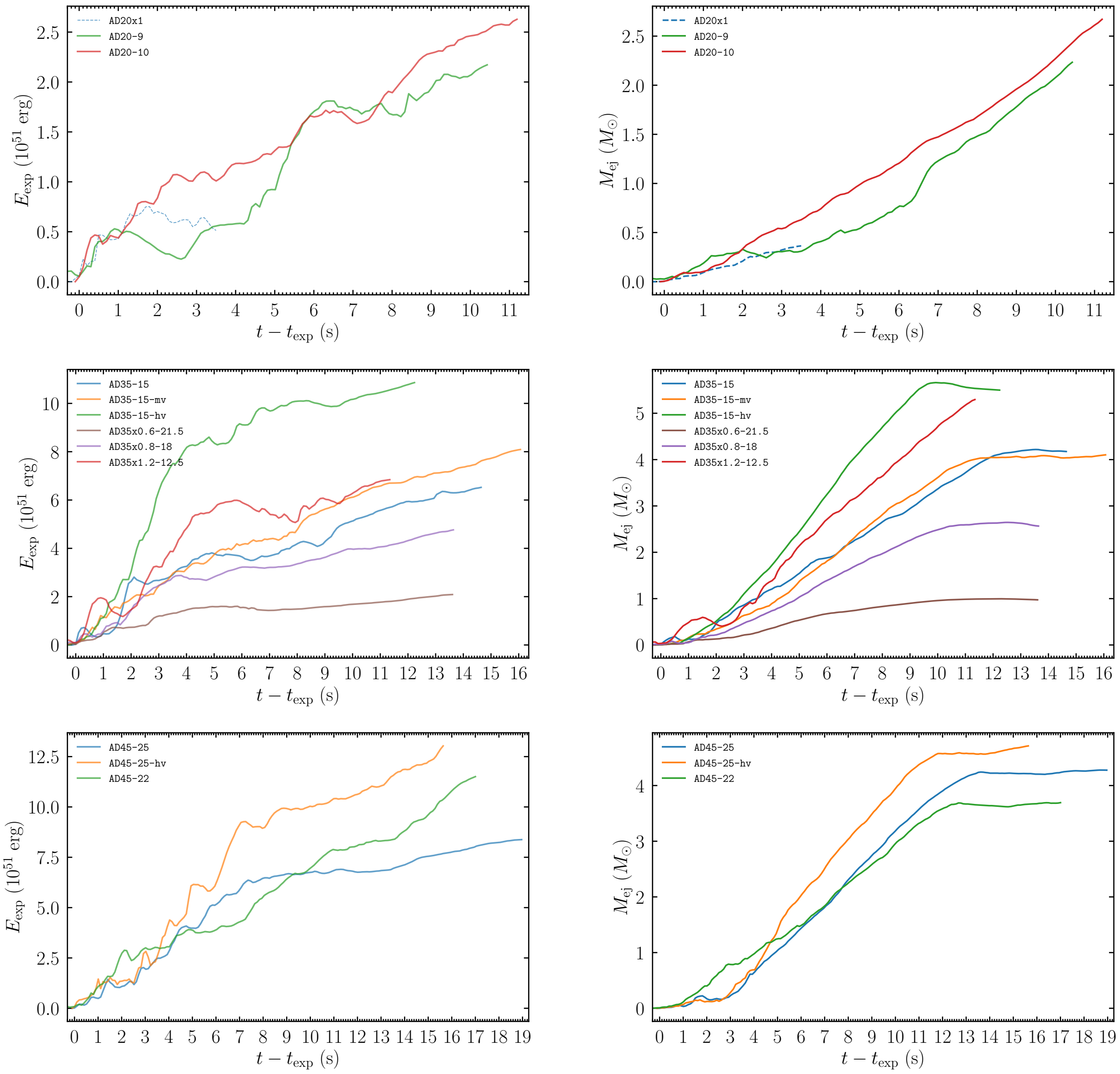

Figure 6.6: Time evolution of the explosion energy (left) and ejecta mass (right) for models of $M_{\rm ZAMS} = 20M_\odot$ (upper panels), $35M_\odot$ (middle panels), and $45M_\odot$ (lower panels). For $M_{\rm ZAMS} = 20M_\odot$, we also plot the result in Ref. [205] by the dashed curves.

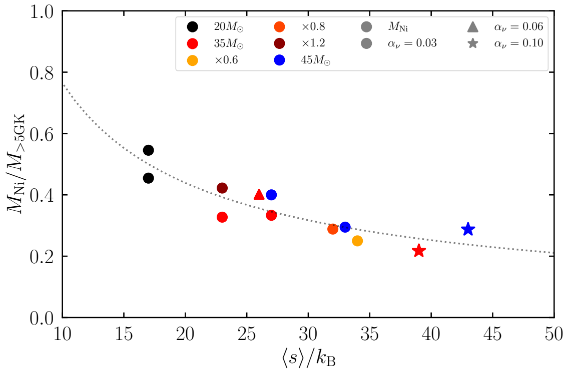

Figure 6.7: $M_{\rm Ni}/M_{>5\,{\rm GK}}$ as a function of $\langle s \rangle / k_{\rm B}$. The dotted curve denotes $(\langle s \rangle / 17k_{\rm B})^{-4/5}/2$.

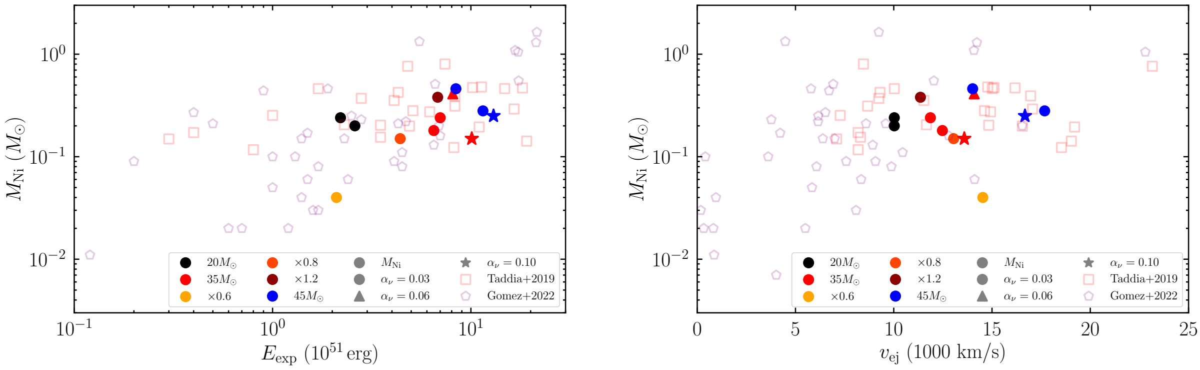

Figure 6.8: $M_{\rm Ni}$ as a function of the explosion energy $E_{\rm exp}$ (left) and average ejecta velocity $v_{\rm ej}$ (right). The open symbols denote the observational data for stripped-envelope supernovae, some of which are broad-lined type Ic supernovae, taken from Refs. [217, 482].

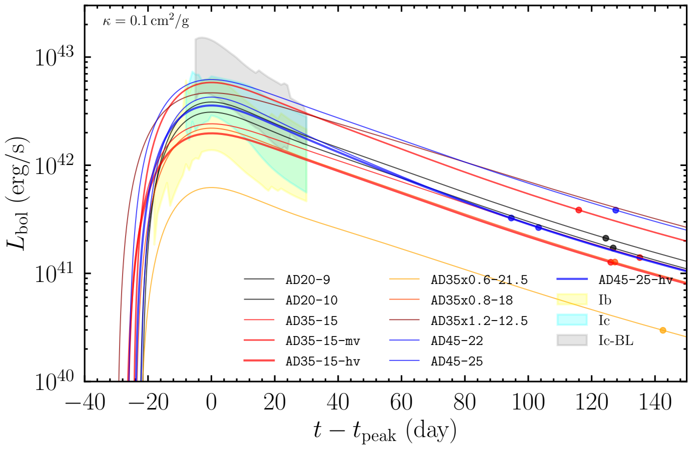

Figure 6.9: Bolometric light curves for all exploded models in this chapter. Light curves for different models are plotted in different colors and line thicknesses. The filled circles along each curve indicate the time at which the ejecta becomes optically thin to thermal photons. The shaded regions denote templates of the bolometric light curves with standard deviations for type Ib, Ic, and Ic-BL taken from Ref. [322].

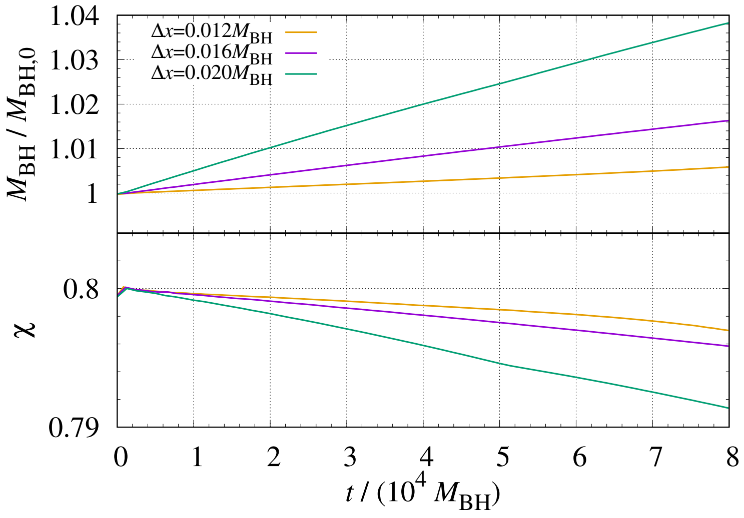

Figure 6.10: Evolution of the mass (upper panel) and dimensionless spin (lower panel) of spinning black holes for $\chi = 0.8$ with the grid resolutions of $\Delta x/M_{\rm BH} = 0.012$, 0.016, and 0.020.

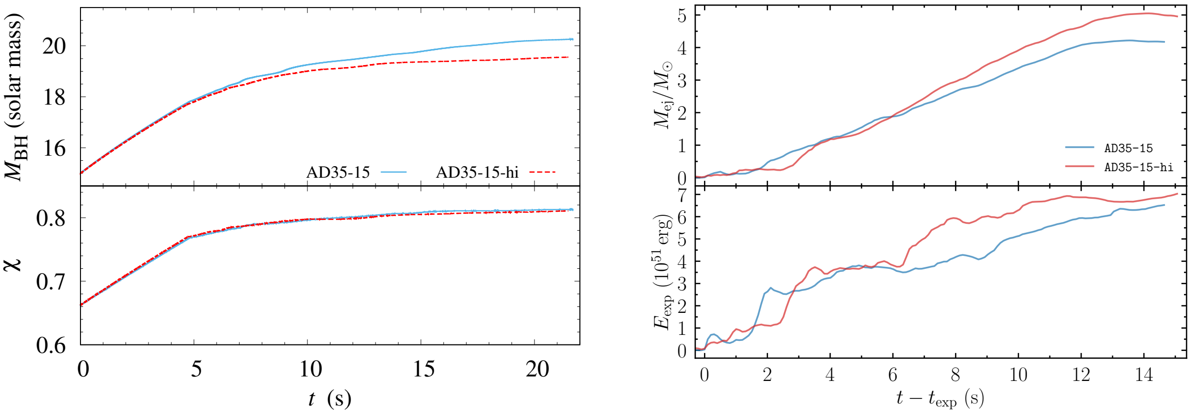

Figure 6.11: Left: The same as the middle panel of Fig. 6.5 but for the comparison between the results of models `AD35-15` (solid curves) and `AD35-15-hi` (dashed curves). Right: The ejecta mass (upper panel) and explosion energy (lower panel) for models `AD35-15` and `AD35-15-hi`.

Chapter 7

SACRA-2D: New axisymmetric general relativistic hydrodynamics code with fixed mesh refinement

Contents

Breakdown of Contribution

This chapter is based on the preprint submitted to Phys. Rev. D: "*SACRA-2D: New axisymmetric general relativistic hydrodynamics code with fixed mesh refinement*" in arXiv:2502.03223 [303] by **A. T.-L. Lam** and M. Shibata. The numerical code `SACRA-2D` was fully developed by me. I carried out all the numerical simulations. The initial data for the test problem of supermassive star collapse was provided by M. Shibata. M. Shibata provided constructive comments on the manuscript written by me.

Overview

In this Chapter, we present `SACRA-2D`, a new MPI and OpenMP parallelized, fully relativistic hydrodynamics (GRHD) code in dynamical spacetime under axial symmetry with the cartoon method using the finite-volume shock-capturing schemes for hydrodynamics. Specifically, we implemented the state-of-the-art Harten-Lax–Van Leer contact Riemann solver and found better accuracy than the standard Total Variation Diminishing Lax-Friedrich Riemann solver.

The spacetime evolves under the Baumgarte-Shapiro-Shibata-Nakamura formalism with Z4c constraint propagation. We demonstrate the accuracy of the code with some benchmark tests and excellent agreement with other codes in the literature. A wide variety of test simulations, including the head-on collision of black holes, the migration and collapse of neutron stars, and the collapse of a rotating supermassive star to a massive black hole and a disk, is also performed to show the robustness of our new code.

7.1 Introduction

In hydrodynamics and magnetohydrodynamics simulations, the finite volume method with the high-resolution shock-capturing (HRSC) scheme is commonly used due to its conservative nature and capability to resolve sharp discontinuities, such as shocks, that often appear in the fluid's motion. One popular HRSC scheme is the family of the Harten, Lax and van Leer (HLL) based approximate Riemann solver [229], which utilizes a subset of waves in the Riemann fan. While most existing numerical relativity (magneto)hydrodynamics codes (e.g., [80, 129, 182, 195, 234, 344, 348, 380, 507]) employ the Harten-Lax–van Leer–Einfeldt solver [297] that includes only shocks and rarefactions, it is known to be very diffusive [236, 336, 337, 493] and the accuracy for long-term simulation could be deteriorated. This is relevant for modeling the long-term evolution of post-merger remnant from neutron-star mergers [214], particularly important when considering the magnetohydrodynamical processes [281]. The authors in [281, 513] have reported a new implementation of the HLL contact (HLLC) solver, which is a more sophisticated Riemann solver that restores the contact discontinuity in the Riemann fan. A recent study also demonstrates its significance even in the inspiral phase of the binary neutron stars, where the dynamical tidal effect on the gravitational waveform can only be manifested with the HLLC solver [295]. Consequently, employing the HLLC solver (or a more accurate solver) for astrophysical simulations is crucial for accurate (magneto)hydrodynamics and gravitational wave signals.

Despite many relativistic astrophysical systems requiring spatially three-dimensional simulation to fully capture the dynamics, such numerical studies are usually computationally expensive, prohibiting us from studying a wider range of parameters. On the other hand, we could approximate specific systems to be axisymmetric, reducing the problem's size to two spatial dimensions and drastically lowering the computation cost for numerical simulation. This allows us to follow the physical system for a much longer time scale beyond the current capability of three-dimensional simulations. Indeed, axisymmetric GRHD code with dynamical spacetime has been used extensively to study various astrophysical systems, such as the dynamics of isolated neutron stars [275, 427, 434] and hypermassive neutron stars [168, 169, 170, 171, 447, 453], stellar collapse [299, 413, 414, 435, 448] and collapsar scenario [204, 207, 209, 456, 458] (see also Chapter 6), collapse of supermassive stars

[208, 315, 342, 438, 451, 451, 498, 499], black hole-torus system [340, 341, 423], higher-dimensional spacetime [534], and merger remnants from binary neutron stars and black hole-neutron star [200, 201, 202, 206, 454, 455].

In addition to astrophysical events, there has recently been an increasing interest in numerical relativity simulations of modified theories of gravity, aiming to search for distinctive features in the strong field regime that may provide shreds of evidence with current and future observations. In particular, a major effort has been put into analyzing the properties of compact objects, including black holes and neutron stars, as well as investigating the gravitational wave signals from the coalescence of binary compact objects in modified gravity theories such as the scalar-tensor theory (STT) [294, 305, 306, 450, 486] (see also Chapters 3 to 5), the scalar Gauss-Bonnet theory [176, 293, 396, 397, 461, 517], the dynamical Chern-Simon gravity [151, 359, 360, 395], and the STT with kinetic screening [88, 440]. However, the three-dimensional setups are computationally too costly to perform numerical experiments to survey new theories systematically, which is particularly important in exploring a well-posed formulation for certain theories. While one-dimensional simulation has been vastly used to explore the effect of the modification in gravity (e.g., [126, 290, 291, 292, 332, 473]), axisymmetric GRHD code can act as a bedrock for an efficient alternative to implementing various alternative theories of gravity and helping to gain new intuition in the regime of non-zero angular momentum. The cartoon method has been shown to be very useful for studying long-term dynamics, for example, core-collapse supernova in STT [298] and the superradiant instability of a Proca field [173, 175].

This Chapter reports the implementation `SACRA-2D`, a new MPI and OpenMP parallelized, fully relativistic GRHD code in dynamical spacetime under axial symmetry with the cartoon method. The code is written in FORTRAN90 with the numerical algorithm and technique closely resembling the three-dimensional moving box numerical relativity code `SACRA-MPI` [278, 526]. We implemented the Baumgarte-Shapiro-Shibata-Nakamura (BSSN) formalism [55, 433] with Z4c constraint propagation [81, 239] to solve Einstein's equations. The finite-volume shock-capturing scheme is employed for GRHD. Specifically, we implemented the total variation diminishing Lax-Friedrichs (TVDLF) solver and the state-of-the-art HLLC solver for the approximate Riemann solver.

In the following, we first outline the grid structure of `SACRA-2D` in Section 7.2.1. We then describe the implementation for dynamical spacetime in Section 7.2.2, specifically the details of the cartoon method in Section 7.2.2.2, followed by the formulation for GRHD in Section 7.2.3. In Section 7.3, we validate our code with several benchmark test problems, addressing the accuracy and performance of `SACRA-2D`. The parallelization efficiency is discussed in Section 7.3.4.

7.2 Formulation

7.2.1 Grid structure

The grid setting of `SACRA-2D` is very similar to that of the "box-in-box" simulation [115, 526]. We employ the two-to-one fixed mesh refinement (FMR) structure in the computational domain, which is composed of a hierarchy of nested concentric grids overlaying on top of each other. It consists of L levels of FMR domains, each of which contains an even number of grids N in both x and z directions with the grid spacing written as

$$\begin{aligned} \Delta x^{(0)} &= x_{\max}/N, & \Delta z^{(0)} &= z_{\max}/N, \\ \Delta x^{(l)} &= \Delta x^{(l-1)}/2, & \Delta z^{(l)} &= \Delta z^{(l-1)}/2, \end{aligned} \tag{7.1}$$

for $l = 1, 2, \cdots, L-1$, where $x_{\max}$ and $z_{\max}$ are the size of computational domain, and levels 0 and $(L-1)$ represent the coarsest and finest levels, respectively. The metric and hydrodynamics variables are assigned at cell-centered positions with coordinates

$$x_j^{(l)} = \left(j - \frac{1}{2}\right) \Delta x^{(l)}, \qquad z_k^{(l)} = \left(k - \frac{1}{2}\right) \Delta z^{(l)}, \tag{7.2}$$

for $j, k \in [1, N]$ on the l-th FMR level. The cell interfaces $x_{j\pm1/2}^{(l)}$ and $z_{k\pm1/2}^{(l)}$ are located at $x_j^{(l)} \pm \Delta x^{(l)}/2$ and $z_k^{(l)} \pm \Delta z^{(l)}/2$, respectively.

In addition to the local N grid cells, extra buffer cells are necessary for calculating derivatives with finite different schemes and reconstructing the hydrodynamics variables. For sixth-order accuracy in spatial derivative, four buffer zones are required to handle the lopsided finite difference for the advection term (see Section 7.2.2) as well as the prolongation scheme at the refinement boundary. We also allocate an additional four buffer cells on top of the original four buffer zones to facilitate the adaptive time update in the time integration scheme (see Section 7.2.4 for more details). Therefore, in `SACRA-2D`, we set up a total of $(4+4)$ buffer cells in each direction for the purpose of time integration. However, the number of buffer cells can be easily adjusted if a higher/lower order scheme is used [e.g., $(3+3)$ for fourth-order accuracy].

7.2.2 Einstein's equations

7.2.2.1 Basic equations

Following the Baumgarte-Shapiro-Shibata-Nakamura (BSSN) formalism [55, 433] introduced in Chapter 1 with Z4c constraint propagation [81, 239], we reformulate the field equations defining a set of geometric variables in Cartesian coordinates below,

$$\tilde{\gamma}_{ij} := \psi^{-4}\gamma_{ij}, \qquad h_{ij} := \tilde{\gamma}_{ij} - f_{ij}, \qquad W := \psi^{-2}, \tag{7.3a}$$

$$K := \gamma_{ij}K^{ij}, \qquad \tilde{A}_{ij} := \psi^{-4}\left(K_{ij} - \frac{1}{3}\gamma_{ij}K\right), \tag{7.3b}$$

$$\tilde{\Gamma}^i := -\partial_j\tilde{\gamma}^{ij}, \qquad \hat{K} := K - 2\Theta, \tag{7.3c}$$

where h_{ij} is the residual of spatial metric, $\Theta := -n_a Z^a$ is a constraint in Z4 system [97, 98, 223], and $\hat{K}$ is a variable used for the evolution equations.

The evolution equations for the geometric variables in Cartesian coordinates are given by

$$(\partial_t - \beta^k\partial_k)W = \frac{1}{3}W\left[\alpha\left(\hat{K} + 2\Theta\right) - \partial_k\beta^k\right], \tag{7.4a}$$

$$(\partial_t - \beta^k\partial_k)h_{ij} = -2\alpha\tilde{A}_{ij} + \tilde{\gamma}_{ik}\partial_j\beta^k + \tilde{\gamma}_{jk}\partial_i\beta^k - \frac{2}{3}\tilde{\gamma}_{ij}\partial_k\beta^k, \tag{7.4b}$$

$$\begin{aligned}(\partial_t - \beta^k\partial_k)\tilde{A}_{ij} = {} & W^2\left[\alpha R_{ij} - D_iD_j\alpha - 8\pi\alpha S_{ij}\right]^{\mathrm{TF}} + \alpha\left[\left(\hat{K} + 2\Theta\right)\tilde{A}_{ij} - 2\tilde{A}_{ik}\tilde{A}_j{}^k\right] \\ & + \tilde{A}_{kj}\partial_i\beta^k + \tilde{A}_{ki}\partial_j\beta^k - \frac{2}{3}\tilde{A}_{ij}\partial_k\beta^k,\end{aligned} \tag{7.4c}$$

$$(\partial_t - \beta^k\partial_k)\hat{K} = 4\pi\alpha(S^i{}_i + rho_h) + \alpha\kappa\Theta + \alpha\left[\tilde{A}_{ij}\tilde{A}^{ij} + \frac{1}{3}\left(\hat{K} + 2\Theta\right)^2\right] - D_iD^i\alpha, \tag{7.4d}$$

$$\begin{aligned}(\partial_t - \beta^k\partial_k)\tilde{\Gamma}^i = {} & -2\tilde{A}^{ij}\partial_j\alpha + 2\alpha\left[\tilde{\Gamma}^i_{jk}\tilde{A}^{jk} - \frac{1}{3}\tilde{\gamma}^{ij}\partial_j\left(\hat{2}K + \Theta\right) - \frac{3}{W}\tilde{A}^{ij}\partial_jW - 8\pi\tilde{\gamma}^{ij}S_j\right] \\ & + \frac{2}{3}\tilde{\gamma}^{jk}\tilde{\Gamma}^i{}_{jk}\partial_l\beta^l + \tilde{\gamma}^{jk}\partial_j\partial_k\beta^i + \frac{1}{3}\tilde{\gamma}^{ij}\partial_j\partial_k\beta^k - \tilde{\gamma}^{kl}\tilde{\Gamma}^j{}_{kl}\partial_j\beta^i - 2\alpha\kappa\left(\tilde{\Gamma}^i - \tilde{\gamma}^{kl}\tilde{\Gamma}^j{}_{kl}\right),\end{aligned} \tag{7.4e}$$

$$(\partial_t - \beta^k\partial_k)\Theta = \frac{1}{2}\alpha\left[R - \tilde{A}_{ij}\tilde{A}^{ij} + \frac{2}{3}\left(\hat{K} + 2\Theta\right)^2\right] - 8\alpha\pi\rho_h - 2\alpha\kappa\Theta, \tag{7.4f}$$

where (ρ_h, S_i, S_{ij}) are the 3 + 1 decomposition of the stress-energy tensor T_{ab} given by Eq. (1.10). The constraint damping parameter κ is chosen to be $\kappa = 5 \times 10^{-3}M^{-1}$ in this work with M being the total mass of the system. We also enforce the following algebraic constraints during the evolution

$$\det(\tilde{\gamma}_{ij}) = 1 \quad \text{and} \quad \tilde{\gamma}^{ij}\tilde{A}_{ij} = 0, \tag{7.5}$$

as the numerical error could induce violations in these constraints. Specifically, we reset the metric variables after each time integration given by

$$\tilde{\gamma}_{ij}^{\rm new} = \det(\tilde{\gamma}_{ij})^{-1/3}\tilde{\gamma}_{ij}, \tag{7.6a}$$

$$W^{\rm new} = \det(\tilde{\gamma}_{ij})^{-1/6}W, \tag{7.6b}$$

$$\tilde{A}_{ij}^{\rm new} = \det(\tilde{\gamma}_{ij})^{-1/3}\left(\tilde{A}_{ij} - \frac{1}{3}\tilde{\gamma}_{ij}\tilde{\gamma}^{kl}\tilde{A}_{kl}\right), \tag{7.6c}$$

$$K^{\rm new} = K + \tilde{\gamma}^{ij}\tilde{A}_{ij}, \tag{7.6d}$$

to satisfy the algebraic constraints.

We adopt the standard moving-puncture gauge condition [26, 42, 119] for the lapse function and shift vector as in Eq. (1.24). We employ the standard initial gauge choice for the lapse function $\alpha = \psi^{-2}$ and the shift vector $\beta^i = 0 = B^i$ for all the tests in Section 7.3 unless stated otherwise.

The spatial derivatives in the right-hand side of BSSN equations, Eq. (7.4), are evaluated with a sixth-order central finite difference, while the sixth-order lopsided finite difference is used for the advection terms in the left-hand side of Eq. (7.4) to guarantee the stability. To reduce high-frequency noise, we include eighth-order Kreiss-Oliger (KO) dissipation for geometric variables Q in x and z directions as

$$(\varepsilon/256)\left(\Delta x^8\partial_x^8 + \Delta z^8\partial_z^8\right)Q, \tag{7.7}$$

with the damping parameter ε set to be 0.5.

7.2.2.2 Cartoon method

We employ the cartoon method [24, 421, 426] to impose the axial symmetry on the geometric variables defined in the Cartesian coordinates. Three extra layers of the computational domain are constructed upon and below the x-z plane with $y = \pm j\Delta y$ ($j = 1, \cdots, 3$) as required by the sixth-order central finite difference. Einstein's equations are solved only on the $y = 0$ plane while the geometric variables $Q(x, \pm j\Delta y, z)$ on the $y = \pm j\Delta y$ planes are obtained by first interpolating the variables $Q^{(0)}(\varpi, 0, z)$ at the same radial distance $\varpi := \sqrt{x^2 + (j\Delta y)^2}$ on the $y = 0$ plane using Lagrange's formula with nine nearby points $[x_j - 4\Delta x, x_j + 4\Delta x]$ along the x direction and then apply rotation using the assumption of axial symmetric as

$$\begin{aligned} Q &= Q^{(0)}, & Q_z &= Q_z^{(0)}, \\ Q_A &= \Lambda_A{}^B Q_B^{(0)}, & Q_{zz} &= Q_{zz}^{(0)}, \\ Q_{Az} &= \Lambda_A{}^B Q_{Bz}^{(0)}, & Q_{AB} &= \Lambda_A{}^C \Lambda_B{}^D Q_{CD}^{(0)}, \end{aligned} \tag{7.8}$$

where Q, Q_i, and Q_{ij} denote, respectively, the scalar, vector, and tensor types of geometric variables, in BSSN formulation, and $\Lambda_A{}^B$ is the rotational matrix given by

$$\Lambda_A{}^B = \begin{pmatrix} \cos\phi & -\sin\phi \\ \sin\phi & \cos\phi \end{pmatrix}, \tag{7.9}$$

with $\tan\phi := \pm j\Delta y/\varpi$. Note that the subscripts A and B run x or y. The interpolated values with eighth-order accuracy result in an expected sixth-order accuracy in the second derivative, and allow us to compute the spatial derivative in the y-direction using the finite difference scheme in the same manner as in 3D Cartesian coordinates. In particular, we enforce the derivatives $\{\partial_y, \partial_{xy}, \partial_{yz}\}$ on $\{Q, Q_z, Q_{zz}\}$ to be zero in all equations to avoid double precision errors arising from the arithmetic operation of finite difference. As we set $\Delta y^{(l)} = \Delta x^{(l)}$ for all FMR levels, the interpolation coefficients remain the same across all the FMR levels. Hence, the coefficients can be easily pre-computed and saved for later use to speed up the calculation.

Since the neighboring nine points $x_j \pm 4\Delta x$ are required for the interpolation, the geometric variables located on the extra layers $y = \pm j\Delta y$ at the edge of the FMR level with grid points $x \in [N+5, N+8]$ cannot be determined, which causes trouble in obtaining the xy-derivative ∂_{xy} for grid points $x \in [N+1, N+4]$. To avoid this problem, we instead adopt the following form

$$\partial_{xy}Q_x = \frac{Q_y}{x^2} - \frac{\partial_x Q_y}{x}, \qquad \partial_{xy}Q_y = -\frac{Q_x}{x^2} + \frac{\partial_x Q_x}{x}, \tag{7.10a}$$

$$\partial_{xy}Q_{xz} = \frac{Q_{yz}}{x^2} - \frac{\partial_x Q_{yz}}{x}, \qquad \partial_{xy}Q_{yz} = -\frac{Q_{xz}}{x^2} + \frac{\partial_x Q_{xz}}{x}, \tag{7.10b}$$

$$\partial_{xy}Q_{xx} = 2\left(\frac{Q_{xy}}{x^2} - \frac{\partial_x Q_{xy}}{x}\right), \qquad \partial_{xy}Q_{yy} = -2\left(\frac{Q_{xy}}{x^2} - \frac{\partial_x Q_{xy}}{x}\right), \tag{7.10c}$$

$$\partial_{xy}Q_{xy} = \frac{Q_{yy} - Q_{xx}}{x^2} + \frac{\partial_x Q_{xx} - \partial_x Q_{yy}}{x}, \tag{7.10d}$$

for the vector Q_i and tensor Q_{ij} quantities located at grid points $x \in [N+1, N+4]$. Although the coordinate singularity $1/x$ appears in the source term of Eq. (7.10), it is justified since the grid points $x \in [N+1, N+4]$ are located at the edge of the refinement boundary far from the symmetric axis with non-zero x.

7.2.2.3 Boundary condition

For the outer boundary, we impose the outgoing boundary condition [433] for metric variables Q located at radial distance r in the form

$$Q^n(r) = \left(1 - \frac{\Delta t}{r}\right) Q^{n-1}(r - \Delta t), \tag{7.11}$$

in order to preserve rQ along the characteristic curves $r - t = \text{constant}$. Here, Q^n and Q^{n-1} are variables in the current t and previous $t - \Delta t$ time step, respectively, and we interpolate Q^{n-1} at $r - \Delta t$ with second-order Lagrange interpolation.

Since the Z4c prescription allows the propagation and damping of constraints by introducing the auxiliary variable Θ, constraint violation will be induced at the outer boundary and propagate inwards if the boundary condition above is used. While one could avoid this by implementing constraint preserving boundary condition [403], we instead adopt a simple treatment for Θ following [300]. We set an effective radius $r_{\rm Z4}$, beyond which the damping parameter κ and the source term for Θ are multiplied by an additional factor $\exp[-(x^2+z^2)/r_{\rm Z4}^2]$ to suppress the propagation of constraint violation terms exponentially. We typically set as $r_{\rm Z4} \lesssim L_{\rm max}/6$ equivalent to a factor of $\sim 10^{-16}$ at the outer boundary, which corresponds to the same order of error as double precision. We found that this simple treatment is good enough to maintain a stable evolution for the long term without any significant growth in constraint violation.

7.2.3 General relativistic hydrodynamics

7.2.3.1 Basic equations

This section briefly summarizes the formulation for general relativistic hydrodynamics (GRHD) under 3+1 decomposition. We refer readers to [392, 430] for more detailed derivation.

The evolution equations for GRHD are based on the conservation of rest-mass and stress-energy momentum tensor,

$$\nabla_a \left(\rho u^a\right) = 0, \tag{7.12a}$$

$$\nabla_b T^{ab} = 0, \tag{7.12b}$$

where ρ, u^a, and P are the rest-mass density, four-velocity, and pressure of the fluid, respectively, and

$$T_{ab} := \rho h u_a u_b + P g_{ab} \tag{7.13}$$

is the stress-energy tensor for perfect fluid with $h := 1 + \epsilon + P/\rho$ being the specific enthalpy and ϵ being the specific internal energy. ∇_a denotes the covariant derivative with respect to g_{ab}.

We adopt the finite volume method using the formulation of, e.g., [45] in the reference metric formalism [127, 343] to solve the hydrodynamical system in cylindrical coordinates (ϖ, ϕ, z) at $\phi = 0$ plane. Under such formulation, the GRHD equations can be written in the following conservative form

$$\partial_t \mathbf{q} + \frac{1}{\sqrt{\hat{\gamma}}} \partial_i \left(\sqrt{\hat{\gamma}} \mathbf{f}^i \right) = \mathbf{s}, \tag{7.14}$$

where $\hat{\gamma}_{ij}$ is the time-independent reference metric chosen to be flat metric in cylindrical coordinates; here $\hat{\gamma}_{ij} := f_{ij} = \mathrm{diag}(1, \varpi, 1)$, $\hat{\gamma} := \det(\hat{\gamma}_{ij})$ is the determinant, $\mathbf{q} := (q_D, q_{S_i}, q_E)$ are the conservative variables defined as

$$\begin{pmatrix} q_D \\ q_{S_i} \\ q_E \end{pmatrix} = \psi^6 \begin{pmatrix} D \\ S_i \\ E \end{pmatrix} = \psi^6 \begin{pmatrix} \rho w \\ \rho h w u_i \\ \rho h w^2 - P \end{pmatrix}, \tag{7.15}$$

$\mathbf{f^i}$ are the flux terms written as

$$\mathbf{f^i} = \begin{pmatrix} (f_D)^i \\ (f_{S_j})^i \\ (f_E)^i \end{pmatrix} = \alpha \psi^6 \begin{pmatrix} D \bar{v}^i \\ S_j \bar{v}^i + P {\delta_j}^i \\ E \bar{v}^i + P \left(\bar{v}^i + \dfrac{\beta^i}{\alpha} \right) \end{pmatrix}, \tag{7.16}$$

with $w := -n_a u^a = \alpha u^t$ being the Lorentz factor measure by an Eulerian observer and $\bar{v}^i := -\beta^i + \gamma^{ij} u_j / u^t$.

Since Einstein's equations are solved in Cartesian coordinates (x, y, z) at $y = 0$ plane, the hydrodynamic variables can be rewritten in Cartesian coordinates as $\varpi = x$ and $u_\phi = x u_y$, which is essentially the same as the conversion to orthonormal frame in reference metric approach [59]. The source term $\mathbf{s} := (s_D, s_{S_i}, s_E)$ in Eq. (7.14) can then be evaluated in

Cartesian coordinates in the forms

$$s_D = 0 \tag{7.17a}$$

$$\begin{aligned} s_{S_\varpi} &= P\partial_x\left(\alpha W^{-3}\right) - W^{-3}\rho h w^2\left[\partial_x\alpha - \bar{v}_i\partial_x\beta^i + \frac{W^2}{2}\alpha\bar{v}_i\bar{v}_j\partial_x\tilde{\gamma}^{ij} + \frac{4}{W}\alpha\bar{v}_i\bar{v}^i\partial_x W\right] \\ &\quad + \frac{(f_{S_\phi})^\phi}{\varpi}, \end{aligned} \tag{7.17b}$$

$$s_{S_\phi} = 0 \tag{7.17c}$$

$$s_{S_z} = P\partial_z\left(\alpha W^{-3}\right) - W^{-3}\rho h w^2\left[\partial_z\alpha - \bar{v}_i\partial_z\beta^i + \frac{W^2}{2}\alpha\bar{v}_i\bar{v}_j\partial_z\tilde{\gamma}^{ij} + \frac{4}{W}\alpha\bar{v}_i\bar{v}^i\partial_z W\right] \tag{7.17d}$$

$$s_E = \alpha K^{ij}S_{ij} - W^{-3}\rho h w^2\bar{v}^i\partial_i\alpha, \tag{7.17e}$$

where the final term $\frac{(f_{S_\phi})^\phi}{\varpi}$ in s_{S_ϖ} comes from the cylindrical geometry (see [127] for detailed derivation of geometrical source term). Note that we have the conservation of angular momentum in axial symmetry. In the conservative form of Eq. (7.14) with $s_D = 0 = s_{S_\phi}$, the conservation of mass and angular momentum can be satisfied numerically with machine precision.

Here, we write down the explicit discretized form of the volume-averaged equations in cylindrical coordinates as follows:

$$\begin{aligned} \partial_t\left\langle \mathbf{q}\right\rangle_{j,k} = \left\langle \mathbf{s}\right\rangle_{j,k} &- \frac{1}{\Delta V_{j,k}} \\ &\times\left\{\left[\left\langle \mathbf{f}\right\rangle^\varpi_{j+\frac{1}{2},k}\Delta A^\varpi_{j+\frac{1}{2},k} - \left\langle \mathbf{f}\right\rangle^\varpi_{j-\frac{1}{2},k}\Delta A^\varpi_{j-\frac{1}{2},k}\right]\right. \\ &\left.+\left[\left\langle \mathbf{f}\right\rangle^z_{j,k+\frac{1}{2}}\Delta A^z_{j,k+\frac{1}{2}} - \left\langle \mathbf{f}\right\rangle^z_{j,k-\frac{1}{2}}\Delta A^z_{j,k-\frac{1}{2}}\right]\right\} \end{aligned} \tag{7.18}$$

where $\Delta V_{j,k}$ and $\Delta A^i_{j,k}$ are the volume and the surface area of the cell (j,k), respectively, given by

$$\Delta V_{j,k} = 2\pi\int_{x_{j-\frac{1}{2}}}^{x_{j+\frac{1}{2}}}\int_{z_{k-\frac{1}{2}}}^{z_{k+\frac{1}{2}}} x\,dx\,dz = 2\pi x_j\Delta x\Delta z, \tag{7.19a}$$

$$\Delta A^\varpi_{j\pm\frac{1}{2},k} = 2\pi\int_{z_{k-\frac{1}{2}}}^{z_{k+\frac{1}{2}}} x_{j\pm\frac{1}{2}}dz = 2\pi x_{j\pm\frac{1}{2}}\Delta z, \tag{7.19b}$$

$$\Delta A^z_{j,k\pm\frac{1}{2}} = 2\pi\int_{x_{j-\frac{1}{2}}}^{x_{j+\frac{1}{2}}} x\,dx = 2\pi x_j\Delta x, \tag{7.19c}$$

$\left\langle \mathbf{q}\right\rangle_{j,k}$ and $\left\langle \mathbf{s}\right\rangle_{j,k}$ are the volume averaged of the corresponding quantities, and $\left\langle \mathbf{f}\right\rangle^i$ are the surface-averaged quantities of the flux terms at the cell interfaces.

7.2.3.2 Riemann Solver

We adopt the HSRC scheme to handle the flux term in hydrodynamics equations. Both Total Variation Diminishing Lax-Friedrich (TVDLF) [269, 495, 529] and HLLC [52, 336, 493] approximate Riemann solvers are implemented in `SACRA-2D`. To obtain the numerical flux, we first reconstruct the left and right states of the primitive variables $\mathbf{p} = (\rho, u_i, P, \epsilon)$ with 3rd-order piecewise parabolic method (PPM) [132, 437] at the cell interface. Since the metric variables are smooth, we employ Lagrangian interpolation to calculate the values at the interface. For the HLLC solver, we perform the tetrad transformation [281, 513] at the cell interface after reconstruction to obtain the numerical flux.

Here, we briefly outline the procedure of the HLLC solver and refer readers to [281, 513, 519] for more details on the implementation. To evaluate the numerical flux in the x-direction, we define a tetrad basis [281, 513] on the surface of $x_{j\pm1/2}$ as

$$e^a_{(\hat{t})} = n^a = \frac{1}{\alpha}\left(1, -\beta^i\right), \tag{7.20a}$$

$$e^a_{(\hat{x})} = W\hat{B}\left(0, \tilde{\gamma}^{xi}\right), \tag{7.20b}$$

$$e^a_{(\hat{y})} = W\hat{D}\left(0, 0, \tilde{\gamma}_{zz}, -\tilde{\gamma}_{yz}\right), \tag{7.20c}$$

$$e^a_{(\hat{z})} = W\hat{C}\left(0, 0, 0, 1\right), \tag{7.20d}$$

where

$$\hat{B} = \frac{1}{\sqrt{\tilde{\gamma}^{xx}}}, \qquad \hat{C} = \frac{1}{\sqrt{\tilde{\gamma}_{zz}}}, \qquad \hat{D} = \frac{1}{\sqrt{\tilde{\gamma}^{xx}\tilde{\gamma}_{zz}}} = \hat{B}\hat{C}, \tag{7.21}$$

with the corresponding covariant components written as

$$e_{(\hat{t})a} = n_a = -\left(\alpha, 0, 0, 0\right), \tag{7.22a}$$

$$e_{(\hat{x})a} = W^{-1}\hat{B}\left(\beta^x, 1, 0, 0\right), \tag{7.22b}$$

$$e_{(\hat{y})a} = W^{-1}\hat{D}\left(-\tilde{\gamma}_{xy}\beta^x + \tilde{\gamma}_{xx}\beta^y, -\tilde{\gamma}_{xy}, \tilde{\gamma}_{xx}, 0\right), \tag{7.22c}$$

$$e_{(\hat{z})a} = W^{-1}\hat{C}\left(\beta_z, \tilde{\gamma}_{iz}\right). \tag{7.22d}$$

This allows us to transform the primitive variables from the Eulerian frame $\mathbf{p}$ to the tetrad frame $\tilde{\mathbf{p}}$ by

$$u_{(\hat{a})} = e_{(\hat{a})}{}^b u_b, \tag{7.23}$$

$$w^2 = 1 + u^{(\hat{i})}u_{(\hat{i})}, \tag{7.24}$$

$$v_{(\hat{i})} = u_{(\hat{i})}/w. \tag{7.25}$$

We can then obtain the left (L) and right (R) states of the conservative variables $\tilde{\mathbf{q}}_{L/R} :=$

$\tilde{\mathbf{q}}(\tilde{\mathbf{p}}_{L/R})$ and the flux terms $\tilde{\mathbf{f}}_{L/R} := \tilde{\mathbf{f}}^{(\hat{x})}(\tilde{\mathbf{p}}_{L/R})$ in the tetrad frame from the corresponding left/right states of the primitive variables $\tilde{\mathbf{p}}_{L/R}$ as

$$\tilde{\mathbf{q}}(\tilde{\mathbf{p}}) = \begin{pmatrix} D \\ S_{(\hat{j})} \\ E \end{pmatrix} = \begin{pmatrix} \rho w \\ \rho h w v_{(\hat{j})} \\ \rho h w^2 + P \end{pmatrix}, \tag{7.26}$$

$$\tilde{\mathbf{f}}^{(\hat{x})}(\tilde{\mathbf{p}}) = \begin{pmatrix} \left(\tilde{f}_D\right)^{(\hat{x})} \\ \left(\tilde{f}_{S_{(\hat{j})}}\right)^{(\hat{x})} \\ \left(\tilde{f}_E\right)^{(\hat{x})} \end{pmatrix} = \begin{pmatrix} D v^{(\hat{x})} \\ S_{(\hat{j})} v^{(\hat{x})} + P \delta^{(\hat{x})}_{(\hat{j})} \\ (E+P)\, v^{(\hat{x})} \end{pmatrix}, \tag{7.27}$$

which essentially have the same expression as in special relativistic hydrodynamics. Now, we can employ the HLLC solver in the local Minkowski spacetime [336] to calculate the numerical flux as

$$\tilde{\mathbf{f}}^{(\hat{x})} = \begin{cases} \tilde{\mathbf{f}}^{(\hat{x})}_{L} & \text{for } \lambda_L > v^{(\hat{x})}_{\text{interface}} \\ \tilde{\mathbf{f}}^{(\hat{x})}_{cL} & \text{for } \lambda_L < v^{(\hat{x})}_{\text{interface}} < \lambda_c \\ \tilde{\mathbf{f}}^{(\hat{x})}_{cR} & \text{for } \lambda_c < v^{(\hat{x})}_{\text{interface}} < \lambda_R \\ \tilde{\mathbf{f}}^{(\hat{x})}_{R} & \text{for } \lambda_R < v^{(\hat{x})}_{\text{interface}} \end{cases}, \tag{7.28}$$

where λ_c is the characteristic speed of the contact discontinuity, $v^{(\hat{x})}_{\text{interface}} = \beta^x / \left(\alpha\sqrt{\gamma^{xx}}\right)$ is the interface velocity [281, 513], $\tilde{\mathbf{f}}^{(\hat{x})}_{cL/cR}$ and $\tilde{\mathbf{q}}^{(\hat{x})}_{cL/cR}$ are the intermediate states obtained from the jump condition

$$\tilde{\mathbf{f}}^{(\hat{x})}_{cL/cR} = \tilde{\mathbf{f}}^{(\hat{x})}_{L/R} + \lambda_{L/R}\left(\tilde{\mathbf{q}}^{(\hat{x})}_{cL/cR} - \tilde{\mathbf{q}}^{(\hat{x})}_{L/R}\right), \tag{7.29}$$

and $\lambda_{L/R}$ are the left/right characteristic speed given by

$$\lambda_L = \min(\lambda(\tilde{\mathbf{p}}_L)^-, \lambda(\tilde{\mathbf{p}}_R)^-), \tag{7.30}$$

$$\lambda_R = \max(\lambda(\tilde{\mathbf{p}}_L)^+, \lambda(\tilde{\mathbf{p}}_R)^+), \tag{7.31}$$

$$\lambda^{\pm}(\tilde{\mathbf{p}}) = \frac{1}{1 - v^2 c_s^2}\left\{ v^{(\hat{x})}\left(1 - c_s^2\right) \pm c_s \sqrt{\left(1 - v^2\right)\left[1 - v^2 c_s^2 - \left(1 - c_s^2\right) v^{(\hat{x})2}\right]} \right\}, \tag{7.32}$$

with $v^2 := v^{(\hat{i})} v_{(\hat{i})}$ and c_s being the sound speed. The characteristic speed λ_c can be obtained by imposing the continuity condition of the pressure across the contact discontinuity as [336]

$$\left(\tilde{f}^{\text{HLL}}_{E}\right)^{(\hat{x})} \lambda_c^2 - \left[E^{\text{HLL}} + \left(\tilde{f}^{\text{HLL}}_{S_{(\hat{x})}}\right)^{(\hat{x})}\right] \lambda_c + S^{\text{HLL}}_{(\hat{x})} = 0, \tag{7.33}$$

where $\tilde{\mathbf{q}}^{\text{HLL}}$ and $\tilde{\mathbf{f}}^{(\hat{x}),\text{HLL}}$ represent the HLL state of the conserved quantities and flux, respectively, given by

$$\tilde{\mathbf{q}}^{\mathrm{HLL}} = \frac{\lambda_R \tilde{\mathbf{q}}_R - \lambda_L \tilde{\mathbf{q}}_L + \tilde{\mathbf{f}}^{(\hat{x})}_L - \tilde{\mathbf{f}}^{(\hat{x})}_R}{\lambda_R - \lambda_L}, \tag{7.34}$$

$$\tilde{\mathbf{f}}^{(\hat{x}),\mathrm{HLL}} = \frac{\lambda_R \tilde{\mathbf{f}}^{(\hat{x})}_L - \lambda_L \tilde{\mathbf{f}}^{(\hat{x})}_R + \lambda_R \lambda_L \left(\tilde{\mathbf{q}}_R - \tilde{\mathbf{q}}_L\right)}{\lambda_R - \lambda_L}. \tag{7.35}$$

The pressure P_c in the intermediate state can be therefore determined by

$$P_c = P_{cL} = P_{cR} = -\lambda_c \left(\tilde{f}^{\mathrm{HLL}}_E\right)^{(\hat{x})} + \left(\tilde{f}^{\mathrm{HLL}}_{S_{(\hat{x})}}\right)^{(\hat{x})}, \tag{7.36}$$

and the conserved quantities in the intermediate cL/cR states can be obtained by

$$D_{cL/cR} = D_{L/R} \frac{\lambda_{L/R} - v^{(\hat{x})}_{L/R}}{\lambda_{L/R} - \lambda_c}, \tag{7.37a}$$

$$\begin{aligned} S_{(\hat{j}),cL/cR} &= \frac{1}{\lambda_{L/R} - \lambda_c} \\ &\times \left[S_{(\hat{j}),L/R} \left(\lambda_{L/R} - v^{(\hat{x})}_{L/R}\right) + \left(P_c - P_{L/R}\right) \delta^{(\hat{x})}_{(\hat{j})} \right], \end{aligned} \tag{7.37b}$$

$$E_{cL/cR} = \frac{E_{L/R} \left(\lambda_{L/R} - v^{(\hat{x})}_{L/R}\right) + P_c \lambda_c - P_{L/R} v^{(\hat{x})}_{L/R}}{\lambda_{L/R} - \lambda_c}. \tag{7.37c}$$

Once the numerical flux in the tetrad frame is evaluated, we can eventually transform it back to the Eulerian observer frame given by

$$\mathbf{f}^x = -\frac{\beta^x}{\alpha} \begin{pmatrix} D \\ e^{(\hat{i})}{}_j S_{(\hat{i})} \\ E \end{pmatrix} + \sqrt{\gamma^{xx}} \begin{pmatrix} \left(\tilde{f}_D\right)^{(\hat{x})} \\ e^{(\hat{i})}{}_j \left(\tilde{f}_{S_{(\hat{i})}}\right)^{(\hat{x})} \\ \left(\tilde{f}_E\right)^{(\hat{x})} \end{pmatrix}. \tag{7.38}$$

7.2.3.3 Equation of state

We implement a hybrid equation of state (EOS) in the current version of `SACRA-2D` where the pressure P and the specific internal energy ϵ are split into the cold part $P_{\mathrm{cold}}/\epsilon_{\mathrm{cold}}$ and thermal part $P_{\mathrm{th}}/\epsilon_{\mathrm{th}}$ as

$$P = P_{\mathrm{cold}} + P_{\mathrm{th}}, \qquad \epsilon = \epsilon_{\mathrm{cold}} + \epsilon_{\mathrm{th}}. \tag{7.39}$$

The cold part is described by a phenomenological piecewise polytropic (PWP) EOS [386] where the realistic EOS is approximated by n pieces of polytrope depending on the transitional density ρ_i. The pressure P_{cold} and the specific internal energy ϵ_{cold} are parameterized by the rest-mass density ρ as

$$\begin{aligned} P_{\text{cold}} &= K_i \rho^{\Gamma_i} \\ \epsilon_{\text{cold}} &= \frac{K_i}{\Gamma_i - 1}\rho^{\Gamma_i - 1} + \Delta\epsilon_i \end{aligned}, \qquad \text{for } \rho_{i-1} \leq \rho < \rho_i \tag{7.40}$$

where i runs from 1 to n with $\rho_0 := 0$, K_i and Γ_i are the polytropic constant and index, respectively, and $\Delta\epsilon_i$ is determined by imposing the continuity condition on the specific internal energy.

In addition to the cold part, we add the thermal part adopting the gamma-law EOS given by

$$P_{\text{th}} = \rho\left(\Gamma_{\text{th}} - 1\right)\epsilon_{\text{th}}, \tag{7.41}$$

where Γ_{th} is a constant typically set to 5/3 in the present work.

7.2.3.4 Recovery of primitive variables

The recovery of primitive variables (ρ, u_i, P, ϵ) from conserved variables $\mathbf{q}$ is non-trivial and can only be done numerically. We implement the primitive recovery procedure for GRHD mentioned in Appendix C of [213]. Here, we briefly outline the implementation of the recovery procedure:

1. Evaluate the rescaled quantities that are fixed in the iterations

$$r := \frac{\sqrt{S_i S^i}}{D}, \qquad q := \frac{E}{D} - 1, \qquad k := \frac{r}{1+q}, \tag{7.42}$$

2. Set the bounds $[z_-, z_+]$ for the root defined as

$$z_- := \frac{k/2}{\sqrt{1 - k^2/4}}, \qquad z_+ := \frac{k}{\sqrt{1-k^2}} \tag{7.43}$$

3. Within the interval $[z_-, z_+]$, we find the root of $f(z) = 0$ with the master function $f(z)$ defined as

$$f(z) := z - \frac{r}{\hat{h}(z)}, \tag{7.44}$$

where

$$\begin{aligned}
\hat{h}(z) &:= (1+\hat{\epsilon})(1+\hat{a}(z)), \\
\hat{P}(z) &:= P(\hat{\rho}(z),\hat{\epsilon}(z)), \\
\hat{a}(z) &:= \frac{\hat{P}(z)}{\hat{\rho}(z)(1+\hat{\epsilon}(z))}, \\
\hat{\rho}(z) &:= \frac{D}{\hat{w}(z)}, \\
\hat{\epsilon}(z) &:= \hat{w}(z)q - zr + \frac{z^2}{1+\hat{w}(z)}, \\
\hat{w}(z) &:= \sqrt{1+z^2}.
\end{aligned} \tag{7.45}$$

In `SACRA_2D`, we numerically solve Eq. (7.44) using the Illinois method for bracketing root-finding. We also set an upper limit for Lorentz factor $w_{\rm max}$ (typically set to be $w_{\rm max} = 100$) and rescale S_i whenever k exceeds certain upper bound following [213]. While this method is robust and always converges to a solution, it does not guarantee that the converged solution satisfies the physical condition. In particular when the obtained specific internal energy falls below the minimum allowed values of EOS ($\epsilon < \epsilon^{\rm EOS}_{\rm min}$), we employ an additional primitive recovery using only the conversed density and momentum (D, S_i) together with the zero temperature EOS $h = h_{\rm cold}(\rho)$ following a similar procedure.

1. Set the bounds $[z_-, z_+]$ for the root defined as

$$z_- := 0, \qquad z_+ := r \tag{7.46}$$

2. Within the interval $[z_-, z_+]$, we find the root of $\tilde{f}(z) = 0$ with the master function $\tilde{f}(z)$ defined as

$$\tilde{f}(z) := z - \frac{r}{h_{\rm cold}(\hat{\rho}(z))}, \tag{7.47}$$

where

$$\hat{\rho}(z) := \frac{D}{\hat{w}(z)} \qquad \hat{w}(z) := \sqrt{1+z^2} \tag{7.48}$$

3. Reset the conversed energy E from primitive variables.

In addition, we impose an artificial atmosphere by defining a lower bound $\rho_{\rm atm}$ and reset the rest-mass density ρ after the primitive recovery whenever it falls below the bound $\rho = \max(\rho, \rho_{\rm atm})$ to maintain stable evolution in the low-density region. The cutoff density $\rho_{\rm atm} := \rho_{\rm max} f_{\rm atm}$ depends on the initial maximum density $\rho_{\rm max}$ where the auxiliary factor $f_{\rm atm}$ is typically set to be $\leq 10^{-15}$.

7.2.4 FMR setting

We adopt the fourth-order explicit Runge-Kutta scheme (RK4) in order to evolve the metric function stably [430]. Following the time update scheme in [115], the adaptive time step is employed using the Berger-Oliger algorithm [76]. We allow sub-cycling of time integration starting from level $l_{\rm fix}$ with a time step for each FMR level set to be

$$\Delta t^{(l)} = \begin{cases} \Delta t^{(l-1)}, & \text{for } 1 \leq l \leq l_{\rm fix}, \\ \Delta t^{(l-1)}/2, & \text{for } l > l_{\rm fix}. \end{cases} \tag{7.49}$$

The parameter $l_{\rm fix}$ limits the time step in the coarse levels to avoid error induced by over-large Δt and reduce the effect from the outer boundary. However, it usually makes no difference practically. The time step in the finest level $\Delta t^{(L-1)}$ is related to the grid size as

$$\Delta t^{(L-1)} = c_{\rm CFL} \min(\Delta x^{(L-1)}, \Delta z^{(L-1)}), \tag{7.50}$$

where the Courant–Friedrichs–Lewy (CFL) factor $c_{\rm CFL}$ is set to be 0.5 unless stated otherwise. In `SACRA-2D`, the buffer zone's $(4+4)$ structure is employed, where the outer 4 buffer cells $[N+5, N+8]$ are used for time interpolation between different time slices, while the inner 4 buffer cells $[N+1, N+4]$ act as a buffer zone to dissipate any oscillatory behavior in the time-interpolated values. This corresponds to the $[1, N+4]$ domain for the first three stages of RK4 time integration and $[1, N]$ for the last stage.

To obtain the buffer zone at the child level from its parent, we employ the eighth-order Lagrange interpolation for geometric variables and minmod limiter to reconstruct the primitive hydrodynamics variables $\mathbf{p}$ for the prolongation in space. For the time interpolation in grid $[N+5, N+8]$, we employ a second-order Lagrange interpolation of three time slices $\{t^{n-1}, t^n, t^{n+1}\}$ of its parent level for time $t^n < t < t^{n+1}$. Since the buffer zone does not affect the conservation of the hydrodynamics quantities in the FMR setting, we interpolate the primitive variables $\mathbf{p}$ and construct the conserved variables directly following [478] to avoid additional primitive recovery in the buffer zone. A limiter procedure is also introduced for fluid variables $\mathbf{p}$ following [526] to maintain numerical stability, where we modify the time interpolation to first order with time levels $\{t^n, t^{n+1}\}$ if the following relation holds:

$$\left(\mathbf{p}^{n+1} - \mathbf{p}^{n}\right)\left(\mathbf{p}^{n} - \mathbf{p}^{n-1}\right) < 0. \tag{7.51}$$

After each time matching step between the child and parent levels, the grid values are transferred from the child level (fine grid) to the parent level (coarse grid) in the overlap region. More specifically, the grids $(x, z) \in ([1, N], [1, N])$ in the child level is mapped to $(x, z) \in ([1, N/2], [1, N/2])$ in the parent level. In this restriction procedure, we employ an eighth-order Lagrange interpolation for the geometric variables, and the following conservative scheme [478]

$$\mathbf{q}_{j,k}^{(l-1)} = \frac{1}{\Delta V_{j,k}^{(l-1)}} \sum_{m=2j-1}^{2j} \sum_{n=2k-1}^{2k} \mathbf{q}_{m,n}^{(l)} \Delta V_{m,n}^{(l)}, \tag{7.52}$$

for the conserved variables $\mathbf{q}$ with $j, k = 1, \cdots, N/2$. The primitive recovery procedure is carried out afterward to obtain the updated primitive variables $\mathbf{p}$.

As the parent and child levels evolve in a different time step, the numerical flux across the refinement boundary becomes inconsistent and introduce violation of conservation in mass and angular momentum. To solve this, we store the numerical flux of all conserved variables at the same refinement boundary for both fine and coarse levels during the time integration. After each level finishes the sub-cycling and matches time with its parent level, we correct the conserved variables next to the refinement boundary in the coarse grid by adding the difference of numerical fluxes between the coarse and fine interface [75, 177, 388].

7.2.5 Hybrid Parallelization

`SACRA-2D` is hybrid parallelized by MPI and OpenMP. We employ a simple domain-based decomposition for MPI parallelization. Each level is divided into $M_{\rm MPI} \times M_{\rm MPI}$ blocks of subdomains ($M_{\rm MPI} \times 2M_{\rm MPI}$ in the absence of the mirror symmetry with respect to the $z = 0$ plane), where $M_{\rm MPI}$ is the number of blocks in x and z directions. The choices of $M_{\rm MPI}$ are limited by the number of grids N, which requires $N/M_{\rm MPI}$ to be an even number. OpenMP further parallelizes the subdomains, with $N_{\rm thr}$ being the number of OpenMP threads in each MPI rank. The total number of cores required for the simulation is then determined by $M_{\rm MPI} \times M_{\rm MPI} \times N_{\rm thr}$.

7.2.6 Diagnostics

7.2.6.1 Constraints, mass, and angular momentum

We monitor the overall constraint violations by computing the corresponding L_2-norm every timestep as

$$||\mathcal{H}||_2 = \int \left(R + K^2 - K_{ij}K^{ij} - 16\pi rho_h\right) dV, \tag{7.53a}$$

$$||\mathcal{M}_i||_2 = \int \left(D_j K^j{}_i - D_i K - 8\pi J_i\right) dV, \tag{7.53b}$$

where $\mathcal{H}$ and $\mathcal{M}_i$ are the Hamiltonian and momentum constraints, respectively. Under axisymmetry, the momentum constraints $\mathcal{M}_x$ and $\mathcal{M}_y$ evaluated are effectively $\mathcal{M}_\varpi$ and $\mathcal{M}_\phi$ in cylindrical coordinates, respectively.

We also compute the total baryon mass and angular momentum as

$$M_b = \int D\sqrt{\gamma}dV = \int W^{-3}\rho w dV, \tag{7.54a}$$

$$J = \int S_\phi\sqrt{\gamma}dV = \int W^{-3}\rho h w u_y x dV, \tag{7.54b}$$

which should be conserved. The gravitational mass and angular momentum of the system are also obtained by analyzing the asymptotic behavior of the geometric quantities.

7.2.6.2 Extraction of gravitational wave

We extract gravitational waves from the numerical data using the outgoing component of Newman-Penrose quantity Ψ_4 [353], which can be expressed by the electric part $E_{ac} := C_{abcd}n^b n^d$ and magnetic part $B_{ac} := \frac{1}{2}C_{abef}\epsilon^{ef}{}_{cd}n^b n^d$ of Weyl tensor C_{abcd} as [371, 526]

$$\Psi_4 = -(E_{ac} - iB_{ac})\bar{m}^a\bar{m}^c, \tag{7.55}$$

where ϵ_{abcd} is the covariant Levi-Civita tensor and $\bar{m}^a$ is part of the null tetrad $(k^a, l^a, m^a, \bar{m}^a)$. Here, k^a and l^a are outgoing and ingoing null vectors, respectively, where m^a is a complex null vector satisfying

$$-k^a l_a = 1 = m^a\bar{m}_a. \tag{7.56}$$

We construct a set of spherical shells at different radii composed of N_θ cell-centered grids for $\theta \in [0, \pi]$ ($\theta \in [0, \pi/2]$ in mirror symmetry) with grid points defined by

$$\theta_j = \frac{\pi}{N_\theta}\left(j - \frac{1}{2}\right), \qquad \text{for } j = 1, 2\cdots, N_\theta, \tag{7.57}$$

and extract Ψ_4 on the surfaces by Lagrange interpolation. We further decompose Ψ_4 into tensor spherical harmonic modes (l, m) [115]

$$\Psi_4^{(l,m)} = \int \Psi_4\bar{Y}^{-2}_{l,m}(\theta, \phi)\, d\Omega, \tag{7.58}$$

where $Y^{-2}_{l,m}$ is the spin-weighted spherical harmonic function with $s = -2$. Due to the axial symmetry, only the $m = 0$ modes are extracted with no ϕ dependence. We adopt the accurate Gauss quadrature scheme for the integration following [371].

7.2.6.3 Apparent horizon finder

To identify the presence of a black hole and to diagnose its properties, we implement an apparent horizon finder in `SACRA-2D`. Assuming that the apparent horizon contains the coordinate center $(x, z) = (0, 0)$, the horizon radius H can be represented as a function of polar angle θ as $r = H(\theta)$. Under an axisymmetric configuration, the elliptic equation for the radius of the apparent horizon is reduced to one-dimensional. We essentially employ the same method in [526] to solve the equation. We note that even if a black hole is located along the z-axis different from $z = 0$, the finder can find the apparent horizon by simply changing the definition of θ.

Once the radius of the apparent horizon is determined, we then evaluate its area A_H, and obtain the irreducible mass $M_{\rm irr}$ and the angular momentum J of the black hole as

$$M_{\rm irr} = \sqrt{\frac{A_H}{16\pi}}, \qquad\qquad J = \frac{1}{8\pi}\oint_{\mathcal{H}} K_{ab}\phi^a s^b dA, \tag{7.59}$$

where $\mathcal{H}$ corresponds to the surface of the apparent horizon, $\phi^a := (\partial/\partial_\phi)^a$, and s^b is the unit radial vector normal to $\mathcal{H}$. As a result, the mass of the black hole can be determined by

$$M = \sqrt{M_{\rm irr}^2 + \frac{J^2}{4M_{\rm irr}^2}}. \tag{7.60}$$

Once the black hole is formed, we excise the fluid quantities by setting $u_i = 0$ and the rest-mass density to zero for $r \leq H(\theta)/2$ to avoid any potential numerical instability which may be caused by extreme values of hydrodynamics quantities inside the black hole.

7.3 Numerical test

This section presents representative examples of the benchmark test problems with `SACRA-2D`. We first examine the metric and GRHD sectors separately with tests considering vacuum spacetime in Section 7.3.1 and fixed background metric in Section 7.3.2, respectively. The code is then fully tested in Section 7.3.3 considering problems that cooperate GRHD in dynamic spacetime.

7.3.1 Vacuum spacetime

7.3.1.1 Trumpet Black hole

We first test our metric solver on a stationary spacetime. Specifically, we consider a non-rotating black hole in the so-called maximal trumpet coordinate, which is time-independent under BSSN formalism with the puncture gauge. The analytic solution of the trumpet-puncture black hole is given by [54, 180]

$$\alpha = \sqrt{1 - \frac{2M}{R} + \frac{27M^4}{16R^4}}, \tag{7.61a}$$

$$\beta^i = \frac{3\sqrt{3}M^2}{4R^3} x^i, \tag{7.61b}$$

$$W = \frac{r}{R}, \tag{7.61c}$$

$$h_{ij} = 0 = K, \tag{7.61d}$$

$$\tilde{A}_{ij} = \frac{3\sqrt{3}M^2}{4R^3} \left(\delta_{ij} - 3\frac{x^i x^j}{r^2} \right), \tag{7.61e}$$

where M is the mass of the black hole, r is the radial coordinate, and R is the areal radius in Schwarzschild metric, which is a function of r written as

$$r = \left(\frac{2R + M + \sqrt{4R^2 + 4MR + 3M^2}}{4} \right) \left[\frac{(4 + 3\sqrt{2})(2R - 3M)}{8R + 6M + 3\sqrt{8R^2 + 8MR + 6M^2}} \right]^{1/\sqrt{2}}. \tag{7.62}$$

In this coordinate, $r = 0$ corresponds to an areal radius of $R = 3M/2$, and the event horizon radius is located at $r \approx 0.78M$. To evolve the trumpet data, we use a gauge condition consistent with the staticity of the solution [402] as

$$\partial_t \alpha = -\alpha (1 - \alpha) K, \tag{7.63a}$$

$$\partial_t \beta^i = \frac{3}{4} B^i, \tag{7.63b}$$

$$\partial_t B^i = \partial_t \tilde{\Gamma}^i - \eta_B B^i, \tag{7.63c}$$

with a damping parameter $\eta_B = 1/M$. The slicing condition in Eq. (7.63), compared to the standard 1+log gauge without advection, gives a lower propagation speed of gauge waves. We found that the numerical result is closer to the analytical trumpet solution under Eq. (7.63) due to a smaller effect from the gauge dynamics. We perform numerical evolution of the trumpet data on a computation domain of $L_{\max} = 1600M$ and 11 FMR boxes with different grid resolutions with $N = 64, 128$, and 256, which corresponds to the grid spacing of $\Delta x = \Delta z = 0.0244M, 0.0122M$ and $0.0061M$, respectively, on the finest level with $L = 1.56M$.

Although the metric variables should remain unchanged analytically under this gauge condition in the trumpet solution, numerical errors from the finite difference scheme and interpolation across the refinement boundaries will induce deviations from the initial values during the evolution. We evolve the trumpet data up to $t = 195M$ and extract the relative error of W, α, and β^r as well as the Hamiltonian constraint violation on the x-axis at $z = 0$ as shown in Fig. 7.1. Regardless of the resolutions, a spike in relative errors appears at

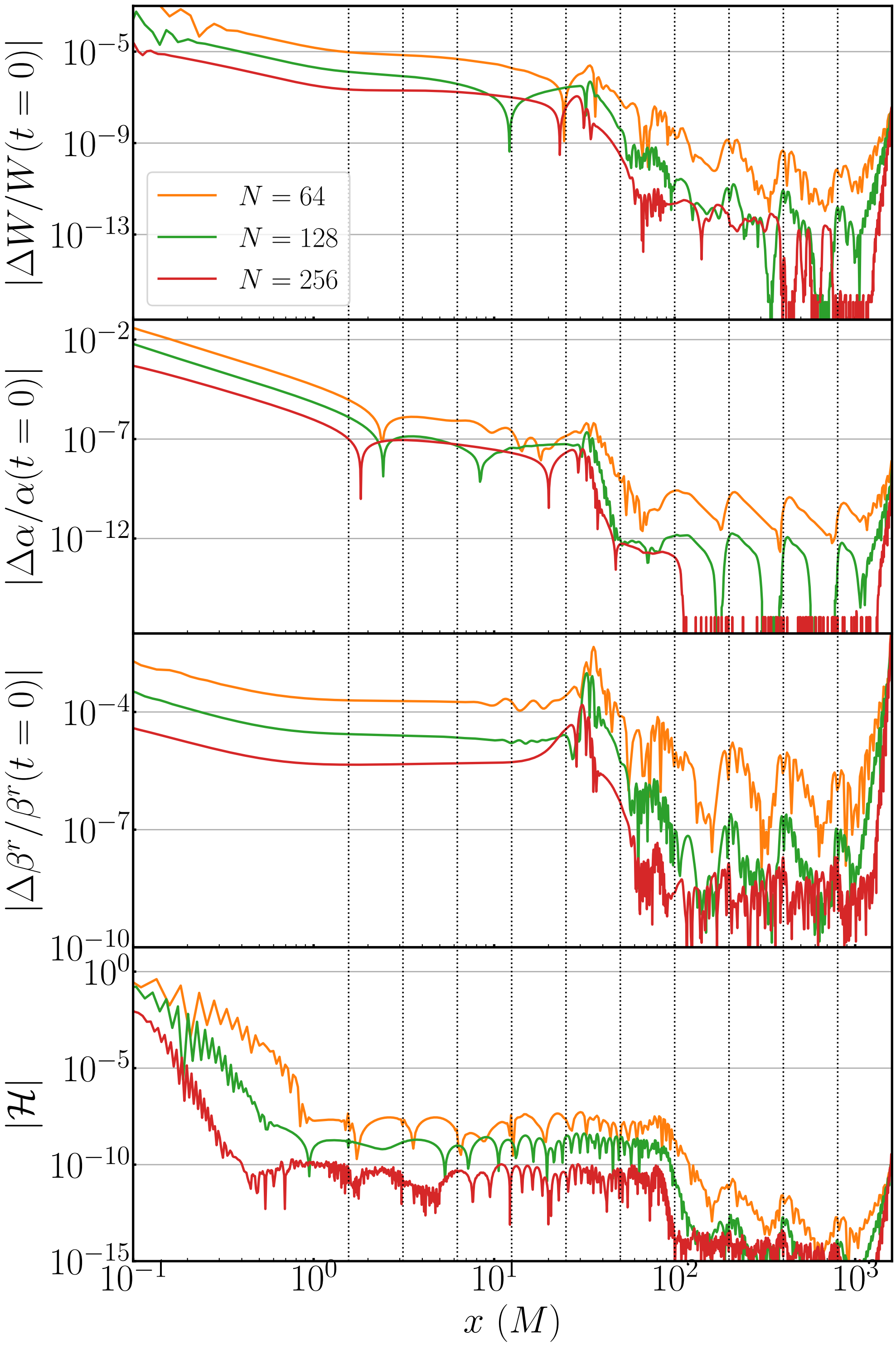

Figure 7.1: The top three panels show the relativity error of $W := \psi^{-2}$, lapse function α, and shift vector β^r along the x-axis extracted at $t = 195M$ for three different grid resolutions $N = 64, 128$, and 256. The bottom panel shows the corresponding absolute violation of Hamiltonian constraints on the same slice. The black dotted vertical lines indicate the location of the refinement boundaries.

$x \approx 30M$, possibly caused by an outgoing gauge wave. This could introduce additional noise and induce a loss of convergence [181]. We can recover an expected sixth-order convergence for metric variables in general, while a roughly fourth-order convergence is found for region $x \lesssim 30M$ where the gauge wave has passed through. Since we start from time-independent initial data that minimizes gauge dynamics, the Hamiltonian constraint violations do not contain non-convergent spikes induced by the gauge evolution that appeared in [181], and convergent results are obtained. In addition, the relative errors and constraint violation show regularly-spaced spikes on a logarithmic space scale in between $x \approx 100M$–$1000M$, which is a common feature for mesh-refinement structure as the metric variables experience the sudden change in grid spacing across the refinement boundary.

7.3.1.2 Spinning Black hole

To further test our metric solver in a system with non-zero angular momentum, we evolve a near-extreme-spin black hole with the dimensionless spin parameter $\chi = 0.95$. We adopt the spinning black hole in quasi-isotropic coordinates under a new radial coordinate r introduced in [316] defined by

$$r_{\mathrm{BL}} = r\left(1 + \frac{r_+}{4r}\right)^2, \tag{7.64}$$

where r_{BL} is the radial coordinate in Boyer-Lindquist coordinates, $r_\pm = M \pm \sqrt{M^2 - a^2}$ is the Boyer-Lindquist radii of inner $(-)$ and outer $(+)$ horizons of the black hole, and M and a are the black hole mass and spin, respectively. The event horizon in this radial coordinate is given by

$$r_h = \frac{1}{4}\left(M + \sqrt{M^2 - a^2}\right), \tag{7.65}$$

which goes to a finite radius $M/4$ when the black hole approaches the maximum spin $a = M$. This gives better initial data for near-extreme-spin black holes compared to quasi-isotropic coordinates in [288], in which the coordinate radius of the event horizon drops to zero for $a \to M$.

The corresponding metric components are written as

$${}^{(3)}ds^2 = \frac{\Sigma\left(r + \frac{r_+}{4}\right)^2}{r^3\left(r_{\mathrm{BL}} - r_-\right)} dr^2 + \Sigma d\theta^2 + \frac{\Xi}{\Sigma}\sin^2\theta d\phi^2, \tag{7.66a}$$

$$K_{r\phi} = K_{\phi r} = \frac{Ma\sin^2\theta}{\Sigma\sqrt{\Xi\Sigma}}\left(1+\frac{r_+}{4r}\right)\frac{1}{\sqrt{r\left(r_{\rm BL}-r_-\right)}} \left[3r_{\rm BL}^4 + 2a^2 r_{\rm BL}^2 - a^4 - a^2\left(r_{\rm BL}^2 - a^2\right)\sin^2\theta\right], \tag{7.66b}$$

$$K_{\theta\phi} = K_{\phi\theta} = -\frac{2a^3 M r_{\rm BL}\cos\theta\sin^3\theta}{\Sigma\sqrt{\Xi\Sigma}}\left(r-\frac{r_+}{4}\right)\sqrt{\frac{r_{\rm BL}-r_-}{r}}, \tag{7.66c}$$

where $\Sigma = r_{\rm BL}^2 + a^2\cos^2\theta$, $\Delta = r_{\rm BL}^2 - 2Mr_{\rm BL} + a^2$, $\Xi = \left(r_{\rm BL} - a^2\right)^2 - \Delta a^2 \sin^2\theta$, and ${}^{(3)}ds^2$ is the spatial line element.

We transform the metric variables to the Cartesian coordinates on the $y = 0$ plane and simulate with $a = 0.95M$. The computational domain is set to be $x_{\rm max} = z_{\rm max} = 2048M$ with 10 FMR levels and three grid resolutions $N = 200, 300$, and 400, which correspond to $\Delta x/M = 0.02, 0.0133$, and 0.01, respectively, with the box size $L = 4M$ at the finest level. We evolve the initial data using the moving puncture gauge of Eq. (1.24) with the gauge parameter $\eta_B = 1/M$. In this configuration, while the black hole spacetime remains stationary, the spatial hypersurface will still evolve under the dynamical gauge conditions and eventually approaches the trumpet puncture [111, 114, 159, 226, 227].

The upper panel of Fig. 7.2 shows the relative error of the mass M and the spin a of the black hole measured for the apparent horizon. As we increase the resolution, the relative error drops and reaches $\sim 10^{-4}$ for the highest resolution with convergence approximately at sixth-order. On the other hand, the coordinate equatorial $r_{\rm eq}$ and polar $r_{\rm p}$ radii of the apparent horizon evolve under the moving puncture gauge and eventually approach constant values of $r_{\rm eq} = 0.428M$ and $r_{\rm p} = 0.281M$ as shown in the bottom panel of Fig. 7.2. Although both $r_{\rm eq}$ and $r_{\rm p}$ are gauge-dependent quantities, the values of $r_{\rm eq}$ and $r_{\rm p}$ drop as a result of the hypersurface approaches the trumpet slice of the near-extreme-spin black hole.

7.3.1.3 Black hole head-on collision

To explore the convergence of gravitational waves numerically extracted, we perform a test simulation of the head-on collision of two non-spinning black holes. Under axial symmetry, we can set up the Brill-Lindquist initial data [108] which consists of two equal-mass black holes in isotropic coordinates located on the rotational axis (z-axis) separated by a distance of $2b$ in the form of

$$\psi = 1 + \frac{M_0}{2r_+} + \frac{M_0}{2r_-}, \tag{7.67}$$

where M_0 is constant and

$$r_\pm = \sqrt{x^2 + (z \pm b)^2}. \tag{7.68}$$

is the radial coordinate distances from the black hole punctures (with $y = 0$).

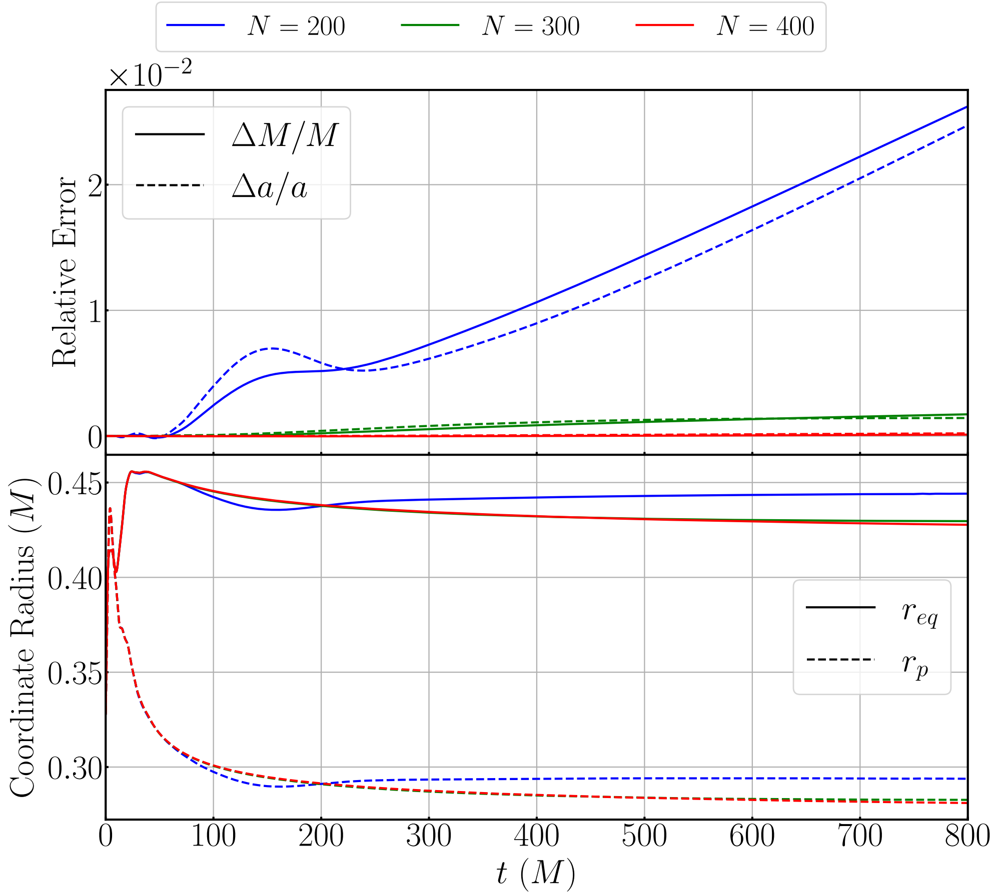

Figure 7.2: The upper panel shows the relative error of black hole mass (solid) and dimensionless spin (dashed) as functions of time with the initial value of $\chi = 0.95$. The bottom panel shows the evolution of equatorial (solid) and polar (dashed) radii of the apparent horizon in the coordinate radius. The initial radius of the apparent horizon is located at $r = 0.328M$. The blue, green, red, and cyan lines indicate the result from $N = 200, 300$, and 400, respectively.

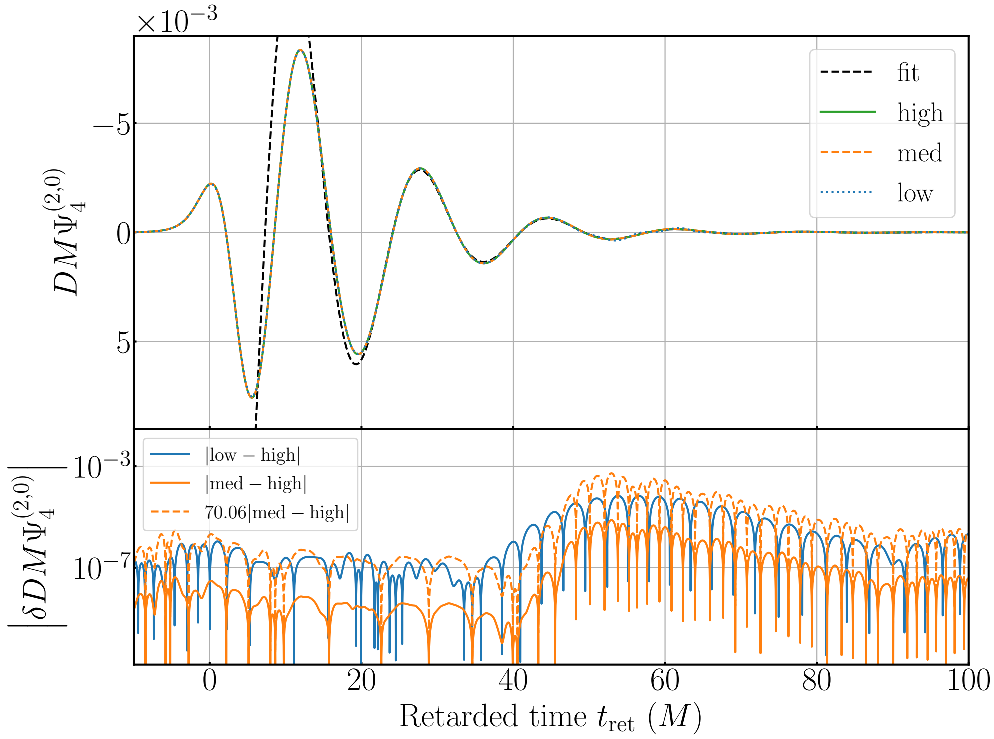

Figure 7.3: $(l,m)=(2,0)$ mode of $DM\Psi_4$ gravitational waves (top) emitted by the head-on collision of two black holes with extraction radius $r_{\rm ex}=30M$ in three different grid resolutions. The grid spacing $\Delta x/M$ in the finest level from low to high are 0.015625, 0.0078125, and 0.005208, respectively. The black dashed line shows the fitted waveform of the analytical ringdown frequency $M\omega \approx 0.3737-0.0890i$. The bottom panel shows the absolution error of the resultant waveform between different resolutions.

We pick $b=M/2=M_0$ following [402] and start the simulation under mirror symmetry. Here, M is the total ADM mass of the system, which also defines the unit of length. In this setup, two black holes are not initially enclosed by the common horizon [424] but merge during the time evolution. The computational domain is set as $x_{\rm max}=z_{\rm max}=1024M$ with 11 FMR levels, which corresponds to the size $L=1M$ in the finest box. We perform the simulations with three grid different resolutions $N=64$ (low), 128 (med), and 192 (high) with corresponding resolutions of $\Delta x/M=0.015625, 0.0078125$, and 0.005208, respectively, in the finest level. The non-spinning black holes are released from rest, accelerating toward each other along the polar axis, and then collide head-on at the origin, forming a perturbed black hole that promptly rings down to a stationary state by emitting gravitational waves.

Fig. 7.3 shows the accompanying gravitational waves signals extracted at $r_{\rm ex}=30M$ as a function of retarded time $t_{\rm ret}$ defined by [278, 280]

$$t_{\rm ret}=t-\left[D+2M\ln\left(\frac{D}{2M}-1\right)\right], \tag{7.69}$$

where $D\approx r\left[1+M/\left(2r\right)\right]^2$ is areal radius of the extraction sphere. The resultant ring-down waveform emitted after the merger forms an exponentially damped oscillation with frequency

$M\omega \approx 0.3737 - 0.0890i$ [86, 402] in the dominant $(l, m) = (2, 0)$ mode. The top panel shows the $(l, m) = (2, 0)$ mode of Ψ_4 in three different grid resolutions, which are all consistent with the analytical frequency. In addition, the bottom panel of Fig. 7.3 indicates the absolute errors between the low ($\Delta x = 0.015625M$) and high ($\Delta x = 0.005208M$) resolutions as well as the medium ($\Delta x = 0.0078125M$) and high ($\Delta x = 0.005208M$) resolutions as blue and orange solid lines, respectively. To examine the order of convergence, we scale up the absolute difference between the medium and high resolutions by a factor of $(0.015625^6 - 0.005208^6)/(0.0078125^6 - 0.005208^6) = 70.06$ as shown in the orange dashed line, which agrees approximately with the blue solid line, suggesting the 6th-order convergence in the waveform. Note that the absolute error of Ψ_4 rises, and the convergence is lost for $t_{\rm ret} \gtrsim 40M$. This is likely caused by the reflection of the outgoing gravitational wave at the refinement boundaries in the coarse domains for which the wavelength of gravitational waves are not well resolved.

7.3.2 GRHD with fixed spacetime

In this section, we consider test problems with a fixed background metric in both flat Minkowski spacetime and curved spacetime (so-called Cowling approximation), focusing on the hydrodynamics sector to validate our Riemann solver and reconstruction scheme, as well as examining the convergence of the hydrodynamics solver.

7.3.2.1 One-dimensional shock-tube test

We carry out a one-dimensional shock-tube test problem following [329], which is commonly used to test the performance of the Riemann solver and reconstruction scheme. For this test, the cylindrical coordinates in `SACRA-2D` are converted to the Cartesian coordinates. Under this setup, the background metric is reduced to the Minkowski flat spacetime with coordinate vector acting as the tetrad basis, thus allowing us to validate our HLLC solver. We consider ideal gas law $P = \rho\,(\Gamma - 1)\,\epsilon$ with $\Gamma = 5/3$ giving the initial left and right states by

$$(\rho, P, v) = \begin{cases} (10, 40/3, 0) & \text{for } x < 0.5, \\ (1, 0, 0) & \text{for } x > 0.5, \end{cases} \tag{7.70}$$

where v is the velocity in the x direction, i.e., $v = u^x/u^t$. The computational domain is set to be $x \in [0, 1]$ with the grid resolution of $N = 800$ ($\Delta x = 0.00125$) and no grid refinement. A third-order PPM scheme is used for reconstruction.

Fig. 7.4 shows the profile of the rest-mass density ρ, pressure P, and velocity v at $t = 0.4$ compared to the analytical solutions generated by `RIEMANN` [1] [329]. The initial discontinuity at $x = 0.5$ creates left and right propagating shock waves and forms a contact discontinuity in

---

[1] The open-source program `RIEMANN` is available here.

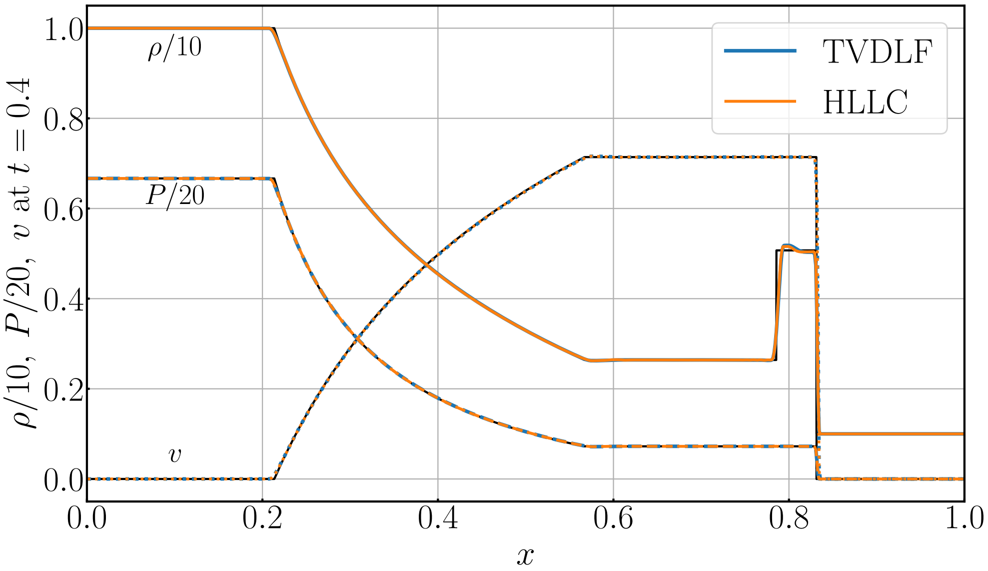

Figure 7.4: The density (solid), pressure (dashed), and velocity (dotted) profile of one-dimensional shock-tube problem at $t = 0.4$ obtained by TVDLF (blue) and HLLC (orange) Riemann solvers. The black solid curve indicates the analytical solution.

between, which is located at $x = 0.786$ for $t = 0.4$. Both TVDLF and HLLC solvers (shown as the blue and orange dots in Fig. 7.4, respectively) can satisfactorily resolve the shocks and contact discontinuity with similar performance, which is consistent with the result in [281] when a 3rd-order reconstruction scheme is employed.

7.3.2.2 Bondi accretion

In this test, we simulate the Bondi accretion [231] consisting of a smooth stationary fluid flow into the black hole that allows us to examine the convergence of hydrodynamics and the tetrad formulation for the HLLC solver under a non-trivial spacetime without shocks. To fit it in the puncture formalism of our code, we consider the Bondi solution in the maximal trumpet coordinate of a non-rotating black hole spacetime [338], which does not exhibit coordinate pathology across the event horizon (see Eq. (7.61) for the background metric). We adopt the same parameters following [513] for our setup with an adiabatic index of $\Gamma = 4/3$, an adiabat of $K = 1$, and a critical radius of $r_c = 8M$ with a mass accretion rate $\dot{M}_{\rm acc} = 0.0848$ where M is the black hole mass. The hydrodynamics quantities within $r = 0.4M$ are fixed as an inner boundary condition. Six different grid resolutions with $N = 32, 64, 128,$ and 256 are considered for the convergence test. The computational domain is $x_{\rm max} = z_{\rm max} = 16M$ without mesh refinement. In addition, we carry out another set of simulations with 3 refinement levels under the same parameters to test our FMR setting, which corresponds to a box size $L = 4M$ and in the finest box. Specifically, we examine the convergence of the profile of the rest-mass density ρ by evaluating the L_1-norm $\epsilon_{\rm L1}$ defined by [513]

$$\epsilon_{\rm L1}(\rho) = \frac{\int |\rho_{\rm initial} - \rho_{\rm final}| \sqrt{-g} dV}{\int |\rho_{\rm initial}| \sqrt{-g} dV}. \tag{7.71}$$

The upper and bottom panels Fig. 7.5 show the radial profiles of the rest-mass density ρ and the radial velocity $-v^r$ of the Bondi flow, respectively. The markers show the profiles extracted at $t = 20M$ in the resolution of $N = 128$ with the TVDLF solver labeled in blue and the HLLC solver labeled in orange, which agrees approximately with the analytical solution indicated by the black dashed curves. The bottom panel of Fig. 7.5 plots the L_1-norm of the error of the rest-mass density ρ concerning the different grid spacing. The TVDLF and HLLC solvers have the same performance due to the smoothness of the accretion flow, as many other studies have shown (e.g., Refs. [281, 348, 437]). The result demonstrates an approximate second-order convergence in both solvers regardless of our FMR setting, which is consistent with the accuracy of our implementation of the Riemann solvers.

7.3.2.3 Rayleigh-Taylor instability from the modified Bondi flow

To further validate our HLLC solver and demonstrate its improvement over the TVDLF solver, we modify the configuration of the Bondi flow to induce Rayleigh-Taylor instability. Following [519], we change the initial setup within a radius $r < 3M[1 + 0.05(\cos(80\theta) + 1)]$ as

$$\rho = 0.1\rho_{\rm bondi}, \qquad P = 50P_{\rm bondi}, \qquad u_r = 0, \tag{7.72}$$

where $\rho_{\rm bondi}$ and $P_{\rm bondi}$ are the density and pressure profiles of the Bondi flow in Section 7.3.2.2, respectively. This introduces a hot, low-density bubble in the inner region with the perturbed interface. The hot bubble rises and pushes through the infalling high-density Bondi flow that later on develops the Rayleigh-Taylor-like instability (or sometimes referred to as the Richtmyer-Meshkov instability). We employ the same grid setup as in Section 7.3.2.2 with a grid resolution of $N = 512$ ($\Delta x = 0.03125M$).

Fig. 7.6 shows the snapshots of the rest-mass density profile extracted at $t/M = 0$ (top row), 25 (middle row), and 50 (bottom row). The left and right columns correspond to the results of the TVDLF solver and the HLLC solver, respectively. When the hot low-density gas expands and compresses the infalling flow, instability fingers develop at $t = 5M$ and eventually spread inwards at $t = 50M$. The HLLC solver can resolve the Richtmyer-Meshkov instability better than the TVDLF solver, with the instability finger's fine structure more sharply captured as illustrated in Fig. 7.6. This demonstrates that the HLLC solver performs better than the TVDLF solver, effectively improving spatial resolution.

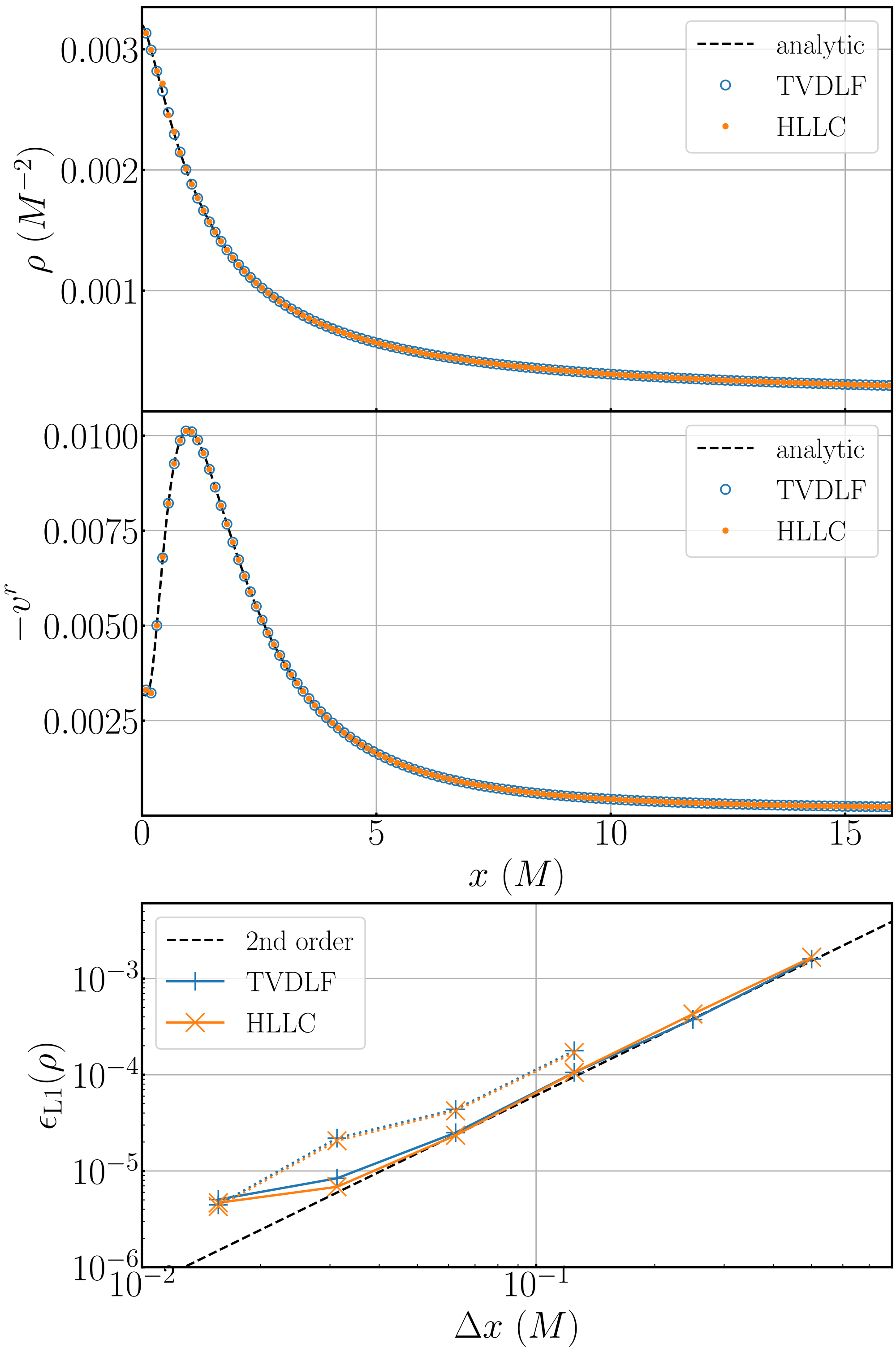

Figure 7.5: Radial profiles of rest-mass density ρ (top) and radial velocity $-v^r$ (middle) extracted at $t = 20M$ with the grid resolution of $N = 128$ using TVDLF (blue) and HLLC (orange) Riemann solvers. The bottom panel shows the L1 norm of the error in rest-mass density $\epsilon_{\rm L1}(\rho)$ with respective to different grid resolutions in the finest box. The solid and dotted lines show the results in the uniform grid setting and the 3 levels FMR setting, respectively. The numerical results are consistent with the second-order convergence (dashed line).

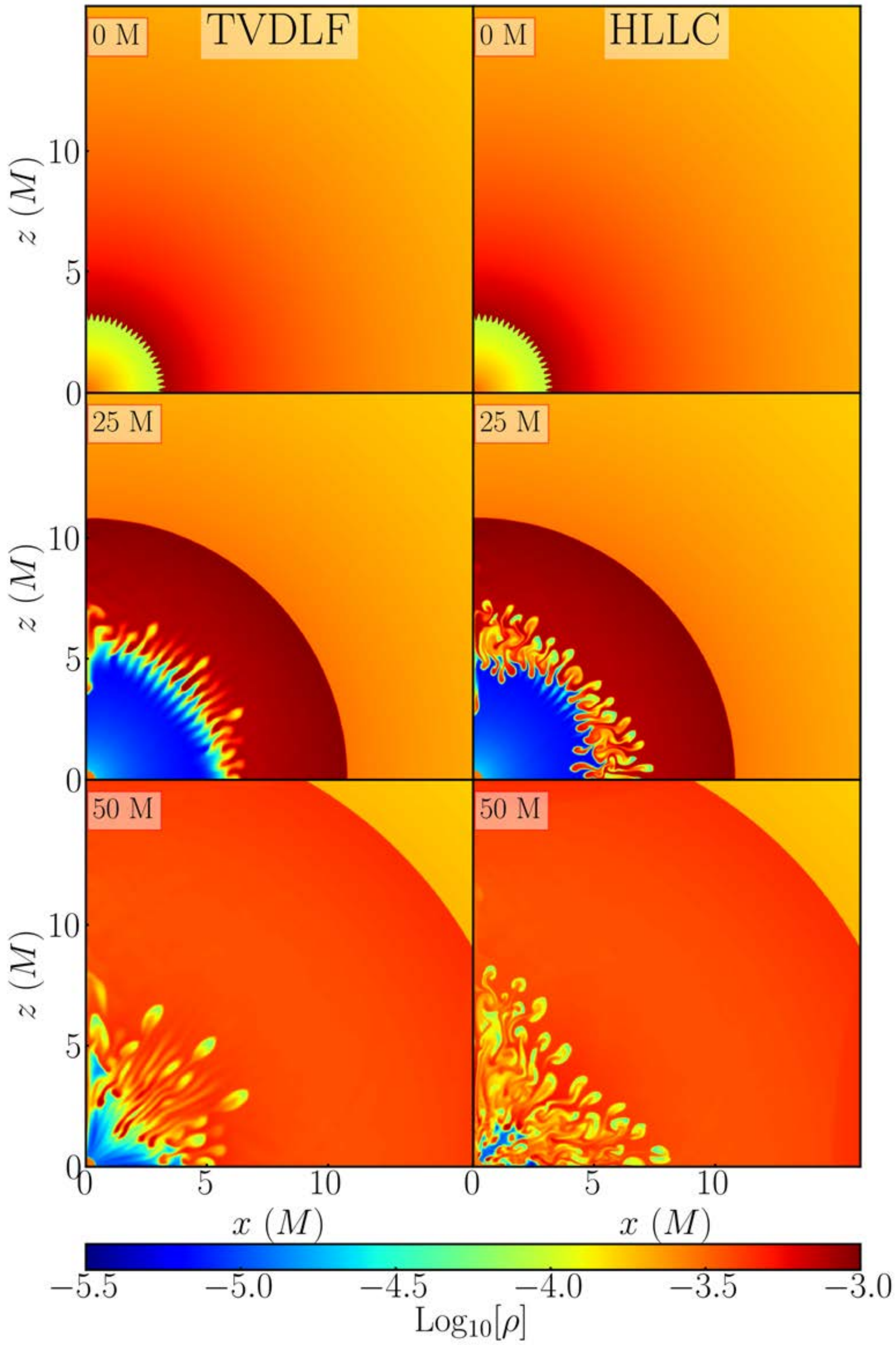

Figure 7.6: Rest-mass density ρ in the modified Bondi flow with TVDLF (left) and HLLC (right) Riemann solvers. The snapshots are extracted at $t/M = 0$ (top), 25 (middle), and 50 (bottom).

7.3.3 GRHD with dynamical spacetime

In this section, we perform test simulations that solve both hydrodynamics and metric sectors to confirm the full capacity of the code.

7.3.3.1 Stable rotating neutron star

We first evolve a stable rotating neutron star in equilibrium configuration with initial data constructed by the open-source code `RNS` [475] using the MPA1 EOS [347]. Specifically, a uniformly rotating neutron star with baryon mass $M_b = 1.80 M_\odot$ and angular momentum $J = 1.80 M_\odot^2$ is considered with the ADM mass $M_{\rm ADM} = 1.65 M_\odot$ and the ratio of rotational kinetic energy to gravitational potential energy $\beta = 0.11$. At such a high angular frequency $\Omega = 6.28 \times 10^3$ rad/s, the neutron star is close to its mass shedding limit. Its shape is flattened to become an oblate spheroid with the ratio between the coordinate radius at pole $r_{\rm p}$ and equator $r_{\rm eq}$ as $r_{\rm p}/r_{\rm eq} = 0.63$. While such a rapidly rotating neutron star may be subjected to non-axisymmetric $m = 2$ bar mode instability [476], it is stable against axial symmetric perturbation. Hence, maintaining the system stable for a long time in the simulation poses a test problem.

We set the computational domain as $x_{\max} = z_{\max} = 4726$ km with 10 FMR levels and grid resolution with $N = 192$, which correspond to the size $L = 9.23$ km and the resolution $\Delta x = \Delta z = 48$ m in the finest box. We also carried out the test with a lower resolution $N = 96$ as a comparison. Since the polar and equatorial radii of the neutron star are $r_p = 8.34$ km and $r_{\rm eq} = 13.25$ km, respectively, the refinement boundary of the finest box in this setup cuts through a part of the neutron star as illustrated in the upper panels of Fig. 7.8. This allows us to test the treatment of fluxes and the reconstruction scheme across the refinement boundary with the adaptive time update scheme. The MPA1 EOS for the cold EOS part and Γ thermal law with $\Gamma_{\rm th} = 5/3$ are employed. We perform two sets of simulations using different Riemann solvers and evolve the neutron star up to $t = 250$ ms, about ~ 250 times the rotational period, which is long enough to examine the quality of the simulation. In both runs, the mirror symmetry with respect to the equatorial plane is imposed, and the atmosphere factor $f_{\rm atm}$ is set to be 10^{-20} and $l_{\rm fix} = 4$.

The top panel of Fig. 7.7 shows the evolution of the rest-mass density at the center ρ_c, which is maintained throughout the simulation with initial oscillation amplitude $\sim 0.1\%$ and $\lesssim 0.2\%$ shift after 250 ms for both TVDLF and HLLC Riemann solvers for $N = 192$. The shift converges approximately at the second order. The oscillation amplitude of ρ_c is noticeably damped out faster for the TVDLF solver than the HLLC solver. This indicates that the diffusive nature of the TVDLF solver numerically dissipates the oscillation energy, as another study [281] also has a similar finding.

The conservation of baryon mass and angular momentum is achieved remarkably well,

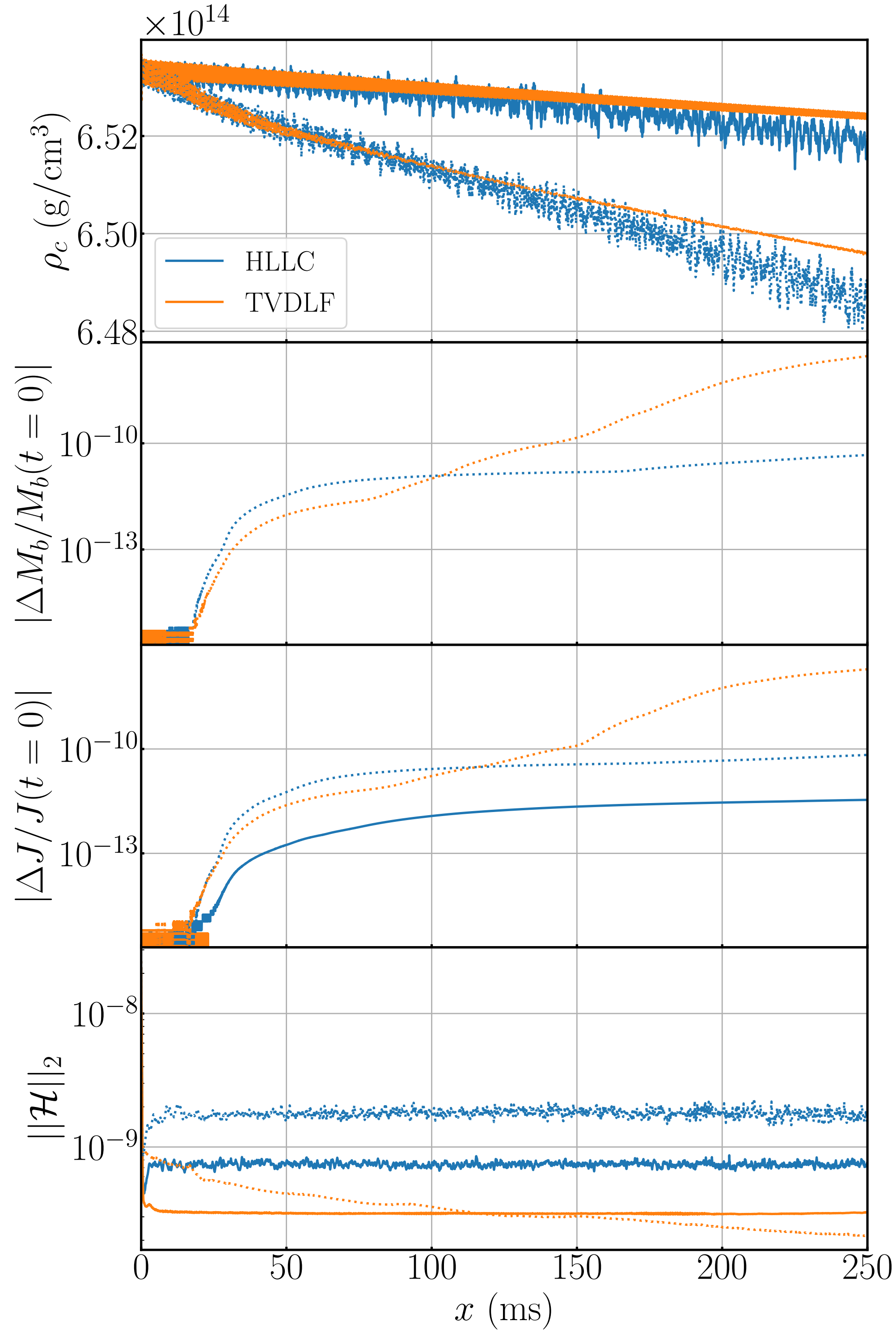

Figure 7.7: From top to bottom, the panels show, respectively, the evolution of central rest-mass density ρ_c, the relative difference of total baryon mass and angular momentum, and the L_2-norm of Hamiltonian constraint violation for the evolution of a rotating neutron star. The solid and dotted lines show the results of $N = 192$ and 96, respectively.

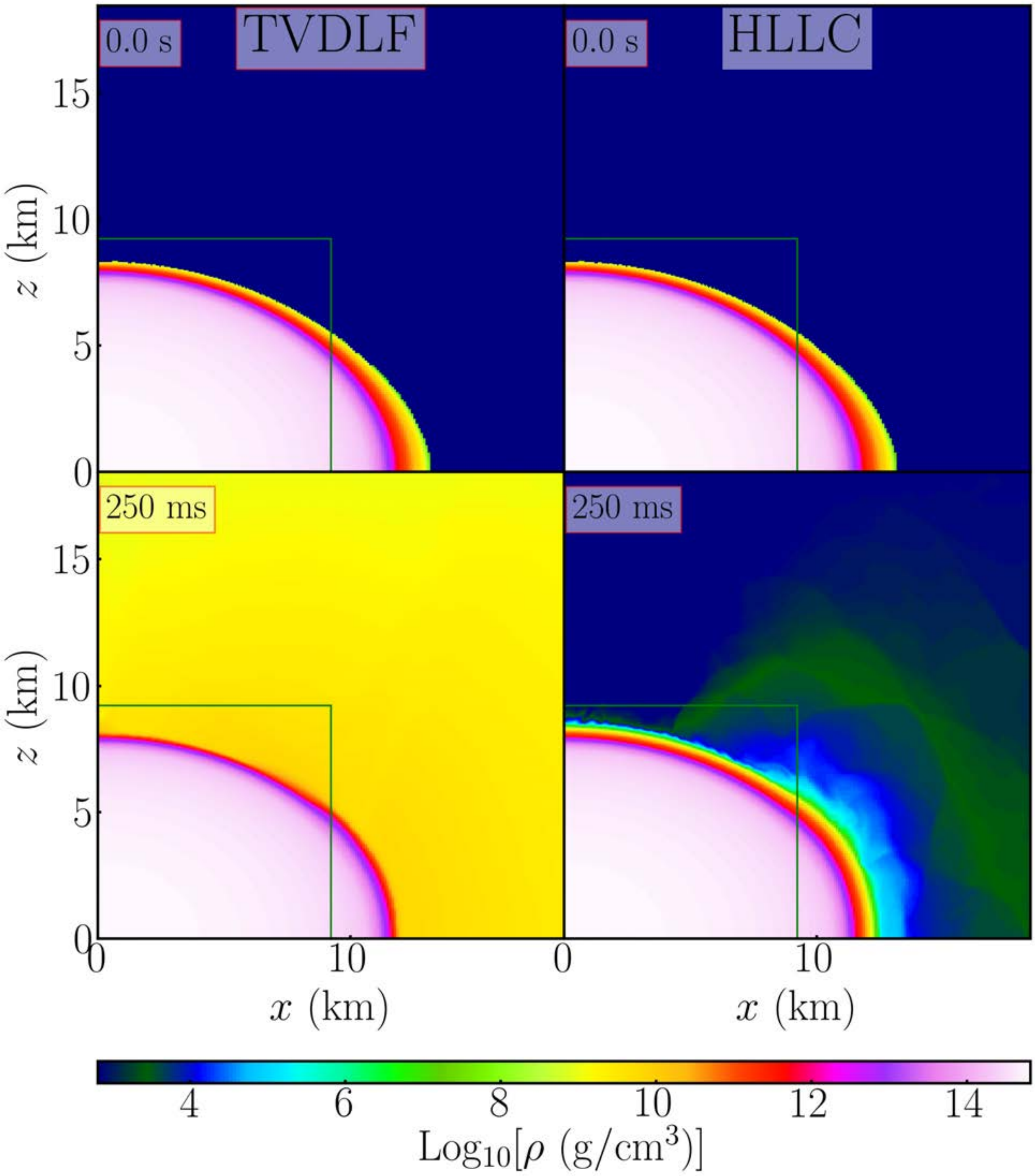

Figure 7.8: Snapshot of the rest-mass density of the rapidly rotating neutron star with TVDLF (left) and HLLC (right) Riemann solvers for $N = 192$. The top and bottom rows are extracted at $t = 0$ s and $t = 250$ ms, respectively. The green solid lines indicate the boundaries of the FMR levels.

as shown in the second and third panels of Fig. 7.7, with an error of machine precision at $\sim$ 10 ms, which validates our treatment of numerical flux across the refinement boundary. Shortly after that, the relative difference raised to $\lesssim 10^{-11}$ irrespective of the grid resolution as the matter on the neutron star surface expanded to the atmosphere due to the artificial heating at the surface. Due to the inability of the TVDLF solver to resolve the contact discontinuity, the effect of the surface heating is much stronger, creating an artificial outflow and an atmosphere with density $\rho \sim 10^9$ g/cm^3 as shown in the bottom left panel of Fig. 7.8. This outflow eventually escapes from the computational domain after $\sim$ 100 ms and continuously increases the relative differences of the rest mass and angular momentum to $\sim 10^{-7}$ at the end of the simulation. On the other hand, these relative differences in the HLLC solver remain $\lesssim 10^{-10}$ at the end of the simulation irrespective of the grid resolution. This is because the HLLC solver resolves the surface of the neutron star (i.e., the contact discontinuity) much better than the TVDLF solver, as shown in the profiles of the rest-mass density ρ in Fig. 7.8. At the end of the simulation ($t = 250$ ms), the rest-mass density in the atmosphere outside the stellar surface is about 10^4–10^5 g/cm^3 for the HLLC solver, which is five orders of magnitude lower than the TVDLF solver, demonstrating a significant improvement in reducing the artificial surface heating. Note that the structure of the neutron star remains intact across the refinement boundary as shown by the green solid line in Fig. 7.10 without any noticeable numerical artifact despite the adaptive time step treatment. This validates our implementation of the FMR scheme.

7.3.3.2 Migration of an unstable neutron star

To further test the nonlinear dynamics of matter and spacetime, we perform one standard test problem that simulates the migration of an unstable neutron star [81, 116, 127, 137, 193, 354]. We construct a Tolman–Oppenheimer–Volkoff (TOV) neutron star in the unstable branch of the mass-radius curve with polytropic EOS $K = 100$, $\Gamma = 2$, and central rest-mass density $\rho_c = 8 \times 10^{-3}$ (in the unit of $c = G = M_\odot = 1$). Since the unstable branch has a smaller absolute value of the binding energy than its stable companion for this EOS, the unstable neutron star would migrate to the corresponding stable state with the same baryon mass in the simulation. The computational domain is set to be $x_{\max} = z_{\max} = 2215$ km in the grid resolution of $N = 128$ with 9 FMR levels, which corresponds to the box size $L = 8.65$ km with the grid spacing $\Delta x = 67.6$ m in the finest level. We carry out two sets of simulations for this system under the mirror symmetry, one using the Γ thermal law with $\Gamma_{\rm th} = 2$, and another adopting the "adiabatic" EOS [193] which neglects the thermal part and enforces zero temperature by discarding the energy equation for E. For both runs, the HLLC Riemann solver is employed with atmosphere factor $f_{\rm atm} = 10^{-15}$ and $l_{\rm fix} = 4$.

The top panel of Fig. 7.9 shows the evolution of the central rest-mass density ρ_c as a function of time for the Γ thermal law EOS and adiabatic EOS shown in blue solid and

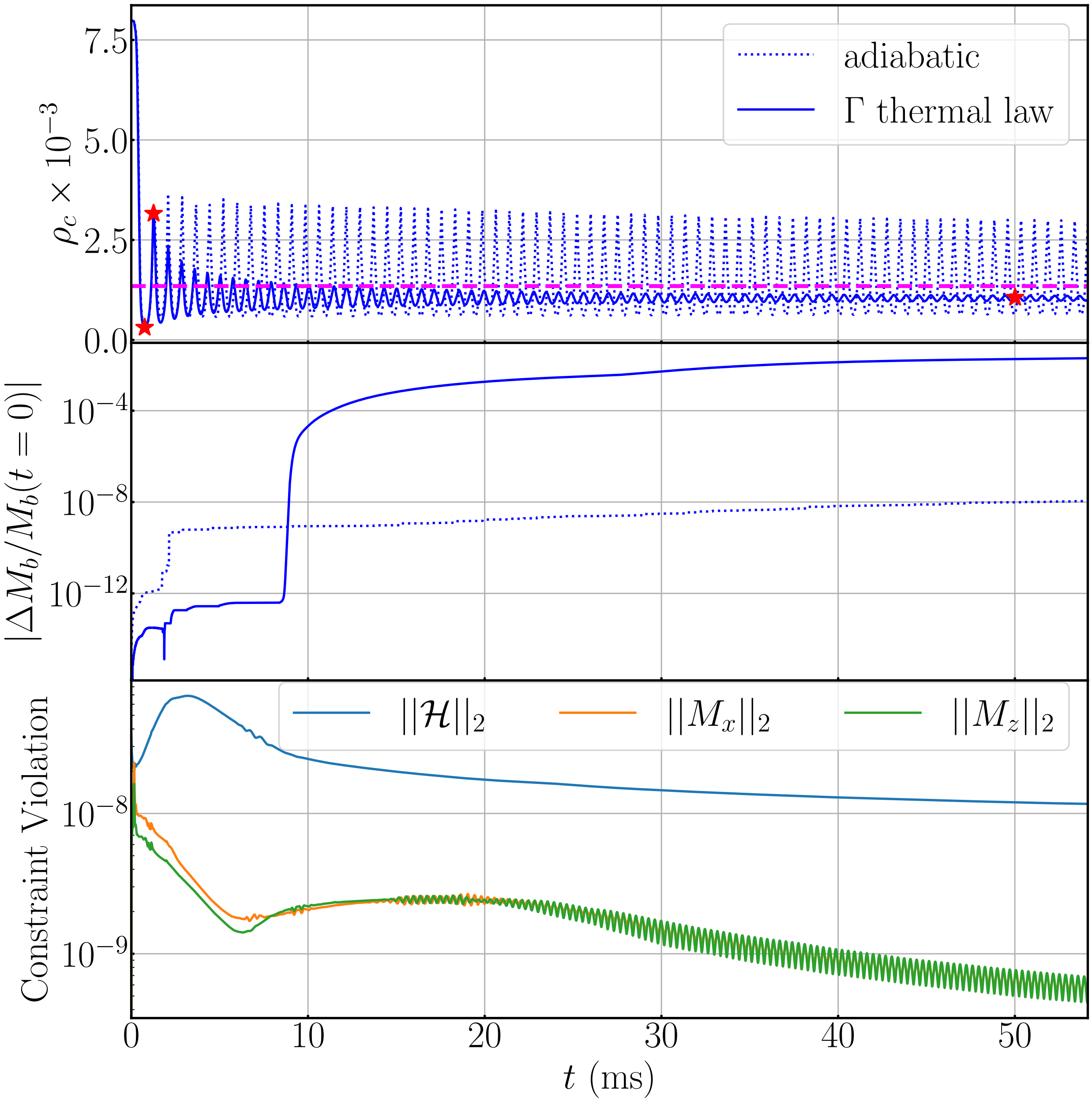

Figure 7.9: The top and middle panels show, respectively, the evolution of the central rest-mass density ρ_c and the relative difference of the total baryon mass M_b as a function of time with the Γ thermal law EOS (solid) and adiabatic EOS (dotted). The magenta dashed line on the top panel indicates central rest-mass density $\rho_s = 1.346 \times 10^{-3}$ of the neutron-star model that lies on the stable branch of the mass-radius curve with the same baryon mass. The red star markers specify the time extracted for the snapshots shown in Fig. 7.10. The bottom panel shows the L_2-norm of constraint violations for the Γ thermal law EOS model.

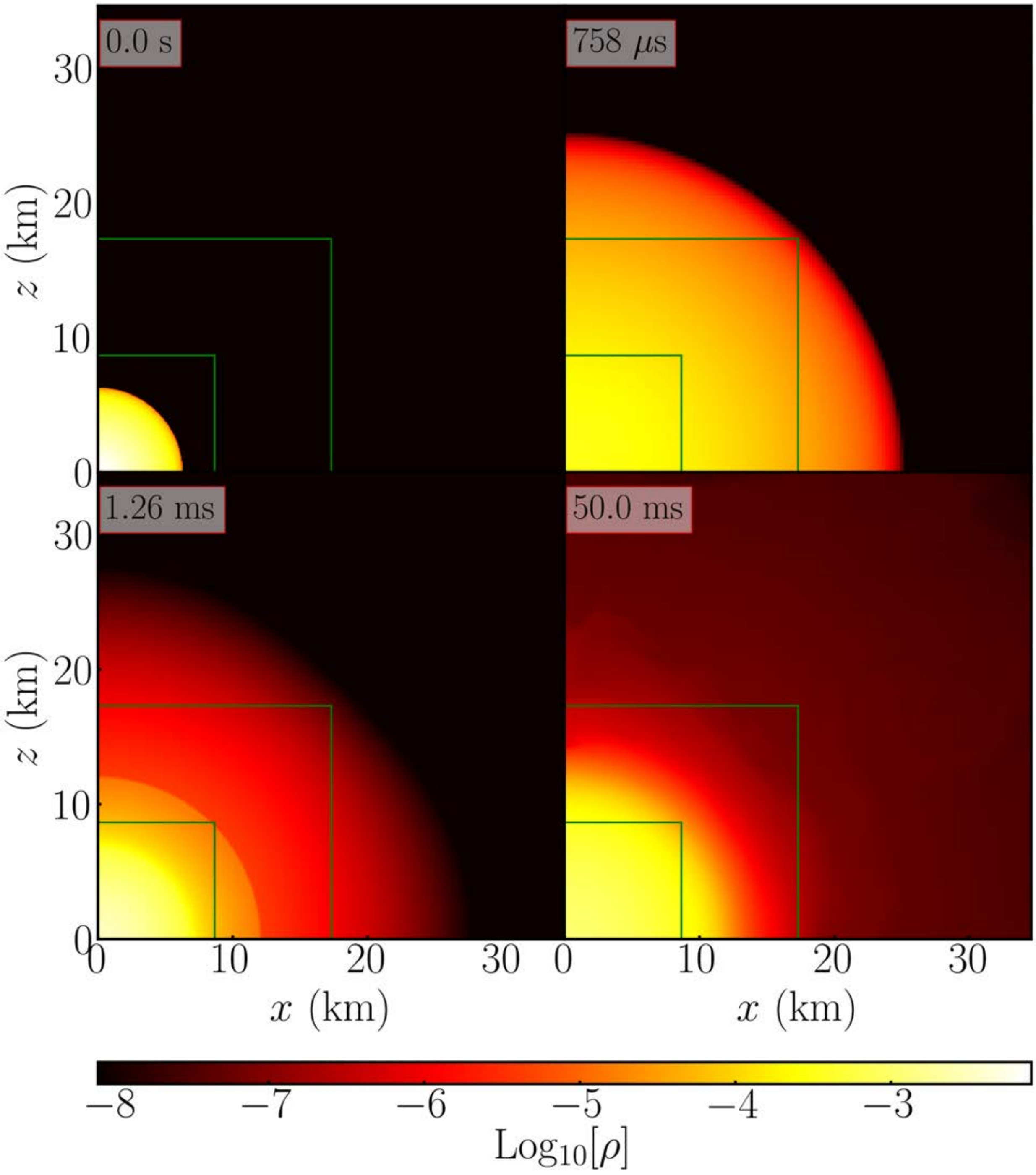

Figure 7.10: Profiles of the rest-mass density ρ of the unstable neutron star in the migration test extracted at $t = 0$ s (top left), 758 μs (top right), 1.26 ms (bottom left), and 50.0 ms (bottom right) with the Γ thermal law EOS employed. The green solid lines indicate the boundaries of the FMR levels.

dotted lines, respectively. The red markers indicate the time extracted for the profiles of rest-mass density shown in Fig. 7.10, and the horizontal magenta dashed line denotes the central rest-mass density $\rho_s = 1.346 \times 10^{-3}$ of the neutron star model on the stable branch with the same baryon mass. Here, we first focus on the result from the Γ thermal law model. At the start, the neutron star with an initial radius of 6.31 km immediately swells and tries to migrate to the corresponding stable state. The central rest-mass density ρ_c rapidly declines and drops below ρ_s to reach its first minimum at $t = 758\ \mu$s, with the stellar radius stretching to almost four times larger. The neutron star compresses and shrinks subsequently until ρ_c reaches its maximum at $t = 1.26$ ms, then expands again and hits the infalling matter, forming a shock wave that propagates outwards and ejects a small amount of matter with a high velocity from the stellar surface to the atmosphere. We find that the highest velocity of the ejecta is $0.98c$ (Lorentz factor of ~ 5), and our code can follow the motion of such a high-velocity component. The matter ejected by this ejection process eventually leaves the computation domain, which accounts for the sudden rise in the relative difference of total baryon mass, as shown in the middle panel of Fig. 7.9.

Nonetheless, the oscillations of ρ_c are gradually damped out in the Γ thermal law EOS since the kinetic energy is dissipated to thermal energy through shock heating. After $t \approx 50$ ms, the neutron star approximately settles to a new stable state with ρ_c slightly below ρ_s. In contrast, the neutron star under the adiabatic EOS oscillates with a nearly constant amplitude in the absence of thermal dissipation as the energy converts back and forth between gravitational binding energy and kinetic energy, which is consistent with the result in [193]. This also explains the lower relative difference of total baryon mass since less matter is ejected without shock heating.

We also monitor the L_2-norm of the constraint violation of the system as shown in the bottom panel of Fig. 7.9. The Hamiltonian and momentum constraints are well under control, with violations damped out and stabilized under the Z4c prescription.

7.3.3.3 Migration of an unstable rotating neutron star

In this test, we simulate the rotating neutron stars that are very close to the turning point of the mass versus energy density ($M_{\rm ADM}$-e_c) curve to examine the performance of `SACRA-2D`. We consider uniformly rotating neutron stars in both the stable and unstable branches indicated as the red crosses in Fig. 7.11 with the same baryon mass $M_b = 3.050 M_\odot$ and angular momentum $J = 1.800 M_\odot^2$ constructed by `RNS` using the MPA1 EOS. The parameters of the stable and unstable models are listed in Table 7.1. Note that the ADM mass at the turning point $M_{\rm ADM} = 2.5113 M_\odot$ is only $\approx 0.04\%$ higher than the models we selected, which poses a challenge for numerical codes in resolving the model accurately.

Since the unstable model has a higher ADM mass and, hence, a smaller absolute value of binding energy than the stable one, the unstable neutron star can migrate to the stable con-

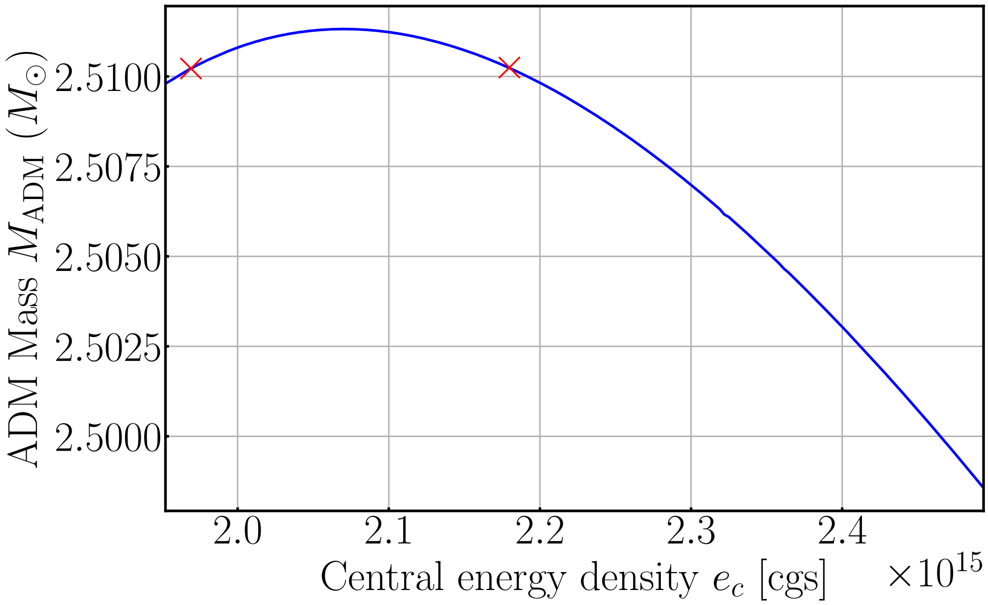

Figure 7.11: The mass versus energy-density (M_{ADM}-e_c) curve of the uniformly rotating neutron star of $J = 1.800 M_\odot^2$ with the MPA1 EOS. The red crosses indicate the models selected for the simulations. The left marker lies on the stable branch, while the right is on the unstable branch. The turning point is located at $e_c = 2.0695 \times 10^{15}$ [cgs] with $M_{\mathrm{ADM}} = 2.5113 M_\odot$.

Table 7.1: The parameters of the stable and unstable models used in the simulations.

Models	stable	unstable
Central energy density $e_c \times 10^{15}$ [cgs]	1.9691	2.1798
Central rest-mass density $\rho_c \times 10^{15}$ [cgs]	1.4219	1.5151
ADM mass M_{ADM} $[M_\odot]$	2.510220	2.510248
Baryon mass M_b $[M_\odot]$	3.0500	3.0500
Angular frequency $\Omega \times 10^3$ [rad/s]	4.6795	4.7925
Equatorial radius r_{eq} [km]	7.425	7.215
Axial ratio $r_{\mathrm{p}}/r_{\mathrm{eq}}$	0.940	0.937

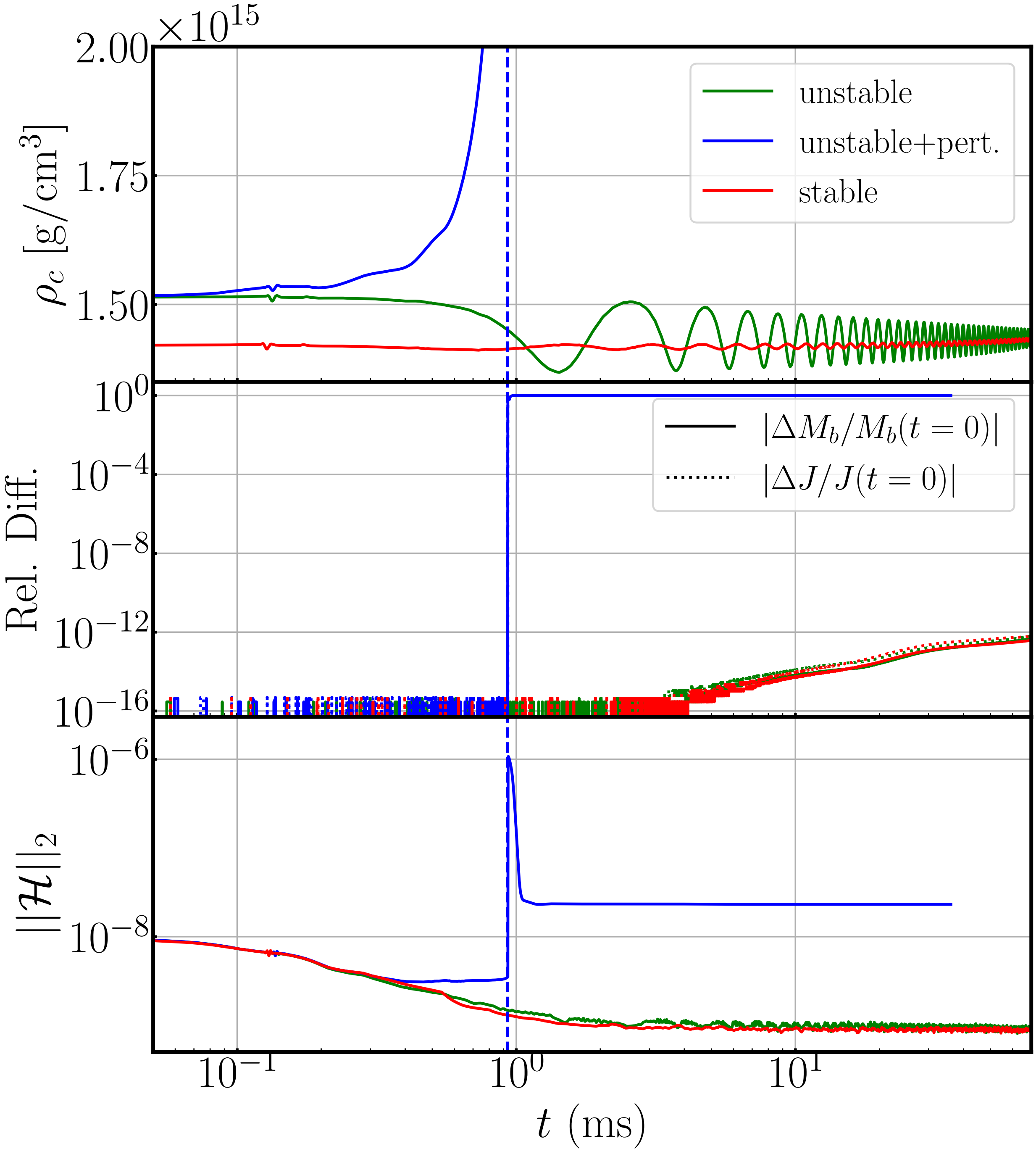

Figure 7.12: The panels show the evolution of central rest-mass density ρ_c (top), the relative difference of total baryon mass M_b and angular momentum J (middle), and the L_2-norm of Hamiltonian constraint violation $||\mathcal{H}||_2$ (bottom) as functions of time. The green, blue, and red solid curves illustrate the results from the unstable model, unstable plus initial perturbation model, and stable model, respectively. The blue vertical dashed line indicates the black hole formation time $t_{\rm AH} = 0.931$ ms for the unstable plus initial perturbation model.

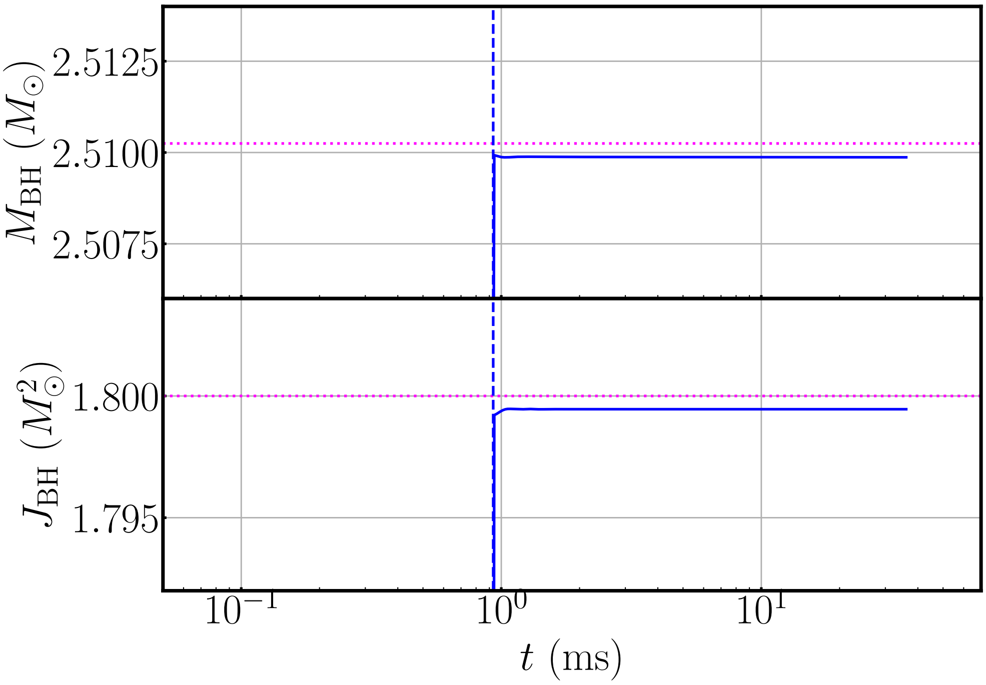

Figure 7.13: The panels show the mass $M_{\rm BH}$ (top) and angular momentum $J_{\rm BH}$ (bottom) of the remnant black hole after collapse for unstable plus initial perturbation model. The blue vertical dashed line indicates the black hole formation time $t_{\rm AH} = 0.931$ ms. The magenta horizontal dotted lines denote the ADM mass $M_{\rm ADM} = 2.510248 M_\odot$ and the angular momentum $J = 1.800 M_\odot^2$ of the rotating neutron star obtained from `RNS`.

figuration similar to the non-rotating case in Section 7.3.3.2, given that the initial numerical perturbation is tiny. On the other hand, to examine the performance of `SACRA-2D` for the black hole formation, we consider an additional run by introducing a small ingoing radial velocity inside the unstable neutron star in forms

$$u_x = -5 \times 10^{-3} x / R_{\rm eq}, \qquad u_z = -5 \times 10^{-3} z / R_{\rm eq}, \tag{7.73}$$

as an initial perturbation to initiate the collapse, where $R_{\rm eq}$ is the star's equatorial coordinate radius. The computational domain is set to be $x_{\rm max} = z_{\rm max} = 4431$ km in the grid resolution of $N = 256$ with 10 FMR levels, which corresponds to the box size $L = 8.65$ km with the grid spacing $\Delta x = 33.8$ m in the finest level. We carry out three sets of simulations in total under the mirror symmetry, including one for stable neutron star, one for unstable neutron star without initial perturbation, and one for unstable neutron star with initial perturbation. We employ the Γ thermal law EOS with $\Gamma_{\rm th} = 5/3$ and the HLLC Riemann solver for all runs with atmosphere factor $f_{\rm atm} = 10^{-20}$ and $l_{\rm fix} = 4$. We perform the simulations up to 70 ms, about ~ 50 cycles of rotation, for models that do not undergo gravitational collapse. If the neutron star collapses, we end the run at 30 ms after the black hole is formed.

Fig. 7.12, from top to bottom, shows the evolution of the central rest-mass density ρ_c, the

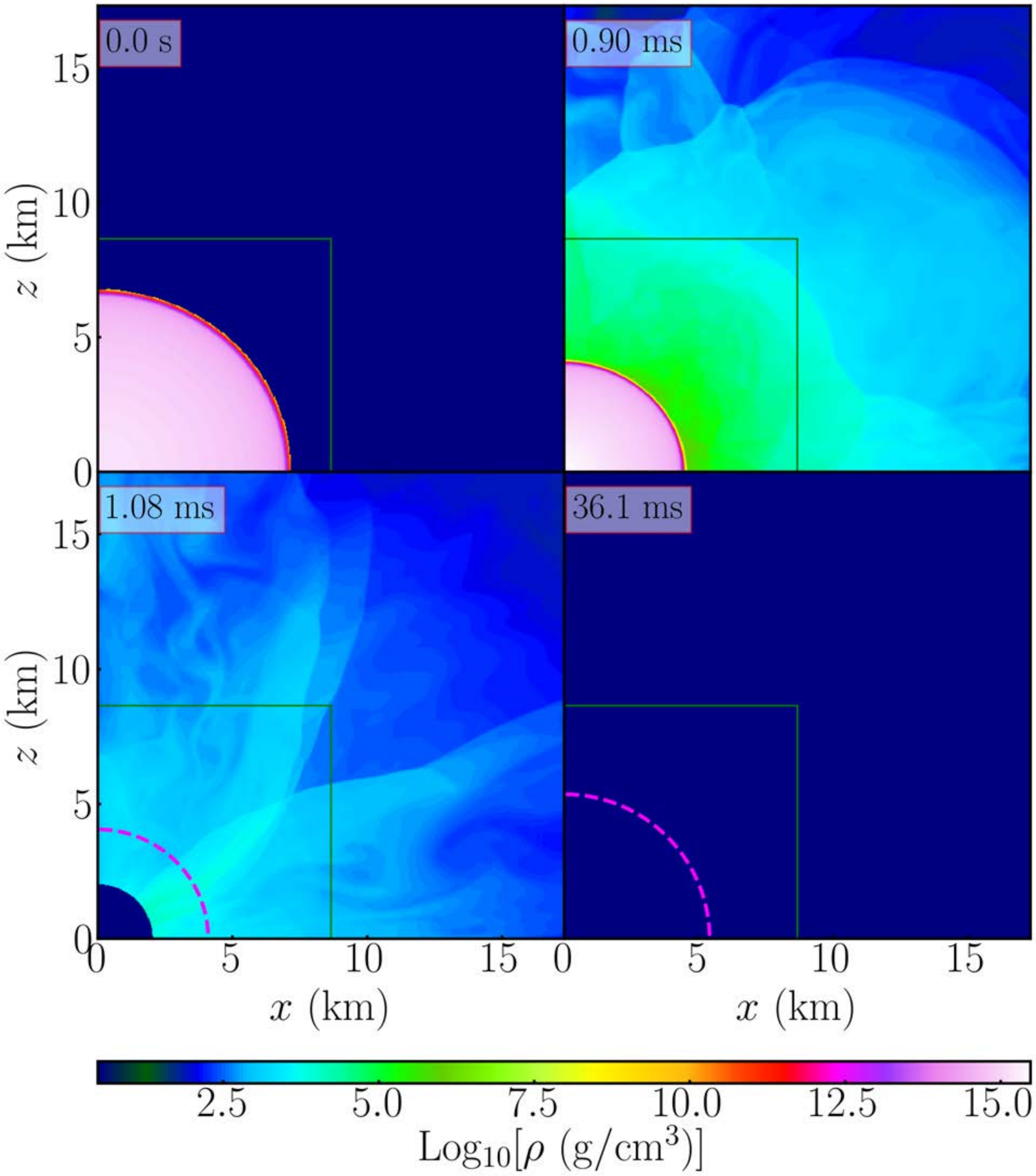

Figure 7.14: The profiles of the rest-mass density ρ of the collapse of an unstable rotating neutron star extracted at $t = 0$ s (top left), 0.90 ms (top right), 1.08 ms (bottom left), and 36.1 ms (bottom right). The green solid lines indicate the boundaries of the FMR levels, and the magenta dashed curves in the bottom panels denote the apparent horizon surface of the black hole.

relative differences of total baryon mass M_b and angular momentum J, and the L_2-norm of the Hamiltonian constraint violation $||\mathcal{H}||_2$ as functions of time. The rotating neutron star on the stable branch remains stable throughout the simulation with oscillation amplitude $\sim 0.5\%$ of the central rest-mass density ρ_c, which agrees with the turning point theorem [198]. In contrast, the central rest-mass density ρ_c of the unstable model (green solid lines) quickly drops and oscillates around the value of its stable counterpart, eventually damped and settling down to the stable state. Despite the central rest-mass density of the unstable neutron star being only 6.6% larger than the stable model, the code can still resolve the migration of the unstable model remarkably well. Since the oscillation is comparably small, no matter is ejected essentially during the migration. As a result, the baryon mass M_b and angular momentum J are well conserved with a relative difference $\lesssim 10^{-12}$.

Nonetheless, if an initial perturbation is introduced in the unstable model (blue lines in Fig. 7.12), the rotating neutron star immediately undergoes gravitational collapse due to the perturbation with an increasing central rest-mass density ρ_c. After a short time, the neutron star compactness becomes so high that ultimately, a black hole is formed at $t_{\rm AH} = 0.931$ ms and swallows the whole star within the black hole, leaving basically nothing outside the apparent horizon at the end, which agrees with the finding in [427] (see the top right and bottom left panels in Fig. 7.14 for the profiles of the rest-mass density ρ before and after the formation of the black hole). The resultant black hole essentially inherits the initial neutron star's ADM mass and angular momentum with negligible loss. The mass $M_{\rm BH}$ and angular momentum $J_{\rm BH}$ of the black hole extracted from the apparent horizon indeed show excellent agreement with derivation $\lesssim 0.03\%$ as shown in Fig. 7.13. This demonstrates the robustness and the accuracy of both the metric solver and the apparent horizon finder. During the collapsing phase, the baryon mass M_b and angular momentum J are conserved down to machine precision until the black hole is formed and the fluid excision is activated. The Hamiltonian constraint violation $||\mathcal{H}||_2$ also experiences a sudden jump at $t_{\rm AH}$ due to the appearance of irregularity at the origin when the puncture is formed and then quickly damped out and stabilized afterward.

In addition, we examine the gravitational wave signal from the collapse scenario of the perturbed unstable model. Since the collapse happens promptly after the start of the simulation, the initial junk radiation will contaminate the subsequent gravitational wave signal that immediately follows under the Z4c constraint propagating description. Therefore, for this particular result shown in Fig. 7.15, we perform the simulation with the BSSN formulation to obtain a cleaner numerical waveform, and we confirm that the overall dynamics of the BSSN run are the same as in the Z4c run shown above. The $(l, m) = (2, 0)$ mode of $D\Psi_4$ black hole ringdown gravitational waves after the collapse is extracted in various radii as a function of $t_{\rm ret} - t_{\rm AH}$ shown in Fig. 7.15, where $t_{\rm ret}$ is the retarded time and $t_{\rm AH}$ is the black hole formation time. The waveforms agree with each other regardless the extraction

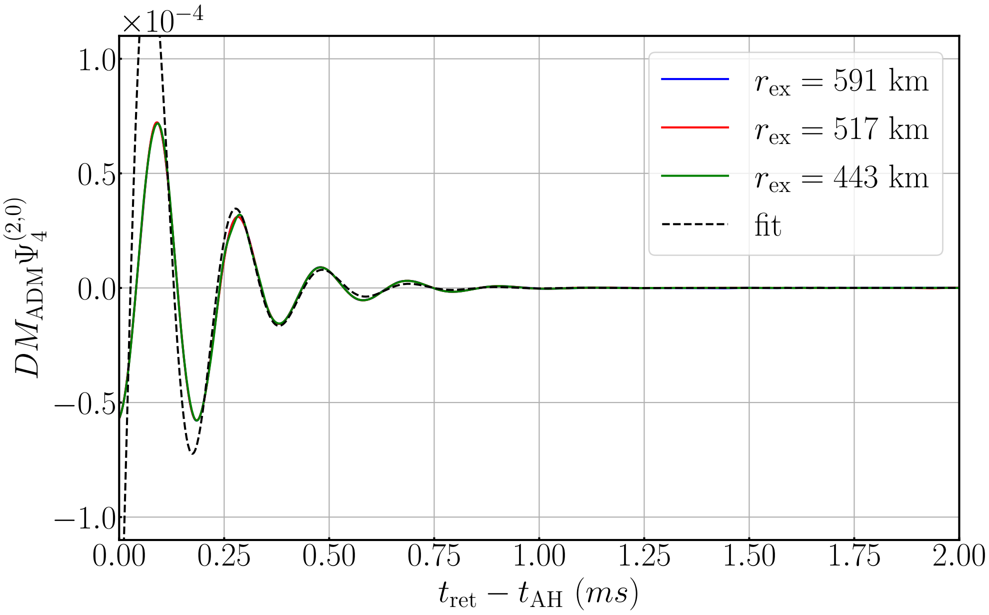

Figure 7.15: $(l, m) = (2, 0)$ mode of $DM_{\rm ADM}\Psi_4$ gravitational waves extracted at $r_{\rm ex} = 591$ km (blue), 517 km (red), and 443 km (green) of the gravitational collapse of the unstable rotating neutron star as a function of retarded time $t_{\rm ret}$.

Table 7.2: The parameters of the SMS and the remnant black hole in the simulations. Γ is the adiabatic index, M is the gravitational mass of the system, β is the ratio of rotational kinetic energy to gravitational potential energy, J is the angular momentum Req is the equatorial circumferential radius, and $M_{\rm BH}$ and χ are the mass and dimensionless spin of the remnant black hole, respectively.

Γ	$M(M_\odot)$	β	J/M^2	$R_{\rm eq}/M$	$M_{\rm BH}/M$	χ
1.3347	1.54×10^5	0.00895	0.826	452.6	0.952	0.701

radii $r_{\rm ex} = 591$ km, 517 km, and 443 km. We also compare our numerical waveform with the analytical black hole quasinormal modes frequency $M_{\rm BH}\omega = 0.3767 - 0.0884i$ [86] considering the final black hole mass $M_{\rm BH} = 2.51 M_\odot$ and the dimensionless spin parameter $\chi = 0.2857$. The fitted analytical ringdown waveform shown as the black dashed line in Fig. 7.15 matches our result. We found the total radiated energy to be $\sim 1.8 \times 10^{-9} M_{\rm ADM}$.

7.3.3.4 Gravitational collapse of a supermassive star

For the final test, we simulate the gravitational collapse of a rotating supermassive star (SMS) to a black hole. In this problem, the SMS with a radius of $\approx 450M$ collapses to a black hole and a disk, and hence, we have to follow a much larger dynamical range than that of neutron-star collapses. For this problem, our FMR algorithm becomes, in particular, the robust tool.

We consider a uniformly rotating supermassive star constructed by the polytropic EOS $P = K\rho^\Gamma$ with the polytropic index $\Gamma = 1.3347$, which approximates the SMS core in helium-burning phase close to the marginally stable state [457] and is approximately the same as the

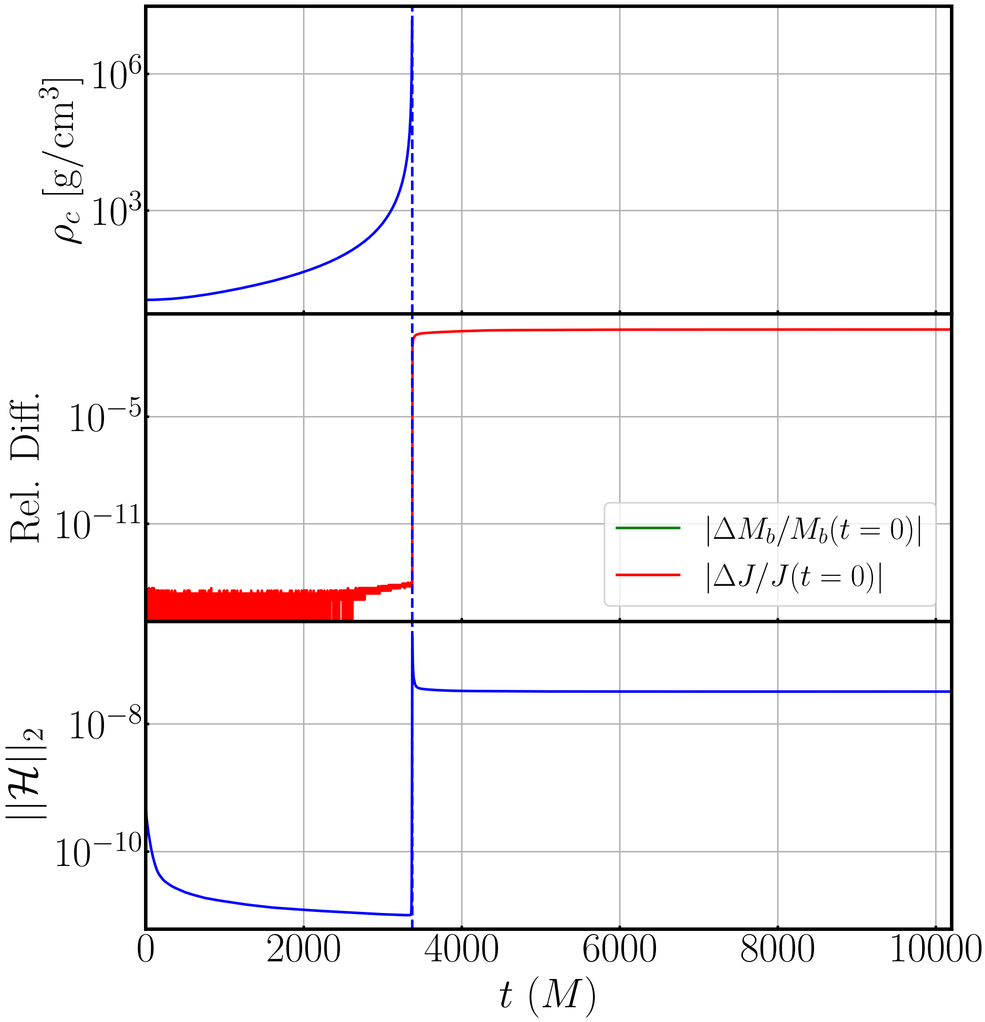

Figure 7.16: The evolution of the central rest-mass density ρ_c (top), relative differences in baryon mass M_b and angular momentum J (middle), and the L2-norm of the Hamiltonian constraint violation $||\mathcal{H}||_2$ as a function of time t in M for the gravitational collapse of the SMS. The blue vertical dashed line indicates the black hole formation time $t_{\rm AH} = 3373M$.

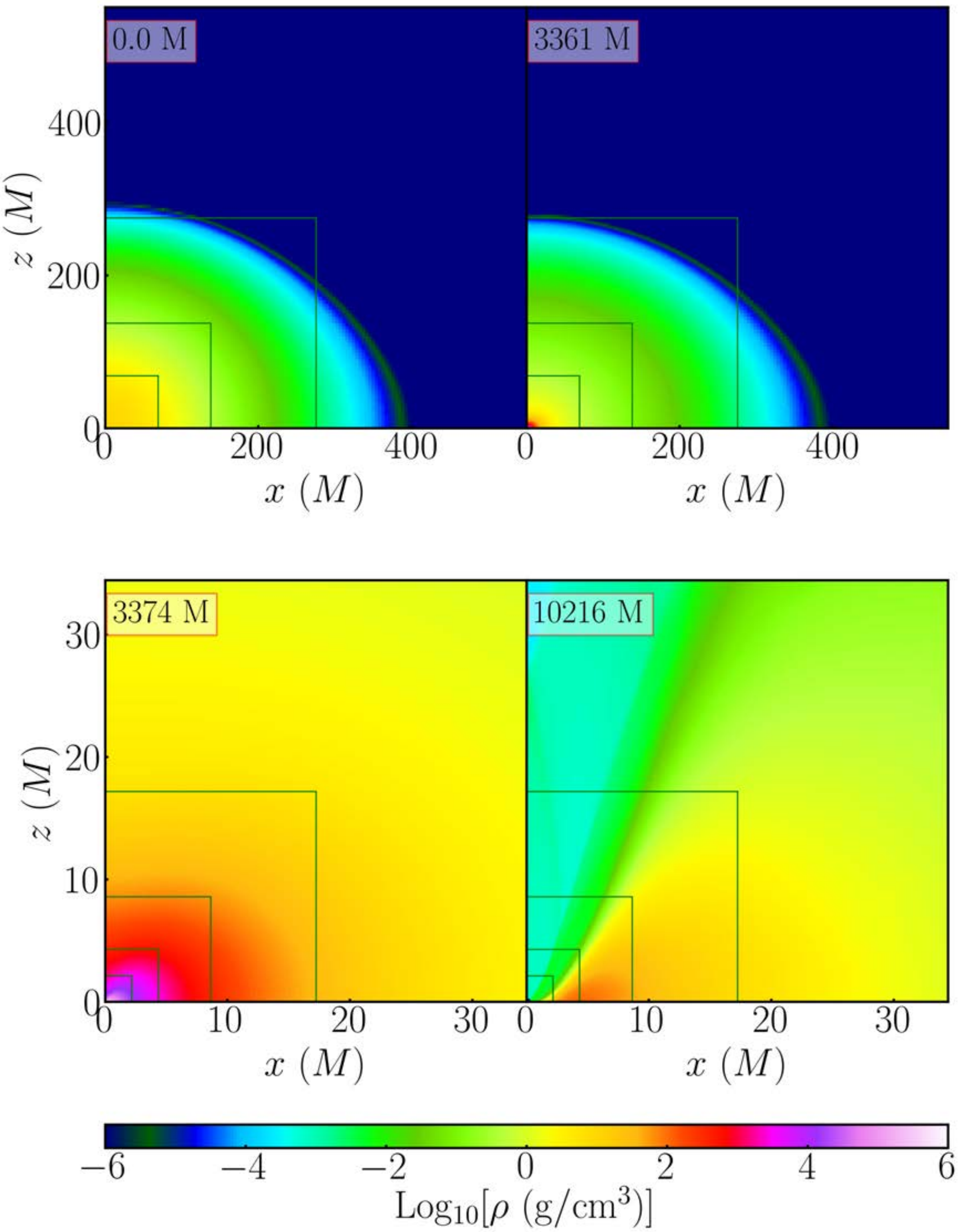

Figure 7.17: The snapshot of the rest-mass density ρ extracted at different time $t = 0.0M$ (top left), $t = 3361M$ (top right), $t = 3374M$ (bottom left), and $t = 10216M$ (bottom right) for the gravitational collapse of the SMS. The green solid lines indicate the boundaries of the FMR levels.

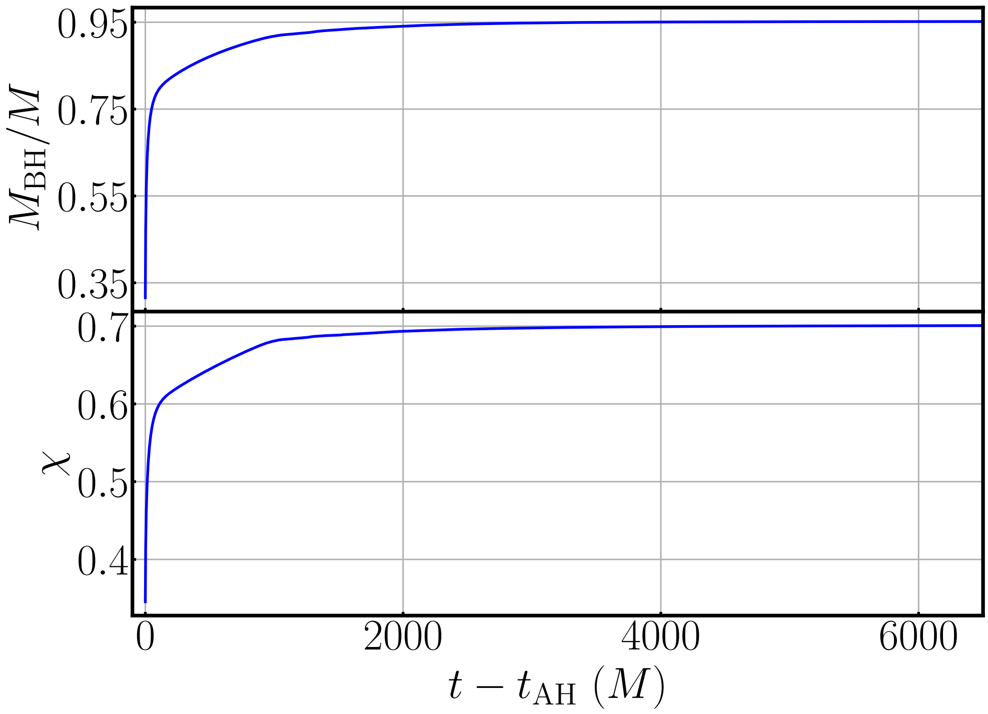

Figure 7.18: The evolution of remnant black hole mass $M_{\rm BH}$ (top) and dimensionless spin parameter χ (bottom) after collapse of the SMS. The black hole is formed at $t_{\rm AH} = 3373M$.

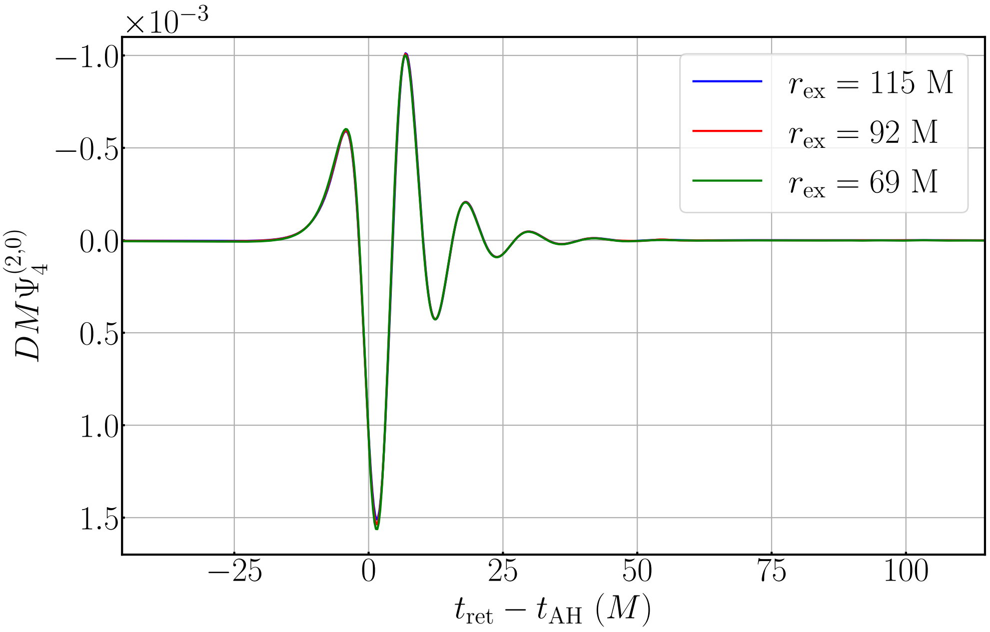

Figure 7.19: $(l, m) = (2, 0)$ mode of $DM\Psi_4$ gravitational waves extracted at $r_{\rm ex} = 115M$ (blue), $92M$ (red), and $69M$ (green) of the gravitational collapse of the SMS as a function of retarded time $t_{\rm ret} - t_{\rm AH}$.

model He4 of [208]. The parameters of the model employed are listed in Table 7.2.

The computational domain is set to be $x_{\rm max} = z_{\rm max} = 1101M$ with $N = 128$ and 10 refinement levels in total, which corresponds to the size of $L = 2.15M$ and the grid resolution $\Delta x = \Delta z = 0.0168M$ in the finest box. The Γ law EOS $P = \rho(\Gamma - 1)\epsilon$ is employed for the simulation with the HLLC solve and the atmospheric factor $f_{\rm atm} = 10^{-20}$. To initiate the collapse, we reduce the pressure by 20% uniformly within the star. With our FMR setup, the computational cost for this simulation is relatively cheap, with the simulation time $t \approx 10800M$ costing about 600 CPUhrs in total under the parallelization setting $[M_{\rm MPI} \times M_{\rm MPI} \times N_{\rm thr} = [4 \times 4 \times 5]$.

Once the pressure is depleted, the matter starts to fall in, resulting in an exponential growth in the central rest-mass density ρ_c. As in [208], about 95% of the SMS collapses into a black hole, and the remaining matter forms a torus around the black hole and ejecta, which is driven by a shock formed around the surface of the torus as shown in the bottom row of the snapshots in Fig. 7.17. The final dimensionless spin of the black hole is ≈ 0.70, which is appreciably smaller than the dimensionless spin of the system (see Table 7.2 and also Fig. 7.18 for the evolution of remnant black hole). The ejecta mass is $\sim 1\%$ of the total mass, and this result agrees with that of [208].

Figure 7.19 plots gravitational waveform (the $(l, m) = (2, 0)$ mode of Ψ_4) during the formation of the black hole. As found in [451], the waveform is composed of a precursor, which is emitted before the formation of the black hole, a burst wave, which is emitted near the formation time of the black hole, and a ring down. The total radiated energy is $\approx 1.08 \times 10^{-6}M$ which agrees with the result in [451].

7.3.4 Strong scaling test

This section presents a test to assess the strong scaling of `SACRA-2D`. The simulations were performed on the cluster Sakura at the Max Planck Computing and Data Facility, which comprises Intel(R) Xeon(R) Gold 6248 CPU with a clock rate of 2.50 GHz. We performed a series of simulations in different parallelization settings using the same configuration in Section 7.3.3.1 except $N = 960$ and 9 FMR levels were adopted here, which corresponds to 35 cycles of RK4 integration in each time iteration, and measured the average computational time required per iteration. A wide range of MPI setting with the number of MPI ranks in each direction $M_{\rm MPI} \in \{2, 4, 8, 16, 24, 32\}$ (see Section 7.2.5 for definition of $M_{\rm MPI}$ and $N_{\rm thr}$), covering 4 to 5120 cores in total. Fig. 7.20 shows the average computational time per iteration in seconds as a function of the number of cores used. The solid line with the same colors denotes models with the same MPI setting but in different numbers of OpenMP threads $N_{\rm thr}$, and the star markers represent the models with $N_{\rm thr} = 1$. The black dashed line indicates the ideal scaling considering 2×2 MPI setting with a single OpenMP thread $N_{\rm thr} = 1$ (i.e. 4 cores in total). The result shows an efficiency of about 70% for a small number of $N_{\rm thr}$,

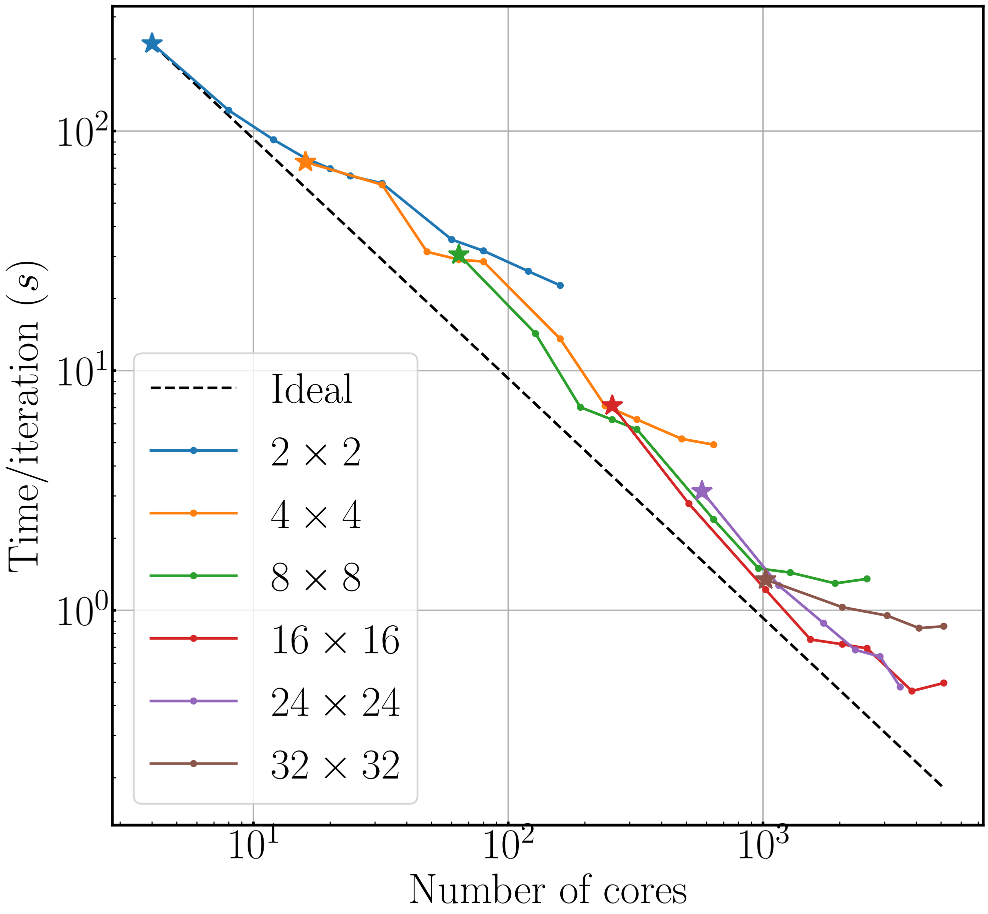

Figure 7.20: The result of the strong scaling test. The legend represents the MPI setting $[M_{\mathrm{MPI}} \times M_{\mathrm{MPI}}]$ for the models. The star markers indicate the result using a single OpenMP thread $N_{\mathrm{thr}} = 1$, while we employed $N_{\mathrm{thr}} > 1$ for the dot markers.

and the performance worsens for an excessive number of OpenMP threads. This suggests the optimal setting to be $N/M_{\rm MPI} \gtrsim 30$ for the MPI setting and $N_{\rm thr} \lesssim N/M_{\rm MPI}/10$ for the OpenMP threads.

7.4 Summary

We present `SACRA-2D`, a new MPI and OpenMP parallelized, fully relativistic hydrodynamics code in dynamical spacetime under axial symmetry with the cartoon method. The code employs a cell-centered grid with FMR and an adaptive time-step scheme. We implement the finite volume method with the state-of-the-art HLLC approximate Riemann solver for hydrodynamics and the Baumgarte-Shapiro-Shibata-Nakamura formalism with Z4c constraint transport for spacetime evolution.

We examined `SACRA-2D` with several benchmark tests, including problems in the vacuum spacetime or the Cowling approximation and simulations of GRHD under dynamics spacetime. We showed a sixth-order convergence of the metric solver and the gravitational waveform in the trumpet black hole and head-on collision tests, respectively. We also demonstrated the power of the HLLC Riemann solver, which effectively improves spatial resolution in the modified Bondi flow test and reduces the artificial shock heating at the stellar surface in the simulation of a stable rotating neutron star. In particular, we show the outstanding robustness and efficiency of `SACRA-2D` in problems like examining the stability of rotating neutron stars adjoining the turning point and resolving the supermassive star collapse. In addition, we performed a strong scaling test and showed an efficiency of about 70%.

In the future, we plan to implement magnetohydrodynamics with the HLLD Riemann solver and the constrained transport scheme [281], as well as implementing radiation hydrodynamics for neutrino physics. We will also use `SACRA-2D` to explore systems in the alternative theories of gravity (see Chapter 8), and astrophysical applications such as black hole-disk collisions [496].

Chapter 8

Axisymmetric stability of neutron stars as extreme rotators in massive scalar-tensor theory

Contents

Breakdown of Contribution

This chapter is based on the preprint submitted to Phys. Rev. D: "*Axisymmetric stability of neutron stars as extreme rotators in massive scalar-tensor theory*" in arXiv:2502.03973 [307] by **A. T.-L. Lam**, K. V. Staykov, H.-J. Kuan, D. D. Doneva and S. S. Yazadjiev. I extended my numerical code `SACRA-2D` to massive scalar-tensor theory. The initial data of the differential rotating neutron star were provided by K. V. Staykov using the code developed K. V. Staykov and D. D. Doneva based on the open-source `RNS` code. All the numerical simulation and data analysis were carried out by me. D. D. Doneva and S. S. Yazadjiev provided constructive comments on the manuscript written partially by me and H.-J. Kuan.

Overview

Differentially rotating scalarized neutron stars, mimickers of binary merger remnants, can possess an enormous angular momentum larger than what could possibly be sustained in a neutron star in general relativity by about one order of magnitude. A natural question to ask is whether these solutions are stable and thus can realize in a binary coalescence. With this motivation in mind, we examine the criterion of dynamical stability against axisymmetric perturbations for these ultra-rotators by numerically tracking their nonlinear evolution in an axisymmetric setup. We demonstrate that the turning-point criterion still serves as a sufficient condition for asymmetric (in)stability. Our findings open an interesting question of whether the merger of two scalarized neutron stars can produce (possibly short-lived) ultra-highly rotating merger remnants.

8.1 Introduction

In the next (5th; expected to start in 2027) observing of the international gravitational wave (GW) network, more binary neutron star (BNS) mergers are expected to be witnessed. The improving sensitivity of the observatory, especially the high-frequency band $\gtrsim 10^3$ Hz, is thought to be promising to further resolve the waveforms produced in the post-merger phases. Although certain important information can already be acquired from the pre-merger waveforms such as the bulk properties of the source and the adiabatic tidal response of the neutron star (NS) members [9, 14], the post-merger segment of the waveforms delivers information supplementary to the aforementioned ones [391, 428, 472, 514]. In particular, the newly formed hypermassive NS (HMNS), which is supported against radial collapse by differential rotation, thermal pressure, and/or magnetic force, carries rich information. For example, the oscillations frequencies and the lifetime of HMNS are not only strongly tied to the internal structure of the star (i.e., to the nuclear equation of state (EOS); e.g., [63, 67, 242, 243, 391, 477]), but closely related to the nature of gravity (e.g., see Chapters 4 and 5).

Scalar-tensor theories of gravity are amongst the most natural and well-motivated alternatives to general relativity (GR). Considering the Damour-Esposito-Farese type of scalar-tensor theory (DEF theory hereafter), current pulsar timing observations severely constrain the massless scalar field sector of the theory [538] while only weak bounds can be imposed in the massive case [28], namely a lower bound of $m_\phi \gtrsim 10^{-15}$ eV [385, 527] on the scalar mass. The constraint on m_ϕ can be pushed further by the null evidence of scalarization in the detected waveform ($\lesssim$ 500 Hz) of GW170817 [15, 16]. In particular, the progenitors of GW170817 are unlikely to be scalarized if the scalar field is massless [331, 537], while a scalarized progenitor can still be reconciled with the observed waveform if the scalar field is sufficiently massive with $> 10^{-12}$ eV [294, 520] (see also Chapter 3). On top of binary systems dynamics, the x-ray pulse profiles emitted by hot spots at NS surfaces infer the mass and radius of NSs [510], which in turn can be used as an independent probe to the EOS and gravitational nature [248, 459, 460, 467, 497].

Within the valid parameter space, Refs. [164, 165, 166, 474] demonstrated in a series of works the existence of stationary, axisymmetric scalarized NSs with an angular momentum exceeding the maximum in GR for a given EOS and rotational law. Such super-rotating NSs have very similar properties to the HMNSs produced after mergers of BNS, which inherit most of the angular momentum of the progenitor binary, thus spinning differentially at a large rate. Although the maximal angular momentum of HMNSs produced by the merger of non-spinning, quasi-circular binaries is roughly bounded as $J \lesssim 8\ M_{\odot}^2$ in GR (e.g, [485, 490, 502]), larger values may be achievable in mergers of dynamically-formed binaries in globular clusters or mergers of NSs having high spins.

The determination of stability of these super-rotating scalarized NSs can be expected to limit the class of HMNSs in the post-merger phase. The turning-point criterion has been shown to be powerful in detecting secular instabilities and in most cases, its results coincide with the ones from perturbation analysis, i.e., the onset of instability is typically associated with an extremum of a properly chosen function of the stellar equilibrium properties [464, 465]. The onset location of secular instability has also been studied by numerical simulations [41, 134, 135, 136, 193, 443], where the validity of the turning-point criterion for uniformly rotating NSs is confirmed.

Here, we briefly recap the turning-point criterion. For axisymmetric spinning NSs and assuming a barotropic EOS, the gravitational mass M_G of an NS can be parameterized by the central energy density ϵ_c, i.e., $M_G = M_G(\epsilon_c)$. In addition, the variations in M_G, angular momentum J, and baryon number N are related via

$$dM_G = \Omega dJ + \mu dN, \tag{8.1}$$

where Ω is the angular velocity of the star, and μ is the chemical potential. The turning-point theorem states that the point where $dJ/d\epsilon_c = dN/d\epsilon_c = 0$ separates the stable segment from the secularly unstable one, and the segment satisfying

$$\frac{d\Omega}{d\epsilon_c}\frac{dJ}{d\epsilon_c} + \frac{d\mu}{d\epsilon_c}\frac{dN}{d\epsilon_c} > 0 \tag{8.2}$$

is on the unstable side [198]. From this, we see that the onset of secular instability is marked by the turn-point of M_G along a one-parameter curve with a fixed J or total baryon mass M_0. In particular, for a sequence of equilibria with a fixed J, the tuning-point,

$$\left.\frac{\partial M_G(\epsilon_c)}{\partial \epsilon_c}\right|_J = 0 \tag{8.3}$$

corresponds to the configuration having the maximal N and thus M_0, while the turning-point for a constant M_0 sequence, i.e.,

$$\left.\frac{\partial M_G(\epsilon_c)}{\partial \epsilon_c}\right|_{M_0} = 0, \tag{8.4}$$

reflects the minimum of J [134]. A remark to be made is that when deriving the theorem for uniformly rotating equilibria, Friedman *et al.* [198] assumed that, due to viscosity, uniformly rotating equilibria will never become differentially rotating as the final state, i.e., the rotational law can be maintained after the perturbation is damped by viscosity. In other words, this criterion is established by comparing neighboring, rigidly rotating configurations along the one-parameter curve.

On the other hand, the applicability of this theorem to NSs obeying a differential rotation law is not established analytically since the rotational law may be altered by any perturbation. Thus, the equilibria do not form a one-parameter family but rather a family of infinite dimensions (to which a turning-point theorem is still possible to hold in some form [465]). While not shown analytically, numerical studies suggest that the turning-point criterion approximately applies to differential rotating NSs [262, 346, 511] in GR. The goal here is to examine the validity of the criterion for high-J stars in scalar-tensor theories, which have no counterparts in GR, through axisymmetric numerical relativity simulations. In particular, we will numerically evolve the stellar profiles to determine if the configuration is stable to a random numerical perturbation, or if some instabilities will operate so that the initial state will migrate to a final state which may be another neutron star configuration or a black hole.

This Chapter is organised as follows: Section 8.2 introduces the basic equations for constructing differentially rotating, scalarized NSs and the scheme for axisymmetric evolution. We provide the numerical results in Section 8.3 and discuss them in Section 8.4.

8.2 Basic Equations

The formulation for constructing initial data in the considered theory will be described in Section 8.2.1. The detailed setup of numerical evolution will then follow in Section 8.2.2.

8.2.1 Profiles from RNS

A modified `RNS` code [475] for generating initial data of equilibrium states of scalarized NSs in the DEF theory has been developed in a series of works [165, 166, 474] from simpler to more sophisticated rotation laws. The code uses a modified [134] Komatsu–Eriguchi–Hachisu (KEH) [283] scheme for constructing rotating equilibrium neutron star models. For mathematical and numerical convenience, the calculation of equilibrium models is performed in the so-called Einstein frame, which is later transformed into the physical Jordan frame used by the evolution code. The two frames are related through a conformal transformation of the metric, and a detailed discussion can be found in [165].

The modified `RNS` code adopts quasi-isotropic coordinate, in which the metric is expressed in the spherical coordinate (r, θ, ϕ) as [183, 283, 284]

$$\begin{aligned} ds^2 &= -e^{\eta+\sigma}dt^2 + e^{\eta-\sigma}r^2\sin^2\theta(d\phi^2 - \varpi dt)^2 \\ &\quad + e^{2\tau}(dr^2 + r^2 d\theta^2) \\ &= -(\alpha^2 - \gamma_{\phi\phi}\varpi^2)dt^2 - 2\varpi\gamma_{\phi\phi}d\phi dt + \gamma_{ij}dx^i dx^j, \end{aligned} \tag{8.5}$$

where α and γ_{ij} is the lapse function and spatial metric, respectively. The shift vector β^i is expressed as (see, e.g., Sec. 4 of [364])

$$\beta^i = -\varpi(\partial_\phi)^i. \tag{8.6}$$

Here, ϖ is the frame-dragging factor, and the spatial metric γ_{ij} is

$$\begin{aligned} \gamma_{ij} &= \psi^4 \begin{pmatrix} e^{-\mathbf{q}} & 0 & 0 \\ 0 & e^{-\mathbf{q}}r^2 & 0 \\ 0 & 0 & e^{2\mathbf{q}}r^2\sin^2\theta \end{pmatrix} \\ &= \psi^4\tilde{\gamma}_{ij} \end{aligned} \tag{8.7}$$

for

$$\psi = e^{(4\tau+\eta-\sigma)/12} \quad \text{and} \quad \mathbf{q} = \frac{2}{3}(2\tau - \eta + \sigma), \tag{8.8}$$

where ψ is the conformal factor and $\tilde{\gamma}_{ij}$ is the conformal spatial metric with its determinant $\det(\tilde{\gamma}_{ij}) = \det(f_{ij})$ same as the flat background metric f_{ij}. In the above expressions, τ, ϖ, σ, and η are all functions of r and θ only since we consider axisymmetric NSs. For non-spinning NSs, we have $e^{\eta-\sigma} = e^{2\tau}$, and thus the metric $\gamma_{ij} = e^{2\tau}f_{ij}$ is conformally flat, while the metric will be distorted from the conformal flatness due to the dragging effect when the star is rotating. The determinant of γ_{ij} in the Cartesian coordinates is $\gamma := \det(\gamma_{ij}) = e^{4\tau+\eta-\sigma}$, which again reduces to $\gamma = e^{6\tau}$ for non-rotating configurations. For the considered gauge and coordinate, the extrinsic curvature tensor, defined as

$$2\alpha K_{ij} = D_i\beta_j + D_j\beta_i, \tag{8.9}$$

has the form (see, e.g., Eqs. (2.43) and (2.44) of [220])

$$K_{ij} = \frac{-e^{\eta} r^2 \sin^2\theta}{2\alpha} \begin{pmatrix} 0 & 0 & \frac{\partial}{\partial r}\varpi \\ \cdot & 0 & \frac{\partial}{\partial \theta}\varpi \\ \cdot & \cdot & 0 \end{pmatrix}, \tag{8.10}$$

where "$\cdot$"s are the ellipsis of the symmetric part and D_i is the covariant derivative associated with the spatial metric γ_{ij}.

For the matter profile, the 4-velocity of matter is expressed as

$$u^a = \frac{w}{\sqrt{\alpha^2 - \gamma_{\phi\phi}\varpi^2}}(1, 0, 0, \Omega), \tag{8.11}$$

with $w := (1 - v^2)^{-1/2}$ being the Lorentz factor and v the proper velocity, given by

$$v = (\Omega - \varpi) r \sin\theta. \tag{8.12}$$

The spin of the star,

$$\Omega(r, \theta) = \frac{u^{\phi}}{u^t}, \tag{8.13}$$

is specified by a certain rotation law as well as the stellar structure. We note that Ω is the same in both the Einstein and Jordan frames, thus not further complicating the transition of the quantities in the two codes.

In the present article, we adopt the 4-parameter differential rotation law introduced by Uryu et al. [503] (see also [251, 252]),

$$\Omega = \Omega_c \frac{1 + \left(\frac{F}{B^2 \Omega_c}\right)^p}{1 + \left(\frac{F}{A^2 \Omega_c}\right)^{p+q}}, \tag{8.14}$$

where $F = u^t u_{\phi}$ is the redshifted angular momentum per unit rest mass. This rotation law allows for the maximum of the angular velocity to be away from the center, which is a common characteristic seen in remnants in merger simulations, e.g., [61, 148, 266]. Here, two constants have been fixed to $p = 1$ and $q = 3$ [251, 252, 539]. This choice allows one to derive an analytical expression for the first integral of the hydrostationary equilibrium, which is required for the `RNS` code. The other two parameters, A and B, are not given explicitly. Instead, the ratios $\lambda_1 = \Omega_{\max}/\Omega_c$ and $\lambda_2 = \Omega_e/\Omega_c$, where Ω_e is the angular velocity at the equator, Ω_c is the angular velocity at the center and $\Omega_{\max}$ is the maximum of the angular velocity, are given. From them, one can obtain and solve an algebraic system for A and B. Those ratios control the shape of the neutron star. In the present article we use $(\lambda_1, \lambda_2) = (1.5, 0.5)$ which correspond to the quasi-toroidal models [474]. When the rotation

Table 8.1: Parameters of different sequences considered in this Chapter, where the scalar mass m_ϕ and coupling constant B (second column), the angular momentum fixed for each sequence (third column), and the central energy density of the NS at the onset of asymmetric instability (last column) are collated.

Sequence name	(m_ϕ, B)	J $(M_\odot^2)$	$\epsilon_{\rm thre}$ $[\times 10^{15}$ cgs$]$
`m0_B12_J8`	(0, 12)	8	1.16
`m0_B12_J12`	(0, 12)	12	1.12
`m0_B12_J20`	(0, 12)	20	1.056
`m0_B12_J40`	(0, 12)	40	NA
`m0.01_B12_J8`	(0.01, 12)	8	1.15
`m0.01_B12_J12`	(0.01, 12)	12	1.08
`m0.01_B12_J20`	(0.01, 12)	20	NA
`m0.01_B12_J30`	(0.01, 12)	30	NA

law F is given, the angular momentum of the star is determined via

$$J = \int_{r<R_\star} \alpha \rho h F \sqrt{\gamma} d^3x, \tag{8.15}$$

for a given rest-mass density ρ and specific enthalpy h distributions inside the star.

8.2.2 Evolution equations

The modified evolution equations in DEF theory under Baumgarte-Shapiro-Shibata-Nakamura (BSSN) formulation [55, 305, 433] (see also Chapter 4) in the Cartesian coordinates are written in Eq. (4.2). We adopted the moving puncture gauge [26, 42, 119] for the lapse function and shift vector given by Eq. (1.24).

The cartoon method [24] has proven to be a robust scheme to evolve axisymmetric spacetime [421, 426, 427, 434]. We extended the 2D cartoon code `SACRA-2D` developed in Chapter 7 to include the evolution equations of DEF theory with Z4c constraint propagation [81, 239]. `SACRA-2D` employs a fixed mesh refinement with 2:1 refinement and imposes equatorial mirror symmetry on the $z = 0$ plane. For the simulations included in this Chapter, the differentially rotating NS is covered by 9 refinement levels with at least 150 grid points covering the equatorial radius of the NS. We adopted 6$^{\rm th}$ order finite difference for the field equations and HLLC Riemann solver [281, 336, 513] for hydrodynamics.

8.3 Numerical results

We construct axis-symmetric, spinning NSs obeying the rotational law (8.14) for several fixed values of J that will be used as initial data for the nonlinear evolution code. The representative sequences are summarized in Table 8.1, where we consider the massless DEF theory and

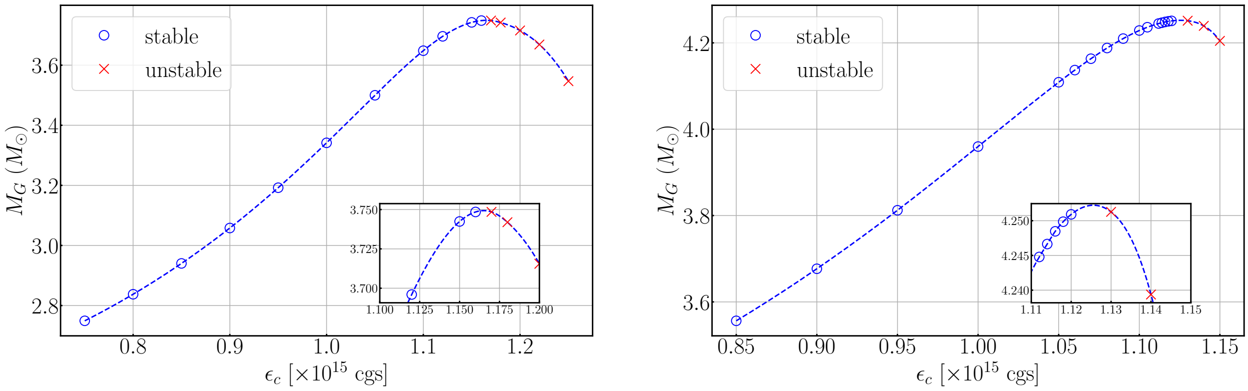

(a) `m0_B12_J8` (b) `m0_B12_J12`

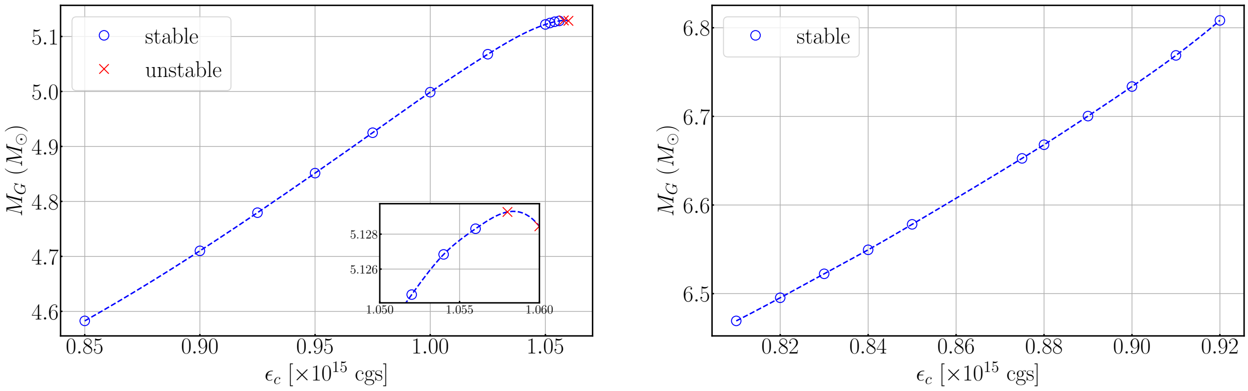

(c) `m0_B12_J20` (d) `m0_B12_J40`

Figure 8.1: Dynamical stability of sequences (a) `m0_B12_J8` (b) `m0_B12_J12` (c) `m0_B12_J20` (d) `m0_B12_J40`. The blue circles and red crosses indicate the regions where the star is dynamically stable and unstable respectively.

a massive scalar field theory with $m_\phi = 0.01$ ($\simeq 1.33 \times 10^{-12}$ eV). We fix $B = 12$ and focus on MPA1 EOS [347] as a representative example. We perform axis-symmetric relativistic simulations for selected models from these sequences, especially close to the maximum mass point, where possible. The goal is to examine the stability and study the outcome of unstable models. We start with the massless theory (Section 8.3.1) followed by a study of the massive scalar field case (Section 8.3.2).

8.3.1 Massless scalar field case

For the massless cases, a turning point can be found for three of the considered angular momenta in Table 8.1, while the sequence with $J = 40$ has no turning point, i.e. no maximum of the mass was reached. A general behavior of the solutions generated by the `RNS` code is that with the increase of the angular momentum, the solution branches get shorter, and they get terminated before reaching the turning point. The reason is numerical – the `RNS` code can not converge to a unique solution. Different numerical schemes may be useful to overcome this problem, such as the spectral method used in [36, 218], that is out of the scope of the present Chapter.

Along each sequence, we study the (asymmetric) stability of 10–20 models, most of which condense near the maximum mass point. The results are summarized in Fig. 8.1, where we see that for cases a), b) and c) the marginally stable model is slightly left to the maximum of the mass, implying that the turning-point criterion approximately predicts the onset of instability for these sequences. For case d), where no turning point was reached in the equilibrium sequence, all neutron star models are stable. For the stable models, the perturbations in the maximum density and central scalar field damp in a dynamical timescale, then settle back to the initial values. Taking the model `m0_B12_J20` as an example, which is very close to the turning-point along the sequence of $J = 20$, the evolution of the maximum rest-mass density and the central value of the scalar field are shown Fig. 8.2 (red), where we see that the initial noise is dissipated after < 5 ms. On the other hand, the unstable models will collapse into a black hole in a dynamical timescale. For one such example `m0_B12_J12`, the evolution of the maximal rest-mass density shows a runaway growth in less than 3 ms (red in Fig. 8.3). After the formation of a black hole, the scalar field dissipates exponentially to $< 10^{-4}$ since black holes in this theory obey the no-hair theorem and thus cannot possess a stationary scalar field [230, 471].

In addition, the rotational law is well-maintained over several dynamical timescales in our simulations for stable models. For one stable example, we plot the profiles of rest-mass density, scalar field, and the specific angular momentum,

$$j := h u_\Phi, \tag{8.16}$$

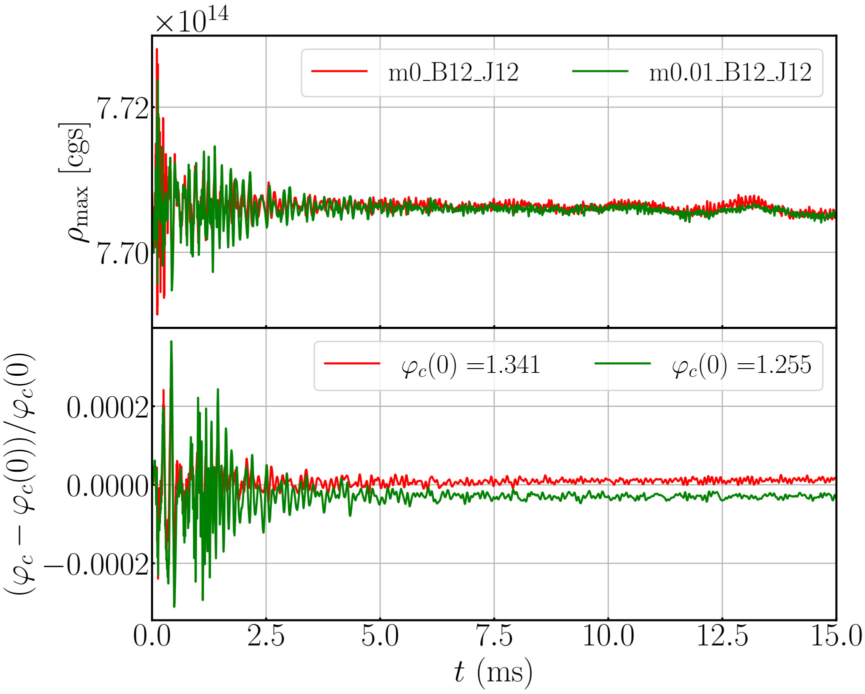

Figure 8.2: Evolution of maximum density $\rho_{\max}$ (top) and central scalar field φ_c (bottom) for two stable models with an initial central energy density $\epsilon_c = 8.5 \times 10^{14}$ g/cm^3.

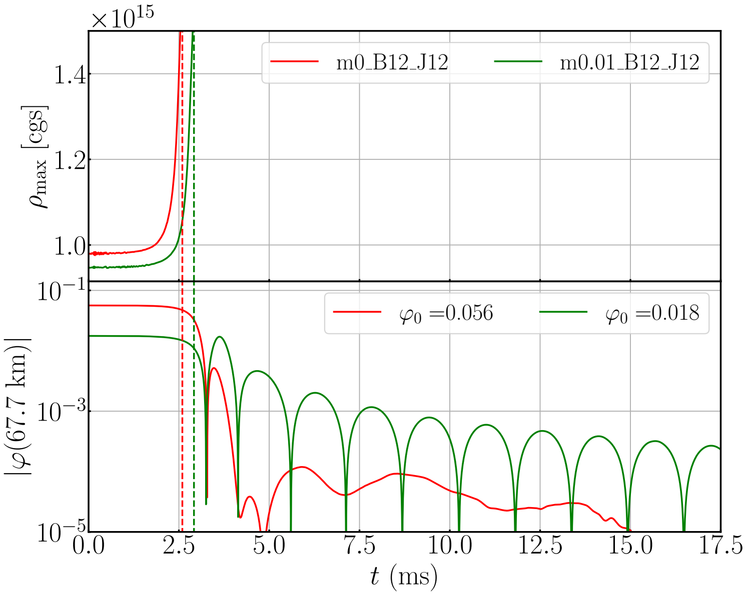

Figure 8.3: Evolution of maximum density $\rho_{\max}$ (top) and absolute value of central scalar field $|\varphi_c|$ (bottom) for unstable models with initial central energy density $\epsilon_c = 1.15 \times 10^{15}$ g/cm^3 (red) and $\epsilon_c = 1.10 \times 10^{15}$ g/cm^3 (green). The colored dashed lines represent the formation time of an apparent horizon for the corresponding models.

at the initial moment and at 15 ms in Fig. 8.4. Apart from a tiny amount of matter that escapes from the surface, the structure of rest-mass density and scalar field remain unaltered to a large extent, i.e., the model is rather stable to axisymmetric perturbations, and the numerical accuracy is robust. In particular, the profile of specific angular momentum within the HMNS is well preserved after 15 ms, showing that the rotational profile is also stable under such perturbations. We also note that the onset of instability is not sensitive to the employed resolutions.

8.3.2 Massive case

We also examine the criterion along fixed-J sequences for a massive scalar field with $m_\phi = 0.01 (\simeq 1.33 \times 10^{-12}$ eV). This value is chosen in order to be in agreement with binary neutron star merger observations [294] (see also Chapter 3). It is a rather large value, and it effectively confines the scalar field in a radius several times larger with respect to the neutron star size.

The chosen models are presented in Fig. 8.5. No turning point is found for the sequences with $J = 20$ and 30 due to the same reason explained above, and the models are stable against axisymmetric perturbations. For the sequences with $J = 8$ and 12, a turning point exists and we find that the onset of instability is in the close vicinity of the turning point, i.e., the turning point criterion approximately holds. In the massive theory, we also demonstrate that unstable models will collapse into a black hole within a dynamical timescale. As a representative example, we plot the evolution of the maximum rest-mass density as well as the scalar field extracted at a certain distance inside the star for `m0.01_B12_J12` (red curves in Figs. 8.1 and 8.5). We again observe a runaway growth in $\rho_{\rm max}$ and a strong suppression in the scalar profile after the black hole forms. Following the collapse, the scalar field decays to a magnitude of $\sim 10^{-3}$ over the dynamical timescale. The decay rate is much slower than the massless case at late times, as shown in the bottom panel of Fig. 8.3, and can be attributed to the dispersion relation of scalar waves [126, 216, 292, 398, 473]. In particular, the propagation group speed of waves at the frequency ω_ϕ is given as Eq. (3.27)

$$v_g = (1 + m_\phi^2 \lambdabar^2)^{-1/2}, \tag{8.17}$$

where $\lambdabar$ denotes the wavelength. It can thus be seen that the scalar waves with wavelengths $\lambdabar \gtrsim 1/m_\phi$ (i.e., $\omega_\phi < m_\phi$) will dissipate over a prolonged damping timescale.

To further assess the turning point criteria, we extract the spectrum of axisymmetric oscillations in the frequency band ≤ 2 kHz for the sequence `m0.01_B12_J8` before the turning point as shown in Fig. 8.6. The modes are extracted by performing Fourier analysis on the central rest-mass density ρ_c and the central scalar field φ_c marked as circles and crosses, respectively, in Fig. 8.6. We observe that two classes of modes emerge in the spectrum, which is speculated to be the quasi-radial $m = 0$ fundamental mode (blue) and ϕ-mode (red). We

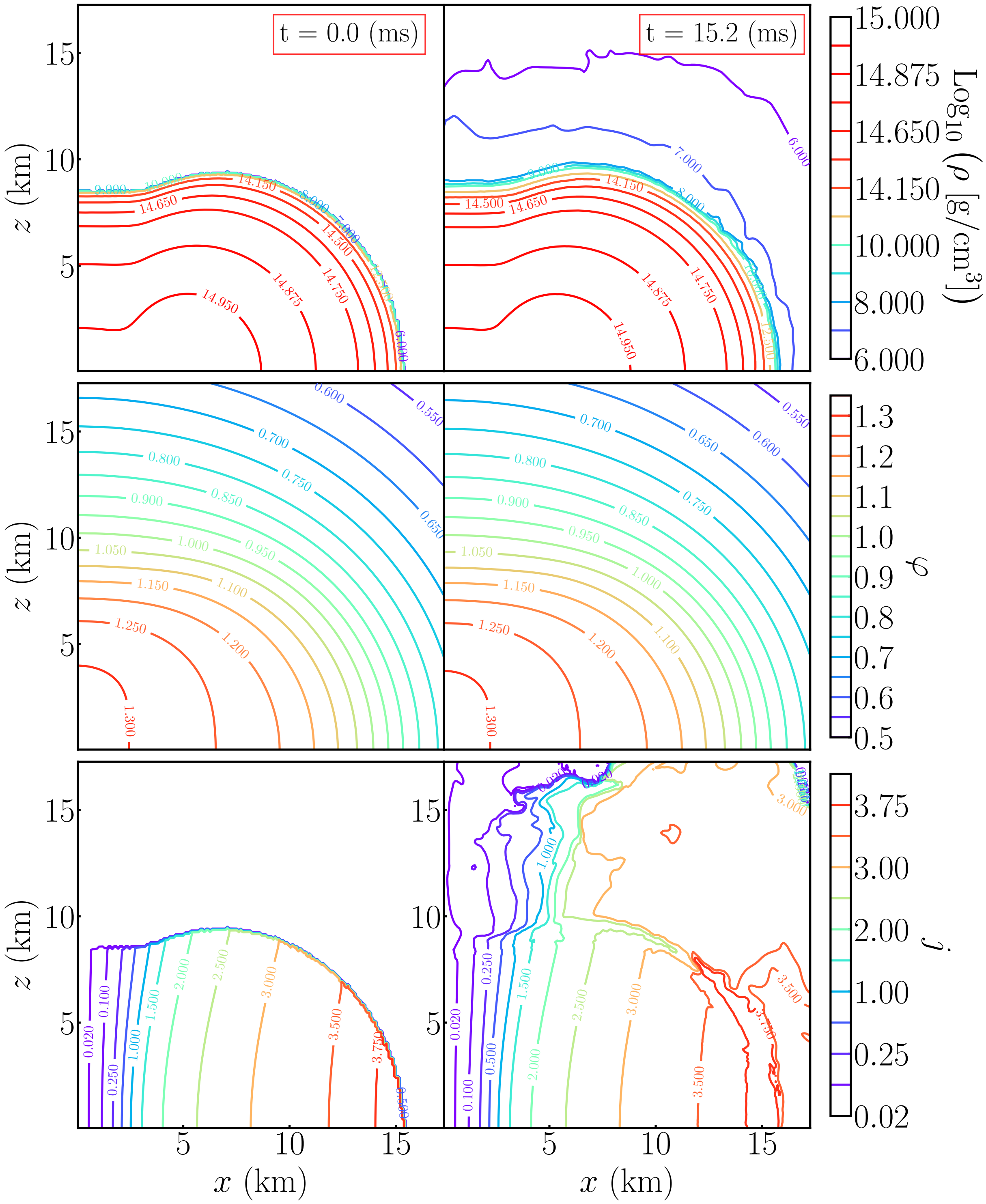

Figure 8.4: Snapshots for a stable model in `m0_B12_J20`, whose central energy density is $\epsilon_c = 1.052 \times 10^{15}$ g/cm^3. The initial profiles are shown in the left column, including rest-mass density (top), scalar field (middle), and specific angular momentum in the code unit (bottom). The profiles at 15.2 ms for them are shown in the right column respectively.

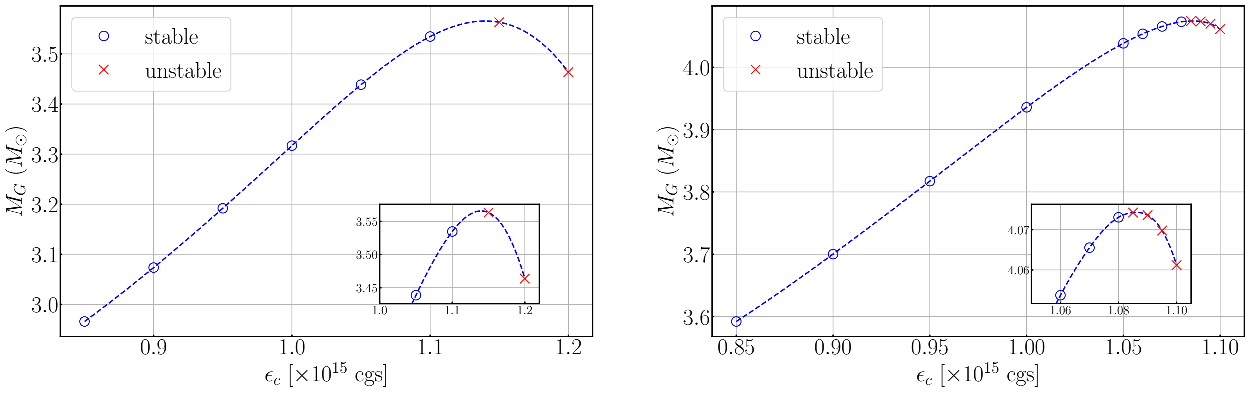

(a) `m0.01_B12_J8` (b) `m0.01_B12_J12`

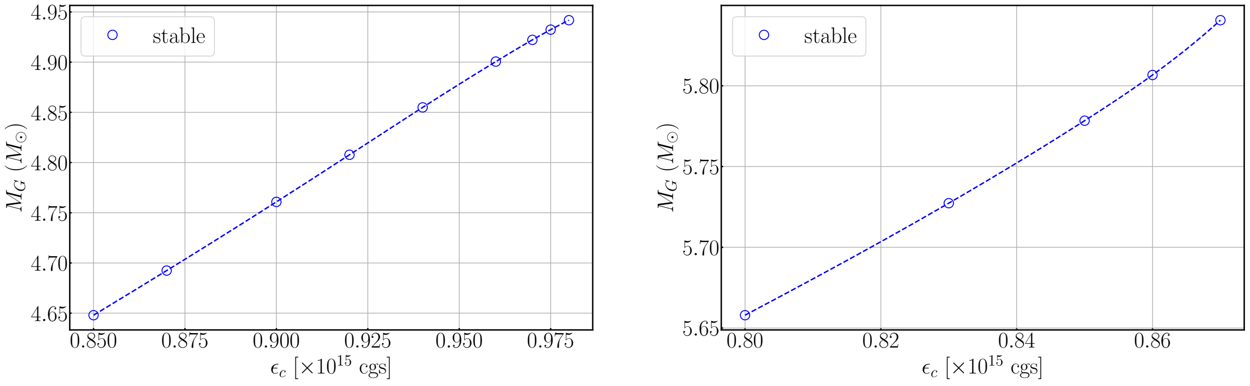

(c) `m0.01_B12_J20` (d) `m0.01_B12_J30`

Figure 8.5: Dynamical stability of sequences (a) `m0.01_B12_J8` (b) `m0.01_B12_J12` (c) `m0.01_B12_J20` (d) `m0.01_B12_J40`. The blue circles and red crosses indicate the regions where the star is dynamically stable and unstable, respectively.

found that the frequency of ϕ-mode decreases as the central internal energy ϵ_c approaches the turning point and eventually reaches a value very close to the Yukawa cutoff frequency of the scalar field $f_c := \omega_\phi/(2\pi)$ in the stable model closest to the turning point. This suggests that the dynamical instability near the turning point arises from the ϕ-mode reaching the cutoff frequency, whereas, in GR, it is triggered by the fundamental mode hitting zero frequency (e.g., [282]). This is similar to the mode analysis in the static case [96, 333, 334].

8.4 Discussion

By performing fully relativistic 2D simulations, we examine the well-known turning-point criterion dictating the condition for one kind of instability among many others. This criterion has been rigorously proven for rigidly rotating configurations by [198] in pure GR, while the extension of it to more general configurations seems only plausible by the use of numerical simulations. In this work, we evolve scalarized neutron stars along constant-angular-momentum sequences to pin down the onset of an axis-symmetric instability for various of the theory

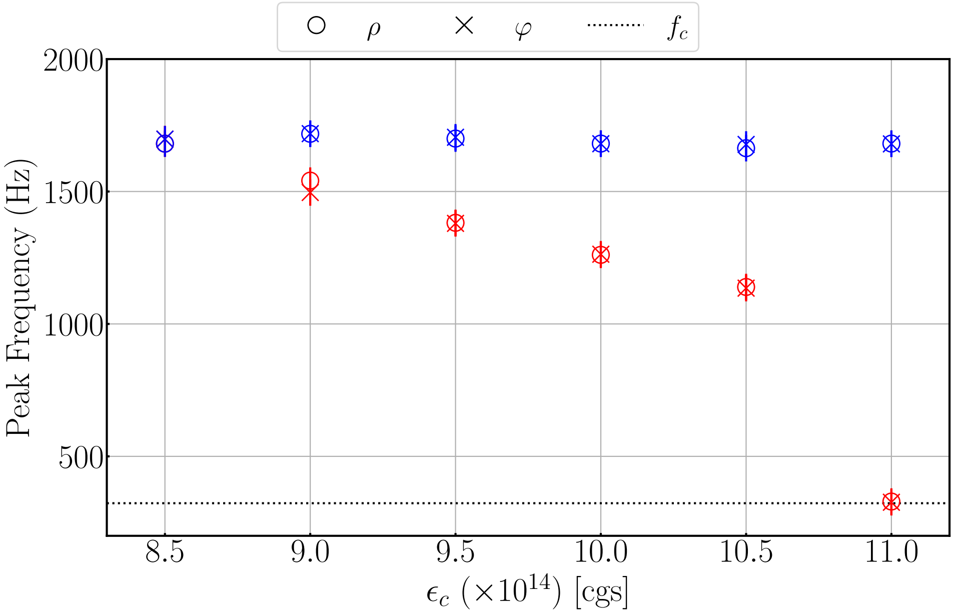

Figure 8.6: Spectrum of the axisymmetric oscillations in the frequency band $\leq$ 2 kHz for the sequence `m0.01_B12_J8` (cf. Fig. 8.5 for its M_G-ϵ_c relation). Two classes of modes are observed, namely, the quasi-radial $m = 0$ fundamental (blue) and ϕ- (red) modes. The modes identified by the Fourier spectrum of oscillating central rest-mass density are marked as circles, while those identified from oscillating central scalar field are denoted as crosses. Agreement between the analysis of either quantity is observed. The Yukawa cutoff $f_c := \omega_\phi/(2\pi)$ is presented as the dotted horizontal line.

parameters as well as J (Table 8.1). Our results suggest that the criterion for rigidly rotating bodies in GR [i.e., Eq. (8.3)] is largely valid also for differentially rotating stars in the DEF theory, and the observed onset of instability agrees within the numerical error at the turning point along the constant–J sequences (Figs. 8.1 and 8.5). For a representative stable model with $J = 20$, we see that the density and scalar profiles as well as the rotational law are perfectly preserved when we terminate the simulation at $\gtrsim$ 15 ms (Fig. 8.4). A word of caution is appropriate here. Other instabilities, such as one-arm and bar-mode instabilities [364], can be activated in reality as 3D simulations suggest [178, 436]. Here, the results are limited to axisymmetric (in)stability that is cared of in the turning-point criterion.

Part IV

Conclusions

Chapter 9

Conclusions and Future work

This thesis discussed some innovative applications of numerical relativity on various astrophysical systems. In Part I, by making use of the new method in numerical relativity that eliminates the leading numerical error from the supermassive black hole, we are able to conduct self-consistently numerical studies on tidal disruption events of a white dwarf by a non-spinning supermassive black hole to study the disruption criteria. Our results show that the tidal disruption takes place for $\beta \gtrsim 0.5$, and an appreciable oscillation of the white dwarfs is induced by the black-hole tidal effect for $\beta \gtrsim 0.4$ for orbits close to the black hole in the $\Gamma = 5/3$ polytropic equation of state, which is consistent with the previous analytical studies. In the next step, we plan to extend the study for spinning black holes. Currently, a popular model for explaining the UV/optical emission of TDE is the stream-stream collision of tidal debris caused by relativistic apsidal precession. If a white dwarf or star is tidally disrupted close to a spinning black hole, the spin-induced precession could avoid stream collisions, causing a significant delay for ~ 10 winding orbitals before stream self-interaction, resulting in a "dark period". However, most studies exploring the spin effect rely on approximation schemes with Post-Newtonian prescriptions. Therefore, it is essential to perform a general relativistic hydrodynamics simulation of a white dwarf tidally disrupted by a spinning black hole in an inclined plane in a self-consistent approach to deepen our understanding of the black hole spin effect on the dynamics of tidal disruption and subsequent mass accretion. A more challenging issue is to follow the long-term hydrodynamics evolution of the tidally disrupted debris to study the subsequent disk formation, which could be a source of electromagnetic counterpart.

In Part II of the thesis, we conducted a series of numerical studies aiming to quantify the non-linear feature of massive DEF theory in binary neutron star mergers and explore distinctive signatures in GW signals, paying particular attention to scalar mass in $\sim 10^{-11}$ eV with corresponding Compton wavelength ~ 20 km, which could have scalar interaction imprinted in the late inspiral phase. Starting from constructing initial data for quasi-equilibrium configurations of binary neutron stars that are self-consistent with DEF theory in Chapter 3, we compared orbital energy obtained from the numerical data with the event GW170817 and suggested a constraint on scalar mass $\gtrsim 10^{-11}$ eV if both neutron stars are scalarized in the inspiral phase. To further understand the scalar effect on the dynamics of the coalescence and the postmerger remnant, we extended the numerical relativity code SACRA-MPI to the massive DEF theory and performed a set of numerical simulations to study comprehensively the dependence on scalar mass and coupling strength in Chapter 4. We found that the modified effect in DEF theory can significantly alter the final fate of the merger remnant and provide various distinctive features that appear in a wide range of binary parameters. The presence of a scalar field could also provide additional support from gravitational collapse. It raises the threshold mass for prompt collapse and prolongs the lifetime of short-lived hypermassive, which can modify the final disk mass around the black hole and subsequent post-merger ejecta. When a hypermassive neutron star is formed after the merger, the scalar field can be dissipated when the core density of the remnant rises to reach an ultra-relativistic regime, leading to descalarization. Such a state transition in the scalar field can introduce a shift in f2 frequency in post-merger GW signal, sharing the similar influence of a phase transition from confined hadronic matter to deconfined quark matter. This motivates us to investigate in Chapter 5 systematically the possible modification in quasi-universal relations of merger waveform in DEF theory. Through analyzing ~ 120 numerical simulations, we demonstrated that a gravitational effect like scalarization could lead to a violation in quasi-universal relations. In the future, we plan to explore the scalar imprint on the inspiral waveform of binary neutron stars to construct a more accurate waveform model.

In the final part of the thesis (Part III), we explore different physical scenarios under axisymmetric configuration. The free-fall initial data model introduced in Chapter 6 allows us to study more efficiently the final fate after the collapse of rotating massive stars that form a black hole and a torus by skipping the initial collapse phase. By performing general relativistic neutrino-radiation viscous-hydrodynamics simulations, we found ^{56}Ni mass $> 0.15\ M_\odot$ and $\sim 3 - 11\%$ of the total ejecta mass for rapidly rotating progenitor stars. The model light curves derived from our numerical results agree with the observational data, which suggests a possibility that some of the high-energy stripped-envelope supernovae may take place from a system of a spinning black hole and a massive torus. In Chapter 7, we present SACRA-2D, a new MPI and OpenMP parallelized, fully relativistic hydrodynamics code in dynamical spacetime under axial symmetry with the cartoon method. The code employs a cell-centered grid with fixed mesh refinement and an adaptive time-step scheme. We implement the finite volume method with the state-of-the-art HLLC approximate Riemann solver for hydrodynamics and the Baumgarte-Shapiro-Shibata-Nakamura formalism with Z4c constraint transport for spacetime evolution. With the new and more efficient code `SACRA-2D`, we examine the well-known turning-point criterion of differentially rotating neutron stars in DEF scalar-tensor theory. By evolving scalarized neutron stars along constant-angular-momentum sequences, we can pin down the onset of an axis-symmetric instability. Our results suggest that the criterion for rigidly rotating bodies in GR are largely valid also for differentially rotating stars in the DEF theory, and the observed onset of instability agrees with the numerical error at the turning point along the constant–momentum sequence. In the future, we plan to implement magnetohydrodynamics with the HLLD Riemann solver and the constrained transport scheme, as well as implement neutrino-radiation viscous-hydrodynamics. With more sophisticated microphysics and magnetohydrodynamics implemented, we can use `SACRA-2D` to explore various systems, including collapsar, supermassive star collapse, and black hole disk system.

Bibliography

[1] J. Aasi et al. Advanced LIGO. *Class. Quant. Grav.*, 32:074001, 2015. doi: 10.1088/0264-9381/32/7/074001.

[2] B. P. Abbott, R. Abbott, T. D. Abbott, M. R. Abernathy, F. Acernese, K. Ackley, C. Adams, T. Adams, P. Addesso, R. X. Adhikari, V. B. Adya, C. Affeldt, M. Agathos, K. Agatsuma, N. Aggarwal, O. D. Aguiar, L. Aiello, A. Ain, P. Ajith, B. Allen, A. Allocca, P. A. Altin, S. B. Anderson, W. G. Anderson, K. Arai, M. A. Arain, M. C. Araya, C. C. Arceneaux, J. S. Areeda, N. Arnaud, K. G. Arun, S. Ascenzi, G. Ashton, M. Ast, S. M. Aston, P. Astone, P. Aufmuth, C. Aulbert, S. Babak, P. Bacon, M. K. M. Bader, P. T. Baker, F. Baldaccini, G. Ballardin, S. W. Ballmer, J. C. Barayoga, S. E. Barclay, B. C. Barish, D. Barker, F. Barone, B. Barr, L. Barsotti, M. Barsuglia, D. Barta, J. Bartlett, M. A. Barton, I. Bartos, R. Bassiri, A. Basti, J. C. Batch, C. Baune, V. Bavigadda, M. Bazzan, B. Behnke, M. Bejger, C. Belczynski, A. S. Bell, C. J. Bell, B. K. Berger, J. Bergman, G. Bergmann, C. P. L. Berry, D. Bersanetti, A. Bertolini, J. Betzwieser, S. Bhagwat, R. Bhandare, I. A. Bilenko, G. Billingsley, J. Birch, I. A. Birney, O. Birnholtz, S. Biscans, A. Bisht, M. Bitossi, C. Biwer, M. A. Bizouard, J. K. Blackburn, C. D. Blair, D. G. Blair, R. M. Blair, S. Bloemen, O. Bock, T. P. Bodiya, M. Boer, G. Bogaert, C. Bogan, A. Bohe, P. Bojtos, C. Bond, F. Bondu, R. Bonnand, B. A. Boom, R. Bork, V. Boschi, S. Bose, Y. Bouffanais, A. Bozzi, C. Bradaschia, P. R. Brady, V. B. Braginsky, M. Branchesi, J. E. Brau, T. Briant, A. Brillet, M. Brinkmann, V. Brisson, P. Brockill, A. F. Brooks, D. A. Brown, D. D. Brown, N. M. Brown, C. C. Buchanan, A. Buikema, T. Bulik, H. J. Bulten, A. Buonanno, D. Buskulic, C. Buy, R. L. Byer, M. Cabero, L. Cadonati, G. Cagnoli, C. Cahillane, J. Calderón Bustillo, T. Callister, E. Calloni, J. B. Camp, K. C. Cannon, J. Cao, C. D. Capano, E. Capocasa, F. Carbognani, S. Caride, J. Casanueva Diaz, C. Casentini, S. Caudill, M. Cavaglià, F. Cavalier, R. Cavalieri, G. Cella, C. B. Cepeda, L. Cerboni Baiardi, G. Cerretani, E. Cesarini, R. Chakraborty, T. Chalermsongsak, S. J. Chamberlin, M. Chan, S. Chao, P. Charlton, E. Chassande-Mottin, H. Y. Chen, Y. Chen, C. Cheng, A. Chincarini, A. Chiummo, H. S. Cho, M. Cho, J. H. Chow, N. Christensen, Q. Chu, S. Chua, S. Chung, G. Ciani, F. Clara, J. A. Clark, F. Cleva, E. Coccia, P. F. Cohadon, A. Colla, C. G. Collette, L. Cominsky, M. Constancio, A. Conte, L. Conti, D. Cook, T. R. Corbitt, N. Cornish, A. Corsi, S. Cortese, C. A. Costa, M. W. Coughlin, S. B. Coughlin, J. P. Coulon, S. T. Countryman, P. Couvares, E. E. Cowan, D. M. Coward, and M. J. Cowart. Observation of Gravitational Waves from a Binary Black Hole Merger. *Phys. Rev. Lett.*, 116(6):061102, February 2016. doi: 10.1103/PhysRevLett.116.061102.

[3] B. P. Abbott et al. Search for Post-merger Gravitational Waves from the Remnant of the Binary Neutron Star Merger GW170817. *Astrophys. J. Lett.*, 851(1):L16, 2017. doi: 10.3847/2041-8213/aa9a35.

[4] B. P. Abbott et al. Multi-messenger Observations of a Binary Neutron Star Merger. *ApJ*, 848(2):L12, October 2017. doi: 10.3847/2041-8213/aa91c9.

[5] B. P. Abbott et al. Gravitational Waves and Gamma-Rays from a Binary Neutron Star Merger: GW170817 and GRB 170817A. *ApJ*, 848(2):L13, October 2017. doi: 10.3847/2041-8213/aa920c.

[6] B. P. Abbott et al. GW170817: Observation of Gravitational Waves from a Binary Neutron Star Inspiral. *Phys. Rev. Lett.*, 119(16):161101, October 2017. doi: 10.1103/PhysRevLett.119.161101.

[7] B. P. Abbott et al. GW170817: Measurements of neutron star radii and equation of state. *Phys. Rev. Lett.*, 121 (16):161101, 2018. doi: 10.1103/PhysRevLett.121.161101.

[8] B. P. Abbott et al. GW170817: Measurements of Neutron Star Radii and Equation of State. *Phys. Rev. Lett.*, 121(16):161101, October 2018. doi: 10.1103/PhysRevLett.121.161101.

[9] B. P. Abbott et al. GW170817: Measurements of neutron star radii and equation of state. *Phys. Rev. Lett.*, 121 (16):161101, 2018. doi: 10.1103/PhysRevLett.121.161101.

[10] B. P. Abbott et al. Tests of General Relativity with GW170817. *Phys. Rev. Lett.*, 123(1):011102, 2019. doi: 10.1103/PhysRevLett.123.011102.

[11] B. P. Abbott et al. Properties of the binary neutron star merger GW170817. *Phys. Rev. X*, 9(1):011001, 2019. doi: 10.1103/PhysRevX.9.011001.

[12] B. P. Abbott et al. GWTC-1: A Gravitational-Wave Transient Catalog of Compact Binary Mergers Observed by LIGO and Virgo during the First and Second Observing Runs. *Phys. Rev. X*, 9(3):031040, 2019. doi: 10.1103/PhysRevX.9.031040.

[13] B. P. Abbott et al. Search for gravitational waves from a long-lived remnant of the binary neutron star merger GW170817. *Astrophys. J.*, 875(2):160, 2019. doi: 10.3847/1538-4357/ab0f3d.

[14] B. P. Abbott et al. Properties of the binary neutron star merger GW170817. *Phys. Rev. X*, 9(1):011001, 2019. doi: 10.1103/PhysRevX.9.011001.

[15] B. P. Abbott et al. Tests of General Relativity with GW170817. *Phys. Rev. Lett.*, 123(1):011102, July 2019. doi: 10.1103/PhysRevLett.123.011102.

[16] B. P. Abbott et al. Properties of the Binary Neutron Star Merger GW170817. *Physical Review X*, 9(1):011001, January 2019. doi: 10.1103/PhysRevX.9.011001.

[17] B. P. Abbott et al. GW190425: Observation of a Compact Binary Coalescence with Total Mass $\sim 3.4 M_{\odot}$. *Astrophys. J. Lett.*, 892(1):L3, 2020. doi: 10.3847/2041-8213/ab75f5.

[18] Benjamin P Abbott et al. Exploring the Sensitivity of Next Generation Gravitational Wave Detectors. *Class. Quant. Grav.*, 34(4):044001, 2017. doi: 10.1088/1361-6382/aa51f4.

[19] R. Abbott, LIGO Scientific Collaboration, and Virgo Collaboration. GWTC-2: Compact Binary Coalescences Observed by LIGO and Virgo during the First Half of the Third Observing Run. *Physical Review X*, 11(2): 021053, April 2021. doi: 10.1103/PhysRevX.11.021053.

[20] F. Acernese et al. Advanced Virgo: a second-generation interferometric gravitational wave detector. *Class. Quant. Grav.*, 32(2):024001, 2015. doi: 10.1088/0264-9381/32/2/024001.

[21] David R. Aguilera-Dena, Norbert Langer, John Antoniadis, and Bernhard Müller. Precollapse Properties of Superluminous Supernovae and Long Gamma-Ray Burst Progenitor Models. *ApJ*, 901(2):114, October 2020. doi: 10.3847/1538-4357/abb138.

[22] A. Akmal, V. R. Pandharipande, and D. G. Ravenhall. Equation of state of nucleon matter and neutron star structure. *Phys. Rev. C*, 58(3):1804–1828, September 1998. doi: 10.1103/PhysRevC.58.1804.

[23] A. Akmal, V. R. Pandharipande, and D. G. Ravenhall. Equation of state of nucleon matter and neutron star structure. *Phys. Rev. C*, 58(3):1804–1828, September 1998. doi: 10.1103/PhysRevC.58.1804.

[24] Miguel Alcubierre, Bernd Brügmann, Daniel Holz, Ryoji Takahashi, Steven Brandt, Edward Seidel, Jonathan Thornburg, and A. Ashtekar. Symmetry Without Symmetry. *International Journal of Modern Physics D*, 10 (3):273–289, January 2001. doi: 10.1142/S0218271801000834.

[25] Miguel Alcubierre, Bernd Bruegmann, Peter Diener, Michael Koppitz, Denis Pollney, Edward Seidel, and Ryoji Takahashi. Gauge conditions for long term numerical black hole evolutions without excision. *Phys. Rev. D*, 67: 084023, 2003. doi: 10.1103/PhysRevD.67.084023.

[26] Miguel Alcubierre, Bernd Brügmann, Peter Diener, Michael Koppitz, Denis Pollney, Edward Seidel, and Ryoji Takahashi. Gauge conditions for long-term numerical black hole evolutions without excision. *Phys. Rev. D*, 67 (8):084023, April 2003. doi: 10.1103/PhysRevD.67.084023.

[27] Kate D. Alexander, Sjoert van Velzen, Assaf Horesh, and B. Ashley Zauderer. Radio Properties of Tidal Disruption Events. *Space Sci. Rev.*, 216(5):81, June 2020. doi: 10.1007/s11214-020-00702-w.

[28] Justin Alsing, Emanuele Berti, Clifford M. Will, and Helmut Zaglauer. Gravitational radiation from compact binary systems in the massive Brans-Dicke theory of gravity. *Phys. Rev. D*, 85(6):064041, March 2012. doi: 10.1103/PhysRevD.85.064041.

[29] Justin Alsing, Emanuele Berti, Clifford M. Will, and Helmut Zaglauer. Gravitational radiation from compact binary systems in the massive Brans-Dicke theory of gravity. *Phys. Rev. D*, 85(6):064041, March 2012. doi: 10.1103/PhysRevD.85.064041.

[30] Zahra Altaha Motahar, Jose Luis Blázquez-Salcedo, Burkhard Kleihaus, and Jutta Kunz. Scalarization of neutron stars with realistic equations of state. *Phys. Rev. D*, 96(6):064046, September 2017. doi: 10.1103/PhysRevD.96.064046.

[31] Pau Amaro-Seoane et al. Laser Interferometer Space Antenna. *arXiv e-prints*, art. arXiv:1702.00786, February 2017.

[32] David Anderson, Paulo Freire, and Nicolás Yunes. Binary pulsar constraints on massless scalar–tensor theories using Bayesian statistics. *Class. Quant. Grav.*, 36(22):225009, 2019. doi: 10.1088/1361-6382/ab3a1c.

[33] David Anderson, Paulo Freire, and Nicolás Yunes. Binary pulsar constraints on massless scalar-tensor theories using Bayesian statistics. *Classical and Quantum Gravity*, 36(22):225009, November 2019. doi: 10.1088/1361-6382/ab3a1c.

[34] Nikolas Andreou, Nicola Franchini, Giulia Ventagli, and Thomas P. Sotiriou. Spontaneous scalarization in generalized scalar-tensor theory. *Phys. Rev. D*, 99(12):124022, June 2019. doi: 10.1103/PhysRevD.99.124022.

[35] Eemeli Annala, Tyler Gorda, Aleksi Kurkela, and Aleksi Vuorinen. Gravitational-Wave Constraints on the Neutron-Star-Matter Equation of State. *Phys. Rev. Lett.*, 120(17):172703, April 2018. doi: 10.1103/PhysRevLett.120.172703.

[36] Marcus Ansorg, Dorota Gondek-Rosinska, and Loic Villain. The Continuous Parametric Transition of Spheroidal to Toroidal Differentially Rotating Stars in General Relativity. *Mon. Not. Roy. Astron. Soc.*, 396:2359, 2009. doi: 10.1111/j.1365-2966.2009.14904.x.

[37] W. D. Arnett. Type I supernovae. I - Analytic solutions for the early part of the light curve. *ApJ*, 253:785–797, February 1982. doi: 10.1086/159681.

[38] Richard Arnowitt, Stanley Deser, and Charles W. Misner. The Dynamics of General Relativity. In *in Gravitation: An Introduction to Current Research (Chap. 7). Edited by Louis Witten. John Wiley & Sons Inc*, page 227. New York Plenum, 1962.

[39] Naomichi Asakawa and Yuichiro Sekiguchi. Constraining self-interactions of a massive scalar field using scalar gravitational waves from stellar core collapse. *Phys. Rev. D*, 108:044060, Aug 2023. doi: 10.1103/PhysRevD.108.044060. URL https://link.aps.org/doi/10.1103/PhysRevD.108.044060.

[40] Josu C. Aurrekoetxea, Pedro G. Ferreira, Katy Clough, Eugene A. Lim, and Oliver J. Tattersall. Where is the ringdown: Reconstructing quasinormal modes from dispersive waves. *Phys. Rev. D*, 106(10):104002, November 2022. doi: 10.1103/PhysRevD.106.104002.

[41] Luca Baiotti, Ian Hawke, Pedro J. Montero, Frank Loffler, Luciano Rezzolla, Nikolaos Stergioulas, Jose A. Font, and Ed Seidel. Three-dimensional relativistic simulations of rotating neutron star collapse to a Kerr black hole. *Phys. Rev. D*, 71:024035, 2005. doi: 10.1103/PhysRevD.71.024035.

[42] John G. Baker, Joan Centrella, Dae-Il Choi, Michael Koppitz, and James van Meter. Gravitational-Wave Extraction from an Inspiraling Configuration of Merging Black Holes. *Phys. Rev. Lett.*, 96(11):111102, March 2006. doi: 10.1103/PhysRevLett.96.111102.

[43] Steven A. Balbus and John F. Hawley. Instability, turbulence, and enhanced transport in accretion disks. *Reviews of Modern Physics*, 70(1):1–53, January 1998. doi: 10.1103/RevModPhys.70.1.

[44] Steven A. Balbus and John F. Hawley. Instability, turbulence, and enhanced transport in accretion disks. *Rev. Mod. Phys.*, 70:1–53, 1998. doi: 10.1103/RevModPhys.70.1.

[45] Francesc Banyuls, José A. Font, José M. Ibáñez, José M. Martí, and Juan A. Miralles. Numerical {3 + 1} General Relativistic Hydrodynamics: A Local Characteristic Approach. *ApJ*, 476(1):221–231, February 1997. doi: 10.1086/303604.

[46] Enrico Barausse, Carlos Palenzuela, Marcelo Ponce, and Luis Lehner. Neutron-star mergers in scalar-tensor theories of gravity. *Phys. Rev. D*, 87(8):081506, April 2013. doi: 10.1103/PhysRevD.87.081506.

[47] James M. Bardeen, William H. Press, and Saul A. Teukolsky. Rotating Black Holes: Locally Nonrotating Frames, Energy Extraction, and Scalar Synchrotron Radiation. *ApJ*, 178:347–370, December 1972. doi: 10.1086/151796.

[48] James M. Bardeen, William H. Press, and Saul A Teukolsky. Rotating black holes: Locally nonrotating frames, energy extraction, and scalar synchrotron radiation. *Astrophys. J.*, 178:347, 1972. doi: 10.1086/151796.

[49] Susanna Barsanti, Andrea Maselli, Thomas P. Sotiriou, and Leonardo Gualtieri. Detecting Massive Scalar Fields with Extreme Mass-Ratio Inspirals. *Phys. Rev. Lett.*, 131(5):051401, August 2023. doi: 10.1103/PhysRevLett.131.051401.

[50] N. H. Barth and S. M. Christensen. Quantizing fourth-order gravity theories: The functional integral. *Phys. Rev. D*, 28(8):1876–1893, October 1983. doi: 10.1103/PhysRevD.28.1876.

[51] A. O. Barvinsky and G. A. Vilkovisky. The generalized Schwinger-Dewitt technique in gauge theories and quantum gravity. *Phys. Rep.*, 119(1):1–74, March 1985. doi: 10.1016/0370-1573(85)90148-6.

[52] P. Batten, N. Clarke, C. Lambert, and D. M. Causon. On the Choice of Wavespeeds for the HLLC Riemann Solver. *SIAM Journal on Scientific Computing*, 18(6):1553–1570, November 1997. doi: 10.1137/S1064827593260140.

[53] Thomas W. Baumgarte. Puncture black hole initial data in the conformal thin-sandwich formalism. *Classical and Quantum Gravity*, 28(21):215003, November 2011. doi: 10.1088/0264-9381/28/21/215003.

[54] Thomas W. Baumgarte and Stephen G. Naculich. Analytical representation of a black hole puncture solution. *Phys. Rev. D*, 75(6):067502, March 2007. doi: 10.1103/PhysRevD.75.067502.

[55] Thomas W. Baumgarte and Stuart L. Shapiro. Numerical integration of Einstein's field equations. *Phys. Rev. D*, 59(2):024007, January 1999. doi: 10.1103/PhysRevD.59.024007.

[56] Thomas W. Baumgarte and Stuart L. Shapiro. *Numerical Relativity: Solving Einstein's Equations on the Computer*. 2010.

[57] Thomas W. Baumgarte, Stuart L. Shapiro, and Masaru Shibata. On the Maximum Mass of Differentially Rotating Neutron Stars. *ApJ*, 528(1):L29–L32, January 2000. doi: 10.1086/312425.

[58] Thomas W. Baumgarte, Niall Ó. Murchadha, and Harald P. Pfeiffer. Einstein constraints: Uniqueness and nonuniqueness in the conformal thin sandwich approach. *Phys. Rev. D*, 75(4):044009, February 2007. doi: 10.1103/PhysRevD.75.044009.

[59] Thomas W. Baumgarte, Pedro J. Montero, Isabel Cordero-Carrión, and Ewald Müller. Numerical relativity in spherical polar coordinates: Evolution calculations with the BSSN formulation. *Phys. Rev. D*, 87(4):044026, February 2013. doi: 10.1103/PhysRevD.87.044026.

[60] A. Bauswein and H. Th. Janka. Measuring neutron-star properties via gravitational waves from binary mergers. *Phys. Rev. Lett.*, 108:011101, 2012. doi: 10.1103/PhysRevLett.108.011101.

[61] A. Bauswein and N. Stergioulas. Unified picture of the post-merger dynamics and gravitational wave emission in neutron star mergers. *Phys. Rev. D*, 91(12):124056, 2015. doi: 10.1103/PhysRevD.91.124056.

[62] A. Bauswein, H. T. Janka, and R. Oechslin. Testing approximations of thermal effects in neutron star merger simulations. *Phys. Rev. D*, 82(8):084043, October 2010. doi: 10.1103/PhysRevD.82.084043.

[63] A. Bauswein, H. T. Janka, K. Hebeler, and A. Schwenk. Equation-of-state dependence of the gravitational-wave signal from the ring-down phase of neutron-star mergers. *Phys. Rev. D*, 86:063001, 2012. doi: 10.1103/PhysRevD.86.063001.

[64] A. Bauswein, T. W. Baumgarte, and H. T. Janka. Prompt Merger Collapse and the Maximum Mass of Neutron Stars. *Phys. Rev. Lett.*, 111(13):131101, September 2013. doi: 10.1103/PhysRevLett.111.131101.

[65] A. Bauswein, N. Stergioulas, and H. T. Janka. Revealing the high-density equation of state through binary neutron star mergers. *Phys. Rev. D*, 90(2):023002, 2014. doi: 10.1103/PhysRevD.90.023002.

[66] Andreas Bauswein and Nikolaos Stergioulas. Semi-analytic derivation of the threshold mass for prompt collapse in binary neutron-star mergers. *MNRAS*, 471(4):4956–4965, November 2017. doi: 10.1093/mnras/stx1983.

[67] Andreas Bauswein, Nikolaos Stergioulas, and Hans-Thomas Janka. Exploring properties of high-density matter through remnants of neutron-star mergers. *Eur. Phys. J. A*, 52(3):56, 2016. doi: 10.1140/epja/i2016-16056-7.

[68] Andreas Bauswein, Niels-Uwe F. Bastian, David B. Blaschke, Katerina Chatziioannou, James A. Clark, Tobias Fischer, and Micaela Oertel. Identifying a First-Order Phase Transition in Neutron-Star Mergers through Gravitational Waves. *Phys. Rev. Lett.*, 122(6):061102, February 2019. doi: 10.1103/PhysRevLett.122.061102.

[69] Andreas Bauswein, Niels-Uwe Friedrich Bastian, David Blaschke, Katerina Chatziioannou, James Alexander Clark, Tobias Fischer, Hans-Thomas Janka, Oliver Just, Micaela Oertel, and Nikolaos Stergioulas. Equation-of-state constraints and the QCD phase transition in the era of gravitational-wave astronomy. In *Xiamen-CUSTIPEN Workshop on the Equation of State of Dense Neutron-Rich Matter in the Era of Gravitational Wave Astronomy*, volume 2127 of *American Institute of Physics Conference Series*, page 020013. AIP, July 2019. doi: 10.1063/1.5117803.

[70] Andreas Bauswein, Sebastian Blacker, Vimal Vijayan, Nikolaos Stergioulas, Katerina Chatziioannou, James A. Clark, Niels-Uwe F. Bastian, David B. Blaschke, Mateusz Cierniak, and Tobias Fischer. Equation of State Constraints from the Threshold Binary Mass for Prompt Collapse of Neutron Star Mergers. *Phys. Rev. Lett.*, 125(14):141103, October 2020. doi: 10.1103/PhysRevLett.125.141103.

[71] Andreas Bauswein, Sebastian Blacker, Georgios Lioutas, Theodoros Soultanis, Vimal Vijayan, and Nikolaos Stergioulas. Systematics of prompt black-hole formation in neutron star mergers. *Phys. Rev. D*, 103(12):123004, June 2021. doi: 10.1103/PhysRevD.103.123004.

[72] Gordon Baym, Tetsuo Hatsuda, Toru Kojo, Philip D. Powell, Yifan Song, and Tatsuyuki Takatsuka. From hadrons to quarks in neutron stars: a review. *Rept. Prog. Phys.*, 81(5):056902, 2018. doi: 10.1088/1361-6633/aaae14.

[73] Gordon Baym, Shun Furusawa, Tetsuo Hatsuda, Toru Kojo, and Hajime Togashi. New Neutron Star Equation of State with Quark-Hadron Crossover. *Astrophys. J.*, 885:42, 2019. doi: 10.3847/1538-4357/ab441e.

[74] David Benisty, Philippe Brax, and Anne-Christine Davis. Stringent pulsar timing bounds on light scalar couplings to matter. *Phys. Rev. D*, 107(6):064049, March 2023. doi: 10.1103/PhysRevD.107.064049.

[75] M. J. Berger and P. Colella. Local Adaptive Mesh Refinement for Shock Hydrodynamics. *Journal of Computational Physics*, 82(1):64–84, May 1989. doi: 10.1016/0021-9991(89)90035-1.

[76] Marsha J. Berger and Joseph Oliger. Adaptive Mesh Refinement for Hyperbolic Partial Differential Equations. *Journal of Computational Physics*, 53(3):484–512, March 1984. doi: 10.1016/0021-9991(84)90073-1.

[77] Laura Bernard. Dipolar tidal effects in scalar-tensor theories. *Phys. Rev. D*, 101(2):021501, January 2020. doi: 10.1103/PhysRevD.101.021501.

[78] Laura Bernard, Luc Blanchet, Guillaume Faye, and Tanguy Marchand. Center-of-mass equations of motion and conserved integrals of compact binary systems at the fourth post-Newtonian order. *Phys. Rev. D*, 97(4):044037, February 2018. doi: 10.1103/PhysRevD.97.044037.

[79] Sebastiano Bernuzzi. Neutron star merger remnants. *General Relativity and Gravitation*, 52(11):108, November 2020. doi: 10.1007/s10714-020-02752-5.

[80] Sebastiano Bernuzzi and Tim Dietrich. Gravitational waveforms from binary neutron star mergers with high-order weighted-essentially-nonoscillatory schemes in numerical relativity. *Phys. Rev. D*, 94(6):064062, September 2016. doi: 10.1103/PhysRevD.94.064062.

[81] Sebastiano Bernuzzi and David Hilditch. Constraint violation in free evolution schemes: Comparing the BSSNOK formulation with a conformal decomposition of the Z4 formulation. *Phys. Rev. D*, 81(8):084003, April 2010. doi: 10.1103/PhysRevD.81.084003.

[82] Sebastiano Bernuzzi, Alessandro Nagar, Simone Balmelli, Tim Dietrich, and Maximiliano Ujevic. Quasiuniversal properties of neutron star mergers. *Phys. Rev. Lett.*, 112:201101, 2014. doi: 10.1103/PhysRevLett.112.201101.

[83] Sebastiano Bernuzzi, Tim Dietrich, and Alessandro Nagar. Modeling the complete gravitational wave spectrum of neutron star mergers. *Phys. Rev. Lett.*, 115(9):091101, 2015. doi: 10.1103/PhysRevLett.115.091101.

[84] Sebastiano Bernuzzi, Alessandro Nagar, Tim Dietrich, and Thibault Damour. Modeling the Dynamics of Tidally Interacting Binary Neutron Stars up to the Merger. *Phys. Rev. Lett.*, 114(16):161103, 2015. doi: 10.1103/PhysRevLett.114.161103.

[85] Sebastiano Bernuzzi, Matteo Breschi, Boris Daszuta, Andrea Endrizzi, Domenico Logoteta, Vsevolod Nedora, Albino Perego, David Radice, Federico Schianchi, Francesco Zappa, Ignazio Bombaci, and Nestor Ortiz. Accretion-induced prompt black hole formation in asymmetric neutron star mergers, dynamical ejecta, and kilonova signals. *MNRAS*, 497(2):1488–1507, September 2020. doi: 10.1093/mnras/staa1860.

[86] Emanuele Berti, Vitor Cardoso, and Andrei O. Starinets. TOPICAL REVIEW: Quasinormal modes of black holes and black branes. *Classical and Quantum Gravity*, 26(16):163001, August 2009. doi: 10.1088/0264-9381/26/16/163001.

[87] Emanuele Berti, Kent Yagi, and Nicolás Yunes. Extreme Gravity Tests with Gravitational Waves from Compact Binary Coalescences: (I) Inspiral-Merger. *Gen. Rel. Grav.*, 50(4):46, 2018. doi: 10.1007/s10714-018-2362-8.

[88] Miguel Bezares, Ricard Aguilera-Miret, Lotte ter Haar, Marco Crisostomi, Carlos Palenzuela, and Enrico Barausse. No Evidence of Kinetic Screening in Simulations of Merging Binary Neutron Stars beyond General Relativity. *Phys. Rev. Lett.*, 128(9):091103, March 2022. doi: 10.1103/PhysRevLett.128.091103.

[89] George David Birkhoff and Rudolph Ernest Langer. *Relativity and modern physics.* 1923.

[90] Sebastian Blacker and Andreas Bauswein. Comprehensive survey of hybrid equations of state in neutron star mergers and constraints on the hadron-quark phase transition. *arXiv: 2406.14669*, 6 2024.

[91] Sebastian Blacker, Niels-Uwe F. Bastian, Andreas Bauswein, David B. Blaschke, Tobias Fischer, Micaela Oertel, Theodoros Soultanis, and Stefan Typel. Constraining the onset density of the hadron-quark phase transition with gravitational-wave observations. *Phys. Rev. D*, 102(12):123023, December 2020. doi: 10.1103/PhysRevD.102.123023.

[92] Luc Blanchet. Gravitational Radiation from Post-Newtonian Sources and Inspiralling Compact Binaries. *Living Reviews in Relativity*, 17(1):2, December 2014. doi: 10.12942/lrr-2014-2.

[93] Luc Blanchet. Analytic approximations in GR and gravitational waves. *International Journal of Modern Physics D*, 28(6):1930011-144, January 2019. doi: 10.1142/S0218271819300118.

[94] R. D. Blandford and D. G. Payne. Hydromagnetic flows from accretion disks and the production of radio jets. *MNRAS*, 199:883–903, June 1982. doi: 10.1093/mnras/199.4.883.

[95] R. D. Blandford and R. L. Znajek. Electromagnetic extraction of energy from Kerr black holes. *MNRAS*, 179:433–456, May 1977. doi: 10.1093/mnras/179.3.433.

[96] Jose Luis Blázquez-Salcedo, Fech Scen Khoo, Jutta Kunz, and Vincent Preut. Polar Quasinormal Modes of Neutron Stars in Massive Scalar-Tensor Theories. *Front. in Phys.*, 9:741427, 2021. doi: 10.3389/fphy.2021.741427.

[97] C. Bona and C. Palenzuela. Dynamical shift conditions for the Z4 and BSSN formalisms. *Phys. Rev. D*, 69(10):104003, May 2004. doi: 10.1103/PhysRevD.69.104003.

[98] C. Bona, T. Ledvinka, C. Palenzuela, and M. Žáček. General-covariant evolution formalism for numerical relativity. *Phys. Rev. D*, 67(10):104005, May 2003. doi: 10.1103/PhysRevD.67.104005.

[99] Silvano Bonazzola and Eric Gourgoulhon. A virial identity applied to relativistic stellar models. *Classical and Quantum Gravity*, 11(7):1775–1784, July 1994. doi: 10.1088/0264-9381/11/7/014.

[100] Gabriel S. Bonilla, Prayush Kumar, and Saul A. Teukolsky. Modeling compact binary merger waveforms beyond general relativity. *Phys. Rev. D*, 107(2):024015, January 2023. doi: 10.1103/PhysRevD.107.024015.

[101] Marica Branchesi et al. Science with the Einstein Telescope: a comparison of different designs. *JCAP*, 07:068, 2023. doi: 10.1088/1475-7516/2023/07/068.

[102] Steven R. Brandt and Edward Seidel. Evolution of distorted rotating black holes. I. Methods and tests. *Phys. Rev. D*, 52(2):856–869, July 1995. doi: 10.1103/PhysRevD.52.856.

[103] Steven R. Brandt and Edward Seidel. Evolution of distorted rotating black holes. II. Dynamics and analysis. *Phys. Rev. D*, 52(2):870–886, July 1995. doi: 10.1103/PhysRevD.52.870.

[104] C. Brans and R. H. Dicke. Mach's Principle and a Relativistic Theory of Gravitation. *Physical Review*, 124(3): 925–935, November 1961. doi: 10.1103/PhysRev.124.925.

[105] Matteo Breschi, Sebastiano Bernuzzi, Francesco Zappa, Michalis Agathos, Albino Perego, David Radice, and Alessandro Nagar. kiloHertz gravitational waves from binary neutron star remnants: time-domain model and constraints on extreme matter. *Phys. Rev. D*, 100(10):104029, 2019. doi: 10.1103/PhysRevD.100.104029.

[106] Matteo Breschi, Sebastiano Bernuzzi, Daniel Godzieba, Albino Perego, and David Radice. Constraints on the Maximum Densities of Neutron Stars from Postmerger Gravitational Waves with Third-Generation Observations. *Phys. Rev. Lett.*, 128(16):161102, 2022. doi: 10.1103/PhysRevLett.128.161102.

[107] Matteo Breschi, Sebastiano Bernuzzi, Kabir Chakravarti, Alessandro Camilletti, Aviral Prakash, and Albino Perego. Kilohertz gravitational waves from binary neutron star mergers: Numerical-relativity informed postmerger model. *Phys. Rev. D*, 109(6):064009, 2024. doi: 10.1103/PhysRevD.109.064009.

[108] Dieter R. Brill and Richard W. Lindquist. Interaction Energy in Geometrostatics. *Physical Review*, 131(1): 471–476, July 1963. doi: 10.1103/PhysRev.131.471.

[109] Richard Brito, Vitor Cardoso, and Paolo Pani. *Superradiance*, volume 906. 2015. doi: 10.1007/978-3-030-46622-0.

[110] Omer Bromberg and Alexander Tchekhovskoy. Relativistic MHD simulations of core-collapse GRB jets: 3D instabilities and magnetic dissipation. *Mon. Not. Roy. Astron. Soc.*, 456(2):1739–1760, 2016. doi: 10.1093/mnras/stv2591.

[111] J. David Brown. Puncture evolution of Schwarzschild black holes. *Phys. Rev. D*, 77(4):044018, February 2008. doi: 10.1103/PhysRevD.77.044018.

[112] Stephanie M. Brown. Tidal Deformability of Neutron Stars in Scalar-Tensor Theories of Gravity for Gravitational Wave Analysis. *arXiv e-prints*, art. arXiv:2210.14025, October 2022. doi: 10.48550/arXiv.2210.14025.

[113] Stephanie M. Brown. Tidal Deformability of Neutron Stars in Scalar-tensor Theories of Gravity. *Astrophys. J.*, 958(2):125, 2023. doi: 10.3847/1538-4357/acfbe5.

[114] Bernd Brügmann. Schwarzschild black hole as moving puncture in isotropic coordinates. *General Relativity and Gravitation*, 41(9):2131–2151, September 2009. doi: 10.1007/s10714-009-0818-6.

[115] Bernd Brügmann, José A. González, Mark Hannam, Sascha Husa, Ulrich Sperhake, and Wolfgang Tichy. Calibration of moving puncture simulations. *Phys. Rev. D*, 77(2):024027, January 2008. doi: 10.1103/PhysRevD.77.024027.

[116] N. Bucciantini and L. Del Zanna. General relativistic magnetohydrodynamics in axisymmetric dynamical spacetimes: the X-ECHO code. *A&A*, 528:A101, April 2011. doi: 10.1051/0004-6361/201015945.

[117] A. Burrows, L. Dessart, E. Livne, C. D. Ott, and J. Murphy. Simulations of Magnetically Driven Supernova and Hypernova Explosions in the Context of Rapid Rotation. *ApJ*, 664(1):416–434, July 2007. doi: 10.1086/519161.

[118] Adam Burrows, David Radice, and David Vartanyan. Three-dimensional supernova explosion simulations of 9-, 10-, 11-, 12-, and 13-$M_\odot$ stars. *MNRAS*, 485(3):3153–3168, May 2019. doi: 10.1093/mnras/stz543.

[119] M. Campanelli, C. O. Lousto, P. Marronetti, and Y. Zlochower. Accurate Evolutions of Orbiting Black-Hole Binaries without Excision. *Phys. Rev. Lett.*, 96(11):111101, March 2006. doi: 10.1103/PhysRevLett.96.111101.

[120] Zach Cano, Shan-Qin Wang, Zi-Gao Dai, and Xue-Feng Wu. The Observer's Guide to the Gamma-Ray Burst Supernova Connection. *Advances in Astronomy*, 2017:8929054, January 2017. doi: 10.1155/2017/8929054.

[121] Collin D. Capano, Ingo Tews, Stephanie M. Brown, Ben Margalit, Soumi De, Sumit Kumar, Duncan A. Brown, Badri Krishnan, and Sanjay Reddy. Stringent constraints on neutron-star radii from multimessenger observations and nuclear theory. *Nature Astronomy*, 4:625–632, March 2020. doi: 10.1038/s41550-020-1014-6.

[122] Katerina Chatziioannou. Neutron star tidal deformability and equation of state constraints. *Gen. Rel. Grav.*, 52(11):109, 2020. doi: 10.1007/s10714-020-02754-3.

[123] Katerina Chatziioannou, James Alexander Clark, Andreas Bauswein, Margaret Millhouse, Tyson B. Littenberg, and Neil Cornish. Inferring the post-merger gravitational wave emission from binary neutron star coalescences. *Phys. Rev. D*, 96(12):124035, 2017. doi: 10.1103/PhysRevD.96.124035.

[124] Katerina Chatziioannou, Carl-Johan Haster, and Aaron Zimmerman. Measuring the neutron star tidal deformability with equation-of-state-independent relations and gravitational waves. *Phys. Rev. D*, 97(10):104036, 2018. doi: 10.1103/PhysRevD.97.104036.

[125] Shichuan Chen, Luohan Wang, Kota Hayashi, Kyohei Kawaguchi, Kenta Kiuchi, and Masaru Shibata. Black hole-neutron star mergers with massive neutron stars in numerical relativity. *Phys. Rev. D*, 110(6):063016, September 2024. doi: 10.1103/PhysRevD.110.063016.

[126] Patrick Chi-Kit Cheong and Tjonnie Guang Feng Li. Numerical studies on core collapse supernova in self-interacting massive scalar-tensor gravity. *Phys. Rev. D*, 100(2):024027, July 2019. doi: 10.1103/PhysRevD.100.024027.

[127] Patrick Chi-Kit Cheong, Alan Tsz-Lok Lam, Harry Ho-Yin Ng, and Tjonnie Guang Feng Li. Gmunu: paralleled, grid-adaptive, general-relativistic magnetohydrodynamics in curvilinear geometries in dynamical space-times. *MNRAS*, 508(2):2279–2301, December 2021. doi: 10.1093/mnras/stab2606.

[128] Takeshi Chiba. Spontaneous scalarization in scalar-tensor theories with conformal symmetry as an attractor. *Progress of Theoretical and Experimental Physics*, 2022(1):013E01, January 2022. doi: 10.1093/ptep/ptab138.

[129] F. Cipolletta, J. V. Kalinani, E. Giangrandi, B. Giacomazzo, R. Ciolfi, L. Sala, and B. Giudici. Spritz: general relativistic magnetohydrodynamics with neutrinos. *Classical and Quantum Gravity*, 38(8):085021, April 2021. doi: 10.1088/1361-6382/abebb7.

[130] J. Clark, A. Bauswein, L. Cadonati, H. T. Janka, C. Pankow, and N. Stergioulas. Prospects For High Frequency Burst Searches Following Binary Neutron Star Coalescence With Advanced Gravitational Wave Detectors. *Phys. Rev. D*, 90(6):062004, 2014. doi: 10.1103/PhysRevD.90.062004.

[131] P. C. M. Clemente and H. P. de Oliveira. Puncture black hole initial data: A single domain Galerkin-collocation method for trumpet and wormhole data sets. *Phys. Rev. D*, 96(2):024035, July 2017. doi: 10.1103/PhysRevD.96.024035.

[132] P. Colella and Paul R. Woodward. The Piecewise Parabolic Method (PPM) for Gas-Dynamical Simulations. *Journal of Computational Physics*, 54:174–201, September 1984. doi: 10.1016/0021-9991(84)90143-8.

[133] Luciano Combi and Daniel M. Siegel. GRMHD Simulations of Neutron-star Mergers with Weak Interactions: r-process Nucleosynthesis and Electromagnetic Signatures of Dynamical Ejecta. *ApJ*, 944(1):28, February 2023. doi: 10.3847/1538-4357/acac29.

[134] Gregory B. Cook, Stuart L. Shapiro, and Saul A. Teukolsky. Spin-up of a Rapidly Rotating Star by Angular Momentum Loss: Effects of General Relativity. *ApJ*, 398:203, October 1992. doi: 10.1086/171849.

[135] Gregory B. Cook, Stuart L. Shapiro, and Saul A. Teukolsky. Rapidly Rotating Polytropes in General Relativity. *ApJ*, 422:227, February 1994. doi: 10.1086/173721.

[136] Gregory B. Cook, Stuart L. Shapiro, and Saul A. Teukolsky. Rapidly Rotating Neutron Stars in General Relativity: Realistic Equations of State. *ApJ*, 424:823, April 1994. doi: 10.1086/173934.

[137] Isabel Cordero-Carrión, Pablo Cerdá-Durán, Harald Dimmelmeier, José Luis Jaramillo, Jérôme Novak, and Eric Gourgoulhon. Improved constrained scheme for the Einstein equations: An approach to the uniqueness issue. *Phys. Rev. D*, 79(2):024017, January 2009. doi: 10.1103/PhysRevD.79.024017.

[138] Gastón Creci, Tanja Hinderer, and Jan Steinhoff. Tidal properties of neutron stars in scalar-tensor theories of gravity. *Phys. Rev. D*, 108(12):124073, 2023. doi: 10.1103/PhysRevD.108.124073.

[139] Gastón Creci, Iris van Gemeren, Tanja Hinderer, and Jan Steinhoff. Tidal effects in gravitational waves from neutron stars in scalar-tensor theories of gravity. *arXiv:2412.06620*, 12 2024.

[140] Sanjana Curtis, Philipp Mösta, Zhenyu Wu, David Radice, Luke Roberts, Giacomo Ricigliano, and Albino Perego. r-process nucleosynthesis and kilonovae from hypermassive neutron star post-merger remnants. *MNRAS*, 518(4):5313–5322, February 2023. doi: 10.1093/mnras/stac3128.

[141] Lixin Dai and Roger D. Blandford. Roche Accretion of stars close to massive black holes. *Mon. Not. Roy. Astron. Soc.*, 434:2948, 2013. doi: 10.1093/mnras/stt1209.

[142] Thibault Damour and Gilles Esposito-Farese. Tensor-multi-scalar theories of gravitation. *Classical and Quantum Gravity*, 9(9):2093–2176, September 1992. doi: 10.1088/0264-9381/9/9/015.

[143] Thibault Damour and Gilles Esposito-Farese. Nonperturbative strong-field effects in tensor-scalar theories of gravitation. *Phys. Rev. Lett.*, 70(15):2220–2223, April 1993. doi: 10.1103/PhysRevLett.70.2220.

[144] Thibault Damour and Gilles Esposito-Farese. Testing gravity to second postNewtonian order: A Field theory approach. *Phys. Rev. D*, 53:5541–5578, 1996. doi: 10.1103/PhysRevD.53.5541.

[145] Thibault Damour and Gilles Esposito-Farèse. Gravitational-wave versus binary-pulsar tests of strong-field gravity. *Phys. Rev. D*, 58(4):042001, August 1998. doi: 10.1103/PhysRevD.58.042001.

[146] Thibault Damour and Alessandro Nagar. Effective one body description of tidal effects in inspiralling compact binaries. *Phys. Rev. D*, 81(8):084016, April 2010. doi: 10.1103/PhysRevD.81.084016.

[147] Soumi De, Daniel Finstad, James M. Lattimer, Duncan A. Brown, Edo Berger, and Christopher M. Biwer. Tidal Deformabilities and Radii of Neutron Stars from the Observation of GW170817. *Phys. Rev. Lett.*, 121(9): 091102, August 2018. doi: 10.1103/PhysRevLett.121.091102.

[148] Roberto De Pietri, Alessandra Feo, José A. Font, Frank Löffler, Michele Pasquali, and Nikolaos Stergioulas. Numerical-relativity simulations of long-lived remnants of binary neutron star mergers. *Phys. Rev. D*, 101(6): 064052, 2020. doi: 10.1103/PhysRevD.101.064052.

[149] Thibaut Arnoulx de Pirey Saint Alby and Nicolás Yunes. Cosmological evolution and Solar System consistency of massive scalar-tensor gravity. *Phys. Rev. D*, 96(6):064040, September 2017. doi: 10.1103/PhysRevD.96.064040.

[150] Juan Carlos Degollado, Néstor Ortiz, and Marcelo Salgado. Dynamical transition to spontaneous scalarization in neutron stars: The massive scalar field scenario. *Phys. Rev. D*, 110(8):084011, 2024. doi: 10.1103/PhysRevD.110.084011.

[151] Térence Delsate, David Hilditch, and Helvi Witek. Initial value formulation of dynamical Chern-Simons gravity. *Phys. Rev. D*, 91(2):024027, January 2015. doi: 10.1103/PhysRevD.91.024027.

[152] Ekrem S. Demirboğa, Yakup Emre Şahin, and Fethi M. Ramazanoğlu. Subtleties in constraining gravity theories with mass-radius data. *Phys. Rev. D*, 108(2):024028, July 2023. doi: 10.1103/PhysRevD.108.024028.

[153] Luc Dessart, D. John Hillier, Stan Woosley, Eli Livne, Roni Waldman, Sung-Chul Yoon, and Norbert Langer. Radiative-transfer models for supernovae IIb/Ib/Ic from binary-star progenitors. *MNRAS*, 453(2):2189–2213, October 2015. doi: 10.1093/mnras/stv1747.

[154] Luc Dessart, D. John Hillier, Stan Woosley, Eli Livne, Roni Waldman, Sung-Chul Yoon, and Norbert Langer. Inferring supernova IIb/Ib/Ic ejecta properties from light curves and spectra: correlations from radiative-transfer models. *MNRAS*, 458(2):1618–1635, May 2016. doi: 10.1093/mnras/stw418.

[155] Kyriakos Destounis, Arthur G. Suvorov, and Kostas D. Kokkotas. Testing spacetime symmetry through gravitational waves from extreme-mass-ratio inspirals. *Phys. Rev. D*, 102(6):064041, September 2020. doi: 10.1103/PhysRevD.102.064041.

[156] Kyriakos Destounis, Arthur G. Suvorov, and Kostas D. Kokkotas. Gravitational Wave Glitches in Chaotic Extreme-Mass-Ratio Inspirals. *Phys. Rev. Lett.*, 126(14):141102, April 2021. doi: 10.1103/PhysRevLett.126.141102.

[157] P. Diener, V. P. Frolov, A. M. Khokhlov, I. D. Novikov, and C. J. Pethick. Relativistic Tidal Interaction of Stars with a Rotating Black Hole. *ApJ*, 479(1):164–178, April 1997. doi: 10.1086/303875.

[158] Tim Dietrich and Bernd Brügmann. Solving the Hamiltonian constraint for 1+log trumpets. *Phys. Rev. D*, 89 (2):024014, January 2014. doi: 10.1103/PhysRevD.89.024014.

[159] Tim Dietrich and Bernd Brügmann. Spinning black hole in the puncture method: Numerical experiments. In *Journal of Physics Conference Series*, volume 490 of *Journal of Physics Conference Series*, page 012155. IOP, March 2014. doi: 10.1088/1742-6596/490/1/012155.

[160] Tim Dietrich, Maximiliano Ujevic, Wolfgang Tichy, Sebastiano Bernuzzi, and Bernd Brügmann. Gravitational waves and mass ejecta from binary neutron star mergers: Effect of the mass ratio. *Phys. Rev. D*, 95(2):024029, January 2017. doi: 10.1103/PhysRevD.95.024029.

[161] Tim Dietrich, David Radice, Sebastiano Bernuzzi, Francesco Zappa, Albino Perego, Bernd Brügmann, Swami Vivekanandji Chaurasia, Reetika Dudi, Wolfgang Tichy, and Maximiliano Ujevic. CoRe database of binary neutron star merger waveforms. *Class. Quant. Grav.*, 35(24):24LT01, 2018. doi: 10.1088/1361-6382/aaebc0.

[162] Tim Dietrich, Michael W. Coughlin, Peter T. H. Pang, Mattia Bulla, Jack Heinzel, Lina Issa, Ingo Tews, and Sarah Antier. Multimessenger constraints on the neutron-star equation of state and the Hubble constant. *Science*, 370(6523):1450–1453, December 2020. doi: 10.1126/science.abb4317.

[163] Tim Dietrich, Tanja Hinderer, and Anuradha Samajdar. Interpreting Binary Neutron Star Mergers: Describing the Binary Neutron Star Dynamics, Modelling Gravitational Waveforms, and Analyzing Detections. *Gen. Rel. Grav.*, 53(3):27, 2021. doi: 10.1007/s10714-020-02751-6.

[164] Daniela D. Doneva and Stoytcho S. Yazadjiev. Rapidly rotating neutron stars with a massive scalar field—structure and universal relations. *JCAP.*, 2016(11):019, November 2016. doi: 10.1088/1475-7516/2016/11/019.

[165] Daniela D. Doneva, Stoytcho S. Yazadjiev, Nikolaos Stergioulas, and Kostas D. Kokkotas. Rapidly rotating neutron stars in scalar-tensor theories of gravity. *Phys. Rev. D*, 88(8):084060, October 2013. doi: 10.1103/PhysRevD.88.084060.

[166] Daniela D. Doneva, Stoytcho S. Yazadjiev, Nikolaos Stergioulas, and Kostas D. Kokkotas. Differentially rotating neutron stars in scalar-tensor theories of gravity. *Phys. Rev. D*, 98(10):104039, November 2018. doi: 10.1103/PhysRevD.98.104039.

[167] Daniela D. Doneva, Fethi M. Ramazanoğlu, Hector O. Silva, Thomas P. Sotiriou, and Stoytcho S. Yazadjiev. Spontaneous scalarization. *Reviews of Modern Physics*, 96(1):015004, March 2024. doi: 10.1103/RevModPhys.96.015004.

[168] Matthew D. Duez, Yuk Tung Liu, Stuart L. Shapiro, and Branson C. Stephens. General relativistic hydrodynamics with viscosity: Contraction, catastrophic collapse, and disk formation in hypermassive neutron stars. *Phys. Rev. D*, 69(10):104030, May 2004. doi: 10.1103/PhysRevD.69.104030.

[169] Matthew D. Duez, Yuk Tung Liu, Stuart L. Shapiro, and Branson C. Stephens. Relativistic magnetohydrodynamics in dynamical spacetimes: Numerical methods and tests. *Phys. Rev. D*, 72:024028, 2005. doi: 10.1103/PhysRevD.72.024028.

[170] Matthew D. Duez, Yuk Tung Liu, Stuart L. Shapiro, and Masaru Shibata. Evolution of magnetized, differentially rotating neutron stars: Simulations in full general relativity. *Phys. Rev. D*, 73:104015, 2006. doi: 10.1103/PhysRevD.73.104015.

[171] Matthew D. Duez, Yuk Tung Liu, Stuart L. Shapiro, Masaru Shibata, and Branson C. Stephens. Collapse of magnetized hypermassive neutron stars in general relativity. *Phys. Rev. Lett.*, 96:031101, 2006. doi: 10.1103/PhysRevLett.96.031101.

[172] William E. East. Gravitational Waves from the Collision of Tidally Disrupted Stars with Massive Black Holes. *ApJ*, 795(2):135, November 2014. doi: 10.1088/0004-637X/795/2/135.

[173] William E. East. Superradiant instability of massive vector fields around spinning black holes in the relativistic regime. *Phys. Rev. D*, 96(2):024004, July 2017. doi: 10.1103/PhysRevD.96.024004.

[174] William E. East and Frans Pretorius. Simulating extreme-mass-ratio systems in full general relativity. *Phys. Rev. D*, 87(10):101502, May 2013. doi: 10.1103/PhysRevD.87.101502.

[175] William E. East and Frans Pretorius. Superradiant Instability and Backreaction of Massive Vector Fields around Kerr Black Holes. *Phys. Rev. Lett.*, 119(4):041101, July 2017. doi: 10.1103/PhysRevLett.119.041101.

[176] William E. East and Frans Pretorius. Binary neutron star mergers in Einstein-scalar-Gauss-Bonnet gravity. *Phys. Rev. D*, 106(10):104055, November 2022. doi: 10.1103/PhysRevD.106.104055.

[177] William E. East, Frans Pretorius, and Branson C. Stephens. Hydrodynamics in full general relativity with conservative adaptive mesh refinement. *Phys. Rev. D*, 85(12):124010, June 2012. doi: 10.1103/PhysRevD.85.124010.

[178] Pedro L. Espino, Vasileios Paschalidis, Thomas W. Baumgarte, and Stuart L. Shapiro. Dynamical stability of quasitoroidal differentially rotating neutron stars. *Phys. Rev. D*, 100(4):043014, August 2019. doi: 10.1103/PhysRevD.100.043014.

[179] Gilles Esposito-Farese. Motion in alternative theories of gravity. *Fundam. Theor. Phys.*, 162:461–489, 2011. doi: 10.1007/978-90-481-3015-3_17.

[180] Frank Estabrook, Hugo Wahlquist, Steven Christensen, Bryce Dewitt, Larry Smarr, and Elaine Tsiang. Maximally Slicing a Black Hole. *Phys. Rev. D*, 7(10):2814–2817, May 1973. doi: 10.1103/PhysRevD.7.2814.

[181] Zachariah B. Etienne, John G. Baker, Vasileios Paschalidis, Bernard J. Kelly, and Stuart L. Shapiro. Improved moving puncture gauge conditions for compact binary evolutions. *Phys. Rev. D*, 90(6):064032, September 2014. doi: 10.1103/PhysRevD.90.064032.

[182] Zachariah B. Etienne, Vasileios Paschalidis, Roland Haas, Philipp Mösta, and Stuart L. Shapiro. IllinoisGRMHD: an open-source, user-friendly GRMHD code for dynamical spacetimes. *Classical and Quantum Gravity*, 32(17):175009, September 2015. doi: 10.1088/0264-9381/32/17/175009.

[183] II Evans, C. R. *A method for numerical relativity: Simulation of axisymmetric gravitational collapse and gravitational radiation generation.* PhD thesis, University of Texas, Austin, January 1984.

[184] Matthew Evans et al. A Horizon Study for Cosmic Explorer: Science, Observatories, and Community. *arXiv:2109.09882*, 9 2021.

[185] Nicholas Farrow, Xing-Jiang Zhu, and Eric Thrane. The Mass Distribution of Galactic Double Neutron Stars. *ApJ*, 876(1):18, May 2019. doi: 10.3847/1538-4357/ab12e3.

[186] F. J. Fattoyev, J. Piekarewicz, and C. J. Horowitz. Neutron Skins and Neutron Stars in the Multimessenger Era. *Phys. Rev. Lett.*, 120(17):172702, April 2018. doi: 10.1103/PhysRevLett.120.172702.

[187] Marc Favata. Systematic parameter errors in inspiraling neutron star binaries. *Phys. Rev. Lett.*, 112:101101, 2014. doi: 10.1103/PhysRevLett.112.101101.

[188] Jacob Fields, Aviral Prakash, Matteo Breschi, David Radice, Sebastiano Bernuzzi, and André da Silva Schneider. Thermal Effects in Binary Neutron Star Mergers. *Astrophys. J. Lett.*, 952(2):L36, 2023. doi: 10.3847/2041-8213/ace5b2.

[189] A. Figura, J. J. Lu, G. F. Burgio, Z. H. Li, and H. J. Schulze. Hybrid equation of state approach in binary neutron-star merger simulations. *Phys. Rev. D*, 102(4):043006, 2020. doi: 10.1103/PhysRevD.102.043006.

[190] Leslie G. Fishbone. The Relativistic Roche Problem. I. Equilibrium Theory for a Body in Equatorial, Circular Orbit around a Kerr Black Hole. *ApJ*, 185:43–68, October 1973. doi: 10.1086/152395.

[191] Éanna É. Flanagan. REPLY TO COMMENT: The conformal frame freedom in theories of gravitation. *Classical and Quantum Gravity*, 21(15):3817–3829, August 2004. doi: 10.1088/0264-9381/21/15/N02.

[192] Eanna E. Flanagan and Tanja Hinderer. Constraining neutron star tidal Love numbers with gravitational wave detectors. *Phys. Rev. D*, 77:021502, 2008. doi: 10.1103/PhysRevD.77.021502.

[193] José A. Font, Tom Goodale, Sai Iyer, Mark Miller, Luciano Rezzolla, Edward Seidel, Nikolaos Stergioulas, Wai-Mo Suen, and Malcolm Tobias. Three-dimensional numerical general relativistic hydrodynamics. II. Long-term dynamics of single relativistic stars. *Phys. Rev. D*, 65(8):084024, April 2002. doi: 10.1103/PhysRevD.65.084024.

[194] Francois Foucart, Roland Haas, Matthew D. Duez, Evan O'Connor, Christian D. Ott, Luke Roberts, Lawrence E. Kidder, Jonas Lippuner, Harald P. Pfeiffer, and Mark A. Scheel. Low mass binary neutron star mergers: Gravitational waves and neutrino emission. *Phys. Rev. D*, 93(4):044019, February 2016. doi: 10.1103/PhysRevD.93.044019.

[195] Francois Foucart, Alexander Chernoglazov, Michael Boyle, Tanja Hinderer, Max Miller, Jordan Moxon, Mark A. Scheel, Nils Deppe, Matthew D. Duez, Francois Hébert, Lawrence E. Kidder, William Throwe, and Harald P. Pfeiffer. High-accuracy waveforms for black hole-neutron star systems with spinning black holes. *Phys. Rev. D*, 103(6):064007, March 2021. doi: 10.1103/PhysRevD.103.064007.

[196] Francois Foucart, Matthew D. Duez, Lawrence E. Kidder, Harald P. Pfeiffer, and Mark A. Scheel. Dynamical ejecta from binary neutron star mergers: Impact of a small residual eccentricity and of the equation of state implementation. *Phys. Rev. D*, 110(2):024003, July 2024. doi: 10.1103/PhysRevD.110.024003.

[197] Paulo C. C. Freire, Norbert Wex, Gilles Esposito-Farèse, Joris P. W. Verbiest, Matthew Bailes, Bryan A. Jacoby, Michael Kramer, Ingrid H. Stairs, John Antoniadis, and Gemma H. Janssen. The relativistic pulsar-white dwarf binary PSR J1738+0333 - II. The most stringent test of scalar-tensor gravity. *MNRAS*, 423(4):3328–3343, July 2012. doi: 10.1111/j.1365-2966.2012.21253.x.

[198] John L. Friedman, James R. Ipser, and Rafael D. Sorkin. Turning Point Method for Axisymmetric Stability of Rotating Relativistic Stars. *ApJ*, 325:722, February 1988. doi: 10.1086/166043.

[199] John L. Friedman, Koji Uryu, and Masaru Shibata. Thermodynamics of binary black holes and neutron stars. *Phys. Rev. D*, 65:064035, 2002. doi: 10.1103/PhysRevD.70.129904. [Erratum: Phys.Rev.D 70, 129904 (2004)].

[200] Sho Fujibayashi, Yuichiro Sekiguchi, Kenta Kiuchi, and Masaru Shibata. Properties of Neutrino-driven Ejecta from the Remnant of a Binary Neutron Star Merger: Pure Radiation Hydrodynamics Case. *ApJ*, 846(2):114, September 2017. doi: 10.3847/1538-4357/aa8039.

[201] Sho Fujibayashi, Masaru Shibata, Shinya Wanajo, Kenta Kiuchi, Koutarou Kyutoku, and Yuichiro Sekiguchi. Mass ejection from disks surrounding a low-mass black hole: Viscous neutrino-radiation hydrodynamics simulation in full general relativity. *Phys. Rev. D*, 101(8):083029, April 2020. doi: 10.1103/PhysRevD.101.083029.

[202] Sho Fujibayashi, Masaru Shibata, Shinya Wanajo, Kenta Kiuchi, Koutarou Kyutoku, and Yuichiro Sekiguchi. Viscous evolution of a massive disk surrounding stellar-mass black holes in full general relativity. *Phys. Rev. D*, 102(12):123014, December 2020. doi: 10.1103/PhysRevD.102.123014.

[203] Sho Fujibayashi, Shinya Wanajo, Kenta Kiuchi, Koutarou Kyutoku, Yuichiro Sekiguchi, and Masaru Shibata. Postmerger Mass Ejection of Low-mass Binary Neutron Stars. *ApJ*, 901(2):122, October 2020. doi: 10.3847/1538-4357/abafc2.

[204] Sho Fujibayashi, Koh Takahashi, Yuichiro Sekiguchi, and Masaru Shibata. Ultra-delayed Neutrino-driven Explosion of Rotating Massive-star Collapse. *ApJ*, 919(2):80, October 2021. doi: 10.3847/1538-4357/ac10cb.

[205] Sho Fujibayashi, Yuichiro Sekiguchi, Masaru Shibata, and Shinya Wanajo. Collapse of rotating massive stars leading to black hole formation and energetic supernovae. *arXiv e-prints*, art. arXiv:2212.03958, December 2022. doi: 10.48550/arXiv.2212.03958.

[206] Sho Fujibayashi, Kenta Kiuchi, Shinya Wanajo, Koutarou Kyutoku, Yuichiro Sekiguchi, and Masaru Shibata. Comprehensive Study of Mass Ejection and Nucleosynthesis in Binary Neutron Star Mergers Leaving Short-lived Massive Neutron Stars. *ApJ*, 942(1):39, January 2023. doi: 10.3847/1538-4357/ac9ce0.

[207] Sho Fujibayashi, Yuichiro Sekiguchi, Masaru Shibata, and Shinya Wanajo. Collapse of Rotating Massive Stars Leading to Black Hole Formation and Energetic Supernovae. *ApJ*, 956(2):100, October 2023. doi: 10.3847/1538-4357/acf5e5.

[208] Sho Fujibayashi, Cédric Jockel, Kyohei Kawaguchi, Yuichiro Sekiguchi, and Masaru Shibata. Powerful explosions from the collapse of rotating supermassive stars. *arXiv e-prints*, art. arXiv:2408.11572, August 2024. doi: 10.48550/arXiv.2408.11572.

[209] Sho Fujibayashi, Alan Tsz-Lok Lam, Masaru Shibata, and Yuichiro Sekiguchi. Supernovalike explosions of massive rotating stars from disks surrounding a black hole. *Phys. Rev. D*, 109(2):023031, January 2024. doi: 10.1103/PhysRevD.109.023031.

[210] Yuki Fujimoto, Kenji Fukushima, Kenta Hotokezaka, and Koutarou Kyutoku. Gravitational Wave Signal for Quark Matter with Realistic Phase Transition. *Phys. Rev. Lett.*, 130(9):091404, 2023. doi: 10.1103/PhysRevLett.130.091404.

[211] Jim Fuller and Wenbin Lu. The spins of compact objects born from helium stars in binary systems. *MNRAS*, 511(3):3951–3964, April 2022. doi: 10.1093/mnras/stac317.

[212] Emanuel Gafton and Stephan Rosswog. Tidal disruptions by rotating black holes: effects of spin and impact parameter. *MNRAS*, 487(4):4790–4808, August 2019. doi: 10.1093/mnras/stz1530.

[213] Filippo Galeazzi, Wolfgang Kastaun, Luciano Rezzolla, and José A. Font. Implementation of a simplified approach to radiative transfer in general relativity. *Phys. Rev. D*, 88(6):064009, September 2013. doi: 10.1103/PhysRevD.88.064009.

[214] Yong Gao, Kota Hayashi, Kenta Kiuchi, Alan Tsz-Lok Lam, Hao-Jui Kuan, and Masaru Shibata. Convective stability analysis of massive neutron stars formed in binary mergers. *arXiv e-prints*, art. arXiv:2501.19053, January 2025.

[215] Chao-Qiang Geng, Hao-Jui Kuan, and Ling-Wei Luo. Viable constraint on scalar field in scalar-tensor theory. *Classical and Quantum Gravity*, 37(11):115001, June 2020. doi: 10.1088/1361-6382/ab86fb.

[216] Chao-Qiang Geng, Hao-Jui Kuan, and Ling-Wei Luo. Inverse-chirp imprint of gravitational wave signals in scalar tensor theory. *European Physical Journal C*, 80(8):780, August 2020. doi: 10.1140/epjc/s10052-020-8359-y.

[217] Sebastian Gomez, Edo Berger, Matt Nicholl, Peter K. Blanchard, and Griffin Hosseinzadeh. Luminous Supernovae: Unveiling a Population between Superluminous and Normal Core-collapse Supernovae. *ApJ*, 941(2):107, December 2022. doi: 10.3847/1538-4357/ac9842.

[218] Dorota Gondek-Rosinska, Izabela Kowalska, Loic Villain, Marcus Ansorg, and Marcin Kucaba. A new view on the maximum mass of differentially rotating neutron stars. *Astrophys. J.*, 837(1):58, 2017. doi: 10.3847/1538-4357/aa56c1.

[219] Ore Gottlieb, Aretaios Lalakos, Omer Bromberg, Matthew Liska, and Alexander Tchekhovskoy. Black hole to breakout: 3D GRMHD simulations of collapsar jets reveal a wide range of transients. *Mon. Not. Roy. Astron. Soc.*, 510(4):4962–4975, 2022. doi: 10.1093/mnras/stab3784.

[220] Eric Gourgoulhon. An introduction to the theory of rotating relativistic stars. *arXiv e-prints*, art. arXiv:1003.5015, March 2010. doi: 10.48550/arXiv.1003.5015.

[221] Eric Gourgoulhon, Philippe Grandclément, Keisuke Taniguchi, Jean-Alain Marck, and Silvano Bonazzola. Quasiequilibrium sequences of synchronized and irrotational binary neutron stars in general relativity: Method and tests. *Phys. Rev. D*, 63(6):064029, March 2001. doi: 10.1103/PhysRevD.63.064029.

[222] James Guillochon and Enrico Ramirez-Ruiz. Hydrodynamical Simulations to Determine the Feeding Rate of Black Holes by the Tidal Disruption of Stars: The Importance of the Impact Parameter and Stellar Structure. *ApJ*, 767(1):25, April 2013. doi: 10.1088/0004-637X/767/1/25.

[223] Carsten Gundlach, Gioel Calabrese, Ian Hinder, and José M. Martín-García. Constraint damping in the Z4 formulation and harmonic gauge. *Classical and Quantum Gravity*, 22(17):3767-3773, September 2005. doi: 10.1088/0264-9381/22/17/025.

[224] Minghao Guo, Junjie Zhao, and Lijing Shao. Extended reduced-order surrogate models for scalar-tensor gravity in the strong field and applications to binary pulsars and gravitational waves. *Phys. Rev. D*, 104(10):104065, November 2021. doi: 10.1103/PhysRevD.104.104065.

[225] Roland Haas, Roman V. Shcherbakov, Tanja Bode, and Pablo Laguna. Tidal Disruptions of White Dwarfs from Ultra-close Encounters with Intermediate-mass Spinning Black Holes. *ApJ*, 749(2):117, April 2012. doi: 10.1088/0004-637X/749/2/117.

[226] Mark Hannam, Sascha Husa, Denis Pollney, Bernd Brügmann, and Niall Ó. Murchadha. Geometry and Regularity of Moving Punctures. *Phys. Rev. Lett.*, 99(24):241102, December 2007. doi: 10.1103/PhysRevLett.99.241102.

[227] Mark Hannam, Sascha Husa, Frank Ohme, Bernd Brügmann, and Niall Ó Murchadha. Wormholes and trumpets: Schwarzschild spacetime for the moving-puncture generation. *Phys. Rev. D*, 78(6):064020, September 2008. doi: 10.1103/PhysRevD.78.064020.

[228] Shamim Haque, Ritam Mallick, and Shashikesh Kumar Thakur. Effects of onset of phase transition on binary neutron star mergers. *Mon. Not. Roy. Astron. Soc.*, 527(4):11575–11586, 2023. doi: 10.1093/mnras/stad3839.

[229] Amiram Harten, Peter D. Lax, and Bram van Leer. On upstream differencing and godunov-type schemes for hyperbolic conservation laws. *SIAM Review*, 25(1):35–61, 1983. doi: 10.1137/1025002. URL `https://doi.org/10.1137/1025002`.

[230] S. W. Hawking. Black holes in the Brans-Dicke: Theory of gravitation. *Communications in Mathematical Physics*, 25(2):167–171, June 1972. doi: 10.1007/BF01877518.

[231] J. F. Hawley, L. L. Smarr, and J. R. Wilson. A numerical study of nonspherical black hole accretion. I Equations and test problems. *ApJ*, 277:296–311, February 1984. doi: 10.1086/161696.

[232] John F. Hawley, Sherwood A. Richers, Xiaoyue Guan, and Julian H. Krolik. Testing Convergence for Global Accretion Disks. *Astrophys. J.*, 772:102, 2013. doi: 10.1088/0004-637X/772/2/102.

[233] Kota Hayashi, Kyohei Kawaguchi, Kenta Kiuchi, Koutarou Kyutoku, and Masaru Shibata. Properties of the remnant disk and the dynamical ejecta produced in low-mass black hole-neutron star mergers. *Phys. Rev. D*, 103(4):043007, February 2021. doi: 10.1103/PhysRevD.103.043007.

[234] Kota Hayashi, Sho Fujibayashi, Kenta Kiuchi, Koutarou Kyutoku, Yuichiro Sekiguchi, and Masaru Shibata. General-relativistic neutrino-radiation magnetohydrodynamic simulation of seconds-long black hole-neutron star mergers. *Phys. Rev. D*, 106(2):023008, July 2022. doi: 10.1103/PhysRevD.106.023008.

[235] James Healy, Tanja Bode, Roland Haas, Enrique Pazos, Pablo Laguna, Deirdre M. Shoemaker, and Nicolás Yunes. Late inspiral and merger of binary black holes in scalar-tensor theories of gravity. *Classical and Quantum Gravity*, 29(23):232002, December 2012. doi: 10.1088/0264-9381/29/23/232002.

[236] Loren E. Held and Henrik N. Latter. Hydrodynamic convection in accretion discs. *MNRAS*, 480(4):4797–4816, November 2018. doi: 10.1093/mnras/sty2097.

[237] Loren E. Held and George Mamatsashvili. MRI turbulence in accretion discs at large magnetic Prandtl numbers. *Mon. Not. Roy. Astron. Soc.*, 517(2):2309–2330, 2022. doi: 10.1093/mnras/stac2656.

[238] S. Hild et al. Sensitivity Studies for Third-Generation Gravitational Wave Observatories. *Class. Quant. Grav.*, 28:094013, 2011. doi: 10.1088/0264-9381/28/9/094013.

[239] David Hilditch, Sebastiano Bernuzzi, Marcus Thierfelder, Zhoujian Cao, Wolfgang Tichy, and Bernd Brügmann. Compact binary evolutions with the Z4c formulation. *Phys. Rev. D*, 88(8):084057, October 2013. doi: 10.1103/PhysRevD.88.084057.

[240] J. G. Hills. Possible power source of Seyfert galaxies and QSOs. *Nature*, 254(5498):295–298, March 1975. doi: 10.1038/254295a0.

[241] Tanja Hinderer. Tidal Love numbers of neutron stars. *Astrophys. J.*, 677:1216–1220, 2008. doi: 10.1086/533487. [Erratum: Astrophys.J. 697, 964 (2009)].

[242] Kenta Hotokezaka, Koutarou Kyutoku, Hirotada Okawa, Masaru Shibata, and Kenta Kiuchi. Binary neutron star mergers: Dependence on the nuclear equation of state. *Phys. Rev. D*, 83(12):124008, June 2011. doi: 10.1103/PhysRevD.83.124008.

[243] Kenta Hotokezaka, Kenta Kiuchi, Koutarou Kyutoku, Takayuki Muranushi, Yu-ichiro Sekiguchi, Masaru Shibata, and Keisuke Taniguchi. Remnant massive neutron stars of binary neutron star mergers: Evolution process and gravitational waveform. *Phys. Rev. D*, 88(4):044026, August 2013. doi: 10.1103/PhysRevD.88.044026.

[244] Kenta Hotokezaka, Kenta Kiuchi, Koutarou Kyutoku, Hirotada Okawa, Yu-ichiro Sekiguchi, Masaru Shibata, and Keisuke Taniguchi. Mass ejection from the merger of binary neutron stars. *Phys. Rev. D*, 87(2):024001, January 2013. doi: 10.1103/PhysRevD.87.024001.

[245] Kenta Hotokezaka, Koutarou Kyutoku, and Masaru Shibata. Exploring tidal effects of coalescing binary neutron stars in numerical relativity. *Phys. Rev. D*, 87(4):044001, February 2013. doi: 10.1103/PhysRevD.87.044001.

[246] Kenta Hotokezaka, Koutarou Kyutoku, Hirotada Okawa, and Masaru Shibata. Exploring tidal effects of coalescing binary neutron stars in numerical relativity. II. Long-term simulations. *Phys. Rev. D*, 91(6):064060, 2015. doi: 10.1103/PhysRevD.91.064060.

[247] Kenta Hotokezaka, Koutarou Kyutoku, Yu-ichiro Sekiguchi, and Masaru Shibata. Measurability of the tidal deformability by gravitational waves from coalescing binary neutron stars. *Phys. Rev. D*, 93(6):064082, 2016. doi: 10.1103/PhysRevD.93.064082.

[248] Zexin Hu, Yong Gao, Rui Xu, and Lijing Shao. Scalarized neutron stars in massive scalar-tensor gravity: X-ray pulsars and tidal deformability. *Phys. Rev. D*, 104(10):104014, November 2021. doi: 10.1103/PhysRevD.104.104014.

[249] Yong-Jia Huang, Luca Baiotti, Toru Kojo, Kentaro Takami, Hajime Sotani, Hajime Togashi, Tetsuo Hatsuda, Shigehiro Nagataki, and Yi-Zhong Fan. Merger and Postmerger of Binary Neutron Stars with a Quark-Hadron Crossover Equation of State. *Phys. Rev. Lett.*, 129(18):181101, 2022. doi: 10.1103/PhysRevLett.129.181101.

[250] Jason D. Immerman and Thomas W. Baumgarte. Trumpet-puncture initial data for black holes. *Phys. Rev. D*, 80(6):061501, September 2009. doi: 10.1103/PhysRevD.80.061501.

[251] Panagiotis Iosif and Nikolaos Stergioulas. Equilibrium sequences of differentially rotating stars with post-merger-like rotational profiles. *MNRAS*, 503(1):850–866, May 2021. doi: 10.1093/mnras/stab392.

[252] Panagiotis Iosif and Nikolaos Stergioulas. Models of binary neutron star remnants with tabulated equations of state. *MNRAS*, 510(2):2948–2967, February 2022. doi: 10.1093/mnras/stab3565.

[253] James A. Isenberg. Waveless Approximation Theories of Gravity. *International Journal of Modern Physics D*, 17(2):265–273, January 2008. doi: 10.1142/S0218271808011997.

[254] Masaki Ishii, Masaru Shibata, and Yasushi Mino. Black hole tidal problem in the Fermi normal coordinates. *Phys. Rev. D*, 71(4):044017, February 2005. doi: 10.1103/PhysRevD.71.044017.

[255] Tamanna Jain, Piero Rettegno, Michalis Agathos, Alessandro Nagar, and Lorenzo Turco. Effective-one-body Hamiltonian in scalar-tensor gravity at third post-Newtonian order. *Phys. Rev. D*, 107(8):084017, April 2023. doi: 10.1103/PhysRevD.107.084017.

[256] H. Th. Janka, Th. Zwerger, and R. Moenchmeyer. Does artificial viscosity destroy prompt type-II supernova explosions? *A&A*, 268(1):360–368, February 1993.

[257] Hans-Thomas Janka. Explosion Mechanisms of Core-Collapse Supernovae. *Annual Review of Nuclear and Particle Science*, 62(1):407–451, November 2012. doi: 10.1146/annurev-nucl-102711-094901.

[258] J. T. Jebsen. On the general spherically symmetric solutions of Einstein's gravitational equations in vacuo. *General Relativity and Gravitation*, 37(12):2253–2259, December 2005. doi: 10.1007/s10714-005-0168-y.

[259] P. Jordan. Zum gegenwärtigen Stand der Diracschen kosmologischen Hypothesen. *Zeitschrift fur Physik*, 157 (1):112–121, February 1959. doi: 10.1007/BF01375155.

[260] Félix-Louis Julié, Vishal Baibhav, Emanuele Berti, and Alessandra Buonanno. Third post-Newtonian effective-one-body Hamiltonian in scalar-tensor and Einstein-scalar-Gauss-Bonnet gravity. *Phys. Rev. D*, 107(10):104044, 2023. doi: 10.1103/PhysRevD.107.104044.

[261] O. Just, M. A. Aloy, M. Obergaulinger, and S. Nagataki. r-process Viable Outflows are Suppressed in Global Alpha-viscosity Models of Collapsar Disks. *Astrophys. J. Lett.*, 934(2):L30, August 2022. doi: 10.3847/2041-8213/ac83a1.

[262] J. D. Kaplan, C. D. Ott, E. P. O'Connor, K. Kiuchi, L. Roberts, and M. Duez. The Influence of Thermal Pressure on Equilibrium Models of Hypermassive Neutron Star Merger Remnants. *ApJ*, 790(1):19, July 2014. doi: 10.1088/0004-637X/790/1/19.

[263] Kazumi Kashiyama and Eliot Quataert. Fast Luminous Blue Transients from Newborn Black Holes. *Mon. Not. Roy. Astron. Soc.*, 451(3):2656–2662, 2015. doi: 10.1093/mnras/stv1164.

[264] Rahul Kashyap, Abhishek Das, David Radice, Surendra Padamata, Aviral Prakash, Domenico Logoteta, Albino Perego, Daniel A. Godzieba, Sebastiano Bernuzzi, Ignazio Bombaci, Farrukh J. Fattoyev, Brendan T. Reed, and André da Silva Schneider. Numerical relativity simulations of prompt collapse mergers: Threshold mass and phenomenological constraints on neutron star properties after GW170817. *Phys. Rev. D*, 105(10):103022, May 2022. doi: 10.1103/PhysRevD.105.103022.

[265] M. M. Kasliwal et al. Illuminating gravitational waves: A concordant picture of photons from a neutron star merger. *Science*, 358(6370):1559–1565, December 2017. doi: 10.1126/science.aap9455.

[266] Wolfgang Kastaun and Filippo Galeazzi. Properties of hypermassive neutron stars formed in mergers of spinning binaries. *Phys. Rev. D*, 91(6):064027, March 2015. doi: 10.1103/PhysRevD.91.064027.

[267] Kyohei Kawaguchi, Masaru Shibata, and Masaomi Tanaka. Diversity of Kilonova Light Curves. *ApJ*, 889(2): 171, February 2020. doi: 10.3847/1538-4357/ab61f6.

[268] Kyohei Kawaguchi, Sho Fujibayashi, Nanae Domoto, Kenta Kiuchi, Masaru Shibata, and Shinya Wanajo. Kilonovae of binary neutron star mergers leading to short-lived remnant neutron star formation. *arXiv e-prints*, art. arXiv:2306.06961, June 2023. doi: 10.48550/arXiv.2306.06961.

[269] R. Keppens, Z. Meliani, A. J. van Marle, P. Delmont, A. Vlasis, and B. van der Holst. Parallel, grid-adaptive approaches for relativistic hydro and magnetohydrodynamics. *Journal of Computational Physics*, 231(3):718–744, February 2012. doi: 10.1016/j.jcp.2011.01.020.

[270] Mohammed Khalil, Noah Sennett, Jan Steinhoff, and Alessandra Buonanno. Theory-agnostic framework for dynamical scalarization of compact binaries. *Phys. Rev. D*, 100(12):124013, December 2019. doi: 10.1103/PhysRevD.100.124013.

[271] Mohammed Khalil, Raissa F. P. Mendes, Néstor Ortiz, and Jan Steinhoff. Effective-action model for dynamical scalarization beyond the adiabatic approximation. *Phys. Rev. D*, 106(10):104016, November 2022. doi: 10.1103/PhysRevD.106.104016.

[272] David K. Khatami and Daniel N. Kasen. Physics of Luminous Transient Light Curves: A New Relation between Peak Time and Luminosity. *ApJ*, 878(1):56, June 2019. doi: 10.3847/1538-4357/ab1f09.

[273] A. Khokhlov, I. D. Novikov, and C. J. Pethick. Weak Tidal Encounters of a Star with a Massive Black Hole. *ApJ*, 418:163, November 1993. doi: 10.1086/173379.

[274] Andrew King. Quasi-periodic eruptions from galaxy nuclei. *MNRAS*, 515(3):4344–4349, September 2022. doi: 10.1093/mnras/stac1641.

[275] Kenta Kiuchi, Masaru Shibata, and Shijun Yoshida. Evolution of neutron stars with toroidal magnetic fields: Axisymmetric simulation in full general relativity. *Phys. Rev. D*, 78(2):024029, July 2008. doi: 10.1103/PhysRevD.78.024029.

[276] Kenta Kiuchi, Yuichiro Sekiguchi, Masaru Shibata, and Keisuke Taniguchi. Long-term general relativistic simulation of binary neutron stars collapsing to a black hole. *Phys. Rev. D*, 80(6):064037, September 2009. doi: 10.1103/PhysRevD.80.064037.

[277] Kenta Kiuchi, Yuichiro Sekiguchi, Masaru Shibata, and Keisuke Taniguchi. Exploring Binary-Neutron-Star-Merger Scenario of Short-Gamma-Ray Bursts by Gravitational-Wave Observation. *Phys. Rev. Lett.*, 104(14): 141101, April 2010. doi: 10.1103/PhysRevLett.104.141101.

[278] Kenta Kiuchi, Kyohei Kawaguchi, Koutarou Kyutoku, Yuichiro Sekiguchi, Masaru Shibata, and Keisuke Taniguchi. Sub-radian-accuracy gravitational waveforms of coalescing binary neutron stars in numerical relativity. *Phys. Rev. D*, 96(8):084060, October 2017. doi: 10.1103/PhysRevD.96.084060.

[279] Kenta Kiuchi, Koutarou Kyutoku, Yuichiro Sekiguchi, and Masaru Shibata. Global simulations of strongly magnetized remnant massive neutron stars formed in binary neutron star mergers. *Phys. Rev. D*, 97(12): 124039, Jun 2018. doi: 10.1103/PhysRevD.97.124039.

[280] Kenta Kiuchi, Kyohei Kawaguchi, Koutarou Kyutoku, Yuichiro Sekiguchi, and Masaru Shibata. Sub-radian-accuracy gravitational waves from coalescing binary neutron stars in numerical relativity. II. Systematic study on the equation of state, binary mass, and mass ratio. *Phys. Rev. D*, 101(8):084006, April 2020. doi: 10.1103/PhysRevD.101.084006.

[281] Kenta Kiuchi, Loren E. Held, Yuichiro Sekiguchi, and Masaru Shibata. Implementation of advanced Riemann solvers in a neutrino-radiation magnetohydrodynamics code in numerical relativity and its application to a binary neutron star merger. *Phys. Rev. D*, 106(12):124041, December 2022. doi: 10.1103/PhysRevD.106.124041.

[282] Kostas. D. Kokkotas and Johannes Ruoff. Radial oscillations of relativistic stars. *Astron. Astrophys.*, 366:565, 2001. doi: 10.1051/0004-6361:20000216.

[283] Hidemi Komatsu, Yoshiharu Eriguchi, and Izumi Hachisu. Rapidly rotating general relativistic stars. I - Numerical method and its application to uniformly rotating polytropes. *MNRAS*, 237:355–379, March 1989. doi: 10.1093/mnras/237.2.355.

[284] Hidemi Komatsu, Yoshiharu Eriguchi, and Izumi Hachisu. Rapidly rotating general relativistic stars. II - Differentially rotating polytropes. *MNRAS*, 239:153–171, July 1989. doi: 10.1093/mnras/239.1.153.

[285] S. S. Komissarov. Electrodynamics of black hole magnetospheres. *Mon. Not. Roy. Astron. Soc.*, 350:407, 2004. doi: 10.1111/j.1365-2966.2004.07446.x.

[286] Sven Köppel, Luke Bovard, and Luciano Rezzolla. A General-relativistic Determination of the Threshold Mass to Prompt Collapse in Binary Neutron Star Mergers. *ApJ*, 872(1):L16, February 2019. doi: 10.3847/2041-8213/ab0210.

[287] M. Kramer et al. Strong-Field Gravity Tests with the Double Pulsar. *Physical Review X*, 11(4):041050, October 2021. doi: 10.1103/PhysRevX.11.041050.

[288] William Krivan and Richard H. Price. Initial data for superposed rotating black holes. *Phys. Rev. D*, 58(10): 104003, November 1998. doi: 10.1103/PhysRevD.58.104003.

[289] Christian J. Krüger and Daniela D. Doneva. Oscillation dynamics of scalarized neutron stars. *Phys. Rev. D*, 103(12):124034, June 2021. doi: 10.1103/PhysRevD.103.124034.

[290] Hao-Jui Kuan, Daniela D. Doneva, and Stoytcho S. Yazadjiev. Dynamical Formation of Scalarized Black Holes and Neutron Stars through Stellar Core Collapse. *Phys. Rev. Lett.*, 127(16):161103, October 2021. doi: 10.1103/PhysRevLett.127.161103.

[291] Hao-Jui Kuan, Jasbir Singh, Daniela D. Doneva, Stoytcho S. Yazadjiev, and Kostas D. Kokkotas. Nonlinear evolution and nonuniqueness of scalarized neutron stars. *Phys. Rev. D*, 104(12):124013, December 2021. doi: 10.1103/PhysRevD.104.124013.

[292] Hao-Jui Kuan, Arthur G. Suvorov, Daniela D. Doneva, and Stoytcho S. Yazadjiev. Gravitational Waves from Accretion-Induced Descalarization in Massive Scalar-Tensor Theory. *Phys. Rev. Lett.*, 129(12):121104, September 2022. doi: 10.1103/PhysRevLett.129.121104.

[293] Hao-Jui Kuan, Alan Tsz-Lok Lam, Daniela D. Doneva, Stoytcho S. Yazadjiev, Masaru Shibata, and Kenta Kiuchi. Dynamical scalarization during neutron star mergers in scalar-Gauss-Bonnet theory. *Phys. Rev. D*, 108 (6):063033, September 2023. doi: 10.1103/PhysRevD.108.063033.

[294] Hao-Jui Kuan, Karim Van Aelst, Alan Tsz-Lok Lam, and Masaru Shibata. Binary neutron star mergers in massive scalar-tensor theory: Quasiequilibrium states and dynamical enhancement of the scalarization. *Phys. Rev. D*, 108(6):064057, September 2023. doi: 10.1103/PhysRevD.108.064057.

[295] Hao-Jui Kuan, Kenta Kiuchi, and Masaru Shibata. Tidal Resonance in Binary Neutron Star Inspirals: A High-Precision Study in Numerical Relativity. *arXiv e-prints*, art. arXiv:2411.16850, November 2024. doi: 10.48550/arXiv.2411.16850.

[296] Pawan Kumar and Eliot J. Quataert. On the Orbital Decay of the PSR J0045-7319 Binary. *ApJ*, 493(1): 412–425, January 1998. doi: 10.1086/305091.

[297] Alexander Kurganov and Eitan Tadmor. New High-Resolution Central Schemes for Nonlinear Conservation Laws and Convection-Diffusion Equations. *Journal of Computational Physics*, 160(1):241–282, May 2000. doi: 10.1006/jcph.2000.6459.

[298] Takami Kuroda and Masaru Shibata. Spontaneous scalarization as a new core-collapse supernova mechanism and its multimessenger signals. *Phys. Rev. D*, 107(10):103025, May 2023. doi: 10.1103/PhysRevD.107.103025.

[299] Takami Kuroda, Kei Kotake, and Tomoya Takiwaki. Fully General Relativistic Simulations of Core-collapse Supernovae with an Approximate Neutrino Transport. *ApJ*, 755(1):11, August 2012. doi: 10.1088/0004-637X/755/1/11.

[300] Koutarou Kyutoku, Masaru Shibata, and Keisuke Taniguchi. Reducing orbital eccentricity in initial data of binary neutron stars. *Phys. Rev. D*, 90(6):064006, September 2014. doi: 10.1103/PhysRevD.90.064006.

[301] Benjamin D. Lackey, Mohit Nayyar, and Benjamin J. Owen. Observational constraints on hyperons in neutron stars. *Phys. Rev. D*, 73(2):024021, January 2006. doi: 10.1103/PhysRevD.73.024021.

[302] Pablo Laguna, Warner A. Miller, and Wojciech H. Zurek. Smoothed Particle Hydrodynamics near a Black Hole. *ApJ*, 404:678, February 1993. doi: 10.1086/172321.

[303] Alan Tsz-Lok Lam and Masaru Shibata. New axisymmetric general relativistic hydrodynamics code with fixed mesh refinement. *Phys. Rev. D*, 111(10):103039, May 2025. doi: 10.1103/PhysRevD.111.103039.

[304] Alan Tsz-Lok Lam, Masaru Shibata, and Kenta Kiuchi. Numerical-relativity simulation for tidal disruption of white dwarfs by a supermassive black hole. *Phys. Rev. D*, 107(4):043033, February 2023. doi: 10.1103/PhysRevD.107.043033.

[305] Alan Tsz-Lok Lam, Hao-Jui Kuan, Masaru Shibata, Karim Van Aelst, and Kenta Kiuchi. Binary neutron star mergers in massive scalar-tensor theory: Properties of postmerger remnants. *Phys. Rev. D*, 110(10):104018, November 2024. doi: 10.1103/PhysRevD.110.104018.

[306] Alan Tsz-Lok Lam, Yong Gao, Hao-Jui Kuan, Masaru Shibata, Karim Van Aelst, and Kenta Kiuchi. Accessing Universal Relations of Binary Neutron Star Waveforms in Massive Scalar-Tensor Theory. *Phys. Rev. Lett.*, 134 (15):151402, April 2025. doi: 10.1103/PhysRevLett.134.151402.

[307] Alan Tsz-Lok Lam, Kalin V. Staykov, Hao-Jui Kuan, Daniela D. Doneva, and Stoytcho S. Yazadjiev. Axisymmetric stability of neutron stars as extreme rotators in massive scalar-tensor theory. *Phys. Rev. D*, 111(10): 104030, May 2025. doi: 10.1103/PhysRevD.111.104030.

[308] Shu Yan Lau and Kent Yagi. Probing hybrid stars with gravitational waves via interfacial modes. *Phys. Rev. D*, 103(6):063015, 2021. doi: 10.1103/PhysRevD.103.063015.

[309] David L. Lee. Conservation laws, gravitational waves, and mass losses in the Dicke-Brans-Jordan theory of gravity. *Phys. Rev. D*, 10(8):2374–2383, October 1974. doi: 10.1103/PhysRevD.10.2374.

[310] A. Lichnerowicz. *Theories relativistes de la gravitation et de l'electromagnetisme. Relativite generale et theories unitaires*. 1955.

[311] Steven L. Liebling, Carlos Palenzuela, and Luis Lehner. Effects of High Density Phase Transitions on Neutron Star Dynamics. *Class. Quant. Grav.*, 38(11):115007, 2021. doi: 10.1088/1361-6382/abf898.

[312] Yeunhwan Lim and Jeremy W. Holt. Neutron star tidal deformabilities constrained by nuclear theory and experiment. *Phys. Rev. Lett.*, 121(6):062701, 2018. doi: 10.1103/PhysRevLett.121.062701.

[313] Itai Linial and Re'em Sari. Unstable Mass Transfer from a Main-Sequence Star to a Supermassive Black Hole and Quasi-Periodic Eruptions. 11 2022.

[314] Georgios Lioutas, Andreas Bauswein, and Nikolaos Stergioulas. Frequency deviations in universal relations of isolated neutron stars and postmerger remnants. *Phys. Rev. D*, 104(4):043011, 2021. doi: 10.1103/PhysRevD.104.043011.

[315] Yuk Tung Liu, Stuart L. Shapiro, and Branson C. Stephens. Magnetorotational collapse of very massive stars to black holes in full general relativity. *Phys. Rev. D*, 76(8):084017, October 2007. doi: 10.1103/PhysRevD.76.084017.

[316] Yuk Tung Liu, Zachariah B. Etienne, and Stuart L. Shapiro. Evolution of near-extremal-spin black holes using the moving puncture technique. *Phys. Rev. D*, 80(12):121503, December 2009. doi: 10.1103/PhysRevD.80.121503.

[317] Carlos O. Lousto, Hiroyuki Nakano, Yosef Zlochower, and Manuela Campanelli. Intermediate-mass-ratio black hole binaries: Intertwining numerical and perturbative techniques. *Phys. Rev. D*, 82(10):104057, November 2010. doi: 10.1103/PhysRevD.82.104057.

[318] Wenbin Lu and Eliot Quataert. Quasi-periodic eruptions from mildly eccentric unstable mass transfer in galactic nuclei. 10 2022.

[319] Jose Luis Blázquez-Salcedo, Fech Scen Khoo, and Jutta Kunz. Ultra-long-lived quasi-normal modes of neutron stars in massive scalar-tensor gravity. *EPL (Europhysics Letters)*, 130(5):50002, June 2020. doi: 10.1209/0295-5075/130/50002.

[320] J. P. Luminet and B. Carter. Dynamics of an Affine Star Model in a Black Hole Tidal Field. *ApJS*, 61:219, June 1986. doi: 10.1086/191113.

[321] J. P. Luminet and J. A. Marck. Tidal squeezing of stars by Schwarzschild black holes. *MNRAS*, 212:57–75, January 1985. doi: 10.1093/mnras/212.1.57.

[322] J. D. Lyman, D. Bersier, P. A. James, P. A. Mazzali, J. J. Eldridge, M. Fraser, and E. Pian. Bolometric light curves and explosion parameters of 38 stripped-envelope core-collapse supernovae. *MNRAS*, 457(1):328–350, March 2016. doi: 10.1093/mnras/stv2983.

[323] Sizheng Ma, Vijay Varma, Leo C. Stein, Francois Foucart, Matthew D. Duez, Lawrence E. Kidder, Harald P. Pfeiffer, and Mark A. Scheel. Numerical simulations of black hole-neutron star mergers in scalar-tensor gravity. *Phys. Rev. D*, 107(12):124051, June 2023. doi: 10.1103/PhysRevD.107.124051.

[324] Morgan MacLeod, Jacqueline Goldstein, Enrico Ramirez-Ruiz, James Guillochon, and Johan Samsing. Illuminating Massive Black Holes with White Dwarfs: Orbital Dynamics and High-energy Transients from Tidal Interactions. *ApJ*, 794(1):9, October 2014. doi: 10.1088/0004-637X/794/1/9.

[325] Kate Maguire, Michael Eracleous, Peter G. Jonker, Morgan MacLeod, and Stephan Rosswog. Tidal Disruptions of White Dwarfs: Theoretical Models and Observational Prospects. *Space Sci. Rev.*, 216(3):39, March 2020. doi: 10.1007/s11214-020-00661-2.

[326] Deborah Mainetti, Alessandro Lupi, Sergio Campana, Monica Colpi, Eric R. Coughlin, James Guillochon, and Enrico Ramirez-Ruiz. The fine line between total and partial tidal disruption events. *A&A*, 600:A124, April 2017. doi: 10.1051/0004-6361/201630092.

[327] J. A. Marck. Solution to the Equations of Parallel Transport in Kerr Geometry; Tidal Tensor. *Proceedings of the Royal Society of London Series A*, 385(1789):431–438, February 1983. doi: 10.1098/rspa.1983.0021.

[328] P. Marronetti, W. Tichy, B. Brügmann, J. González, and U. Sperhake. High-spin binary black hole mergers. *Phys. Rev. D*, 77(6):064010, March 2008. doi: 10.1103/PhysRevD.77.064010.

[329] Jose Maria Martí and Ewald Müller. Numerical Hydrodynamics in Special Relativity. *Living Reviews in Relativity*, 2(1):3, December 1999. doi: 10.12942/lrr-1999-3.

[330] Andrea Maselli, Vitor Cardoso, Valeria Ferrari, Leonardo Gualtieri, and Paolo Pani. Equation-of-state-independent relations in neutron stars. *Phys. Rev. D*, 88(2):023007, 2013. doi: 10.1103/PhysRevD.88.023007.

[331] Ajit Kumar Mehta, Alessandra Buonanno, Roberto Cotesta, Abhirup Ghosh, Noah Sennett, and Jan Steinhoff. Tests of general relativity with gravitational-wave observations using a flexible theory-independent method. *Phys. Rev. D*, 107(4):044020, February 2023. doi: 10.1103/PhysRevD.107.044020.

[332] Raissa F. P. Mendes and Néstor Ortiz. Highly compact neutron stars in scalar-tensor theories of gravity: Spontaneous scalarization versus gravitational collapse. *Phys. Rev. D*, 93(12):124035, June 2016. doi: 10.1103/PhysRevD.93.124035.

[333] Raissa F. P. Mendes and Néstor Ortiz. New Class of Quasinormal Modes of Neutron Stars in Scalar-Tensor Gravity. *Phys. Rev. Lett.*, 120(20):201104, May 2018. doi: 10.1103/PhysRevLett.120.201104.

[334] Raissa F. P. Mendes, Néstor Ortiz, and Nikolaos Stergioulas. Nonlinear dynamics of oscillating neutron stars in scalar-tensor gravity. *Phys. Rev. D*, 104(10):104036, 2021. doi: 10.1103/PhysRevD.104.104036.

[335] Brian D. Metzger, Nicholas C. Stone, and Shmuel Gilbaum. Interacting Stellar EMRIs as Sources of Quasi-periodic Eruptions in Galactic Nuclei. *Astrophys. J.*, 926(1):101, 2022. doi: 10.3847/1538-4357/ac3ee1.

[336] A. Mignone and G. Bodo. An HLLC Riemann solver for relativistic flows - I. Hydrodynamics. *MNRAS*, 364(1): 126–136, November 2005. doi: 10.1111/j.1365-2966.2005.09546.x.

[337] A. Mignone, M. Ugliano, and G. Bodo. A five-wave Harten-Lax-van Leer Riemann solver for relativistic magnetohydrodynamics. *MNRAS*, 393(4):1141–1156, March 2009. doi: 10.1111/j.1365-2966.2008.14221.x.

[338] August J. Miller and Thomas W. Baumgarte. Bondi accretion in trumpet geometries. *Classical and Quantum Gravity*, 34(3):035007, February 2017. doi: 10.1088/1361-6382/aa51fe.

[339] Miquel Miravet-Tenés, Davide Guerra, Milton Ruiz, Pablo Cerdá-Durán, and José A. Font. Identifying thermal effects in neutron star merger remnants with model-agnostic waveform reconstructions and third-generation detectors. *arXiv:2401.02493*, 1 2024.

[340] Pedro J. Montero, José A. Font, and Masaru Shibata. Nada: A new code for studying self-gravitating tori around black holes. *Phys. Rev. D*, 78(6):064037, September 2008. doi: 10.1103/PhysRevD.78.064037.

[341] Pedro J. Montero, José A. Font, and Masaru Shibata. Influence of Self-Gravity on the Runaway Instability of Black-Hole-Torus Systems. *Phys. Rev. Lett.*, 104(19):191101, May 2010. doi: 10.1103/PhysRevLett.104.191101.

[342] Pedro J. Montero, Hans-Thomas Janka, and Ewald Müller. Relativistic Collapse and Explosion of Rotating Supermassive Stars with Thermonuclear Effects. *ApJ*, 749(1):37, April 2012. doi: 10.1088/0004-637X/749/1/37.

[343] Pedro J. Montero, Thomas W. Baumgarte, and Ewald Müller. General relativistic hydrodynamics in curvilinear coordinates. *Phys. Rev. D*, 89(8):084043, April 2014. doi: 10.1103/PhysRevD.89.084043.

[344] E. R. Most, L. Jens Papenfort, and L. Rezzolla. Beyond second-order convergence in simulations of magnetized binary neutron stars with realistic microphysics. *MNRAS*, 490(3):3588–3600, December 2019. doi: 10.1093/mnras/stz2809.

[345] Elias R. Most, L. Jens Papenfort, Veronica Dexheimer, Matthias Hanauske, Stefan Schramm, Horst Stöcker, and Luciano Rezzolla. Signatures of quark-hadron phase transitions in general-relativistic neutron-star mergers. *Phys. Rev. Lett.*, 122(6):061101, 2019. doi: 10.1103/PhysRevLett.122.061101.

[346] Nishad Muhammed, Matthew D. Duez, Pavan Chawhan, Noora Ghadiri, Luisa T. Buchman, Francois Foucart, Patrick Chi-Kit Cheong, Lawrence E. Kidder, Harald P. Pfeiffer, and Mark A. Scheel. Stability of hypermassive neutron stars with realistic rotation and entropy profiles. *arXiv e-prints*, art. arXiv:2403.05642, March 2024. doi: 10.48550/arXiv.2403.05642.

[347] H. Müther, M. Prakash, and T. L. Ainsworth. The nuclear symmetry energy in relativistic Brueckner-Hartree-Fock calculations. *Physics Letters B*, 199(4):469–474, December 1987. doi: 10.1016/0370-2693(87)91611-X.

[348] Philipp Mösta, Bruno C Mundim, Joshua A Faber, Roland Haas, Scott C Noble, Tanja Bode, Frank Löffler, Christian D Ott, Christian Reisswig, and Erik Schnetter. Grhydro: a new open-source general-relativistic magnetohydrodynamics code for the einstein toolkit. *Classical and Quantum Gravity*, 31(1):015005, nov 2013. doi: 10.1088/0264-9381/31/1/015005. URL `https://dx.doi.org/10.1088/0264-9381/31/1/015005`.

[349] T. Nakamura, K. Oohara, and Y. Kojima. General Relativistic Collapse to Black Holes and Gravitational Waves from Black Holes. *Progress of Theoretical Physics Supplement*, 90:1–218, January 1987. doi: 10.1143/PTPS.90.1.

[350] Hiroyuki Nakano. A note on gravitational wave extraction from binary simulations. *Classical and Quantum Gravity*, 32(17):177002, September 2015. doi: 10.1088/0264-9381/32/17/177002.

[351] Hiroyuki Nakano, James Healy, Carlos O. Lousto, and Yosef Zlochower. Perturbative extraction of gravitational waveforms generated with numerical relativity. *Phys. Rev. D*, 91(10):104022, May 2015. doi: 10.1103/PhysRevD.91.104022.

[352] Vsevolod Nedora, Federico Schianchi, Sebastiano Bernuzzi, David Radice, Boris Daszuta, Andrea Endrizzi, Albino Perego, Aviral Prakash, and Francesco Zappa. Mapping dynamical ejecta and disk masses from numerical relativity simulations of neutron star mergers. *Classical and Quantum Gravity*, 39(1):015008, January 2022. doi: 10.1088/1361-6382/ac35a8.

[353] Ezra Newman and Roger Penrose. An Approach to Gravitational Radiation by a Method of Spin Coefficients. *Journal of Mathematical Physics*, 3(3):566–578, May 1962. doi: 10.1063/1.1724257.

[354] Harry Ho-Yin Ng, Jin-Liang Jiang, Carlo Musolino, Christian Ecker, Samuel D. Tootle, and Luciano Rezzolla. Hybrid approach to long-term binary neutron-star simulations. *Phys. Rev. D*, 109(6):064061, March 2024. doi: 10.1103/PhysRevD.109.064061.

[355] M. Obergaulinger and M. Á. Aloy. Magnetorotational core collapse of possible GRB progenitors - III. Three-dimensional models. *MNRAS*, 503(4):4942–4963, May 2021. doi: 10.1093/mnras/stab295.

[356] M. Obergaulinger and M. Á. Aloy. Magnetorotational core collapse of possible gamma-ray burst progenitors - IV. A wider range of progenitors. *MNRAS*, 512(2):2489–2507, May 2022. doi: 10.1093/mnras/stac613.

[357] Evan O'Connor and Christian D. Ott. Black Hole Formation in Failing Core-Collapse Supernovae. *ApJ*, 730 (2):70, April 2011. doi: 10.1088/0004-637X/730/2/70.

[358] Roland Oechslin and H. T. Janka. Gravitational waves from relativistic neutron star mergers with nonzero-temperature equations of state. *Phys. Rev. Lett.*, 99:121102, 2007. doi: 10.1103/PhysRevLett.99.121102.

[359] Maria Okounkova, Leo C. Stein, Mark A. Scheel, and Saul A. Teukolsky. Numerical binary black hole collisions in dynamical Chern-Simons gravity. *Phys. Rev. D*, 100(10):104026, November 2019. doi: 10.1103/PhysRevD.100.104026.

[360] Maria Okounkova, Leo C. Stein, Jordan Moxon, Mark A. Scheel, and Saul A. Teukolsky. Numerical relativity simulation of GW150914 beyond general relativity. *Phys. Rev. D*, 101(10):104016, May 2020. doi: 10.1103/PhysRevD.101.104016.

[361] Carlos Palenzuela, Enrico Barausse, Marcelo Ponce, and Luis Lehner. Dynamical scalarization of neutron stars in scalar-tensor gravity theories. *Phys. Rev. D*, 89(4):044024, February 2014. doi: 10.1103/PhysRevD.89.044024.

[362] Paolo Pani and Emanuele Berti. Slowly rotating neutron stars in scalar-tensor theories. *Phys. Rev. D*, 90(2): 024025, July 2014. doi: 10.1103/PhysRevD.90.024025.

[363] L. Jens Papenfort, Samuel D. Tootle, Philippe Grandclément, Elias R. Most, and Luciano Rezzolla. New public code for initial data of unequal-mass, spinning compact-object binaries. *Phys. Rev. D*, 104(2):024057, July 2021. doi: 10.1103/PhysRevD.104.024057.

[364] Vasileios Paschalidis and Nikolaos Stergioulas. Rotating stars in relativity. *Living Reviews in Relativity*, 20(1): 7, November 2017. doi: 10.1007/s41114-017-0008-x.

[365] L. Perivolaropoulos. PPN parameter γ and solar system constraints of massive Brans-Dicke theories. *Phys. Rev. D*, 81(4):047501, February 2010. doi: 10.1103/PhysRevD.81.047501.

[366] Scott E. Perkins, Nicolás Yunes, and Emanuele Berti. Probing Fundamental Physics with Gravitational Waves: The Next Generation. *Phys. Rev. D*, 103(4):044024, 2021. doi: 10.1103/PhysRevD.103.044024.

[367] Dimitrios Pesios, Ioannis Koutalios, Dimitris Kugiumtzis, and Nikolaos Stergioulas. Predicting Binary Neutron Star Postmerger Spectra Using Artificial Neural Networks. *arXiv: 2405.09468*, 5 2024.

[368] P. C. Peters. Gravitational Radiation and the Motion of Two Point Masses. *Physical Review*, 136(4B):1224–1232, November 1964. doi: 10.1103/PhysRev.136.B1224.

[369] Loren I. Petrich, Stuart L. Shapiro, and Saul A. Teukolsky. Oppenheimer-Snyder collapse with maximal time slicing and isotropic coordinates. *Phys. Rev. D*, 31(10):2459, 1985. doi: 10.1103/PhysRevD.31.2459.

[370] Tsvi Piran. The physics of gamma-ray bursts. *Reviews of Modern Physics*, 76(4):1143–1210, October 2004. doi: 10.1103/RevModPhys.76.1143.

[371] Denis Pollney, Christian Reisswig, Erik Schnetter, Nils Dorband, and Peter Diener. High accuracy binary black hole simulations with an extended wave zone. *Phys. Rev. D*, 83(4):044045, February 2011. doi: 10.1103/PhysRevD.83.044045.

[372] Aviral Prakash, David Radice, Domenico Logoteta, Albino Perego, Vsevolod Nedora, Ignazio Bombaci, Rahul Kashyap, Sebastiano Bernuzzi, and Andrea Endrizzi. Signatures of deconfined quark phases in binary neutron star mergers. *Phys. Rev. D*, 104(8):083029, 2021. doi: 10.1103/PhysRevD.104.083029.

[373] Aviral Prakash, Ish Gupta, Matteo Breschi, Rahul Kashyap, David Radice, Sebastiano Bernuzzi, Domenico Logoteta, and B. S. Sathyaprakash. Detectability of QCD phase transitions in binary neutron star mergers: Bayesian inference with the next generation gravitational wave detectors. *Phys. Rev. D*, 109(10):103008, 2024. doi: 10.1103/PhysRevD.109.103008.

[374] Geraint Pratten, Patricia Schmidt, and Natalie Williams. Impact of Dynamical Tides on the Reconstruction of the Neutron Star Equation of State. *Phys. Rev. Lett.*, 129(8):081102, 2022. doi: 10.1103/PhysRevLett.129.081102.

[375] W. H. Press and S. A. Teukolsky. On formation of close binaries by two-body tidal capture. *ApJ*, 213:183–192, April 1977. doi: 10.1086/155143.

[376] Anna Puecher, Tim Dietrich, Ka Wa Tsang, Chinmay Kalaghatgi, Soumen Roy, Yoshinta Setyawati, and Chris Van Den Broeck. Unraveling information about supranuclear-dense matter from the complete binary neutron star coalescence process using future gravitational-wave detector networks. *Phys. Rev. D*, 107(12):124009, 2023. doi: 10.1103/PhysRevD.107.124009.

[377] M. Punturo et al. The Einstein Telescope: A third-generation gravitational wave observatory. *Class. Quant. Grav.*, 27:194002, 2010. doi: 10.1088/0264-9381/27/19/194002.

[378] Miguel Quartin, Shinji Tsujikawa, Luca Amendola, and Riccardo Sturani. Constraining Horndeski theory with gravitational waves from coalescing binaries. *JCAP.*, 2023(8):049, August 2023. doi: 10.1088/1475-7516/2023/08/049.

[379] David Radice, Filippo Galeazzi, Jonas Lippuner, Luke F. Roberts, Christian D. Ott, and Luciano Rezzolla. Dynamical mass ejection from binary neutron star mergers. *MNRAS*, 460(3):3255–3271, August 2016. doi: 10.1093/mnras/stw1227.

[380] David Radice, Sebastiano Bernuzzi, Albino Perego, and Roland Haas. A new moment-based general-relativistic neutrino-radiation transport code: Methods and first applications to neutron star mergers. *MNRAS*, 512(1):1499–1521, May 2022. doi: 10.1093/mnras/stac589.

[381] Carolyn A. Raithel. Constraints on the Neutron Star Equation of State from GW170817. *Eur. Phys. J. A*, 55(5):80, 2019. doi: 10.1140/epja/i2019-12759-5.

[382] Carolyn A. Raithel and Elias R. Most. Characterizing the Breakdown of Quasi-universality in Postmerger Gravitational Waves from Binary Neutron Star Mergers. *Astrophys. J. Lett.*, 933(2):L39, 2022. doi: 10.3847/2041-8213/ac7c75.

[383] Carolyn A. Raithel and Elias R. Most. Degeneracy in the Inference of Phase Transitions in the Neutron Star Equation of State from Gravitational Wave Data. *Phys. Rev. Lett.*, 130(20):201403, 2023. doi: 10.1103/PhysRevLett.130.201403.

[384] Carolyn A. Raithel and Vasileios Paschalidis. Detectability of finite-temperature effects from neutron star mergers with next-generation gravitational wave detectors. *Phys. Rev. D*, 110(4):043002, 2024. doi: 10.1103/PhysRevD.110.043002.

[385] Fethi M. Ramazanoğlu and Frans Pretorius. Spontaneous scalarization with massive fields. *Phys. Rev. D*, 93 (6):064005, March 2016. doi: 10.1103/PhysRevD.93.064005.

[386] Jocelyn S. Read, Benjamin D. Lackey, Benjamin J. Owen, and John L. Friedman. Constraints on a phenomenologically parametrized neutron-star equation of state. *Phys. Rev. D*, 79(12):124032, June 2009. doi: 10.1103/PhysRevD.79.124032.

[387] Jocelyn S. Read, Luca Baiotti, Jolien D. E. Creighton, John L. Friedman, Bruno Giacomazzo, Koutarou Kyutoku, Charalampos Markakis, Luciano Rezzolla, Masaru Shibata, and Keisuke Taniguchi. Matter effects on binary neutron star waveforms. *Phys. Rev. D*, 88:044042, 2013. doi: 10.1103/PhysRevD.88.044042.

[388] C. Reisswig, R. Haas, C. D. Ott, E. Abdikamalov, P. Mösta, D. Pollney, and E. Schnetter. Three-dimensional general-relativistic hydrodynamic simulations of binary neutron star coalescence and stellar collapse with multipatch grids. *Phys. Rev. D*, 87(6):064023, March 2013. doi: 10.1103/PhysRevD.87.064023.

[389] Christian Reisswig and Denis Pollney. Notes on the integration of numerical relativity waveforms. *Classical and Quantum Gravity*, 28(19):195015, October 2011. doi: 10.1088/0264-9381/28/19/195015.

[390] David Reitze et al. Cosmic Explorer: The U.S. Contribution to Gravitational-Wave Astronomy beyond LIGO. *Bull. Am. Astron. Soc.*, 51(7):035, 2019.

[391] Luciano Rezzolla and Kentaro Takami. Gravitational-wave signal from binary neutron stars: A systematic analysis of the spectral properties. *Phys. Rev. D*, 93(12):124051, June 2016. doi: 10.1103/PhysRevD.93.124051.

[392] Luciano Rezzolla and Olindo Zanotti. *Relativistic Hydrodynamics*. Oxford University Press, USA, 2013.

[393] Luciano Rezzolla, Luca Baiotti, Bruno Giacomazzo, David Link, and José A. Font. Accurate evolutions of unequal-mass neutron-star binaries: properties of the torus and short GRB engines. *Classical and Quantum Gravity*, 27(11):114105, June 2010. doi: 10.1088/0264-9381/27/11/114105.

[394] Luciano Rezzolla, Elias R. Most, and Lukas R. Weih. Using Gravitational-wave Observations and Quasi-universal Relations to Constrain the Maximum Mass of Neutron Stars. *ApJ*, 852(2):L25, January 2018. doi: 10.3847/2041-8213/aaa401.

[395] Chloe Richards, Alexandru Dima, and Helvi Witek. Black holes in massive dynamical Chern-Simons gravity: Scalar hair and quasibound states at decoupling. *Phys. Rev. D*, 108(4):044078, August 2023. doi: 10.1103/PhysRevD.108.044078.

[396] Justin L. Ripley and Frans Pretorius. Gravitational collapse in Einstein dilaton-Gauss-Bonnet gravity. *Classical and Quantum Gravity*, 36(13):134001, July 2019. doi: 10.1088/1361-6382/ab2416.

[397] Justin L. Ripley and Frans Pretorius. Scalarized black hole dynamics in Einstein-dilaton-Gauss-Bonnet gravity. *Phys. Rev. D*, 101(4):044015, February 2020. doi: 10.1103/PhysRevD.101.044015.

[398] Roxana Rosca-Mead, Ulrich Sperhake, Christopher J. Moore, Michalis Agathos, Davide Gerosa, and Christian D. Ott. Core collapse in massive scalar-tensor gravity. *Phys. Rev. D*, 102(4):044010, August 2020. doi: 10.1103/PhysRevD.102.044010.

[399] E. M. Rossi, N. C. Stone, J. A. P. Law-Smith, M. Macleod, G. Lodato, J. L. Dai, and I. Mandel. The Process of Stellar Tidal Disruption by Supermassive Black Holes. *Space Sci. Rev.*, 217(3):40, April 2021. doi: 10.1007/s11214-021-00818-7.

[400] S. Rosswog, E. Ramirez-Ruiz, and W. R. Hix. Tidal Disruption and Ignition of White Dwarfs by Moderately Massive Black Holes. *ApJ*, 695(1):404–419, April 2009. doi: 10.1088/0004-637X/695/1/404.

[401] Stephan Rosswog, Enrico Ramirez-Ruiz, and William R. Hix. Atypical Thermonuclear Supernovae from Tidally Crushed White Dwarfs. *ApJ*, 679(2):1385–1389, June 2008. doi: 10.1086/528738.

[402] Ian Ruchlin, Zachariah B. Etienne, and Thomas W. Baumgarte. SENR /NRPy + : Numerical relativity in singular curvilinear coordinate systems. *Phys. Rev. D*, 97(6):064036, March 2018. doi: 10.1103/PhysRevD.97.064036.

[403] Milton Ruiz, David Hilditch, and Sebastiano Bernuzzi. Constraint preserving boundary conditions for the Z4c formulation of general relativity. *Phys. Rev. D*, 83(2):024025, January 2011. doi: 10.1103/PhysRevD.83.024025.

[404] Taeho Ryu, Julian Krolik, Tsvi Piran, and Scott C. Noble. Tidal Disruptions of Main-sequence Stars. I. Observable Quantities and Their Dependence on Stellar and Black Hole Mass. *ApJ*, 904(2):98, December 2020. doi: 10.3847/1538-4357/abb3cf.

[405] Taeho Ryu, Julian Krolik, Tsvi Piran, and Scott C. Noble. Tidal Disruptions of Main-sequence Stars. II. Simulation Methodology and Stellar Mass Dependence of the Character of Full Tidal Disruptions. *ApJ*, 904(2):99, December 2020. doi: 10.3847/1538-4357/abb3cd.

[406] Taeho Ryu, Julian Krolik, Tsvi Piran, and Scott C. Noble. Tidal Disruptions of Main-sequence Stars. III. Stellar Mass Dependence of the Character of Partial Disruptions. *ApJ*, 904(2):100, December 2020. doi: 10.3847/1538-4357/abb3ce.

[407] Taeho Ryu, Julian Krolik, Tsvi Piran, and Scott C. Noble. Tidal Disruptions of Main-sequence Stars. IV. Relativistic Effects and Dependence on Black Hole Mass. *ApJ*, 904(2):101, December 2020. doi: 10.3847/1538-4357/abb3cc.

[408] Taeho Ryu, Julian Krolik, and Tsvi Piran. Extremely Relativistic Tidal Disruption Events. *ApJ*, 946(2):L33, April 2023. doi: 10.3847/2041-8213/acc390.

[409] Laura Sampson, Nicolás Yunes, Neil Cornish, Marcelo Ponce, Enrico Barausse, Antoine Klein, Carlos Palenzuela, and Luis Lehner. Projected constraints on scalarization with gravitational waves from neutron star binaries. *Phys. Rev. D*, 90(12):124091, December 2014. doi: 10.1103/PhysRevD.90.124091.

[410] R. Saxton, S. Komossa, K. Auchettl, and P. G. Jonker. Correction to: X-Ray Properties of TDEs. Space Science Reviews, Volume 217, Issue 1, article id.18, February 2021.

[411] Mark A. Scheel, Stuart L. Shapiro, and Saul A. Teukolsky. Collapse to black holes in Brans-Dicke theory. I. Horizon boundary conditions for dynamical spacetimes. *Phys. Rev. D*, 51(8):4208–4235, April 1995. doi: 10.1103/PhysRevD.51.4208.

[412] Mark A. Scheel, Stuart L. Shapiro, and Saul A. Teukolsky. Collapse to black holes in Brans-Dicke theory. II. Comparison with general relativity. *Phys. Rev. D*, 51(8):4236–4249, April 1995. doi: 10.1103/PhysRevD.51.4236.

[413] Yu-Ichirou Sekiguchi and Masaru Shibata. New criterion for direct black hole formation in rapidly rotating stellar collapse. *Phys. Rev. D*, 70(8):084005, October 2004. doi: 10.1103/PhysRevD.70.084005.

[414] Yu-Ichirou Sekiguchi and Masaru Shibata. Axisymmetric collapse simulations of rotating massive stellar cores in full general relativity: Numerical study for prompt black hole formation. *Phys. Rev. D*, 71(8):084013, April 2005. doi: 10.1103/PhysRevD.71.084013.

[415] Noah Sennett and Alessandra Buonanno. Modeling dynamical scalarization with a resummed post-Newtonian expansion. *Phys. Rev. D*, 93(12):124004, June 2016. doi: 10.1103/PhysRevD.93.124004.

[416] Brian C. Seymour and Kent Yagi. Probing massive scalar fields from a pulsar in a stellar triple system. *Classical and Quantum Gravity*, 37(14):145008, July 2020. doi: 10.1088/1361-6382/ab9933.

[417] N. I. Shakura and R. A. Sunyaev. Reprint of 1973A&A....24..337S. Black holes in binary systems. Observational appearance. *A&A*, 500:33–51, June 1973.

[418] Lijing Shao. Degeneracy in studying the supranuclear equation of state and modified gravity with neutron stars. In *Xiamen-CUSTIPEN Workshop on the Equation of State of Dense Neutron-Rich Matter in the Era of Gravitational Wave Astronomy*, volume 2127 of *American Institute of Physics Conference Series*, page 020016, July 2019. doi: 10.1063/1.5117806.

[419] Lijing Shao, Noah Sennett, Alessandra Buonanno, Michael Kramer, and Norbert Wex. Constraining Nonperturbative Strong-Field Effects in Scalar-Tensor Gravity by Combining Pulsar Timing and Laser-Interferometer Gravitational-Wave Detectors. *Physical Review X*, 7(4):041025, October 2017. doi: 10.1103/PhysRevX.7.041025.

[420] Ji-Ming Shi, James M. Stone, and Chelsea X. Huang. Saturation of the magnetorotational instability in the unstratified shearing box with zero net flux: convergence in taller boxes. *Mon. Not. Roy. Astron. Soc.*, 456(3): 2273–2289, 2016. doi: 10.1093/mnras/stv2815.

[421] M. Shibata. Axisymmetric Simulations of Rotating Stellar Collapse in Full General Relativity —Criteria for Prompt Collapse to Black Holes—. *Progress of Theoretical Physics*, 104(2):325–358, August 2000. doi: 10.1143/PTP.104.325.

[422] M. Shibata and T. Nakamura. Evolution of three-dimensional gravitational waves: Harmonic slicing case. *Phys. Rev. D*, 52:5428–5444, November 1995. doi: 10.1103/PhysRevD.52.5428.

[423] M. Shibata and Y. Sekiguchi. Radiation Magnetohydrodynamics for Black Hole-Torus System in Full General Relativity: A Step toward Physical Simulation. *Progress of Theoretical Physics*, 127(3):535–559, March 2012. doi: 10.1143/PTP.127.535.

[424] Masaru Shibata. Apparent horizon finder for a special family of space-times in 3-D numerical relativity. *Phys. Rev. D*, 55:2002–2013, 1997. doi: 10.1103/PhysRevD.55.2002.

[425] Masaru Shibata. Fully general relativistic simulation of coalescing binary neutron stars: Preparatory tests. *Phys. Rev. D*, 60(10):104052, November 1999. doi: 10.1103/PhysRevD.60.104052.

[426] Masaru Shibata. Axisymmetric general relativistic hydrodynamics: Long-term evolution of neutron stars and stellar collapse to neutron stars and black holes. *Phys. Rev. D*, 67(2):024033, January 2003. doi: 10.1103/PhysRevD.67.024033.

[427] Masaru Shibata. Collapse of Rotating Supramassive Neutron Stars to Black Holes: Fully General Relativistic Simulations. *ApJ*, 595(2):992–999, October 2003. doi: 10.1086/377435.

[428] Masaru Shibata. Constraining Nuclear Equations of State Using Gravitational Waves from Hypermassive Neutron Stars. *Phys. Rev. Lett.*, 94(20):201101, May 2005. doi: 10.1103/PhysRevLett.94.201101.

[429] Masaru Shibata. Rotating black hole surrounded by self-gravitating torus in the puncture framework. *Phys. Rev. D*, 76(6):064035, September 2007. doi: 10.1103/PhysRevD.76.064035.

[430] Masaru Shibata. *Numerical Relativity*. World Scientific, 2016. doi: 10.1142/9692.

[431] Masaru Shibata and Kenta Hotokezaka. Merger and Mass Ejection of Neutron Star Binaries. *Annual Review of Nuclear and Particle Science*, 69:41–64, October 2019. doi: 10.1146/annurev-nucl-101918-023625.

[432] Masaru Shibata and Kyohei Kawaguchi. Virial relation and first law of thermodynamics in scalar-tensor theories of gravity. *Phys. Rev. D*, 87(10):104031, May 2013. doi: 10.1103/PhysRevD.87.104031.

[433] Masaru Shibata and Takashi Nakamura. Evolution of three-dimensional gravitational waves: Harmonic slicing case. *Phys. Rev. D*, 52(10):5428–5444, November 1995. doi: 10.1103/PhysRevD.52.5428.

[434] Masaru Shibata and Yu-Ichirou Sekiguchi. Gravitational waves from axisymmetrically oscillating neutron stars in general relativistic simulations. *Phys. Rev. D*, 68(10):104020, November 2003. doi: 10.1103/PhysRevD.68.104020.

[435] Masaru Shibata and Yu-Ichirou Sekiguchi. Gravitational waves from axisymmetric rotating stellar core collapse to a neutron star in full general relativity. *Phys. Rev. D*, 69(8):084024, April 2004. doi: 10.1103/PhysRevD.69.084024.

[436] Masaru Shibata and Yu-Ichirou Sekiguchi. Three-dimensional simulations of stellar core collapse in full general relativity: Nonaxisymmetric dynamical instabilities. *Phys. Rev. D*, 71(2):024014, January 2005. doi: 10.1103/PhysRevD.71.024014.

[437] Masaru Shibata and Yu-Ichirou Sekiguchi. Magnetohydrodynamics in full general relativity: Formulation and tests. *Phys. Rev. D*, 72(4):044014, August 2005. doi: 10.1103/PhysRevD.72.044014.

[438] Masaru Shibata and Stuart L. Shapiro. Collapse of a rotating supermassive star to a supermassive black hole: Fully relativistic simulations. *Astrophys. J. Lett.*, 572:L39–L44, 2002. doi: 10.1086/341516.

[439] Masaru Shibata and Keisuke Taniguchi. Merger of binary neutron stars to a black hole: Disk mass, short gamma-ray bursts, and quasinormal mode ringing. *Phys. Rev. D*, 73(6):064027, March 2006. doi: 10.1103/PhysRevD.73.064027.

[440] Masaru Shibata and Dina Traykova. Properties of scalar wave emission in a scalar-tensor theory with kinetic screening. *Phys. Rev. D*, 107(4):044068, February 2023. doi: 10.1103/PhysRevD.107.044068.

[441] Masaru Shibata and K. ōji Uryū. Simulation of merging binary neutron stars in full general relativity: Γ=2 case. *Phys. Rev. D*, 61(6):064001, March 2000. doi: 10.1103/PhysRevD.61.064001.

[442] Masaru Shibata and K. ōji Uryū. Computation of gravitational waves from inspiraling binary neutron stars in quasiequilibrium circular orbits: Formulation and calibration. *Phys. Rev. D*, 64(10):104017, November 2001. doi: 10.1103/PhysRevD.64.104017.

[443] Masaru Shibata, Thomas W. Baumgarte, and Stuart L. Shapiro. Stability and collapse of rapidly rotating, supramassive neutron stars: 3D simulations in general relativity. *Phys. Rev. D*, 61(4):044012, February 2000. doi: 10.1103/PhysRevD.61.044012.

[444] Masaru Shibata, Keisuke Taniguchi, and Kōji Uryū. Merger of binary neutron stars of unequal mass in full general relativity. *Phys. Rev. D*, 68(8):084020, October 2003. doi: 10.1103/PhysRevD.68.084020.

[445] Masaru Shibata, Kōji Uryū, and John L. Friedman. Deriving formulations for numerical computation of binary neutron stars in quasicircular orbits. *Phys. Rev. D*, 70(4):044044, August 2004. doi: 10.1103/PhysRevD.70.044044.

[446] Masaru Shibata, Keisuke Taniguchi, and Kōji Uryū. Merger of binary neutron stars with realistic equations of state in full general relativity. *Phys. Rev. D*, 71(8):084021, April 2005. doi: 10.1103/PhysRevD.71.084021.

[447] Masaru Shibata, Matthew D. Duez, Yuk Tung Liu, Stuart L. Shapiro, and Branson C. Stephens. Magnetized hypermassive neutron star collapse: A Central engine for short gamma-ray bursts. *Phys. Rev. Lett.*, 96:031102, 2006. doi: 10.1103/PhysRevLett.96.031102.

[448] Masaru Shibata, Yuk Tung Liu, Stuart L. Shapiro, and Branson C. Stephens. Magnetorotational collapse of massive stellar cores to neutron stars: Simulations in full general relativity. *Phys. Rev. D*, 74(10):104026, November 2006. doi: 10.1103/PhysRevD.74.104026.

[449] Masaru Shibata, Koutarou Kyutoku, Tetsuro Yamamoto, and Keisuke Taniguchi. Gravitational waves from black hole-neutron star binaries: Classification of waveforms. *Phys. Rev. D*, 79(4):044030, February 2009. doi: 10.1103/PhysRevD.79.044030.

[450] Masaru Shibata, Keisuke Taniguchi, Hirotada Okawa, and Alessandra Buonanno. Coalescence of binary neutron stars in a scalar-tensor theory of gravity. *Phys. Rev. D*, 89(8):084005, April 2014. doi: 10.1103/PhysRevD.89.084005.

[451] Masaru Shibata, Yuichiro Sekiguchi, Haruki Uchida, and Hideyuki Umeda. Gravitational waves from supermassive stars collapsing to a supermassive black hole. *Phys. Rev. D*, 94(2):021501, July 2016. doi: 10.1103/PhysRevD.94.021501.

[452] Masaru Shibata, Sho Fujibayashi, Kenta Hotokezaka, Kenta Kiuchi, Koutarou Kyutoku, Yuichiro Sekiguchi, and Masaomi Tanaka. Modeling GW170817 based on numerical relativity and its implications. *Phys. Rev. D*, 96(12):123012, 2017. doi: 10.1103/PhysRevD.96.123012.

[453] Masaru Shibata, Kenta Kiuchi, and Yu-ichiro Sekiguchi. General relativistic viscous hydrodynamics of differentially rotating neutron stars. *Phys. Rev. D*, 95(8):083005, April 2017. doi: 10.1103/PhysRevD.95.083005.

[454] Masaru Shibata, Sho Fujibayashi, and Yuichiro Sekiguchi. Long-term evolution of a merger-remnant neutron star in general relativistic magnetohydrodynamics: Effect of magnetic winding. *Phys. Rev. D*, 103(4):043022, February 2021. doi: 10.1103/PhysRevD.103.043022.

[455] Masaru Shibata, Sho Fujibayashi, and Yuichiro Sekiguchi. Long-term evolution of neutron-star merger remnants in general relativistic resistive magnetohydrodynamics with a mean-field dynamo term. *Phys. Rev. D*, 104(6):063026, September 2021. doi: 10.1103/PhysRevD.104.063026.

[456] Masaru Shibata, Sho Fujibayashi, Alan Tsz-Lok Lam, Kunihito Ioka, and Yuichiro Sekiguchi. Outflow energy and black-hole spin evolution in collapsar scenarios. *Phys. Rev. D*, 109(4):043051, February 2024. doi: 10.1103/PhysRevD.109.043051.

[457] Masaru Shibata, Sho Fujibayashi, Cédric Jockel, and Kyohei Kawaguchi. Threshold Mass of the General-relativistic Instability for Supermassive Star Cores. *Astrophys. J.*, 978(1):58, 2025. doi: 10.3847/1538-4357/ad93a4.

[458] Masaru Shibata, Sho Fujibayashi, Shinya Wanajo, Kunihito Ioka, Alan Tsz-Lok Lam, and Yuichiro Sekiguchi. Self-consistent scenario for jet and stellar explosions in collapsar: General relativistic magnetohydrodynamics simulation with a dynamo. *Phys. Rev. D*, 111(12):123017, June 2025. doi: 10.1103/msy2-fwhx.

[459] Hector O. Silva and Nicolás Yunes. Neutron star pulse profiles in scalar-tensor theories of gravity. *Phys. Rev. D*, 99(4):044034, February 2019. doi: 10.1103/PhysRevD.99.044034.

[460] Hector O. Silva and Nicolás Yunes. Neutron star pulse profile observations as extreme gravity probes. *Classical and Quantum Gravity*, 36(17):17LT01, September 2019. doi: 10.1088/1361-6382/ab3560.

[461] Hector O. Silva, Helvi Witek, Matthew Elley, and Nicolás Yunes. Dynamical Descalarization in Binary Black Hole Mergers. *Phys. Rev. Lett.*, 127(3):031101, July 2021. doi: 10.1103/PhysRevLett.127.031101.

[462] Kyle Slinker, Charles R. Evans, and Mark Hannam. Trumpet initial data for boosted black holes. *Phys. Rev. D*, 98(4):044014, August 2018. doi: 10.1103/PhysRevD.98.044014.

[463] Larry Smarr and James W. York, Jr. Kinematical conditions in the construction of spacetime. *Phys. Rev. D*, 17(10):2529–2551, May 1978. doi: 10.1103/PhysRevD.17.2529.

[464] R. Sorkin. A Criterion for the Onset of Instability at a Turning Point. *ApJ*, 249:254, October 1981. doi: 10.1086/159282.

[465] R. D. Sorkin. A Stability Criterion for Many Parameter Equilibrium Families. *ApJ*, 257:847, June 1982. doi: 10.1086/160034.

[466] Hajime Sotani. Scalar gravitational waves from relativistic stars in scalar-tensor gravity. *Phys. Rev. D*, 89(6): 064031, March 2014. doi: 10.1103/PhysRevD.89.064031.

[467] Hajime Sotani. Pulse profiles from a pulsar in scalar-tensor gravity. *Phys. Rev. D*, 96(10):104010, November 2017. doi: 10.1103/PhysRevD.96.104010.

[468] Hajime Sotani and Kostas D. Kokkotas. Probing strong-field scalar-tensor gravity with gravitational wave asteroseismology. *Phys. Rev. D*, 70:084026, 2004. doi: 10.1103/PhysRevD.70.084026.

[469] Hajime Sotani and Kostas D. Kokkotas. Maximum mass limit of neutron stars in scalar-tensor gravity. *Phys. Rev. D*, 95(4):044032, February 2017. doi: 10.1103/PhysRevD.95.044032.

[470] Thomas P. Sotiriou. Black holes and scalar fields. *Classical and Quantum Gravity*, 32(21):214002, November 2015. doi: 10.1088/0264-9381/32/21/214002.

[471] Thomas P. Sotiriou and Valerio Faraoni. Black Holes in Scalar-Tensor Gravity. *Phys. Rev. Lett.*, 108(8):081103, February 2012. doi: 10.1103/PhysRevLett.108.081103.

[472] Theodoros Soultanis, Andreas Bauswein, and Nikolaos Stergioulas. Analytic models of the spectral properties of gravitational waves from neutron star merger remnants. *Phys. Rev. D*, 105(4):043020, February 2022. doi: 10.1103/PhysRevD.105.043020.

[473] Ulrich Sperhake, Christopher J. Moore, Roxana Rosca, Michalis Agathos, Davide Gerosa, and Christian D. Ott. Long-Lived Inverse Chirp Signals from Core-Collapse in Massive Scalar-Tensor Gravity. *Phys. Rev. Lett.*, 119 (20):201103, November 2017. doi: 10.1103/PhysRevLett.119.201103.

[474] Kalin V. Staykov, Daniela D. Doneva, Lavinia Heisenberg, Nikolaos Stergioulas, and Stoytcho S. Yazadjiev. Differentially rotating scalarized neutron stars with realistic post-merger profile. *arXiv e-prints*, art. arXiv:2303.07769, March 2023. doi: 10.48550/arXiv.2303.07769.

[475] Nikolaos Stergioulas and John L. Friedman. Comparing Models of Rapidly Rotating Relativistic Stars Constructed by Two Numerical Methods. *ApJ*, 444:306, May 1995. doi: 10.1086/175605.

[476] Nikolaos Stergioulas and John L. Friedman. Nonaxisymmetric Neutral Modes in Rotating Relativistic Stars. *ApJ*, 492(1):301–322, January 1998. doi: 10.1086/305030.

[477] Nikolaos Stergioulas, Andreas Bauswein, Kimon Zagkouris, and Hans-Thomas Janka. Gravitational waves and non-axisymmetric oscillation modes in mergers of compact object binaries. *MNRAS*, 418(1):427–436, November 2011. doi: 10.1111/j.1365-2966.2011.19493.x.

[478] James M. Stone, Kengo Tomida, Christopher J. White, and Kyle G. Felker. The Athena++ Adaptive Mesh Refinement Framework: Design and Magnetohydrodynamic Solvers. *ApJS*, 249(1):4, July 2020. doi: 10.3847/1538-4365/ab929b.

[479] Lami Suleiman and Jocelyn Read. Quasiuniversal relations in the context of future neutron star detections. *Phys. Rev. D*, 109(10):103029, 2024. doi: 10.1103/PhysRevD.109.103029.

[480] R. Surman, G. C. McLaughlin, and N. Sabbatino. Nucleosynthesis of Nickel-56 from Gamma-Ray Burst Accretion Disks. *ApJ*, 743(2):155, December 2011. doi: 10.1088/0004-637X/743/2/155.

[481] Takeru K. Suzuki and Shu-ichiro Inutsuka. Magnetohydrodynamic Simulations of Global Accretion Disks with Vertical Magnetic Fields. *Astrophys. J.*, 784:121, 2014. doi: 10.1088/0004-637X/784/2/121.

[482] F. Taddia, J. Sollerman, C. Fremling, C. Barbarino, E. Karamehmetoglu, I. Arcavi, S. B. Cenko, A. V. Filippenko, A. Gal-Yam, D. Hiramatsu, G. Hosseinzadeh, D. A. Howell, S. R. Kulkarni, R. Laher, R. Lunnan, F. Masci, P. E. Nugent, A. Nyholm, D. A. Perley, R. Quimby, and J. M. Silverman. Analysis of broad-lined Type Ic supernovae from the (intermediate) Palomar Transient Factory. *A&A*, 621:A71, January 2019. doi: 10.1051/0004-6361/201834429.

[483] Kentaro Takami, Luciano Rezzolla, and Luca Baiotti. Constraining the Equation of State of Neutron Stars from Binary Mergers. *Phys. Rev. Lett.*, 113(9):091104, August 2014. doi: 10.1103/PhysRevLett.113.091104.

[484] Kentaro Takami, Luciano Rezzolla, and Luca Baiotti. Spectral properties of the post-merger gravitational-wave signal from binary neutron stars. *Phys. Rev. D*, 91(6):064001, March 2015. doi: 10.1103/PhysRevD.91.064001.

[485] Keisuke Taniguchi and Masaru Shibata. Binary Neutron Stars in Quasi-equilibrium. *ApJS*, 188(1):187–208, May 2010. doi: 10.1088/0067-0049/188/1/187.

[486] Keisuke Taniguchi, Masaru Shibata, and Alessandra Buonanno. Quasiequilibrium sequences of binary neutron stars undergoing dynamical scalarization. *Phys. Rev. D*, 91(2):024033, January 2015. doi: 10.1103/PhysRevD.91.024033.

[487] T. M. Tauris, M. Kramer, P. C. C. Freire, N. Wex, H. T. Janka, N. Langer, Ph. Podsiadlowski, E. Bozzo, S. Chaty, M. U. Kruckow, E. P. J. van den Heuvel, J. Antoniadis, R. P. Breton, and D. J. Champion. Formation of Double Neutron Star Systems. *ApJ*, 846(2):170, September 2017. doi: 10.3847/1538-4357/aa7e89.

[488] J. Teunissen and R. Keppens. A geometric multigrid library for quadtree/octree AMR grids coupled to MPI-AMRVAC. *Computer Physics Communications*, 245:106866, December 2019. doi: 10.1016/j.cpc.2019.106866.

[489] The LIGO Scientific Collaboration, the Virgo Collaboration, and the KAGRA Collaboration. GWTC-3: Compact Binary Coalescences Observed by LIGO and Virgo During the Second Part of the Third Observing Run. *arXiv e-prints*, art. arXiv:2111.03606, November 2021. doi: 10.48550/arXiv.2111.03606.

[490] Wolfgang Tichy. Constructing quasi-equilibrium initial data for binary neutron stars with arbitrary spins. *Phys. Rev. D*, 86(6):064024, September 2012. doi: 10.1103/PhysRevD.86.064024.

[491] F. X. Timmes, R. D. Hoffman, and S. E. Woosley. An Inexpensive Nuclear Energy Generation Network for Stellar Hydrodynamics. *ApJS*, 129(1):377–398, July 2000. doi: 10.1086/313407.

[492] L. Tonetto and G. Lugones. Discontinuity gravity modes in hybrid stars: assessing the role of rapid and slow phase conversions. *Phys. Rev. D*, 101(12):123029, 2020. doi: 10.1103/PhysRevD.101.123029.

[493] E. F. Toro, M. Spruce, and W. Speares. Restoration of the contact surface in the HLL-Riemann solver. *Shock Waves*, 4(1):25–34, July 1994. doi: 10.1007/BF01414629.

[494] Andoni Torres-Rivas, Katerina Chatziioannou, Andreas Bauswein, and James Alexander Clark. Observing the post-merger signal of GW170817-like events with improved gravitational-wave detectors. *Phys. Rev. D*, 99(4):044014, 2019. doi: 10.1103/PhysRevD.99.044014.

[495] Gábor Tóth and Dušan Odstrčil. Comparison of Some Flux Corrected Transport and Total Variation Diminishing Numerical Schemes for Hydrodynamic and Magnetohydrodynamic Problems. *Journal of Computational Physics*, 128(1):82–100, October 1996. doi: 10.1006/jcph.1996.0197.

[496] Alan Tsz-Lok Lam, Masaru Shibata, Kyohei Kawaguchi, and Joaquin Pelle. Black hole-accretion disk collision in general relativity: Axisymmetric simulations. *arXiv e-prints*, art. arXiv:2504.17016, April 2025. doi: 10.48550/arXiv.2504.17016.

[497] Semih Tuna, Kıvanç I. Ünlütürk, and Fethi M. Ramazanoğlu. Constraining scalar-tensor theories using neutron star mass and radius measurements. *Phys. Rev. D*, 105(12):124070, June 2022. doi: 10.1103/PhysRevD.105.124070.

[498] Haruki Uchida, Masaru Shibata, Takashi Yoshida, Yuichiro Sekiguchi, and Hideyuki Umeda. Gravitational collapse of rotating supermassive stars including nuclear burning effects. *Phys. Rev. D*, 96(8):083016, October 2017. doi: 10.1103/PhysRevD.96.083016.

[499] Haruki Uchida, Masaru Shibata, Koh Takahashi, and Takashi Yoshida. Black Hole Formation and Explosion from Rapidly Rotating Very Massive Stars. *ApJ*, 870(2):98, January 2019. doi: 10.3847/1538-4357/aaf39e.

[500] K. ōji Uryū, Masaru Shibata, and Yoshiharu Eriguchi. Properties of general relativistic, irrotational binary neutron stars in close quasiequilibrium orbits: Polytropic equations of state. *Phys. Rev. D*, 62(10):104015, November 2000. doi: 10.1103/PhysRevD.62.104015.

[501] Kōji Uryū, François Limousin, John L. Friedman, Eric Gourgoulhon, and Masaru Shibata. Binary Neutron Stars: Equilibrium Models beyond Spatial Conformal Flatness. *Phys. Rev. Lett.*, 97(17):171101, October 2006. doi: 10.1103/PhysRevLett.97.171101.

[502] Kōji Uryū, François Limousin, John L. Friedman, Eric Gourgoulhon, and Masaru Shibata. Nonconformally flat initial data for binary compact objects. *Phys. Rev. D*, 80(12):124004, December 2009. doi: 10.1103/PhysRevD.80.124004.

[503] Kōji Uryū, Antonios Tsokaros, Luca Baiotti, Filippo Galeazzi, Keisuke Taniguchi, and Shin'ichirou Yoshida. Modeling differential rotations of compact stars in equilibriums. *Phys. Rev. D*, 96(10):103011, November 2017. doi: 10.1103/PhysRevD.96.103011.

[504] Iris van Gemeren, Banafsheh Shiralilou, and Tanja Hinderer. Dipolar tidal effects in gravitational waves from scalarized black hole binary inspirals in quadratic gravity. *Phys. Rev. D*, 108(2):024026, July 2023. doi: 10.1103/PhysRevD.108.024026.

[505] Sjoert van Velzen, Thomas W. S. Holoien, Francesca Onori, Tiara Hung, and Iair Arcavi. Optical-Ultraviolet Tidal Disruption Events. *Space Sci. Rev.*, 216(8):124, October 2020. doi: 10.1007/s11214-020-00753-z.

[506] Michelle Vick, Dong Lai, and Jim Fuller. Tidal dissipation and evolution of white dwarfs around massive black holes: an eccentric path to tidal disruption. *MNRAS*, 468(2):2296–2310, June 2017. doi: 10.1093/mnras/stx539.

[507] Daniele Viganò, Ricard Aguilera-Miret, Federico Carrasco, Borja Miñano, and Carlos Palenzuela. General relativistic MHD large eddy simulations with gradient subgrid-scale model. *Phys. Rev. D*, 101(12):123019, June 2020. doi: 10.1103/PhysRevD.101.123019.

[508] Stamatis Vretinaris, Nikolaos Stergioulas, and Andreas Bauswein. Empirical relations for gravitational-wave asteroseismology of binary neutron star mergers. *Phys. Rev. D*, 101(8):084039, 2020. doi: 10.1103/PhysRevD.101.084039.

[509] Leslie Wade, Jolien D. E. Creighton, Evan Ochsner, Benjamin D. Lackey, Benjamin F. Farr, Tyson B. Littenberg, and Vivien Raymond. Systematic and statistical errors in a bayesian approach to the estimation of the neutron-star equation of state using advanced gravitational wave detectors. *Phys. Rev. D*, 89(10):103012, 2014. doi: 10.1103/PhysRevD.89.103012.

[510] Anna L. Watts, Nils Andersson, Deepto Chakrabarty, Marco Feroci, Kai Hebeler, Gianluca Israel, Frederick K. Lamb, M. Coleman Miller, Sharon Morsink, Feryal Özel, Alessandro Patruno, Juri Poutanen, Dimitrios Psaltis, Achim Schwenk, Andrew W. Steiner, Luigi Stella, Laura Tolos, and Michiel van der Klis. Colloquium: Measuring the neutron star equation of state using x-ray timing. *Reviews of Modern Physics*, 88(2):021001, April 2016. doi: 10.1103/RevModPhys.88.021001.

[511] Lukas R. Weih, Elias R. Most, and Luciano Rezzolla. On the stability and maximum mass of differentially rotating relativistic stars. *MNRAS*, 473(1):L126–L130, January 2018. doi: 10.1093/mnrasl/slx178.

[512] Lukas R. Weih, Matthias Hanauske, and Luciano Rezzolla. Postmerger Gravitational-Wave Signatures of Phase Transitions in Binary Mergers. *Phys. Rev. Lett.*, 124(17):171103, May 2020. doi: 10.1103/PhysRevLett.124.171103.

[513] Christopher J. White, James M. Stone, and Charles F. Gammie. An Extension of the Athena++ Code Framework for GRMHD Based on Advanced Riemann Solvers and Staggered-mesh Constrained Transport. *ApJS*, 225 (2):22, August 2016. doi: 10.3847/0067-0049/225/2/22.

[514] Marcella Wijngaarden, Katerina Chatziioannou, Andreas Bauswein, James A. Clark, and Neil J. Cornish. Probing neutron stars with the full premerger and postmerger gravitational wave signal from binary coalescences. *Phys. Rev. D*, 105(10):104019, 2022. doi: 10.1103/PhysRevD.105.104019.

[515] J. R. Wilson and G. J. Mathews. Relativistic hydrodynamics. In Charles R. Evans, Lee S. Finn, and David W. Hobill, editors, *Frontiers in Numerical Relativity*, pages 306–314. 1989.

[516] J. R. Wilson and G. J. Mathews. Instabilities in Close Neutron Star Binaries. *Phys. Rev. Lett.*, 75(23):4161–4164, December 1995. doi: 10.1103/PhysRevLett.75.4161.

[517] Helvi Witek, Leonardo Gualtieri, Paolo Pani, and Thomas P. Sotiriou. Black holes and binary mergers in scalar Gauss-Bonnet gravity: Scalar field dynamics. *Phys. Rev. D*, 99(6):064035, March 2019. doi: 10.1103/PhysRevD.99.064035.

[518] S. E. Woosley. Gamma-Ray Bursts from Stellar Mass Accretion Disks around Black Holes. *ApJ*, 405:273, March 1993. doi: 10.1086/172359.

[519] Xiaoyi Xie and Alan Tsz-Lok Lam. Bridging relativistic jets from black hole scales to long-term electromagnetic radiation distances: A moving-mesh general relativistic hydrodynamics code with the HLLC Riemann solver. *Phys. Rev. D*, 109(8):084070, April 2024. doi: 10.1103/PhysRevD.109.084070.

[520] Yiqi Xie, Adrian Ka-Wai Chung, Thomas P. Sotiriou, and Nicolás Yunes. Bayesian search of massive scalar fields from LIGO-Virgo-KAGRA binaries. *arXiv:2410.14801*, 10 2024.

[521] Kent Yagi and Michael Stepniczka. Neutron stars in scalar-tensor theories: Analytic scalar charges and universal relations. *Phys. Rev. D*, 104(4):044017, August 2021. doi: 10.1103/PhysRevD.104.044017.

[522] Kent Yagi and Nicolas Yunes. I-Love-Q Relations in Neutron Stars and their Applications to Astrophysics, Gravitational Waves and Fundamental Physics. *Phys. Rev. D*, 88(2):023009, 2013. doi: 10.1103/PhysRevD.88.023009.

[523] Kent Yagi and Nicolas Yunes. I-Love-Q. *Science*, 341:365–368, 2013. doi: 10.1126/science.1236462.

[524] Kent Yagi and Nicolas Yunes. Binary Love Relations. *Class. Quant. Grav.*, 33(13):13LT01, 2016. doi: 10.1088/0264-9381/33/13/13LT01.

[525] Kent Yagi and Nicolás Yunes. Approximate Universal Relations for Neutron Stars and Quark Stars. *Phys. Rept.*, 681:1–72, 2017. doi: 10.1016/j.physrep.2017.03.002.

[526] Tetsuro Yamamoto, Masaru Shibata, and Keisuke Taniguchi. Simulating coalescing compact binaries by a new code (SACRA). *Phys. Rev. D*, 78(6):064054, September 2008. doi: 10.1103/PhysRevD.78.064054.

[527] Stoytcho S. Yazadjiev, Daniela D. Doneva, and Dimitar Popchev. Slowly rotating neutron stars in scalar-tensor theories with a massive scalar field. *Phys. Rev. D*, 93(8):084038, April 2016. doi: 10.1103/PhysRevD.93.084038.

[528] Stoytcho S. Yazadjiev, Daniela D. Doneva, and Kostas D. Kokkotas. Tidal Love numbers of neutron stars in f(R) gravity. *European Physical Journal C*, 78(10):818, October 2018. doi: 10.1140/epjc/s10052-018-6285-z.

[529] HC YEE. A class of high-resolution explicit and implicit shock capturing methods. *NASA TM-101088*, 1989.

[530] James W. York. Gravitational Degrees of Freedom and the Initial-Value Problem. *Phys. Rev. Lett.*, 26(26): 1656–1658, June 1971. doi: 10.1103/PhysRevLett.26.1656.

[531] James W. York. Role of Conformal Three-Geometry in the Dynamics of Gravitation. *Phys. Rev. Lett.*, 28(16): 1082–1085, April 1972. doi: 10.1103/PhysRevLett.28.1082.

[532] Jr. York, J. W. Kinematics and dynamics of general relativity. In L. L. Smarr, editor, *Sources of Gravitational Radiation*, pages 83–126, January 1979.

[533] Jr. York, James W. Conformal “Thin-Sandwich” Data for the Initial-Value Problem of General Relativity. *Phys. Rev. Lett.*, 82(7):1350–1353, February 1999. doi: 10.1103/PhysRevLett.82.1350.

[534] Hirotaka Yoshino and Masaru Shibata. Higher-dimensional numerical relativity: Formulation and code tests. *Phys. Rev. D*, 80(8):084025, October 2009. doi: 10.1103/PhysRevD.80.084025.

[535] Nicolás Yunes, Paolo Pani, and Vitor Cardoso. Gravitational waves from quasicircular extreme mass-ratio inspirals as probes of scalar-tensor theories. *Phys. Rev. D*, 85(10):102003, May 2012. doi: 10.1103/PhysRevD.85.102003.

[536] Jun Zhang, Zhenwei Lyu, Junwu Huang, Matthew C. Johnson, Laura Sagunski, Mairi Sakellariadou, and Huan Yang. First Constraints on Nuclear Coupling of Axionlike Particles from the Binary Neutron Star Gravitational Wave Event GW170817. *Phys. Rev. Lett.*, 127(16):161101, 2021. doi: 10.1103/PhysRevLett.127.161101.

[537] Junjie Zhao, Lijing Shao, Zhoujian Cao, and Bo-Qiang Ma. Reduced-order surrogate models for scalar-tensor gravity in the strong field regime and applications to binary pulsars and GW170817. *Phys. Rev. D*, 100(6): 064034, September 2019. doi: 10.1103/PhysRevD.100.064034.

[538] Junjie Zhao, Paulo C. C. Freire, Michael Kramer, Lijing Shao, and Norbert Wex. Closing a spontaneous-scalarization window with binary pulsars. *Classical and Quantum Gravity*, 39(11):11LT01, June 2022. doi: 10.1088/1361-6382/ac69a3.

[539] Enping Zhou, Antonios Tsokaros, Kōji Uryū, Renxin Xu, and Masaru Shibata. Differentially rotating strange star in general relativity. *Phys. Rev. D*, 100(4):043015, August 2019. doi: 10.1103/PhysRevD.100.043015.

[540] Jiaxiang Zhu, Chuming Wang, Chengjun Xia, Enping Zhou, and Yiqiu Ma. Probing phase transitions in neutron stars via the crust-core interfacial mode. *Phys. Rev. D*, 107(8):083023, 2023. doi: 10.1103/PhysRevD.107.083023.